Westfälische
Wilhelms-Universität
Münster

Studies on the reaction $p + d \rightarrow {}^3He + \eta$ and search for C violation in the decay $\eta \rightarrow \pi^0 + e^+ + e^-$ with WASA-at-COSY

Dissertation zur Erlangung des Doktorgrades der
Naturwissenschaften im Fachbereich Physik der
Mathematisch-Naturwissenschaftlichen Fakultät der
Westfälischen Wilhelms-Universität Münster

vorgelegt von

Florian Sebastian Bergmann

– Münster, im April 2017 –

Dekan:	Prof. Dr. Michael Klasen
Erster Gutachter:	Prof. Dr. Alfons Khoukaz
Zweiter Gutachter:	Prof. Dr. Johannes P. Wessels
Tag der Disputation:	21.07.2017
Tag der Promotion:	21.07.2017

Abstract

The reaction p+d $\rightarrow$ ^{3}He+η was measured with the WASA-at-COSY experimental setup during two beam times in 2008 and 2009. Most of the data were recorded at an excess energy of $Q = 59.8\,\mathrm{MeV}$, while data were collected at $Q = 48.8\,\mathrm{MeV}$ during one day of the 2009 beam time.

In the first part of this thesis the production reaction $\mathrm{p} + \mathrm{d} \rightarrow {}^3\mathrm{He} + \eta$ was investigated utilizing a part of the data collected in 2009 at $Q = 59.8\,\mathrm{MeV}$ and the full data measured at $Q = 48.8\,\mathrm{MeV}$. The data were used to determine the differential cross sections for 23 angular bins in the range from $\cos\vartheta_\eta^{\mathrm{CMS}} = -0.92$ to $\cos\vartheta_\eta^{\mathrm{CMS}} = 0.92$. The resulting distributions can be described by polynomial distributions of third order. Furthermore, the total cross section ratio of $\frac{\sigma_\eta(48.8\,\mathrm{MeV})}{\sigma_\eta(59.8\,\mathrm{MeV})} = 0.77 \pm 0.06$ was extracted. This result indicates a distinct and unexpected fluctuation of the total cross section between $Q = 20\,\mathrm{MeV}$ and $Q = 60\,\mathrm{MeV}$, which might indicate a possible variation of the production mechanism in this energy range. Due to these results a new beam time was conducted with WASA-at-COSY in 2014 covering the excess energy range from 13.6 MeV to 80.9 MeV.

The second part of the thesis was based on both the 2008 and the 2009 data set with the goal to search for the decay $\eta \rightarrow \pi^0 + \mathrm{e}^+ + \mathrm{e}^-$ in regards to a C parity violating process. It was possible to extract an improved upper limit for the branching ratio of the decay $\eta \rightarrow \pi^0 + \gamma^* \rightarrow \pi^0 + \mathrm{e}^+ + \mathrm{e}^-$ of 7.52×10^{-6} (CL = 90 %) and for the branching ratio of the decay $\eta \rightarrow \pi^0 + \mathrm{e}^+ + \mathrm{e}^-$ according to three-particle phase space of 9.49×10^{-6} (CL = 90 %).

Zusammenfassung

Die Reaktion p+d $\rightarrow$ ^{3}He+η wurde mit Hilfe des WASA-at-COSY Experimentes im Verlauf von zwei Strahlzeiten in den Jahren 2008 und 2009 gemessen. Dabei wurden die meisten Daten bei einer Überschussenergie von $Q = 59{,}8\,\mathrm{MeV}$ aufgezeichnet, während für einen Tag der Strahlzeit in 2009 Daten bei $Q = 48{,}8\,\mathrm{MeV}$ gemessen wurden.

Im ersten Teil der Arbeit wurde die Produktionsreaktion $\mathrm{p} + \mathrm{d} \rightarrow {}^3\mathrm{He} + \eta$ untersucht. Hierfür wurde ein Teil der in 2009 bei $Q = 59{,}8\,\mathrm{MeV}$ gesammelten Daten verwendet sowie der gesamte bei $Q = 48{,}8\,\mathrm{MeV}$ gemessene Datensatz. Diese Daten wurden verwendet, um die differentiellen Wirkungsquerschnitte für 23 Winkelbins im Bereich von $\cos\vartheta_\eta^{\mathrm{CMS}} = -0{,}92$ bis $\cos\vartheta_\eta^{\mathrm{CMS}} = 0{,}92$ zu bestimmen. Die so extrahierten Winkelverteilungen können mit Hilfe von Polynomen dritter Ordnung beschrieben werden. Neben den differentiellen Wirkungsquerschnitten wurde das Verhältnis der totalen Wirkungsquerschnitte zu $\frac{\sigma_\eta(48{,}8\,\mathrm{MeV})}{\sigma_\eta(59{,}8\,\mathrm{MeV})} = 0{,}77 \pm 0{,}06$ bestimmt. Dieses Ergebnis deutet auf eine ausgeprägte und unerwartete Fluktuation des totalen Wirkungsquerschnittes im Bereich von $Q = 20\,\mathrm{MeV}$ bis $Q = 60\,\mathrm{MeV}$ hin, was wiederum ein Hinweis für eine mögliche Variation des Produktionsmechanismuses sein könnte. Auf Grund dieser Ergebnisse wurde im Jahr 2014 mit dem WASA-at-COSY Experiment eine neue Strahlzeit durchgeführt, die den Überschussenergiebereich von 13,6 MeV bis 80,9 MeV abdeckte.

Der zweite Teil der Arbeit basiert sowohl auf dem Datensatz von 2008 als auch auf dem von 2009. Ziel war es, nach dem Zerfall $\eta \rightarrow \pi^0 + \mathrm{e}^+ + \mathrm{e}^-$ in Hinsicht auf einen C-Parität verletzenden Prozess zu suchen. Hierbei war es möglich, eine verbesserte Obergrenze für das Verzweigungsverhältnis des Zerfalls $\eta \rightarrow \pi^0 + \gamma^* \rightarrow \pi^0 + \mathrm{e}^+ + \mathrm{e}^-$ zu $7{,}52 \times 10^{-6}$ (CL = 90 %) sowie für den Zerfall $\eta \rightarrow \pi^0 + \mathrm{e}^+ + \mathrm{e}^-$ gemäß Dreiteilchenphasenraum zu $9{,}49 \times 10^{-6}$ (CL = 90 %) zu bestimmen.

Contents

1. Introduction

The question about the structure of matter is one of the oldest in human history. First thoughts about matter as a composition of indivisible, fundamental particles go back to ancient Greece. Democritus (ca. 460 BC – 370 BC) developed the hypothesis that matter is composed of "atoms" (Greek ἄτομος = indivisible), which he described as physically indivisible particles [Bar02]. It took until the beginning of the 20th century before the existence of atoms as the basic component of matter was finally proven, and further 50 years until single atoms could be observed. At about the same time as the existence of atoms was commonly accepted, it already became clear that atoms themselves have a substructure. Experiments by J. J. Thomson, E. Rutherford, and J. Chadwick identified the components of the atoms, namely protons and neutrons in the nucleus surrounded by electrons [Tho01, Rut11, Cha35]. While according to the current scientific knowledge electrons are point-like, indivisible particles, protons and neutrons consist of quarks and gluons. In modern physics the interaction of these particles is described by the so-called standard model of particle physics.

For the studies of the substructure of matter particle accelerators play an important part. In experiments with these accelerators a lot of subatomic, short lived particles were discovered. In particle physics these particles are divided into leptons and hadrons. While the former are supposed to be elementary, the latter can be grouped into baryons consisting of three quarks and mesons containing one quark and one antiquark. Further combinations of quarks and antiquarks are so-called exotics and are object of research of several modern experiments.

Besides the identification of new particles, the study of the production, interaction, and decay of these particles is an important part of particle physics. For instance, protons and neutrons are known to be bound in atomic nuclei, whereas the interactions between nucleons and mesons or nuclei and mesons are known with less precision. Several experiments were conducted in order to study these interactions. In case of the η meson and a ^{3}He nucleus, for example,

measurements were performed based on the reaction $p + d \rightarrow {}^3He + \eta$. Close to the η production threshold, which was the focus of most such experiments, the data showed a strong final state interaction between the helium nucleus and the η meson [M$^+$96, S$^+$07, M$^+$07]. However, there are less measurement results for increasing energies. In addition, there are deviations between the results of some experiments. While the shape of the total cross section for the reaction $p + d \rightarrow {}^3He + \eta$ agrees with a plateau for excess energies Q ranging from 40 MeV to 120 MeV according to results from the ANKE and the WASA/PROMICE experiment [B$^+$02, B$^+$04, R$^+$09], the results obtained with GEM at $Q = 48.8\,\text{MeV}$ indicate a larger cross section [B$^+$00], although still in agreement with the plateau within their large systematic uncertainties. Furthermore, theoretical models fail to properly describe the total and differential cross section distributions obtained for these energies. For the development and test of new models, more data are required with higher accuracy than currently available. Therefore, as one major part of this thesis, the reaction $p + d \rightarrow {}^3He + \eta$ will be investigated at the two excess energies $Q = 48.8\,\text{MeV}$ and $Q = 59.8\,\text{MeV}$. Here, aside from the development of the total cross section, the differential cross sections are of great importance as these distributions allow for a more detailed test of the different theoretical models. Thus, in this thesis the differential cross sections will be determined with high precision, as well as the ratio of the total cross section at these energies (see chapters 4 and 5). The obtained results will help future theoretical investigations of the production mechanism and interactions of particles involved.

In addition to the investigation of interactions of particles in production reactions, the research of particle decays allows to study the properties of the three fundamental forces. There are quantities that are conserved during these interactions. The conservation of these quantities is directly connected to symmetries utilized in the description of the fundamental forces in the standard model of particle physics. A violation of such a conserved quantity is thus related to a breaking of the corresponding symmetry. In fact, there are quantities which are broken for some interactions. One example is the C parity, which is conserved in the electromagnetic and strong interaction according to the current scientific knowledge, but can be violated in the weak interaction. A violation of the C parity conservation in either the electromagnetic or the strong interaction is not allowed in the standard model. Hence, an observation of a C parity violation in one of these two interactions would be a discovery of physics beyond the standard model.

Thus, the search for a C parity violating electromagnetic or strong process is an important task in particle physics.

However, in contrast to C parity conserving processes, C violating processes are expected to be suppressed if they exist at all. In case of the η meson, all decays via the electromagnetic or strong interaction are either forbidden or suppressed in first order. Accordingly, the η meson is perfectly suited for the search of rare or forbidden decays. For instance, the decay $\eta \to \pi^0 + \gamma^* \to \pi^0 + e^+ + e^-$ is a process that would violate the C parity conservation. In fact, this decay has not been observed yet, but an upper limit for the branching ratio of the decay of 4×10^{-5} was determined by M. R. Jane et al. in 1975 [J$^+$75]. The C conserving decay $\eta \to \pi^0 + \gamma^* + \gamma^* \to \pi^0 + e^+ + e^-$ has an expected branching ratio of less than 10^{-8} [JS02]. Thus, there are three orders of magnitude room to search for the C violating process. The search for the decay $\eta \to \pi^0 + e^+ + e^-$ is the second major topic of this thesis (see chapters 6 and 7). It is important to note that there is no common theoretical model for C violation in either strong or electromagnetic interactions. As a consequence, results from the search for other C violating processes like the decay $\pi^0 \to \gamma + \gamma + \gamma$ cannot be directly compared to results from the search for the decay $\eta \to \pi^0 + \gamma^* \to \pi^0 + e^+ + e^-$. Therefore, it is necessary to search for a possible C violation whenever there is room for such a process and the precision of an experiment allows to search for it.

The measurements utilized for the analyses in this thesis were performed with the WASA-at-COSY experimental setup [HR$^+$04] (see chapter 3). COSY, located at Forschungszentrum Jülich, is a storage ring which can provide polarized as well as unpolarized proton or deuteron beams with momenta of up to $3.7\,\mathrm{GeV}\,c^{-1}$. These beam particles can collide with the protons or deuterons of the internal WASA pellet target. The forward detector of the WASA experimental setup is used for the reconstruction of forward scattered ejectiles like protons, deuterons, and helium nuclei and it is perfectly suited for the $p + d \to {}^3He + \eta$ cross section analysis based on the missing mass method. The 4π central detector allows to detect, reconstruct, and identify all decay particles of a meson decay like the η meson decay of interest $\eta \to \pi^0 + e^+ + e^-$.

For the η decay studies based on η mesons produced in the reaction $p + d \to {}^3He + \eta$, two beam times were performed in 2008 and 2009 at an excess energy of 59.8 MeV with a total number of about 3×10^7 η mesons produced [A$^+$16b]. In addition, in 2009 data were collected at $Q = 48.8\,\mathrm{MeV}$ for the cross section studies.

The analysis with regard to the $p + d \rightarrow {}^3He + \eta$ cross section is based on parts of the 2009 data set, whereas the decay studies utilize the full 2008 and 2009 data sets. The full statistics are necessary to achieve the best possible result for the branching ratio of the decay $\eta \rightarrow \pi^0 + e^+ + e^-$.

2. Theory

2.1. Standard model of particle physics

In particle physics the standard model is the general theory for the description of three of the four fundamental forces, namely the electromagnetic, the weak and the strong force. Not yet included in this theory is the fourth force, gravitation, which is well described by Einstein's general relativity. On particle scale, however, the effects caused by gravitation are very small and, hence, can be neglected.

According to quantum field theory, an antiparticle exists for each particle of the standard model with the same mass, spin and multiplicative quantum numbers like parity, but opposite additive quantum numbers. An example for an additive quantum number is the electrical charge. If all additive quantum numbers are equal to zero, a particle can be its own antiparticle. For instance, the photon is its own antiparticle.

The standard model distinguishes between particles as fermions with half integer spin and bosons with integer spin, as listed in figure 2.1. A more detailed list of all fermions and bosons with their masses, spins, and electrical charges is presented in table 2.1. The bosons are separated in twelve gauge bosons with spin 1 and the scalar Higgs boson with spin 0. Under the terms of the standard model, the twelve gauge bosons mediate the electromagnetic, the strong and the weak force between particles. The massless photon transmits the electromagnetic interaction, which is described by the quantum electrodynamics theory (QED). It couples to the electric charge of a particle, but is electrically neutral itself. Further gauge bosons are the eight gluons, which couple to the color charge of a particle. Like the photon the gluons have no mass and are electrically neutral. Each gluon itself carries a color and an anticolor and, thus, does not only mediate the strong force, but can also interact with one another. The theory describing the strong interaction is the quantum chromodynamics (QCD). Unlike the photon and the gluons the $W^{\pm}$ and Z^0 bosons coupling to the weak charge have a mass, and - in case of the $W^{\pm}$

Table 2.1.: Properties of the standard model particles. The upper limit for the electron neutrino mass is given under the assumption that antineutrinos and neutrinos have the same mass [P+16].

Quark	El. charge	Spin	Mass	
u	$+2/3\,e$	1/2	$2.2^{+0.6}_{-0.4}$	MeV/c^2
d	$-1/3\,e$	1/2	$4.7^{+0.5}_{-0.4}$	MeV/c^2
c	$+2/3\,e$	1/2	1.27 ± 0.03	GeV/c^2
s	$-1/3\,e$	1/2	96^{+8}_{-4}	MeV/c^2
t	$+2/3\,e$	1/2	$173.21 \pm 0.51 \pm 0.71$	GeV/c^2
b	$-1/3\,e$	1/2	$4.18^{+0.04}_{-0.03}$	GeV/c^2
Lepton	**El. charge**	**Spin**	**Mass**	
ν_e	$0\,e$	1/2	< 2	eV/c^2
e	$-1\,e$	1/2	0.510 998 946 1(31)	MeV/c^2
ν_μ	$0\,e$	1/2	< 0.19	MeV/c^2
μ	$-1\,e$	1/2	105.658 374 5(24)	MeV/c^2
ν_τ	$0\,e$	1/2	< 18.2	MeV/c^2
τ	$-1\,e$	1/2	1776.86 ± 0.12	MeV/c^2
Boson	**El. charge**	**Spin**	**Mass**	
γ	$0\,e$	1	0	eV/c^2
g	$0\,e$	1	0	eV/c^2
Z^0	$0\,e$	1	91.1876 ± 0.0021	GeV/c^2
$W^\pm$	$\pm 1\,e$	1	80.385 ± 0.015	GeV/c^2
H^0	$0\,e$	0	$125.09 \pm 0.21 \pm 0.11$	GeV/c^2

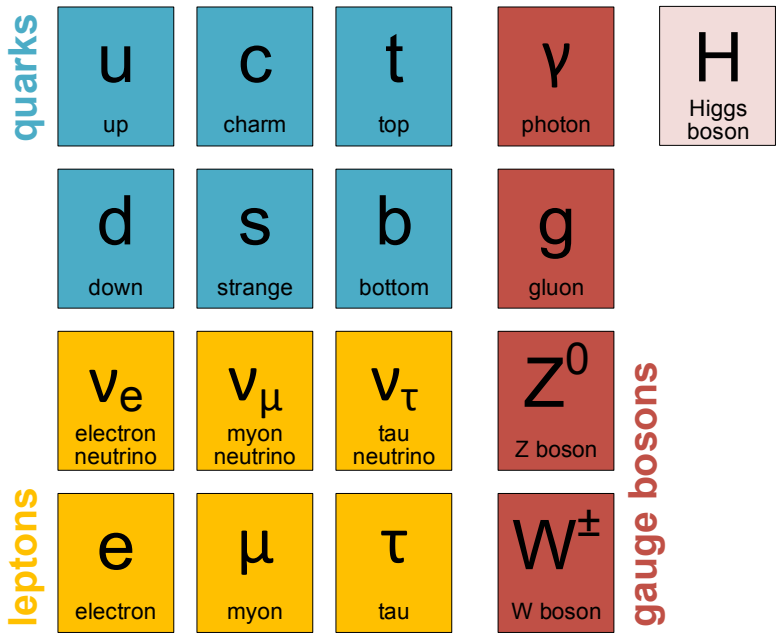

Figure 2.1.: Standard model particles grouped into twelve fermions (divided into six quarks and six leptons), twelve gauge bosons, and the Higgs boson.

bosons - carry an electrical charge. During the 1960s Glashow, Salam, Ward, and Weinberg combined the description of the weak and the electromagnetic interaction in the electroweak interaction [Gla61, SW64, Wei67]. In the same decade, namely in 1964, the Higgs mechanism was introduced as an addition to the standard model giving an explanation for the masses of the gauge bosons of the weak interaction [EB64, Hig64a, Hig64b]. As a consequence of this theory a scalar boson, the Higgs boson, was predicted, and recently discovered [ATL12, CMS12, A$^+$15a].

The fermions are grouped into leptons and quarks, which are separated into three generations each. While the three leptons electron, myon, and tau have the electrical charge $-1\,e$, the corresponding neutrinos are electrically neutral and only interact weakly. Like the electron, myon, and tau, the six quarks have an electrical charge, too. Each quark generation consists of one quark with positive charge $(+2/3\,e)$ and one with negative charge $(-1/3\,e)$. Furthermore, all quarks have a color charge and, therefore, are subject to the strong interaction. The color of a quark can either be red, green, or blue (antired, antigreen, and antiblue for antiquarks, respectively). A special characteristic of the quantum chromodynamics is that the exchange particles of the strong force, the gluons, interact with each other. Moreover, only color neutral particles can be observed. This principle is

called confinement. Therefore, quarks cannot be isolated, but build hadrons. These hadrons are grouped in baryons (antibaryons) consisting of three quarks (qqq) (or antiquarks ($\bar{q}\bar{q}\bar{q}$)) and mesons with one quark and one antiquark ($q\bar{q}$). In case of the baryons, the quarks have the colors red, green, and blue, while the quark and the antiquark of a meson have a color and the corresponding anticolor. In principle, color neutral particles can also be formed with other numbers of quarks and antiquarks. Two examples are pentaquarks consisting of four quarks and one antiquark [DPP97] and dibaryons made of six quarks [G$^+$89]. Resonances consistent with pentaquark states have been observed recently at LHCb [A$^+$15b] and a potential dibaryon was detected with WASA-at-COSY [A$^+$14c]. Further theoretically possible color neutral particles are glueballs consisting only of gluons and hybrids of quarks and gluons. The searches for such exotic particles are ongoing [PAN09, CW09, Yua15, Car06, The16].

The quarks and antiquarks that determine the quantum numbers of a hadron are called valence quarks. Additionally, hadrons contain a large number of virtual quark-antiquark pairs, so-called sea quarks, as well as virtual gluons. All these particles interact with each other, resulting in a more complex structure of the hadrons than described above. Moreover, these particles and their interactions are responsible for the main part of a hadron's mass.

2.2. Pseudoscalar mesons

Mesons are hadrons made of a quark-antiquark pair ($q\bar{q}$). The spins of the quark and antiquark can either be parallel ($\uparrow\uparrow$) or antiparallel ($\uparrow\downarrow$). This results in a possible total spin of $s = 1$ or $s = 0$. With no additional orbital angular momentum between q and $\bar{q}$ ($l = 0$) the quantum number of the total angular momentum defined as

$$\vec{J} = \vec{s} + \vec{l} \tag{2.1}$$

can either be $J = 1$ or $J = 0$. Mesons with an orbital angular momentum of zero and a total angular momentum of one are called vector mesons, while those with $l = 0$ and $J = 0$ are pseudoscalar mesons. Unlike scalar particles, pseudoscalar particles have a negative parity P which is defined as

$$P = (-1)^{l+1} \tag{2.2}$$

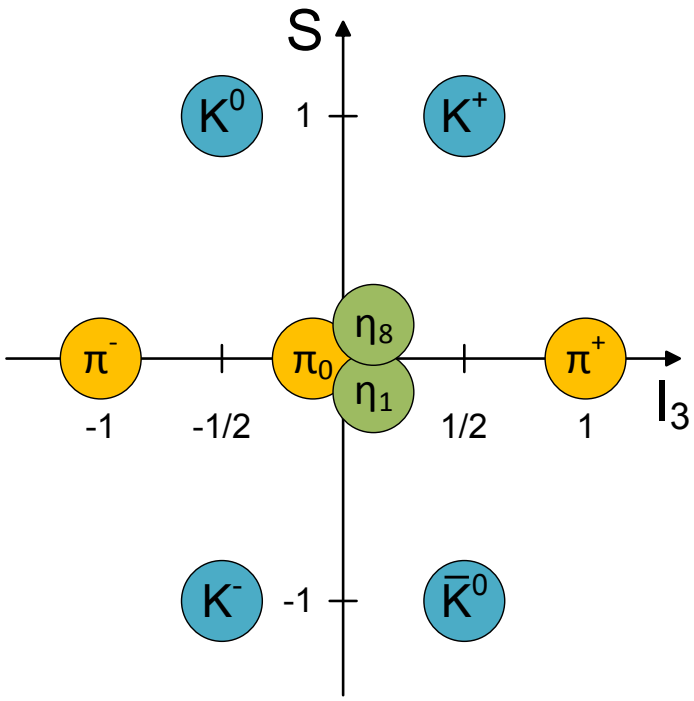

Figure 2.2.: Nonet of the pseudoscalar mesons. The mesons are plotted depending on their strangeness S and the third component of their isospin I_3.

in a fermion antifermion system.

In total there are $6^2 = 36$ possible $q\bar{q}$ pairs, when taking all quarks and antiquarks into account. Considering only the three lightest quarks up (u), down (d), and strange (s) the number of combinations is reduced to $3^2 = 9$. Figure 2.2 shows the nine pseudoscalar mesons in a nonet with their strangeness S and the value of the third component of their isospin I_3. For a hadron the strangeness is defined as the number of $\bar{s}$ quarks minus the number of s quarks. The isospin differs from zero only for u and d quarks and their antiparticles, whereas it is zero for all other particles. Its third component is $I_3 = +1/2$ for the up quark and $I_3 = -1/2$ for the down quark, and it has the opposite sign for their antiparticles.

Mathematically the combination of a $q\bar{q}$ pair can be described by the SU(3) flavor symmetry for the three lightest quarks u, d, and s [GM64, Zwe64]. As a consequence, the light meson states are grouped into an octet and a singlet. While the states $|d\bar{s}\rangle$, $|s\bar{d}\rangle$, $|u\bar{s}\rangle$ and $|s\bar{u}\rangle$ can be identified with the physically observable kaons K^0, $\bar{K}^0$, K^+ and K^-, and the two $|I_3| = 1$ states $|u\bar{d}\rangle$ and $|d\bar{u}\rangle$ are the two

charged pions[1] π^+ and π^-, the states $|u\bar{u}\rangle$, $|d\bar{d}\rangle$ and $|s\bar{s}\rangle$ can mix with each other, as they have the same quantum numbers J, P, S, and I_3. According to SU(3) flavor symmetry, the mixed states $|\pi_0\rangle$ and $|\eta_8\rangle$ are grouped into an octet together with the other $|q\bar{q}\rangle$ states, while the third mixed state $|\eta_1\rangle$ is a singlet state orthogonal to the other states. Typically, these mixed states are defined as

$$|\pi_0\rangle = \frac{1}{\sqrt{2}}\left(|u\bar{u}\rangle - |d\bar{d}\rangle\right) , \tag{2.3}$$

$$|\eta_8\rangle = \frac{1}{\sqrt{6}}\left(|u\bar{u}\rangle + |d\bar{d}\rangle - 2\,|s\bar{s}\rangle\right) , \text{ and} \tag{2.4}$$

$$|\eta_1\rangle = \frac{1}{\sqrt{3}}\left(|u\bar{u}\rangle + |d\bar{d}\rangle + |s\bar{s}\rangle\right) . \tag{2.5}$$

The three pion states which only contain up and down quarks can be grouped into an isospin triplet. Table 2.2 lists all pseudoscalar meson states with their quark content.

While the state $|\pi_0\rangle$ matches with the physical particle π^0, there are no pure $|\eta_1\rangle$ and $|\eta_8\rangle$ states in nature. Instead, the physical particles η and η' are linear combinations of those two states:

$$\eta = \eta_8 \cos\vartheta - \eta_1 \sin\vartheta\,, \tag{2.6}$$

$$\eta' = \eta_8 \sin\vartheta + \eta_1 \cos\vartheta \tag{2.7}$$

with a mixing angle ϑ in the range of $-10°$ to $-20°$ [P+16].

2.2.1. The η meson

The η meson is a pseudoscalar meson ($J = 0$, $P = -1$) with no electric charge and an isospin of $I = 0$ [P+16]. Its mass has been determined to be $m = (547.862 \pm 0.017)\,\mathrm{MeV}\,c^{-2}$ with a full width of $\Gamma = (1.31 \pm 0.05)\,\mathrm{keV}\,c^{-2}$ equaling to a mean life time of $\tau = (5.02 \pm 0.19) \times 10^{-19}\,\mathrm{s}$. Due to its short mean life time it is not observed directly, but by means of the missing mass or invariant mass methods (see chapter 2.5). All additive quantum numbers of the η meson are equal to zero as the η meson is its own antiparticle (see chapter 2.1).

[1] Note that here for simplification the quark is always the first particle in the wave function and the antiquark is the second one. In a more precise description the mesons' wave functions have to be symmetrized and antisymmetrized, respectively, with regard to the order of the quark and antiquark in the wave function. For example, the wave function of the π^+ meson is $|\pi^+\rangle = \frac{1}{\sqrt{2}}\left(|u\bar{d}\rangle + |\bar{d}u\rangle\right)$ [Ber06].

Table 2.2.: List of pseudoscalar mesons with their quark content, electrical charge Q, absolute isospin value I, third component of the isospin I_3, and strangeness S.

	Meson	Quark content		Q	I	I_3	S
Octet	π_0	$\left(u\bar{u} - d\bar{d}\right)/\sqrt{2}$	Isospin triplet	$0\,e$	1	0	0
	π^+	$u\bar{d}$		$+1\,e$	1	$+1$	0
	π^-	$d\bar{u}$		$-1\,e$	1	-1	0
	K^0	$d\bar{s}$		$0\,e$	1/2	$-1/2$	$+1$
	$\bar{K}^0$	$s\bar{d}$		$0\,e$	1/2	$+1/2$	-1
	K^+	$u\bar{s}$		$+1\,e$	1/2	$+1/2$	$+1$
	K^-	$s\bar{u}$		$-1\,e$	1/2	$-1/2$	-1
	η_8	$\left(u\bar{u} + d\bar{d} - 2s\bar{s}\right)/\sqrt{6}$		$0\,e$	0	0	0
Singlet	η_1	$\left(u\bar{u} + d\bar{d} + s\bar{s}\right)/\sqrt{3}$		$0\,e$	0	0	0

Particles that are their own antiparticles have a well defined C parity which is the eigenvalue of the $\bar{C}$ operator. The $\bar{C}$ operator changes the sign of all additive quantum numbers turning a particle into its antiparticle, for example an electron into a positron:

$$\bar{C}\,|e^-\rangle = a\,|e^+\rangle \tag{2.8}$$

with a phase factor a. Applying the $\bar{C}$ operator a second time turns the antiparticle back into its particle counter part. If a particle is its own antiparticle, it is therefore an eigenstate of the $\bar{C}$ operator with the only possible eigenvalues being $C = +1$ or $C = -1$. An example is the photon with a negative C parity. As the C parity is a multiplicative quantum number which, according to theory, is conserved in strong and electromagnetic interactions, the C parity of a particle can be calculated from an observed decay. Using the decay $\eta \to \gamma\gamma$, for example, one obtains:

$$\begin{aligned} C(\eta) = C(\gamma\gamma) &= C(\gamma) \cdot C(\gamma) \\ &= (-1) \cdot (-1) = (+1)\ . \end{aligned} \tag{2.9}$$

Therefore, the C parity of the η meson is $C = +1$.

Table 2.3.: Properties of the η meson [P+16].

Mass (m)	$(547.862 \pm 0.017)\,\mathrm{MeV}\,c^{-2}$
Full width (Γ)	$(1.31 \pm 0.05)\,\mathrm{keV}\,c^{-2}$
Mean life time (τ)	$(5.02 \pm 0.19) \times 10^{-19}\,\mathrm{s}$
Charge (Q)	$0\,e$
Isospin (I)	0
Total angular momentum (J)	$0\,\hbar$
Parity (P)	-1
C parity (C)	$+1$
G parity (G)	$+1$
Strangeness (S)	0

As the C parity is only defined for particles which are their own antiparticle, the G parity is introduced as a generalization of the C parity for multiplets. It is conserved in the strong interaction in lowest order, but not in the weak or electromagnetic interaction. Since the strong interaction is independent of a particle's charge, the G parity for charged and neutral pions is identical. The operator of the G parity is defined as

$$\bar{G} = \bar{C} e^{-i\pi \bar{I}_2} \tag{2.10}$$

where $e^{-i\pi \bar{I}_2}$ is a rotation around the isospin I_2 axis by 180°. Hence, the G parity of the η meson is $G = +1$. Table 2.3 lists the quantum numbers and other properties of the η meson.

The η meson decays via either the strong or the electromagnetic interaction with roughly 28 % proceeding in charged decay modes and 72 % in neutral decay modes [P+16]. Over 99 % of the decays are covered by the four most common decay channels. Table 2.4 lists all decay modes of the η meson that have been observed so far.

As all η decays via the strong and electromagnetic interaction are forbidden or suppressed in first order, the η meson is well suited for studies on or searches for rare or forbidden decays. The decay $\eta \to (\pi + \pi)^0$, for example, violates P and CP conservation. While the η meson has a total angular momentum of $J = 0$, an orbital angular momentum of $l = 0$, and its parity is $P = -1$, the parity of the ππ system is

$$P\,(\pi\pi) = P(\pi) \cdot P(\pi) \cdot (-1)^l\,. \tag{2.11}$$

Table 2.4.: Observed decay modes of the η meson with their branching ratios [P+16].

η decay modes	Fraction (Γ_i/Γ)
Neutral modes	72.12 ± 0.34 %
$\eta \to \gamma + \gamma$	39.41 ± 0.20 %
$\eta \to \pi^0 + \pi^0 + \pi^0$	32.68 ± 0.23 %
$\eta \to \pi^0 + \gamma + \gamma$	$2.56 \pm 0.22 \times 10^{-4}$
Charged modes	28.10 ± 0.34 %
$\eta \to \pi^+ + \pi^- + \pi^0$	22.92 ± 0.28 %
$\eta \to \pi^+ + \pi^- + \gamma$	4.22 ± 0.08 %
$\eta \to e^+ + e^- + \gamma$	$6.9 \pm 0.4 \times 10^{-3}$
$\eta \to \mu^+ + \mu^- + \gamma$	$3.1 \pm 0.4 \times 10^{-4}$
$\eta \to \mu^+ + \mu^-$	$5.8 \pm 0.8 \times 10^{-6}$
$\eta \to e^+ + e^- + e^+ + e^-$	$2.40 \pm 0.22 \times 10^{-5}$
$\eta \to \pi^+ + \pi^- + e^+ + e^-(+\gamma)$	$2.68 \pm 0.11 \times 10^{-4}$

Since the total angular momentum is conserved, this decay would therefore violate the parity conservation. Similarly, decays into four pions also violate the parity and CP conservation. Furthermore, the decay $\eta \to (\pi + \pi + \pi)^0$ is not allowed in first order because it does not conserve the G parity:

$$\begin{aligned} G(\pi\pi\pi) &= G(\pi) \cdot G(\pi) \cdot G(\pi) \\ &= (-1) \cdot (-1) \cdot (-1) = -1 \\ &\neq +1 = G(\eta)\,. \end{aligned} \tag{2.12}$$

Due to the charge difference of the up and down quark, however, the isospin is not conserved in electromagnetic processes. Moreover, because of the mass differences of the the up and down quark, the isospin is not strictly conserved in strong processes, as well. Hence, the isospin and the G parity conservation, respectively, can be violated allowing the decay $\eta \to (\pi + \pi + \pi)^0$. The electromagnetic decay channels $\eta \to \pi^0 + \gamma$, $\eta \to \pi^0 + \pi^0 + \gamma$ and $\eta \to \pi^0 + \pi^0 + \pi^0 + \gamma$ are forbidden, as they do not conserve the C parity. In case of the decay $\eta \to \pi^0 + \gamma$, the angular momentum conservation would also be violated (see chapter 2.4.1). The decay $\eta \to \pi^+ + \pi^- + \gamma$ is the only allowed first order electromagnetic decay, but suppressed [Red10]. The

most prominent possible η decay is the second order decay $\eta \rightarrow \gamma + \gamma$ with a branching ratio of $(39.41 \pm 0.20)\,\%$ [P+16].

2.3. The reaction $p + d \rightarrow {}^3He + \eta$

Mesons can be produced in many different nuclear reactions. At the WASA-at-COSY experiment η mesons are typically produced by either colliding a proton beam with a proton target and looking for the reaction $p + p \rightarrow p + p + \eta$ or by fusion of proton beam particles with target deuterons to ^{3}He nuclei. The latter reaction $p + d \rightarrow {}^3He + \eta$ is the basis of the analyses presented in this thesis and will be discussed in more detail in the following chapters.

2.3.1. Kinematics of two particle reactions

The reactions $p + d \rightarrow {}^3He + \eta$ and $d + p \rightarrow {}^3He + \eta$ have two particles in the initial and two particles in the final state and differ only by alternating the beam and target particle. Generally, two particle reactions can be written as

$$a + b \rightarrow c + d\,. \tag{2.13}$$

For simplification the convention

$$\hbar = c = 1 \tag{2.14}$$

often used in nuclear and particle physics will be used throughout the thesis.

According to energy and momentum conservation, the sum of the four-momenta of the initial particles p_a^μ and p_b^μ is equal to the sum of the four-momenta p_c^μ and p_d^μ of the final state particles:

$$p_a^\mu + p_b^\mu = p_c^\mu + p_d^\mu\,. \tag{2.15}$$

The absolute value of these sums of four-momenta is the total energy $\sqrt{s}$ in the center of mass system (CMS):

$$\sqrt{s} = |p_a + p_b| = |p_c + p_d|\ . \tag{2.16}$$

This center of mass energy is then converted into the masses of the final state particles c and d and kinetic energy Q according to Einstein's mass-energy equivalence formula $E = m$:

$$\sqrt{s} = m_\mathrm{c} + m_\mathrm{d} + Q\,. \tag{2.17}$$

A reaction can only occur if $Q \geq 0\,\mathrm{eV}$, as the conservation of energy would be violated otherwise. The case $Q = 0\,\mathrm{eV}$ defines the threshold for the reaction $\mathrm{a}+\mathrm{b} \to \mathrm{c}+\mathrm{d}$ when there is just enough energy available to produce the particles c and d. Q is therefore the excess energy of a given reaction for a certain center of mass energy.

The sum of the three-momenta of the initial state particles is equal to the sum of the momenta of the final state particles according to momentum conservation. Per definition both sums are equal to zero in the center of mass rest frame:

$$\vec{p}_\mathrm{a}^{\,\mathrm{CMS}} + \vec{p}_\mathrm{b}^{\,\mathrm{CMS}} = \vec{p}_\mathrm{c}^{\,\mathrm{CMS}} + \vec{p}_\mathrm{d}^{\,\mathrm{CMS}} = \vec{0}\,. \tag{2.18}$$

Thus, the absolute values of the three-momenta of particles c and d have to be equal and define the final state momentum p_f, which only depends on the center of mass energy for a given reaction:

$$p_\mathrm{f} = \left|\vec{p}_\mathrm{c}^{\,\mathrm{CMS}}\right| = \left|\vec{p}_\mathrm{d}^{\,\mathrm{CMS}}\right|\,. \tag{2.19}$$

Therefore, in case of a two particle reaction, all momenta of the final state particles c and d allowed by energy and momentum conservation lie on the surface of a momentum sphere with the radius p_f. It is hence reasonable to use a spherical coordinate system.

Figure 2.3 shows a sketch of the kinematics of the two-particle reaction $\mathrm{a} + \mathrm{b} \to \mathrm{c} + \mathrm{d}$ in the center of mass system. The scattering angle $\vartheta_\mathrm{c}^{\mathrm{CMS}}$ is defined as the angle between the beam particle's momentum $\vec{p}_\mathrm{a}^{\,\mathrm{CMS}}$ and the outgoing final state particle's momentum $\vec{p}_\mathrm{c}^{\,\mathrm{CMS}}$. In the same way the scattering angle $\vartheta_\mathrm{d}^{\mathrm{CMS}}$ can be defined as the angle between $\vec{p}_\mathrm{a}^{\,\mathrm{CMS}}$ and $\vec{p}_\mathrm{d}^{\,\mathrm{CMS}}$. From

$$\vartheta_\mathrm{d}^{\mathrm{CMS}} = \pi + \vartheta_\mathrm{c}^{\mathrm{CMS}} \tag{2.20}$$

it follows that

$$\cos\vartheta_\mathrm{d}^{\mathrm{CMS}} = -\cos\vartheta_\mathrm{c}^{\mathrm{CMS}}\,. \tag{2.21}$$

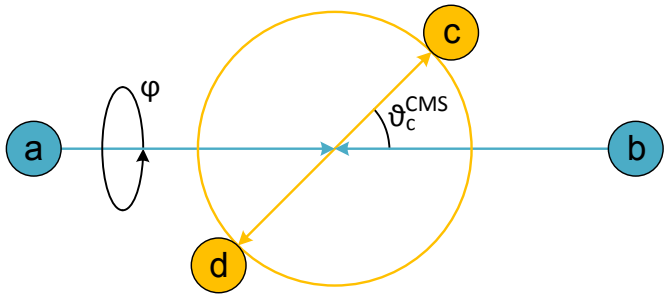

Figure 2.3.: Schematic sketch of the kinematics of the two particle reaction a+b → c+d in the center of mass system.

The azimuthal angle φ defines the rotation around the beam axis.

Purely according to kinematics, there is no reason why the final state momenta should not be equally spread over the indicated momentum sphere for a two particle reaction. Deviations from this so-called "phase space" distribution can be explained by higher partial waves, caused by interactions of the initial or final state particles, or can originate from production mechanisms. In order to study the contribution of the partial waves, the wave function of a moving particle can be expanded in eigenfunctions of the angular momentum, the spherical harmonics. In case of lower excess energies and due to the low range of the strong interaction, it is often sufficient to consider only a few partial waves. These are labeled s, p, d, f, and so on, depending on the angular momentum. Measurements with polarized beams and/or targets are particularly well suited for studies of the partial waves. For unpolarized measurements, like the ones presented in this thesis, there is no dependence of the momentum distribution on the azimuthal angle φ, but only on $\cos\vartheta_c^{CMS}$. In case of pure s-waves the final state particles' momenta are equally spread over the momentum sphere and, hence, equally distributed depending on $\cos\vartheta_c^{CMS}$.

Lorentz transformation and momentum ellipsis

So far the two particles kinematics were discussed in the center of mass rest frame, whereas in the experiment the particles are observed in a different system (laboratory system). In order to obtain the center of mass momenta, the measured laboratory momenta can be transformed into CMS via a Lorentz transformation. In case of the WASA experiment with the target particle being at rest in the laboratory

system and the beam particle moving in z direction, a particle's four-momentum p_μ is transformed to the four-momentum p'_μ according to:

$$\begin{aligned} E' &= \gamma\,(E - \beta p_z) \\ p'_x &= p_x \\ p'_y &= p_y \\ p'_z &= \gamma\,(p_z - \beta E) \end{aligned} \tag{2.22}$$

with $\beta = v/c$. Here v is the velocity of the CMS system in z direction compared to the laboratory system.

Similar to the momenta, the scattering angles differ in the CMS and laboratory system. While the azimuthal scattering angles are identical, the polar scattering angle ϑ of a particle c is transformed according to:

$$\cos\vartheta_{\mathrm{c}}^{\mathrm{CMS}} = \frac{-\frac{\beta}{\beta_{\mathrm{c}}^{\mathrm{CMS}}}\gamma^2\tan^2\vartheta_{\mathrm{c}} \pm \sqrt{1+\gamma^2\tan^2\vartheta_{\mathrm{c}}\left(1-\left(\frac{\beta}{\beta_{\mathrm{c}}^{\mathrm{CMS}}}\right)^2\right)}}{1+\gamma^2\tan^2\vartheta_{\mathrm{c}}} \tag{2.23}$$

with

$$\begin{aligned} \gamma &= \frac{1}{\sqrt{1-\beta^2}} \\ \vec{\beta} &= \frac{\vec{p}_{\mathrm{a}}+\vec{p}_{\mathrm{b}}}{E_{\mathrm{a}}+E_{\mathrm{b}}} = \frac{p_{\mathrm{a}}}{E_{\mathrm{a}}+E_{\mathrm{b}}}\vec{e}_z \\ \beta_{\mathrm{c}}^{\mathrm{CMS}} &= \frac{\sqrt{\left(T_{\mathrm{c}}^{\mathrm{CMS}}\right)^2 + 2T_{\mathrm{c}}^{\mathrm{CMS}}m_{\mathrm{c}}}}{T_{\mathrm{c}}^{\mathrm{CMS}}+m_{\mathrm{c}}} \\ T_{\mathrm{c}}^{\mathrm{CMS}} &= \frac{T_f^{\mathrm{CMS}}}{2}\frac{T_f^{\mathrm{CMS}}+2m_{\mathrm{d}}}{E_{\mathrm{CMS}}} \\ T_f^{\mathrm{CMS}} &= E_{\mathrm{CMS}} - (m_{\mathrm{c}}+m_{\mathrm{d}}) \\ E_{\mathrm{CMS}} &= \sqrt{\left(E_{\mathrm{a}}+E_{\mathrm{b}}\right)^2 - \left(\vec{p}_{\mathrm{a}}+\vec{p}_{\mathrm{b}}\right)^2} = \sqrt{\left(E_{\mathrm{a}}+E_{\mathrm{b}}\right)^2 - \vec{p}_{\mathrm{a}}^{\,2}} \\ E_{\mathrm{a,b}} &= T_{\mathrm{a,b}} + m_{\mathrm{a,b}} \\ p_{\mathrm{a}} &= \frac{1}{c}\sqrt{T_{\mathrm{a}}^2 + 2T_{\mathrm{a}}m_{\mathrm{a}}}\,. \end{aligned} \tag{2.24}$$

For sufficiently high beam momenta, in the laboratory system all particles are scattered in the forward direction. This results in a maximum scattering angle

$$\tan \vartheta_{\mathrm{c}}^{\max} = \frac{1}{\gamma} \frac{1}{\sqrt{\left(\frac{\beta}{\beta_{\mathrm{c}}^{\mathrm{CMS}}}\right)^2 - 1}} \,. \tag{2.25}$$

As this relation between the beam momentum and $\vartheta_{\mathrm{c}}^{\max}$ is unambiguous, the maximum scattering angle observed in data can be used to determine the beam momentum during the experiment.

2.3.2. Energy dependence of the differential cross sections

The probability that an incoming particle (projectile) interacts with a second particle (target) can be quantified by the cross section σ. Its dimension is that of a surface with the unit barn ($1\,\mathrm{b} = 10^{-28}\,\mathrm{m}^2$). For the definition of the cross section it is assumed that an interaction occurs if a point-like particle hits a surface of the size σ. This definition has no further practical meaning, as the geometrical profile of the particle is typically not in the same order as the cross section. The differential cross section $\mathrm{d}\sigma/\mathrm{d}\Omega$ gives the probability of an ejectile to be scattered in a given solid angle $\mathrm{d}\Omega$. Besides this general definition of the cross section, a cross section σ can be defined for a certain reaction giving the probability of this reaction to occur.

In case of a reaction of the type $\mathrm{a} + \mathrm{b} \to \mathrm{c} + \mathrm{d}$, the cross section depends on the initial state interaction (ISI)[2], the production mechanism, and the final state interaction (FSI)[3]. These interactions are combined in the scattering amplitude

$$f_{\mathrm{scat}} = f_{\mathrm{ISI}} \cdot f_{\mathrm{prod}} \cdot f_{\mathrm{FSI}} \tag{2.26}$$

with the production amplitude f_{prod} and the terms f_{ISI} and f_{FSI} for the initial and final state interaction, respectively. Without ISI and FSI and close to the production threshold assuming pure s-wave behavior, this value solely depends on the center of mass energy $\sqrt{s}$ of the reaction[4]. In this region the excess energy Q

[2]Interaction of the initial projectiles.
[3]Interaction of the outgoing ejectiles.
[4]Note that it is furthermore assumed that there are no narrow resonances close the production threshold.

is much smaller than the sum of the masses m_c and m_d of the final state particles. Hence, the center of mass energy

$$\sqrt{s} = m_\mathrm{c} + m_\mathrm{d} + Q \approx m_\mathrm{c} + m_\mathrm{d} \tag{2.27}$$

can be assumed to be constant. Due to the pure $\sqrt{s}$ dependency of f_prod, the production amplitude can be assumed to be constant, as well.

The differential cross section of a reaction is given by the integral over all allowed states in phase space for a given solid angle $\mathrm{d}\sigma/\mathrm{d}\Omega$. For a two particle reaction this results in a dependency of the differential cross section in the center of mass system on the momentum p_i of the incoming projectiles and the momentum p_f of the outgoing ejectiles:

$$\frac{\mathrm{d}\sigma}{\mathrm{d}\Omega} = \frac{p_f}{p_i} \cdot |f_\mathrm{scat}|^2 \ . \tag{2.28}$$

Close to the production threshold the kinetic energy Q of the outgoing particles is given as

$$Q = \frac{{p_f}^2}{2 \cdot m_\mathrm{red}} \tag{2.29}$$

with the reduced mass m_red of the ejectiles c and d:

$$m_\mathrm{red} = \frac{m_\mathrm{c} m_\mathrm{d}}{m_\mathrm{c} + m_\mathrm{d}} \ . \tag{2.30}$$

Furthermore, for small excess energies the initial momentum p_i does not change by much and can be assumed to be constant. Together with equation 2.28, this results in the dependency

$$\frac{\mathrm{d}\sigma}{\mathrm{d}\Omega} \propto \sqrt{Q} \tag{2.31}$$

of the differential cross section close to the production threshold without ISI and FSI.

2.3.3. Models for the reaction $\mathrm{p} + \mathrm{d} \rightarrow {}^3\mathrm{He} + \eta$

In theory the reaction $\mathrm{p} + \mathrm{d} \rightarrow {}^3\mathrm{He} + \eta$ can be described by different models which differ considerably in the production mechanism assumed. While the available data can be well described by a two-step model for small excess energies below $Q = 12\,\mathrm{MeV}$, until now theoretical calculations according to this model fail to describe the data at higher excess energies (see chapter 2.3.4). For these energies

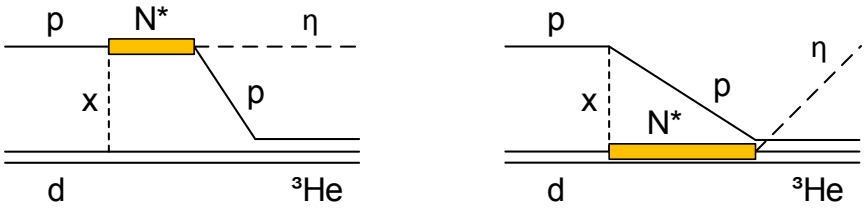

Figure 2.4.: Schematic diagrams of a resonant production mechanism for the reaction $p + d \rightarrow {}^3He + \eta$ with an excitation of the beam proton (left) or a target nucleon (right) to the S_{11} resonance $N^*(1535)$. The exchange mesons x can be π, ρ, ω and η mesons.

there are approaches to describe the η meson production by the production of intermediate nucleon resonances. So far no commonly accepted theoretical model was found capable of describing the available data over the full energy range. A short description of a resonance model and the two-step model is given in the following sections.

Resonance model

One approach for the theoretical description of the reaction $p + d \rightarrow {}^3He + \eta$ is the production of the η meson via an excitation of one nucleon to a nucleon resonance and its decay into a nucleon and an η meson (see figure 2.4). Such an approach was chosen to describe the data measured at GEM in [B+00]. In detail, Betigeri et al. suggested the intermediate excitation of a S_{11} resonance $N^*(1535)$. They fitted their cross section data point and previously published data depending on the excitation energy E using the relation

$$\sigma(E) = \frac{p_\eta^{\mathrm{CMS}}}{p_\mathrm{p}^{\mathrm{CMS}}} |M(E)|^2 \ . \tag{2.32}$$

The excitation energy dependence of the Breit Wigner Matrix element $M(E)$ is given by:

$$|M(E)|^2 = \frac{A\Gamma_R^2}{(E - m_R)^2 + \Gamma(E)^2} \tag{2.33}$$

with

$$\Gamma(E) = \Gamma_R \cdot \left(\mathrm{BR}_\eta \cdot \frac{p_\eta^{\mathrm{CMS}}}{p_{\eta,R}^{\mathrm{CMS}}} + \mathrm{BR}_\pi \cdot \frac{p_\pi^{\mathrm{CMS}}}{p_{\pi,R}^{\mathrm{CMS}}} + \mathrm{BR}_{\pi\pi} \right) \ . \tag{2.34}$$

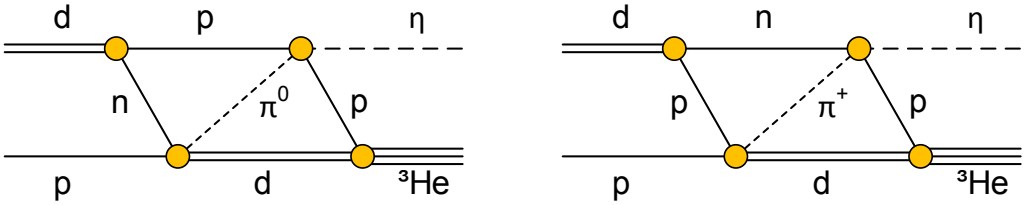

Figure 2.5.: Schematic diagrams of the two-step model for the reaction $\mathrm{p} + \mathrm{d} \rightarrow {}^3\mathrm{He} + \eta$ with a π^0 meson (left) or a π^+ meson (right) produced in the first step.

All momenta in equations 2.32 and 2.34 are in the center of mass rest frame, those with index R are momenta at the resonance position. Due to the large uncertainties of the decay branching ratios of the S_{11} resonance $N^*(1535)$, the averages $BR_\eta = 0.47$, $BR_\pi = 0.48$, and $BR_{\pi\pi} = 0.05$ were chosen for the decays $N^* \rightarrow N + \eta$, $N^* \rightarrow N + \pi$, and $N^* \rightarrow N + \pi + \pi$, respectively, according to [C+98]. For their fit Betigeri et al. fixed the mass of the $N^*(1535)$ to $m_R = 1540\,\mathrm{MeV}\,c^{-2}$ and the resonance width to $\Gamma_R = 200\,\mathrm{MeV}\,c^{-2}$, keeping the strength A as the only free parameter. A comparison of their obtained fit with the available cross section data base is presented in chapter 2.3.4.

Two-step model

The cross sections of the reaction $\mathrm{p} + \mathrm{d} \rightarrow {}^3\mathrm{He} + \eta$ have two remarkable properties close to the η meson threshold: first, the rapid change within the first MeV of excess energy and second, the absolute height of the total cross section. Assuming a production process with only two of the nucleons taking part, the amplitude of the cross section is underestimated by at least a factor of the order of four [GW89]. Therefore, a two-step model including all three nucleons in the production process was independently developed by Laget and Lecolley and by Kilian and Nann [LL88, KN91].

Schematic diagrams of the two reactions possible in the two-step model are shown in figure 2.5. According to this model, the η meson is produced in two steps. In the first step the proton interacts with one nucleon of the target deuteron, producing a deuteron and a pion. The π meson can either be neutral or positively charged. In the second step this pion reacts with the remaining nucleon, forming a proton

and the η meson. The deuteron formed in the first step and the nucleon from the second step fuse to a ^{3}He nucleus.

While the height of the cross sections calculated with this model is in good agreement with measured data, the shape of the total cross section near threshold cannot be explained by the two-step model without further assumptions. As presented in chapter 2.3.4, a description can only be achieved if a final state interaction between the ^{3}He nucleus and the η meson is included [FW95].

2.3.4. The available data base

Compared to similar reactions, the reaction $p + d \rightarrow {}^3He + \eta$ shows a significantly different behavior. For instance, the total cross sections of the reactions $p + d \rightarrow {}^3He + \pi^0$ and $p + d \rightarrow {}^3He + \eta$ are similar close to their respective threshold, although the momentum transfer associated with the latter reaction is much larger [GW89]. Thus, several measurements were performed since the 1970s to investigate this reaction. In the following these measurements are summarized and the obtained cross sections will be discussed.

The first cross sections of the reaction $d + p \rightarrow {}^3He + \eta$ were published by Banaigs et al. in 1973 [B$^+$73]. The corresponding experiment was carried out at Saturne, and the differential cross sections at $\cos\vartheta^{\mathrm{CMS}}_{^3\mathrm{He}} = -1$ were determined for the three excess energies 74 MeV, 134 MeV, and 163 MeV. Furthermore, for $Q \approx 86$ MeV differential cross sections were measured at four different $\cos\vartheta^{\mathrm{CMS}}_{^3\mathrm{He}}$.

Berthet et al. measured differential cross sections of the reaction $p + d \rightarrow {}^3He + \eta$ for 16 excess energies and up to five different scattering angles in the excess energy range from 15.6 MeV to 711 MeV. For $Q = 847$ MeV they were able to determine an upper limit for the differential cross section at $\vartheta^{\mathrm{LAB}}_{^3\mathrm{He}} = 3°$. The measurements were conducted at the SPES-IV spectrometer and published in 1985 [B$^+$85].

In 1988 Berger et al. published cross sections at $\cos\vartheta^{\mathrm{CMS}}_{^3\mathrm{He}} = -1$ and $\cos\vartheta^{\mathrm{CMS}}_{^3\mathrm{He}} = 1$, as well as analyzing powers for the excess energies 0.84 MeV, 2.2 MeV, and 4.6 MeV [B$^+$88]. While the corresponding measurements were also carried out at the SPES-IV experiment, a polarized deuteron beam was used instead of a proton beam. The obtained data showed a stronger energy dependence of the scattering amplitude than anticipated for phase space behavior which led to an increased theoretical and experimental interest in this reaction.

Results of further measurements of the reaction $p + d \rightarrow {}^3He + \eta$ close to the η production threshold at SPES-II were published in 1996 by Mayer et al. [M$^+$96].

The data at eight excess energies ranging from 0.12 MeV to 6.2 MeV also showed a strong energy dependence of the scattering amplitude, and the shape was explained by a strong final state interaction and a two-step model [FW95] (see chapter 2.3.3).

Total and differential cross sections measured at GEM were released in 2000 by Betigeri et al. at an excess energy of 48.8 MeV [B$^+$00]. For the first time differential cross sections at $\cos\vartheta_\eta^{\mathrm{CMS}} = 0$ were measured. Instead of explaining the data with a strong final state interaction and a two-step model, the results were interpreted by an excitation of one nucleon to a nucleon resonance as the major production mechanism neglecting a final state interaction (see chapter 2.3.3).

In 2002 Bilger et al. published differential and total cross sections for the excess energies 20.0 MeV, 38.8 MeV, 77.9 MeV, and 112.6 MeV obtained with the WASA/PROMICE experimental setup [B$^+$02, B$^+$04].

To close the gap between the near η threshold measurements performed at SPES-II and SPES-IV and the higher energy measurements at WASA/PROMICE and GEM, differential and total cross sections were measured with the COSY-11 experiment at the five intermediate excess energies 4.5 MeV, 10.3 MeV, 14.6 MeV, 19.4 MeV, and 40.0 MeV[5], and the results were published by Adam et al. in 2007 [A$^+$07].

In the same year Smyrski et al. released total and differential cross sections measured with the same experiment using a deuteron beam covering 19 additional excess energies close to threshold ranging from 0.3 MeV to 8.3 MeV [S$^+$07].

Since the results of the different measurements close to the η meson threshold as well as for higher excess energies showed discrepancies, measurements of the total and differential cross sections for both excess energy regions were performed in two parts at the ANKE experiment with a deuteron beam. One part was realized with a ramping beam covering excess energies from threshold up to about 11.2 MeV. The resulting 195 data points for the total cross section were published by Mersmann et al. in 2007 [M$^+$07]. Moreover, for 48 excess energies differential cross sections covering the whole angular range were determined. The second part was performed at the fixed excess energies 19.5 MeV, 39.4 MeV, and 59.4 MeV, and total and differential cross sections for these energies were published in 2009 by Rausmann

[5] The excess energies 5.0 MeV, 10.8 MeV, 15.1 MeV, 19.9 MeV, and 40.6 MeV in ref. [A$^+$07] were calculated from the proton beam momenta 1.581 GeV c^{-1}, 1.593 GeV c^{-1}, 1.602 GeV c^{-1}, 1.612 GeV c^{-1}, and 1.655 GeV c^{-1} under the assumption of an η meson mass of $m_\eta = 547.3\,\mathrm{MeV}\,c^{-2}$. The values quoted here were recalculated using the current value of $m_\eta = 547.862\,\mathrm{MeV}\,c^{-2}$ for the η meson mass [P$^+$16].

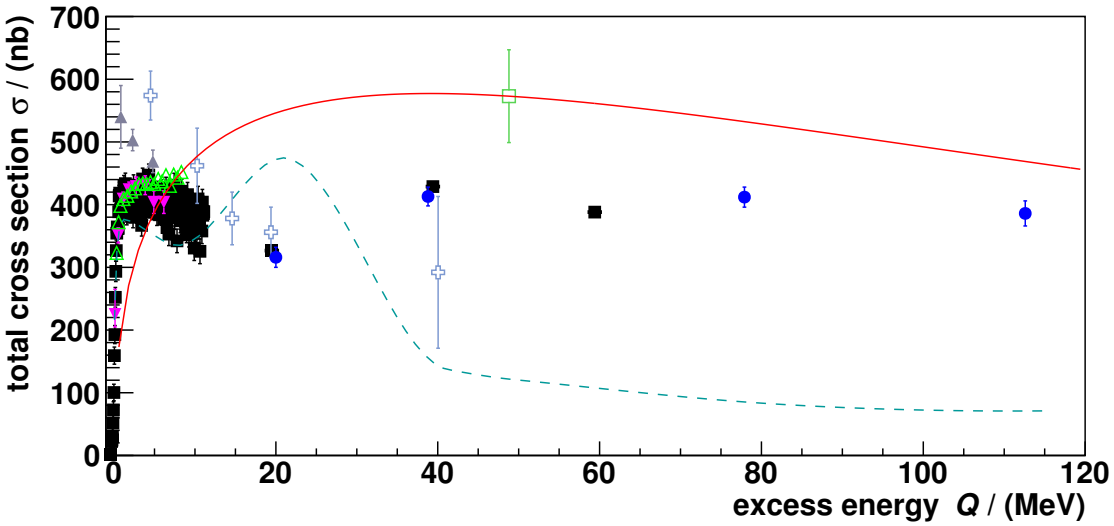

Figure 2.6.: Total cross section σ as a function of the excess energy Q for the reactions p+d $\rightarrow$ ^{3}He+η and d+p $\rightarrow$ ^{3}He+η. Data points from publications before 2014 are shown. Uncertainties due to normalization are not included. The data stem from the experiments SPES-IV (filled gray triangles [B$^+$88]), SPES-II (inverted purple triangles [M$^+$96]), GEM (open green square [B$^+$00]), WASA/PROMICE (filled blue circles [B$^+$02, B$^+$04]), COSY-11 (open light blue crosses [A$^+$07] and open green triangles [S$^+$07]), and ANKE (filled black squares [M$^+$07, R$^+$09]). Illustrated by the red solid curve is a theoretical description of the η meson production via an excitation of a N*(1535) resonance [B$^+$00], while the turquoise dashed line represents a two-step model description [KKJ07].

et al. [R$^+$09]. For the first time cross sections were determined for excess energies ranging from threshold up to 59.4 MeV conducted by one experiment. As a result, uncertainties due to different normalization procedures could be excluded.

Discussion of the total cross sections data base

The available total cross sections of the reactions p+d $\rightarrow$ ^{3}He+η and d+p $\rightarrow$ ^{3}He+η for excess energies up to $Q = 120$ MeV are shown in figure 2.6. All data points are presented without systematic uncertainties due to normalization which are in the order of 7 % (SPES-II [M$^+$96]) to 15 % (ANKE [R$^+$09]). These uncertainties only influence the absolute height of the cross sections, but not the shape of the cross section determined in the individual measurements. The data basis is divided into a close to threshold part with excess energies up to about 12 MeV, which can be explained by a two-step model including final state interaction [FW95], and a second part with higher excess energies.

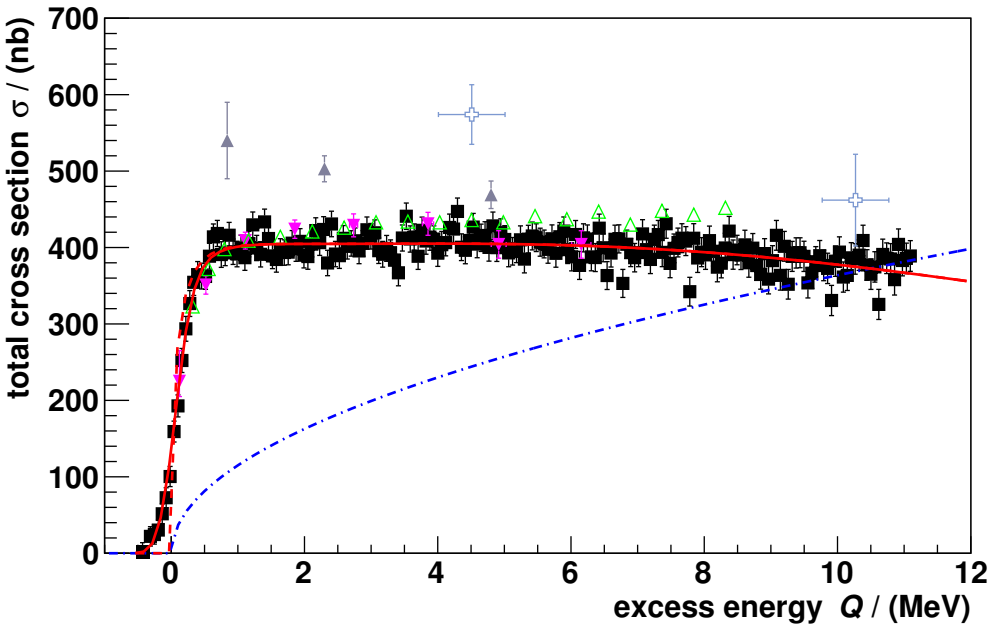

Figure 2.7.: Total cross section σ as a function of the excess energy Q for the reactions p+d $\rightarrow$ ^{3}He+η and d+p $\rightarrow$ ^{3}He+η close to threshold. Uncertainties due to normalization are not included. The data stem from the experiments SPES-IV (filled gray triangles [B$^+$88]), SPES-II (inverted purple triangles [M$^+$96]), COSY-11 (open light blue crosses [A$^+$07] and open green triangles [S$^+$07]), and ANKE (filled black squares [M$^+$07]). While the arbitrarily scaled phase space function $\sigma(Q) \propto \sqrt{Q}$ is indicated as a blue dashed dotted curve, the red solid curve is a fit to the ANKE data as obtained in [M$^+$07]. Without the consideration of the finite excess energy resolution of the ANKE data, the fit model results in the red dashed curve.

Figure 2.7 shows an enlarged view of the total cross section for excess energies below $Q = 12\,\text{MeV}$. Without any initial and final state interaction the cross section is expected to increase proportionally to the square root of Q as shown in chapter 2.3.2 and illustrated by the arbitrarily scaled blue dashed dotted curve in figure 2.7. The data from SPES-II [M$^+$96], COSY-11 [S$^+$07], and ANKE [M$^+$07], however, exhibit a much steeper increase of the cross section within the first few MeV of excess energy. This can be explained by a strong final state interaction [FW95]. For increasing excess energies, the observed behavior differs between the various experiments. The ANKE and SPES-II data indicate a slightly dropping cross section for higher Q values, whereas the COSY-11 data published by Smyrski et al. suggest a cross section that increases further. A theoretical model capable to describe the enhancement and slope seen by the ANKE measurements is the two-step model including a strong final state interaction [M$^+$07]. It is illustrated by the red solid curve shown in figure 2.7. Note that for the fit the finite excess energy resolution of the experiment was considered. The red dashed curve presents the shape of this model for an infinite excess energy resolution.

As can be seen in figure 2.6, the data measured at about 20 MeV excess energy with the ANKE [R$^+$09] and WASA/PROMICE [B$^+$02, B$^+$04] experiments, which are in good agreement with each other, agree with the decrease observed by ANKE [M$^+$07] and SPES-II [M$^+$96]. Furthermore, both the ANKE [R$^+$09] and WASA/PROMICE [B$^+$02, B$^+$04] data exhibit a plateau at a slightly higher total cross section value for excess energies above $Q = 40\,\text{MeV}$. Whilst the cross sections measured at COSY-11 and published by Adam et al. [A$^+$07] agree with the data from these experiments within uncertainties, they indicate a continuous drop of the cross section, which is steeper than the one suggested by SPES-II [M$^+$96] and ANKE [M$^+$07]. The measured cross sections close to the η meson threshold can be explained by the two-step model including final state interaction, while no commonly approved theoretical two-step model approach exists which can describe the cross sections observed in data for higher excess energies. The turquoise dashed curve shown in figure 2.6 illustrates a two-step model including s-wave for the final state interaction and s-, p- and d-waves in the reaction mechanism [KKJ07]. Although it is able to reproduce the shape of the data for excess energies close to threshold, it fails to describe the data at higher energies. It should be noted that the peak-like structure at about 20 MeV excess energy is an artifact of the model being limited to lower excess energies and has no physical meaning [KKJ12].

The total cross section at $Q = 48.8\,\mathrm{MeV}$ measured at GEM [B$^+$00] is considerably larger than the plateau observed by WASA/PROMICE and ANKE. Betigeri et al. explained their data with an excitation of a N*(1535) resonance in the intermediate state as the major production mechanism illustrated by the red solid curve in figure 2.6 (see chapter 2.3.3). As the strength of the resonance was scaled to agree with their determined total cross section, it fails to describe the data obtained by WASA/PROMICE and ANKE. Furthermore, the enhancement close to threshold cannot be reproduced. However, considering the statistical and systematic uncertainties, the GEM data point is compatible with a plateau in the total cross section. In order to clarify the situation, in 2009 data were recorded with the WASA-at-COSY detector setup at $Q = 48.8\,\mathrm{MeV}$ excess energy for the reaction $\mathrm{p} + \mathrm{d} \rightarrow {}^3\mathrm{He} + \eta$ in addition to the $Q = 59.8\,\mathrm{MeV}$ data collected for the η meson decay studies. A first analysis of these data was done by A. Passfeld in her diploma thesis [Pas10] and subsequently continued as a major part of this thesis.

Discussion of the differential cross section data base

The two reactions $\mathrm{p} + \mathrm{d} \rightarrow {}^3\mathrm{He} + \eta$ and $\mathrm{d} + \mathrm{p} \rightarrow {}^3\mathrm{He} + \eta$ differ in the beam particle used, resulting in an opposite angular distribution in the center of mass system for the same final state particle. As there are only two particles in the final state of these reactions, equation 2.21 applies:

$$\cos\vartheta_\eta^{\mathrm{CMS}} = -\cos\vartheta_{^3\mathrm{He}}^{\mathrm{CMS}}\,. \tag{2.35}$$

Therefore, the differential distribution of $\cos\vartheta_\eta^{\mathrm{CMS}}$ determined for the reaction $\mathrm{p} + \mathrm{d} \rightarrow {}^3\mathrm{He} + \eta$ is equal to the differential distribution of $\cos\vartheta_{^3\mathrm{He}}^{\mathrm{CMS}}$ extracted from the reaction $\mathrm{d} + \mathrm{p} \rightarrow {}^3\mathrm{He} + \eta$ at the same excess energy. In the following the differential cross sections will be shown depending on $\cos\vartheta_\eta^{\mathrm{CMS}}$ for the reaction $\mathrm{p} + \mathrm{d} \rightarrow {}^3\mathrm{He} + \eta$ and on $\cos\vartheta_{^3\mathrm{He}}^{\mathrm{CMS}}$ for the reaction $\mathrm{d} + \mathrm{p} \rightarrow {}^3\mathrm{He} + \eta$, respectively. For simplification the label $\cos\vartheta_{\mathrm{CMS}}$ will be used in both cases.

As already mentioned in chapter 2.3.1, the differential cross section distributions depending on $\cos\vartheta_{\mathrm{CMS}}$ are expected to be flat in case of simple phase space behavior. Deviations from this expectation allow to study the contributions of other partial waves. These studies contribute to the investigation of different production models.

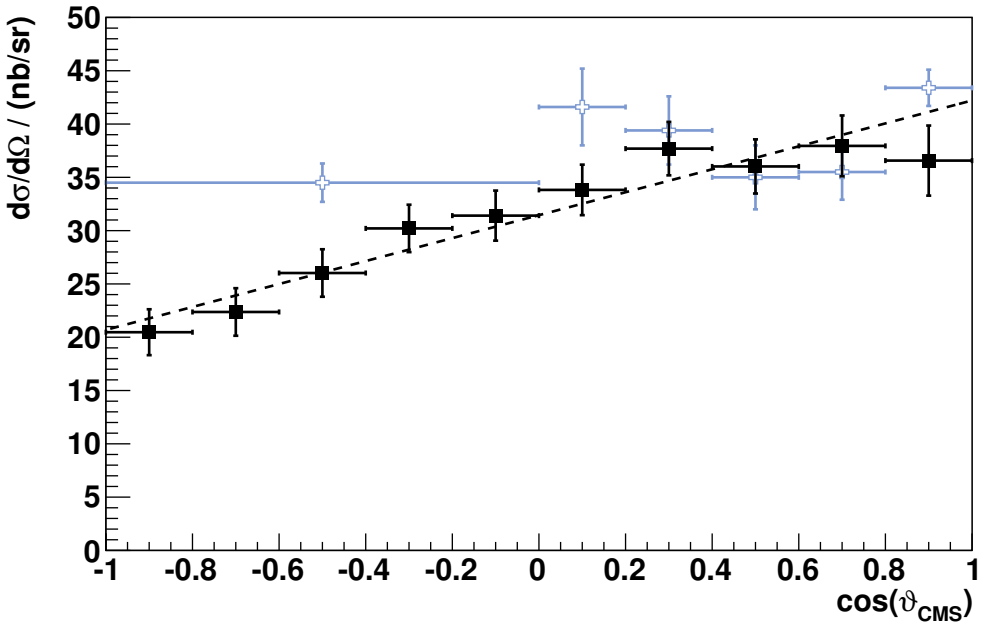

Figure 2.8.: Differential cross sections of the $Q = 10.74\,\mathrm{MeV}$ ANKE data (filled black squares [M$^+$07]) and the $Q = 10.3\,\mathrm{MeV}$ COSY-11 data (open light blue crosses [A$^+$07]). The black dashed line is a linear fit to the ANKE data. The horizontal bars indicate the angular bin widths.

First measurements close to the η meson threshold were limited to differential cross sections at $\cos\vartheta_{\mathrm{CMS}} = -1$ and $\cos\vartheta_{\mathrm{CMS}} = 1$ [B$^+$88, M$^+$96]. Since detailed measurements at the COSY-11 and at the ANKE experiment were performed, it is possible to study the angular distributions in this energy region in more detail [S$^+$07, M$^+$07]. Both data sets show no asymmetry in the differential cross section distribution for excess energies below $Q = 2\,\mathrm{MeV}$, indicating a pure s-wave behavior.

For $Q > 2\,\mathrm{MeV}$ an asymmetry of the angular distribution has been observed both by Mersmann et al. and Smyrski et al., whereas the measurements published by Adam et al. do not show this asymmetry for the $Q = 4.5\,\mathrm{MeV}$ and $Q = 10.3\,\mathrm{MeV}$ data [A$^+$07]. Possible reasons might be the complex detector acceptances and, thus, systematic uncertainties of the latter data sets [Rau09]. Furthermore, the data only contain one value for $\cos\vartheta_{\mathrm{CMS}} < 0$. Figure 2.8 shows the differential cross sections measured at ANKE at $Q = 10.74\,\mathrm{MeV}$ by Mersmann et al. [M$^+$07] and those measured at COSY-11 at $Q = 10.3\,\mathrm{MeV}$ by Adam et al. [A$^+$07]. The black dashed line is a linear fit to the ANKE data. In addition to s-wave contributions, the

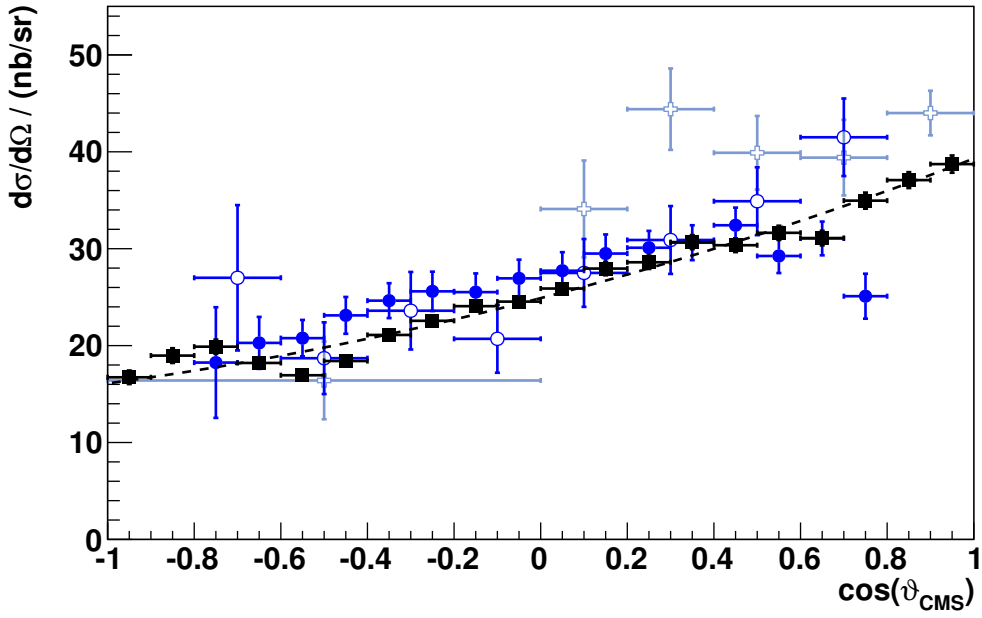

Figure 2.9.: Differential cross sections of the $Q = 20.0\,\text{MeV}$ WASA/PROMICE data (blue circles [B$^+$02, B$^+$04]), the $Q = 19.4\,\text{MeV}$ COSY-11 data (open light blue crosses [A$^+$07]), and the $Q = 19.5\,\text{MeV}$ ANKE data (filled black squares [R$^+$09]). The filled blue circles show the WASA/PROMICE data from the analysis requiring only a ^{3}He detected, while the open circles represent the data from the $\eta \to \gamma + \gamma$ analysis. The black dashed line is a fit to the ANKE data. The horizontal bars indicate the angular bin widths.

linear rise of the distribution observed by Mersmann et al. indicates contributions by p-waves.

Figure 2.9 shows the differential cross sections determined with the experiments WASA/PROMICE [B$^+$02, B$^+$04], COSY-11 [A$^+$07], and ANKE [R$^+$09] at an excess energy of about 20 MeV. From the WASA/PROMICE publication both results determined in an analysis requiring only a ^{3}He detected and by a $\eta \to \gamma + \gamma$ decay analysis are shown. Due to the additional requirement of two photons detected in the central detector, the data points of the latter analysis have significantly larger statistical uncertainties. Just like for the other excess energies, there is only one data point with $\cos\vartheta_{\text{CMS}} < 0$ measured by Adam et al. For the angular bins with $\cos\vartheta_{\text{CMS}} \leq 0.7$ the distributions determined at WASA/PROMICE and ANKE are in good agreement. Nonetheless, for $\cos\vartheta_{\text{CMS}} > 0.7$ both experiments show a different behavior. The WASA data derived by the ^{3}He missing mass analysis shows a decrease of the cross section, whereas the ANKE data as well as the WASA η decay analysis data show a further increase. This difference in the observed

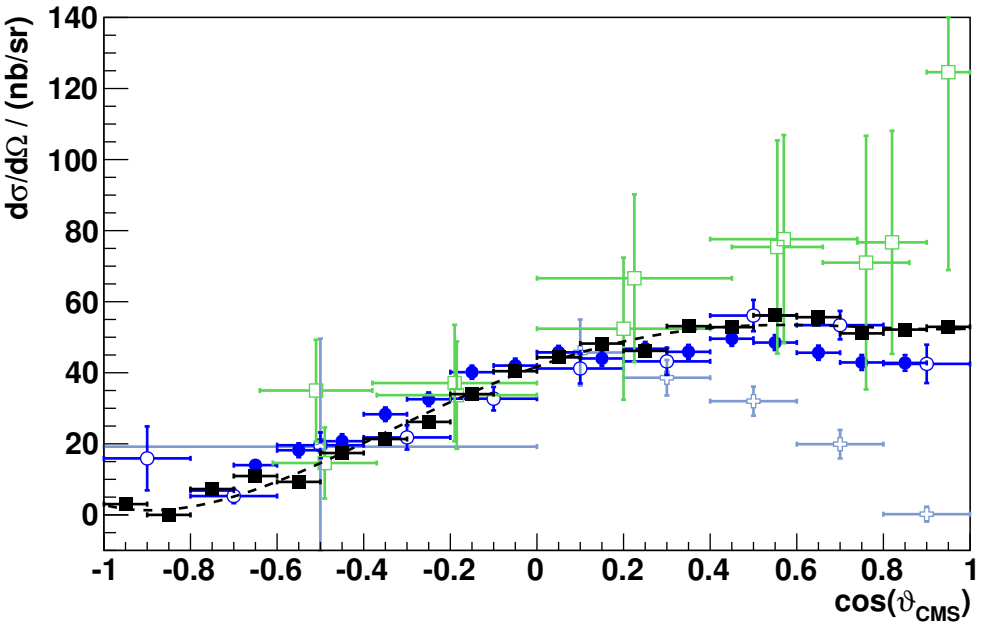

Figure 2.10.: Differential cross sections of the $Q = 48.8\,\mathrm{MeV}$ GEM data (open green squares [B$^+$00]), the $Q = 38.8\,\mathrm{MeV}$ WASA/PROMICE data (blue circles [B$^+$02, B$^+$04]), the $Q = 40.0\,\mathrm{MeV}$ COSY-11 data (open light blue crosses [A$^+$07]), and the $Q = 39.4\,\mathrm{MeV}$ ANKE data (filled black squares [R$^+$09]). The filled blue circles show the WASA/PROMICE data from the analysis requiring only a ^{3}He detected, while the open circles represent the data from the $\eta \to \gamma + \gamma$ analysis. The black dashed line is a fit to the ANKE data. The horizontal bars indicate the angular bin widths.

behavior might be explained by systematic uncertainties of the low acceptances of the WASA/PROMICE experiment for ^{3}He with very low laboratory scattering angles. The black dashed curve presented in figure 2.9 is a fit to the ANKE data by a second order polynomial. Therefore, contributions of s- and p-waves are sufficient for a description of the shape of the angular distribution at this excess energy [Rau09].

Next to differential cross sections measured at WASA/PROMICE [B$^+$02, B$^+$04], COSY-11 [A$^+$07], and ANKE [R$^+$09] at an excess energy of about $Q = 40\,\mathrm{MeV}$, differential cross sections measured at GEM [B$^+$00] at $Q = 48.8\,\mathrm{MeV}$ are presented in figure 2.10. While all measurements are in good agreement for $\cos\vartheta_{\mathrm{CMS}} \leq 0.2$, showing a linear rise of the differential cross section, they disagree for $\cos\vartheta_{\mathrm{CMS}} > 0.2$. The data from ANKE indicate a constant cross section for $\cos\vartheta_{\mathrm{CMS}} > 0.4$. With the exception of the $\cos\vartheta_{\mathrm{CMS}} = 0.9$ data point, the results of the WASA/PROMICE $\eta \to \gamma+\gamma$ analysis agree very well with this behavior. The ^{3}He missing mass analysis data from the same experiment either indicate a plateau starting already at smaller

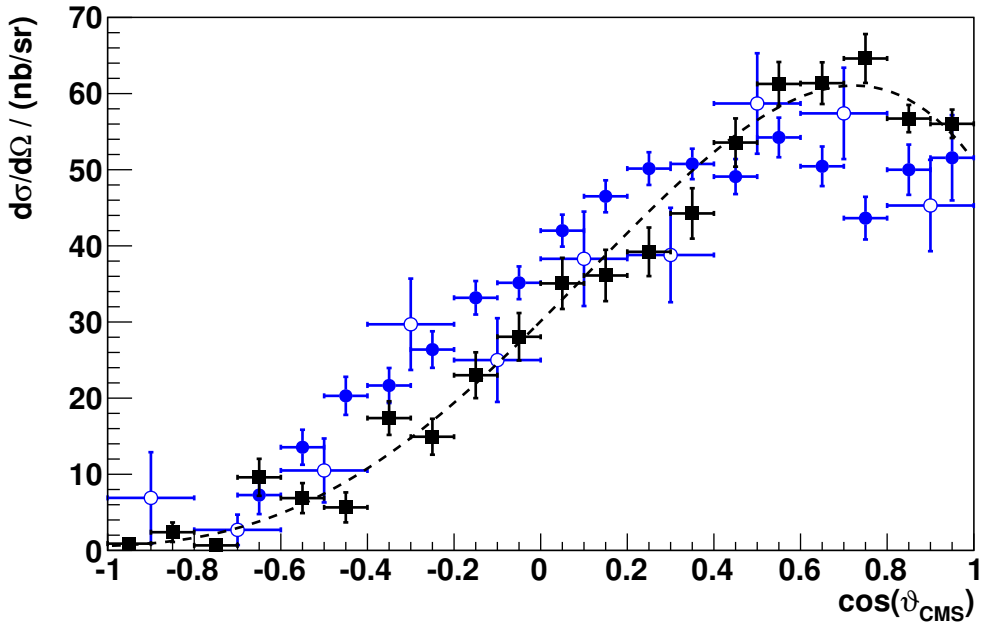

Figure 2.11.: Differential cross sections of the $Q = 77.9\,\text{MeV}$ WASA/PROMICE data (blue circles [B$^+$02, B$^+$04]) and the $Q = 59.4\,\text{MeV}$ ANKE data (filled black squares [R$^+$09]). The filled blue circles show the WASA/PROMICE data from the analysis requiring only a ^{3}He detected, while the open circles represent the data from the $\eta \rightarrow \gamma+\gamma$ analysis. The black dashed line is a fit to the ANKE data. The horizontal bars indicate the angular bin widths.

angular bins ($\cos\vartheta_{\text{CMS}} > 0$) or a small decrease for $\cos\vartheta_{\text{CMS}} > 0.4$. Compared to the results of COSY-11 and GEM, the differences of the shapes between the WASA/PROMICE and ANKE experiments are small and might be explained by systematic uncertainties due to the low acceptances of WASA/PROMICE for low laboratory scattering angles. The decrease of the cross section observed by Adam et al. with COSY-11 is much steeper than the one possibly seen in the WASA/PROMICE data. On the other hand, the GEM data suggest a continuous rise of the cross section for increasing $\cos\vartheta_{\text{CMS}}$. Nevertheless, the GEM data are compatible with the shape found at ANKE and WASA/PROMICE due to their large uncertainties. Therefore, further data at an excess energy of about 48.8 MeV with much lower uncertainties are needed for clarification. Such measurements were done in 2009 at the WASA-at-COSY experiment and the results will be presented in this thesis. Except for the GEM data, the shape of the angular distribution cannot be described by solely s- and p-wave contributions, but does additionally require higher partial waves, like d-waves.

The studies of the η decay $\eta \to \pi^0 + e^+ + e^-$ presented in this thesis are based on $p + d \to {}^3He + \eta$ production runs at an excess energy of about 60 MeV. For reliable analysis results, and reliable acceptance corrections in detail, the knowledge of the differential cross section at this energy is crucial. Figure 2.11 shows the differential cross section depending on $\cos\vartheta_{CMS}$ as determined with the ANKE data at 59.4 MeV excess energy [R$^+$09] as well as the WASA/PROMICE data at $Q = 77.9$ MeV. The black dashed line is a fourth order polynomial fit to the ANKE data. While the shape of the distributions change noticeably between $Q = 20$ MeV and $Q = 40$ MeV, there are only minor differences for the excess energies 40 MeV, 60 MeV, and 80 MeV according to the results from ANKE and WASA/PROMICE. Compared to the 20 MeV and 40 MeV ANKE measurements, the uncertainties of the differential cross sections at 60 MeV are larger.

If there was an enhancement of the total cross section at about 50 MeV excess energy as indicated by the GEM data, this might also be visible in the differential cross sections at this energy, if compared to the distributions at 40 MeV and 60 MeV excess energy. Thus, the differential cross section distribution was determined at $Q \approx 60$ MeV in addition to the one at about 50 MeV as a part of this thesis. As a result systematic uncertainties due to measurements at different experiments are avoided.

Further detailed discussions of the differential and total cross sections for the reactions $p + d \to {}^3He + \eta$ and $d + p \to {}^3He + \eta$ close to the η meson threshold can be found in the doctoral thesis of T. Mersmann [Mer07] as well as in the doctoral thesis of T. Rausmann in case of higher excess energies [Rau09].

2.4. The η meson decay $\eta \to \pi^0 + e^+ + e^-$

The η meson decay $\eta \to \pi^0 + e^+ + e^-$ is well suited to search for a violation of the C parity conservation in electromagnetic interactions [BFL65, PC65, RK65, B$^+$67a, B$^+$67b, B$^+$68, J$^+$75, KW11]. If the decay occurs as

$$\eta \to \pi^0 + \gamma^* \to \pi^0 + e^+ + e^- \tag{2.36}$$

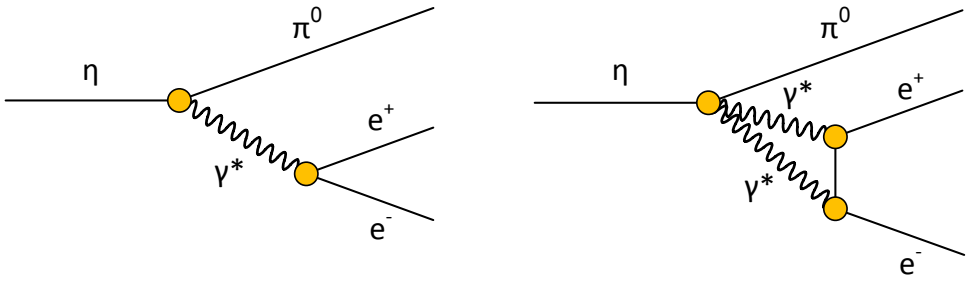

Figure 2.12.: Schematic diagram of the η meson decay $\eta \to \pi^0 + e^+ + e^-$ for a C parity violating decay via one virtual photon (left) and for a C parity conserving decay via two virtual photons (right).

(see figure 2.12, left), it violates C parity conservation, as

$$\begin{aligned} C(\pi^0\gamma^*) &= C(\pi^0) \cdot C(\gamma^*) \\ &= (+1) \cdot (-1) = -1 \\ &\neq +1 = C(\eta)\,. \end{aligned} \tag{2.37}$$

In previous measurements this η decay channel has not been observed yet, but an upper limit for the branching ratio of the decay was determined to be

$$\frac{\Gamma(\eta \to \pi^0 + e^+ + e^-)}{\Gamma(\eta \to \text{all})} < 4 \times 10^{-5} \qquad (\text{CL} = 90\,\%)\,[\text{P}^+16]. \tag{2.38}$$

Besides performing as a decay via one virtual photon, the decay $\eta \to \pi^0 + e^+ + e^-$ may perform via two virtual photons as

$$\eta \to \pi^0 + \gamma^* + \gamma^* \to \pi^0 + e^+ + e^- \tag{2.39}$$

(see right of figure 2.12). In this case the C parity is conserved:

$$\begin{aligned} C(\pi^0\gamma^*\gamma^*) &= C(\pi^0) \cdot C(\gamma^*) \cdot C(\gamma^*) \\ &= (+1) \cdot (-1) \cdot (-1) = +1 \\ &= C(\eta)\,. \end{aligned} \tag{2.40}$$

Since this decay is a fourth order electromagnetic process, it is suppressed and has an expected branching ratio orders of magnitude below the current upper limit

of 4×10^{-5} (CL = 90 %) [P+16]. Theoretical calculations for the branching ratio of this decay mode are based on the already observed η decay $\eta \to \pi^0 + \gamma + \gamma$ with a branching ratio of $(2.56 \pm 0.22) \times 10^{-4}$ [P+16], and the extracted branching ratios vary between 10^{-11} to 10^{-8} [Che67, Smi68, NP93, JS02]. The differences between these calculated branching ratios originate from differences of the models and assumptions used. While vector meson dominance model (VMD) calculations by T. P. Cheng result in an expected branching ratio of about 10^{-8}, he pointed out that this ratio might be lower by an order of magnitude if one assumes pure s-wave coupling for $\eta \to \pi^0 + \gamma + \gamma$ and VMD for $\eta \to \pi^0 + e^+ + e^-$ [Che67]. Calculations by J. Smith, on the other hand, result in a branching ratio for the C conserving decay $\eta \to \pi^0 + e^+ + e^-$ in the order of 10^{-11} under the assumption of pure s-wave interaction and neglecting possibly large contributions of p-wave terms by virtual vector mesons [Smi68]. Newer calculations by J. N. Ng and D. J. Peters suggest a branching ratio of about 3×10^{-9} utilizing a vector meson dominance model and a branching ratio in the range of 1×10^{-9} to 6×10^{-9} using a quark box diagram for the calculations [NP93].

In summary, an observation of the decay $\eta \to \pi^0 + e^+ + e^-$ with a branching ratio significantly above 10^{-8} would indicate a violation of the C parity conservation in the electromagnetic interaction. The search for the decay $\eta \to \pi^0 + e^+ + e^-$ is one major part of this thesis (see chapter 6).

For the search for the C parity violating decay $\eta \to \pi^0 + \gamma^* \to \pi^0 + e^+ + e^-$ the knowledge of the decay amplitude is important, as it can influence the choice of selection conditions and the reconstruction efficiency of this decay (see chapters 6.7 and 7). In order to determine the decay amplitude, certain constraints have to be taken into account. For instance, the η decay $\eta \to \pi^0 + \gamma$, which is the on-shell analog of the off-shell decay $\eta \to \pi^0 + \gamma^*$, does not only violate the C parity conservation, but also the angular momentum conservation, as will be shown in chapter 2.4.1 [Sak64, KW11, Wir17]. Since it is reasonable to assume a conservation of the angular momentum, there should be no on-shell contribution to the decay $\eta \to \pi^0 + \gamma^*$. Apart from angular momentum conservation, the global gauge invariance forbids the on-shell decay (see chapter 2.4.2). The implications of this on the amplitude for the decay $\eta \to \pi^0 + \gamma^* \to \pi^0 + e^+ + e^-$ will be discussed in chapter 2.4.2.

In addition to the decay $\eta \to \pi^0 + e^+ + e^-$, further η-decays can be investigated to search for a C parity violation (see also chapter 2.2.1). For example, the C parity

conservation can be tested in the decays $\eta \to \pi^+ + \pi^- + \gamma$ and $\eta \to \pi^+ + \pi^- + \pi^0$. Here a violation results in an asymmetry of the energy distributions of the π^+ and π^- meson [BFL65, Lee65] or is visible in the pion angular distribution [BT66]. Analyses of these decays were performed with the WASA-at-COSY facility, too. Details about the analyses of the decay $\eta \to \pi^+ + \pi^- + \gamma$, including studies of the pion angular distribution, can be found in [Red10, Ler14], whereas more information about asymmetry studies for the decay $\eta \to \pi^+ + \pi^- + \pi^0$ is given in [Adl12].

2.4.1. Violation of angular momentum conservation in $\eta \to \pi^0 + \gamma$

The η meson is a pseudoscalar meson with the total angular momentum $J = 0$ and spin $S = 0$ (see chapter 2.2). In order to investigate the total angular momentum of the final state of the decay $\eta \to \pi^0 + \gamma$, the axis of quantization (z) is chosen along the $\pi^0 - \gamma$ decay line [Sak64, Wir17]. Consequently, it is $L_z = 0$ for the final state. Furthermore, it is $S(\pi^0) = S_z(\pi^0) = 0$, as the π^0 is a pseudoscalar meson, as well, and $S_z(\gamma) = \pm 1$. This results in a total angular momentum of $J_z = S_z(\gamma) = \pm 1$, which is in contradiction to $J_z(\eta) = 0$. Thus, the decay $\eta \to \pi^0 + \gamma$ does not only violate C parity conservation, but also angular momentum conservation. Under the reasonable assumption of angular momentum conservation the amplitude of the on-shell decay $\eta \to \pi^0 + \gamma$ must vanish, accordingly [KW11, Wir17].

2.4.2. Amplitude of the decay $\eta \to \pi^0 + \gamma^* \to \pi^0 + e^+ + e^-$

For the process $\eta \to \pi^0 + \gamma^*$ the matrix element $K^\mu(x; p_\eta, p_\pi)$ of the transition current $\mathcal{J}^\mu$ in general has the form

$$\begin{aligned} K^\mu(x; p_\eta, p_\pi) &\equiv \left\langle \pi^0(p_\pi) \left| \mathcal{J}^\mu(x) \right| \eta(p_\eta) \right\rangle \\ &= \left[f_1(q^2)\,(p_\eta + p_\pi)^\mu - f_2(q^2)\,(p_\eta - p_\pi)^\mu \right] e^{-i(p_\eta - p_\pi)\cdot x} \\ &= \left[f_1(q^2)\,(p_\eta + p_\pi)^\mu - f_2(q^2) q^\mu \right] e^{-iq\cdot x} \text{ [Wir17]} \end{aligned} \tag{2.41}$$

with the four-momenta p_η and p_π of the η and π^0 meson and the form factors $f_1(q^2)$ and $f_2(q^2)$, which only depend on the four-momentum transfer

$$q^2 = (p_\eta - p_\pi)^2 \text{ [BFL65, Wir17]}. \tag{2.42}$$

Due to global gauge invariance in QED the transition current has to be conserved [BFL65, Wir17]:

$$\begin{aligned} 0 &= \partial_\mu K^\mu\left(x; p_\eta, p_\pi\right) \equiv \partial_\mu \left\langle \pi^0(p_\pi) \left| \mathcal{J}^\mu(x) \right| \eta(p_\eta) \right\rangle \\ &= -i\left[f_1(q^2)\left(p_\eta + p_\pi\right)\cdot q - f_2(q^2)q^2\right] e^{-iq\cdot x} \\ &= -i\left[f_1(q^2)\left(p_\eta^2 - p_\pi^2\right) - f_2(q^2)q^2\right] e^{-iq\cdot x} \\ &= -i\left[f_1(q^2)\left(m_\eta^2 - m_\pi^2\right) - f_2(q^2)q^2\right] e^{-iq\cdot x}\,. \end{aligned} \tag{2.43}$$

As a consequence it is

$$f_1(q^2)\left(m_\eta^2 - m_\pi^2\right) = f_2(q^2)q^2\,, \tag{2.44}$$

which results in two valid approaches for the calculation of K^μ, namely:

$$f_1(q^2) = f_2(q^2)\frac{q^2}{m_\eta^2 - m_\pi^2} \tag{2.45}$$

$$\Rightarrow K^\mu\left(x; p_\eta, p_\pi\right) = \frac{f_2(q^2)}{m_\eta^2 - m_\pi^2}\left[\left(p_\eta + p_\pi\right)^\mu q^2 - \left(m_\eta^2 - m_\pi^2\right) q^\mu\right] e^{-iq\cdot x}\,, \tag{2.46}$$

as used in [BFL65], and

$$f_2(q^2) = f_1(q^2)\frac{m_\eta^2 - m_\pi^2}{q^2} \tag{2.47}$$

$$\Rightarrow \tilde{K}^\mu\left(x; p_\eta, p_\pi\right) = f_1(q^2)\left[\left(p_\eta + p_\pi\right)^\mu - \frac{m_\eta^2 - m_\pi^2}{q^2} q^\mu\right] e^{-iq\cdot x}\,, \tag{2.48}$$

as used in [B$^+$68].

Under the assumption that $\lim\limits_{q^2\to 0} f_i(q^2) = f_i(0)$ is finite, a smooth $q^2 \to 0$ limit exists for the first alternative $K^\mu\left(x; p_\eta, p_\pi\right)$ (see equation 2.46). Furthermore, when coupled to the polarized four-vector $\varepsilon_\mu^*(q)$ of an on-shell photon with momentum q, it is

$$\lim_{q^2\to 0} K^\mu\left(x; p_\eta, p_\pi\right)\varepsilon_\mu^*(q) = 0\,, \tag{2.49}$$

since $q^\mu \varepsilon_\mu^*(q) = 0$ and $\lim\limits_{q^2\to 0}\left(\left(p_\eta + p_\pi\right)^\mu q^2\right) = 0$ [Wir17].

In case of the second alternative $\tilde{K}^\mu\left(x; p_\eta, p_\pi\right)$ (see equation 2.48), the second term $\frac{m_\eta^2 - m_\pi^2}{q^2} q^\mu$ excludes a smooth $q^2 \to 0$ limit. However, when coupled to a conserved current $j_\mu(\mathrm{e^+e^-})$ via a photon propagator, this term vanishes and a

smooth $q^2 \to 0$ limit exists. Nevertheless, when coupled to a real photon, the first term $(p_\eta + p_\pi)^\mu$ does not vanish for the $q^2 \to 0$ limit, as it should (see chapter 2.4.1), except for the case of $f_1(q^2)$ being proportional to q^2 for small q^2. Yet then $f_1(q^2)$ can just be replaced by $q^2 \frac{f_2(q^2)}{m_\eta^2 - m_\pi^2}$, which results in the first alternative given in equation 2.46.

As a consequence only the first term $(p_\eta + p_\pi)^\mu q^2$ contributes if $K^\mu(x; p_\eta, p_\pi)$ is coupled to $j_\mu(\mathrm{e^+e^-})$, as the second term $\left(m_\eta^2 - m_\pi^2\right) q^\mu$ vanishes, since $q^\mu j_\mu(\mathrm{e^+e^-}) = 0$. Moreover, the $\frac{1}{q^2}$ pole of the photon propagator $\frac{g_{\mu\nu}}{q^2}$ exactly cancels with the q^2 numerator of the first term of K^μ.

In summary, the decay amplitude $\mathcal{A}(\eta \to \pi^0 + \gamma^* \to \pi^0 + \mathrm{e^+} + \mathrm{e^-})$ is given by

$$\begin{aligned}
&\mathcal{A}\left(\eta \to \pi^0 + \gamma^* \to \pi^0 + \mathrm{e^+} + \mathrm{e^-}\right) \\
&= K^\mu(x; p_\eta, p_\pi) \left(-i\frac{g_{\mu\nu}}{q^2}\right) \left(ij^\nu(\mathrm{e^+e^-})\right) \\
&= \frac{f_1(q^2)}{q^2} \left[(p_\eta + p_\pi)^\mu - \frac{m_\eta^2 - m_\pi^2}{q^2} q^\mu\right] j_\mu(\mathrm{e^+e^-}) \\
&= \frac{f_1(q^2)}{q^2} (p_\eta + p_\pi)^\mu \, j_\mu(\mathrm{e^+e^-}) \, [\mathrm{Wir17}].
\end{aligned} \tag{2.50}$$

For the calculation of the squared amplitude it can be assumed that the spins of the leptons are not measured, as it is the case in the analysis presented in this thesis. Therefore, the projection tensor $\mathcal{O}_{\mu\mu'}(\mathrm{e^+e^-})$ is constructed from the bilinear combination of the current $j_\mu(\mathrm{e^+e^-}) = j_\mu(p_\mathrm{e}^+, s_\mathrm{e}^+; p_\mathrm{e}^-, s_\mathrm{e}^-)$ summing over all spins s_e^- and s_e^+ of the electron-positron pair. According to [Pet10], the resulting projection tensor is calculated as

$$\mathcal{O}_{\mu\mu'}(\mathrm{e^+e^-}) \equiv \sum_{s_\mathrm{e}^+ = -1/2}^{+1/2} \sum_{s_\mathrm{e}^- = -1/2}^{+1/2} j_\mu(p_\mathrm{e}^+, s_\mathrm{e}^+; p_\mathrm{e}^-, s_\mathrm{e}^-) j_{\mu'}^\dagger(p_\mathrm{e}^+, s_\mathrm{e}^+; p_\mathrm{e}^-, s_\mathrm{e}^-) \tag{2.51}$$

$$= 2e^2 p_\mathrm{e}^2 \left[-\left(g_{\mu\mu'} - \frac{p_{\mathrm{e},\mu} p_{\mathrm{e},\mu'}}{p_\mathrm{e}^2}\right) - \frac{\left(p_\mathrm{e}^+ - p_\mathrm{e}^-\right)_\mu \left(p_\mathrm{e}^+ - p_\mathrm{e}^-\right)_{\mu'}}{p_\mathrm{e}^2}\right] \tag{2.52}$$

with the electrical charge e, the four-momenta $p_{\mathrm{e},\mu}^+$ and $p_{\mathrm{e},\mu}^-$ of the positron and electron, and the four-momentum transfer $q = p_{\mathrm{e},\mu} = p_{\mathrm{e},\mu}^+ + p_{\mathrm{e},\mu}^-$. Utilizing this

tensor and equation B.7 from appendix B.1, the absolute amplitude squared for the decay $\eta \to \pi^0 + \gamma^* \to \pi^0 + e^+ + e^-$ is:

$$\left|\mathcal{A}\left(\eta \to \pi^0 + \gamma^* \to \pi^0 + e^+ + e^-\right)\right|^2 \tag{2.53}$$

$$= \left(\frac{f_1(q^2)}{q^2}\right)^2 (p_\eta + p_\pi)^\mu \, \mathcal{O}_{\mu\mu'}(e^+e^-) \, (p_\eta + p_\pi)^{\mu'} \tag{2.54}$$

$$= \frac{|f_1(q^2)|^2}{(q^2)^2} 2e^2 \left(-4m_\eta^2 q^2 + 16 m_\eta^2 E_{e^+} E_{e^-}\right) \tag{2.55}$$

with the positron and electron energies E_{e^+} and E_{e^-}.

In the case of vector meson dominance, the form factor $f_1(q^2)$ can be written as

$$f_1(q^2) = \frac{e\lambda q^2}{m_x^2 - q^2 - i\sqrt{q^2}\Gamma_x(q)} \tag{2.56}$$

$$\Rightarrow \left|f_1(q^2)\right|^2 = \frac{e^2\lambda^2 (q^2)^2}{(m_x^2 - q^2)^2 + q^2\Gamma_x^2(q^2)} \tag{2.57}$$

with λ as a constant factor [Wir17]. The width $\Gamma_x(q^2)$ of the vector meson x is given by

$$\Gamma_x(q^2) = \begin{cases} 0 & \text{if } q^2 < 4m_\pi^2 \\ g_{m_x} \frac{q^2}{m_x^2} \left(\frac{1 - \frac{4m_\pi^2}{q^2}}{1 - \frac{4m_\pi^2}{m_x^2}}\right)^{\frac{3}{2}} & \text{if } q^2 \geq 4m_\pi^2 \end{cases} \tag{2.58}$$

with $g_{m_x} = 149.1\,\mathrm{MeV}\,c^{-2}$ [EW88, Pet10] and the charged pion mass $m_\pi = 139.570\,18(35)\,\mathrm{MeV}\,c^{-2}$ [P+16]. Since the vector meson dominance model is dominated by the ρ meson for the decay $\eta \to \pi^0 + \gamma^* \to \pi^0 + e^+ + e^-$, the ρ mass m_ρ can be assumed in equation 2.56 [Wir17]. Inserting the form factor squared from equation 2.57 with $m_x = m_\rho = (775.26 \pm 0.25)\,\mathrm{MeV}\,c^{-2}$ [P+16] in equation 2.55, gives the final absolute amplitude squared

$$\begin{aligned} &\left|\mathcal{A}_{\mathrm{VMD}}\left(\eta \to \pi^0 + \gamma^* \to \pi^0 + e^+ + e^-\right)\right|^2 \\ &= \frac{1}{\cancel{(q^2)^2}} \frac{e^2\lambda^2\cancel{(q^2)^2}}{(m_\rho^2 - q^2)^2 + q^2\Gamma_\rho^2(q^2)} 2e^2 \left(-4m_\eta^2 q^2 + 16 m_\eta^2 E_{e^+} E_{e^-}\right) \\ &= \frac{e^2\lambda^2}{(m_\rho^2 - q^2)^2 + q^2\Gamma_\rho^2(q^2)} 2e^2 \left(-4m_\eta^2 q^2 + 16 m_\eta^2 E_{e^+} E_{e^-}\right) \end{aligned} \tag{2.59}$$

as utilized for the Monte Carlo simulations in this thesis (see chapter 6.3.1).

2.5. Missing mass and invariant mass method

The η meson produced in the reaction $p + d \rightarrow {}^3He + \eta$ cannot be detected directly due to its short life time of $\tau = (5.02 \pm 0.19) \times 10^{-19}\,s$ [P+16] (see table 2.3). It decays before it reaches a detector. Instead, the η meson is detected indirectly using either the information of its decay particles (invariant mass method) or the information of all incoming and all other outgoing particles (missing mass method).

2.5.1. Missing mass method

If a particle cannot be detected directly, it is possible to reconstruct its four-momentum from the four-momenta of the ingoing projectiles and all other outgoing ejectiles. In case of the reaction p+d $\rightarrow$ ^{3}He+η, energy and momentum conservation give:

$$p_p^\mu + p_d^\mu = p_{^3He}^\mu + p_\eta^\mu \,. \tag{2.60}$$

As the absolute value of a particle's four-momentum is its rest mass, solving equation 2.60 for p_η^μ and taking the absolute value, one obtains:

$$m_\eta = |p_\eta| = |p_p + p_d - p_{^3He}| \,. \tag{2.61}$$

Besides η mesons, other particles can be produced in reactions of the type p+d $\rightarrow$ ^{3}He+X. At the beam momenta used during the given beam times, these are one to four pions. A plot of the missing mass $m_X = |p_p + p_d - p_{^3He}|$ for a data sample from the WASA-at-COSY $p + d \rightarrow {}^3He + X$ beam time measured in August/September 2009 is presented in figure 2.13. The reaction $p + d \rightarrow {}^3He + \eta$ is visible as a peak at the η mass $m_\eta = (547.862 \pm 0.017)\,MeV\,c^{-2}$ [P+16] with a width due to the limited detector resolution, while the two-, three-, and four-pion productions form the continuous background below the peak. In this thesis the missing mass m_X will be referred to as ^{3}He missing mass.

2.5.2. Invariant mass method

A particle that decays before it reaches a detector can be reconstructed with the four-momenta of its decay particles. Due to energy and momentum conservation

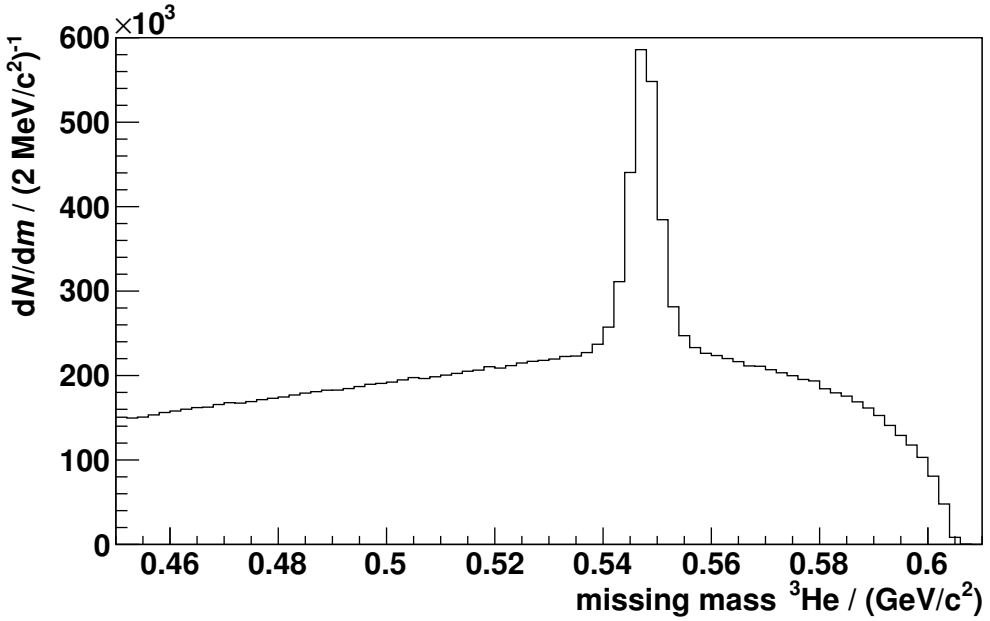

Figure 2.13.: ^{3}He missing mass of a $Q = 59.8\,\mathrm{MeV}$ data sample measured at WASA-at-COSY in August/September 2009. Adapted from [A$^+$14b].

the four-momentum of a particle a decaying into n particles $\mathrm{b}_1, \ldots, \mathrm{b}_n$ is given by:

$$p_\mathrm{a}^\mu = \sum_{i=1}^{n} p_{\mathrm{b}_i}^\mu \,. \tag{2.62}$$

Taking the absolute value of the four-momentum vectors results in the invariant mass

$$m_\mathrm{a} = |p_\mathrm{a}| = \left| \sum_{i=1}^{n} p_{\mathrm{b}_i} \right| \,. \tag{2.63}$$

For example, a π^0 meson that decays into two photons can be reconstructed by:

$$m_{\pi^0} = |p_{\pi^0}| = |p_\gamma + p_\gamma| \,. \tag{2.64}$$

Figure 2.14 shows the invariant mass of two neutral particles calculated with the four-momenta reconstructed with the WASA central detector for a data sample recorded in August/September 2009. The decay $\pi^0 \to \gamma + \gamma$ is visible as a peak at the π^0 mass $m_{\pi^0} \approx 135\,\mathrm{MeV}\,c^{-2}$. The continuous background is formed by photons that originate from other reactions and not from a decay of a single particle into two photons.

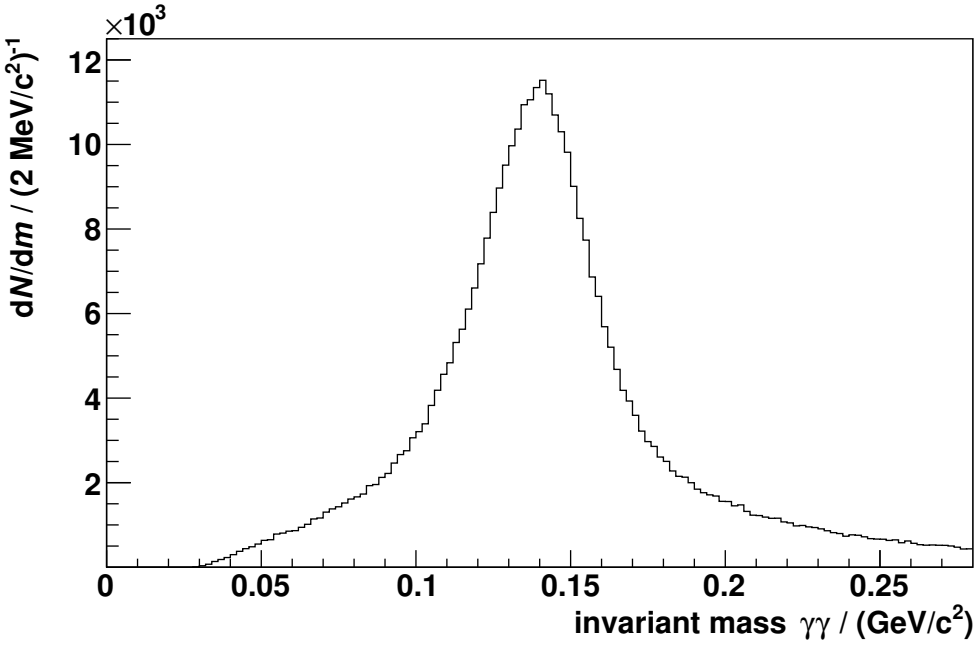

Figure 2.14.: Invariant mass of two photons for a data sample measured at WASA-at-COSY in August/September 2009. The data were preselected using the conditions presented in chapter 6.5.

2.6. Kinematic fitting

A common method utilized in the analysis with regard to a reaction of interest is kinematic fitting. It is a least square fit with constraints that minimizes a χ^2 function [Kup95]. The constraints are implemented by Lagrange multipliers. In the standard version of the implementation used at WASA-at-COSY only energy and momentum conservation of the full system is required, but it is possible to add further constraints to the fit. Examples for such constraints are secondary meson decays like $\pi^0 \to \gamma + \gamma$, where the invariant mass $m_{\gamma\gamma} = |p_\gamma + p_\gamma|$ is fixed to the π^0 mass.

The χ^2 function implemented in the WASA-at-COSY software is:

$$\chi^2 = \sum_{i=1}^{m} \left(\frac{\varepsilon_i}{\Delta v_i} \right)^2 + 2 \sum_{\mu} \lambda_\mu F_\mu(\varepsilon_1, \ldots, \varepsilon_m) \tag{2.65}$$

with the difference $\varepsilon_i = x_i - v_i$ between the fitted values x_i and the measured values v_i, the uncertainty Δv_i of the measured values v_i, and the Lagrange multipliers λ_μ and constraint equations $F_\mu(\varepsilon_1, \ldots, \varepsilon_m)$ for the μ constraints and m kinematic variables.

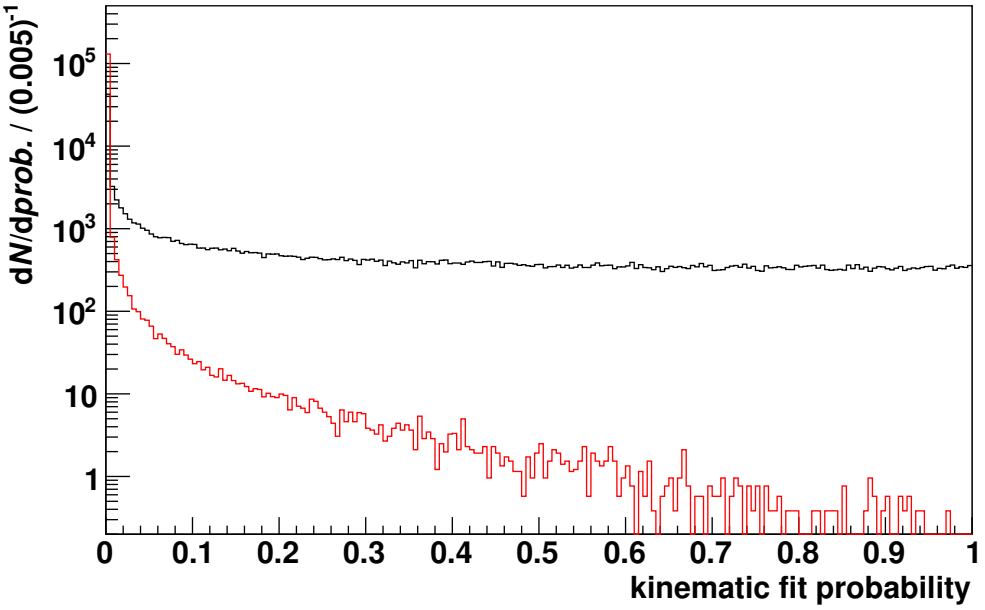

Figure 2.15.: χ^2 probability for the kinematic fit hypothesis of the reaction p+d $\rightarrow$ ^{3}He+ e^++e^-+γ+γ for the simulated reaction p+d $\rightarrow$ ^{3}He+η with $\eta \rightarrow (\pi^0 \rightarrow \gamma + \gamma)$+$e^+$+$e^-$ and $\eta \rightarrow \pi^+ + \pi^- + (\pi^0 \rightarrow \gamma + \gamma)$ (black and red histogram, respectively). The data were preselected using the conditions presented in chapter 6.5.

In order to minimize equation 2.65, its first derivative is set equal to zero and solved for all ε_i. For an estimate of the derivative for the constraint equations, a Taylor series around the measured values v_i is taken, allowing to compute a solution for the Lagrange multipliers λ_μ and the corrections ε_i.

For the method of kinematic fitting the uncertainties Δv_i of the measured values must be known. In this thesis a kinematic fit is used for the analysis with regard to the decay $\eta \rightarrow \pi^0 + e^+ + e^-$, which is based on a common analysis module (see chapter 3.5.3) and requires only energy and momentum conservation without further constraints. The determination of the uncertainties of the measured values was done as part of this common analysis class [BCHW17, Cod12, Wur13].

In the analysis the χ^2 probability of the kinematic fit hypothesis is used to improve the signal to background ratio. As an example figure 2.15 shows the distribution of the χ^2 probability for the hypothesis of the reaction $p + d \rightarrow {}^3He + e^+ + e^- + \gamma + \gamma$ for the simulated reaction $p + d \rightarrow {}^3He + \eta$ with $\eta \rightarrow (\pi^0 \rightarrow \gamma + \gamma) + e^+ + e^-$ and $\eta \rightarrow \pi^+ + \pi^- + (\pi^0 \rightarrow \gamma + \gamma)$ (black and red histogram, respectively). A cut on this probability will be applied to reject events from background reactions (see chapter 6.7).

2.7. Luminosity

In order to determine the cross section of a measured reaction, the obtained results have to be normalized. For this purpose the luminosity of the experiment is used. The luminosity L is the proportional factor between the cross section σ and the rate of events $\mathrm{d}N/\mathrm{d}t$ expected during the experiment:

$$\frac{\mathrm{d}N}{\mathrm{d}t} = L \cdot \sigma \,, \tag{2.66}$$

and it is independent of the reaction. In case of a storage ring like COSY (see chapter 3.1) with a fixed target and full beam-target overlap, it can be calculated from the areal density of the target ρ_{target}, the number of beam particles N_{beam} stored in the ring, and the orbital frequency f:

$$L = \rho_{\mathrm{target}} \cdot N_{\mathrm{beam}} \cdot f \,. \tag{2.67}$$

However, in the analyses presented in this thesis a relative normalization is performed to a second reaction with a known cross section and based on the same triggers (see chapter 4.11). That way uncertainties due to, for example, different trigger efficiencies are avoided.

2.8. Confidence level and upper limit

Typically the results for measurements of rare phenomena are given with a certain confidence level. For example, a given interval $[s_0, s_1]$ with a confidence level $\mathrm{CL} = 90\,\%$ means that if the measurement is repeated several times, in $90\,\%$ of the cases the interval $[s_0, s_1]$ will contain the mean value of an infinite number of such measurements. In case a reaction is not observed, it is also possible to define an upper limit which is an interval of the type $[0, N_{\mathrm{S,up}}]$.

For measurements of rare processes with a low number of events, it is important to consider that these obey the Poisson statistics. In such measurements the upper limit for the number of signal events $N_{\mathrm{S,up}}$ depends on the number of events n observed in data as well as on the number of events b expected from background reactions.

In classical statistics the confidence interval (also called confidence belt) or the upper (confidence) limit is determined using a Neyman construction [Ney37].

Nonetheless, this method suffers from a few disadvantages like the so-called under coverage [Zhu07]. Moreover, according to Feldman and Cousins, the manual choice between an upper limit or a two-sided interval based on the measured data leads to intervals that do not fulfill the properties of a confidence interval [FC98]. Therefore, Feldman and Cousins introduced a new, so-called unified approach for the analysis of small signals.

According to [Zhu07], this method has some drawbacks as well, especially for the case of fewer events being observed than expected. In addition, their method does not take into account systematic uncertainties of the signal efficiency or of the number of events expected from background reactions. For these reasons Zhu introduced an alternative method to consider the mentioned drawbacks and systematic uncertainties of the measurement. It is a Bayesian approach and will be described in the following chapter 2.8.1.

2.8.1. Bayesian approach

In a Bayesian approach a prior probability density function (pdf) for the signal is required for the upper limit calculation. This prior pdf is used as input for the calculation of a posterior pdf with the aid of Bayes' theorem [BP63]. In case of n observed events, and assuming s is the unknown number of signal events, the posterior pdf $h(s|n)$ is given by:

$$h(s|n) = \frac{p(n|s)\pi(s)}{\int_0^\infty p(n|s)\pi(s)\mathrm{d}s} \tag{2.68}$$

with the conditional pdf $p(n|s)$ of observing n events with s given signal events and the prior pdf $\pi(s)$ [Zhu07]. This posterior pdf can be utilized to either calculate a confidence interval $[s_0, s_1]$ or the upper limit $N_{\mathrm{S,up}}$ for the number of signal events and a given confidence level CL by solving

$$\mathrm{CL} = \int_{s_0}^{s_1} h(s|n)\mathrm{d}s \text{ and} \tag{2.69}$$

$$\mathrm{CL} = \int_0^{N_{\mathrm{S,up}}} h(s|n)\mathrm{d}s \text{ , respectively.} \tag{2.70}$$

In general, there are two approaches for the prior pdf $\pi(s)$: an informative and a non-informative prior. The informative prior uses the information available from previous measurements. However, this approach induces difficulties if the

results should be combined afterwards. Thus, in [Zhu07] the non-informative prior approach was chosen. It estimates the prior pdf of the signal to deduce the posterior pdf.

There are different choices for the prior distribution. The most conservative and most commonly chosen one is a flat prior, as suggested by Bayes [BP63]. Nevertheless, there is no mathematical reason that excludes other choices. Two alternatives are $\pi(s) = 1/(s+b)$ and $\pi(s) = 1/\sqrt{s+b}$ derived by Jeffreys [Jef98, Jef46], Jaynes [Jay68], and Box [BT92] with s and b being the expectations for the number of signal and background events.

According to [Nar00a, Nar00b], the prior pdf $\pi(s) = 1/\sqrt{s+b}$ is the most versatile choice for a Bayesian approach to upper limit determination, whereas a flat prior is the most conservative choice [P$^+$16]. For that reason the latter was chosen for the presented analysis, and equation 2.68 simplifies to:

$$h(s|n) = \frac{p(n|s)}{\int_0^\infty p(n|s)\mathrm{d}s}\,. \tag{2.71}$$

Under the assumption that the number of signal events and the number of background events are Poisson variables with the unknown expectation s and known expectation b, respectively, the conditional pdf $p(n|s)$ is

$$p(n|s) = e^{-(s+b)}\frac{(s+b)^n}{n!}\ \text{[Zhu07]}. \tag{2.72}$$

Utilizing this pdf and equation 2.71 in equation 2.69 and 2.70, a confidence interval $[s_0, s_1]$ and an upper limit $N_{\mathrm{S,up}}$ for the number of signal events, respectively, can be calculated assuming b background events in case of n observed events for a given confidence level CL.

However, at this stage no uncertainties of the signal reconstruction efficiency ε_{S} and the expected number of background events b have been included in the calculation. The uncertainties can be incorporated by replacing $p(n|s)$ with

$$q\left(n|s\right)_b = \int_0^\infty \int_0^\infty p\left(n|s\varepsilon\right)_{b'} f_{b'}(b,\sigma_b) f_\varepsilon(1,\sigma_\varepsilon)\mathrm{d}b'\mathrm{d}\varepsilon\,, \tag{2.73}$$

as stated in [Zhu07]. Here $f_{b'}(b,\sigma_b)$ is a pdf with the mean b and the standard deviation σ_b, and $f_\varepsilon(1,\sigma_\varepsilon)$ is a pdf with the mean 1 and the standard deviation σ_ε. These probability density functions represent the distribution of the background

expectation and the distribution of the relative efficiency ε with respect to the mean signal efficiency ε_{S}, respectively. The conditional pdf $p\left(n|s\varepsilon\right)_{b'}$ is given by:

$$p\left(n|s\varepsilon\right)_{b'} = e^{-(s\varepsilon+b')}\frac{\left(s\varepsilon+b'\right)^{n}}{n!}\,. \tag{2.74}$$

Zhu provided a program (BPULE) for the upper limit calculation utilizing the above mentioned method [Zhu07]. In this program the functions $f_{b'}(b,\sigma_b)$ and $f_{\varepsilon}(1,\sigma_{\varepsilon})$ can either be Gaussian, Log-Gaussian or flat distributions. Nevertheless, these functions can be replaced by any other pdf, as performed in an algorithm written by A. Kupść [Kup17] and utilized in this thesis (see chapter 7.2). Hence, with this algorithm it is possible to consider asymmetric uncertainties with individual distributions.

2.8.2. Branching ratio

A major part of this thesis is the search for the decay $\eta \to \pi^0 + \mathrm{e}^+ + \mathrm{e}^-$ with the aim to either determine a branching ratio, in case of an observation, or to give a new upper limit for the branching ratio of the decay. For this purpose a relative normalization to the decay $\eta \to \pi^+ + \pi^- + \pi^0$ will be performed. In case of an upper limit $N_{\mathrm{S,up}}$ for the number of signal events, the relative branching ratio is

$$\frac{\Gamma\left(\eta \to \pi^0 + \mathrm{e}^+ + \mathrm{e}^-\right)}{\Gamma\left(\eta \to \pi^+ + \pi^- + \pi^0\right)} < \frac{N_{\mathrm{S,up}}}{N^{\mathrm{produced}}_{\eta\to\pi^+\pi^-\pi^0}\cdot\varepsilon_{\mathrm{S}}} \tag{2.75}$$

with the signal reconstruction efficiency ε_{S} and the number $N^{\mathrm{produced}}_{\eta\to\pi^+\pi^-\pi^0}$ of $\eta \to \pi^+ + \pi^- + \pi^0$ decays in the collected data, which already comprises the reconstruction efficiency and corresponds to the actual number of occurred reactions.

3. WASA-at-COSY

The **W**ide **A**ngle **S**hower **A**pparatus (WASA) was developed for studies of light meson production mechanisms and their decays [HR$^+$04]. Originally it was constructed and operated at the storage ring CELSIUS in Uppsala. After the shutdown of the CELSIUS accelerator in 2005 the WASA experiment was transported to Forschungszentrum Jülich and installed at the cooler synchrotron COSY (see chapter 3.1). Here several beam times were held between August 2006 and June 2014. The analysis of the collected data covers production and decay studies of the π^0 meson [A$^+$13a, A$^+$13d, A$^+$14a], the η meson [A$^+$09, A$^+$12b, A$^+$13e, A$^+$14b, A$^+$14d, A$^+$16b, A$^+$17], the ω meson, and the η' meson as well as studies of the $\pi\pi$ production [A$^+$11, A$^+$12a, A$^+$12c, A$^+$13b, A$^+$13c, A$^+$14c, A$^+$14e, A$^+$15c, A$^+$15d, A$^+$16a] and 4π production [A$^+$16c], and studies are still ongoing. During its operation the WASA detector setup was changed a few times to comply the needs of the different experiments. The last modification was done in spring 2014 [Sit15] for the "Investigation of total cross section structures in the pd $\rightarrow$ ^{3}Heη reaction at WASA-at-COSY" and the "Search for the η-mesic ^{3}He with WASA-at-COSY" [KM14].

The following chapters describe the COSY accelerator and the WASA setup during the p + d $\rightarrow$ ^{3}He + X beam times in September/October 2008 and August/September 2009 on which the analyses presented in this thesis are based.

3.1. Cooler synchrotron (COSY)

The **CO**oler **SY**nchrotron (COSY) [Mai97] is a 184 m long storage ring at the Nuclear Physics Institute at Forschungszentrum Jülich. In 2008 and 2009 the experimental setups WASA, ANKE, and PAX as well as the EDDA detector used as a beam polarimeter were available for operation and located in the two 40 m long straight parts of the accelerator (see figure 3.1). Additionally, the beam can

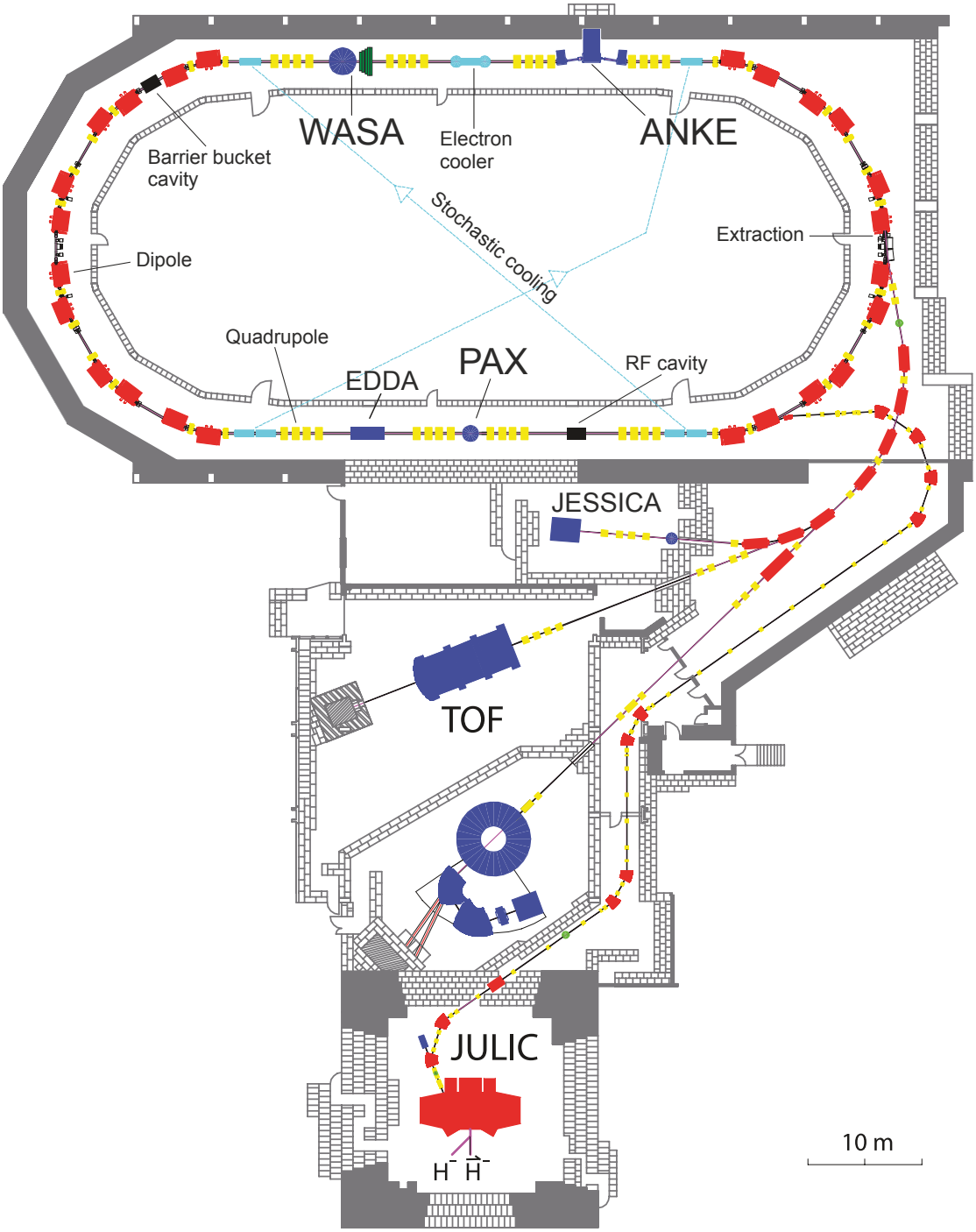

Figure 3.1.: Schematic representation of the COSY accelerator facility with its pre-accelerating cyclotron JULIC and external and internal experimental setups. Adapted from [HR+04].

be extracted to external experimental setups like the now dismantled TOF setup or to the JESSICA area where detectors can be tested.

COSY is operated with either protons or deuterons as beam particles [D+02]. These are provided by two ion sources as polarized or unpolarized H^- and D^- ions. As a minimum energy is required for the acceleration in the COSY ring, the ions are pre-accelerated by the attached cyclotron JULIC to energies of up to 45 MeV/nucleon [B+03]. Afterwards they are induced into the storage ring via a 100 m long injection beam pipe and strip off their electrons at a carbon foil before entering the ring. Here the protons and deuterons reach momenta ranging from 0.3 GeV c^{-1} to 3.7 GeV c^{-1} [HR+04, Wol07].

COSY provides two beam cooling mechanisms to reduce the momentum spread and emittance of the beam. For small proton momenta of up to 600 MeV c^{-1} an electron cooler can be used, while for higher momenta between 1.5 GeV c^{-1} and 3.4 GeV c^{-1} a stochastic cooling system can be applied [P+00]. The electron cooler works by injecting and superimposing an electron beam with the same velocity as the ion beam. The electrons and ions interact with each other, which reduces the phase space and momentum spread of the ion beam. The stochastic cooling system consists of two parts – one 4 m long pickup tank and a 2 m long kicker. Two such pickup-kicker pairs are used to correct the horizontal and the vertical plane, respectively. The signal of the pickup tank is sent to the kicker at the opposite side of the COSY ring which adjusts the beam position accordingly. The stochastic cooling has been designed for an operation with target thicknesses as provided by the ANKE cluster jet target. For the higher thicknesses of the WASA pellet target both cooling methods are insufficient and a different method is applied to compensate the mean energy loss. Since 2007 a barrier bucket cavity has been installed at COSY in addition to the accelerating and decelerating radio frequency cavity (RF cavity) [S+08]. When this barrier bucket cavity is used, the beam particles are grouped in a single bunch and the mean energy loss due to interactions with the target is compensated by the barrier bucket cavity. Using this mechanism, the typical life time of the COSY beam is in the order of one minute if a pellet target is used, and several minutes in case of an operation with a cluster jet target, before new particles are pre-accelerated and injected into the COSY ring, which defines the start of a new cycle.

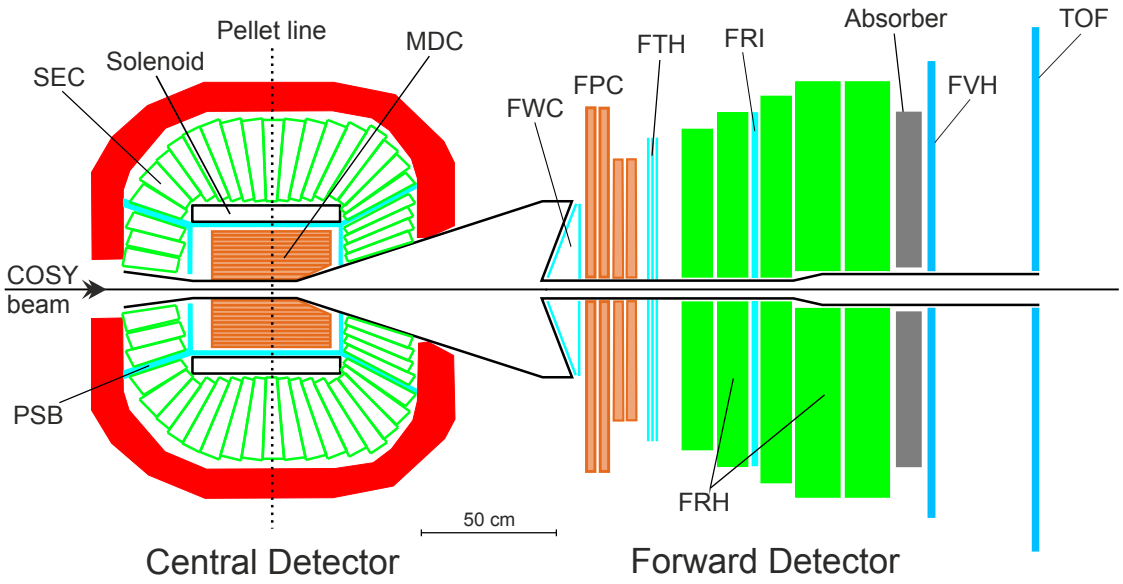

Figure 3.2.: Schematic diagram of the WASA-at-COSY detector setup. The individual components of the central detector (left) and the forward detector (right) are described in the following chapters. Adapted from [HR+04].

3.2. WASA detector setup

The main components of the WASA-at-COSY experimental setup are the pellet target (see chapter 3.2.1), the 4π central detector (see chapter 3.2.2), and the forward detector (see chapter 3.2.3). Figure 3.2 shows a schematic diagram of the WASA detector. The different components are described in the following chapters.

3.2.1. Pellet target

The physics studies done with the WASA experiment have high requirements for the target. For example, in order to reconstruct a meson decay, the vertex needs to be known with high precision. Furthermore, high statistics and therefore high luminosities are needed to search for rare decays. The pellet target fulfills all these requirements. Its high effective thickness of $> 10^{15}\,\mathrm{atoms/cm^2}$ allows for a luminosity of $> 10^{32}\,\mathrm{cm^{-2}\,s^{-1}}$ [E+96, HR+04]. The low pellet beam diameter of 2 mm to 3 mm results in a well defined vertex position [Tro95]. In addition, the pellet generator is installed above the WASA central detector and only a narrow beam pipe through the detector for the pellet target is needed, leading to a high geometrical acceptance. Typical parameters for the WASA-at-COSY pellet target operation are shown in table 3.1.

Table 3.1.: Typical parameters for the WASA-at-COSY pellet target operation. Adapted from [B$^+$09, Win11].

Pellet rate (H_2)	8000 pellets/s
Pellet rate (D_2)	20 000 pellets/s
Pellet diameter	20 µm to 35 µm
Target thickness (H_2)	4×10^{15} atoms/cm^2
Target thickness (D_2)	8×10^{15} atoms/cm^2
Pellet velocity	60 m s^{-1}
Pellet distance	5 mm
Target diameter at interaction point	
with 0.7 mm skimmer diameter	2.5 mm
with 1.0 mm skimmer diameter	3.5 mm
Skimmer diameter	0.7 mm or 1.0 mm
Nozzle diameter	13.2 µm
Nozzle temperature (H_2)	15 K
Nozzle temperature (D_2)	20 K
Pressure in droplet chamber (H_2)	20 mbar
Pressure in droplet chamber (D_2)	60 mbar

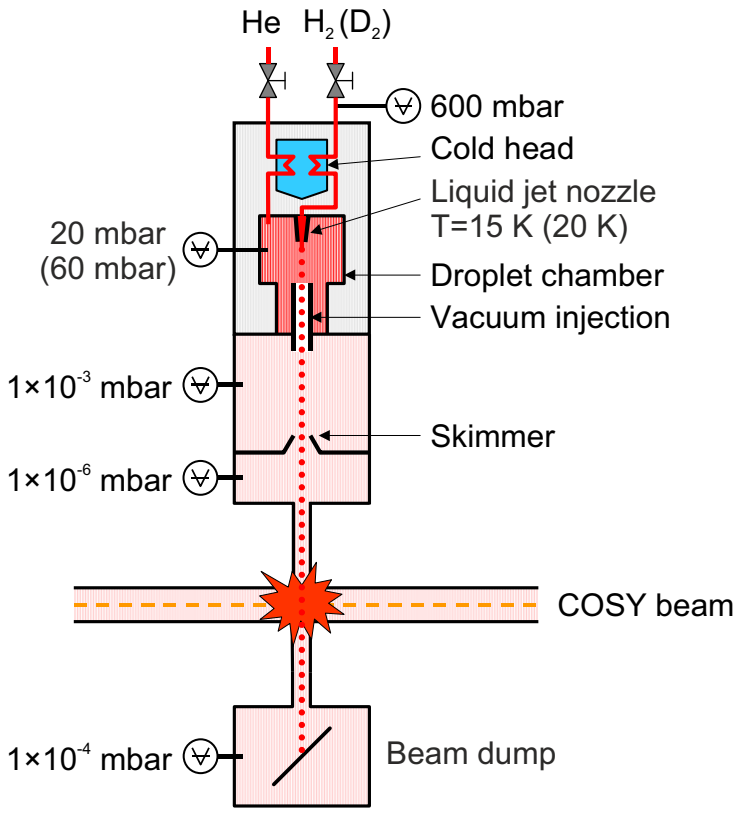

Figure 3.3.: Schematic diagram of the WASA-at-COSY pellet target with typical pressures and nozzle temperatures for the operation with hydrogen (deuterium). Adapted from [Nor04].

The WASA-at-COSY pellet target can be operated with hydrogen as well as deuterium as target material. Its main components are the pellet generator, the differential pumping system, which is needed to achieve the required vacuum conditions, and the pellet beam dump. Figure 3.3 shows a schematic diagram of the pellet target without the pumps.

The target material and helium are cooled down by a cold head to temperatures of around 15 K for the operation with hydrogen and to around 20 K for the deuterium case, which is close to their triple point temperatures (hydrogen: 13.84 K, deuterium: 18.63 K [ÇT05]). The liquified hydrogen/deuterium is led through a glass nozzle with a pressure of typically 400 mbar to 800 mbar into the droplet chamber. This chamber is filled with helium at a pressure of 20 mbar or 60 mbar, respectively. Thus, freezing of the nozzle and evaporation or freezing of the droplets are prevented. The nozzle, having a typical diameter of about 13 µm, is driven by a piezoelectric transducer, which breaks up the liquid beam into droplets with

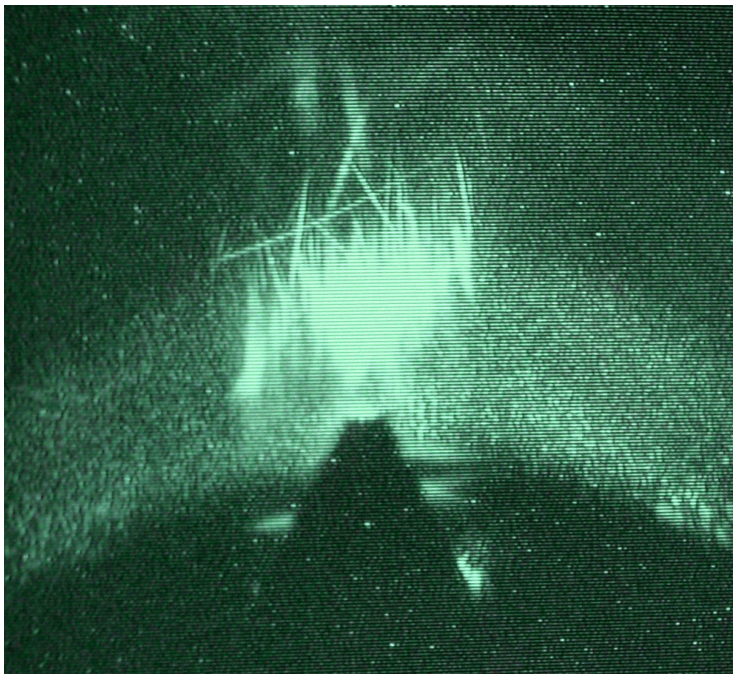

Figure 3.4.: Picture of the skimmer. Above the skimmer (dark truncated cone) the pellet beam (bright spot) and reflected pellets (line traces) illuminated by a laser are visible.

a diameter of approximately 50 µm. The frequency of the piezoelectric crystal is typically in the range of 40 kHz to 80 kHz. After the droplets have flown through the chamber with a velocity of about $26\,\mathrm{m\,s^{-1}}$, they are injected through a glass capillary into the skimmer chamber. The pressure in this chamber is reduced to the order of 10^{-3} mbar by a differential pumping system, which causes the droplets to freeze out into pellets with a diameter of about 20 µm to 35 µm and a velocity of about $60\,\mathrm{m\,s^{-1}}$.

Because of the pressure difference between the two chambers, turbulences emerge in the capillary enlarging the pellet beam diameter. To obtain a well defined narrow pellet beam, a skimmer is installed in the beam path after about 70 cm, which reflects all pellets with too large angles back into the chamber (see figure 3.4). Below the skimmer chamber the pressure is reduced further to the order of 10^{-6} mbar. By using a skimmer with a 0.7 mm diameter, a pellet beam of about 2.5 mm diameter at the interaction point can be created. During the beam times in September/October 2008 and August/September 2009 a skimmer with a diameter of 1.0 mm was used, increasing the pellet beam diameter at the interaction point to about 3.5 mm. This way the pellet rate could be improved significantly to 8000 pellets/s using hydrogen

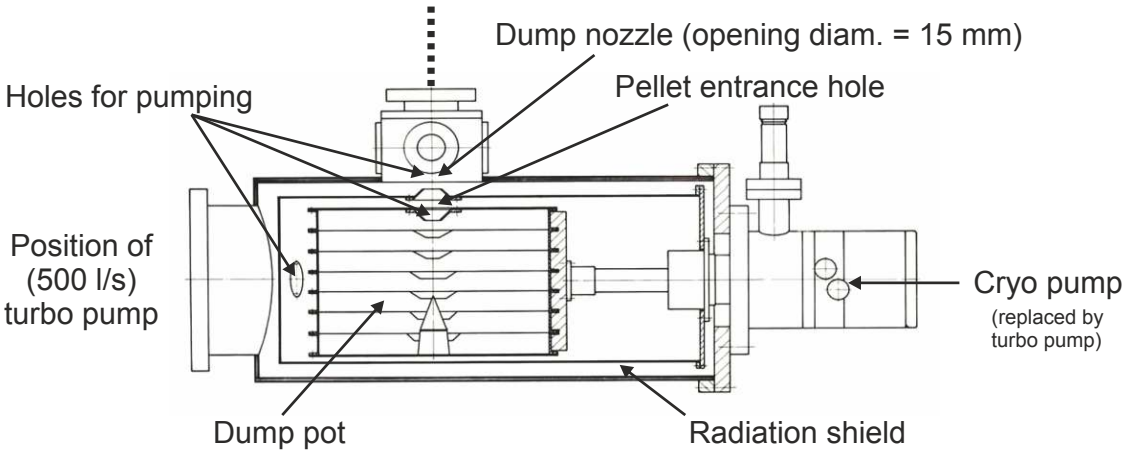

Figure 3.5.: Schematic diagram of the beam dump. The shown kryo pump has been replaced by a second turbo pump for the operation at COSY. Adapted from [Cal08].

and to 20 000 pellets/s using deuterium as target material without increasing the background pressure in the reaction chamber. The typical distance between the individual pellets is about 5 mm, which is slightly larger than the COSY beam diameter. Thereby secondary reactions are avoided.

After the interaction with the COSY beam the pellets are deflected in the beam dump, which is seated below the WASA central detector, where they vaporize (see figure 3.5). The gas in the beam dump is pumped away by two turbo pumps. This way background reactions caused by pellets reflected back into the reaction chamber and interacting with the COSY beam are avoided.

For the operation of the WASA-at-COSY pellet target the used gas has to be of high purity and leaks in the gas system have to be avoided, as the smallest impurity in the gas system can cause the nozzle to block. To achieve this goal both for hydrogen and deuterium pellet production, palladium gas purifiers are used (see figure 3.6). Only hydrogen and deuterium can pass through the membrane of the purifier resulting in a target gas of highest purity. A second purifier from the ANKE experiment in addition to the one directly at the target was used during the beam times in September/October 2008 and August/September 2009. This purifier is connected to the gas supply, which is used by both experiments and located outside of the COSY ring about 30 m away from the WASA-at-COSY experimental setup. While the hydrogen gas is provided by gas bottles, a deuterium generator is used to produce the deuterium gas out of heavy water via electrolysis. The deuterium from the generator has a higher purity than the one from gas bottles. In order to avoid a blocking of the pellet target nozzle due to foreign particles which may enter

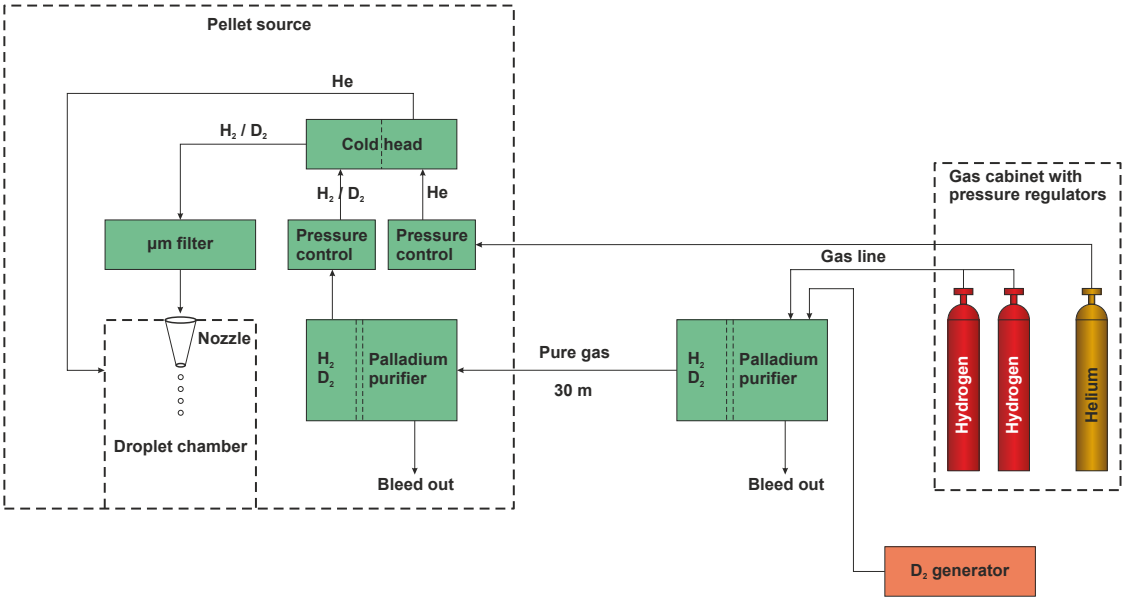

Figure 3.6.: Schematic diagram of the pellet target gas system. Adapted from [Ber09], based on [Kho09].

the gas system during maintenance work, a sinter filter with a pore size of 2 µm is melted into the glass nozzle [W$^+$08a].

A reliable production of pellets requires precise parameter settings matching with each other. The set nozzle temperature must be low enough to create a well defined droplet stream, but not too low to avoid a freezing of the nozzle. The same holds true for the helium pressure in the droplet chamber. The target gas pressure, on the other hand, must be in agreement with the frequency of the piezoelectric transducer which drives the nozzle to produce a proper and stable droplet beam with a constant distance between the individual droplets. Otherwise, the losses due to injection into the skimmer chamber would be too high and a constant pellet rate could not be achieved. Further details about the pellet target and its operation can be found in [B$^+$09, E$^+$96, Tro95, Win11].

3.2.2. Central detector

The central detector (CD) of the WASA experiment has been designed for the detection, identification, and reconstruction of the decay particles of the produced mesons, such as the η meson. It is used to determine the deposited energy and momentum of photons, electrons, and positrons as well as charged pions. The main components of the central detector are the mini drift chamber (MDC)

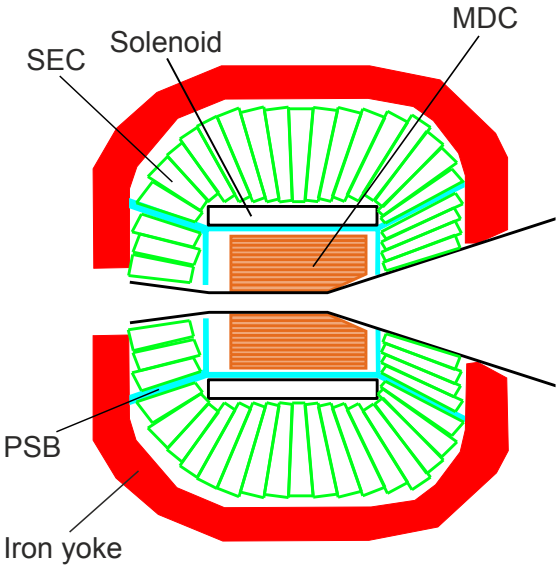

Figure 3.7.: Schematic diagram of the central detector. It contains a mini drift chamber (MDC), a plastic scintillator barrel (PSB), a superconducting solenoid (SCS), and a scintillator electromagnetic calorimeter (SEC) and is surrounded by an iron yoke. The COSY beam direction is from left to right. Adapted from [HR+04].

for momentum and track reconstruction of charged decay particles, the plastic scintillator barrel (PSB) as a veto for photon detection, the superconducting solenoid (SCS), which creates the magnetic field needed for the momentum determination, and a scintillator electromagnetic calorimeter (SEC) to determine the particle energy (see figure 3.7). The whole central detector is surrounded by a 5-ton iron yoke as return path of the magnetic flux and to shield the photomultipliers of the SEC [Koc04].

In order to avoid interactions of the particles with passive material, the amount of used material is reduced as much as possible. For example, the pellet beam pipe through the central detector is made of 1.2 mm thick beryllium [HR+04]. The small atomic size of the beryllium further reduces the possibility of interactions. Thanks to its design the central detector has a geometrical acceptance of 96 %. The individual components of the central detector are described in the following sections.

Mini drift chamber (MDC)

The mini drift chamber is mounted around the scattering chamber (see figure 3.8) and is used for the vertex determination and momentum reconstruction of charged

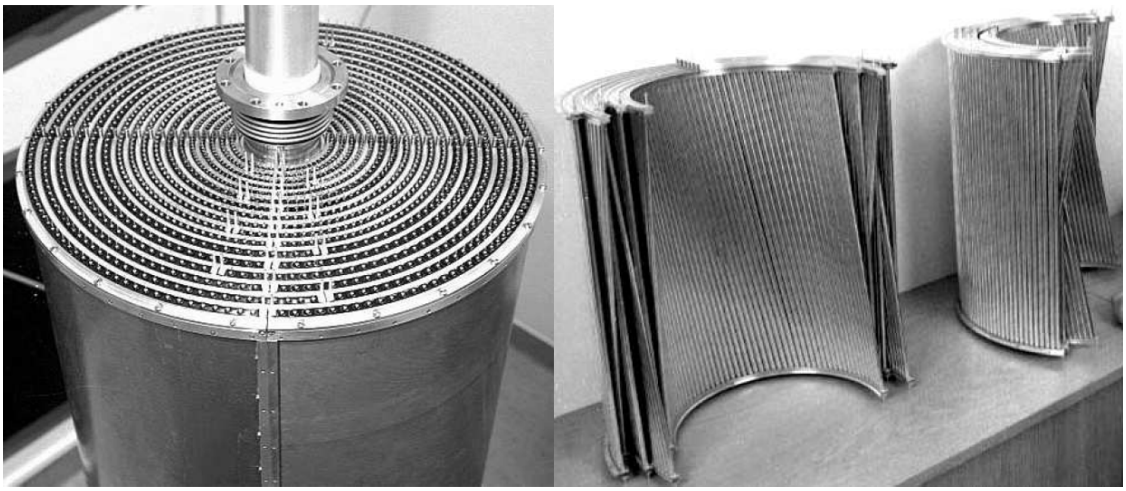

Figure 3.8.: Pictures of the mini drift chamber. Left: Fully assembled around the scattering chamber and surrounded by a Al-Be cylinder. Right: Drift tubes of the different MDC layers. Note the alternating assignment of the layers [HR$^+$04].

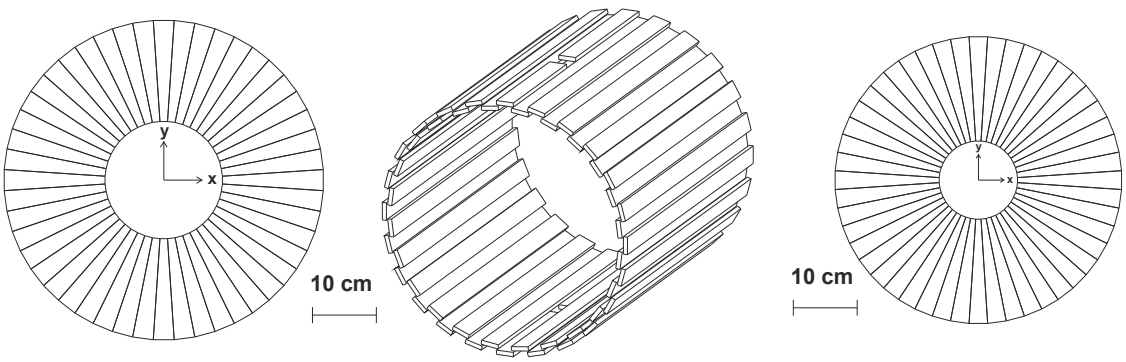

Figure 3.9.: Schematic drawing of the three PSB parts: The front cap, the central part and the backward cap. Note the recesses in the central part for the pellet beam pipe. Adapted from [HR$^+$04].

particles. It covers a scattering angle range of 24° to 159° and consists of 1738 drift tubes (straw tubes) in 17 cylindrical layers. Their diameters range from 4 mm for the inner most layers to 8 mm for the outer layers. In nine layers the straws are parallel to the COSY beam pipe, whereas they are skewed by 6° to 9° in the other eight layers with respect to the beam axis. The hit positions of a charged particle in the different layers allow to reconstruct its trace, and, together with the magnetic field provided by the superconducting solenoid, it is possible to determine its momentum. Further details about the MDC can be found in [Jac04].

Plastic scintillator barrel (PSB)

The plastic scintillator barrel is placed around the MDC and provides fast signals which can be used for a preselection during the data acquisition (first level trigger). Its signals are used as a veto for the photon identification. Together with the signals from the MDC and the SEC, it is employed for the charged particle identification via the $\Delta E - E$ and $\Delta E - p$ methods. It consists of three parts – a cylindrical central part and two end caps (see figure 3.9) – and contains in total 146 strip-shaped elements with a thickness of 8 mm. The central part contains 48(+2) elements with a length of 550 mm and a width of 38 mm. The elements are aligned in two layers and the neighboring elements have a small overlap of 6 mm to avoid acceptance gaps. Two of the elements are divided into two parts with a small gap for the pellet beam pipe. The end caps are radial-shaped with 48 elements each. While the forward part is flat and has an outer and an inner diameter of 51 cm and 19 cm, the backward part forms a conical surface and has an outer and an inner diameter of 42 cm and 12 cm. An acrylic light guide is glued to each scintillator. These light guides are connected to photo multipliers outside of the iron yoke. Further details about the PSB can be found in [HR+04].

Superconducting solenoid (SCS)

The super conducting solenoid (see figure 3.10) surrounds the PSB and provides a magnetic field parallel to the COSY beam axis, which is needed for the momentum reconstruction of charged particles via the MDC. The tracks of the charged particles are bent by the applied magnetic field and their curvature can be determined with the help of the mini drift chamber allowing a calculation of the particle momentum.

The solenoid is made of NbTi/Cu, which is superconducting at low temperatures and, therefore, cooled down to about 4.5 K using liquid helium. A maximum central magnetic flux density of 1.3 T can be produced by the SCS. Its return path is provided by the iron yoke, which also works as a mechanical support structure for the calorimeter crystals. The solenoid's wall thickness of 80 mm equals 0.18 radiation lengths, allowing a highly accurate measurement of the energy deposited in the calorimeter. Further details about the solenoid are available in [Rub99].

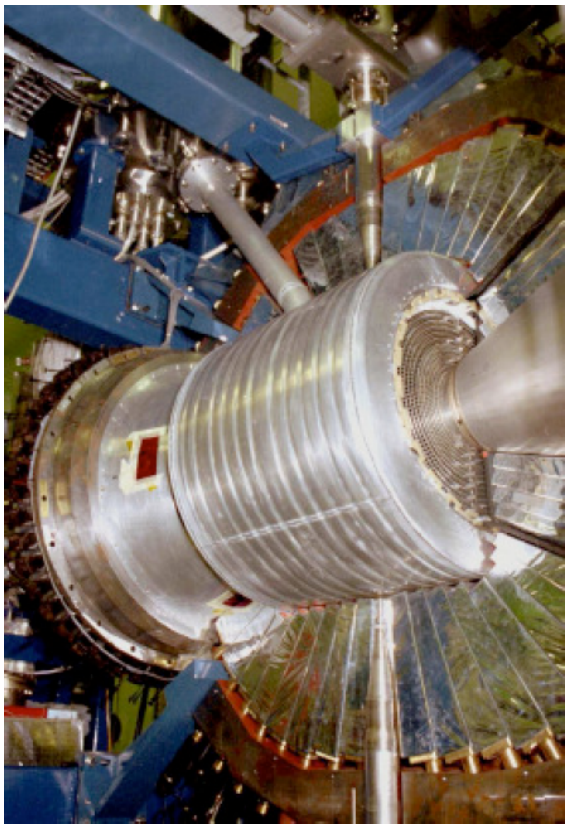

Figure 3.10.: Picture of the superconducting solenoid mounted in the central detector with one yoke half rolled out [WAS17].

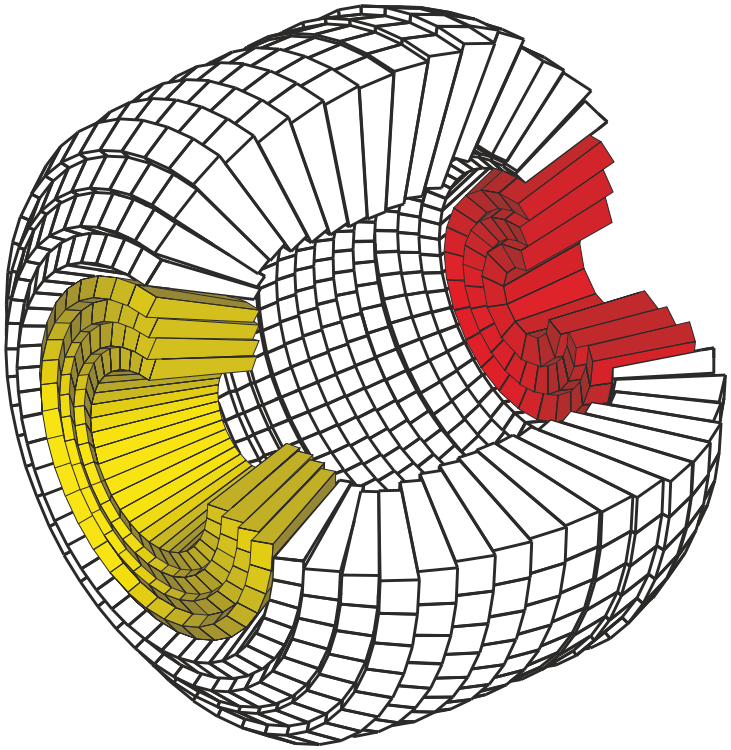

Figure 3.11.: Schematic diagram of the scintillator electromagnetic calorimeter. The SEC is divided into three parts: the forward part (yellow), the central part (white), and the backward part (red). Adapted from [HR+04].

Scintillator electromagnetic calorimeter (SEC)

The scintillator electromagnetic calorimeter is the outer most part of the central detector and can measure photons, electrons, and positrons with energies of up to 800 MeV. The minimum energy for photons is 2 MeV and the maximum kinetic energy for $\pi^{\pm}$/p/d stopping in the SEC is 190 MeV/400 MeV/500 MeV. The calorimeter is made of 1012 sodium-doped CsI scintillating crystals. These are shaped as truncated pyramids and aligned in 24 rings around the COSY beam pipe. The SEC is divided into three main parts – the forward, the backward, and the central part (see figure 3.11) – and covers in total a polar angle range of 20° to 169°. The forward part consists of four rings with 36 crystal elements each covering a polar angle range of 20° to 36°, and the central part has 17 rings with 48 elements each and covers an angle range of 36° to 150°. The backward part contains three rings of which two have 24 crystal elements and the one closest to the beam pipe has twelve elements. It covers an angular range of 150° to 169°. Except for spare areas for the pellet beam pipe and for the helium gas line required for the solenoid, the calorimeter has azimuthal angle coverage of 360°. This results in a total geometrical acceptance of the SEC of 96 %. Further details about the scintillator electromagnetic calorimeter can be found in [Koc04].

3.2.3. Forward detector

The forward detector (FD) (see figure 3.12) is designed to detect particles with a small scattering angle ranging from 3° to 18°. These are mainly scattered projectiles and charged recoil particles like protons, deuterons, and helium nuclei. Furthermore, it is possible to measure charged pions and neutrons. In total the forward detector contains 364 scintillating elements whose information can be used for the first level trigger logic. The precise energy measurement and particle trace reconstruction allow for particle identification via the $\Delta E - E$ method and use of the missing mass method for mass determination of the produced mesons. Some basic properties of the forward detector are listed in table 3.2. The individual parts of the detector are described in the following sections.

Forward window counter (FWC)

The first detector of the forward detector in COSY beam direction is the forward window counter, which consists of two layers with 24 plastic scintillator elements

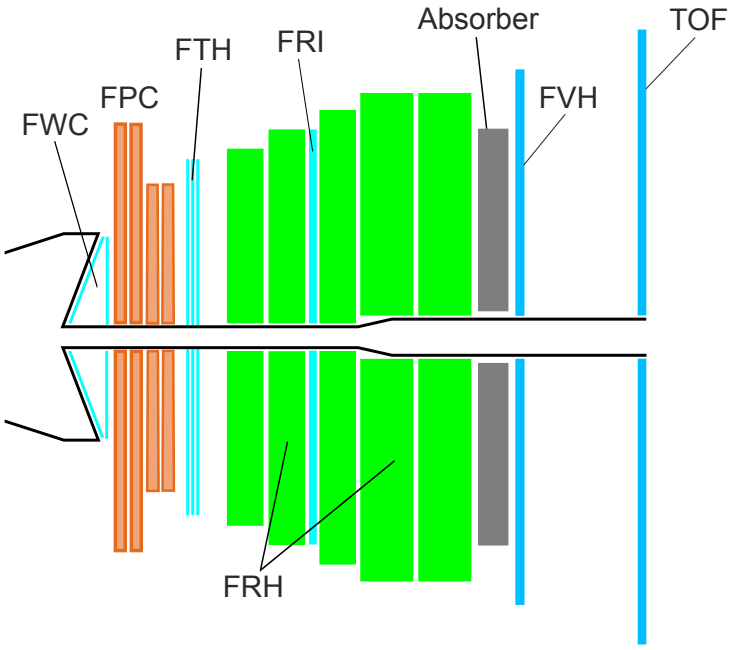

Figure 3.12.: Schematic diagram of the forward detector. It consists of the forward window counter (FWC), the forward proportional chamber (FPC), the forward trigger hodoscope (FTH), the forward range hodoscope (FRH), the forward range interleaving hodoscope (FRI), the forward veto hodoscope (FVH), the time of flight detector (TOF), and a removable absorber. Adapted from [HR+04].

Table 3.2.: Overview of some basic properties of the forward detector. Adapted from [Pé14b, Vla08].

Number of scintillating elements	364
Scattering angle coverage	3° to 18°
Scattering angle resolution	0.2°
E_{kin} to reach FRH layer 1 $\pi^{\pm}$/p/d/^{3}He/^{4}He	25/60/80/215/240 MeV
E_{kin} to punch through FRH layer 5 $\pi^{\pm}$/p/d/^{3}He/^{4}He	200/370/485/1325/1475 MeV
Time resolution	< 3 ns
Relative energy resolution stopped particles $E_{\text{kin}} < E_{\text{stop}}$ particles with $E_{\text{stop}} < E_{\text{kin}} < 2E_{\text{stop}}$	 1.5 % to 3 % 3 % to 8 %
Particle identification	$\Delta E - E$

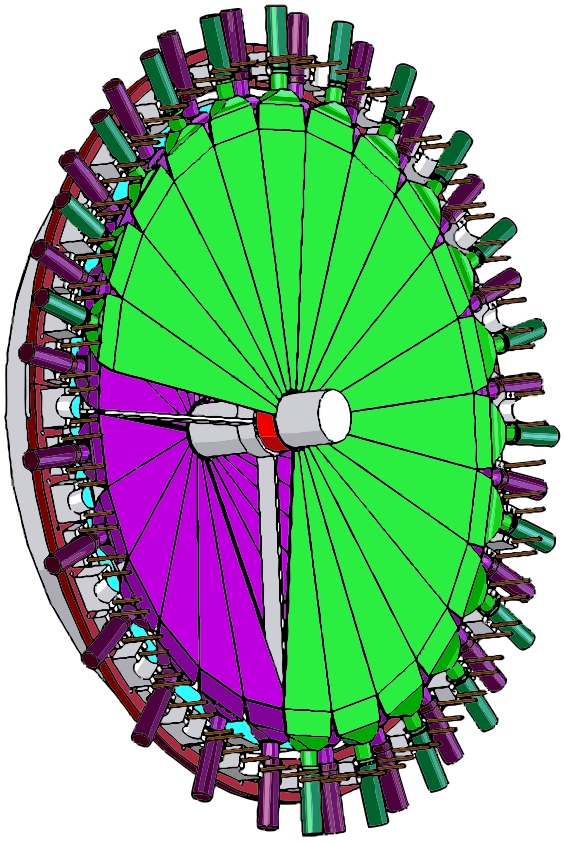

Figure 3.13.: Schematic view of the forward window counter. Some elements of the second layer (green) are not shown so that the first layer (purple) is visible. Adapted from [Pri10].

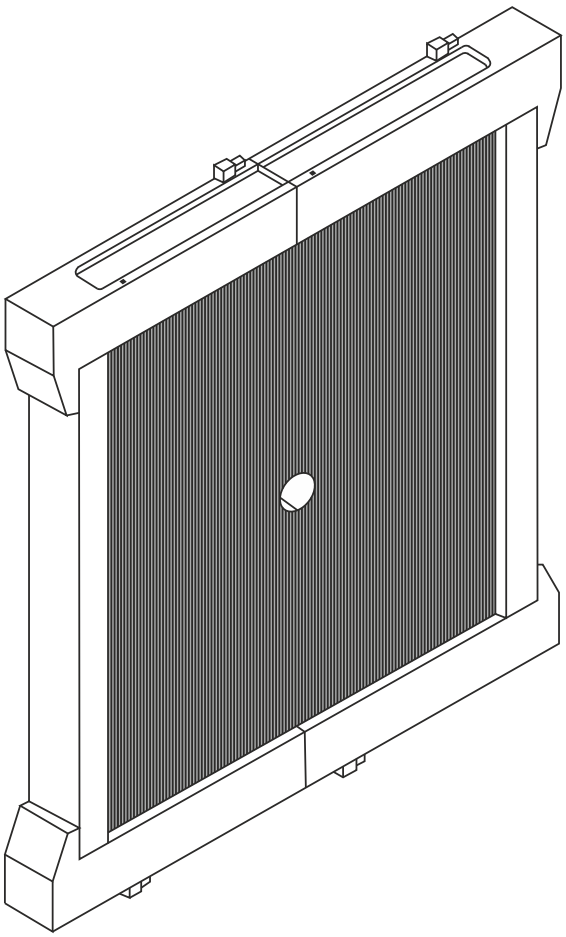

Figure 3.14.: Schematic drawing of one of the forward proportional chamber modules. Adapted from [HR+04].

each (see figure 3.13). While the first layer is tilted by 20° relative to the beam line, the second layer is planar. The 3 mm thick elements of the two layers are overlapping, giving a granularity of 48 zones. The signals of the FWC serve as a first level trigger and can be used to define the origin of the forward scattered particles, which helps to reduce the background from cosmic particles. Further details about the forward window counter are available in [Pri10].

Forward proportional chamber (FPC)

The next detector behind the forward window counter is the forward proportional chamber. It consists of four modules which are rotated by 45° with respect to each other perpendicularly to the beam axis [C+96]. Each module has four layers of 122 8 mm thick proportional drift tubes. The FPC is used for the track reconstruction

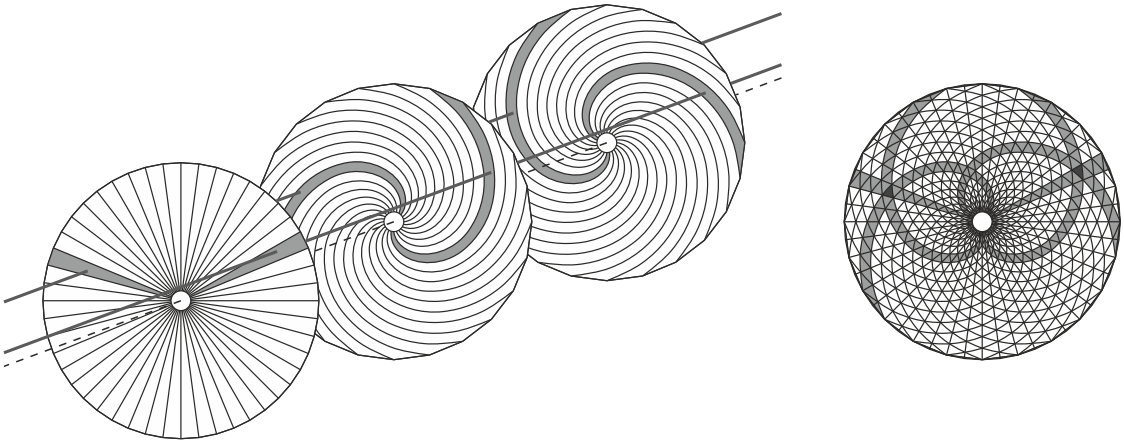

Figure 3.15.: Schematic diagram of the forward trigger hodoscope. Left: An explosion view of the detector. Right: Pixel structure formed by the layer overlap. The overlap of the hit elements (dark) allows a narrowed definition of the hit position.

providing a precise angle of the particles originating from the interaction point. Figure 3.14 shows one module of the forward proportional chamber.

Forward trigger hodoscope (FTH)

The forward trigger hodoscope is located directly after the FPC. The first layer of its three 5 mm thick plastic scintillator layers has 48 radially assigned elements (see figure 3.15), while the other two layers consist of 24 elements each forming oppositely arranged archimedian spirals. The overlap of the three layers gives a pixel structure allowing the measurement of the azimuthal scattering angle with a constant angular resolution. Details about the forward trigger hodoscope detector design can be found in [D$^+$94]. The FTH is mainly used as trigger and the information about the energy loss in this detector can be used for the particle identification via the $\Delta E - E$ method.

Forward range hodoscope (FRH)

The forward range hodoscope consists of five layers, each with 24 cake shaped elements (see figure 3.16). The layers' diameters range from 1.2 m (first layer) to 1.8 m (last two layers) [C$^+$07]. The first three layers are 11 cm thick, while the last two layers have a thickness of 15 cm. The FRH is used for energy reconstruction with an energy resolution of up to 1.5 % to 3 % in case of particles stopped in the detector [Vla08], and 3 % to 8 % for particles with up to twice the stopping energy,

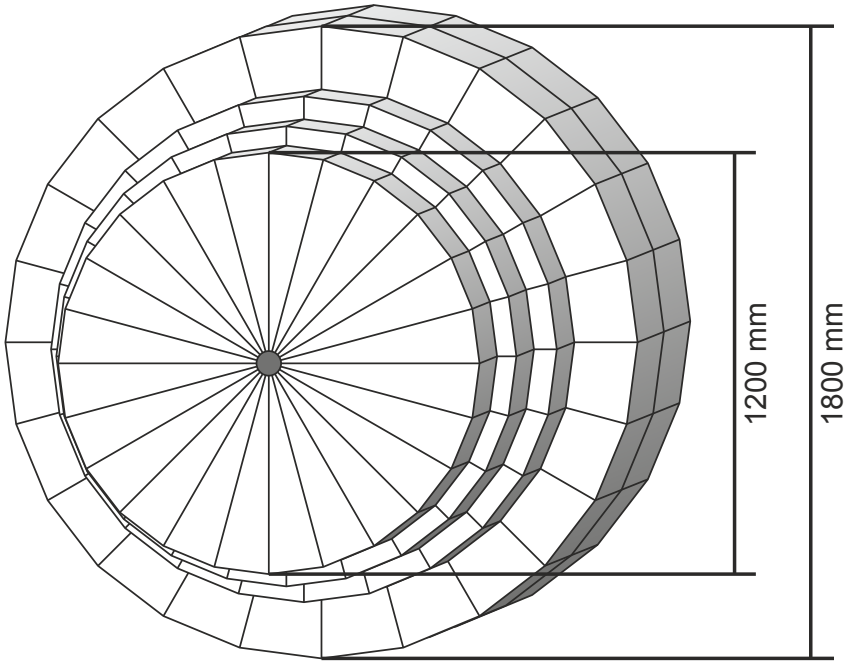

Figure 3.16.: Schematic diagram of the forward range hodoscope.

respectively. By comparing the energy loss in the different layers, it is possible to identify the measured particle via the $\Delta E - E$ method.

Forward range interleaving hodoscope (FRI)

The forward range interleaving hodoscope (see figure 3.17) is seated between the second and third layer of the forward range hodoscope. It is divided into two layers containing 32 plastic scintillator stripes with a thickness of 5 mm. The stripes in one layer are vertically orientated, whilst they are horizontal in the other one resulting in a X-Y pixel structure, which is required for a scattering angle determination of neutrons. Detailed information about the forward range interleaving hodoscope can be found in [Pau06].

Since the ^{3}He nuclei investigated in the analyses presented in this thesis are stopped in the first or second layer of the FRH, the information of the FRI are not used here.

Forward veto hodoscope (FVH)

The next detector behind the FRH is the forward veto hodoscope (see figure 3.18). It consists of twelve horizontally arranged plastic scintillator barrels with

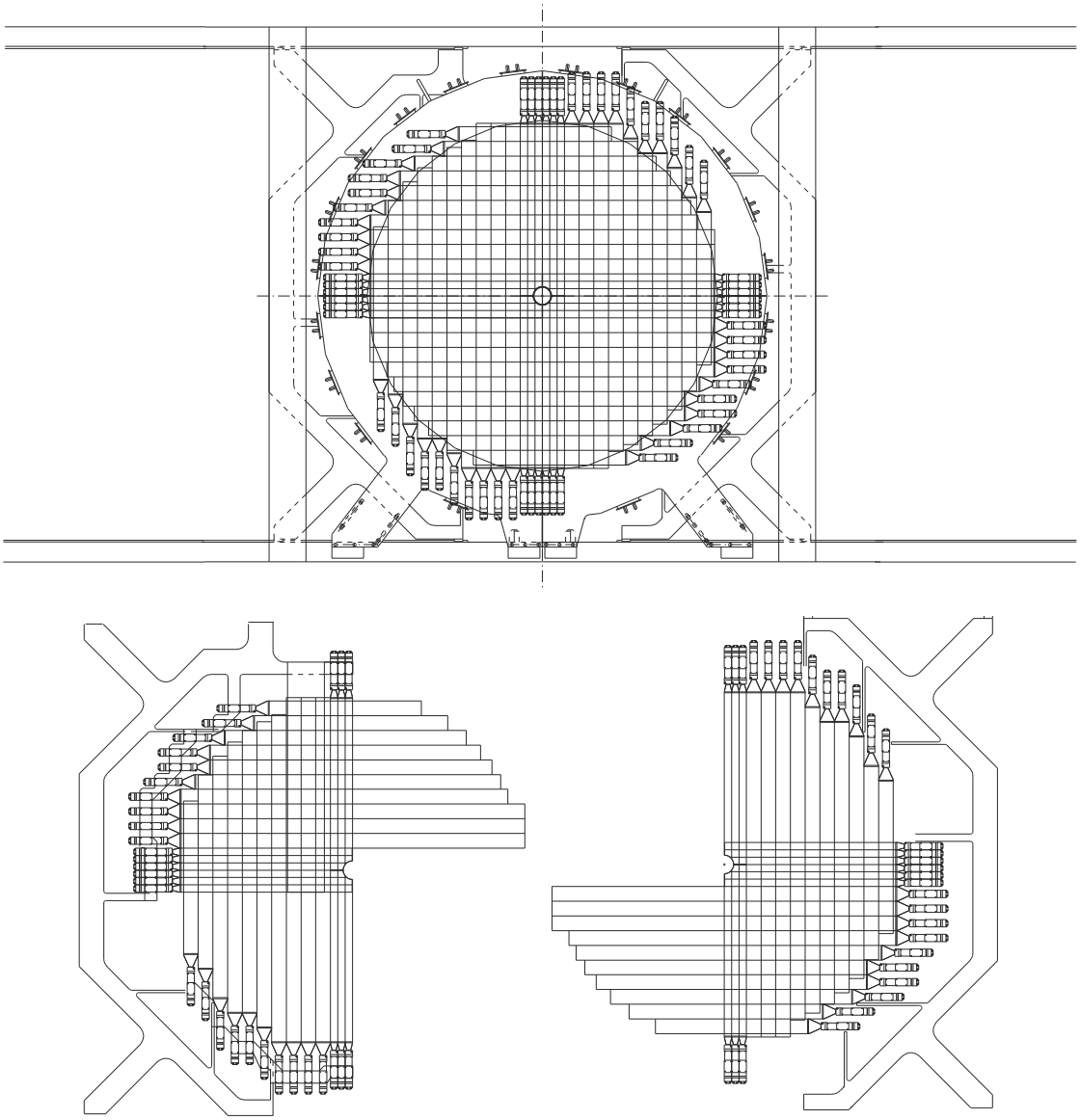

Figure 3.17.: Schematic view of the forward range interleaving hodoscope. In the upper part the whole detector is shown, while the lower part illustrates the detector divided into two parts [HR+04].

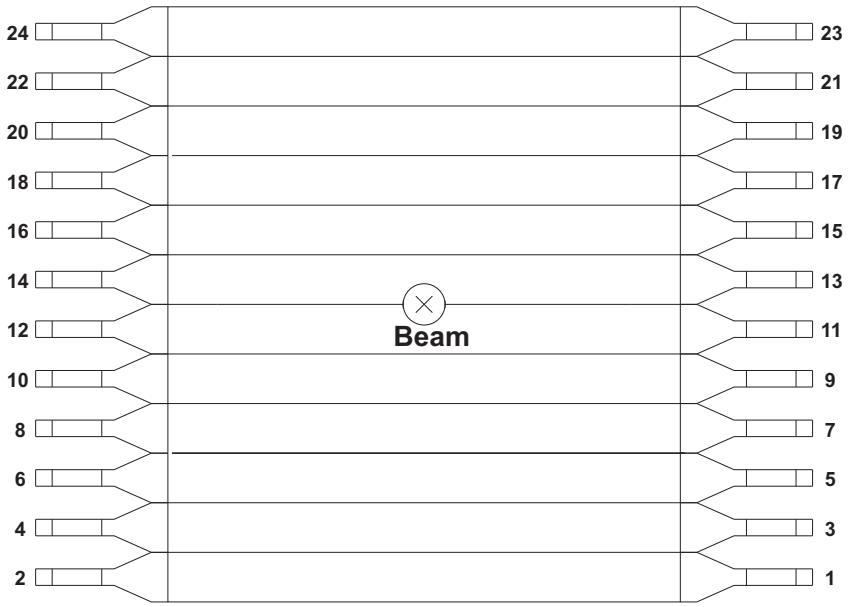

Figure 3.18.: Schematic drawing of the forward veto hodoscope. Adapted from [HR+04].

the dimensions 165 cm × 13.7 cm × 2 cm. The readout of the elements is possible via photomultipliers at both ends. By using the time information, the hit position within a stripe can be determined. The signals of the FVH can be utilized as a veto for particles with too high energies passing through the whole FRH. A detailed description of the FVH is available in [Bro95].

Forward range absorber (FRA)

The forward range absorber is an optional absorber made of iron, which can be put between the last layer of the FRH and the FVH [HR+04]. Its thickness can be set between 5 mm and 100 mm. The absorber was, for example, used during pp → ppη beam times with a beam energy of about 1400 MeV. Protons from this reaction are stopped in the FRA, whereas faster protons from other reactions like pp → ppπ^0 reach the FVH producing a veto signal.

Second forward veto hodoscope (FVH2)/Time of flight detector (TOF)

The FVH does not cover the full angular range of 3° to 18° of the WASA forward detector. Therefore, since 2008 a second forward veto hodoscope (see figure 3.19) covering the full range has been installed as the last detector in beam direction. It consists of 22 vertically aligned plastic scintillator stripes forming a rectangular pixel structure together with the elements of the first veto hodoscope. Additionally,

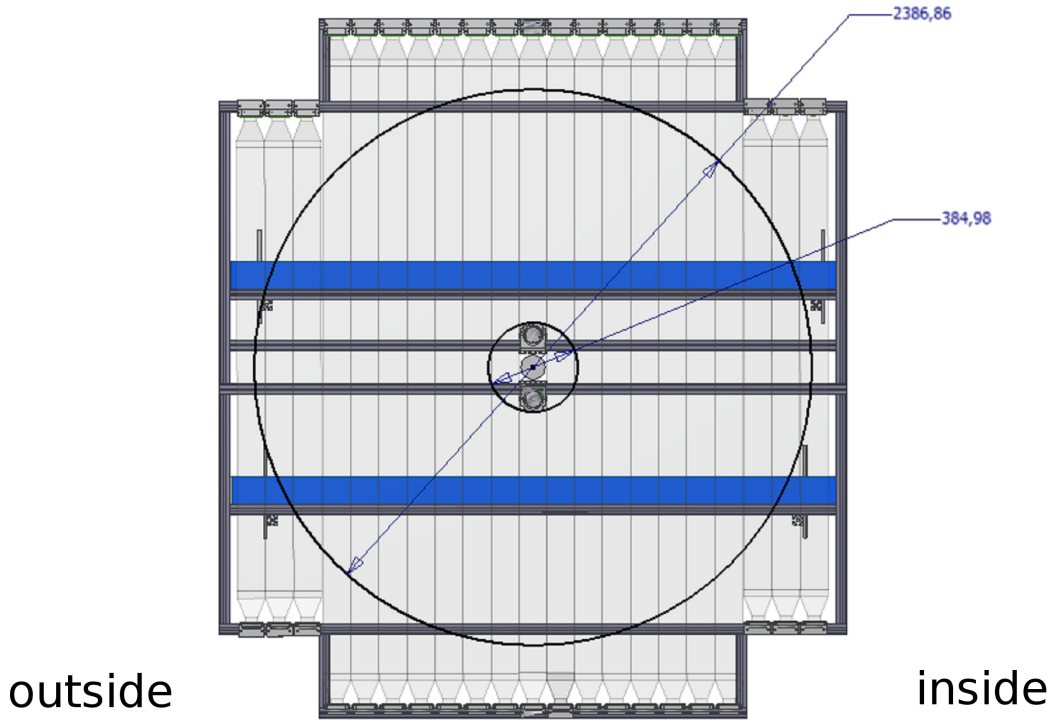

Figure 3.19.: Schematic diagram of the second forward veto hodoscope/time of flight detector [Pé09].

it has two horizontal elements which can be positioned along the vertical axis. Just like the first FVH, its elements have a double readout. Using the signals from the FWC as start and those from FVH2 as stop signals, the time of flight method can be applied for particle identification. Hence, the second veto hodoscope is also called time of flight detector. In [Pé09] further information about the TOF can be found. None of the forward veto hodoscopes were used in the analyses done for this thesis.

3.3. Data acquisition (DAQ)

The WASA data acquisition system is designed for the desired luminosities of the experiment and is based on the third generation of DAQ systems for experiments operated at COSY [K$^+$06]. The event rate is limited by the writing speed of the used hard disks for event storage to about 80 MB s^{-1}, resulting in a manageable trigger rate of 10 kHz assuming a typical event size of 8 kB [Red10]. The achieved dead time of the WASA DAQ is about 20 µs [W$^+$08b].

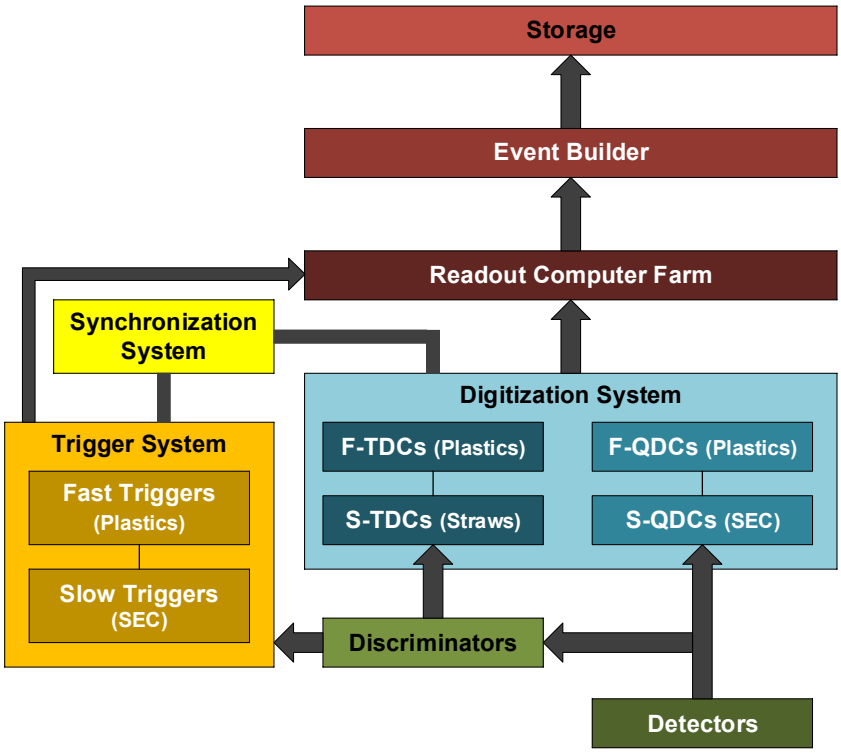

Figure 3.20.: Flow chart of the DAQ system for WASA-at-COSY.

Figure 3.20 illustrates a sketch of the data acquisition utilized at WASA. The analog signals from the different plastic scintillators are sent through a splitter box to so-called F-QDCs (Fast Charge to Digital Converters) with a sampling rate of 160 MHz and to discriminators. Signals above the discriminator threshold are sent to Fast TDCs (Time to Digital Converters) based on the GPX ASIC [K$^+$08, aca06] as well as to the trigger logic. In case of the forward window counter, two splitter boxes are used, allowing to apply a low and a high threshold in parallel.

For the signals from the calorimeter crystals, active splitters provide the input for the S-QDCs (Slow Charge to Digital Converters) with a sampling rate of 80 MHz and additionally build an analog sum of crystal groups. These groups contain 4×3 crystals in case of the forward SEC part, 4×4 crystals in the central part and 3×3 crystals for the backward part. The signal sums are sent to dual threshold discriminators whose outputs serve as inputs for the trigger logic. The signals from the straw tubes are amplified, discriminated and sent to the Slow TDCs, which are based on the F1 ASIC [aca01].

All QDC and TDC signals are stored in a buffer and only saved in case of a trigger signal. The synchronization of the digitization system and the trigger system is done in EMS (Experiment Message Specification) framework which is also used by other experiments operated at the COSY accelerator [Z$^+$94].

3.4. Trigger system

With WASA-at-COSY luminosities of above $10^{32}\,\mathrm{cm}^{-2}\,\mathrm{s}^{-1}$ the event rates exceed the maximum rate of 10 000 events/s that can be saved on disk. Therefore, a trigger system is needed to reduce the number of events and to select only events fulfilling certain basic conditions [Fra02]. The WASA-at-COSY trigger system is organized in two levels, both hardware based.

The first level trigger uses the fast signals from the plastic scintillators as input for multiplicity units. Hits in adjacent elements within a coincidence time window of 20 ns are combined into clusters and the cluster multiplicity of each detector plane is calculated, which can be used for triggering.

In addition, the WASA trigger system allows to apply a more complex condition for triggering, namely the matching trigger. It involves both planes of the FWH, the radial plane of the FTH and the first FRH plane. The hits in these planes are tested for alignment. If a hit in the first layer of the forward trigger hodoscope

is found to be in coincidence with hits in one of the two forward window counter planes and the first layer of the forward range hodoscope at the same azimuthal angle, it will be validated. It is possible to use two different discriminator thresholds for the FWC layers for the matching trigger. The efficiency of the trigger has been found to be in the range of 79.2 % to 98.7 % [Zhe09].

The second level trigger involves the slower signals from the calorimeter. The information about the deposited energies in the individual crystals are summed in groups of nine elements to 16 elements, so-called hardware clusters. The sums are sent to dual threshold discriminators and the resulting logic signals for low and high energy deposits are checked for geometrical coincidence with clusters in the plastic scintillator barrel to define charged or neutral hits. The multiplicity of charged and neutral tracks are calculated for low and high energy deposits. In addition to the energy sums of the hardware clusters, energy sums over the whole calorimeter or parts of the detector can be used for triggering.

The signals from both the first level and the second level triggers can be combined in coincidence matrices. Up to 32 such matrices can be applied at the same time. In order to reduce the amount of events written to disk, it is possible to prescale the individual triggers. For example, a prescaling factor of 5 means that only every fifth event is written to disk.

The trigger conditions used for the acquisition of the analyzed data sets are presented in chapters 4.1 and 6.1.

3.5. Software

The Software used at WASA-at-COSY is divided into two parts, a simulation part and an analysis part. The software packages used in the presented thesis are described in the following sections. Table 3.3 lists the revisions of the software used for the analyses presented in this thesis.

3.5.1. Simulation software

Simulations at WASA are done in two steps. First the events are generated, then the output of the generator is sent through a detector simulation software. The event generation is done by the Monte Carlo tool Pluto [F+07]. Pluto was originally developed for the experiment HADES at the GSI. It is based on the software package ROOT [BR97], which itself is based on C++. ROOT was developed at

Table 3.3.: Software revisions used for the analyses.

Software	Revision used for η cross section analysis	Revision used for $\eta \to \pi^0 + e^+ + e^-$ analysis
ROOT	5-34-05	5-34-08
Pluto	5.31.1 (SVN-58)	5.38 (SVN-74)
WMC	SVN-284	SVN-294
RootSorter	SVN-3490	SVN-3813

CERN specifically for the usage in nuclear and particle physics. It offers additional classes valuable for studies in these scientific fields, like the class of Lorentz vectors.

In order to use the Pluto event generator, the reactions and particle decays of interest are written in macros which are processed with the compiler provided by the ROOT software package. Besides simple reactions it is possible to create cocktails of Monte Carlo simulations containing several different decays with the correct branching ratios. One advantage of the Pluto event generator is the option to implement decay or reaction models replacing the phase space distribution assumed by default. Some more complex decay models are already implemented in the current version of Pluto and can easily be switched on or off.

The reaction data created by Pluto macros are used as an input for the WASA Monte Carlo simulation program (WMC). The WMC software is based on GEANT 3 (GEometry ANd Tracking) developed at CERN [CER93] and simulates the whole WASA detector setup including particle interactions with the active detector material as well as the passive parts of the detector. The output of the simulation program contains hit positions, timings, and information about the energy losses and is saved in the same format as the data collected during beam times. This allows to use the same analysis framework for simulations and for data.

3.5.2. Analysis software

For data and simulation analysis the RootSorter framework based on ROOT is used. It was originally developed for the ANKE experiment [HHM03]. Currently it is utilized by the ANKE, PAX, and WASA-at-COSY collaborations. The reconstruction of the collected data as well as of the Monte Carlo simulations are described in the following.

At first the collected experimental data are calibrated, while the output from WASA Monte Carlo is smeared. This is the only step where data and simulations are treated differently. The resulting information are stored separately for each detector in hit banks. Hits are signals from single detector elements. Adjacent hits, which are expected to originate from the same particle, are combined in clusters by cluster finding algorithms. These clusters are then saved in cluster banks. Clusters from the different detectors originating from the same particle are combined to tracks and saved in track banks. These tracks can be accessed within analyses written in C++ classes. A track contains all information of a single particle. This modular structure of the reconstruction provides an intuitive analysis structure and allows simple changes or replacements in the reconstruction algorithms.

3.5.3. Common base class PDEtaAnalysisBase

As mentioned in chapter 2.2.1, the η meson allows to study rare decay processes. Therefore, the data collected during the $p + d \rightarrow {}^3He + X$ beam times in September/October 2008 and August/September 2009 and used for this thesis are the basis for several other η decay studies [Adl12, Cod12, Hod12, Jan10, Lal10, Red10, Win11, Wur13, Yur11]. Since 2012 a common analysis class for η-decay studies (PDEtaAnalysisBase) has been developed and optimized for the September/October 2008 and August/September 2009 data sets. This way it is not only assured that the analyses based on this class use the same calibration and Monte Carlo smearing settings, but also that the major data analysis steps are identical for all decay studies. All conditions and parameters used in the base class are adjustable by RootSorter options. The optimization of these parameters, including the detector calibration, was done by a task force consisting of postdoctoral researchers and PhD students.

The differential cross section studies of the reaction $p + d \rightarrow {}^3He + \eta$ based on the data of the August/September 2009 beam time, which are part of this thesis (see chapter 4), require a precise calibration of the forward detector, especially the forward range hodoscope. Thus, methods for a fine calibration of the FRH were developed. These methods were applied to the full $p + d \rightarrow {}^3He + X$ data sets from September/October 2008 and August/September 2009 and are included in the PDEtaAnalysisBase class (see chapter 6.2). This class is the basis for the studies of the η decay $\eta \rightarrow \pi^0 + e^+ + e^-$.

Table 3.4.: Models used for the common $p + d \rightarrow {}^3He + \eta$ Monte Carlo simulation pool.

η decay channel	Kinematic distribution
$\eta \rightarrow \gamma + \gamma$	Phase space
$\eta \rightarrow \pi^0 + \pi^0 + \pi^0$	Phase space Dalitz decay of π^0 with proper kinematics [F$^+$07]
$\eta \rightarrow \pi^+ + \pi^- + \pi^0$	Matrix element [F$^+$07, A$^+$95] Dalitz decay of π^0 with proper kinematics [F$^+$07]
$\eta \rightarrow \pi^+ + \pi^- + \gamma$	Matrix element [F$^+$07, Pet10]
$\eta \rightarrow e^+ + e^- + \gamma$	Phase space e^+e^- distribution based on Quantum Electrodynamics (QED) [F$^+$07]
$\eta \rightarrow e^+ + e^- + e^+ + e^-$	Dilepton distribution based on QED [F$^+$07]
$\eta \rightarrow \pi^+ + \pi^- + e^+ + e^-$	Matrix element [F$^+$07, Pet10] QED dilepton mass distribution Vector meson form factor for e^+e^- pair

In addition to the common base class, a common set of Monte Carlo simulations was created and common settings for further simulations were defined. For all simulated η decays the angular distribution of the reaction $p + d \rightarrow {}^3He + \eta$ derived during the studies presented in chapters 4 and 5 was applied. Furthermore, more complex models derived from previous studies were applied for the simulations of η decays where the phase space kinematic distribution assumed by Pluto by default is known to be inadequate. Table 3.4 shows a summary of the kinematics applied for the Monte Carlo simulations of η decays used in the common analyses. As part of this thesis the common Monte Carlo basis was significantly extended, especially for background reactions like $p + d \rightarrow {}^3He + (\pi + \pi)^0$ (see chapter 6.3).

4. Analysis of the reaction $p + d \rightarrow {}^3He + \eta$

The reaction $p + d \rightarrow {}^3He + \eta$ has remarkable properties when compared to similar reactions and other η meson production reactions. Its very high cross sections for small excess energies are unexpected and can only be explained by a strong final state interaction (see chapter 2.3.3) [FW95]. At higher excess energies it shows an interesting behavior, too. For instance, the data determined by WASA/PROMICE and ANKE show a plateau of the total cross section for excess energies above 40 MeV [B$^+$02, B$^+$04, R$^+$09]. The $Q = 48.8$ MeV data measured with GEM, on the other hand, indicates a total cross section value possibly well above this plateau [B$^+$00]. Moreover, the shape of their obtained differential cross section distribution hints at a possible difference from those distributions obtained with WASA/PROMICE and ANKE for slightly different excess energies. However, within their comparably large uncertainties the total and differential cross sections determined with GEM are compatible with the results from these experiments. In order to clarify this, new measurements at $Q = 48.8$ MeV were performed with WASA-at-COSY in 2009. Additionally, the differential cross sections were determined for $Q = 59.8$ MeV. This way systematic uncertainties are avoided when comparing the differential distributions. Due to the high statistics of the WASA-at-COSY measurements and the hence low uncertainties, the obtained differential cross sections will help new theoretical studies [K$^+$13]. Furthermore, the η production reaction $p + d \rightarrow {}^3He + \eta$ at $Q = 59.8$ MeV is used for the search for the decay $\eta \rightarrow \pi^0 + e^+ + e^-$. A proper description of the data by Monte Carlo simulations is essential for the analysis and, therefore, the angular distribution of the reaction $p + d \rightarrow {}^3He + \eta$ has to be known. The analysis of this reaction for a determination of the differential cross sections had already been started by A. Passfeld [Pas10] and was continued as part of this thesis. The results were published in 2014 [A$^+$14b].

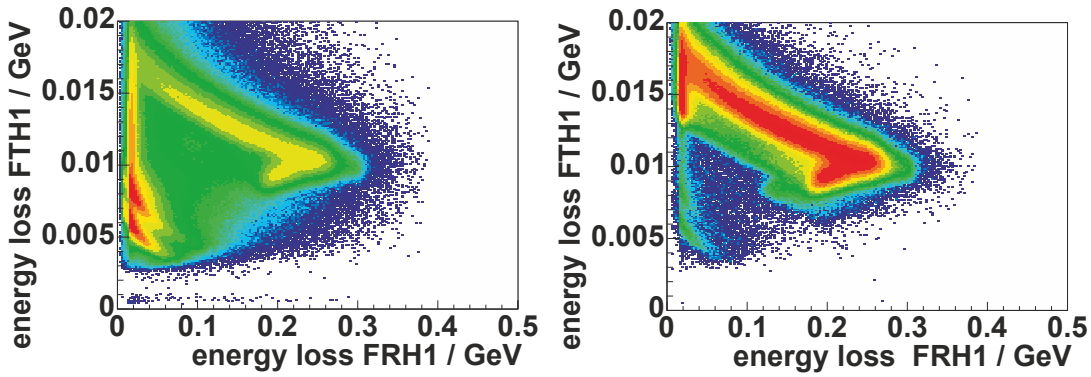

Figure 4.1.: Energy loss in the first layer of the forward trigger hodoscope plotted against the energy loss in the first layer of the forward range hodoscope for a sample of raw data (left) and for the same sample after preselection (right) in logarithmic scale. Adapted from [Pas10].

4.1. Database and preselection

The analysis of the reaction $\mathrm{p} + \mathrm{d} \rightarrow {}^3\mathrm{He} + \eta$ presented in this chapter is based on data gathered during the WASA-at-COSY beam time in August/September 2009 (separated in files with run numbers 13 969 to 15 944). While most data were collected at a proton kinetic beam energy of $T_{\mathrm{beam}} = 1000\,\mathrm{MeV}$ equaling an excess energy of $Q = 59.8\,\mathrm{MeV}$, the runs 15 276 to 15 296 were recorded at $T_{\mathrm{beam}} = 980\,\mathrm{MeV}$ equaling an excess energy of $Q = 48.8\,\mathrm{MeV}$. The data were recorded using the following trigger conditions:

- at least one geometrically matching hit in the first layer of FRH and FTH as well as one hit in either the first or second FWC layer,
- at least one hit in each FWC layer, and
- high threshold for the energies deposited in the FWC.

In order to reduce the amount of background reactions further and improve the analysis performance, the data were preselected by J. Złomańczuk using graphical cuts in the energy loss spectra. These cuts were determined with ODIN, an alternative framework to the RootSorter analysis software. As part of her diploma thesis A. Passfeld compared raw data with preselected data determining the number of $\mathrm{p} + \mathrm{d} \rightarrow {}^3\mathrm{He} + \eta$ events in each data set [Pas10].

Figure 4.1 shows the energy loss of a track in the first layer of the FTH plotted against the energy loss in the first FRH layer for a sample of 22 data runs recorded

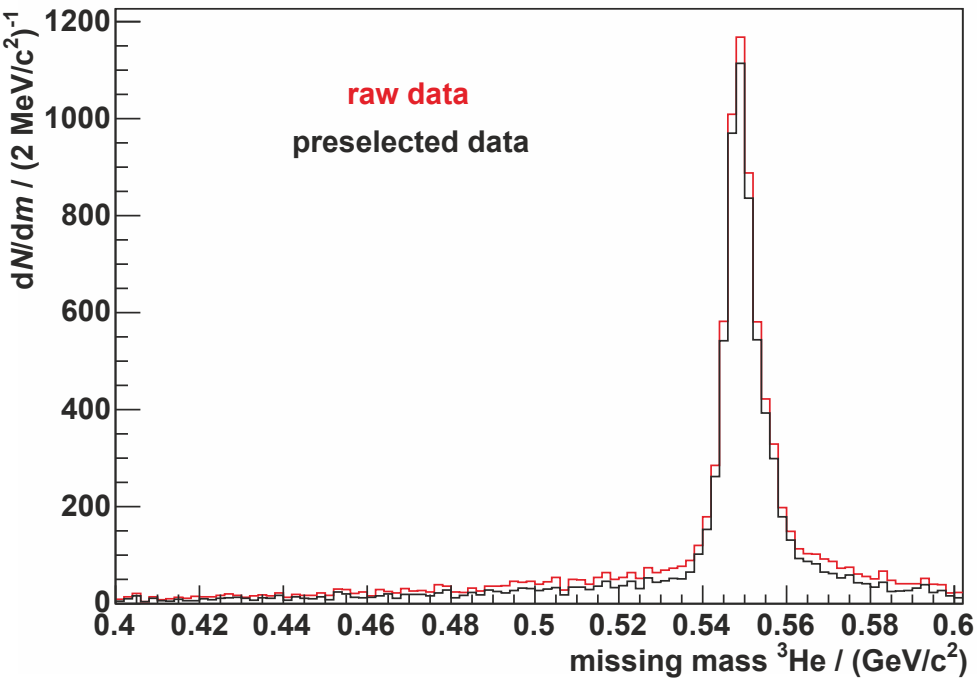

Figure 4.2.: ^{3}He missing mass for 22 sample runs of the 59.8 MeV data with the requirement of exactly one charged particle detected in the forward detector and exactly six neutral particles in the central detector. Raw data are shown in red and preselected data in black. Adapted from [Pas10].

at $Q = 59.8\,\mathrm{MeV}$ before (left figure) and after preselection (right figure). The chosen data runs were analyzed requiring exactly six neutral particles detected in the central detector to select the η meson decay $\eta \to \pi^0 + \pi^0 + \pi^0$ with the pions decaying into two photons each. This way the multi-pion background from direct $(\pi\pi)^0$ and $\pi^+\pi^-\pi^0$ production as well as from $(\pi\pi\pi\pi)^0$ production was reduced significantly.

The kinetic energy of a ^{3}He nucleus was reconstructed by using the information of the deposited energy in the forward range hodoscope and the laboratory azimuthal scattering angle which, together with the polar scattering angle, was determined with the help of the forward proportional chamber. The ^{3}He four-momentum extracted in this way and the known four-momenta of the beam and target allowed to identify the produced particles via the missing mass method (see chapter 2.5). Figure 4.2 shows the missing mass of the ^{3}He nuclei for the raw and preselected data sample. The difference in the number of reconstructed η mesons is quite small.

According to the analysis of A. Passfeld, $(98 \pm 2)\,\%$ of the $\mathrm{p} + \mathrm{d} \rightarrow {}^3\mathrm{He} + \eta$ events reconstructed in the raw data are also found in the preselected data [Pas10].

4.2. Simulation of the reaction $\mathrm{p} + \mathrm{d} \rightarrow {}^3\mathrm{He} + \eta$ and possible background reactions

The numbers of $\mathrm{p} + \mathrm{d} \rightarrow {}^3\mathrm{He} + \eta$ events were extracted from missing mass spectra of the ^{3}He by either fitting the background with a polynomial or a Monte Carlo simulation cocktail and subsequently subtracting the determined background from the data. For this purpose ten million events were simulated for each of the following background reactions using the WMC framework for each of the two excess energies $Q = 48.8\,\mathrm{MeV}$ and $Q = 59.8\,\mathrm{MeV}$:

- $\mathrm{p} + \mathrm{d} \rightarrow {}^3\mathrm{He} + \pi^0$
- $\mathrm{p} + \mathrm{d} \rightarrow {}^3\mathrm{He} + \pi^0 + \pi^0$
- $\mathrm{p} + \mathrm{d} \rightarrow {}^3\mathrm{He} + \pi^+ + \pi^-$
- $\mathrm{p} + \mathrm{d} \rightarrow {}^3\mathrm{He} + \pi^0 + \pi^0 + \pi^0$
- $\mathrm{p} + \mathrm{d} \rightarrow {}^3\mathrm{He} + \pi^+ + \pi^- + \pi^0$
- $\mathrm{p} + \mathrm{d} \rightarrow {}^3\mathrm{He} + \pi^0 + \pi^0 + \pi^0 + \pi^0$
- $\mathrm{p} + \mathrm{d} \rightarrow {}^3\mathrm{He} + \pi^+ + \pi^- + \pi^0 + \pi^0$
- $\mathrm{p} + \mathrm{d} \rightarrow {}^3\mathrm{He} + \pi^+ + \pi^- + \pi^+ + \pi^-$

Furthermore, 10^7 events of the signal channel $\mathrm{p} + \mathrm{d} \rightarrow {}^3\mathrm{He} + \eta$ were simulated with the η meson decaying into three π^0. All multi-pion simulations and the simulation of the signal channel were done assuming pure phase space production, and all produced π^0 were simulated to decay into two photons.

4.3. Application of the ^{3}He selection conditions to simulations

As mentioned in chapter 4.1, the collected data were preselected using a graphical cut around the ^{3}He band in the energy loss spectra. In order to avoid systematic

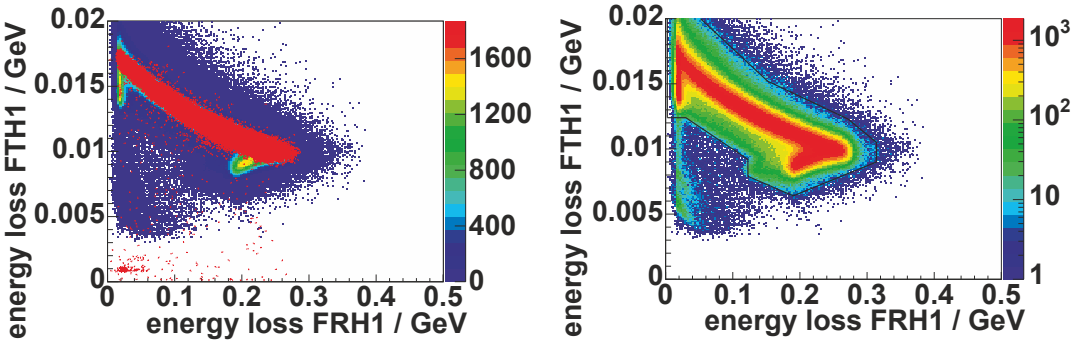

Figure 4.3.: Energy loss in the first layer of the FTH plotted against the energy loss in the first FRH layer for the sample of 20 runs of the $Q = 59.8\,\mathrm{MeV}$ data used for the detector calibration. In the left histogram simulated events are shown in red in addition. The right histogram is plotted in logarithmic scale with a black line indicating the used graphical cut. Adapted from [Pas10].

uncertainties, the data and simulations had to be preselected applying the same cut conditions. Due to the differences between the ODIN framework used for the preselection and the RootSorter framework utilized for the analysis, such as small differences in the calibration settings, the exact graphical cut used for the data preselection could not be applied to the Monte Carlo simulations. Instead a new graphical cut for the helium selection was defined by A. Passfeld [Pas10].

Figure 4.3 shows the energy loss in the first FTH layer (FTH1) plotted against the energy loss in the first layer of the FRH (FRH1) for a sample of 20 runs at $Q = 59.8\,\mathrm{MeV}$. These 20 runs, namely run 14450 to run 14469, were already used for the detector calibration. In the left figure the measured distribution is superimposed with Monte Carlo simulations of the reaction $\mathrm{p+d} \rightarrow {}^3\mathrm{He+\eta}$ shown in red, while the right figure shows the plot in logarithmic scale and includes the graphical cut around the ^{3}He band (black line). In addition to this graphical cut, both for data and simulations exactly one charged particle in the forward detector was required with at least 1 MeV energy deposited in each of the FWC and FTH layers as well as in the first layer of the FRH.

The stability of the detector calibration needs to be checked for the whole beam time. Due to adjustments of the WASA detector and/or the pellet target during the beam time, not all runs could be used for the analysis and, therefore, were excluded for the check. In the WASA-at-COSY collaboration Wiki a list of runs recommended for the analysis is available as well as a list containing 10 % of these recommended runs [WAS17]. The latter cover the whole beam time and, hence,

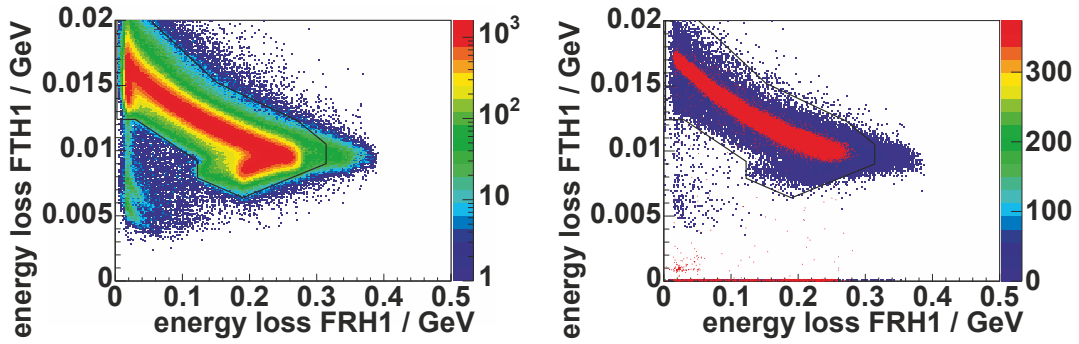

Figure 4.4.: Energy loss in the first FTH layer plotted against the energy loss in the first layer of the FRH for the first 20 recommended data runs with an excess energy of $Q = 59.8\,\text{MeV}$. The left histogram is in logarithmic scale. In the right histogram a hit in the 20th element of FRH1 is required. Monte Carlo simulations are shown in red for comparison. Adapted from [Pas10].

were analyzed in order to check the calibration. It was found that the calibration of the forward detector was not correct for all elements over the whole beam time [Pas10]. Figure 4.4 shows the energy loss in FTH1 versus FRH1 for the first 20 data runs from the recommended list (10 %) recorded at $Q = 59.8\,\text{MeV}$. It is visible that the ^{3}He band extends beyond the chosen graphical cut (see left figure). The right figure shows the data for the same runs if the ^{3}He nuclei were detected in the 20th element of FRH1. For comparison the simulated $\text{p} + \text{d} \rightarrow {}^3\text{He} + \eta$ reaction is shown in red. It is visible that the measured helium band deviates from the simulations.

Such a shift for certain detector elements is to be expected for a long beam time. In case of the analysis of the reaction $\text{p} + \text{d} \rightarrow {}^3\text{He} + \eta$ with the aim to determine differential cross sections, it is not necessary to analyze the whole $Q = 59.8\,\text{MeV}$ data set. Instead, runs which are suitable for the analysis and, thus, already have correctly calibrated detectors were chosen by A. Passfeld [Pas10]. However, an analysis based on the complete data set like η meson decay studies relies on a careful run dependent detector calibration (see chapter 6.2). In case of the $Q = 48.8\,\text{MeV}$ data set, all recorded 15 runs were found to be calibrated correctly. The analyzed runs with $Q = 48.8\,\text{MeV}$ and $Q = 59.8\,\text{MeV}$, respectively, are listed in appendix A.2. Figure 4.5 shows the energy loss histogram for all $Q = 48.8\,\text{MeV}$ data runs (left figure) and for all $Q = 59.8\,\text{MeV}$ data runs used (right figure). The chosen graphical cut is identical for both data sets.

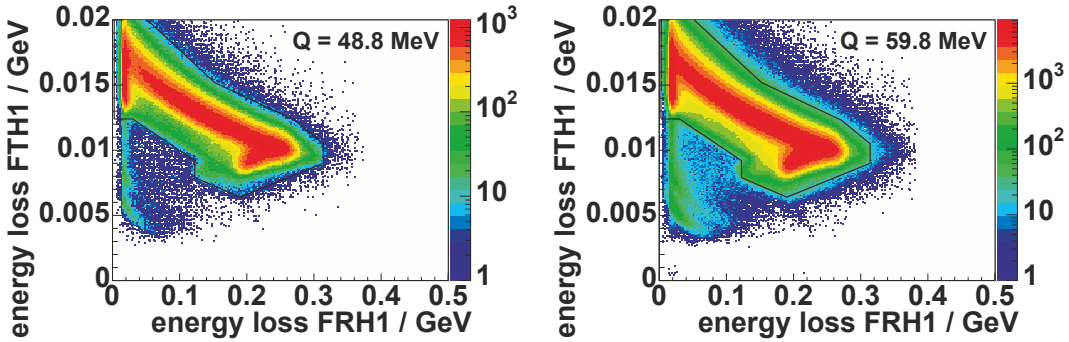

Figure 4.5.: Energy loss in FTH1 versus the energy loss in FRH1 in logarithmic scale. The left histogram shows all $Q = 48.8\,\mathrm{MeV}$ data runs, the right one all $Q = 59.8\,\mathrm{MeV}$ data runs used for the analysis. The applied graphical cut is drawn in black. Adapted from [Pas10].

4.4. Angular reconstruction

An appropriate angular binning for the differential cross sections is defined by the detector energy as well as scattering angle resolution. To check the latter, the resolution of the ^{3}He laboratory scattering angle was obtained by A. Passfeld using Monte Carlo simulations of the reaction $\mathrm{p} + \mathrm{d} \rightarrow {}^3\mathrm{He} + \eta$ [Pas10]. Figure 4.6 shows the reconstructed laboratory ^{3}He scattering angle plotted against the scattering angle originally generated by Monte Carlo.

In order to identify a possible shift of the laboratory angle during reconstruction, as well as to determine the angular resolution, the reconstructed scattering angle was plotted for small ranges of generated $\vartheta_{\mathrm{LAB}}^{\mathrm{gen}}$ and fitted by a Gaussian distribution. The difference between the extracted mean values of $\vartheta_{\mathrm{LAB}}^{\mathrm{rec}}$ and the mean values of the original scattering angle $\vartheta_{\mathrm{LAB}}^{\mathrm{gen}}$ is shown in the left of figure 4.7, while the right shows the determined standard deviation σ for the different generated laboratory scattering angles, which is below 0.2° for the angular range of interest. It is visible that the differences of the mean scattering angles are smaller by about a factor of 20 than the standard deviations of the reconstructed laboratory angle $\vartheta_{\mathrm{LAB}}^{\mathrm{rec}}$, which most likely originate from smearing effects during the reconstruction. Hence, the systematic deviations are only marginal and can be neglected.

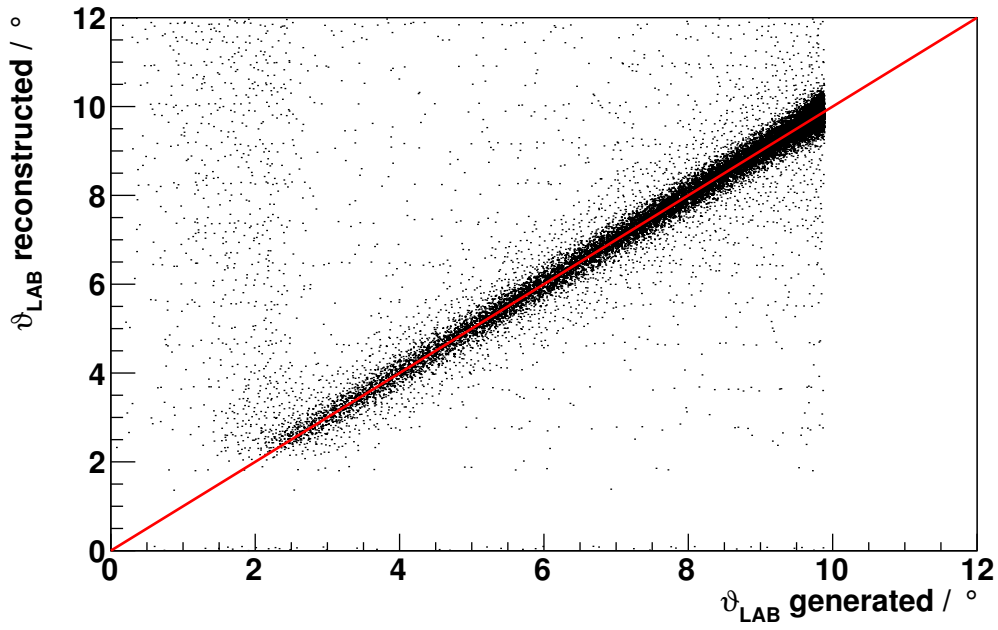

Figure 4.6.: Laboratory scattering angle of the reconstructed ^{3}He plotted against its generated laboratory scattering angle for the simulated reaction $p + d \rightarrow {}^3He + \eta$. The bisectrix is shown in red. Adapted from [Pas10].

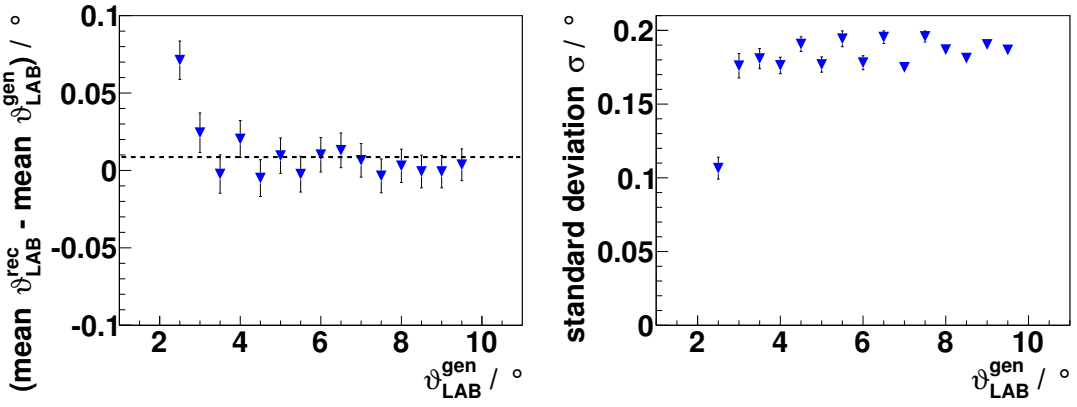

Figure 4.7.: Difference between the mean reconstructed laboratory scattering angle ϑ^{rec}_{LAB} and the mean generated laboratory scattering angle ϑ^{gen}_{LAB} of the ^{3}He depending on ϑ^{gen}_{LAB} for the simulated reaction $p + d \rightarrow {}^3He + \eta$ (left figure). A fit with a constant is indicated by a black dashed line. The right figure shows the standard deviation σ of the reconstructed ^{3}He scattering angle ϑ^{rec}_{LAB} depending on ϑ^{gen}_{LAB}. Adapted from [Pas10].

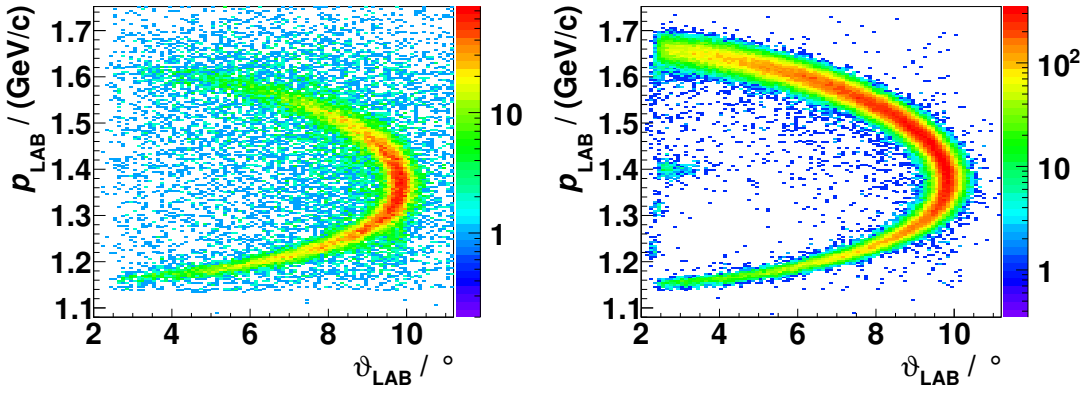

Figure 4.8.: ^{3}He laboratory momenta plotted against the corresponding laboratory angle for the $Q = 59.8\,\mathrm{MeV}$ data (left) and Monte Carlo simulations of the reaction $\mathrm{p} + \mathrm{d} \rightarrow {}^3\mathrm{He} + \eta$ at the same excess energy (right) in logarithmic scale. Six neutral particles detected in the central detector were required.

4.5. Calibration of the ^{3}He laboratory momenta

After the reconstruction of the laboratory scattering angles had been checked using Monte Carlo simulations (see chapter 4.4), the calibration of the forward detector was investigated. This was done in two major steps. At first the measured data were compared with Monte Carlo simulations and the measured laboratory momenta were shifted to agree with the simulations (see chapters 4.5.1 and 4.5.2). Then the reconstructed laboratory momenta of Monte Carlo simulations were compared with the corresponding generated momenta (see chapter 4.5.3) and corrected if needed. This correction was applied to both Monte Carlo simulations and measured data. In chapter 4.5.4 the calibrated data will be compared to expectations from two-particle kinematics.

4.5.1. Adaptation of the measured laboratory momenta to simulations

Figure 4.8 displays the absolute value of the laboratory momenta of ^{3}He plotted against the laboratory scattering angle ϑ_{LAB} for the measured data (left figure) and for simulations (right figure) at an excess energy of 59.8 MeV. In order to reduce the background, six neutral particles, which are expected to mostly originate from the η decay $\eta \rightarrow \pi^0 + \pi^0 + \pi^0$ with the pions decaying into two photons each, were

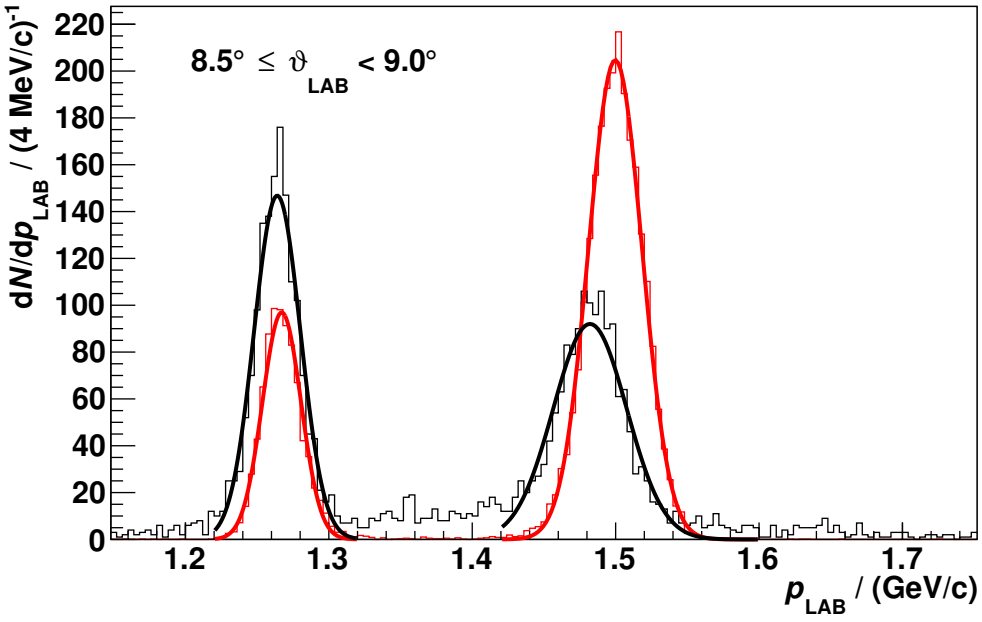

Figure 4.9.: Laboratory momenta of ^{3}He for the angular range $8.5° \leq \vartheta_{\mathrm{LAB}} < 9.0°$ for an excess energy of $Q = 59.8\,\mathrm{MeV}$. Measured data are shown in black, simulated data in red. Both peaks of the measured and simulated data are fitted by Gaussian distributions (black and red curves). Note that the simulations are scaled by an arbitrary factor for better illustration.

required to be detected in the central detector. This condition was only applied for the forward detector energy calibration and not during the final analysis.

Since the reaction $\mathrm{p} + \mathrm{d} \rightarrow {}^3\mathrm{He} + \eta$ is a two particle reaction, each laboratory momentum of the ^{3}He corresponds to one laboratory scattering angle ϑ_{LAB}[1]. While the distribution along the ^{3}He band can differ between Monte Carlo simulations and measured data due to an angular distribution different from phase space, the position and shape should be identical. Indeed, there is no shift visible in ϑ_{LAB} direction (see also chapter 4.5.4, figure 4.14), but there is a clear deviation of the ^{3}He band position and shape in p_{LAB} direction.

In order to check this in more detail and to obtain a correction function for the measured laboratory momenta, the momenta in simulations and in measured data were compared for different ϑ_{LAB} angular ranges. This method was introduced by A. Passfeld [Pas10], and it was optimized for the analysis presented in this thesis by improved fitting procedures. In figure 4.9 the ^{3}He laboratory momenta for the

[1]The other way does not hold true, since, except for the maximum scattering angle $\vartheta_{\mathrm{LAB}}^{\mathrm{max}}$, there are two possible laboratory momenta for each laboratory angle ϑ_{LAB}.

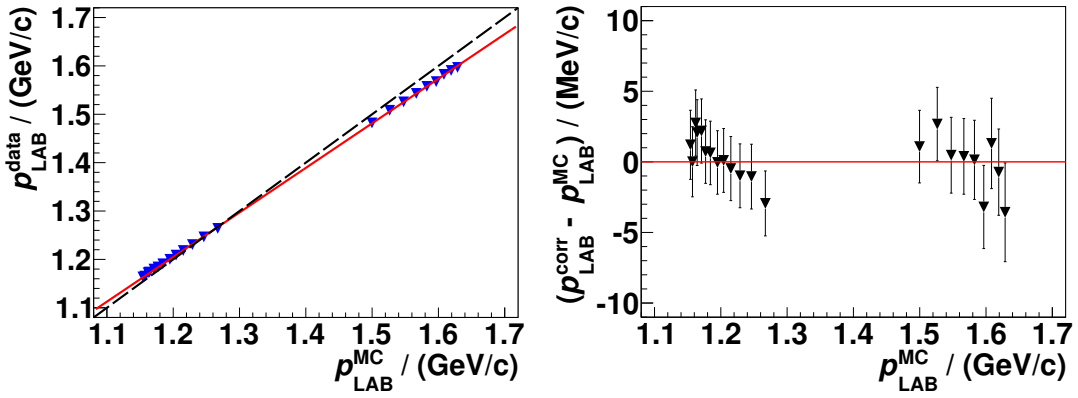

Figure 4.10.: Left: Laboratory momenta $p^{\mathrm{data}}_{\mathrm{LAB}}$ of the measured 59.8 MeV data plotted against the laboratory momenta $p^{\mathrm{MC}}_{\mathrm{LAB}}$ of the simulated 59.8 MeV data. The data points are fitted by a linear fit (red line), and an ideal calibration is indicated by the black dashed line. Right: Residual $p^{\mathrm{corr}}_{\mathrm{LAB}} - p^{\mathrm{MC}}_{\mathrm{LAB}}$ after the correction. The data points agree with zero (red line) within uncertainties.

measured 59.8 MeV data presented in black are compared to those for simulations (red) for an angular range of $8.5° \leq \vartheta_{\mathrm{LAB}} < 9.0°$. The peaks were fitted with Gaussian distributions to determine their position. It should be noted that the different relative heights of the peaks in data and simulations are caused by the assumption of phase space behavior in the Monte Carlo simulations which does not have to be the case in nature.

Figure 4.10 (left) shows the obtained mean laboratory momenta of the measured data plotted against the laboratory momenta of the simulations obtained at the same scattering angle for $Q = 59.8$ MeV excess energy. The data points are fitted by a linear function (red line). For an ideally calibrated detector the points should lie on the bisectrix (black dashed line). In the right of figure 4.10 the residual $p^{\mathrm{corr}}_{\mathrm{LAB}} - p^{\mathrm{MC}}_{\mathrm{LAB}}$ is plotted after correcting the laboratory momenta by applying the obtained function:

$$p^{\mathrm{corr}}_{\mathrm{LAB}}\left(^3\mathrm{He}\right) = \left(p^{\mathrm{data}}_{\mathrm{LAB}}\left(^3\mathrm{He}\right) - 0.0987(14)\,\mathrm{GeV}\,c^{-1}\right)/0.9217(11)\,. \tag{4.1}$$

The residuals agree with zero (red line) within their uncertainties.

Due to the much lower statistics of the $Q = 48.8$ MeV data set, it is not feasible to determine a dedicated correction function for this data set. Instead, equation 4.1 was applied to the $Q = 48.8$ MeV data as well, resulting in a good agreement of Monte Carlo simulations with data (see chapter 4.9, figures 4.21 and 4.22).

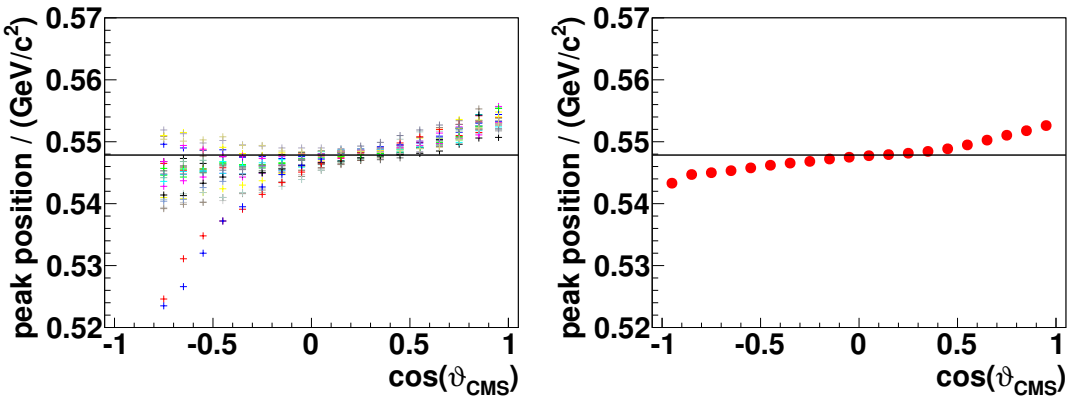

Figure 4.11.: η meson peak position in the missing mass of ^{3}He depending on $\cos\vartheta_{\mathrm{CMS}}$ of the produced η meson for different FRH1 elements for the 59.8 MeV data (left) and for Monte Carlo simulations (right). In the left figure the peak positions for the various FRH1 elements are presented in different colors. The black lines indicate the η mass according to [P$^+$16].

4.5.2. Detector element resolved fine calibration of the measured laboratory momenta

Since the first layer of the forward range hodoscope, which is used for the determination of the ^{3}He momenta, consists of 24 elements, the laboratory momenta had to be also checked separately for each element. The corresponding analysis had been started by A. Passfeld after her diploma thesis and was continued and optimized as part of this thesis.

Figure 4.11 (left) shows the obtained η meson peak position in the ^{3}He missing mass spectra depending on $\cos\vartheta_{\mathrm{CMS}}$ of the produced η meson for the various detector elements for the 59.8 MeV data. The full $\cos\vartheta_{\mathrm{CMS}}$ angular range was divided into 20 bins, and the different colors correspond to different FRH elements. Due to the low statistics in the first two bins, only peak positions for the other 18 bins were determined and plotted. For comparison the η meson peak positions depending on $\cos\vartheta_{\mathrm{CMS}}$ are shown for Monte Carlo simulations in the right of figure 4.11.

It is visible that the measured peak position varies for all detector elements as well as for the different $\cos\vartheta_{\mathrm{CMS}}$ bins. These deviations are due to shifts of the ^{3}He laboratory momenta p_{LAB} depending on $\cos\vartheta_{\mathrm{CMS}}$, which itself depends on p_{LAB}, and need to be corrected. As seen in the right of figure 4.11, the simulations also show a dependency of the peak position on $\cos\vartheta_{\mathrm{CMS}}$, although less prominent. While this

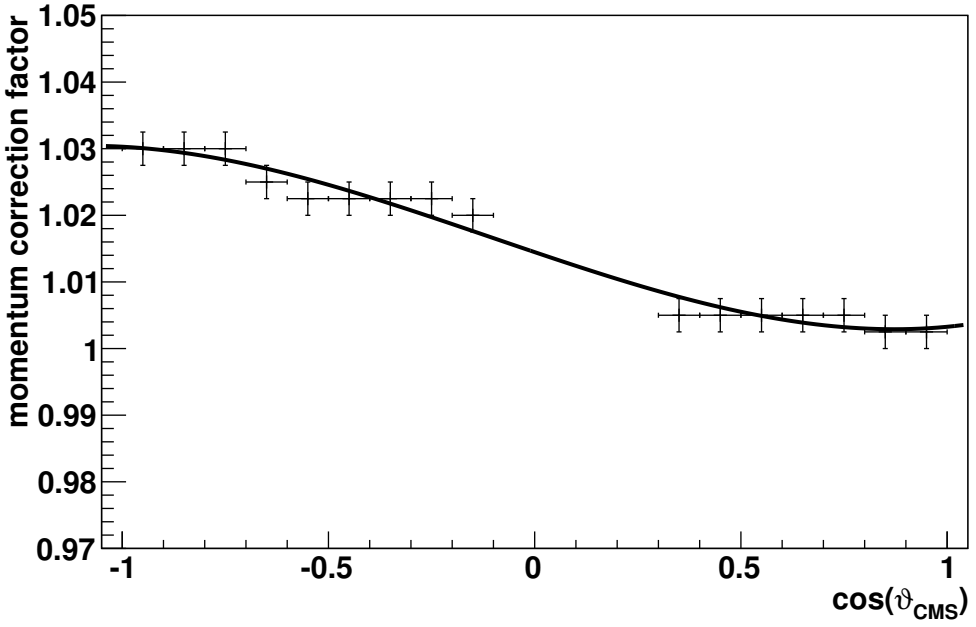

Figure 4.12.: Laboratory momentum correction factor for the 15th element of the first FRH layer depending on $\cos\vartheta_{\mathrm{CMS}}$ of the produced η meson fitted with a third order polynomial (black line).

effect will be addressed in chapter 4.5.3, the measured laboratory momenta were first adjusted to the simulated momenta for all 24 elements of the first FRH layer. Afterwards the correction function determined in chapter 4.5.3 will be applied to the data, as well. In order to align the laboratory momenta of the measured data to the simulations, the laboratory momenta were compared for all FRH1 elements depending on $\cos\vartheta_{\mathrm{CMS}}$ and subsequently correction factors were determined.

In figure 4.12 the laboratory momentum correction factors are presented for the 15th FRH1 element depending on $\cos\vartheta_{\mathrm{CMS}}$ of the produced η. As it can be seen, the $\cos\vartheta_{\mathrm{CMS}}$ bins between -0.1 and 0.3 corresponding to laboratory scattering angles close to $\vartheta_{\mathrm{LAB}}^{\mathrm{max}}$ were excluded. This is due to the fact that a distinct assignment of the laboratory momenta to laboratory scattering angles is not possible for these values because of the finite detector resolution. The obtained factors were fitted with a third order polynomial, which was then in turn used in the analysis to shift the laboratory momenta and, hence, the η meson peak to the position extracted for simulations. As the statistics of the $Q = 48.8\,\mathrm{MeV}$ data set is too low to extract separate correction factors for all 24 elements of the first FRH layer, the same corrections as those determined for the $Q = 59.8\,\mathrm{MeV}$ data set were applied to the 48.8 MeV data. This is reasonable, since both data sets were recorded during the

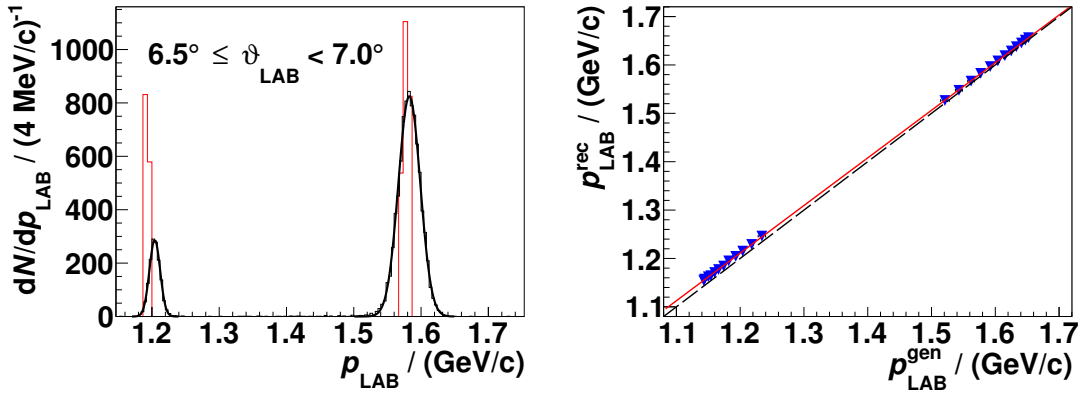

Figure 4.13.: Left: Laboratory momentum of ^{3}He for laboratory scattering angles in the range of $6.5° \leq \vartheta_{\mathrm{LAB}} < 7.0°$ for the simulated reaction $\mathrm{p} + \mathrm{d} \rightarrow {}^3\mathrm{He} + \eta$. The generated laboratory momenta are shown in red and the reconstructed momenta in black with a fit by a Gaussian distribution. Right: Mean reconstructed laboratory momenta obtained from the Gaussian fit distribution plotted against the mean generated laboratory momenta of the corresponding scattering angle range. The uncertainties are smaller than the marker size. A linear fit is shown in red. The dashed line indicates an ideal reconstruction.

same beam time and no shift of the detector calibration was observed between the $Q = 48.8\,\mathrm{MeV}$ and $Q = 59.8\,\mathrm{MeV}$ runs (see chapter 4.3).

4.5.3. Laboratory momentum reconstruction

As already mentioned at the beginning of chapter 4.5, the laboratory momentum reconstruction needs to be checked similar to the angular reconstruction (see chapter 4.4). Due to the higher angular resolution of the WASA-at-COSY forward detector compared to the energy and momentum resolution, respectively, the momentum reconstruction can be tested depending on the laboratory scattering angle ϑ_{LAB} of the ^{3}He. Therefore, the laboratory momenta were plotted for the different angular ranges for the generated and reconstructed Monte Carlo simulations of the reaction $\mathrm{p} + \mathrm{d} \rightarrow {}^3\mathrm{He} + \eta$. An example is presented in the left of figure 4.13 for the angular range of $6.5° \leq \vartheta_{\mathrm{LAB}} < 7.0°$ and an excess energy of $Q = 59.8\,\mathrm{MeV}$. Here the generated momenta are drawn in red and the reconstructed data in black[2]. The two peaks of the reconstructed momenta were

[2]Note that the energy smearing of the FRH was set to default values and not optimized. The optimization will be done in chapter 4.6.

fitted by a Gaussian distribution (black curve), while for the generated momenta the mean value was used.

The obtained mean values of the generated and reconstructed momenta were plotted against each other and fitted by a linear function (see figure 4.13, right). Applying the same procedure for the simulated data with an excess energy of $Q = 48.8\,\mathrm{MeV}$, the following correction functions were determined for both excess energies:

$$p_{\mathrm{LAB}}^{\mathrm{corr}}\left({}^3\mathrm{He}\right) = \left(p_{\mathrm{LAB}}^{\mathrm{rec}}\left({}^3\mathrm{He}\right) - 0.0366(9)\,\mathrm{GeV}\,c^{-1}\right)/0.9798(6) \text{ for } Q = 48.8\,\mathrm{MeV}\,, \tag{4.2}$$

$$p_{\mathrm{LAB}}^{\mathrm{corr}}\left({}^3\mathrm{He}\right) = \left(p_{\mathrm{LAB}}^{\mathrm{rec}}\left({}^3\mathrm{He}\right) - 0.0296(13)\,\mathrm{GeV}\,c^{-1}\right)/0.9845(11) \text{ for } Q = 59.8\,\mathrm{MeV}\,. \tag{4.3}$$

These functions are applied to both the simulated and the measured data for momentum correction.

4.5.4. Comparison of measured data with expectations from two-particle kinematics

After all corrections presented in chapters 4.5.1, 4.5.2, and 4.5.3 had been applied to the measured data, the calibration of the data was checked by comparing the ^{3}He laboratory momenta depending on the ^{3}He laboratory scattering angle ϑ_{LAB} with theoretical expectations from two-particle kinematics. Figure 4.14 shows the according plot for the $Q = 59.8\,\mathrm{MeV}$ data compared to a theoretical curve for the reaction $\mathrm{p} + \mathrm{d} \rightarrow {}^3\mathrm{He} + \eta$ with an excess energy of $Q = 59.8\,\mathrm{MeV}$. The ^{3}He band in data is in very good agreement with the theoretical expectation.

The laboratory momenta depending on ϑ_{LAB} of the $Q = 48.8\,\mathrm{MeV}$ data are plotted in figures 4.15. In the left figure the theoretical expectation for the reaction $\mathrm{p} + \mathrm{d} \rightarrow {}^3\mathrm{He} + \eta$ at $Q = 48.8\,\mathrm{MeV}$ (equaling a proton beam energy of $T_{\mathrm{beam}} = 980\,\mathrm{MeV}$ and a beam momentum of $p_{\mathrm{beam}} = 1.673\,\mathrm{GeV}\,c^{-1}$) is drawn as a black curve and compared to the data. All results presented in [A$^+$14b] are based on this value.

Small deviations of the measured laboratory momenta from the theoretical line are expected due to the fact that the detector calibration was optimized for the $Q = 59.8\,\mathrm{MeV}$ data. While the theoretical curve and the measured data are in good

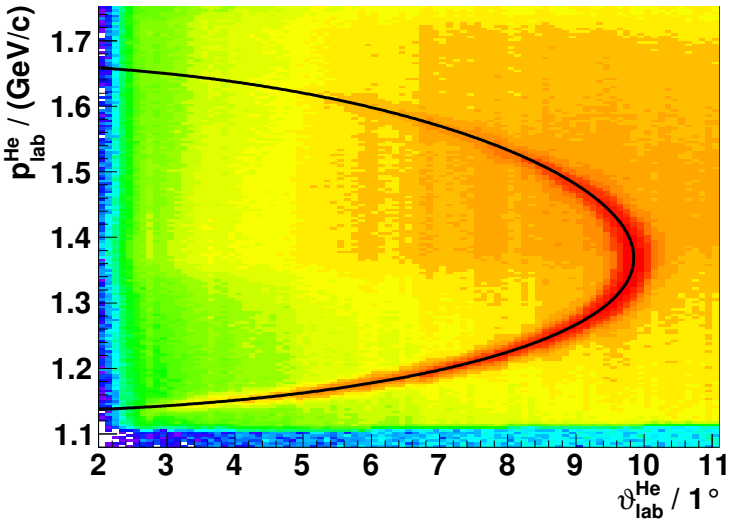

Figure 4.14.: ^{3}He laboratory momenta plotted against the corresponding laboratory angle for the calibrated $Q = 59.8\,\mathrm{MeV}$ data in logarithmic scale. The black line indicates the theoretically expected relationship between laboratory ^{3}He momentum and scattering angle for the reaction $\mathrm{p} + \mathrm{d} \rightarrow {}^3\mathrm{He} + \eta$ at $Q = 59.8\,\mathrm{MeV}$ as calculated from relativistic kinematics [A$^+$14b].

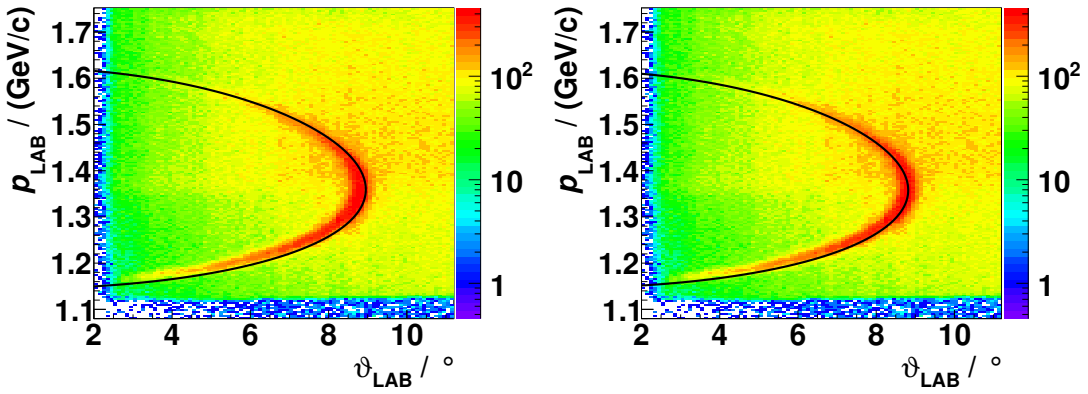

Figure 4.15.: ^{3}He laboratory momenta plotted against the corresponding laboratory angle for the $Q = 48.8\,\mathrm{MeV}$ data after calibration in logarithmic scale. The black lines indicate theoretical expectations for the reaction $\mathrm{p} + \mathrm{d} \rightarrow {}^3\mathrm{He} + \eta$ at $Q = 48.8\,\mathrm{MeV}$ (left) and at $Q = 47.3\,\mathrm{MeV}$ (right) as calculated from relativistic kinematics.

agreement considering the forward detector resolution, a slightly better agreement is observed assuming a proton beam momentum of $p_{\mathrm{beam}} = 1.670\,\mathrm{GeV}\,c^{-1}$, which equals an excess energy of $Q = 47.3\,\mathrm{MeV}$ and a beam energy of $T_{\mathrm{beam}} = 977.3\,\mathrm{MeV}$ (see right of figure 4.15, black line). This equates a deviation of the COSY proton beam momentum of less than 0.2 % from the nominal beam momentum $p_{\mathrm{beam}} = 1.673\,\mathrm{GeV}\,c^{-1}$. However, the expected uncertainty is 0.1 % [Mai97].

The value $p_{\mathrm{beam}} = 1.673\,\mathrm{GeV}\,c^{-1}$ equaling an excess energy of $Q = 48.8\,\mathrm{MeV}$ was used in the analysis presented as well as in the published results [A$^+$14b]. Possible consequences of differences in the assumed proton beam momentum will be discussed in appendix A.1.

4.6. Determination of the energy smearing in Monte Carlo simulations

After calibration of the measured laboratory momenta, the energy smearing of the Monte Carlo simulations had to be adjusted to agree with the energy resolution observed in data. For this reason the laboratory momenta of the measured $Q = 59.8\,\mathrm{MeV}$ data were compared with those of the reconstructed Monte Carlo simulations depending on the ^{3}He laboratory angle.

Figure 4.16 shows the laboratory momenta for the angular range $6.5^\circ \leq \vartheta_{\mathrm{LAB}} < 7.0^\circ$ for data in black and for simulations in red. The peaks were fitted by Gaussian distributions (black and red curve) to extract the standard deviations. The same procedure was applied to each angular range. A relative energy smearing of 3 % in the FRH for the Monte Carlo simulations was found to agree best with the measured data.

4.7. Determination of the angular binning

The differential cross section distributions of the reaction $\mathrm{p} + \mathrm{d} \rightarrow {}^3\mathrm{He} + \eta$ are determined depending on the cosine of the center of mass scattering angle $\vartheta_\eta^{\mathrm{CMS}}$. As already mentioned in chapter 2.3.4, $\cos\vartheta_\eta^{\mathrm{CMS}}$ is equal to the cosine of the ^{3}He scattering angle $\vartheta_{^3\mathrm{He}}^{\mathrm{CMS}}$ but with opposite sign. In the following $\vartheta_\eta^{\mathrm{CMS}}$ will be referred to as ϑ_{CMS}.

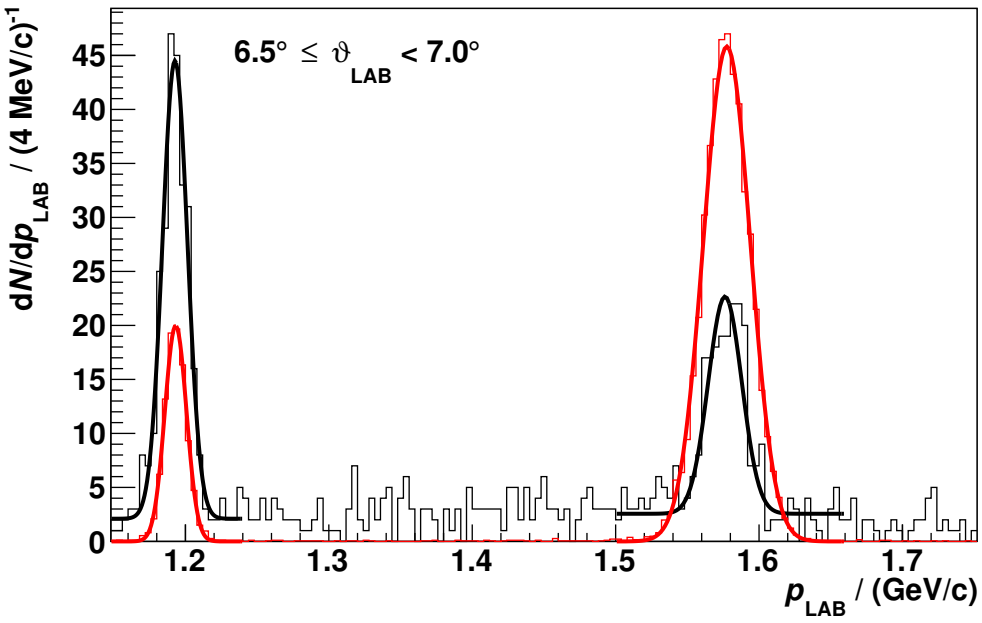

Figure 4.16.: ^{3}He laboratory momenta for the ^{3}He laboratory angular range $6.5° \leq \vartheta_{\mathrm{LAB}} < 7.0°$. The $Q = 59.8\,\mathrm{MeV}$ data are shown in black and the simulations in red. Both measured and simulated data were fitted by Gaussian distributions (black and red curve, respectively). Note that the simulations are scaled by an arbitrary factor for better illustration.

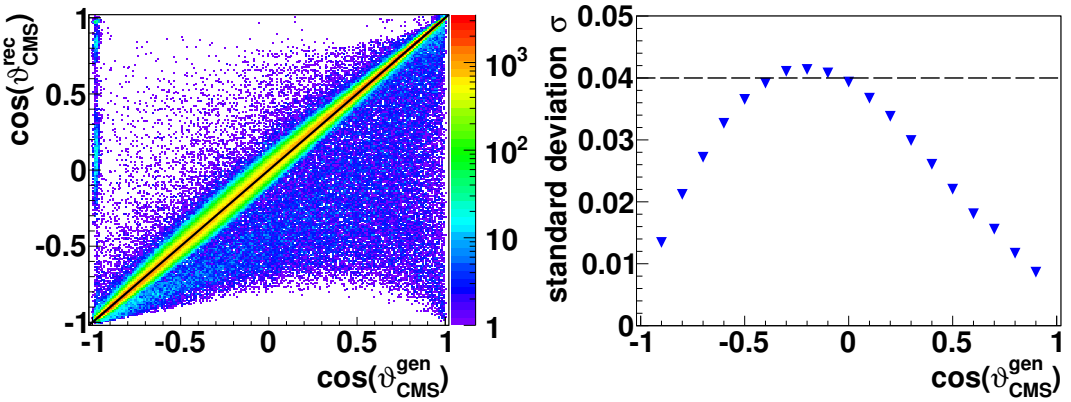

Figure 4.17.: Left: Cosine of the reconstructed CMS scattering angle plotted against the cosine of the generated CMS scattering angle in logarithmic z-scale. The black line indicates the expected bisectrix. Right: Standard deviation of $\cos\vartheta^{\mathrm{rec}}_{\mathrm{CMS}}$ depending on $\cos\vartheta^{\mathrm{gen}}_{\mathrm{CMS}}$. The black dashed line represents the half angular bin width chosen.

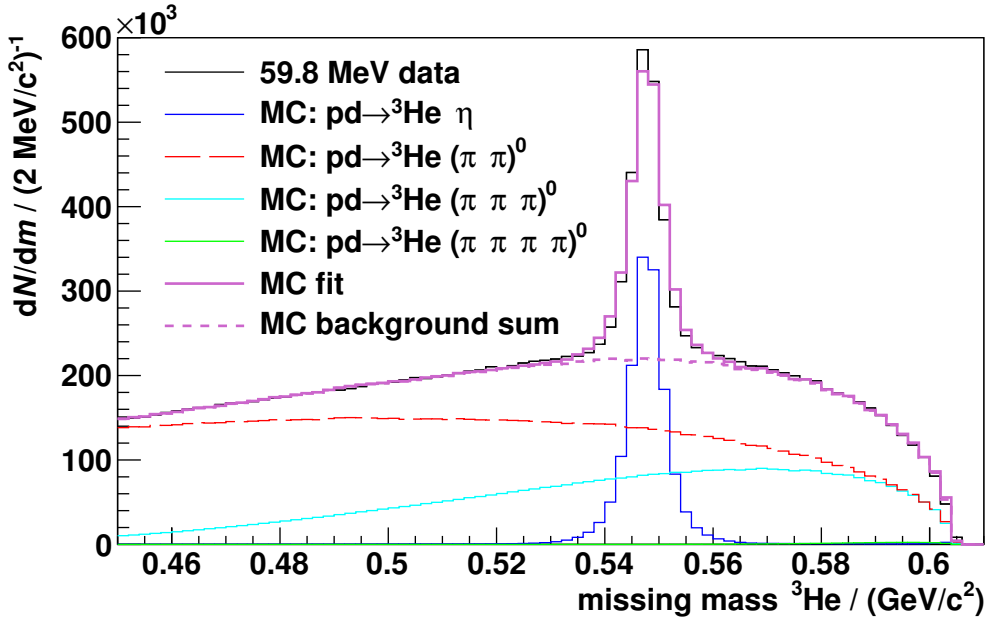

Figure 4.18.: ^{3}He missing mass of the $Q = 59.8\,\mathrm{MeV}$ data for the full angular range fitted by Monte Carlo simulations. Adapted from [A$^+$14b].

The binning of $\cos\vartheta_{\mathrm{CMS}}$ is limited by the detector resolution. Thus, the generated and reconstructed $\cos\vartheta_{\mathrm{CMS}}$ values of Monte Carlo simulations of the reaction $\mathrm{p} + \mathrm{d} \rightarrow {}^3\mathrm{He} + \eta$ at an excess energy of 59.8 MeV were compared. Figure 4.17 (left) shows the two values plotted against each other. The expected bisecting line is drawn in black. Projections of the reconstructed $\cos\vartheta^{\mathrm{rec}}_{\mathrm{CMS}}$ were fitted by Gaussian distributions for different angular ranges of $\cos\vartheta^{\mathrm{gen}}_{\mathrm{CMS}}$ to extract the standard deviation σ presented in figure 4.17 (right). The standard deviation is smallest for $\cos\vartheta^{\mathrm{gen}}_{\mathrm{CMS}} = \pm 1$ and largest with $\sigma_{\mathrm{max}} \approx 0.04$ for $\cos\vartheta^{\mathrm{gen}}_{\mathrm{CMS}}$ close to zero. Hence, an angular bin width of $2 \cdot \sigma_{\mathrm{max}} = 0.08$ was chosen for the determination of the angular distributions. This equates to 25 bins over the full $\cos\vartheta_{\mathrm{CMS}}$ range.

4.8. Number of $\mathrm{p} + \mathrm{d} \rightarrow {}^3\mathrm{He} + \eta$ events per φ bin

The numbers of η mesons produced in the reaction $\mathrm{p} + \mathrm{d} \rightarrow {}^3\mathrm{He} + \eta$ were extracted from ^{3}He missing mass spectra. For this purpose the spectra were fitted by a cocktail of Monte Carlo simulations (see chapter 4.2 for details), using the amplitudes of the different reactions as free parameters. Figure 4.18 shows such a fit by Monte Carlo simulations for the full angular range of the $Q = 59.8\,\mathrm{MeV}$ data. For a better

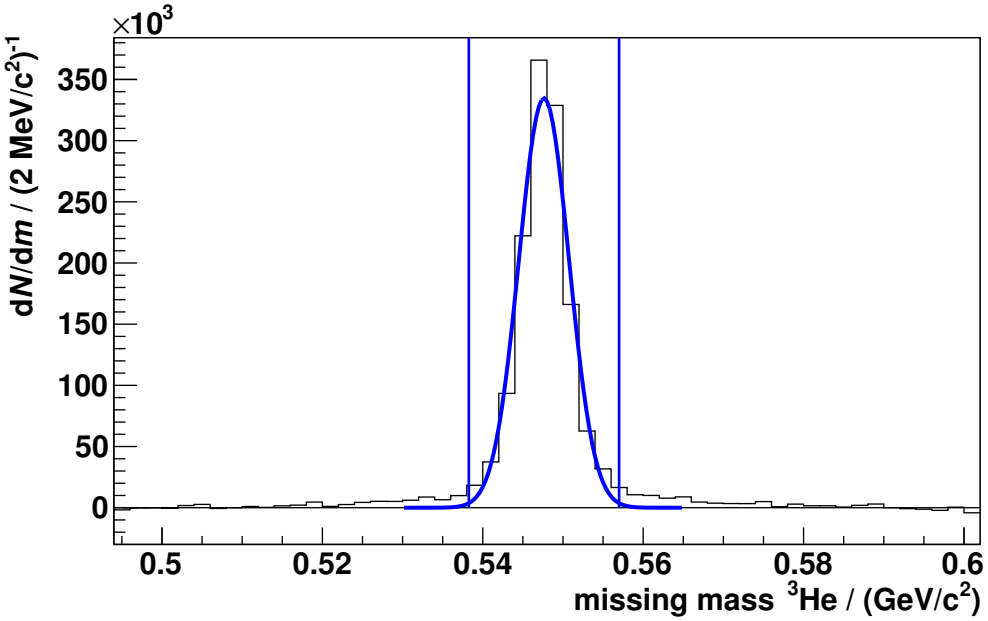

Figure 4.19.: ^{3}He missing mass of the $Q = 59.8\,\mathrm{MeV}$ data for the full angular range after background subtraction fitted by a Gaussian distribution (blue curve). The left and right vertical blue lines indicate the $\pm 3\sigma$ environment. Adapted from [A$^+$14b].

visualization the contributions of multi-pion production reactions with the same number of final state pions were merged in this figure, but treated separately in the fit. It is important to mention that the assumption of phase space behavior is known not to hold true for the multi-pion production. Especially the so-called ABC effect heavily influences the distribution for the two-pion production [ABC60, BAC61, Pé14b]. This is important for the η meson decay studies presented in chapter 6, whereas the determination of the number of η mesons produced can be achieved with any proper description of the background shape close to the η meson mass in the missing mass spectra. A fit by the mentioned Monte Carlo simulation cocktail was found to describe the spectra very well.

After the background distribution had been described, it was subtracted from the missing mass spectrum of the data. The distribution obtained in this way has a clear peak right at the η meson mass (see figure 4.19). This peak was then fitted by a Gaussian distribution and the number of events N_{signal} in the histogram were counted in the 3σ environment. Similarly, the number of background events $N_{\mathrm{background}}$ were determined in the same environment to obtain the statistical uncertainty

$$\Delta \mathrm{N}_{\mathrm{signal}} = \sqrt{\mathrm{N}_{\mathrm{signal}} + \mathrm{N}_{\mathrm{background}}}\,. \tag{4.4}$$

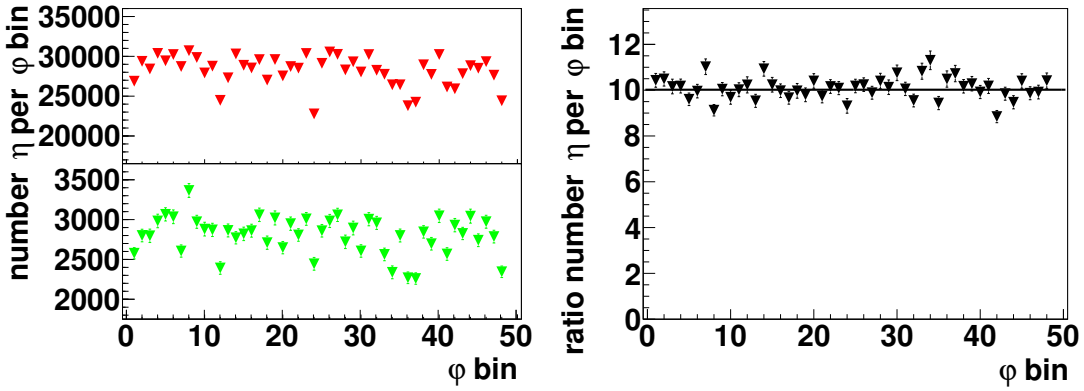

Figure 4.20.: Left: Number of extracted η mesons for different φ bins defined by the detector elements of FTH1. The $Q = 59.8\,\text{MeV}$ data are shown in red, the $Q = 48.8\,\text{MeV}$ data in green. Right: Ratio of the numbers of extracted η mesons depending on φ fitted by a constant (black line) with $\chi^2/ndf \approx 2.42$. All data points are presented with their statistical uncertainties.

Not all events of the reaction p+d $\rightarrow$ ^{3}He+η are within the 3σ environment of the Gaussian distribution and the extracted number had to be corrected for this. Since the measured peak does not necessarily have to be a perfect Gaussian distribution, it is not sufficient to assume about 99.7 % of the events to be located in the 3σ environment. Hence, the η peak in the ^{3}He missing mass of the simulations was fitted by a Gaussian distribution as well, and the events within a 3σ environment were counted. The ratio of this number and the number of events in the full missing mass histogram of the simulated data was used as a correction factor for the number of η events obtained for the measured data.

As the $Q = 48.8\,\text{MeV}$ and $Q = 59.8\,\text{MeV}$ data were measured using an unpolarized proton beam and an unpolarized deuteron target, the number of produced p + d $\rightarrow$ ^{3}He + η reactions should be independent of the azimuthal scattering angle φ. To check this, the number of η mesons was determined using the above mentioned method depending on the element of FTH1 in which the ^{3}He was detected, defining 48 azimuthal scattering angular bins. In figure 4.20 (left) the numbers of observed η mesons are plotted for all φ bins. Both the $Q = 48.8\,\text{MeV}$ data and the $Q = 59.8\,\text{MeV}$ data exhibit a dependence between the number of η mesons reconstructed and the azimuthal scattering angle of ^{3}He in the laboratory system. They show a clear dependence of the η numbers on the detector element which detected the ^{3}He. Possible reasons for this effect are dead material in the forward detector or detector alignment effects.

Since the $Q = 48.8\,\mathrm{MeV}$ data were normalized to the $Q = 59.8\,\mathrm{MeV}$, only a dependence of the ratio of observed η meson numbers on the azimuthal scattering angle φ had to be taken into account. This ratio is plotted in figure 4.20 (right), fitted by a constant. Considering that the data were fitted without systematic uncertainties originating from the procedure used for the η meson number determination, the data points are in good agreement with a constant. As the $Q = 48.8\,\mathrm{MeV}$ and $Q = 59.8\,\mathrm{MeV}$ data are affected in the same way, the φ dependence of the observed $\mathrm{p+d} \rightarrow {}^3\mathrm{He}+\eta$ events does not have to be considered.

4.9. Extraction of the number of $\mathrm{p} + \mathrm{d} \rightarrow {}^3\mathrm{He} + \eta$ events depending on $\cos\vartheta_{\mathrm{CMS}}$

The numbers of $\mathrm{p} + \mathrm{d} \rightarrow {}^3\mathrm{He} + \eta$ events were extracted for 25 angular bins in $\cos\vartheta_{\mathrm{CMS}}$ using the method described in chapter 4.8. Figures 4.21, 4.22, 4.23, and 4.24 show the ^{3}He missing mass distributions for the measured $Q = 48.8\,\mathrm{MeV}$ and $Q = 59.8\,\mathrm{MeV}$ data for all 25 $\cos\vartheta_{\mathrm{CMS}}$ angular bins. For each $\cos\vartheta_{\mathrm{CMS}}$ bin the data were described by a cocktail of Monte Carlo simulations. In case of the three angular bins between $\cos\vartheta_{\mathrm{CMS}} = -0.92$ and -0.68 as well as the three bins between $\cos\vartheta_{\mathrm{CMS}} = 0.76$ and 1.00, the background in the missing mass distributions of the $Q = 48.8\,\mathrm{MeV}$ data were fitted by a third order polynomial, giving a better description of the data in these bins than a fit by a Monte Carlo cocktail. For the same reason the background in the $Q = 59.8\,\mathrm{MeV}$ missing mass histograms for the angular ranges between $\cos\vartheta_{\mathrm{CMS}} = -0.92$ and -0.76 as well as between $\cos\vartheta_{\mathrm{CMS}} = 0.76$ and 1.00 was fitted by a third order polynomial.

After subtraction of the background the peaks located at the η meson mass were described by Gaussian distributions and the number of η mesons was extracted with the procedure already described in chapter 4.8. In order to check the systematic uncertainties of the fits, the fit range was varied by up to $60\,\mathrm{MeV}\,c^{-2}$ and considered for later analysis, if larger than the statistical uncertainties.

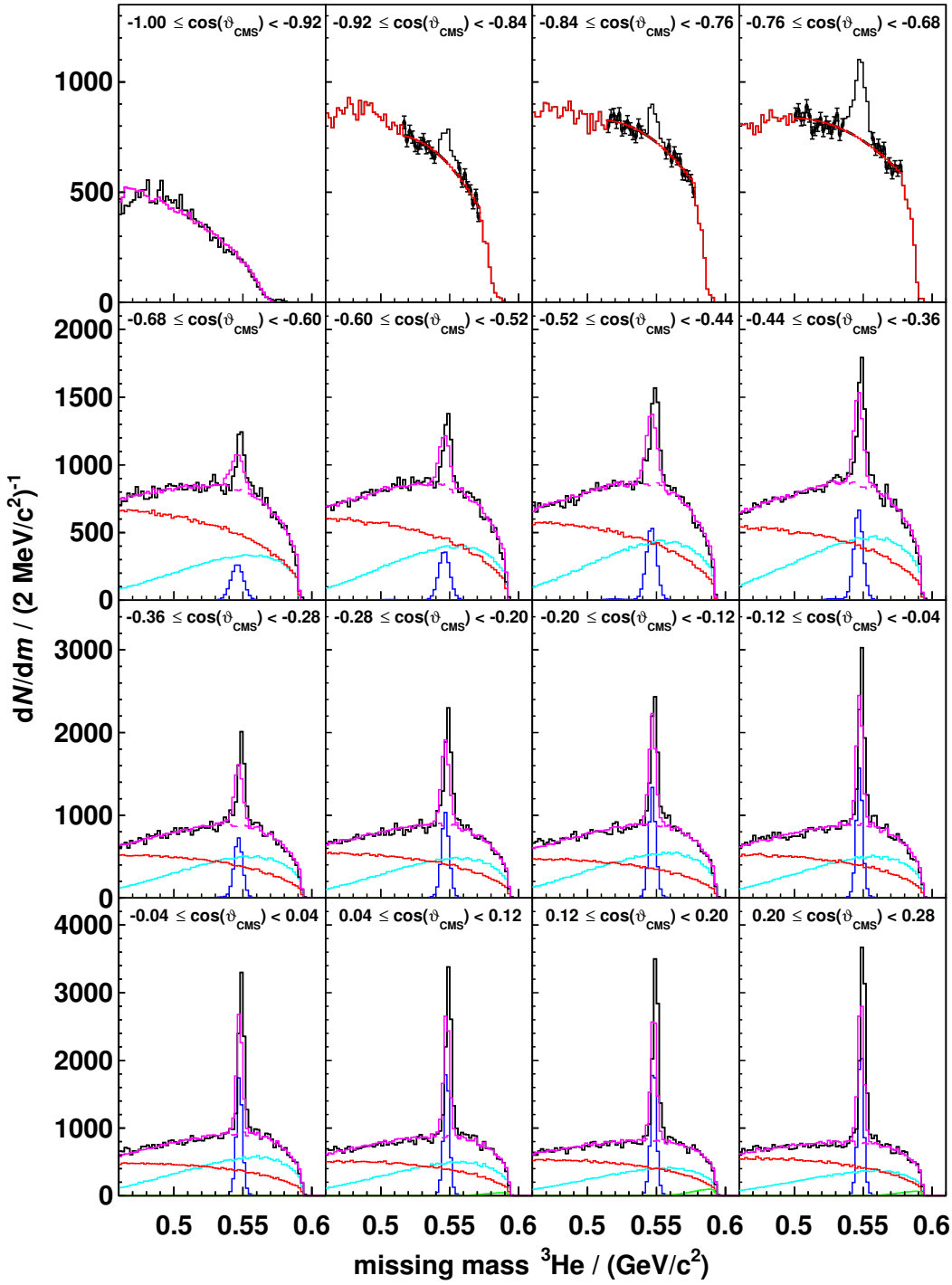

Figure 4.21.: ^{3}He missing mass of the $Q = 48.8\,\mathrm{MeV}$ data for the 16 η meson angular bins ranging from $\cos\vartheta_{\mathrm{CMS}} = -1.00$ to 0.28 fitted by Monte Carlo simulations. For the color code see figure 4.18. The background for the three angular bins ranging from -0.92 to -0.68 is fitted by a third order polynomial within the fit range marked by black points.

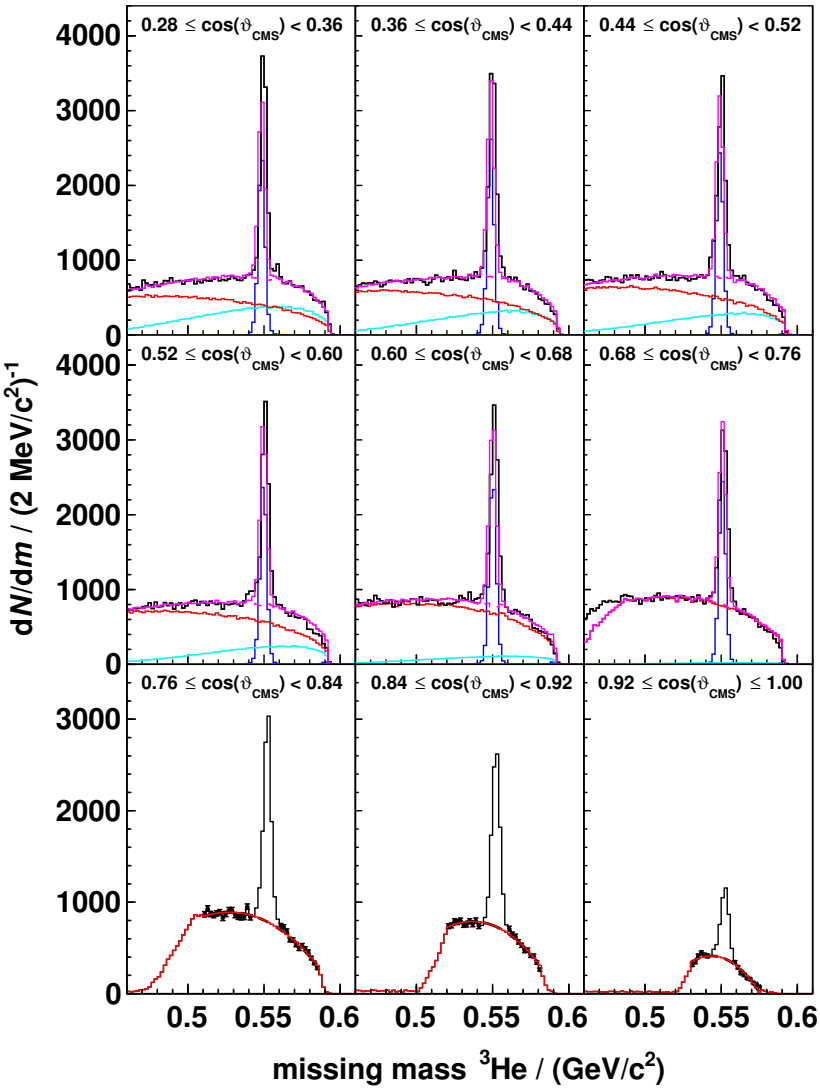

Figure 4.22.: ^{3}He missing mass of the $Q = 48.8\,\mathrm{MeV}$ data for the nine η meson angular bins ranging from $\cos\vartheta_{\mathrm{CMS}} = 0.28$ to 1.00 fitted by Monte Carlo simulations. For the color code see figure 4.18. The background for the three angular bins ranging from 0.76 to 1.00 is fitted by a third order polynomial within the fit range marked by black points.

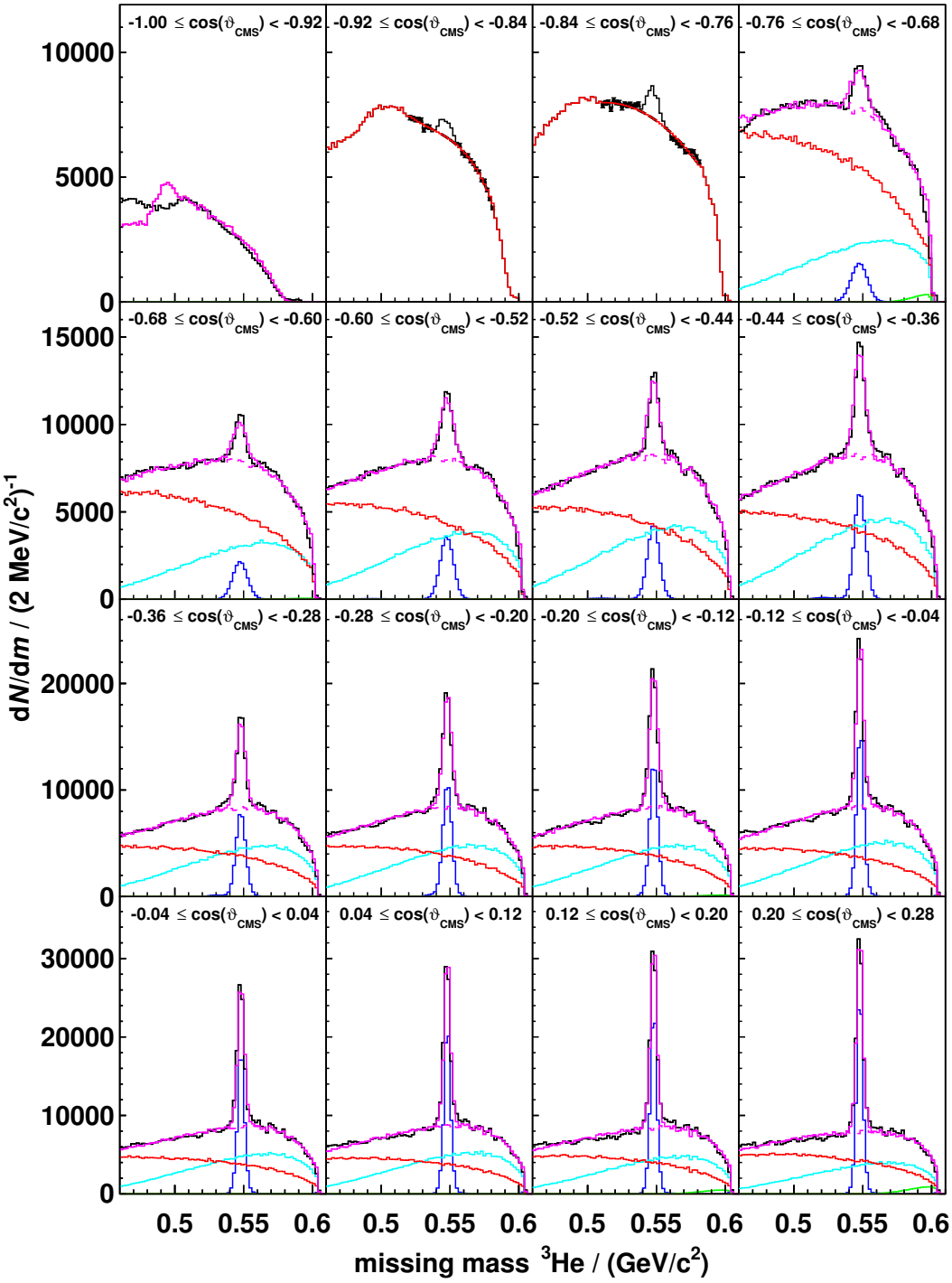

Figure 4.23.: ^{3}He missing mass of the $Q = 59.8\,\mathrm{MeV}$ data for the 16 η meson angular bins ranging from $\cos\vartheta_{\mathrm{CMS}} = -1.00$ to 0.28 fitted by Monte Carlo simulations. For the color code see figure 4.18. The background for the two angular bins ranging from -0.92 to -0.76 is fitted by a third order polynomial within the fit range marked by black points.

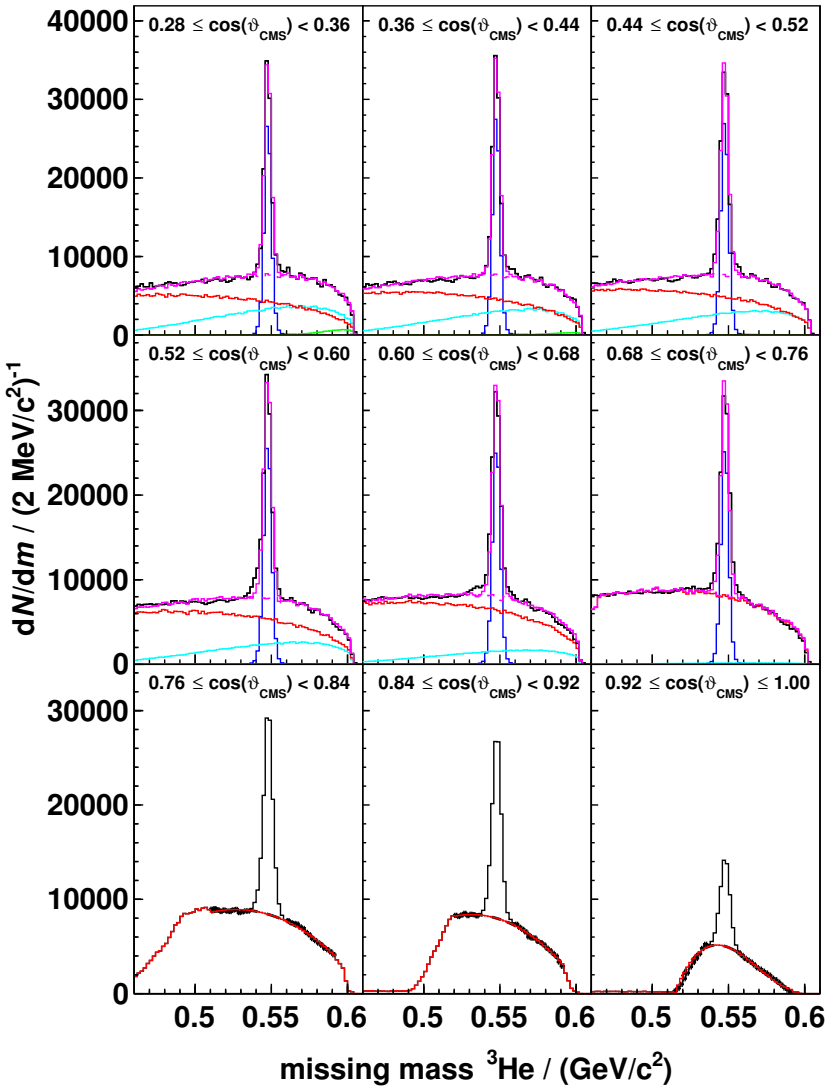

Figure 4.24.: ^{3}He missing mass of the $Q = 59.8\,\mathrm{MeV}$ data for the nine η meson angular bins ranging from $\cos\vartheta_{\mathrm{CMS}} = 0.28$ to 1.00 fitted by Monte Carlo simulations. For the color code see figure 4.18. The background for the three angular bins ranging from 0.76 to 1.00 is fitted by a third order polynomial within the fit range marked by black points.

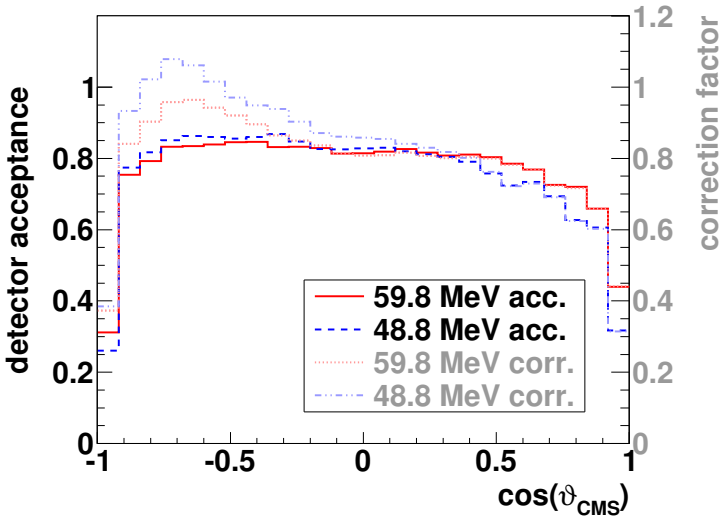

Figure 4.25.: Detector acceptance for the reaction $p + d \rightarrow {}^3He + \eta$ at $Q = 48.8\,MeV$ (blue dashed line) and $Q = 59.8\,MeV$ (red solid line) and the corresponding correction factors for $Q = 48.8\,MeV$ (blue dashed dotted line) and $Q = 59.8\,MeV$ (red dotted line) according to Monte Carlo simulations [A$^+$14b].

4.10. Acceptance and efficiency corrections

Not all ^3He nuclei produced in the reaction $p + d \rightarrow {}^3He + \eta$ were detected and subsequently reconstructed in the analysis. Hence, the extracted number of η mesons has to be corrected for the detector acceptance, which is the product of the geometrical acceptance and the track reconstruction efficiency. This was done by comparing the number of ^3He nuclei generated in Monte Carlo simulations of the reaction $p + d \rightarrow {}^3He + \eta$ with the number of reconstructed ^3He.

Figure 4.25 shows the detector acceptances depending on $\cos\vartheta_{CMS}$ of the η meson for the simulated $Q = 48.8\,MeV$ (blue dashed line) and $Q = 59.8\,MeV$ (red solid line) data sets. In the uncertainties, which are in the size of the line width, the systematic uncertainties of up to 0.8 % introduced by the finite COSY beam momentum resolution of 0.1 % are included [Mai97]. Except for the very first and very last bin, the acceptance varies smoothly within the range of 60 % to 86 %. The drop close to $\cos\vartheta_{CMS} = -1$ and $\cos\vartheta_{CMS} = 1$ is caused by ^3He escaping through the COSY beam pipe. Therefore, the very first and the last $\cos\vartheta_{CMS}$ bin were excluded from further analysis.

In addition to the corrections regarding the geometrical acceptance and the track reconstruction efficiency, the number of extracted $p + d \rightarrow {}^3He + \eta$ events has to be corrected for effects resulting from the finite momentum resolution of

the WASA detector. The inclusion of the latter was done by using the angular distribution extracted from data as input for the angular distribution in Monte Carlo simulation, which was then in turn used to recalculate the efficiency with the more realistic angular dependency of the reaction. Afterwards the newly determined correction factors were used for the extraction of an updated angular distribution. This method was performed iteratively until convergence was reached. The resulting correction factors including all previously mentioned effects are presented in figure 4.25 for $Q = 48.8\,\mathrm{MeV}$ (blue dashed dotted line) and $Q = 59.8\,\mathrm{MeV}$ (red dotted line).

4.11. Data normalization

In order to compare the two extracted angular distributions and to determine the ratio of the total cross sections at the excess energies $Q = 48.8\,\mathrm{MeV}$ and $Q = 59.8\,\mathrm{MeV}$, the data have to be normalized. For an absolute normalization the luminosity of the two measurements has to be known. With a known luminosity L the extracted numbers $N_{\eta,i}$ of $\mathrm{p + d \rightarrow {}^3He + \eta}$ events for the different angular bins can be converted into the differential cross section in the given bin i:

$$\left(\frac{\mathrm{d}\sigma}{\mathrm{d}\Omega}\right)_i = \frac{1}{2\pi} \cdot \frac{1}{L} \cdot \frac{\mathrm{d}N_{\eta,i}}{\mathrm{d}\cos\vartheta_{\mathrm{CMS},i}}\,. \tag{4.5}$$

The total cross section σ_{total} of the reaction $\mathrm{p + d \rightarrow {}^3He + \eta}$ is then defined as the sum of all differential cross sections:

$$\int_0^{2\pi}\int_0^{\pi} \frac{\mathrm{d}\sigma}{\mathrm{d}\Omega}\mathrm{d}\cos\vartheta_{\mathrm{CMS}}\mathrm{d}\varphi\,. \tag{4.6}$$

Typically, reactions with well known cross sections are used to determine luminosities, like, e.g. the pd elastic scattering. Since the analyzed data set was recorded with trigger settings optimized for the reaction $\mathrm{p + d \rightarrow {}^3He + X}$, it is reasonable to choose a normalization reaction with a ^{3}He nucleus in the final state. This way systematic effects due to, e.g. dead times are avoided. Therefore, the reaction $\mathrm{p + d \rightarrow {}^3He + \pi^0}$ was used for normalization purposes, since a broad data base of differential cross sections is available for $\cos\vartheta_{\pi^0}^{\mathrm{CMS}} = -1$ [B$^+$85, K$^+$86]. With these cross sections a relative normalization was done, as, besides the determination of the angular distributions, the ratio of the total cross sections at $Q = 48.8\,\mathrm{MeV}$

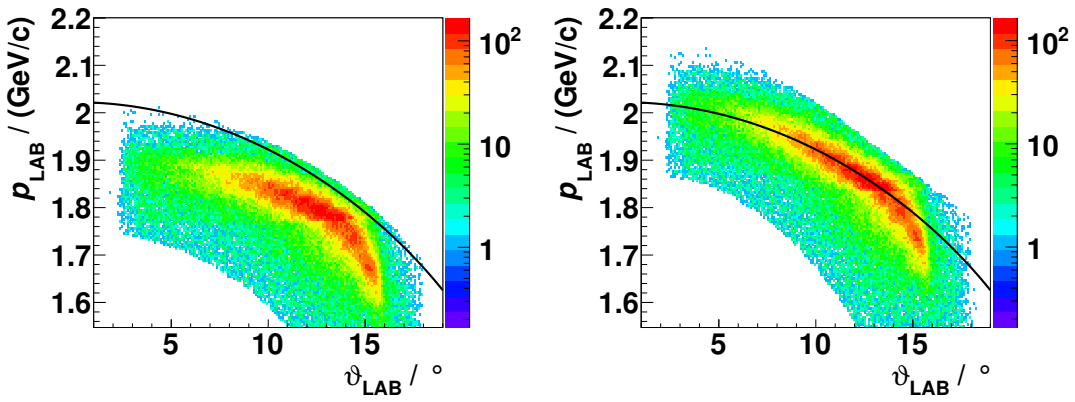

Figure 4.26.: Laboratory momenta of ^{3}He detected in the second FRH layer plotted against the corresponding laboratory polar angle after application of a rough cut around the $p+d \rightarrow {}^3He+\pi^0$ band. The black line is the expected position of the band according to two-particle kinematics. The $T_{beam} = 1000\,MeV$ data is shown before (left) and after fine tuning of the calibration (right).

and $Q = 59.8\,MeV$ is of big interest. What cancel are systematic effects due to the ^{3}He nucleus being stopped in the second FRH layer instead of the first one for $\cos\vartheta_{\pi^0}^{CMS}$ close to -1.

For simplification, in the following the labeling $\cos\vartheta_{CMS}$ will be used for $\cos\vartheta_{\pi^0}^{CMS}$ (compare to chapter 2.3.4).

4.11.1. Calibration tuning of the second FRH layer

Since the ^{3}He nuclei stemming from the reaction $p+d \rightarrow {}^3He+\pi^0$ with $\cos\vartheta_{CMS} \approx -1$ were stopped in the second FRH layer, the calibration of this detector layer has to be checked and adjusted, if necessary. For this purpose the same method as the one described in chapter 4.5.1 was applied.

In figure 4.26 the absolute values of the ^{3}He laboratory momenta are plotted against the corresponding laboratory angles for data recorded at a proton beam energy of $T_{beam} = 1000\,MeV$ ($Q_\eta = 59.8\,MeV$) and compared to the expected position of the ^{3}He band according to theoretical expectations from two-particle kinematics (black line). Data before the fine calibration are presented in the left histogram and the same data after calibration in the right one. For a better visualization of the $p + d \rightarrow {}^3He + \pi^0$ band, a rough cut was applied to the data before plotting. A good agreement between the expectations and the measured data after fine calibration is visible for $\vartheta_{LAB} < 13.5°$. The deviations observed for higher scattering angles are caused by ^{3}He nuclei being stopped in the dead material

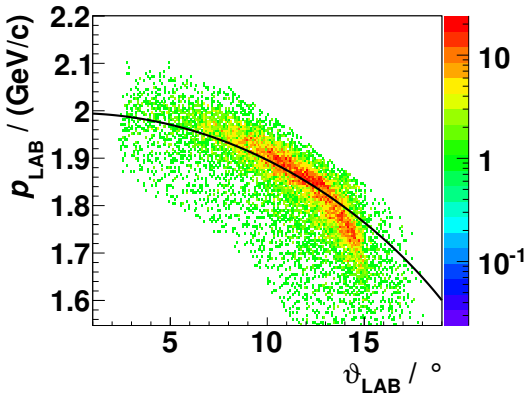

Figure 4.27.: Laboratory momenta of ^{3}He detected in the second FRH layer plotted against the corresponding laboratory polar angle after application of a rough cut around the $p + d \rightarrow {}^3He + \pi^0$ band. The $T_{beam} = 980\,MeV$ data is presented after applying the fine calibration. For comparison the expected position of the ^{3}He band is plotted in black.

between the first and second layer of the FRH or close to it. For the normalization only scattering angles below 13.5° are relevant (see also chapter 4.11.3).

Due to the lower statistics for the data recorded at $T_{beam} = 980\,MeV$ the same fine calibration parameters were used as for the $T_{beam} = 1000\,MeV$ data. Although the fine calibration was optimized for the $T_{beam} = 1000\,MeV$ data, a good agreement between theoretical expectations and the $T_{beam} = 980\,MeV$ data was achieved after applying the fine calibration for the relevant scattering angles. The resulting distribution is presented in figure 4.27.

4.11.2. Extraction of the number of $p + d \rightarrow {}^3He + \pi^0$ events

The reaction $p + d \rightarrow {}^3He + \pi^0$ was identified and subsequently quantified by using the information of the detected ^{3}He. For background reduction exactly two neutral particles expected from the decay $\pi^0 \rightarrow \gamma + \gamma$ are required to be detected in the central detector. Although this condition was applied both to the $T_{beam} = 1000\,MeV$ and the $T_{beam} = 980\,MeV$ data sets and no absolute but a relative normalization was performed, the changes in the detector acceptance might be influenced differently. This will be tested in chapter 4.11.3.

Due to the lower mass of the π^0 meson compared to the η meson in combination with the finite detector resolution, it is possible that the squared missing mass

$$|p_p + p_d - p_{^3He}|^2 = (T_p + m_p + T_d + m_d - T_{^3He} - m_{^3He})^2 - (\vec{p}_p + \vec{p}_d - \vec{p}_{^3He})^2 \quad (4.7)$$

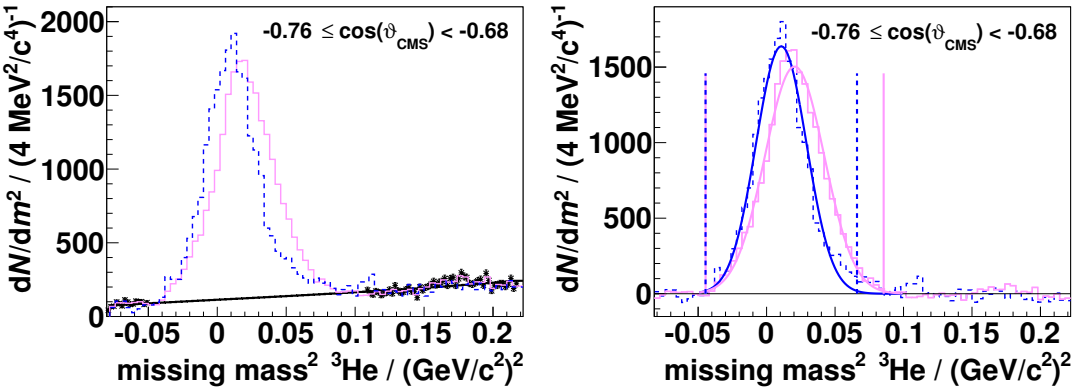

Figure 4.28.: Left: Squared ^{3}He missing mass with the background fitted by a second order polynomial for the measured $T_{\text{beam}} = 1000\,\text{MeV}$ data (purple solid line) and the $T_{\text{beam}} = 980\,\text{MeV}$ data (blue dashed line) for the π^0 angular range $-0.76 \leq \cos\vartheta_{\text{CMS}} < -0.68$. The background fit area is indicated by the black points. Two neutral particles detected in the central detector are required. Right: Same spectra after background subtraction with the peaks fitted by Gaussian distributions. The purple solid lines and blue dashed lines to the left and to the right of the peaks indicate the 3σ environment of the Gaussian distributions.

is negative. Computing the square root would therefore result in complex masses. Hence, not ^{3}He missing masses but squared ^{3}He missing masses were studied to extract the number of π^0 mesons produced depending on $\cos\vartheta_{\text{CMS}}$. For the angular bins the same width as for the η number extraction was used.

Figure 4.28 displays the squared missing mass of the ^{3}He for the angular range $-0.76 \leq \cos\vartheta_{\text{CMS}} < -0.68$ before (left) and after background subtraction (right). If the background of the $T_{\text{beam}} = 1000\,\text{MeV}$ data and the $T_{\text{beam}} = 980\,\text{MeV}$ data is fitted independently, systematic effects due to the background fit mimicking enhancements in the peak region for one or the other beam energy can be observed. To avoid this systematic effect, the background regions $-0.080\,(\text{GeV}/c^2)^2$ to $-0.050\,(\text{GeV}/c^2)^2$ and $0.108\,(\text{GeV}/c^2)^2$ to $0.218\,(\text{GeV}/c^2)^2$ (indicated by the black points in the left histogram of figure 4.28) of the $T_{\text{beam}} = 1000\,\text{MeV}$ and $T_{\text{beam}} = 980\,\text{MeV}$ data were used to scale the histograms to each other, and a common fit by a second order polynomial distribution was applied to describe the background (black line). This way for both beam energies a good background description was achieved for all angular ranges relevant for the normalization (see chapter 4.11.3).

After background subtraction (see figure 4.28, right) the peaks at the squared π^0 mass in the distributions of the squared ^{3}He missing mass were fitted by Gaussian

distributions for both beam energies, and the number of events within the 3σ environment of the Gaussian distributions indicated by the blue dashed and purple solid lines were determined. The difference of the peak position visible in figure 4.28 (right) is due to the calibration being optimized for the $T_{\mathrm{beam}} = 1000\,\mathrm{MeV}$ data, but as in case of the analysis regarding the η meson, this has no influence on the determined integrals. Since not all $\mathrm{p} + \mathrm{d} \rightarrow {}^3\mathrm{He} + \pi^0$ events are located within the 3σ environment of the fit, the extracted number has to be corrected. Similar to the extraction of the η meson number, this was done by fitting Monte Carlo simulations with a Gaussian distribution and comparing the number of all detected $\mathrm{p}+\mathrm{d} \rightarrow {}^3\mathrm{He}+\pi^0$ events with those within the 3σ environment (see chapter 4.8). This factor was then used to correct the numbers determined for the measured data.

4.11.3. Acceptance and efficiency correction for $\mathrm{p} + \mathrm{d} \rightarrow {}^3\mathrm{He} + \pi^0$

Similar to the determined number of η mesons, the extracted number of $\mathrm{p} + \mathrm{d} \rightarrow {}^3\mathrm{He} + \pi^0$ events has to be corrected for the acceptance of the WASA detector. Therefore, the numbers of events generated in Monte Carlo simulations were compared to those reconstructed in the analysis.

Figure 4.29 (left) displays the detector acceptance for the reaction $\mathrm{p} + \mathrm{d} \rightarrow {}^3\mathrm{He} + \pi^0$ determined with Monte Carlo simulations depending on $\cos\vartheta_{\mathrm{CMS}}$ of the π^0 meson. The acceptance in case of the beam energy $T_{\mathrm{beam}} = 1000\,\mathrm{MeV}$ is drawn in purple, while that for $T_{\mathrm{beam}} = 980\,\mathrm{MeV}$ is plotted in blue. Alongside the acceptance without the additional requirement of two neutral particles detected in the CD (dashed lines), the acceptance with this requirement is shown (solid lines). This requirement reduces the detector acceptance by a factor of about two.

For the relative normalization it is important to exclude systematic effects depending on the beam energy due to changes of the acceptance by the application of a signature cut in the central detector. Therefore, the ratios of the acceptances at both beam energies with and without the additional CD requirement (black solid line and red dashed line, respectively) are compared in the right of figure 4.29. Except for the angular bins above $\cos\vartheta_{\mathrm{CMS}} = -0.52$, the ratios agree within their uncertainties. The gray shaded areas indicate the angular ranges not used for the relative data normalization. The angular range $-1.00 \leq \cos\vartheta_{\mathrm{CMS}} < -0.92$

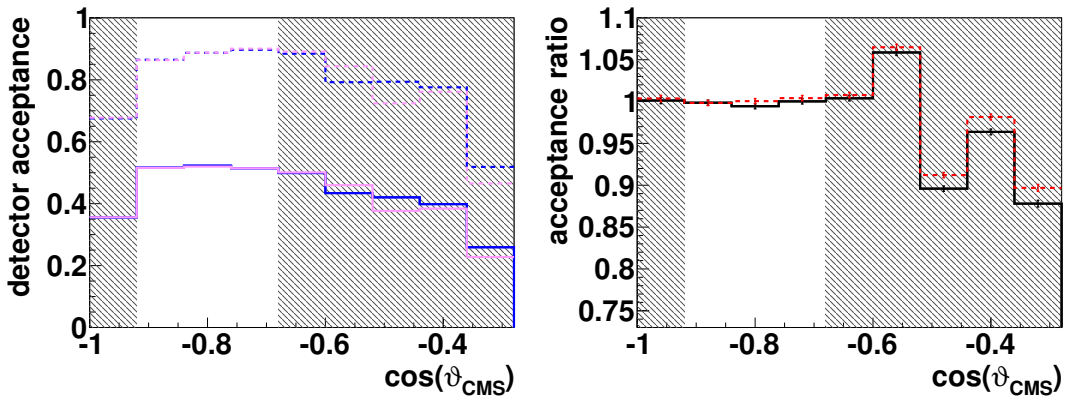

Figure 4.29.: Left: Detector acceptance for the simulated reaction $p + d \rightarrow {}^3He + \pi^0$ depending on $\cos\vartheta_{CMS}$ of the π^0 meson for the kinetic beam energy $T_{beam} = 1000\,MeV$ (purple lines) and for $T_{beam} = 980\,MeV$ (blue lines) with and without requiring two neutral particles detected in the central detector (solid and dashed lines, respectively). Only the area not shaded in gray was used for the analysis. Right: Ratio of the $T_{beam} = 1000\,MeV$ and $T_{beam} = 980\,MeV$ detector acceptance without requirements in the CD (red dashed line) and requiring two neutral particles detected in the CD (black solid line) as derived from simulations.

was excluded due to the drop of the acceptance caused by ^3He nuclei escaping through the COSY beam pipe. While the detector acceptance ratios agree with one within their uncertainties for the angular range $-1.00 \leq \cos\vartheta_{CMS} < -0.60$, they fluctuate for higher values of $\cos\vartheta_{CMS}$. Hence, these bins were excluded from the analysis, as well. As mentioned in chapter 4.11.1, ^3He nuclei with laboratory scattering angles above 13.5° can be stopped in the dead material between the first and second layer of the FRH or close to it. Thus, only the three angular bins in the range of $-0.92 \leq \cos\vartheta_{CMS} < -0.68$ were utilized for the normalization. The chosen angular range is reasonable, as no data with $\cos\vartheta_{CMS} \geq -0.68$ are required for the extrapolation of the differential cross section ratio to $\cos\vartheta_{CMS} = -1$ (see chapter 4.11.4).

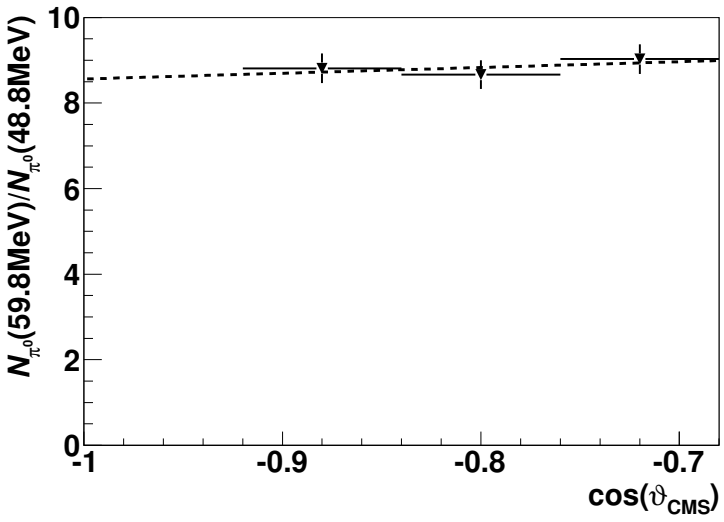

Figure 4.30.: Relative π^0 yield for the measurements at the beam energies $T_{\text{beam}} = 1000\,\text{MeV}$ and $T_{\text{beam}} = 980\,\text{MeV}$ equaling η meson excess energies of $Q = 59.8\,\text{MeV}$ and $Q = 48.8\,\text{MeV}$, respectively, depending on $\cos\vartheta_{\text{CMS}}$ of the π^0 meson. The data points are presented with statistical uncertainties (vertical bars) and the bin width is indicated by the horizontal bars. A fit by a first order polynomial is drawn as a dashed line. Adapted from [A$^+$14b].

4.11.4. Relative normalization

After applying the acceptance correction, the ratio of the determined numbers of $\text{p}+\text{d} \rightarrow {}^3\text{He}+\pi^0$ events was investigated depending on $\cos\vartheta_{\text{CMS}}$. Figure 4.30 shows the ratio of the acceptance corrected numbers of the single-pion production at $T_{\text{beam}} = 1000\,\text{MeV}$ and $T_{\text{beam}} = 980\,\text{MeV}$ corresponding to η meson excess energies $Q_\eta = 59.8\,\text{MeV}$ and $Q_\eta = 48.8\,\text{MeV}$ for the angular range $-0.92 \leq \cos\vartheta_{\text{CMS}} < -0.68$ fitted by a first order polynomial of the form

$$\frac{N_{\pi^0}\,(59.8\,\text{MeV})}{N_{\pi^0}\,(48.8\,\text{MeV})} = a_0 + a_1 \cdot (\cos\vartheta_{\text{CMS}} + 1) \tag{4.8}$$

to extract the ratio at $\cos\vartheta_{\text{CMS}} = -1$.

The uncertainty of the obtained ratio

$$\frac{N_{\pi^0}\,(T_{\text{beam}} = 1000\,\text{MeV})}{N_{\pi^0}\,(T_{\text{beam}} = 980\,\text{MeV})} = 8.6 \pm 0.6 \tag{4.9}$$

is dominated by the lower statistics of the $T_{\text{beam}} = 980\,\text{MeV}$ data [A$^+$14b]. For the relative normalization of the η meson measurements the differential cross section

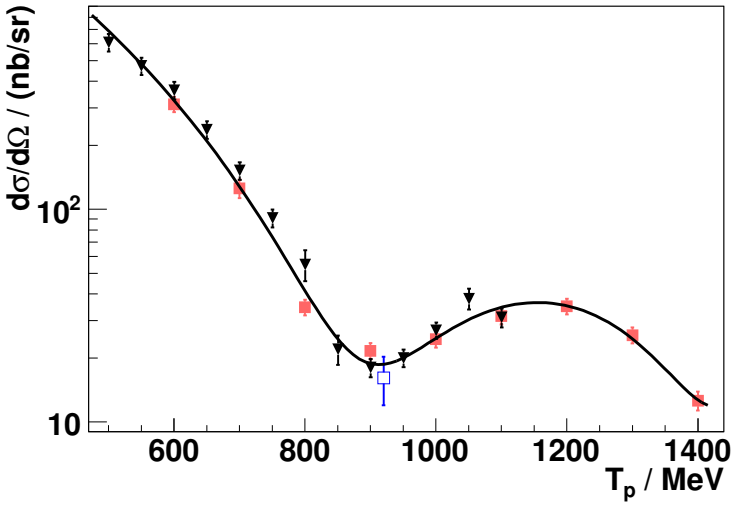

Figure 4.31.: Differential cross sections for $\cos\vartheta_{\mathrm{CMS}} = -1$ depending on the proton beam energy T_{p}. The data are taken from [K$^+$86] for the reaction $\mathrm{d} + \mathrm{p} \to {}^3\mathrm{He} + \pi^0$ (black triangles) as well as from [B$^+$85] for the reactions $\mathrm{p} + \mathrm{d} \to {}^3\mathrm{He} + \pi^0$ (open blue square) and $\mathrm{p} + \mathrm{d} \to \mathrm{t} + \pi^+$ (red filled squares, scaled by an isospin factor of 0.5). All data points are shown with statistical and systematic uncertainties and were fitted by a fifth order polynomial (black line) [A$^+$14b].

ratio of the reaction $\mathrm{p} + \mathrm{d} \to {}^3\mathrm{He} + \pi^0$ at $\cos\vartheta_{\mathrm{CMS}} = -1$ needs to be known in addition.

In figure 4.31 the differential cross sections at $\cos\vartheta_{\mathrm{CMS}} = -1$ are displayed for different proton beam energies T_{beam} (labeled as T_{p} in the figure) available in literature. The black triangles are data from [K$^+$86] for the reaction $\mathrm{d}+\mathrm{p} \to {}^3\mathrm{He}+\pi^0$ and the open blue square and red filled squares are from [B$^+$85] for the reactions $\mathrm{p} + \mathrm{d} \to {}^3\mathrm{He} + \pi^0$ and $\mathrm{p} + \mathrm{d} \to \mathrm{t} + \pi^+$, respectively. The latter are scaled by an isospin factor of 0.5. All data points are shown with statistical and systematic uncertainties.

In order to obtain the differential cross sections at kinetic beam energies of $T_{\mathrm{beam}} = 980\,\mathrm{MeV}$ and $T_{\mathrm{beam}} = 1000\,\mathrm{MeV}$, the data points were fitted by a fifth order polynomial. As already published in [A$^+$14b], the ratio of the extracted differential cross sections at these energies amounts to

$$\frac{\sigma_{\pi^0}\left(T_{\mathrm{beam}} = 980\,\mathrm{MeV}\right)}{\sigma_{\pi^0}\left(T_{\mathrm{beam}} = 1000\,\mathrm{MeV}\right)} = 0.914 \pm 0.009\,. \tag{4.10}$$

The given uncertainty includes statistical as well as systematic uncertainties. Using the results presented in equations 4.9 and 4.10, the cross section ratio is determined by

$$\begin{aligned}\frac{\sigma_\eta\,(48.8\,\mathrm{MeV})}{\sigma_\eta\,(59.8\,\mathrm{MeV})} &= \frac{\sigma_{\pi^0}\,(T_\mathrm{beam} = 980\,\mathrm{MeV})}{\sigma_{\pi^0}\,(T_\mathrm{beam} = 1000\,\mathrm{MeV})} \cdot \frac{N_{\pi^0}\,(T_\mathrm{beam} = 1000\,\mathrm{MeV})}{N_{\pi^0}\,(T_\mathrm{beam} = 980\,\mathrm{MeV})} \\ &\quad \cdot \frac{N_\eta\,(48.8\,\mathrm{MeV})}{N_\eta\,(59.8\,\mathrm{MeV})} \\ &= (0.914 \pm 0.009) \cdot (8.6 \pm 0.6) \cdot \frac{N_\eta\,(48.8\,\mathrm{MeV})}{N_\eta\,(59.8\,\mathrm{MeV})}\end{aligned} \tag{4.11}$$

with the acceptance corrected meson yields N_i [A$^+$14b].

5. Results of the $p + d \rightarrow {}^3He + \eta$ analysis

In order to determine the total cross section ratio $\sigma_\eta\,(48.8\,\mathrm{MeV})\,/\sigma_\eta\,(59.8\,\mathrm{MeV})$ using equation 4.11, the meson yields for the whole angular range have to be derived. Due to the missing acceptance of the WASA forward detector at $\cos\vartheta_{\mathrm{CMS}} = \pm 1.0$, the according values have to be extrapolated from the information in the other angular bins. This will be done in chapter 5.1, where the obtained angular distributions will be compared to differential cross sections at similar excess energies available in literature (see chapter 5.1.1) as well as with theoretical expectations (see chapter 5.1.2). In chapter 5.2 the determined total cross section ratio will be utilized to calculate a total cross section at $Q = 48.8\,\mathrm{MeV}$ by scaling the WASA-at-COSY at $Q = 59.8\,\mathrm{MeV}$ data to the $Q = 59.4\,\mathrm{MeV}$ ANKE data [R+09].

5.1. Angular distributions of the reaction $p + d \rightarrow {}^3He + \eta$

The angular distributions extracted in the scope of this thesis are presented with regard to the cosine of the scattering angle of the η meson in the CMS, $\cos\vartheta_\eta^{\mathrm{CMS}}$. For a better comparison angular distributions from literature measured using a deuteron beam will be given as a function of $\cos\vartheta_{^3\mathrm{He}}^{\mathrm{CMS}}$. Both will be referred to as $\cos\vartheta_{\mathrm{CMS}}$.

Figure 5.1 (a) shows the angular distribution of the determined η meson yields for the two excess energies $Q = 48.8\,\mathrm{MeV}$ (filled blue circles) and $Q = 59.8\,\mathrm{MeV}$ (open red circles). All data points are presented in arbitrary units with both statistical and systematic uncertainties. The latter include uncertainties in the fits of the missing mass histograms (see chapter 4.9) and uncertainties introduced by the finite COSY beam momentum resolution with a precision of 0.1 % [Mai97] (see chapter 4.10).

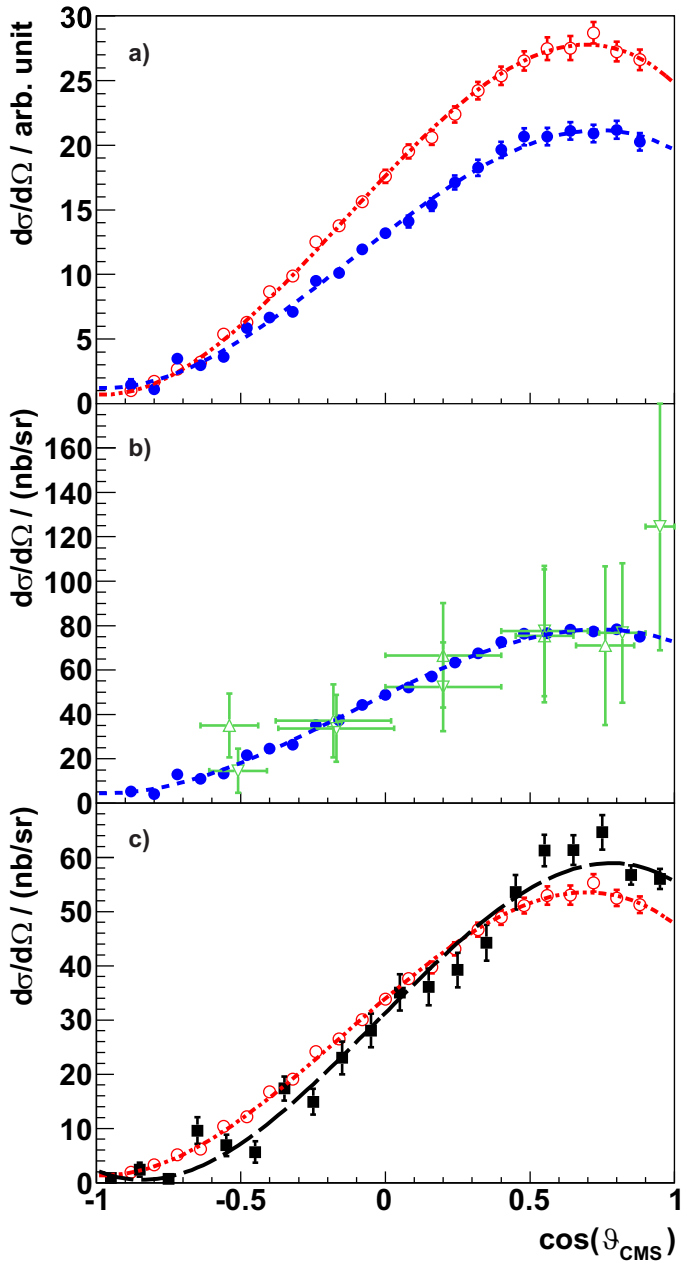

Figure 5.1.: Angular distributions measured at an excess energy of $Q = 48.8\,\text{MeV}$ (filled blue circles) and $Q = 59.8\,\text{MeV}$ (open red circles). (a) $Q = 48.8\,\text{MeV}$ and $Q = 59.8\,\text{MeV}$ data normalized relatively in arbitrary units. (b) $Q = 48.8\,\text{MeV}$ data scaled to the data obtained at GEM at the same excess energy (open green squares) [B$^+$00]. (c) $Q = 59.8\,\text{MeV}$ data scaled to the data measured at ANKE at an excess energy of 59.4 MeV (black squares) [R$^+$09]. The parameters of the third order polynomial fits (shown in blue, red, and black) are given in table 5.2. Figures published in [A$^+$14b].

Table 5.1.: Extracted angular distributions for $Q = (48.8 \pm 0.8)$ MeV and $Q = (59.8 \pm 0.8)$ MeV in arbitrary units [A$^+$14b].

$\cos\vartheta_\eta^{\mathrm{CMS}}$	$\frac{\mathrm{d}\sigma}{\mathrm{d}\Omega}$ / arb. unit	
	$Q = (48.8 \pm 0.8)$ MeV	$Q = (59.8 \pm 0.8)$ MeV
−0.92 – −0.84	1.43 ± 0.47	1.00 ± 0.16
−0.84 – −0.76	1.10 ± 0.23	1.71 ± 0.20
−0.76 – −0.68	3.49 ± 0.22	2.66 ± 0.22
−0.68 – −0.60	2.98 ± 0.19	3.21 ± 0.12
−0.60 – −0.52	3.61 ± 0.22	5.38 ± 0.18
−0.52 – −0.44	5.87 ± 0.27	6.29 ± 0.20
−0.44 – −0.36	6.66 ± 0.29	8.67 ± 0.33
−0.36 – −0.28	7.10 ± 0.29	9.89 ± 0.34
−0.28 – −0.20	9.51 ± 0.35	12.53 ± 0.36
−0.20 – −0.12	10.13 ± 0.37	13.77 ± 0.39
−0.12 – −0.04	11.95 ± 0.41	15.62 ± 0.45
−0.04 – 0.04	13.21 ± 0.44	17.58 ± 0.50
0.04 – 0.12	14.09 ± 0.47	19.52 ± 0.55
0.12 – 0.20	15.40 ± 0.50	20.61 ± 0.58
0.20 – 0.28	17.12 ± 0.55	22.38 ± 0.63
0.28 – 0.36	18.26 ± 0.62	24.22 ± 0.68
0.36 – 0.44	19.64 ± 0.62	25.38 ± 0.71
0.44 – 0.52	20.66 ± 0.66	26.53 ± 0.75
0.52 – 0.60	20.68 ± 0.68	27.49 ± 0.88
0.60 – 0.68	21.12 ± 0.67	27.52 ± 0.93
0.68 – 0.76	20.91 ± 0.67	28.71 ± 0.84
0.76 – 0.84	21.19 ± 0.69	27.25 ± 0.78
0.84 – 0.92	20.27 ± 0.67	26.62 ± 0.78

The corresponding values were published in 2014 [A$^+$14b] and are presented in table 5.1.

To extrapolate the values for the missing η meson angular ranges $-1.0 \leq \cos\vartheta_{\mathrm{CMS}} < -0.92$ and $0.92 \leq \cos\vartheta_{\mathrm{CMS}} \leq 1.0$, the angular distributions were fitted by polynomial functions of the type:

$$\frac{\mathrm{d}\sigma}{\mathrm{d}\Omega} = a_0 \cdot \left[1 + \sum_{i=1}^{n} a_i \left(\cos\vartheta_{\mathrm{CMS}}\right)^i\right] \tag{5.1}$$

with $n = 3$, which describe the distributions very well for both excess energies. The corresponding fit parameters are presented in table 5.2. With the extrapolated η meson yields

$$\frac{\mathrm{d}\sigma}{\mathrm{d}\Omega}(-1\,\text{–}\,{-0.92}) = \int_{-1}^{-0.92} a_0 \cdot \left[1 + \sum_{i=1}^{3} a_i \left(\cos\vartheta_{\mathrm{CMS}}\right)^i\right] \mathrm{d}\cos\vartheta_{\mathrm{CMS}}\,, \tag{5.2}$$

$$\frac{\mathrm{d}\sigma}{\mathrm{d}\Omega}(0.92\,\text{–}\,1) = \int_{0.92}^{1} a_0 \cdot \left[1 + \sum_{i=1}^{3} a_i \left(\cos\vartheta_{\mathrm{CMS}}\right)^i\right] \mathrm{d}\cos\vartheta_{\mathrm{CMS}}\,, \tag{5.3}$$

and equation 4.11 the total cross section ratio for η meson production in $\mathrm{p} + \mathrm{d} \to {}^3\mathrm{He} + \eta$ was found to be

$$\frac{\sigma_\eta\,(48.8\,\mathrm{MeV})}{\sigma_\eta\,(59.8\,\mathrm{MeV})} = 0.77 \pm 0.06\,, \tag{5.4}$$

as published in [A$^+$14b]. The quoted uncertainty includes contributions from the determination of the number of η mesons produced, detector acceptances at both $Q = 48.8\,\mathrm{MeV}$ (0.8 %) and $Q = 59.8\,\mathrm{MeV}$ (0.5 %), as well as uncertainties introduced during the normalization using the reaction $\mathrm{p} + \mathrm{d} \to {}^3\mathrm{He} + \pi^0$ (7.7 %).

In Figure 5.1 (b) the data measured at $Q = 48.8\,\mathrm{MeV}$ are compared to the data obtained at the GEM experiment at the same excess energy [B$^+$00]. For this purpose the WASA-at-COSY data were scaled to the GEM data by a factor of $3.70\,\mathrm{nb\,sr^{-1}}$. Both data sets show the same asymmetric behavior. While the $\cos\vartheta_{\mathrm{CMS}} = 0.95$ GEM data point indicates a continued rise of the angular distribution, this is not observed in the WASA-at-COSY data derived in this thesis. Instead, the new data indicate a saturation or light decrease of the differential cross section for this angular range. Considering the large uncertainties of the $\cos\vartheta_{\mathrm{CMS}} = 0.95$ data point, the same behavior is seen in the GEM data set.

Figure 5.1 (c) displays the new $Q = 59.8\,\mathrm{MeV}$ WASA-at-COSY data together with the $Q = 59.4\,\mathrm{MeV}$ ANKE data scaled to the latter by a factor of $1.93\,\mathrm{nb\,sr^{-1}}$. The ANKE data were fitted with a third order polynomial of the form described in equation 5.1. The corresponding fit parameters are given in table 5.2. Both the new WASA-at-COSY data and the ANKE data show a rise in the differential cross sections with increasing $\cos\vartheta_{\mathrm{CMS}}$ and a constant behavior or light decrease for $\cos\vartheta_{\mathrm{CMS}}$ close to +1. However, the slopes of the two data sets differ slightly. This needs to be considered when scaling the integral of the $Q = 59.8\,\mathrm{MeV}$ WASA-at-

COSY angular distribution to the integral of the distribution obtained at ANKE in order to derive a total cross section value at $Q = 48.8\,\mathrm{MeV}$ (see chapter 5.2). Compared to the ANKE data, the 23 new data points determined in the scope of this thesis have much lower uncertainties due to the higher statistics. Therefore, the very good description of the newly measured angular distribution by the third order polynomial fit will be used as an input in Monte Carlo simulations for the search for the η meson decay $\eta \rightarrow \pi^0 + e^+ + e^-$ (see chapter 6.3).

5.1.1. Comparison of the available high statistics data for excess energies between 20 MeV and 80 MeV

Along with a comparison of the newly determined angular distributions with data at about the same excess energies, it is reasonable to look at these developments of the distributions for a wider excess energy range. Hence, the angular distributions of the high statistics ANKE and WASA/PROMICE data with excess energies ranging roughly from 20 MeV to 80 MeV are discussed and compared to the newly derived WASA-at-COSY data [R$^+$09, B$^+$02, B$^+$04, A$^+$14b]. Due to their larger uncertainties, the data published in [A$^+$07] and [B$^+$00], as well as the $\eta \rightarrow \gamma + \gamma$ data from [B$^+$02], are not considered. Furthermore, all angular distributions were fitted by a third order polynomial of the same type as the new data set:

$$\frac{\mathrm{d}\sigma}{\mathrm{d}\Omega} = a_0 \cdot \left[1 + \sum_{i=1}^{n} a_i \left(\cos\vartheta_{\mathrm{CMS}}\right)^i\right] . \tag{5.5}$$

The parameters corresponding to the individual fits are given in table 5.2. In case of the WASA/PROMICE data measured at the excess energies 20.0 MeV, 38.8 MeV, and 77.9 MeV, the parameters are those derived in [B$^+$02]. Since the ANKE data at the excess energies 19.5 MeV, 39.4 MeV, and 59.4 MeV published in [R$^+$09] were fitted by polynomial functions parametrized in a different way, a new fit to the data with the quoted parametrization was performed. In case of the $Q = 19.5\,\mathrm{MeV}$ ANKE data, the parameter a_3 was set to zero, as no higher order is required to describe the data (compare to [Rau09]).

In figure 5.2 the angular distributions of the 20.0 MeV WASA/PROMICE data (filled blue circles) [B$^+$02, B$^+$04] and the 19.5 MeV ANKE data (black squares) [R$^+$09] are plotted. The blue dashed line and black dashed line correspond to the polynomial fits to the data with the parameters as given in table 5.2.

Table 5.2.: Parameters of third order polynomial fits of the form given in equation 5.1 to angular distributions determined at WASA-at-COSY, ANKE, and WASA/PROMICE [A$^+$14b, R$^+$09, B$^+$02, B$^+$04]. For the $Q = 39.4 \pm 0.8$ ANKE data parameters of a fourth order polynomial fit are given in addition.

Experiment	Q / MeV	a_1	a_2	a_3	a_4	χ^2/ndf
WASA-at-COSY	48.8 ± 0.8	1.300 ± 0.028	-0.211 ± 0.029	-0.60 ± 0.06	–	3.10
WASA-at-COSY	59.8 ± 0.8	1.337 ± 0.017	-0.277 ± 0.024	-0.65 ± 0.04	–	1.37
ANKE	19.5 ± 0.8	0.463 ± 0.012	0.115 ± 0.023	–	–	3.90
ANKE	39.4 ± 0.8	1.149 ± 0.031	-0.403 ± 0.017	-0.54 ± 0.04	–	6.56
ANKE	59.4 ± 0.8	1.72 ± 0.06	-0.08 ± 0.05	-0.87 ± 0.08	–	2.17
ANKE (4th order pol. fit)	39.4 ± 0.8	1.070 ± 0.032	-0.87 ± 0.07	-0.48 ± 0.04	0.54 ± 0.08	4.04
WASA/PROMICE	20.00 ± 0.55	0.33 ± 0.07	-0.36 ± 0.11	-0.10 ± 0.15	–	0.35
WASA/PROMICE	38.80 ± 0.55	0.81 ± 0.05	-0.64 ± 0.07	-0.56 ± 0.09	–	1.27
WASA/PROMICE	77.90 ± 0.55	1.10 ± 0.06	-0.48 ± 0.07	-0.65 ± 0.10	–	0.75

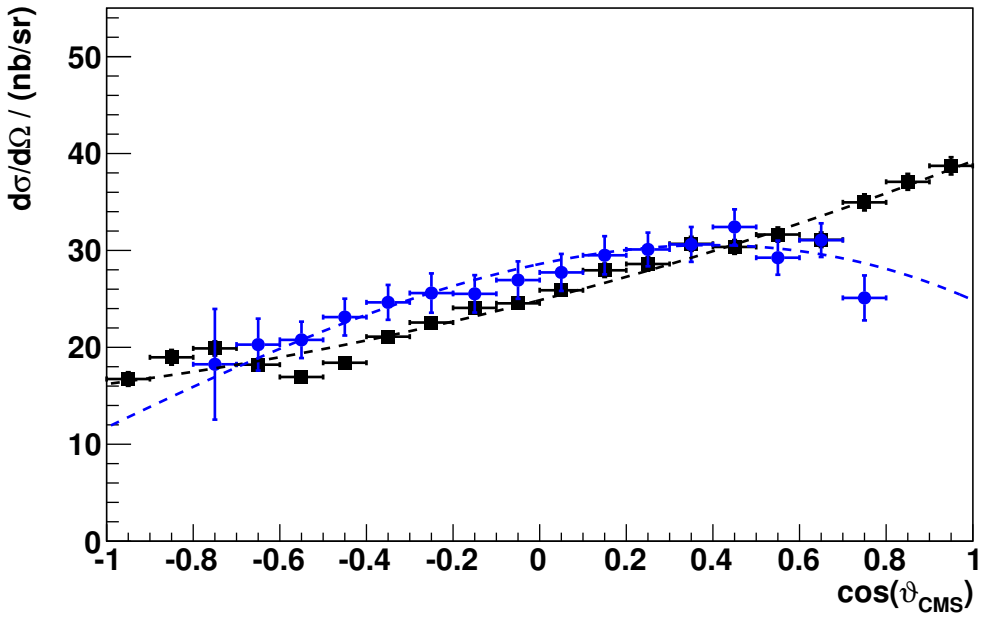

Figure 5.2.: Angular distributions of the 19.5 MeV ANKE data (black squares) [R$^+$09] and the 20.0 MeV WASA/PROMICE data (filled blue circles) [B$^+$02, B$^+$04]. The latter were fitted by a third order polynomial (blue dashed line) and the ANKE data by a second order polynomial distribution (black dashed line). The fit parameters are given in table 5.2. The horizontal bars indicate the angular bin widths.

While the ANKE data were fitted with a second order polynomial [R$^+$09], the 20.0 MeV WASA/PROMICE data are described by a third order polynomial. Since the fit parameter $a_3 = -0.10 \pm 0.15$ agrees with zero within its uncertainties for the 20.0 MeV WASA/PROMICE data, a second order polynomial would be adequate, as well. Thus, contributions from s- and p-waves are sufficient to describe the shape of these angular distributions from both measurements. As already mentioned in chapter 2.3.4, the WASA/PROMICE and ANKE data are in good agreement for $\cos\vartheta_{\mathrm{CMS}} \leq 0.7$, but suggest a different behavior when including higher angular bins. This is reflected in an opposite sign of the quadratic fit parameter a_2 for the two data sets and a steeper slope at $\cos\vartheta_{\mathrm{CMS}} = 0$ of the ANKE fit compared to the WASA/PROMICE one (parameter a_1). Possible reasons might be unknown systematic effects in either of the two measurements not included in the systematic uncertainties. For the theoretical interpretation of the angular distributions at $Q = 20$ MeV, these differences, especially the opposite sign of a_2, might be relevant. Hence, new measurements with high precision will greatly aid in solving this question [KM14, Hü17].

Figure 5.3 displays the angular distributions of the new 48.8 MeV WASA-at-COSY data (red stars) [A$^+$14b] together with the 39.4 MeV ANKE data (black squares) [R$^+$09] and 38.8 MeV WASA/PROMICE data (filled blue circles) [B$^+$02, B$^+$04]. The WASA-at-COSY data were scaled to the ANKE data by a factor of 2.78 nb sr^{-1}, and all data sets were fitted by third order polynomial fits (dashed red, black, and blue lines) with the parameters given in table 5.2.

While the WASA/PROMICE and WASA-at-COSY data can be described well by a third order polynomial distribution, a third order polynomial fit of the 39.4 MeV ANKE data with a reduced χ^2/ndf of 6.56 leads to a worse description than the fourth order polynomial fit presented in [R$^+$09] ($\chi^2/ndf = 1.9$). Thus, a fit of the 39.4 MeV ANKE data with a fourth order polynomial of the type given in equation 5.5 was performed in addition. It is plotted as a gray dashed dotted line in figure 5.3. The corresponding fit parameters are given in table 5.2. All three data sets show the same behavior of a steep rise of the differential cross section from a nearly vanishing value for $\cos\vartheta_{\mathrm{CMS}} = -1$ to a maximum above $\cos\vartheta_{\mathrm{CMS}} = 0$ whose exact position differs between the three experiments. Although the third order polynomial fits suggest a decrease for further increasing $\cos\vartheta_{\mathrm{CMS}}$, the WASA-at-COSY, ANKE, and WASA/PROMICE data agree with a constant behavior at large $\cos\vartheta_{\mathrm{CMS}}$ within their uncertainties, as well. Especially the precisely measured 48.8 MeV

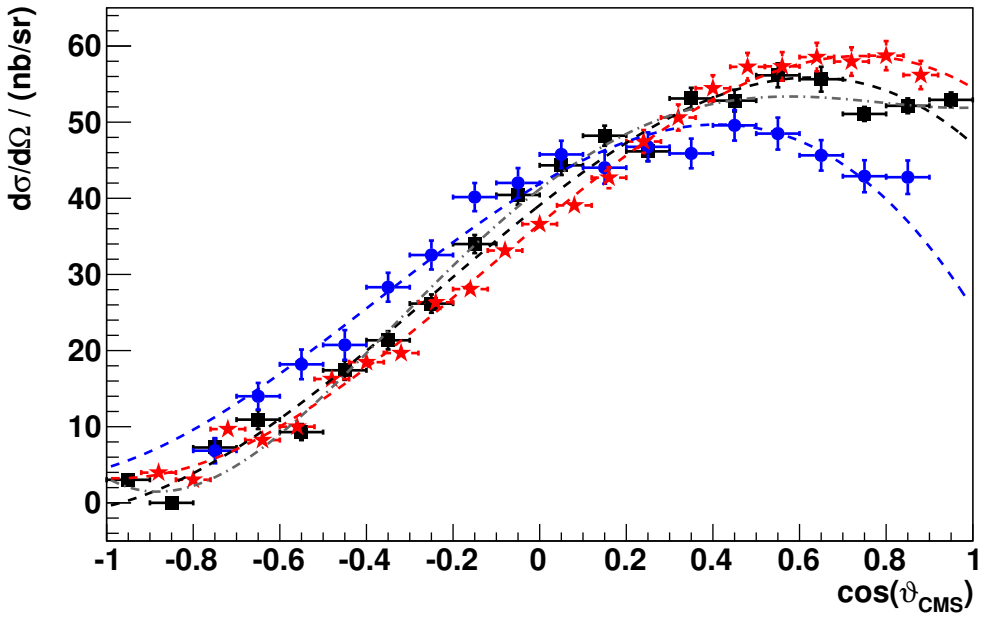

Figure 5.3.: Angular distributions of the 39.4 MeV ANKE data (black squares) [R$^+$09], 38.8 MeV WASA/PROMICE data (filled blue circles) [B$^+$02, B$^+$04], and 48.8 MeV WASA-at-COSY data (red stars) [A$^+$14b]. The WASA-at-COSY data are scaled to the 39.4 MeV ANKE data by a factor of 2.78 nb sr^{-1}. All data sets were fitted by third order polynomial distributions (dashed blue, black, and red lines), and the corresponding fit parameters are given in table 5.2. A fit by a fourth order polynomial distribution to the ANKE data is shown in addition (gray dashed dotted line). The horizontal bars indicate the angular bin widths.

WASA-at-COSY and 39.4 MeV ANKE data allow for this interpretation. Since the data of all three measurements cannot be described by second order polynomials, but require at least a third order polynomial to reach a good agreement between data and fit (or even a fourth order polynomial in case of the 39.4 MeV ANKE data), s- and p-waves are not sufficient for a good description of the shape seen in the data. Higher order partial waves are required.

While the general shape of the 38.8 MeV WASA/PROMICE, 39.4 MeV ANKE, and 48.8 MeV WASA-at-COSY data is similar, there are differences that are larger than the given uncertainties. In case of the WASA-at-COSY data, these might be due to the excess energy about 10 MeV larger. As the WASA/PROMICE and ANKE data were measured at about the same excess energy ($Q \approx 39$ MeV), these two data sets should agree within their uncertainties. Similar to the $Q \approx 20$ MeV data sets, these differences might originate from unknown systematic effects of either of the two measurements not included in their calculated uncertainties. New measurements with high precision at this energy could help to clarify this [KM14, Hü17].

Figure 5.4 shows the 59.8 MeV WASA-at-COSY data (red stars) [A$^+$14b] compared to the 59.4 MeV ANKE data (black squares) [R$^+$09] with the WASA-at-COSY data scaled to the 59.4 MeV ANKE data by a factor of 1.93 nb sr^{-1}. In addition, the 77.9 MeV WASA/PROMICE data [B$^+$02, B$^+$04] are presented as filled blue circles. All three data sets were fitted by third order polynomial distributions (dashed red, black, and blue lines) with the parameters given in table 5.2.

The 39.4 MeV ANKE, 38.8 MeV WASA/PROMICE, and 48.8 MeV WASA-at-COSY data and, as already mentioned in the introduction of chapter 5.1, the 59.4 MeV ANKE and 59.8 MeV WASA-at-COSY data as well as the 77.9 MeV WASA/PROMICE data show a similar increase of the cross section from about zero for $\cos\vartheta_{\mathrm{CMS}} = -1$ to a maximum value. While the position of the maximum is reached at about the same value $\cos\vartheta_{\mathrm{CMS}} \approx 0.7$ for both the 59.4 MeV ANKE and the 59.8 MeV WASA-at-COSY data, the 77.9 MeV WASA/PROMICE data reaches its maximum already for lower $\cos\vartheta_{\mathrm{CMS}} \approx 0.5$. Furthermore, the slope at $\cos\vartheta_{\mathrm{CMS}} = 0$ and, hence, parameter a_1 of the fits differ for all three experiments, ranging from 1.10 ± 0.06 for the WASA/PROMICE data over 1.337 ± 0.017 for the WASA-at-COSY data to 1.72 ± 0.06 for the ANKE data. In case of the WASA-at-COSY data, it was found that a consideration of the finite momentum resolution of the WASA forward detector has a great impact on the parameter a_1 (see also

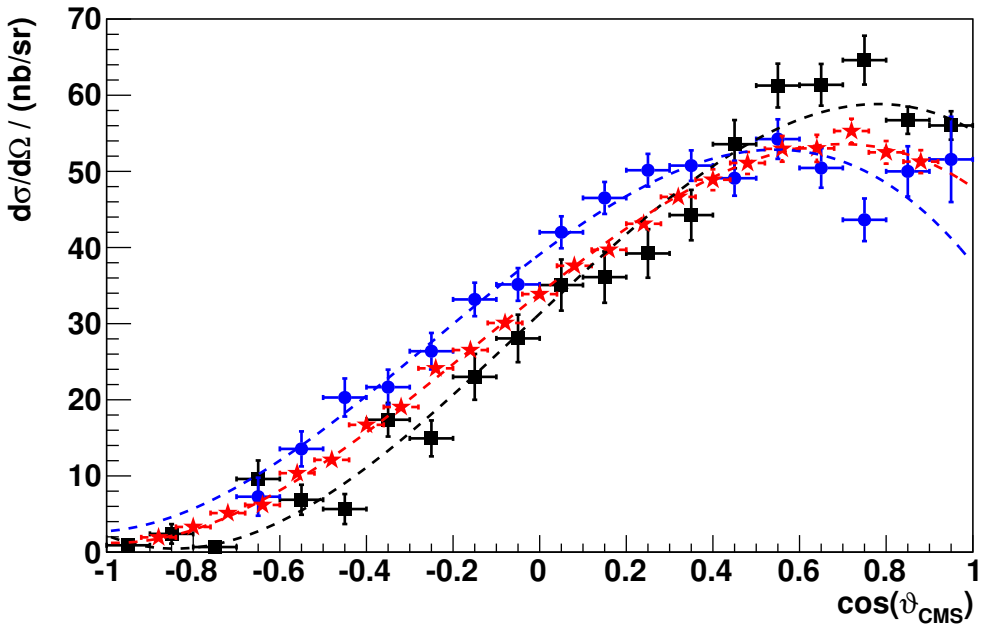

Figure 5.4.: Angular distributions of the 59.4 MeV ANKE data (black squares) [R$^+$09], 77.9 MeV WASA/PROMICE data (filled blue circles) [B$^+$02, B$^+$04], and 59.8 MeV WASA-at-COSY data (red stars) [A$^+$14b]. The WASA-at-COSY data are scaled to the 59.4 MeV ANKE data by a factor of 1.93 nb sr^{-1}. All data sets were fitted by third order polynomial distributions (dashed blue, black, and red lines) and the corresponding fit parameters are given in table 5.2. The horizontal bars indicate the angular bin widths.

chapter 4.10, figure 4.25). Previous preliminary analysis results which did not consider this effect led to a lower value of $a_1 = 1.20 \pm 0.02$ [Pas10]. Therefore, it is obvious that a correction of this effect is required, as presented in chapter 4.10. It is not known if something similar was considered for the results published in [B$^+$02] or [R$^+$09]. In case of the WASA/PROMICE data, an analogical behavior is expected due to a very similar forward detector design. If not included, this could lead to a better agreement between the WASA-at-COSY and the WASA/PROMICE data, although the measurements were performed at different excess energies. For the ANKE data it is unclear how, if at all, the efficiencies would be effected due to the very different detector design. Newer analyses of measurements at ANKE which will include the method for the efficiency determination sketched in chapter 4.10 might give a better insight to this phenomenon at ANKE although these measurements were performed at lower excess energies [Fri17].

When comparing the excess energy dependence of the polynomial fit parameters of the three experiments, some common trends can be observed. The WASA/PROMICE, ANKE, and WASA-at-COSY data all show an increase of parameter a_1 with rising Q. The exact values differ, though, with ANKE observing the highest a_1 values and WASA/PROMICE observing the lowest values. The WASA-at-COSY data are located between the results of those two experiments. For parameter a_2 no common trend is observed. Except for the 19.5 MeV ANKE data, all measurements determined negative values of a_2. According to the results from ANKE and WASA/PROMICE, parameter a_3 agrees with zero for $Q \approx 20$ MeV and decreases to negative values for higher excess energies. The WASA-at-COSY fit parameters are in good agreement with this observation. For a further, more detailed discussion of the polynomial fits in the excess energy region 20 MeV to 80 MeV, results from new measurements performed at WASA-at-COSY in 2014 are required and are currently being analyzed [Hü17].

In figure 5.5 the angular distributions of both WASA-at-COSY data sets are plotted. Here the 48.8 MeV data (filled blue circles) are scaled to the 59.8 MeV data by a factor of 0.77^{-1} to allow for a better comparison of the shape of the distribution. The third order polynomial fits are presented as dashed blue and red lines. Although measured at excess energies differing by about 10 MeV, the two data sets are in very good agreement. Furthermore, the data can be described very well by the third order polynomial fits. The good agreement of the two data sets is also visible when comparing the parameters of the third order polynomial fits

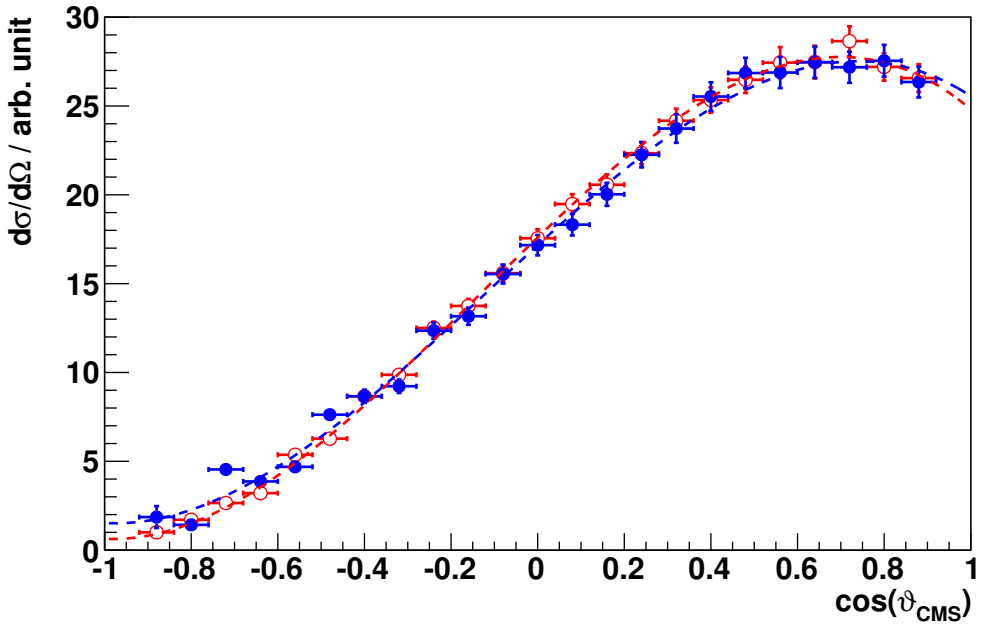

Figure 5.5.: Angular distributions of the 48.8 MeV (filled blue circles) and 59.8 MeV WASA-at-COSY data (open red circles) in arbitrary units [A$^+$14b]. The 48.8 MeV data are scaled to the 59.8 MeV data by a factor of 1.30. The parameters of the third order polynomial fits to the data (dashed blue and red lines) are given in table 5.2. The horizontal bars indicate the angular bin widths.

which agree with each other within their uncertainties under consideration of the reduced χ^2/ndf of the two fits. Thus, the two angular distributions suggest no rapid change of the η meson production mechanisms for these two excess energies.

Compared to the measurements at ANKE and WASA/PROMICE, the WASA-at-COSY experimental setup has proven to be able to yield angular distributions with very low uncertainties. Moreover, due to the high laboratory angle and momentum resolution, a narrow $\cos\vartheta_{\mathrm{CMS}}$ binning can be chosen. Therefore, the WASA-at-COSY experiment is perfectly suited to obtain angular distributions for the given excess energy range of 20 MeV to 80 MeV [KM14]. New measurements for the proton beam momenta 1.60 GeV c^{-1} to 1.74 GeV c^{-1}, corresponding to an excess energy range of 13.6 MeV to 80.9 MeV, were performed at WASA-at-COSY in 2014 to provide differential cross section distributions as well as total cross sections for 15 excess energies. The data are currently being analyzed by N. Hüsken [Hü17]. Very first analysis results are in good agreement with the results presented here and even suggest only minor changes of the differential cross section distributions for the excess energy range from 40 MeV to 80 MeV, if normalized to unity.

5.1.2. Comparison of the determined angular distributions with theoretical expectations

Comparison with two-step model

In chapter 2.3.3 a two-step model was presented for the theoretical description of the reaction p + d $\rightarrow$ ^{3}He + η. Including final state interaction, it is in very good agreement with near threshold data [M$^+$07]. For higher excess energies ($Q >$ 12 MeV) no commonly approved theoretical calculations for the two-step model yet exist which can reproduce the differential cross section distributions observed in data.

Figure 5.6 compares calculations by Khemchandani et al. [KKJ12, Rau09] to the WASA-at-COSY results presented in this thesis [A$^+$14b]. For this theoretical model partial waves s, p, and d were included in the reaction mechanism, whereas s-waves were used for the final state interaction. It is visible that the theoretical calculations and the measured data show a different behavior. While the differential cross section decreases depending on $\cos\vartheta_{\mathrm{CMS}}$ according to the two-step model, the data show a positive slope of the distribution.

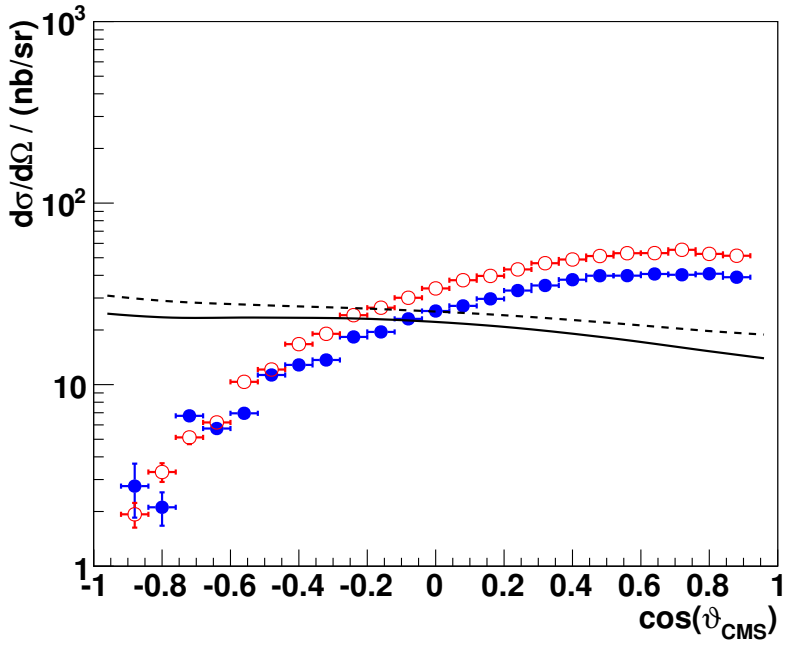

Figure 5.6.: Angular distributions of the 48.8 MeV (filled blue circles) and 59.8 MeV WASA-at-COSY data (open red circles) scaled to the 59.4 MeV ANKE data by a factor of 1.93 nb sr^{-1} [A$^+$14b, R$^+$09], compared to theoretical expectations according to two-step model calculations by Khemchandani et al. [KKJ12, Rau09]. The black solid curve results from calculations for an excess energy of $Q = 60$ MeV, while the black dashed curve illustrates the results for $Q = 40$ MeV. The horizontal bars of the data points indicate the angular bin widths.

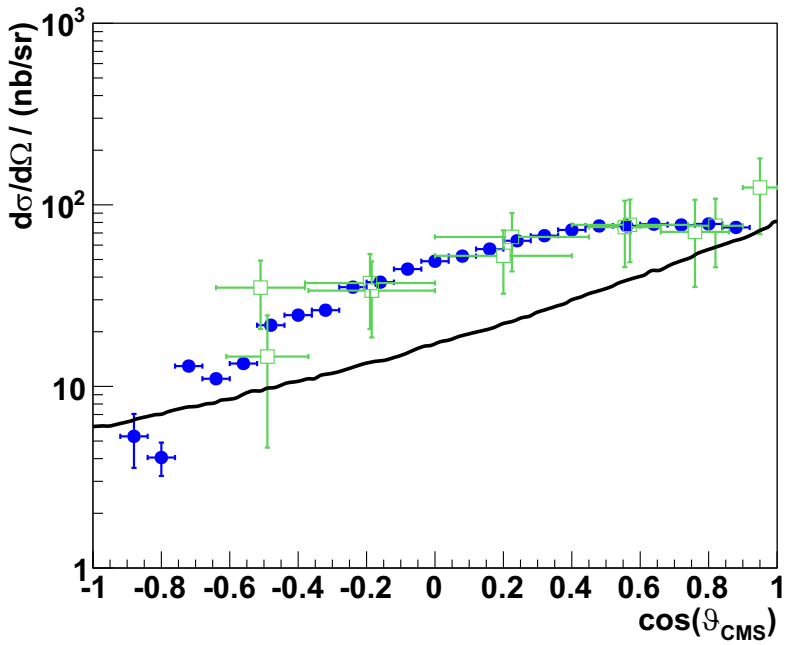

Figure 5.7.: Angular distributions of the 48.8 MeV WASA-at-COSY data (filled blue circles) scaled to the data obtained at GEM at the same excess energy (open green squares) by a factor of 3.70 nb sr^{-1} [A$^+$14b, B$^+$00], compared to theoretical expectations according to resonance model calculations by A. B. Santra and B. K. Jain (black curve) [SJ01]. The horizontal bars of the data points indicate the angular bin widths.

As suggested in [Rau09], possible reasons for that might be the changing of components of the two-step model or the lack of them. However, changes to the components of the two-step model did not help to solve this issue so far. Another possible explanation is that different production mechanisms start to play an important role at excess energies above $Q = 12$ MeV (see next section).

Comparison with resonance model

Betigeri et al. suggested an excitation of a N*(1535) resonance in the intermediate state of the reaction p+d $\rightarrow$ ^{3}He+η as the major production mechanism [B$^+$00] (see chapter 2.3.3). In contrast to the presented two-step model, their model does not include final state interaction. While it fails to describe the close to threshold data, it might lead to a better description for higher excess energies. Calculations for a resonance model with respect to the GEM data were performed by A. B. Santra and B. K. Jain [SJ01] and are compared to the results obtained with WASA-at-COSY at $Q = 48.8$ MeV in figure 5.7. Contrary to the two-step model, the calculations of the

resonance model show a positive slope of the differential cross section distribution as is observed in data. However, while the slope increases with $\cos\vartheta_{\mathrm{CMS}}$ according to the theoretical model, a decrease of the slope is seen in data for $\cos\vartheta_{\mathrm{CMS}} > 0$. Due to the noticeable higher accuracy of the WASA-at-COSY results compared to the GEM data, these differences cannot be explained by uncertainties. Hence, at higher excess energies the presented resonance model approach fails to fully describe the measured data, as well.

A theoretical approach which includes the two-step model with strong FSI close to the η threshold and the resonance model approach might lead to a better agreement between data and theory for excess energies $Q > 12\,\mathrm{MeV}$. Since high precision measurements of the differential cross section, such as those presented in this thesis, help to verify theoretical models, an increased high precision data base will help further theoretical investigations. Such measurements were performed for the excess energy range from 13.6 MeV to 80.9 MeV with WASA-at-COSY in 2014 and are currently analyzed and will be compared to ongoing theoretical calculations [Hü17].

5.2. Total Cross Sections of the reaction $\mathbf{p + d \rightarrow {}^3He + \eta}$

In chapter 5.1 (equation 5.4) the relative total cross section ratio was found to be $\sigma_\eta\,(48.8\,\mathrm{MeV})/\sigma_\eta\,(59.8\,\mathrm{MeV}) = 0.77 \pm 0.06$ [A$^+$14b]. By scaling the WASA-at-COSY data at an excess energy of 59.8 MeV to the $Q = 59.4\,\mathrm{MeV}$ ANKE data, a total cross section for $Q = 48.8\,\mathrm{MeV}$ can be calculated, which can then be compared to the available total cross section data base. According to the measurements at ANKE [R$^+$09], the total cross section at $Q = (59.4 \pm 0.8)\,\mathrm{MeV}$ is

$$\sigma\,(59.4\,\mathrm{MeV}) = (388.1 \pm 7.1 \pm 58.0)\,\mathrm{nb}\,. \tag{5.6}$$

Here the latter uncertainty of 58.0 nb (15 %) originates from the absolute normalization via the pd elastic scattering. As mentioned in chapter 5.1, the shapes of the angular distributions obtained by ANKE and WASA-at-COSY at about 60 MeV differ slightly. This has to be taken into account as a systematic uncertainty of the $Q = 48.8\,\mathrm{MeV}$ total cross section. For this purpose the angular distributions of the 59.4 MeV ANKE and 59.8 MeV WASA-at-COSY data were divided into five

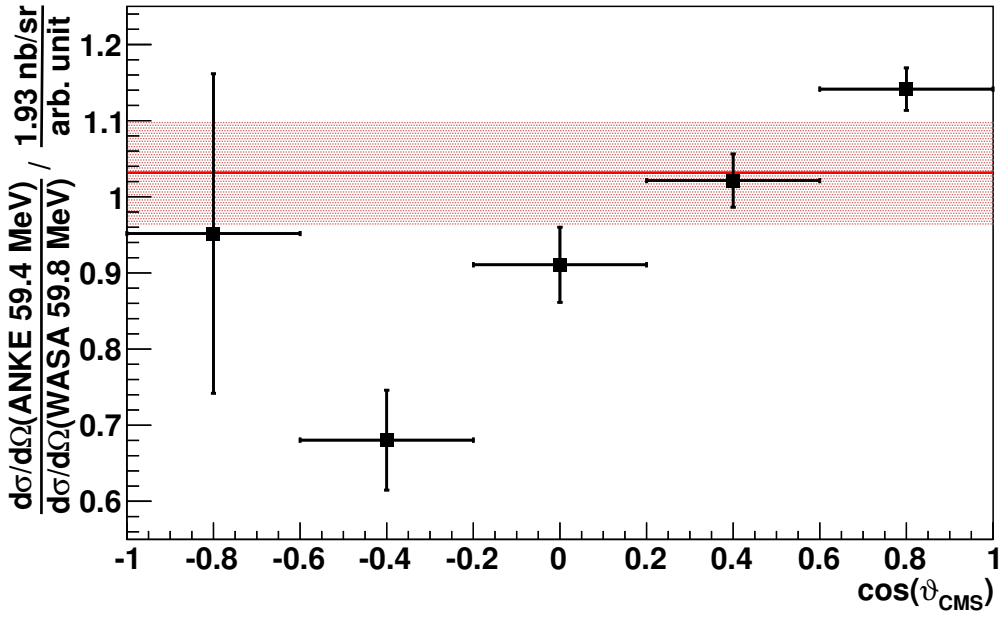

Figure 5.8.: Scaling factors $\mathrm{d}\sigma/\mathrm{d}\Omega$ (ANKE 59.4 MeV) /$\mathrm{d}\sigma/\mathrm{d}\Omega$ (WASA 59.8 MeV) divided by the global scaling factor $1.93\,\mathrm{nb\,sr^{-1}}$ as a function of $\cos\vartheta_{\mathrm{CMS}}$. The horizontal error bars indicate the angular bin width. The weighted mean is plotted as a red line with its uncertainty (red shaded area) under consideration of the reduced χ^2/ndf.

equally sized angular bins to extract separate scaling factors for these bins. These factors were then compared to the global scaling factor of $1.93\,\mathrm{nb\,sr^{-1}}$.

Figure 5.8 shows the extracted factors divided by $1.93\,\mathrm{nb\,sr^{-1}}$. The uncertainty of the weighted mean value of these factors (red line) is used as systematic uncertainty of the scaling. Considering the reduced χ^2/ndf of the weighted mean value, it corresponds to 6.7 % (red shaded area).

Scaling the 59.8 MeV WASA-at-COSY data to the 59.4 MeV ANKE data and subsequently using the relative normalization factor from equation 5.4, the cross section at $Q = (48.8 \pm 0.8)\,\mathrm{MeV}$ results in

$$\sigma\left((48.8 \pm 0.8)\,\mathrm{MeV}\right) = (298 \pm 24 \pm 49)\,\mathrm{nb}\,, \tag{5.7}$$

as published in [A$^+$14b]. The first uncertainty is the statistical one and dominated by the statistical uncertainty of 7.7 % of the extracted η meson production ratio. Furthermore, it includes the statistical uncertainty of the 59.4 MeV ANKE data cross section which corresponds to 1.9 %. The second one is the systematic

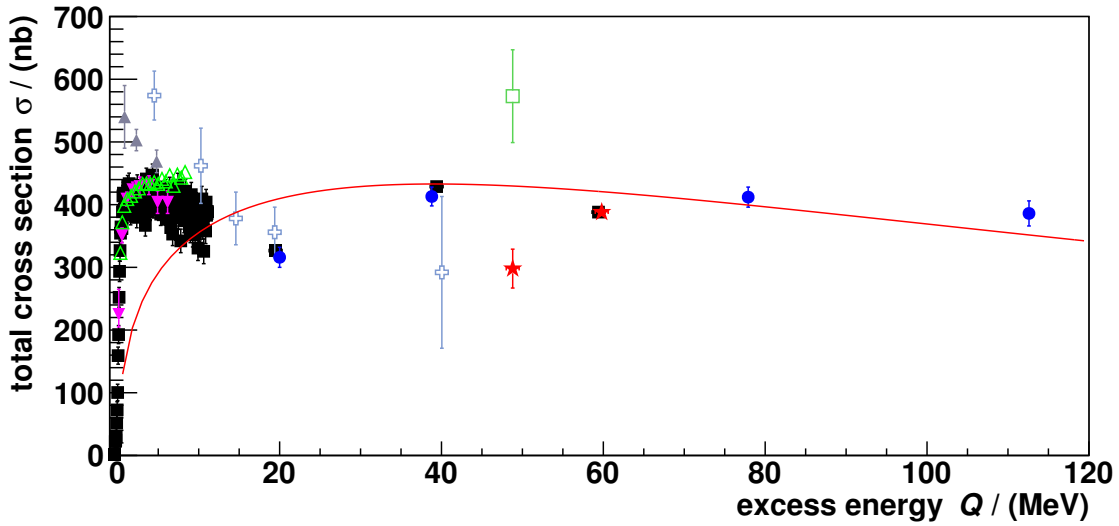

Figure 5.9.: Total cross section σ as a function of the excess energy Q for the reactions $p + d \rightarrow {}^3He + \eta$ and $d + p \rightarrow {}^3He + \eta$. Uncertainties due to absolute normalization are not included. Besides the new WASA-at-COSY data (red stars [A$^+$14b]), data from the experiments SPES-IV (filled gray triangles [B$^+$88]), SPES-II (inverted purple triangles [M$^+$96]), GEM (open green square [B$^+$00]), WASA/PROMICE (filled blue circles [B$^+$02, B$^+$04]), COSY-11 (open light blue crosses [A$^+$07] and open green triangles [S$^+$07]), and ANKE (filled black squares [M$^+$07, R$^+$09]) are shown. The WASA-at-COSY data are arbitrarily scaled to the Q = 59.4 MeV ANKE data point. Illustrated by the red solid curve is a theoretical description of the η meson production via an excitation of a N*(1535) resonance by Betigeri et al., arbitrarily scaled by a factor of 0.75 [B$^+$00].

uncertainty, including the 15 % normalization uncertainty of the 59.4 MeV ANKE data and the uncertainty from scaling to this data point (6.7 %).

In figure 5.9 the total cross sections of the scaled WASA-at-COSY data (red stars) are plotted together with data from the experiments SPES-IV (filled gray triangles [B$^+$88]), SPES-II (inverted purple triangles [M$^+$96]), GEM (open green square [B$^+$00]), WASA/PROMICE (filled blue circles [B$^+$02, B$^+$04]), COSY-11 (open light blue crosses [A$^+$07] and open green triangles [S$^+$07]), and ANKE (filled black squares [M$^+$07, R$^+$09]). Similar to figure 2.6 in chapter 2.3.4, all data points are shown without uncertainties due to absolute normalization. The uncertainties of the 48.8 MeV WASA-at-COSY data point include the uncertainty introduced by the scaling to the 59.4 MeV ANKE data point.

Unlike the 48.8 MeV GEM data point, which indicates a possible increase of the total cross section, but is still in agreement with a constant cross section

for the excess energy range from 40 MeV to 80 MeV within its uncertainties[1], the 48.8 MeV WASA-at-COSY data point suggests the presence of a distinct change of the total cross section for excess energies between 20 MeV and 60 MeV. Especially the extracted total cross section ratio, which does not rely on the scaling to the ANKE data, shows a variation of the total cross section that cannot be explained by normalization uncertainties. This behavior is unexpected, since no change in the angular distributions is observed (compare 5.1.1).

In order to compare the results obtained in this thesis together with the available data to the resonance model as suggested by Betigeri et al., the calculated theoretical total cross sections presented in [B$^+$00] were scaled by a factor of 0.75 and are illustrated in figure 5.9 by a red solid curve. As discussed in 2.3.4, the model fails to reproduce the enhancement close to threshold. While the total cross sections obtained with ANKE and WASA/PROMICE are compatible with this scaled model for excess energies larger than about 40 MeV, the scaled model cannot reproduce the lower cross sections at about 20 MeV measured with the same experiments. Especially the decrease of the cross section at $Q = 48.8$ MeV presented in this thesis and published in [A$^+$14b] cannot be reproduced by this calculation.

In summary, the results for the total cross section ratio presented in this thesis lead to further questions which cannot be answered by theory yet. They make the energy region starting at about $Q = 20$ MeV even more interesting than predicted in 2009, when the beam time for the presented measurements was conducted. Therefore, new measurements with high precision both for the total and differential cross section are crucial in order to quantify new theoretical approaches. This motivated the beam time performed in 2014 which was dedicated to high precision measurements of the total and differential cross sections of the reaction $\mathrm{p + d \rightarrow {}^3He + \eta}$ at 15 excess energies ranging from 13.6 MeV to 80.9 MeV [KM14]. Modifications made to the WASA-at-COSY detector design and further optimizations of the data acquisition will allow not only to do a normalization via the reaction $\mathrm{p + d \rightarrow {}^3He + \pi^0}$, but also by using the pd elastic scattering as an alternative normalization channel for cross checks [Hü17]. This way, possible, yet unknown effects due to properties of the normalization channel can be tested. Very first preliminary analysis results concerning the normalization will be discussed in the following chapter 5.2.1.

[1] According to [B$^+$00], the total cross section at $Q = 48.8$ MeV is $\sigma(48.8\,\mathrm{MeV\ GEM}) = (573 \pm 74 \pm 69)$ nb. The latter (systematic) uncertainty introduced by an independent absolute normalization is not included in figure 5.9.

5.2.1. Very first look at the normalization of the new 2014 data

The insights discussed in this chapter regarding the ongoing analysis of the p + d $\rightarrow$ ^{3}He + X data recorded in 2014 are very preliminary and may still change considerably [Hü17]. They are discussed here to give a hint whether there might be systematic effects yet unknown in the normalization via the reaction p + d $\rightarrow$ ^{3}He + π^0. Hence, they will be discussed only qualitatively.

For the relative normalization of the data published in [A$^+$14b], it is assumed that the differential cross sections of the reaction p + d $\rightarrow$ ^{3}He + π^0 do not change significantly in the angular range and for the beam energies used. This assumption is regarded as reasonable, as the phase space volume being in first order proportional to the square root of the excess energy of this reaction changes by only

$$\sqrt{\frac{Q_{\pi^0}(T_{\mathrm{beam}} = 1000\,\mathrm{MeV})}{Q_{\pi^0}(T_{\mathrm{beam}} = 980\,\mathrm{MeV})}} = \sqrt{\frac{472.6\,\mathrm{MeV}}{461.7\,\mathrm{MeV}}} \approx 1.01\,. \tag{5.8}$$

Indeed, the ratios of the π^0 meson yields for the angular range $-0.92 \leq \cos\vartheta_{\mathrm{CMS}} < -0.68$ show only a slight linear decrease to lower values of $\cos\vartheta_{\mathrm{CMS}}$ (see chapter 4.11.4). However, the low amount of angular bins might hide a more complex behavior.

Thanks to the optimizations done for the 2014 beam time, a noticeably smaller binning can be chosen for the determination of the π^0 meson yields [Sit15]. A very first look at the π^0 meson yields for the beam momenta $p_{\mathrm{beam}} = 1.670\,\mathrm{GeV}\,c^{-1}$ and $p_{\mathrm{beam}} = 1.700\,\mathrm{GeV}\,c^{-1}$, equaling η meson excess energies of 47.3 MeV and 61.7 MeV, show the same linear behavior for $-0.92 \leq \cos\vartheta_{\mathrm{CMS}} < -0.68$ as observed in the data published in [A$^+$14b].

The smaller binning also allows the inclusion of meson yields extracted for lower values of $\cos\vartheta_{\mathrm{CMS}} < -0.92$. Very first investigations of the yield ratio for these $\cos\vartheta_{\mathrm{CMS}}$ values show a possible deviation from a linear behavior [Hü17]. Since these angular bins are already very close to the COSY beam pipe, such effects could also be produced by minor differences between the WASA detector implementation in Monte Carlo and the actual physical detector setup, resulting in systematic uncertainties of the detector acceptances. Thus, for the normalization of the data from 2014 the pd elastic scattering will be used in addition. The precise angular binning and high statistics for the reaction p + d $\rightarrow$ ^{3}He + π^0 will also help to

increase the differential cross section data base for this particular reaction. First test analyses were done as part of the master thesis of K. Sitterberg [Sit15].

6. Analysis with regard to the η meson decay $\eta \rightarrow \pi^0 + e^+ + e^-$

Studies of rare or forbidden η meson decays are particularly well suited for searching physics beyond the standard model (see chapter 2.2.1). As mentioned in chapter 2.4, the decay $\eta \rightarrow \pi^0 + e^+ + e^-$, the search for which is a major part of this thesis, violates the C parity conservation if it occurs via an intermediate state virtual photon ($\eta \rightarrow \pi^0 + \gamma^* \rightarrow \pi^0 + e^+ + e^-$). For the analysis of such rare or forbidden decays high statistics of η mesons produced are very important. During the operation of WASA-at-COSY two reactions were used to produce large sets of η mesons for their decays to be studied. These are the reactions $p + p \rightarrow p + p + \eta$ and $p + d \rightarrow {}^3He + \eta$. While the first reaction has a noticeably higher total cross section of $(9.8 \pm 1.0 \pm 1.5)\,\mu b$ at $T_{beam} = 1.4\,GeV$ [C$^+$94] compared to the $(388.1 \pm 7.1 \pm 58.0)\,nb$ cross section at $T_{beam} = 1.0\,GeV$ for the latter reaction [R$^+$09], the signal to background ratio is much better for the p + d fusion reaction [Cod12]. Furthermore, the higher beam momentum required for the p+p → p+p+η production reaction leads to a larger Lorentz boost resulting in a higher fraction of η meson decay products being scattered at lower polar angles. As the mini drift chamber can only reconstruct the tracks of charged particles with polar angles above 24°, the chance of missed particles increases with a higher Lorentz boost. Hence, the reconstruction efficiency, especially of decays with charged decay particles, is lower for η mesons produced in p + p collisions than for those produced in p + d fusion reactions. The analysis of the decay $\eta \rightarrow \pi^0 + e^+ + e^-$, which is presented in this thesis, is based on data sets using the production channel $p + d \rightarrow {}^3He + \eta$ (see chapter 4.1). A previous analysis of the decay $\eta \rightarrow \pi^0 + e^+ + e^-$ by A. Winnemöller was based on about one third of the same data set and was focused on low invariant masses of the electron-positron pair [Win11]. The $p + p \rightarrow p + p + \eta$ data sets are being analyzed by K. Demmich in regard to the decay $\eta \rightarrow \pi^0 + e^+ + e^-$ [Dem17].

First investigations of a part of these data sets with respect to this decay channel confirm the potential of the $p + p \to p + p + \eta$ production reaction [Ste17].

Since different η meson decays are studied by different PhD students and postdoctoral researchers using the same $p + d \to {}^3He + \eta$ data sets, a common analysis base class for η decay studies has been developed and then subsequently optimized for this production channel (see chapter 3.5.3). This does include common optimizations of detector calibration parameters, which are mandatory for the analysis of rare or forbidden η meson decays. As part of this thesis the calibration parameters of the forward detector have been optimized and implemented into the common analysis class (see chapter 6.2).

Studies of η meson decays in which no clear signals are expected, as in the case of the decay $\eta \to \pi^0 + e^+ + e^-$, require a fully correct description of the measured data by Monte Carlo simulations in order to obtain reliable results. Therefore, high statistics simulations including physics models for the various reactions and decays were created (see chapter 6.3) and then used to give a proper description of the data (see chapter 6.6). With the aid of these simulations optimal selection conditions for the η meson decay of interest were determined (see chapter 6.7) and applied to the data afterwards (see chapter 7).

6.1. Database

The analysis of the η meson decay $\eta \to \pi^0 + e^+ + e^+$ presented in this thesis is based on two data sets recorded with the WASA-at-COSY experimental setup in September/October 2008 and August/September 2009, respectively. For the measurements a proton beam with a kinetic beam energy of about 1 GeV was brought to collision with a deuterium pellet target with the aim to produce η mesons in the fusion reaction $p + d \to {}^3He + \eta$. While doing so, a COSY cycle time of 100 s was used. In total 19.7 TB of data separated in 1212 files (runs) were collected in the 2008 beam time and 42.9 TB separated in 2464 runs in 2009. Not all runs were used for the analysis, as adjustments of the pellet target, the COSY accelerator, or the WASA detector settings were performed during some runs. Excluding these runs, 822 runs from the 2008 beam time in the range of run numbers 10 392 to 11 525 and 1842 runs from the 2009 beam time with run numbers ranging from 13 969 to 15 944 are used for the analysis. The runs 11 302 to 11 456

and 15 276 to 15 296 are excluded, as they were performed at different kinetic beam energies, namely 1800 MeV and 980 MeV, respectively.

While the 2009 data set was recorded using the same proton beam settings for all runs recorded, the 2008 data set was collected with two different COSY operation modes. During the first part of the beam time (runs 10 392 to 10 965) the barrier bucket cavity was used to compensate the beam energy loss caused by the interaction with the pellet target (a procedure that was also used for the whole 2009 beam time). This cavity was not functional during the second part of the beam time (runs 10 966 to 11 525), resulting in a time-in-cycle dependency of the beam momentum p_{beam}. The exact beam momenta for the different run periods were determined and will be discussed in chapter 6.2.

The logic trigger conditions utilized for both the 2008 and 2009 data are identical, while individual detector thresholds might vary. As already mentioned in chapter 4.1, these were:

- at least one geometrically matching hit in the first layer of FRH and FTH, as well as one matching hit in either the first or second FWC layer,
- at least one hit in each FWC layer, and
- high threshold for the energies deposited in the FWC.

Both data sets were preselected on ^{3}He nuclei detected in the forward detector using a graphical cut in the energy loss spectra (see chapter 4.1).

6.2. Detector calibration

In order to search for rare or forbidden decays such as the η meson decay $\eta \rightarrow \pi^0 + e^+ + e^-$, a precise calibration of the different WASA detector components is very important. As already mentioned at the beginning of chapter 6, the optimization of the calibration of the various detectors was allocated among PhD students and postdoctoral researchers analyzing the same data sets. During the studies of the cross sections of the reaction $p + d \rightarrow {}^3\mathrm{He} + \eta$, techniques were developed for the optimization of the forward detector calibration (see chapter 4). These techniques were utilized to obtain an optimal calibration of this detector part for the given beam times as part of this thesis.

While a good calibration had already been achieved for the 2009 data set runs utilized for the cross section analysis, some of the runs excluded from the

analysis indicated a run dependency of the detector calibration (see chapter 4.3). Furthermore, a calibration of the 2008 data set had not been performed. In the following chapters an optimization of the calibration of the different forward detector components will be presented, starting with the forward proportional chamber (see chapters 6.2.1, 6.2.2, and 6.2.3). Afterwards a fine tuning of the formula for the kinetic energy determination will be explained in chapter 6.2.4.

6.2.1. Forward proportional chamber calibration: Shift of the vertex position

A possibility to statistically distinguish between a signal channel and various background channels is provided by kinematic fitting (see chapter 2.6). In order to obtain reliable results of this fit, it is important to not only know the uncertainties of the measured energy losses of the detected particles with high precision, but also those of the measured scattering angles. In case of forward scattered particles, the determination of these angles depends on the hit position in the FPC layers as well as on the position of the interaction vertex of the COSY beam with the pellet target. The latter is correlated to the COSY beam orbit whose exact position in the x-y plane perpendicular to the proton beam depends on the COSY accelerator settings and is not known a priori. The z position of the vertex, on the other hand, solely depends on the path of the pellet stream through the COSY beam pipe. As the orifice of the pellet beam pipe has a diameter of 3 mm [HR$^+$04], the path of the pellet beam through the scattering chamber should not vary by more than a tenth of a millimeter, since the pressure in the scattering chamber would otherwise increase leading to unwanted background reactions (see also chapter 3.2.1). Hence, such an increase of the pressure was avoided during data recording and the vertex z position can be assumed to be stable at $z = 0$ mm with an uncertainty of 0.1 mm. This uncertainty is small compared to the expected target diameter of 3.5 mm at the interaction point and, thus, can be neglected. To test if the vertex position in the x-y plane agrees with the assumed position at $x = y = 0$ mm, a kinematic relation of the two-particle reaction $\mathrm{p} + \mathrm{d} \to {}^3\mathrm{He} + \eta$ can be utilized (see chapter 2.3.1). According to this kinematic relation, the laboratory scattering angle ϑ_{LAB} of the helium nuclei has a maximum value $\vartheta_{\mathrm{LAB}}^{\mathrm{max}}$ which does not depend on the azimuthal angle φ.

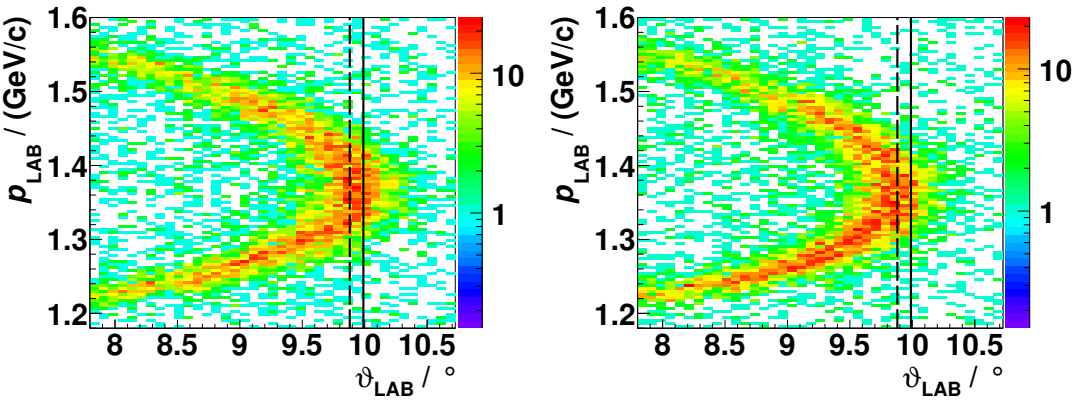

Figure 6.1.: ^{3}He laboratory momenta p_{LAB} plotted against the corresponding laboratory angle ϑ_{LAB} for the data runs 10 705 to 10 965 in logarithmic scale requiring a hit in the sixth element of FRH1 (left) or a hit in the 18th element of FRH1 (right). The black solid line indicates the extracted maximum $\vartheta^{\mathrm{max}}_{\mathrm{LAB}}$ scattering angle for the sixth element, while the black dashed line indicates the maximum $\vartheta^{\mathrm{max}}_{\mathrm{LAB}}$ for the 18th element. Only events with six neutral particles reconstructed in the central detector are presented.

Assuming the nominal vertex position of $(0, 0, 0)$, the polar scattering angles ϑ_{LAB} of the helium nuclei have been determined from the FPC hit positions. In figure 6.1 the corresponding laboratory momenta of the ^{3}He nuclei are plotted against the angles requiring a hit in the sixth or 18th element of FRH1 (left and right figure, respectively) for runs 10 705 to 10 965. In order to extract the maximum polar scattering angles, projections on the ϑ_{LAB} axis for momentum ranges with a width of 4 MeV c^{-1} were fitted by Gaussian distributions. The obtained maxima for ϑ_{LAB} for the sixth and 18th[1] element are indicated by the black solid and black dashed lines, respectively. A clear deviation of the maxima by about 0.2° is visible originating from an incorrectly assumed vertex position.

To extract the correct vertex position in the x-y plane, the above mentioned method was applied to all 24 elements of FRH1 for the various run periods. Figure 6.2 illustrates the determined maxima ϑ_{LAB} of the ^{3}He nuclei depending on the azimuthal scattering angle φ for runs 10 705 to 10 965. The data points are fitted by a sinusoidal function (red curve) of the type:

$$\vartheta^{\mathrm{max}}_{\mathrm{LAB}}(n) = a \cdot \sin\left(\varphi + \varphi_0\right) + \vartheta_{\mathrm{max}} \,. \tag{6.1}$$

[1]Note that the mean azimuthal angles of the sixth and 18th element of the FRH differ by 180°.

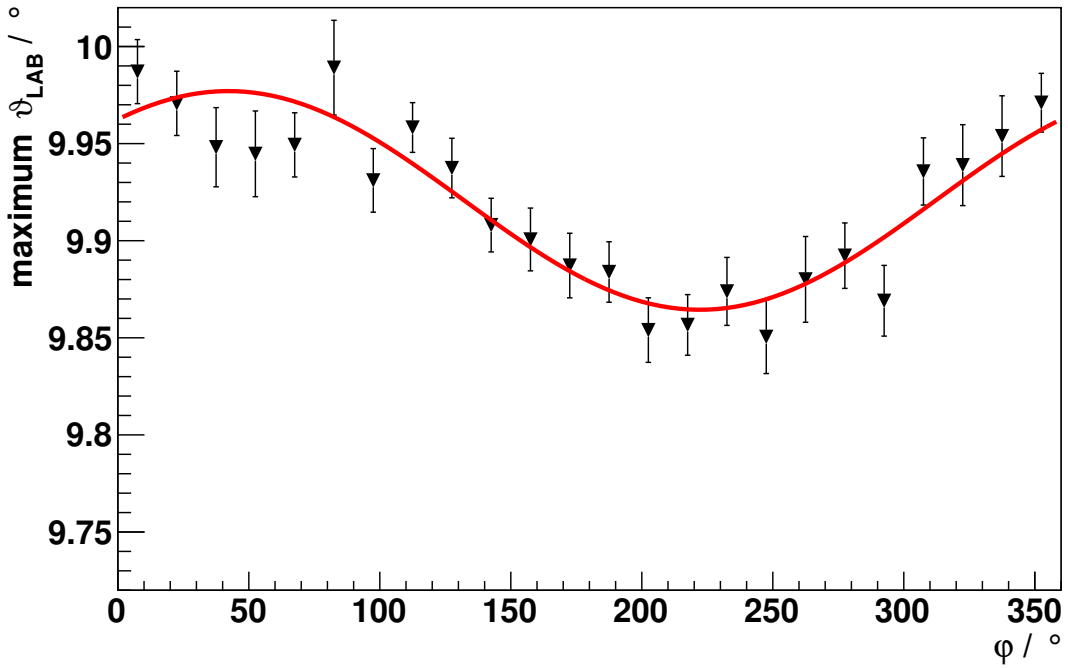

Figure 6.2.: Extracted maximum polar scattering angles ϑ_{LAB} of the ^{3}He nuclei for the reaction $\mathrm{p} + \mathrm{d} \rightarrow {}^3\mathrm{He} + \eta$ for the data runs 10 705 to 10 965, depending on the azimuthal scattering angle φ. The red curve is a fit by a sinusoidal function.

Table 6.1.: Shift parameters for the global FPC position perpendicular to the COSY beam pipe as applied in the analysis for the various run periods.

run numbers	x shift / mm	y shift / mm
10 392 – 10 528	−1.07	−1.02
10 529 – 10 704	−1.06	−1.18
10 705 – 10 965	−1.53	−0.84
10 966 – 11 525	−1.64	−0.63
13 969 – 15 944	+1.44	−1.22

Here the parameter $\vartheta_{\max}$ corresponds to the actual maximum scattering angle, while a is the amplitude of the deviation from this value. The observed oscillations can be corrected for by either shifting the assumed vertex position or by adjusting the position of the FPC assumed in the analysis. In the first case the influence of the magnetic field of the solenoid on the helium trajectories has to be considered first in order to correctly calculate the vertex position. This is not needed for the second method where a purely geometrical calculation is sufficient. Since the resolution of the central detector is not high enough to observe the vertex shift using its information, an additional shift of the central detector component positions assumed in the analysis is not required for the second method. Hence, it was decided to apply the second method to the correction [BCHW17].

Table 6.1 lists the x and y shift parameters of the global FPC position for the various run number ranges calculated from the fits[2]. While for the beam time recorded in 2009 one shift parameter set is sufficient and no changes in the vertex position over the runs 13 969 to 15 944 were observed, the 2008 data is divided into four parts. The separation of runs 10 392 to 10 528 and runs 10 529 to 10 704 originates from major adjustments of WASA detector settings after run 10 528, leading to different calibration parameters for the two run periods [BCHW17]. The minor adjustments of the COSY beam settings performed between these run periods lead to only small changes in the vertex position. After run 10 704 the COSY beam target overlap was optimized, which results in a noticeable change in the interaction vertex position. As the runs 10 966 to 11 525 were recorded using

[2] The actual FPC position does, of course, not vary between the runs, but only the position assumed in the analysis to compensate the shift of the interaction vertex position.

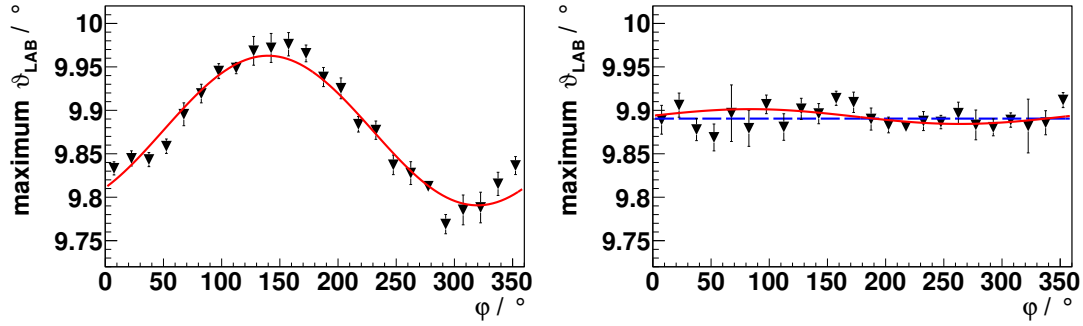

Figure 6.3.: Extracted maximum scattering angles ϑ_{LAB} of the ^{3}He nuclei for the reaction $\mathrm{p} + \mathrm{d} \to {}^3\mathrm{He} + \eta$ for a sample of data runs recorded in 2009 depending on the azimuthal scattering angle φ. The red curves are fits by sinusoidal functions. Left: The data sample without applying a shift of the FPC position in the analysis. Right: The data sample after applying a shift of the FPC position in the analysis. The blue dashed line is a fit by a constant.

a different accelerator setting with a cycle time dependent beam momentum, shift parameters were determined separately for this run period.

In figure 6.3 the dependencies of the extracted maximum polar scattering angles ϑ_{LAB} of the ^{3}He nuclei on the azimuthal angle φ are compared before and after the application of the FPC shift for the 2009 data (left and right figure, respectively). While a sinusoidal function is required to describe the uncorrected data (red curve), a constant fit is sufficient after the correction leading to a reduced χ^2/ndf of about 1.43 (blue dashed line) compared to $\chi^2/ndf \approx 1.25$ for a fit with a sinusoidal function (red curve). Furthermore, the latter would indicate a shift of the vertex position by less than 0.1 mm, which is the same as the uncertainty of the z position of the vertex and can be neglected.

After applying the correction, the extracted maximum scattering angle $\vartheta_{\mathrm{LAB}}^{\mathrm{max}}$ of the helium nucleus can be utilized to calculate the COSY beam momentum using a relation between $\vartheta_{\mathrm{LAB}}^{\mathrm{max}}$ and p_{beam} derived from relativistic kinematics. For the run periods 10 392 to 10 528, 10 529 to 10 704, and 10 705 to 10 965 a proton beam momentum of $p_{\mathrm{beam}} = 1.6986\,\mathrm{GeV}\,c^{-1}$ was determined, whereas for the runs 13 969 to 15 944 a slightly lower beam momentum of $p_{\mathrm{beam}} = 1.6970\,\mathrm{GeV}\,c^{-1}$ was found to describe the data best[3]. In case of runs 10 966 to 11 525, only an average beam

[3]The quoted beam momentum determined for the 2009 data set differs by less than $1\,\mathrm{MeV}\,c^{-1}$ compared to the beam momentum equaling $T_{\mathrm{beam}} = 1000\,\mathrm{GeV}$ and used for the cross section determination in chapters 4 and 5. This can be explained by the higher statistics utilized for the decay analysis, and, in particular, for the beam momentum determination, and the difference is well below the uncertainty of the COSY beam momentum of 0.1 % [Mai97].

momentum can be determined using this method, as the nominal beam momentum depends on the time in the COSY cycle. It corresponds to 1.694 GeV c^{-1}. The exact beam momentum with its cycle time dependency will be presented in chapter 6.2.6.

6.2.2. Forward range hodoscope calibration

To fully reconstruct a detected helium nucleus, information about both its trajectory and its energy are required. While the first can be determined with the help of the FPC, for the calculation of the latter the knowledge of the projectile's energy loss in the FRH is needed. In case of the reaction $p + d \rightarrow {}^3He + \eta$ with a proton beam momentum of roughly 1.7 GeV c^{-1}, the helium nucleus is stopped in the first layer of the FRH. Hence, for the calculation of its kinetic energy the measured energy loss in FRH1 and the polar scattering angle are sufficient and only the calibration of the first of the five FRH layers needs to be optimized.

In chapter 4.5 an optimization of the FRH1 calibration was performed for about 10 % of the $p + d \rightarrow {}^3He + X$ data recorded in 2009 within the context of the cross section determination of the reaction $p + d \rightarrow {}^3He + \eta$ at $Q = 48.8$ MeV and $Q = 59.8$ MeV. For the precise cross section determination 10 % of the recorded data with stable conditions in the sense of the detector calibration were sufficient, whereas the full data set is required for the analysis of rare or forbidden η meson decays. Furthermore, for the latter analysis a detailed check of the data recorded in 2008 is necessary, which has not yet been performed. Since a run dependency of the calibration parameters for the various detector elements has been observed in chapter 4.3, this needs to be checked and corrected in a first step before a fine calibration is performed.

Run dependency of the forward range hodoscope calibration

To investigate the run dependency of the FRH1 calibration parameters, a calibration tool developed by K. Demmich as part of his master thesis was used [Dem13]. The interface of this program is presented in figure 6.4. In the right part the energy losses recorded for one element of the first layer of the FRH are plotted against the energy losses in the corresponding two FTH1 elements. Here data points of particles stopped in FRH1 are drawn in red, whilst those passing through FRH1 are presented in blue. The black points illustrate the expected mean of the distributions

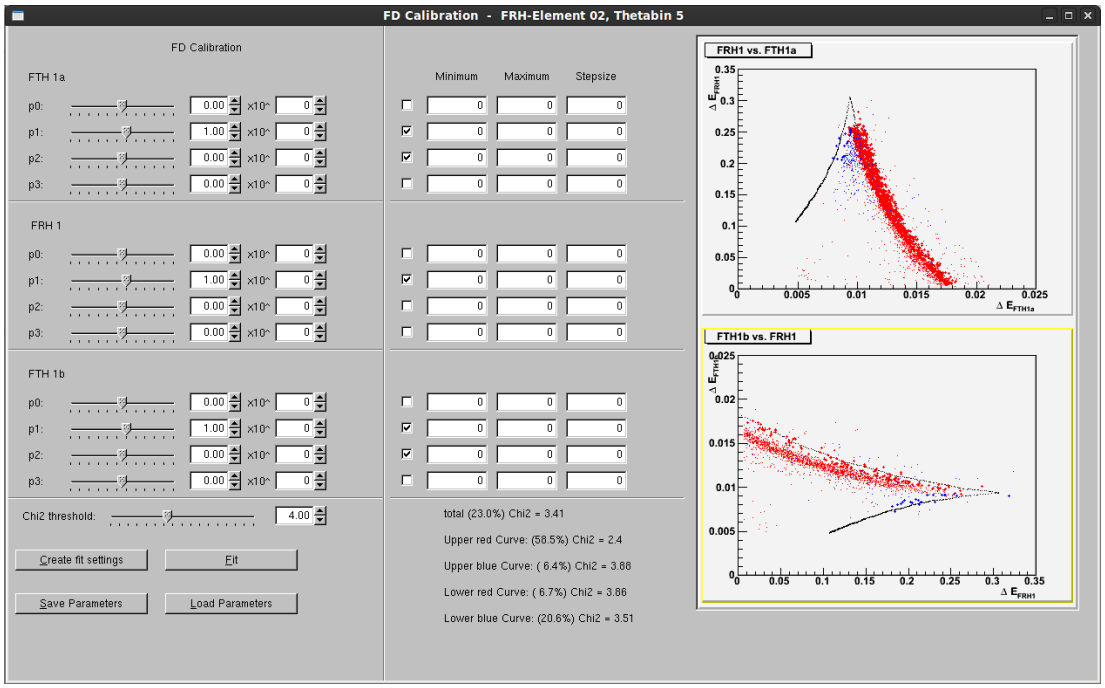

Figure 6.4.: Graphical interface for the calibration of the first layer of the forward range hodoscope developed by K. Demmich. The plots show the energy loss of a particle in element 2 of the first FRH layer plotted against the energy loss in element 3 of the first FTH layer (upper plot) and the energy loss in element 4 of the first FTH layer plotted against the energy loss in element 2 of FRH1 (lower plot), respectively. Entries from particles stopped in the first FRH layer are shown in red and entries from those passing through the first FRH layer are presented in blue. Black points correspond to energy losses according to simulations of ^{3}He with different energies. The tool allows to set calibration parameters for the three detector elements. A detailed description is given in [Dem13].

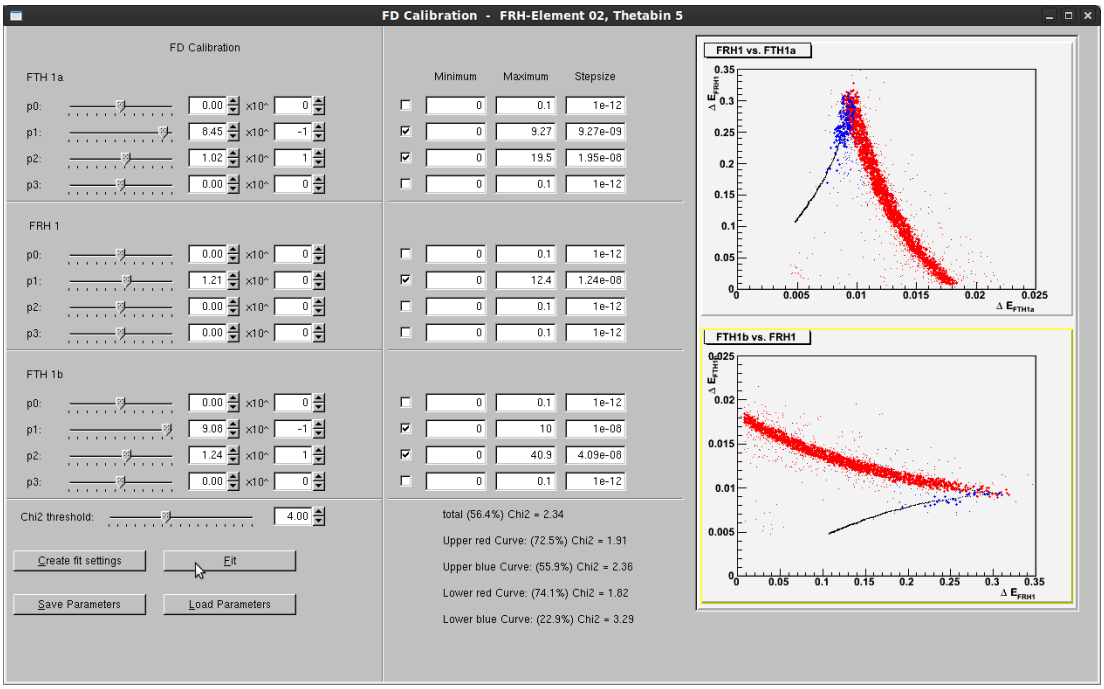

Figure 6.5.: Graphical interface for the calibration of the first layer of the forward range hodoscope developed by K. Demmich after fitting the data (red and blue points) to the Monte Carlo simulations (black points).

according to Monte Carlo simulations. In the left part the start parameters p_n of the calibration functions of the type

$$f\left(\Delta E\right) = \sum_{n=0}^{3} p_n \cdot \Delta E^n \tag{6.2}$$

can be set. While in the standard version of the calibration tool ADC (Analog to Digital Converter) values are used as an input, already calibrated energy losses ΔE are used as input here instead. As the data were already well calibrated, only the linear parameter p_1 was varied by the fit to adjust the energy deposited in FRH1, as well as parameters p_1 and p_2 for FTH1. Changes to these parameters are sufficient to obtain a good agreement between Monte Carlo and data (see figure 6.5). For a more detailed description of the calibration program refer to [Dem13].

In order to extract run dependent correction factors for all 24 elements of the first layer of the FRH, both the 2008 and the 2009 data set were divided into blocks of 20 runs. For each set of 20 runs and each FRH1 detector element a correction factor was determined using the above mentioned tool. In figure 6.6 these scaling factors are plotted against the corresponding mean run number for element 21

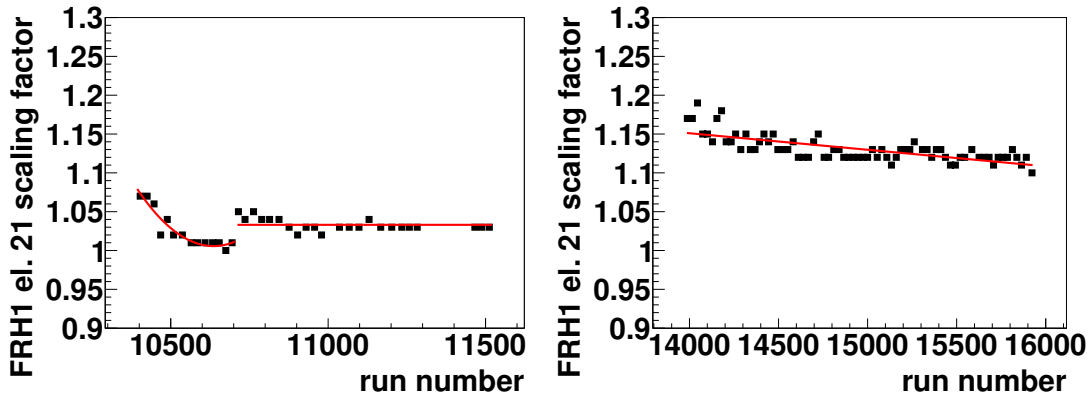

Figure 6.6.: Extracted run number dependent scaling factors for the 21st element of FRH1 for the 2008 data set (left) and for the 2009 data set (right). The continual segments are fitted by polynomial functions of up to the second order (red lines).

for the data recorded in 2008 and for the 2009 data set (left and right figure). If the previous calibration of the FRH1 elements had been ideal and there was no run dependency, the scaling factors would have been constant at one, which is clearly not the case. Not only can a run dependency be observed, but it is also noticeable that all extracted scaling factors are larger than one. This originates from the fitting procedure utilized by the calibration program, which leads to a global overestimation of the scaling factors. Since this effect is independent of the run number, the tool is applicable to studies of the run dependence of the FRH calibration, while the overall magnitude of the scaling was adjusted by means of an additional calibration step presented in the following chapter. The discontinuities observed for both data sets are caused by adjustments of WASA detector settings done between two runs. In order to extract scaling factors for the whole analyzed beam times, the different segments were fitted by polynomial functions up to the second order (red lines).

Elemental fine calibration of the forward range hodoscope

As already done for a part of the analyzed data set recorded in 2009 and described in chapter 4.5, a fine calibration of the helium nucleus momentum can be achieved with the aid of its precisely measured polar scattering angle and Monte Carlo simulations. Instead of the laboratory momenta, the energies ΔE deposited in the first layer of the FRH are corrected. However, they are directly connected to the helium momenta.

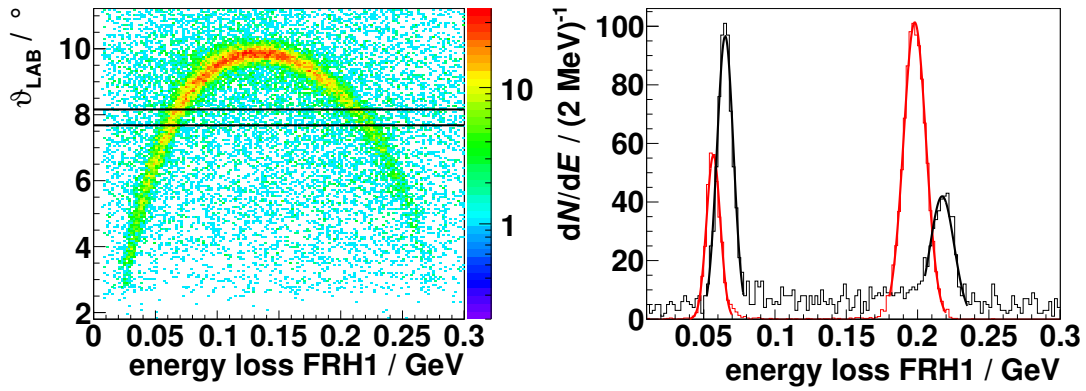

Figure 6.7.: Left: Laboratory ^{3}He polar scattering angle ϑ_{LAB} plotted against the corresponding energy loss in the 21st element of the first FRH layer for the 2009 data set in logarithmic scale. Right: Energy loss spectrum for $7.68° \leq \vartheta_{LAB} < 8.16°$ (indicated by the black lines in the left figure) for the data recorded in 2009 (black) and Monte Carlo simulations of the reaction $\mathrm{p} + \mathrm{d} \rightarrow {}^3\mathrm{He} + \eta$ with the η meson decaying into three neutral pions (red). The peaks are fitted by Gaussian distributions (black and red curves, respectively) to extract their peak position. Note that the Monte Carlo simulations are arbitrarily scaled to the recorded data. In both figures six neutral particles detected in the central detector were required to reduce the multi-pion background.

In the left of figure 6.7 the measured polar scattering angles ϑ_{LAB} of the ^{3}He nuclei are plotted against the corresponding energy losses in the first layer of the FRH for helium nuclei detected in the 21st element of FRH1 for the 2009 data set. For calibration purposes the presented data were preselected requiring exactly six neutral particles detected in the central detector, mainly expected to originate from the decay $\eta \rightarrow \pi^0 + \pi^0 + \pi^0$ in order to reduce the multi-pion background. Projections for ϑ_{LAB} ranges were compared to those of Monte Carlo simulations of the reaction $\mathrm{p} + \mathrm{d} \rightarrow {}^3\mathrm{He} + \eta$ with the η meson decaying into three neutral pions. As an example the energy distributions for $7.68° \leq \vartheta_{LAB} < 8.16°$ (indicated by the black lines) are presented in the right of figure 6.7. Due to the different beam momenta of the run periods 10 392 to 10 965, 10 966 to 11 525, and 13 969 to 15 944, separate simulations were created with the beam momenta determined in the previous chapter. In case of the runs 10 966 to 11 525, the mean beam momentum $p_{\mathrm{beam}} = 1.694\,\mathrm{GeV}\,c^{-1}$ was used. For both the data (black) and Monte Carlo simulations (red) the two peaks in the energy spectra were fitted by Gaussian distributions (black and red curves, respectively) to extract the peak positions for the selected angular range. This method was applied to angular ranges up to $\vartheta_{\mathrm{LAB}} < 9.6°$ for each of the 24 elements of FRH1. For higher angular ranges

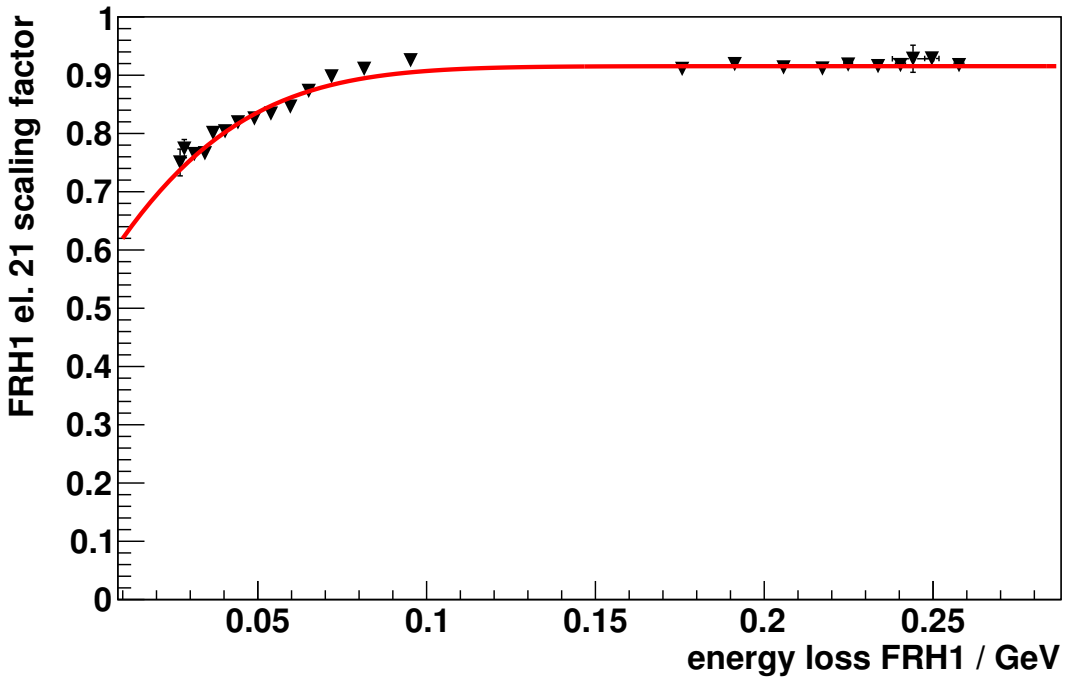

Figure 6.8.: Scaling factors for the energy losses of the helium nuclei detected in the 21st element of FRH1 for the 2009 data set. The data points are fitted by a function as described in equation 6.3 (red curve).

the two peaks in the energy loss spectra cannot be separated and, thus, they were excluded from the calibration process. Similarly, some higher energy losses were excluded due to too low statistics in the corresponding angular ranges.

To determine elemental fine calibration factors, the ratio of the energy loss as expected according to simulations and the energy loss as seen in data was plotted against the energy loss according to the measured data. Figure 6.8 shows such a plot for the 21st element of FRH1 for the 2009 data set. As expected, all scaling factors are smaller than one and, hence, compensate the overestimated global scaling obtained in the previous chapter. The data points were fitted by a function of the type:

$$f(E_{\mathrm{dep}}) = a_0 + \mathrm{erf}\left(\frac{E_{\mathrm{dep}} - a_1}{a_2}\right) - 1 \tag{6.3}$$

with the error function $\mathrm{erf}\,(x)$ defined as

$$\mathrm{erf}\,(x) = \frac{2}{\sqrt{\pi}} \int_0^x e^{-y^2} \mathrm{d}y\,. \tag{6.4}$$

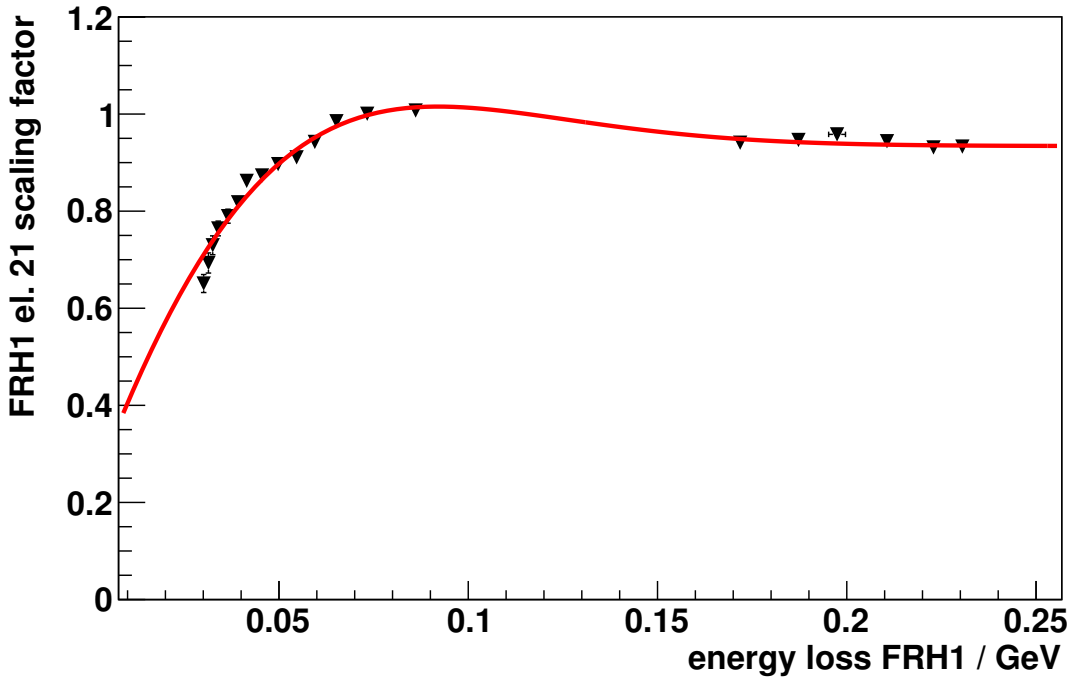

Figure 6.9.: Scaling factors for the energy losses of the helium nuclei detected in the 21st element of FRH1 for runs 10 705 to 10 965. The data points are fitted by a function as described in equation 6.5 (red curve).

While this fit function is able to describe the distributions of all 24 elements of the FRH1 very well for the 2009 data set and was found to be stable during the beam time, an extended function is required for a proper description of the 2008 data set:

$$f(E_{\mathrm{dep}}) = a_0 + \left(\mathrm{erf}\left(\frac{E_{\mathrm{dep}} - a_1}{a_2}\right) - 1\right) \cdot (a_3 + a_4 \cdot E_{\mathrm{dep}}) \ . \tag{6.5}$$

Furthermore, due to major adjustments of WASA detector settings after runs 10 528, 10 704, 10 965, and 11 301, the 2008 data set was divided into five parts, for each of which separate correction functions were determined. Figure 6.9 illustrates the fitted scaling factors for the energy losses in the 21st element of the FRH for runs 10 705 to 10 965.

6.2.3. Forward trigger hodoscope calibration

The helium nuclei produced in the reaction $\mathrm{p} + \mathrm{d} \rightarrow {}^3\mathrm{He} + \mathrm{X}$ are identified via their energy losses in the first layer of the forward range hodoscope and in the first layer of the forward trigger hodoscope. As already mentioned in chapter 4.3,

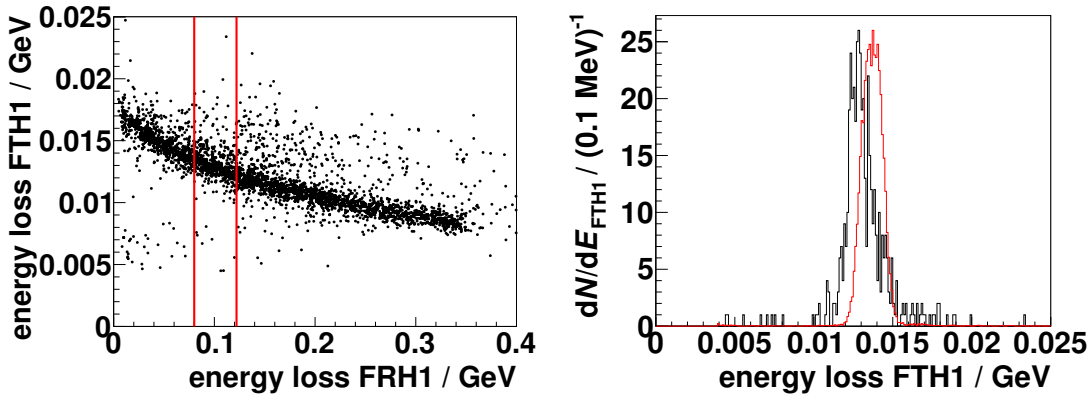

Figure 6.10.: Left: Energy loss in the 42nd element of the first FTH layer plotted against the energy loss of the same particle in the first FRH layer. The red lines indicate the selected projection range. Right: Energy loss in the 42nd element of the first FTH layer for the selected FRH1 energy loss range. Data from run number 14 091 are shown in black, while Monte Carlo simulations are presented in red. Note that the latter are arbitrarily scaled to the data.

the calibration settings of some FTH1 elements show a dependence on the run number. Therefore, only runs with constant calibration parameters were used for the analysis presented in chapter 4. Since the analysis of rare or forbidden η meson decays requires the full available statistic, a run dependent correction of the FTH1 calibration settings was performed for both the full 2008 and the 2009 data set.

Instead of using the FTH1 calibration parameters obtained with the aid of the calibration tool presented in the previous chapter, the already well calibrated first layer of the FRH was utilized to derive run dependent scaling factors for the first layer of the FTH. Figure 6.10 (left) shows the energy loss in the 42nd element of FTH1 plotted against the energy loss in FRH1 for run 14 091. In the energy range indicated by the red lines, the energy loss in the given FTH1 element was compared to the expected energy loss according to Monte Carlo simulations of the reaction $p + d \rightarrow {}^3He + \eta$ as presented in the right of figure 6.10. To obtain a scaling factor that can be used to correct the FTH1 calibration, the distribution of the data as well as the one from simulations were fitted by a Gaussian distribution. The expected energy loss value according to simulations divided by the extracted peak position can then be used as a scaling factor.

This method was applied to all 48 FTH1 elements for all runs of the 2008 and 2009 data sets. While for the data recorded in 2009 a separate scaling factor could be determined for each run, a scaling factor for a set of five runs was extracted

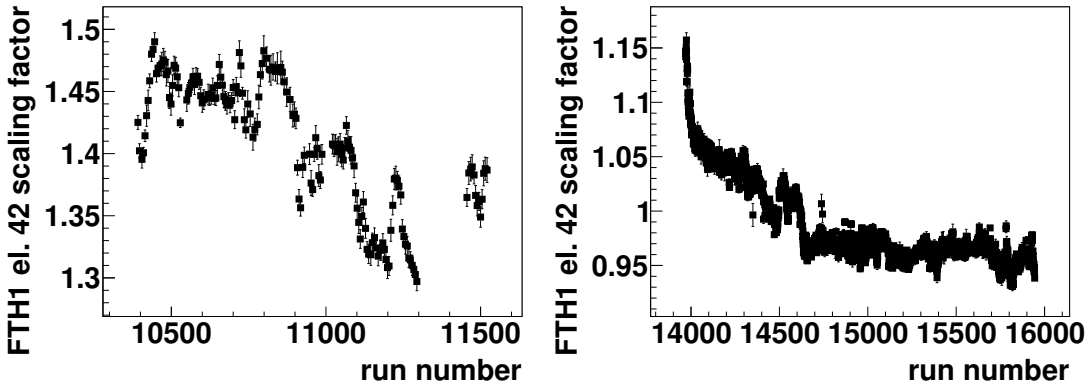

Figure 6.11.: Scaling factors for the 42nd element of the first FTH layer depending on the run number for the data recorded in 2008 (left) as well as for the data recorded in 2009 (right).

for the runs of the 2008 data set due to lower statistics per run. In figure 6.11 the scaling factors for the energy loss in the 42nd FTH1 element are presented for the 2008 and 2009 data sets depending on the run number. These scaling factors were used in the later analysis to account for the run dependency of the FTH1 calibration.

6.2.4. Reconstruction of the kinetic energy

In chapter 4.5.3 functions were determined with the aid of Monte Carlo simulations correcting the reconstructed ^{3}He momenta to match the generated ones. A similar correction is required for the η meson decay studies. Due to the layout of the common PDEtaAnalysisBase class, a correction was applied to the kinetic energies of the helium nuclei rather than to their momenta. For the aforementioned purpose Monte Carlo simulations of the reaction $p + d \rightarrow {}^3He + \eta$ were analyzed. The resulting energy correction function

$$E_{\mathrm{kin}}^{\mathrm{corr}}\left({}^3\mathrm{He}\right) = \left(E_{\mathrm{kin}}^{\mathrm{rec}}\left({}^3\mathrm{He}\right) - 0.003\,714(84)\,\mathrm{GeV}\right)/0.990\,09(36) \tag{6.6}$$

was applied both to data and Monte Carlo simulations, as the 2008 and 2009 data sets were calibrated to agree with Monte Carlo simulations (see previous chapters).

6.2.5. Fine tuning of the FRH1 calibration with regard to the η mass

The η meson is known to have a mass of $m_\eta = (547.862 \pm 0.017)\,\mathrm{MeV}\,c^{-2}$ [P+16]. Since the energy calibration of the forward range hodoscope was performed with respect to the η meson production reaction $\mathrm{p} + \mathrm{d} \to {}^3\mathrm{He} + \eta$, the peak position in the ^{3}He missing mass spectrum corresponding to the η meson can be used to check and further optimize this calibration.

The best agreement between the observed peak position depending on $\cos\vartheta_\eta^{\mathrm{CMS}}$ and the η meson mass was obtained if a minor correction was applied to the ^{3}He energies deposited in FRH1:

$$\begin{aligned} E_{\mathrm{dep}}^{\mathrm{corr}}\left({}^3\mathrm{He}\right) = {} & E_{\mathrm{dep}}^{\mathrm{FRH}}\left({}^3\mathrm{He}\right) + 0.0024(3)\,\mathrm{GeV} \\ & - 0.013(1) \cdot E_{\mathrm{dep}}^{\mathrm{FRH}}\left({}^3\mathrm{He}\right) - 0.002(1)\,\mathrm{GeV} \cdot \vartheta_{\mathrm{LAB}} \end{aligned} \tag{6.7}$$

for the 2008 data set and

$$\begin{aligned} E_{\mathrm{dep}}^{\mathrm{corr}}\left({}^3\mathrm{He}\right) = {} & E_{\mathrm{dep}}^{\mathrm{FRH}}\left({}^3\mathrm{He}\right) + 0.0012(1)\,\mathrm{GeV} \\ & - 0.006(1) \cdot E_{\mathrm{dep}}^{\mathrm{FRH}}\left({}^3\mathrm{He}\right) - 0.002(1)\,\mathrm{GeV} \cdot \vartheta_{\mathrm{LAB}} \end{aligned} \tag{6.8}$$

for the 2009 data set. These adjustments of the helium energy are smaller than the uncertainties of the calibration methods presented in chapter 6.2.2, but lead to a slightly better agreement of the missing mass peak position with the η mass[4].

In figure 6.12 the peak positions in the ^{3}He missing mass spectra determined for the 2008 and 2009 data sets (red triangles and blue inverted triangles, respectively) are compared to the η meson mass (black dashed line) and Monte Carlo simulations of the reaction $\mathrm{p} + \mathrm{d} \to {}^3\mathrm{He} + \eta$ with $\eta \to \pi^+ + \pi^- + \pi^0$ (black squares) depending on $\cos\vartheta_\eta^{\mathrm{CMS}}$. All extracted peak positions deviate from $m_\eta = 547.862\,\mathrm{MeV}\,c^{-2}$ by less than $500\,\mathrm{keV}\,c^{-2}$, except for the two angular ranges below $\cos\vartheta_\eta^{\mathrm{CMS}} = -0.6$. Furthermore, for these two angular bins Monte Carlo and data show a different behavior. While the peak positions in simulations are below the η mass, they are above it for data. Only very few η mesons of all η mesons produced in the reaction $\mathrm{p} + \mathrm{d} \to {}^3\mathrm{He} + \eta$ are scattered with $\cos\vartheta_\eta^{\mathrm{CMS}} < -0.6$ for $Q = 59.8\,\mathrm{MeV}$ (less than 3 %, see chapter 5.1). Moreover, the angular range $-1.0 \leq \cos\vartheta_\eta^{\mathrm{CMS}} < -0.6$

[4]Note that these adjustments were determined by a manual iterative method. Changes of the parameters by the given uncertainties do not lead to a further improvement.

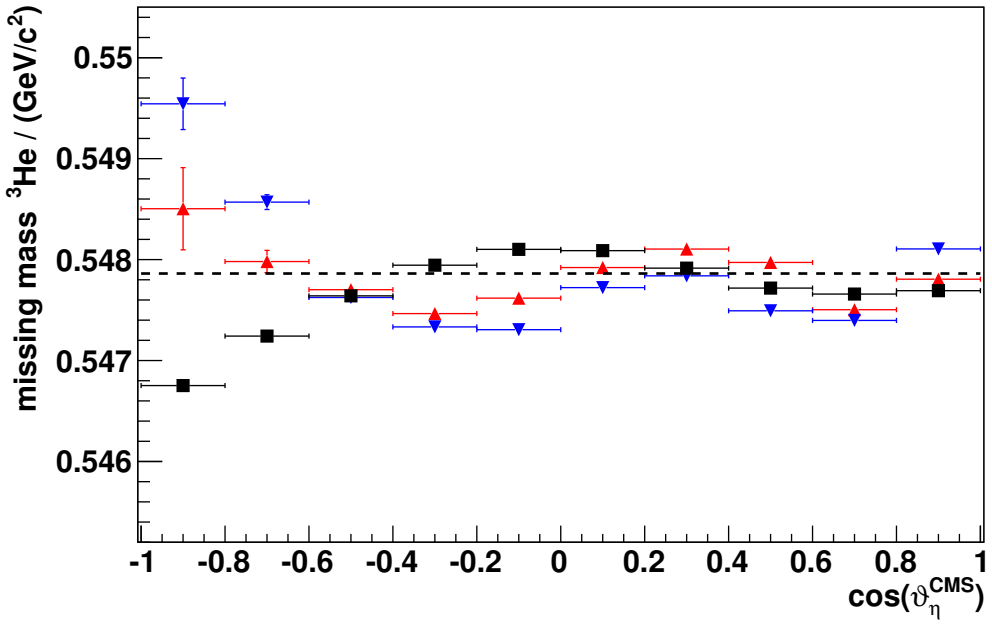

Figure 6.12.: Extracted η meson peak position in the ^{3}He missing mass spectra depending on $\cos\vartheta_\eta^{\mathrm{CMS}}$ for the 2008 and 2009 data sets (red triangles and blue inverted triangles, respectively) compared to Monte Carlo simulations of the reaction $\mathrm{p} + \mathrm{d} \rightarrow {}^3\mathrm{He} + \eta$ with $\eta \rightarrow \pi^+ + \pi^- + \pi^0$ (black squares). The horizontal error bars indicate the bin width, whereas the vertical error bars are purely statistical uncertainties. The black dashed line indicates the η meson mass position at $m_\eta = 547.862\,\mathrm{MeV}\,c^{-2}$. All shown data samples were preselected with the conditions described in chapter 6.5, and the second part of the 2008 data set (runs 10 966 to 11 525) was analyzed with the beam momenta as given in chapter 6.2.6.

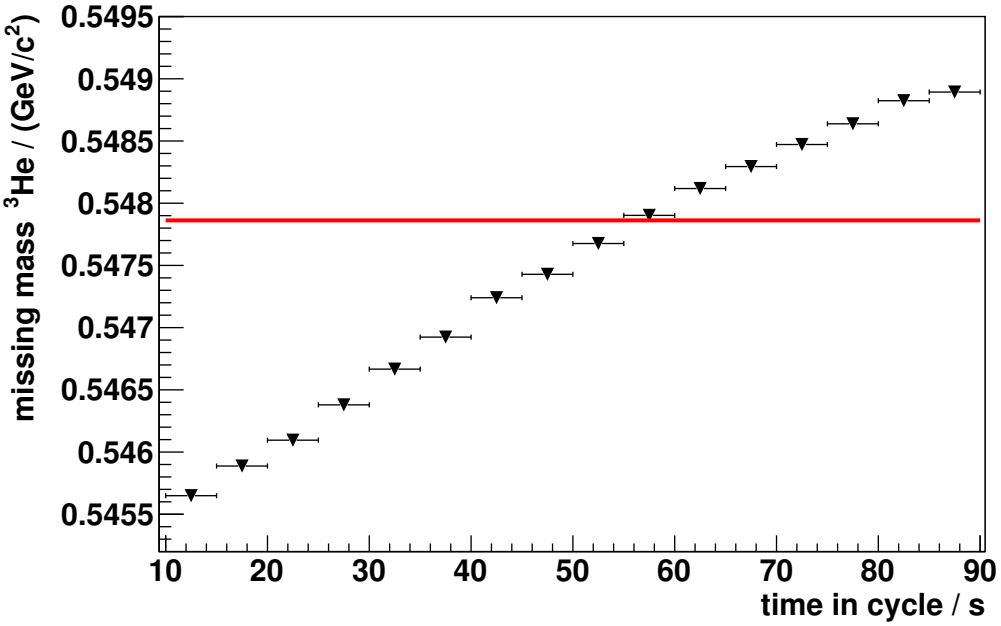

Figure 6.13.: η meson peak position in the ^{3}He missing mass spectrum depending on the time in cycle for runs 10 966 to 11 525. The red line presents the correct η meson mass position at $m_\eta = (547.862 \pm 0.017)\,\mathrm{MeV}\,c^{-2}$ [P$^+$16], and the horizontal error bars indicate the chosen bin width.

is excluded from the later analysis (see chapter 6.6). Thus, the deviations for $\cos\vartheta_\eta^{\mathrm{CMS}} < -0.6$ can be neglected.

6.2.6. Cycle time dependency of the proton beam momentum

As mentioned in chapter 6.1, the COSY beam momentum p_{beam} varies depending on the time in cycle for the second part of the 2008 data set (runs 10 966 to 11 525). The assumption of a constant proton beam momentum of $1.694\,\mathrm{GeV}\,c^{-1}$ in the analysis results in a variation of the η meson peak position in the spectrum of the ^{3}He missing mass depending on the cycle time as presented in figure 6.13.

The dependency of the beam momentum p_{beam} on the time in cycle t_{cycle} can be described by the function

$$\begin{aligned} p_{\mathrm{beam}}\,(t_{\mathrm{cycle}}) = {} & 1.6998(1)\,\mathrm{GeV}\,c^{-1} - 1.00(30) \times 10^{-4}\,\mathrm{GeV}\,c^{-1}\,\mathrm{s}^{-1} \cdot t_{\mathrm{cycle}} \\ & - 5.6(32) \times 10^{-7}\,\mathrm{GeV}\,c^{-1}\,\mathrm{s}^{-2} \cdot t_{\mathrm{cycle}}^2 \\ & + 6.7(21) \times 10^{-9}\,\mathrm{GeV}\,c^{-1}\,\mathrm{s}^{-3} \cdot t_{\mathrm{cycle}}^3\,, \end{aligned} \tag{6.9}$$

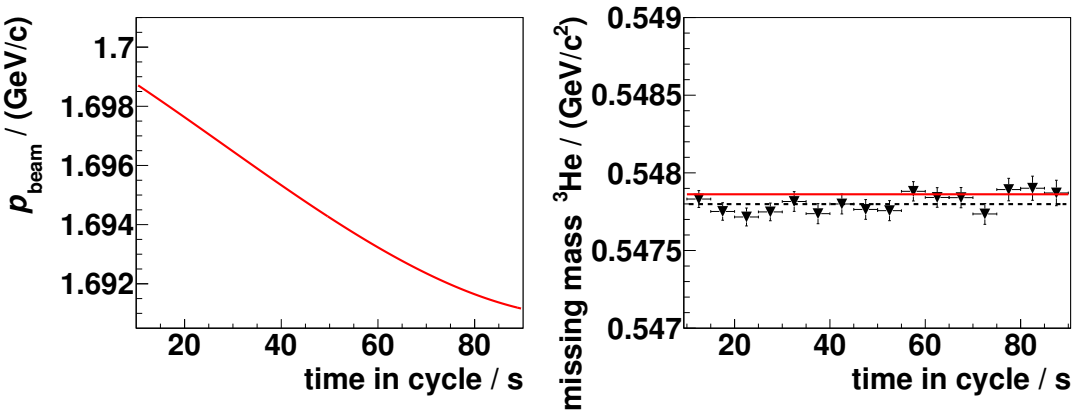

Figure 6.14.: Left: Function to describe the dependency of the proton beam momentum p_{beam} on the time in cycle for runs 10 966 to 11 525. Right: η meson peak position in the ^{3}He missing mass spectrum depending on the time in cycle for runs 10 966 to 11 525 using equation 6.9 for the proton beam momentum. The red solid line presents the correct η meson mass position at $m_\eta = (547.862 \pm 0.017)\,\mathrm{MeV}\,c^{-2}$ [P$^+$16], and the horizontal error bars indicate the chosen bin width. A fit by a constant is illustrated by the black dashed line ($\chi^2/ndf = 0.89$). The presented data were preselected with the conditions described in chapter 6.5.

which is illustrated in the left of figure 6.14. Utilizing this function in the analysis leads to an η meson peak position that does not depend on the time in cycle anymore (see figure 6.14 right). Moreover, the fitted mean value (black dashed line) deviates from $m_\eta = (547.862 \pm 0.017)\,\mathrm{MeV}\,c^{-2}$ [P$^+$16] (red solid line) by only $60\,\mathrm{keV}\,c^{-2}$, which is less than the uncertainty of the η peak position depending on $\cos\vartheta_\eta^{\mathrm{CMS}}$ (see chapter 6.2.5) and below the uncertainty given by the resolution of the COSY beam momentum [Mai97].

6.3. Monte Carlo simulations

As mentioned in chapter 3.5.3, a common set of Monte Carlo simulations was created, which includes models for η and π^0 decays with angular distributions known to differ from phase space behavior. This common set was simulated with a constant proton beam momentum of $p_{\mathrm{beam}} = 1.700\,\mathrm{GeV}\,c^{-1}$. During the work on this thesis the amount of statistics of Monte Carlo simulations was increased in order to avoid a limitation of the determination of the branching ratio or its upper limit of the decay channel $\eta \to \pi^0 + e^+ + e^-$ by the number of simulated background events. For this purpose millions of events were simulated for all η meson decays that have been observed so far [P$^+$16]. A list of these decays including

Table 6.2.: List of all simulated background η meson decay channels with their corresponding number of simulated events.

η decay channel	Number of events simulated
$\eta \to \gamma + \gamma$	4.0×10^7
$\eta \to \pi^0 + \pi^0 + \pi^0$	4.0×10^7
$\eta \to \pi^0 + \gamma + \gamma$	1.0×10^7
$\eta \to \pi^+ + \pi^- + (\pi^0 \to \gamma + \gamma)$	3.0×10^7
$\eta \to \pi^+ + \pi^- + (\pi^0 \to e^+ + e^- + \gamma)$	1.0×10^7
$\eta \to \pi^+ + \pi^- + \gamma$	1.0×10^7
$\eta \to e^+ + e^- + \gamma$	1.0×10^7
$\eta \to \mu^+ + \mu^- + \gamma$	1.0×10^7
$\eta \to e^+ + e^- + e^+ + e^-$	1.0×10^7
$\eta \to \pi^+ + \pi^- + e^+ + e^-$	1.0×10^7

the numbers of simulated events is given in table 6.2. While in case of the decay channel $\eta \to \pi^+ + \pi^- + \pi^0$, which will be utilized for normalization in the later analysis, separate simulations were created for the two π^0 meson decays $\pi^0 \to \gamma + \gamma$ and $\pi^0 \to e^+ + e^- + \gamma$, the decay of the π^0 meson was handled by the Pluto event generator respecting the π^0 decay branching ratios in the other cases.

Additionally, a large set of reactions of the type

$$p + d \to {}^3He + (n \cdot \pi)^0 \text{ with } n = 1 \ldots 4 \tag{6.10}$$

was simulated (see table 6.3). All direct pion production channels were simulated assuming a distribution according to phase space, except for the two reaction channels $p + d \to {}^3He + \pi^0 + \pi^0$ and $p + d \to {}^3He + \pi^+ + \pi^-$, where a major deviation from phase space behavior is observed, the so-called ABC effect [ABC60, BAC61, Pé14b] (see chapter 6.3.2). Due to their large cross sections, these channels greatly contribute to the background of the $\eta \to \pi^0 + e^+ + e^-$ decay analysis. In case of the reaction $p + d \to {}^3He + \pi^0 + \pi^0$, a total cross section was determined by E. Pérez del Río based on the same data set as used for the analysis

Table 6.3.: List of all simulated multi-pion production reactions with their corresponding number of simulated events. In case of the reaction $p + d \to {}^3He + \pi^0 + \pi^0$ additional 6.0×10^8 events were simulated for the efficiency determination (see chapter 7).

Reaction channel	Number of events simulated
$p + d \to {}^3He + \pi^0$	1.4×10^7
$p + d \to {}^3He + \pi^0 + \pi^0$	$5.0 \times 10^8 + 6.0 \times 10^8$
$p + d \to {}^3He + \pi^0 + \pi^0 + \pi^0$	5.0×10^7
$p + d \to {}^3He + \pi^0 + \pi^0 + \pi^0 + \pi^0$	3.0×10^7
$p + d \to {}^3He + \pi^+ + \pi^-$	3.0×10^9
$p + d \to {}^3He + \pi^+ + \pi^- + \pi^0$	5.0×10^7
$p + d \to {}^3He + \pi^+ + \pi^- + \pi^0 + \pi^0$	3.0×10^7
$p + d \to {}^3He + \pi^+ + \pi^- + \pi^+ + \pi^-$	3.0×10^7

presented in this thesis and recorded in August/September 2009 [Pé14b, A$^+$15c]. It corresponds to

$$\sigma\left({}^3He\pi^0\pi^0\right) = (2.28 \pm 0.04 \pm 0.40)\,\mu b \text{ at } \sqrt{s} = 3.416\,GeV\,, \tag{6.11}$$

with the first uncertainty being statistical and the latter being systematic. The overall systematic normalization uncertainty of 30 % is not included in the quoted cross section. This value exceeds the total cross section of the reaction $p + d \to {}^3He + \eta$ determined at ANKE [R$^+$09] by a factor of about six:

$$\sigma\left({}^3He\eta\right) = (388.1 \pm 7.1 \pm 58.0)\,nb \text{ at } \sqrt{s} = 3.416\,GeV\,. \tag{6.12}$$

In addition to the simulations of the background reactions, simulations for the signal channel $\eta \to \pi^0 + e^+ + e^-$ were created. These will be presented in more detail in the following chapter 6.3.1.

Due to the very high luminosities during the beam times in 2008 and 2009, event overlaps are possible. These can be caused by multiple reactions between the COSY proton beam and a single deuterium pellet, for example. A method to consider this effect in Monte Carlo simulations will be discussed in chapter 6.3.3.

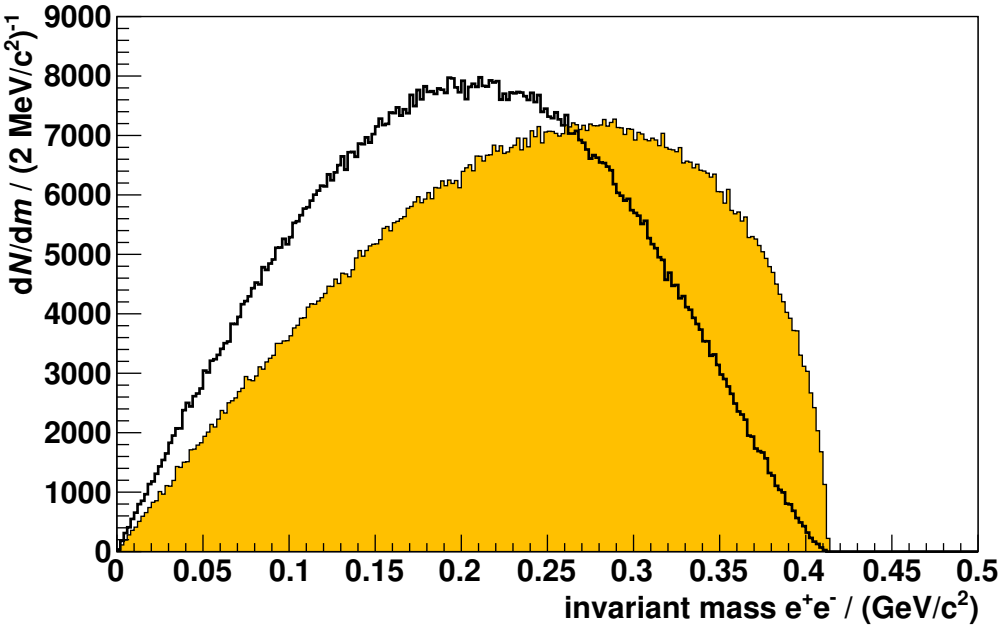

Figure 6.15.: Invariant mass of the e^+e^- pair in the simulated η meson decay $\eta \to \pi^0 + e^+ + e^-$. A distribution of a decay via a virtual photon (black) is compared to a distribution according to three-particle phase space (shadowed in orange). For both decays 1×10^6 events were generated.

6.3.1. η meson decay $\eta \to \pi^0 + e^+ + e^-$

As discussed in chapter 2.4, the decay $\eta \to \pi^0 + e^+ + e^-$ can theoretically proceed through different intermediate channels. Besides a decay via a single virtual photon, which violates C parity conservation, a decay via two virtual photons conserving C parity is possible. Therefore, in order to search for the η meson decay $\eta \to \pi^0 + e^+ + e^-$, Monte Carlo simulations based on these different assumptions were created.

The simplest assumption is a decay according to three-particle phase space. This leads to a distribution of the invariant mass of the e^+e^- pair as illustrated by the orange shadowed histogram in figure 6.15.

In chapter 2.4.2 it has been shown that the absolute amplitude squared of the decay $\eta \to \pi^0 + \gamma^* \to \pi^0 + e^+ + e^-$ is

$$|\mathcal{A}_{\mathrm{VMD}}|^2 = \frac{e^2\lambda^2}{(m_\rho^2 - q^2)^2 + q^2\Gamma_\rho^2(q^2)} 2e^2 \left(-4m_\eta^2 q^2 + 16m_\eta^2 E_{e^+} E_{e^-}\right) \tag{6.13}$$

Table 6.4.: List of simulated $\eta \to \pi^0 + e^+ + e^-$ decay models with their corresponding number of simulated events.

Decay model	Number of events simulated
Phase space	1 000 000
$\eta \to \pi^0 + \gamma^* \to \pi^0 + e^+ + e^-$	1 250 000

assuming vector meson dominance. While the elementary charge e and the factor λ as well as the ρ meson mass m_ρ and the η mass m_η are constants in the Monte Carlo simulations, the invariant mass q of the e^+e^- pair, the width $\Gamma_\rho(q^2)$ of the ρ meson, and the kinetic energies E_{e^+} and E_{e^-} in the η meson rest frame vary. Implementing the amplitude squared from equation 6.13 into Pluto leads to an invariant mass distribution of the e^+e^- pair as illustrated in figure 6.15 (black line). A clear shift of the distribution to lower masses compared to the three-particle phase space simulations is visible.

In table 6.4 the simulated $\eta \to \pi^0 + e^+ + e^-$ decay models are listed with their corresponding number of simulated events.

In addition to a decay via one or two virtual photons, a decay via a hypothetical dark boson in the intermediate state might be possible. This will be discussed in more detail in the outlook (see chapter 8.3).

6.3.2. Two-pion production $p + d \to {}^3He + (\pi + \pi)^0$

The direct two-pion production reactions $p + d \to {}^3He + (\pi + \pi)^0$ have a total cross section which is roughly one order of magnitude larger than the total cross section for $p + d \to {}^3He + \eta$ at a proton beam momentum of $p_{beam} = 1.700\,\mathrm{GeV}\,c^{-1}$ (see introduction of chapter 6.3). Moreover, the two neutral pions from the reaction $p+d \to {}^3He+\pi^0+\pi^0$ can mimic the signature of the η meson decay $\eta \to \pi^0+e^+e^-$ if one of the two pions performs a Dalitz decay ($\pi^0 \to e^+ + e^- + \gamma$) and the photon is missed in the reconstruction. Even though the branching ratio of this π^0 decay channel is just $(1.174 \pm 0.035)\,\%$, a large number of such reactions were recorded due to the high cross section of the two-pion production. Hence, high statistics of Monte Carlo simulations with a correct physics model for the two-pion production are essential for the η meson decay analysis presented in this thesis.

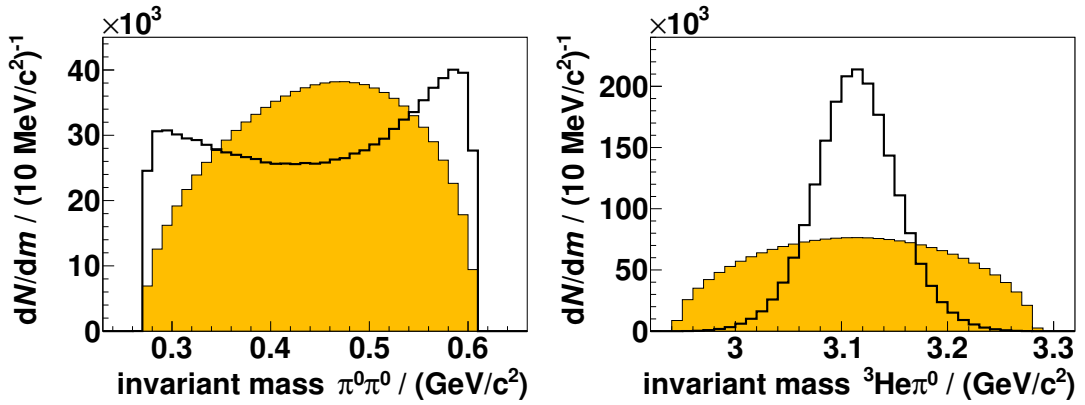

Figure 6.16.: Monte Carlo simulations of the reaction $p + d \to {}^3He + \pi^0 + \pi^0$. Left: Invariant mass of $\pi^0\pi^0$ according to three-particle phase space (orange shadowed area) and to the ABC model from [Pé14a, Pé14b] (black line). Right: Invariant mass of ${}^3He\pi^0$ for simulations according to three-particle phase space and to the ABC model from [Pé14a, Pé14b] (orange shadowed and black lined histogram, respectively).

As part of her doctoral thesis E. Pérez del Río further developed a Monte Carlo simulation program including the production model created by M. Bashkanov for the reaction $p + d \to {}^3He + (\pi + \pi)^0$ [Pé14a, Pé14b]. This program was used to create a large Monte Carlo data sample for the two-pion production with respect to the $d^*(2380)$ resonance and the t-channel $\Delta\Delta$ process. In figure 6.16 (left) the invariant mass distribution of the two pions according to the model implemented in Monte Carlo is compared to a distribution according to three-particle phase space (black lined and orange shadowed histogram, respectively). For the given beam momentum of $p_{\text{beam}} = 1.700\,\text{GeV}\,c^{-1}$ both the excitation of the d^* s-channel resonance at low masses and the enhancement at higher masses caused by the $\Delta\Delta$ t-channel are clearly visible. In the right of figure 6.16 the invariant mass of a pion and the ${}^3He$ nucleus is illustrated. The peak in the distribution for the simulations that include the ABC effect is caused by a strong $\Delta \to N\pi$ contribution as predicted by both production mechanisms. For a more detailed description of the ABC model used for the Monte Carlo simulations refer to [Pé14b].

6.3.3. Event overlap

As mentioned in the introduction of chapter 6.3, the very high luminosity during the measurements in 2008 and 2009 can lead to a temporal overlap of two events. In order to reduce these random coincidences, cuts are applied to the time difference

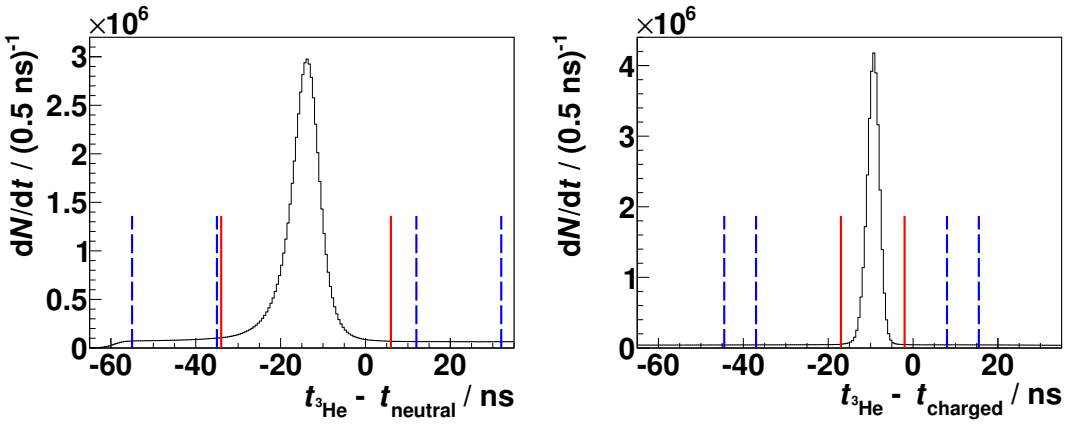

Figure 6.17.: Time difference between the ^{3}He nuclei detected in the forward detector and neutral and charged particles detected in the central detector for the 2008 data set (left and right figure, respectively). Only central detector particles in the time windows indicated by the red solid lines are used in the data analysis. Particles in the lower and upper time windows (blue dashed lines) are combined with Monte Carlo simulations to describe the effect of events overlapping.

between the ^{3}He nucleus detected in the forward detector and particles detected in the central detector. The time cuts applied to the 2008 data set are indicated as red solid lines in figure 6.17 for the neutral particles and charged particles (left and right figure, respectively). Nevertheless, a few particles from event overlaps remain after application of these cuts.

There are two possible approaches to include this effect into Monte Carlo simulations. In the first approach the particles from random coincidences are generated by Monte Carlo simulations. This approach can lead to systematic uncertainties, though, as the distributions of these particles have to be known precisely in advance. In the second approach particles from the measured data are used that did not pass the time cut and thus do not originate from the analyzed event. For this purpose particles from one event lying within one of the two time windows indicated by the blue dashed lines in figure 6.17 are added to one event from Monte Carlo simulations. The total width of these time windows is identical to the width of the time window indicated by the red solid lines. With this method the proper distributions of the particles' momenta from the random event overlap are naturally included.

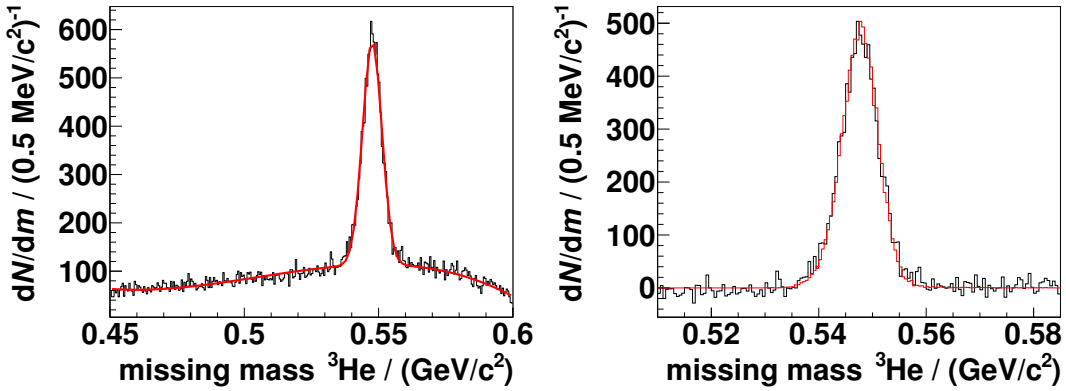

Figure 6.18.: Missing mass of ^{3}He for the angular range $-0.6 \leq \cos\vartheta_\eta^{\mathrm{CMS}} < -0.4$ for the 2008 data set. Left: Fitted by a Gaussian distribution plus a third order polynomial (red). Right: After background subtraction (black) compared to Monte Carlo simulations (red) using the smearing parameters listed in table 6.5.

6.4. Determination of the smearing settings for the Monte Carlo simulations

In order to obtain reliable results for studies with regard to rare or forbidden η meson decays, a good agreement between the measured data and Monte Carlo simulations is of great importance. Therefore, the detector resolution observed in data must be identical to the one assumed in simulations. In the following chapters the smearing settings for Monte Carlo simulations will be discussed and compared to the detector resolution of the measured data for the forward detector as well as the central detector (chapters 6.4.1 and 6.4.2).

6.4.1. Forward detector smearing settings

The missing mass spectrum of the ^{3}He nucleus detected in the forward detector is perfectly suited to investigate the resolution of the forward detector components utilized in the analysis, as the energy loss in FRH1 and the polar scattering angle of the ^{3}He derived from hit positions in the FPC are required for the calculation of the missing mass. For this purpose the standard deviation σ of the η meson peak in the ^{3}He missing mass spectrum was determined for ten $\cos\vartheta_\eta^{\mathrm{CMS}}$ intervals covering the full angular range. This was done by fitting the spectra with a third order polynomial added to a Gaussian distribution. In the left of figure 6.18 such a fit is presented for the 2008 data set for $-0.6 \leq \cos\vartheta_\eta^{\mathrm{CMS}} < -0.4$. The extracted

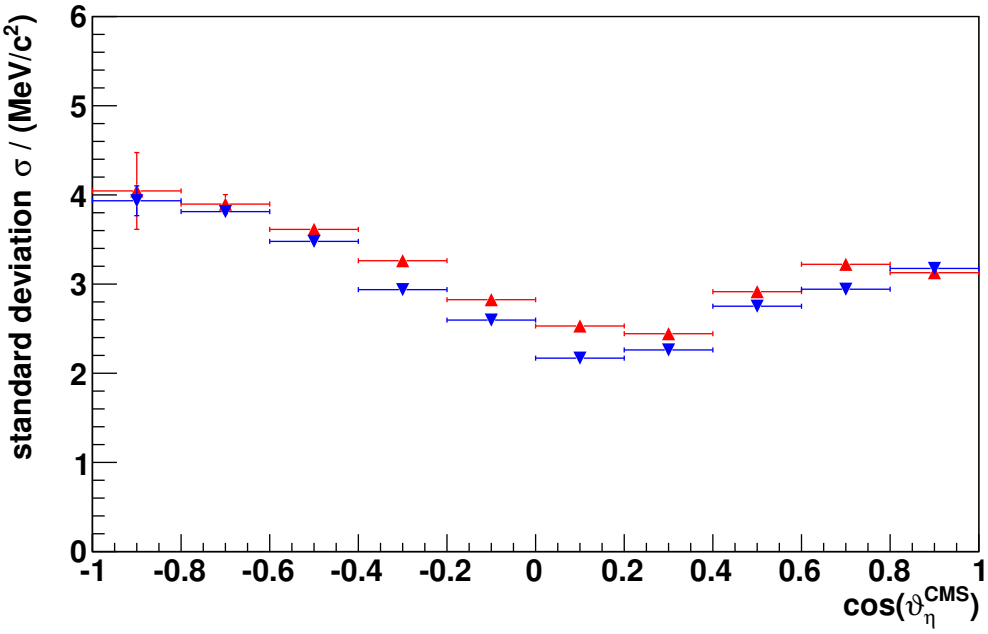

Figure 6.19.: Standard deviation σ of the η meson peak in the ^{3}He missing mass spectra depending on $\cos\vartheta_\eta^{\mathrm{CMS}}$ for the 2008 and 2009 data sets (red triangles and blue inverted triangles, respectively). The horizontal bars indicate the bin width.

Table 6.5.: Monte Carlo smearing parameters for the forward detector.

Data set	ΔE / MeV	ΔE_{rel}	*p.e.* / MeV	$\Delta\vartheta_{\mathrm{rel}}$
2008	0.0025	0.013	85	0.014
2009	0.0025	0.013	85	0.010

standard deviations of the Gaussian fits are shown in figure 6.19 for the 2008 data set (red triangles) and the 2009 data set (blue inverted triangles) depending on $\cos\vartheta_\eta^{\mathrm{CMS}}$. A good agreement between the two data sets is visible for $\cos\vartheta_\eta^{\mathrm{CMS}}$ close to ±1, whereas minor differences exist for $\cos\vartheta_\eta^{\mathrm{CMS}} \approx 0$. Hence, separate smearing parameters for Monte Carlo simulations were determined for the 2008 and 2009 data sets.

In the standard RootSorter the smearing for the FRH is parametrized by an absolute energy smearing parameter ΔE, a relative smearing parameter ΔE_{rel}, and the average number of photo-electrons per MeV (*p.e.* / MeV). These parameters cannot account for the deviation seen for $\cos\vartheta_\eta^{\mathrm{CMS}} \approx 0$, since for this angular range the missing mass resolution is mostly limited by the angular resolution. Thus, an

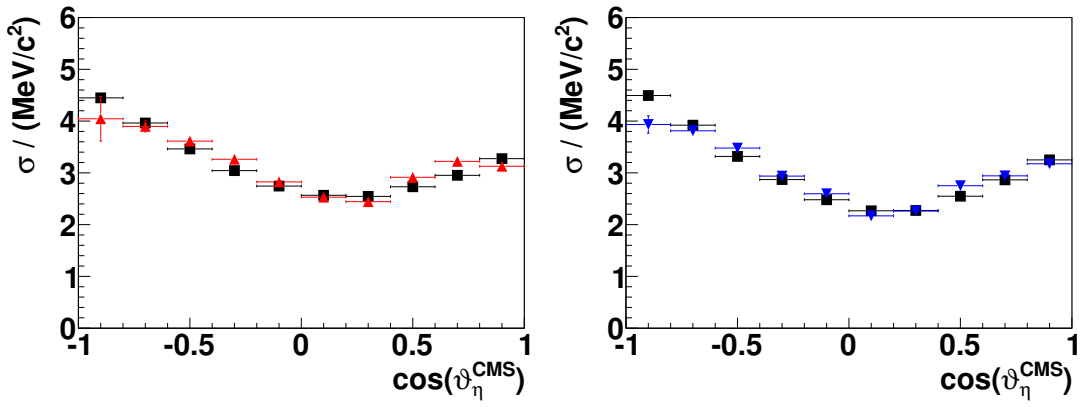

Figure 6.20.: Standard deviation σ of the η meson peak in the ^{3}He missing mass spectra depending on $\cos\vartheta_\eta^{\mathrm{CMS}}$. Left: The 2008 data set compared with Monte Carlo simulations (red triangles and black squares, respectively). Right: The 2009 data set compared with Monte Carlo simulations (blue inverted triangles and black squares, respectively). The horizontal bars indicate the bin width.

Table 6.6.: Monte Carlo smearing parameters for the central detector optimized for the decay $\pi^0 \to \gamma + \gamma$.

ΔE / MeV	ΔE_{rel}	*p.e.* / MeV	Scaling factor
0.0005	0.055	0.625	1.142

additional relative smearing parameter for the polar angle $\Delta\vartheta_{\mathrm{rel}}$ is required for a good description of the data. A possible reason for the different polar angular resolutions are changes of the pumping system of the pellet target between the beam time executed in 2008 and the beam time in 2009. These led to a better spatial resolution along the COSY beam axis for the 2009 beam time and, hence, a better polar angular resolution. The Monte Carlo smearing parameters found to describe the data best are listed in table 6.5 for both data sets. In figure 6.20 the standard deviations of the η meson peak using these smearing parameters are compared to the standard deviations observed in the 2008 and 2009 data sets depending on $\cos\vartheta_\eta^{\mathrm{CMS}}$ (left and right figure, respectively). A very good agreement between Monte Carlo simulations and data is clearly visible (see also figure 6.18, right).

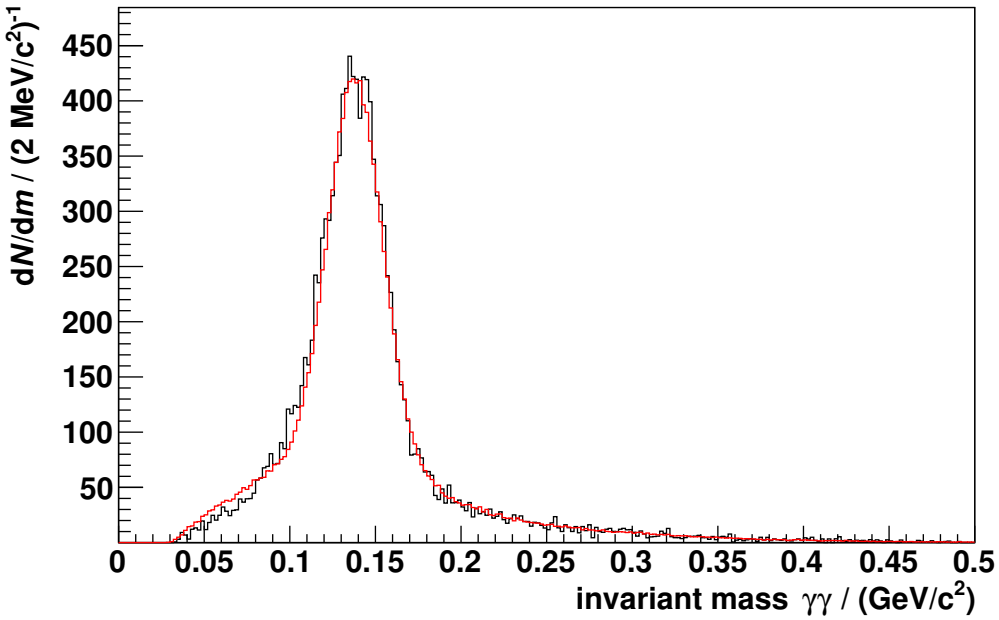

Figure 6.21.: Invariant mass of two photons for the angular range $0.0 \leq \cos\vartheta_{\eta}^{\mathrm{CMS}} < 0.2$ for the 2008 data set (black) fitted by a cocktail of Monte Carlo simulations (red). All shown data samples were preselected with the conditions described in chapter 6.5.

6.4.2. Central detector smearing settings

While optimal Monte Carlo smearing parameters for the forward detector were determined as part of this thesis, optimal parameters for the central detector components were determined by other members of the task force analyzing the data collected in 2008 and 2009 [BCHW17]. In particular, these are the parameters for the MDC, the PSB, and the SEC. For the SEC two different smearing parameter sets were determined. The standard set was optimized with regard to the two photons from the η meson decay channel $\eta \rightarrow \gamma + \gamma$ and a good match of their invariant mass with the η mass, whereas the second set led to a good agreement of the invariant mass of two photons from the π^0 decay $\pi^0 \rightarrow \gamma + \gamma$ with the π^0 mass. In the decay $\eta \rightarrow \pi^0 + e^+ + e^-$ photons originate from the decay of the π^0. Therefore, the latter set of smearing parameters was used for the analysis (listed in table 6.6). Besides the parameters ΔE, ΔE_{rel}, and *p.e.* / MeV, a linear factor is required to obtain a good agreement of the energy losses between Monte Carlo simulations and data. In figure 6.21 the invariant mass of two photons detected in the central detector of a sample from the 2008 data set is compared to a fit by Monte Carlo simulations. It can be seen that a good agreement was achieved.

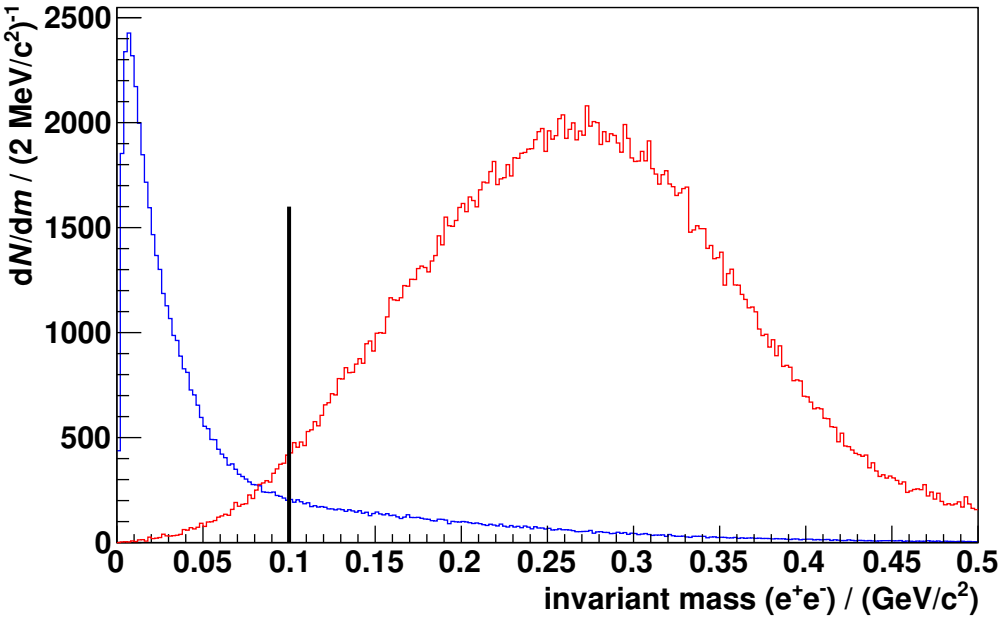

Figure 6.22.: Invariant mass of the two charged particles detected in the central detector assuming electron masses for the simulated η meson decays $\eta \to e^+ + e^- + \gamma$ (blue) and $\eta \to \pi^+ + \pi^- + \gamma$ (red). The spectrum for the decay $\eta \to e^+ + e^- + \gamma$ is scaled to the latter with respect to their relative branching ratios [P+16]. A cut at an invariant mass of 100 MeV c^{-2} is indicated by the black line.

The energy loss information of the SEC is not only used for the determination of the photon four-momenta, but together with the information provided by the MDC also for the particle identification of charged particles in the central detector. Since the scaling factor for the energy loss in the SEC can differ depending on the particle type, data and Monte Carlo simulations will be compared individually for electrons, positrons, and charged pions in the following sections. In case of deviations between data and simulations, correction functions will be determined for the simulations to obtain a good agreement with the well calibrated energy losses in data [BCHW17]. Furthermore, the other smearing settings will be checked.

e^+ and e^- adjustments

In the recorded data the energy loss distribution of charged particles measured in the central detector is dominated by charged pions. In order to investigate the energy losses of electrons and positrons in the SEC, the 2008 and 2009 data sets were preselected with the following requirements:

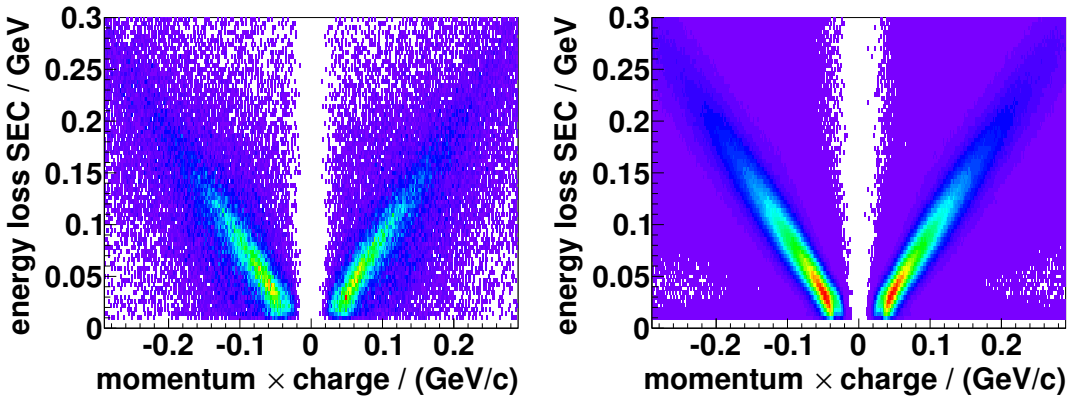

Figure 6.23.: Energy loss of the charged particles in the SEC plotted against their momentum times charge in linear scale. Both the data recorded in 2009 (left) and the Monte Carlo simulations of the η meson decay $\eta \to e^+ + e^- + \gamma$ (right) were preselected with the conditions given in the text.

- Exactly one negatively charged particle detected in the central detector,
- exactly one positively charged particle detected in the central detector,
- exactly one neutral particle detected in the central detector,
- and the invariant mass of the electron-positron pair candidate must be less or equal to $100\,\mathrm{MeV}\,c^{-2}$.

With these requirements most of the remaining charged particles are electrons and positrons originating from the η meson decay $\eta \to e^+ + e^- + \gamma$. The invariant mass of an electron and positron from a Dalitz decay peaks well below $100\,\mathrm{MeV}\,c^{-2}$, while the invariant mass distribution of charged pions from reactions like $\eta \to \pi^+ + \pi^- + \gamma$ or direct pion production and misidentified as an electron-positron pair is spread over a wider mass range (see figure 6.22).

In figure 6.23 the energy losses of the charged particles in the SEC are plotted against their respective momentum times charge as reconstructed by the MDC under the conditions mentioned previously. Neither for the 2009 data set nor for Monte Carlo simulations of the decay $\eta \to e^+ + e^- + \gamma$ pion bands are visible, while clear positron and electron bands can be identified. Since the MDC had been well calibrated before, showing a good agreement with Monte Carlo simulations [BCHW17], projections of the energy losses for various momentum ranges were used to compare data and simulations. Figure 6.24 illustrates such a projection of the energy loss in the SEC for the momentum range $0.065\,\mathrm{GeV}\,c^{-1}$ to $0.083\,\mathrm{GeV}\,c^{-1}$

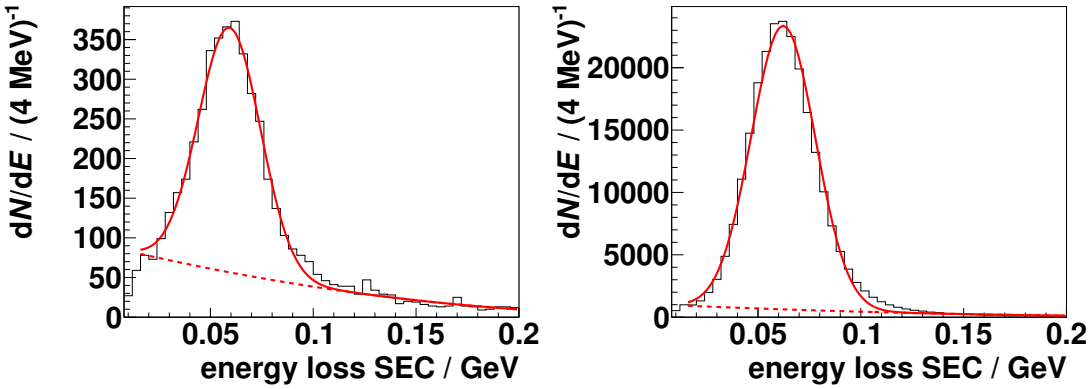

Figure 6.24.: Energy loss of the negatively charged particle in the SEC for the momentum range 0.065 GeV c^{-1} to 0.083 GeV c^{-1} for data recorded in 2009 and Monte Carlo simulations (left and right figure, respectively). Each histogram was fitted by a Gaussian and a second order polynomial distribution (red lines). The contributions of the polynomials are illustrated by the red dashed lines.

Table 6.7.: Correction functions for the energy losses of electrons and positrons in the SEC for Monte Carlo simulations to agree with the 2008 and 2009 data sets.

Data set	Particle type	Energy loss correction function
2008	electron	$0.999(8) \cdot E_{\text{dep}}^{\text{SEC}} - 0.0028(6)$ GeV
2008	positron	$0.997(8) \cdot E_{\text{dep}}^{\text{SEC}} - 0.0029(6)$ GeV
2009	electron	$0.959(6) \cdot E_{\text{dep}}^{\text{SEC}} - 0.0014(4)$ GeV
2009	positron	$0.969(6) \cdot E_{\text{dep}}^{\text{SEC}} - 0.0018(5)$ GeV

for negatively charged particles, both for data and simulations (left and right figure, respectively), each fitted by a Gaussian and a second order polynomial distribution (red lines).

Afterwards the mean of the Gaussian fits to the measured data and the simulations were plotted against each other (see figure 6.25 as an example) in order to extract the correction functions for the energy losses of the positrons and electrons in the SEC presented in table 6.7. Applying these functions to Monte Carlo simulations, a very good agreement of the energy losses of electrons and positrons in the SEC between data and simulations was obtained, as can be seen in figure 6.26. Both the peak positions of electrons and positrons in the energy loss spectra after background subtraction and the peak width show a good agreement.

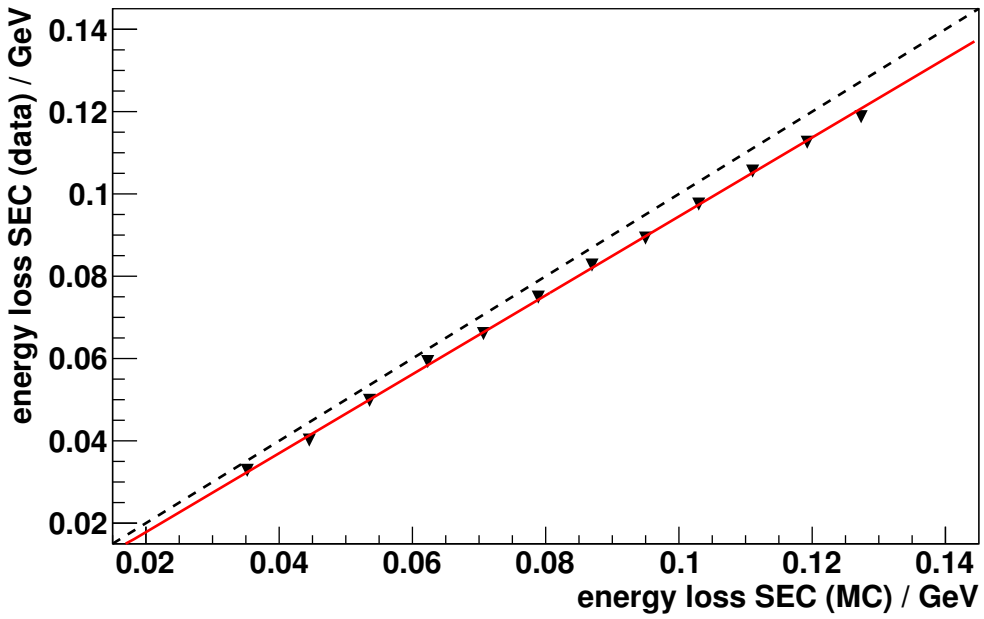

Figure 6.25.: Mean energy loss of electrons in the SEC for a given momentum range determined for the 2009 data set plotted against the mean energy loss according to Monte Carlo simulations. The data points are fitted by a first order polynomial (red line) and the bisectrix is illustrated by the black dashed line.

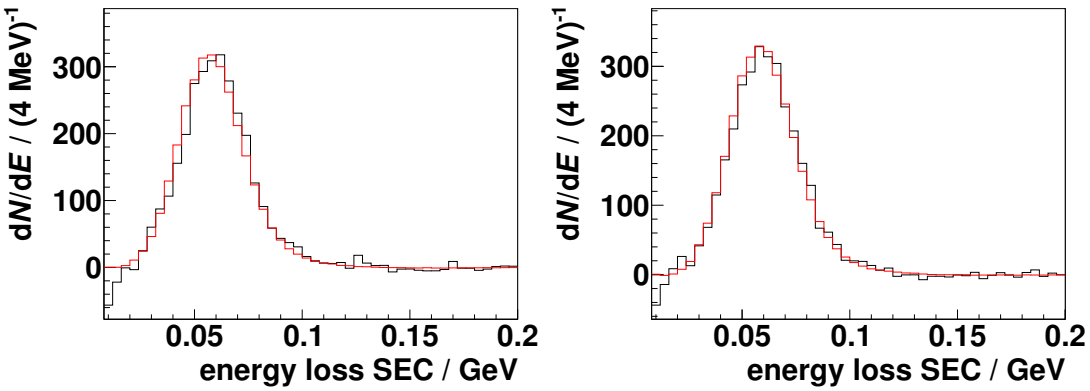

Figure 6.26.: Energy loss of the negatively and positively charged particles in the SEC for the momentum range 0.065 GeV c^{-1} to 0.083 GeV c^{-1} (left and right figure, repsectively) after background subtraction. The data recorded in 2009 are presented in black, while the Monte Carlo simulations (scaled to the data) are shown in red.

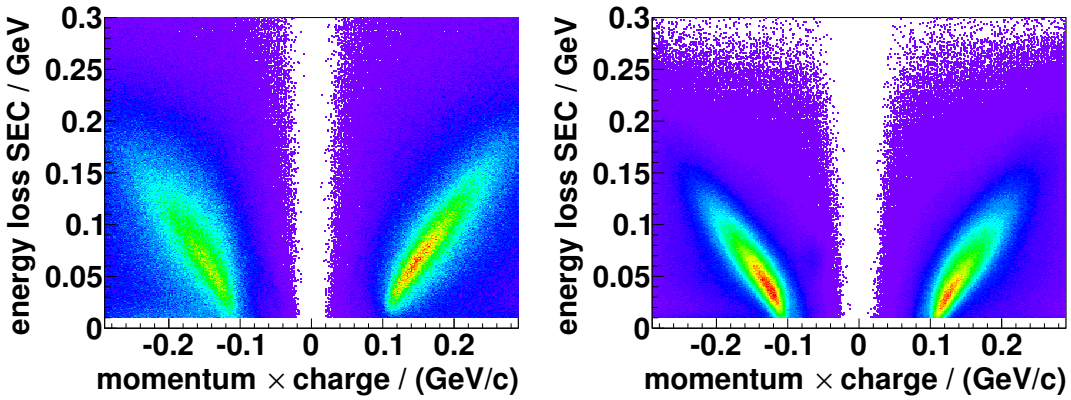

Figure 6.27.: Energy loss of charged particles in the SEC plotted against their momentum times charge in linear scale. Both the data recorded in 2009 (left) and Monte Carlo simulations of the reaction $\mathrm{p} + \mathrm{d} \to {}^3\mathrm{He} + \pi^+ + \pi^- + \pi^0$ (right) were preselected with the conditions given in the text.

π^+ and π^- adjustments

Similar to the approach applied to the adjustment of the energy losses of electrons and positrons, the data need to be preselected for studying the energy losses of charged pions. For this purpose the recorded data were preselected with regard to the direct $\pi^+\pi^-\pi^0$ production and the η meson decay $\eta \to \pi^+ + \pi^- + \pi^0$ using the following conditions:

- At least one negatively charged particle detected in the central detector,
- at least one positively charged particle detected in the central detector,
- at least two neutral particles detected in the central detector,
- and the invariant mass of the two charged particles must be greater than $100\,\mathrm{MeV}\,c^{-2}$ assuming electron masses for the charged particles.

In the left of figure 6.27 the energy losses of the pion candidates in the SEC are plotted against the corresponding momentum times charge after application of these conditions to the 2009 data set. For comparison the same histogram is shown in the right part of figure 6.27 for Monte Carlo simulations of the reaction $\mathrm{p} + \mathrm{d} \to {}^3\mathrm{He} + \pi^+ + \pi^- + \pi^0$ after applying the same cuts. In both cases bands corresponding to π^+ and π^- mesons are clearly visible. Compared to the electron and positron bands presented in figure 6.23, these are not only wider, but the continuous background below the bands is larger, too. The differences of the

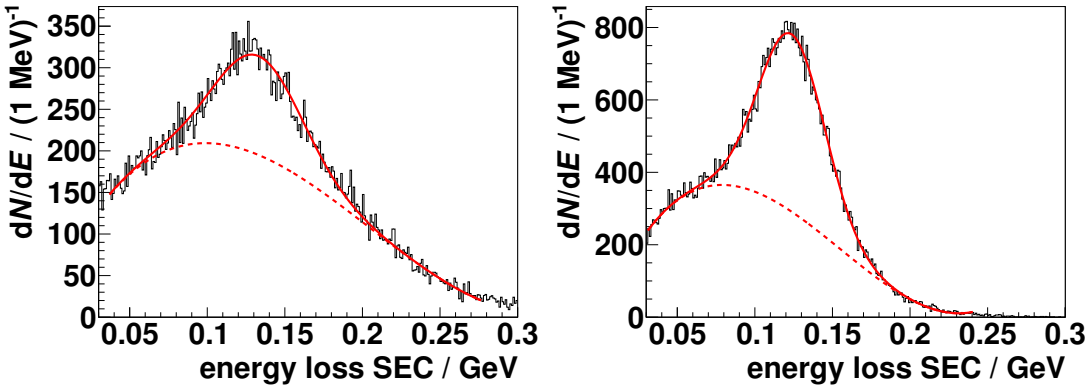

Figure 6.28.: Energy loss of the negatively charged particle in the SEC for the momentum range 0.217 GeV c^{-1} to 0.225 GeV c^{-1} fitted by a Gaussian and a third order polynomial distribution (red lines). The contributions of the polynomials are illustrated by the red dashed lines. Left: Data recorded in 2009. Right: Monte Carlo simulations of the reaction $p + d \rightarrow {}^3He + \pi^+ + \pi^- + \pi^0$.

background originate from the larger invariant mass range selected for the pion investigations and the looser conditions on the signature of the reaction products compared to those applied in the previous section. They are more visible in the projections of the energy loss in the SEC for the different momentum ranges. Figure 6.28 illustrates such a projection for the momentum range 0.217 GeV c^{-1} to 0.225 GeV c^{-1} for negatively charged particles, both for data (left) and simulations (right). While all entries in the right histogram originate from the simulated reaction $p + d \rightarrow {}^3He + \pi^+ + \pi^- + \pi^0$, the left histogram contains entries from other reactions, as well. This leads to a different ratio of the peak to the background for the data compared to the simulations. In order to match the peak positions in both spectra, the histograms were fitted with Gaussian distributions and a third order polynomial (red lines)[5].

The mean energy losses of the π^- mesons in the SEC for different momentum ranges in the 2009 data set plotted against the corresponding energy losses according to simulations are presented in the left of figure 6.29. Unlike for the energy losses of electrons and positrons, a linear function is not sufficient to properly

[5]Note that in case of the simulated reaction $p + d \rightarrow {}^3He + \pi^+ + \pi^- + \pi^0$, the part of the energy loss distribution described by a third order polynomial function originates from charged pions, as well. In case of the measured data, other particles contribute to this background below the peak in addition. Hence, only the peaks of the distributions are compared as both for data and MC only charged pions contribute to them.

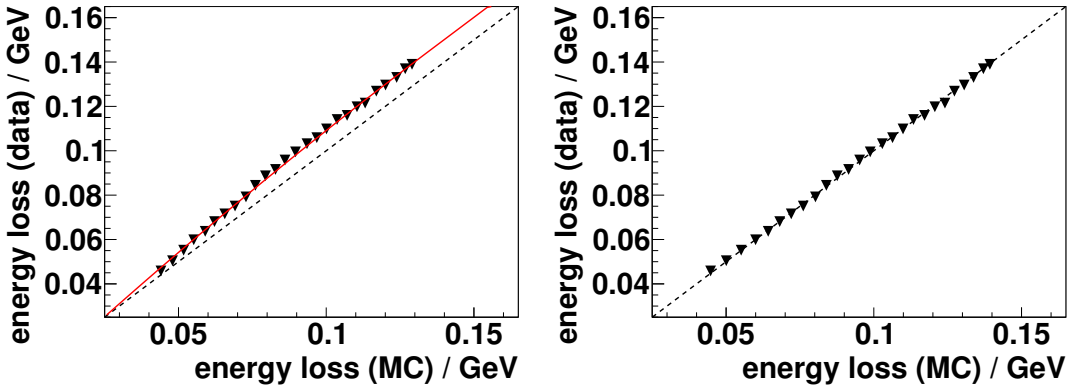

Figure 6.29.: Mean energy losses of π^- mesons in the SEC for certain momentum ranges in the 2009 data set plotted against the mean energy losses according to Monte Carlo simulations before and after correction (left and right figure, respectively). The bisectrix is illustrated by the black dashed lines and the correction function given in equation 6.14 is shown in red (left figure).

describe the distribution of the data points. Instead, a continuous combination of a second order polynomial and a first order polynomial is used:

$$E_{\text{dep}}^{\text{corr}} = \begin{cases} f\left(E_{\text{dep}}^{\text{SEC}}\right) = a \cdot \left(E_{\text{dep}}^{\text{SEC}}\right)^2 + b \cdot E_{\text{dep}}^{\text{SEC}} + c & \text{if } \frac{\mathrm{d}f\left(E_{\text{dep}}^{\text{SEC}}\right)}{\mathrm{d}E_{\text{dep}}^{\text{SEC}}} \geq m \\ m \cdot E_{\text{dep}}^{\text{SEC}} + d & \text{if } \frac{\mathrm{d}f\left(E_{\text{dep}}^{\text{SEC}}\right)}{\mathrm{d}E_{\text{dep}}^{\text{SEC}}} < m \end{cases} \tag{6.14}$$

with

$$\begin{aligned} d &= f\left(E_1\right) - m \cdot E_1 \,, \\ E_1 &= \frac{m-b}{2a} \,. \end{aligned} \tag{6.15}$$

The corresponding parameters are listed in table 6.8. For the determination of the given parameters constrains of the fit were set manually to ascertain a not unphysical behavior outside of the fit range. The parameters are presented with the last digit being the significant one.

After applying the correction functions, the mean energy losses in simulations and those determined for the measured data are in good agreement (see figure 6.29, right). Besides these mean energy losses, the width of the energy distributions agree very well, as can be seen in figure 6.30 where the energy losses of the negatively and positively charged particles in simulations and in data are compared

Table 6.8.: Parameters of the correction function 6.14 for the energy losses of negatively and positively charged pions in the SEC for Monte Carlo simulations to agree with the 2008 and 2009 data sets.

Data set	Particle type	a / GeV^{-1}	b	c / GeV	m
2008	π^+	-0.91	1.14	8.6×10^{-3}	0.975
2008	π^-	-0.77	1.24	-3.9×10^{-3}	1.05
2009	π^+	-0.52	1.06	9.4×10^{-3}	0.96
2009	π^-	-0.81	1.22	-4.8×10^{-3}	1.00

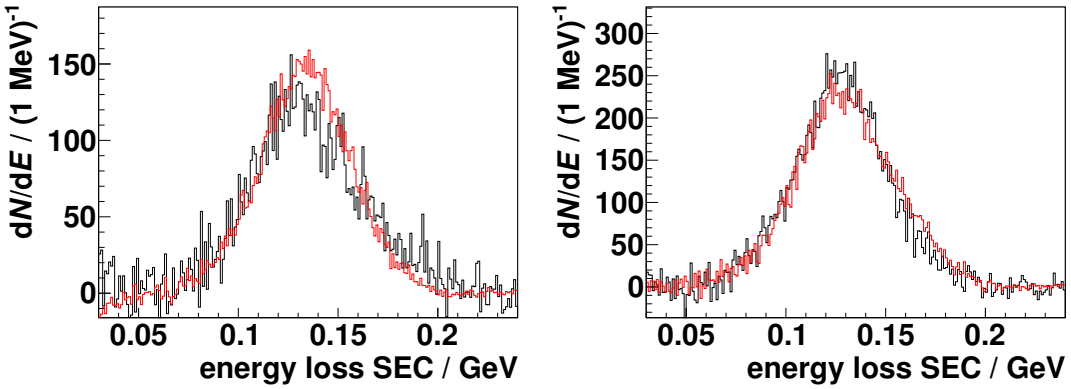

Figure 6.30.: Energy loss of the negatively and positively charged particles in the SEC for the momentum range 0.217 GeV c^{-1} to 0.225 GeV c^{-1} (left and right figure, respectively) after background subtraction. The data recorded in 2009 are presented in black, while the Monte Carlo simulations scaled to the data are shown in red.

in the momentum range $0.217\,\mathrm{GeV}\,c^{-1}$ to $0.225\,\mathrm{GeV}\,c^{-1}$ after subtraction of the polynomial function (left and right figure, respectively).

6.5. Preselection and general background reduction

Before the contributions of certain reaction channels to the measured data can be determined by fitting the data with Monte Carlo simulations, various preselection conditions have to be applied. This is necessary for a few reasons. In general, a preselection into so-called ROOT-trees significantly improves the performance of an analysis, since not all analysis steps have to be done each time for all events and each analysis iteration. In case of the presented analysis, all simulated reactions are of the type $\mathrm{p} + \mathrm{d} \rightarrow {}^3\mathrm{He} + \mathrm{X}$. Background from non-fusion reactions should be removed from the data samples. As mentioned in chapters 4.1 and 6.1, first selection conditions for ^{3}He nuclei detected in the forward detector were applied to the 2008 and 2009 data sets in a first level preselection. To reduce the background further, additional cuts (described in chapter 6.5.1) were applied.

The reconstruction of particles described by Monte Carlo simulations are known to have larger uncertainties for particles detected at the geometrical detector edges. In order to obtain reliable acceptances, those particles detected at the edge of the detector were excluded from the analysis. In the following chapters the conditions of the preselection applied both to data and to simulations will be presented.

6.5.1. Selection of ^{3}He

As shown in chapter 6.2, the forward detector is well calibrated both for the 2008 and the 2009 beam time. Furthermore, Monte Carlo simulations and data are in good agreement. Thus, for data and simulations the same conditions can be used to select ^{3}He nuclei. For this purpose a graphical cut was applied to the energy loss in the first layer of the FRH and the corresponding energy loss in the first layer of the FTH (see figure 6.31). It was required that the detected particle is stopped in FRH1, as all ^{3}He nuclei produced in the reaction $\mathrm{p} + \mathrm{d} \rightarrow {}^3\mathrm{He} + \eta$ are stopped in this layer according to simulations. While the energy loss of the ^{3}He candidate in FRH1 must be in the range of 0.003 GeV to 0.35 GeV, its energy loss must not exceed 0.003 GeV in the FRH detector layers two to five. As can be seen in figure 6.31, the ^{3}He band is located above the black cut line for simulations and data, while protons, deuterons, and pions are rejected (bands below the cut line in the upper figures). The minor

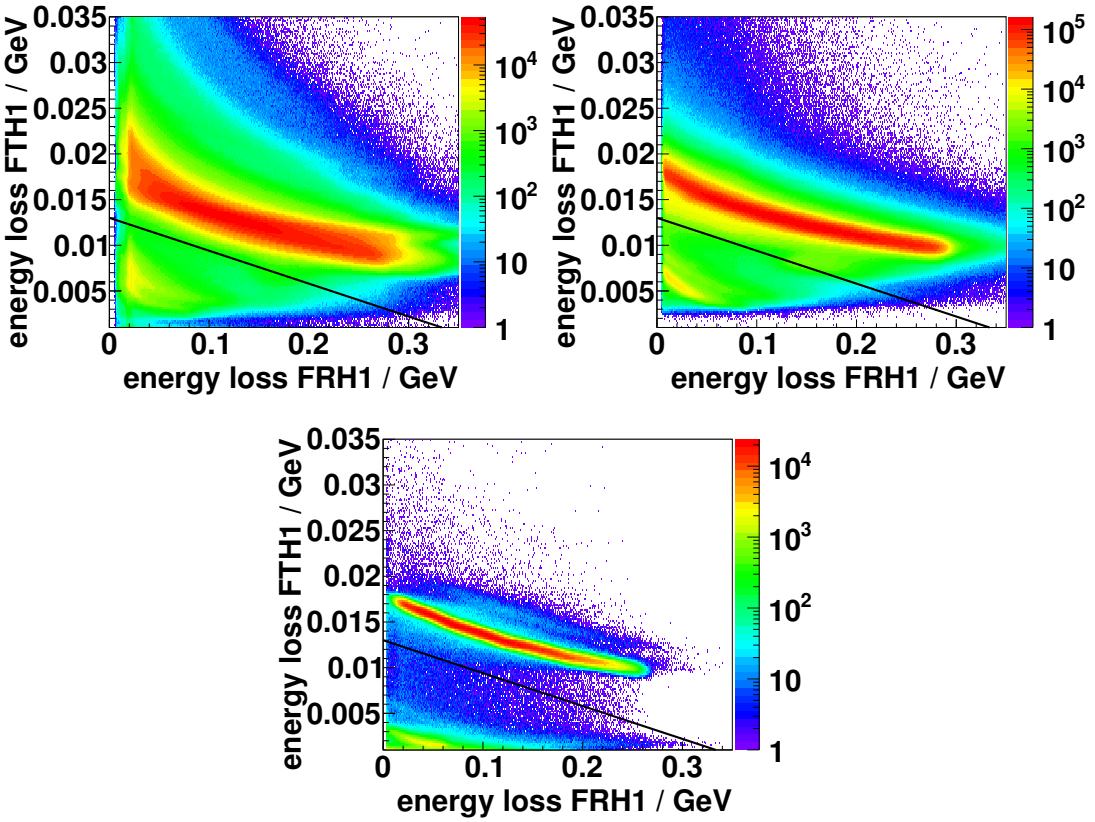

Figure 6.31.: Energy loss in the first FTH layer plotted against the energy loss of the same particle in the first FRH layer in logarithmic scale. Particles below the black line are excluded in the preselection. In the upper left figure data recorded in 2008 are presented, while data from 2009 and Monte Carlo simulations of the reaction $p + d \rightarrow {}^3He + \eta$ are shown in the upper right and in the lower histogram, respectively.

differences[6] in the FTH1 detector resolution observed for the 2008 data set, the 2009 data set, and Monte Carlo can be neglected, because in all cases the full ^{3}He band remains after the cut. Moreover, for the normalization another η meson decay is used with the η originating from the reaction $p + d \to {}^3He + \eta$. This relative normalization is independent of the ^{3}He detection efficiency. Additionally, the energy loss information in the FTH is only required for the ^{3}He selection and not used for the determination of the particle's kinetic energy. Therefore, the mentioned uncertainties have no influence on the cuts utilized in the later analysis.

The WASA forward detector is designed to reconstruct particles with polar scattering angles in the range of 3° to 18° (see chapter 3.2.3). To avoid systematic effects at the edge of the detector, the scattering angle ϑ_{LAB} of the helium has to be in this range. In the analysis it was required that ϑ_{LAB} is in the range of 3° to 17°. As all ^{3}He nuclei from the reaction $p + d \to {}^3He + \eta$ at the given excess energy have a polar scattering angle below 11°, applying a stricter cut at 17° instead of at 18° rejects no signal helium nuclei. In order to keep more events from other reaction channels for a proper determination of their contribution to the data sample, an upper border larger than 11° was chosen for the preselection.

A ^{3}He data sample with high purity could be obtained by requiring exactly one particle fulfilling the above mentioned preselection conditions.

6.5.2. Signature of the decay $\eta \to \pi^0 + e^+ + e^-$

To search for the decay $\eta \to \pi^0 + e^+ + e^-$, a large data sample and billions of simulated events needed to be analyzed (see chapter 6.3). The performance of the analysis can be significantly improved if both the measured data and the Monte Carlo simulations are preselected into ROOT-trees on the signature of the decay $\eta \to (\pi^0 \to \gamma{+}\gamma){+}e^+{+}e^-$. For this purpose at least one negatively charged particle, at least one positively charged particle, and at least two neutral particles detected in the central detector were requested in addition to the ^{3}He detected in the forward detector. No strict conditions were demanded because events can overlap due to the high luminosity during the studied beam times, leading to additional particles observed in the central detector. Hence, strict conditions would reduce the amount of possible signal events, as well.

[6] The differences between the 2008 and the 2009 data set originate from the different and independent calibration of the FTH for these data sets.

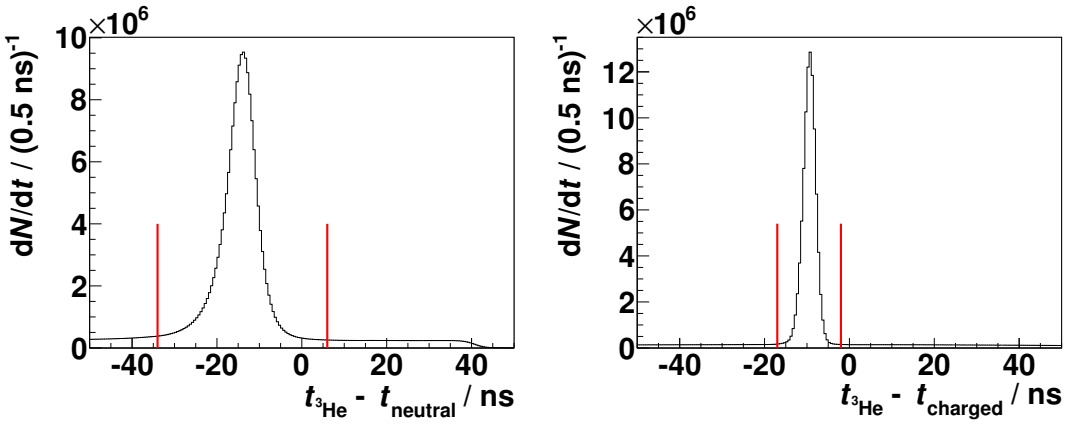

Figure 6.32.: Time difference between the ^{3}He nuclei detected in the forward detector and neutral or charged particles detected in the central detector for the 2008 data set (left and right figure, respectively). Only central detector particles in the time windows indicated by the red lines are used in the data analysis.

In the η decay analysis based on the PDEtaAnalysisBase class the type of a particle detected in the CD is defined by the detectors it produced a signal in. Neutral tracks must not be recorded in the MDC and must have an energy loss of at least 20 MeV in the calorimeter, but not more than 1 GeV. A veto on the plastic scintillator is not requested in the PDEtaAnalysisBase class, as that reduces the reconstruction efficiency of neutral particles noticeably [BCHW17].

Charged particles must be reconstructed by the MDC, and the direction of their deflection defines their charge. Furthermore, the energy loss of a charged particle in the SEC must be at least 20 MeV, and, in case it does not give a signal in the SEC, it must have deposited energy in the PSB.

Additionally, both for charged and neutral particles conditions on the time difference between CD and FD are requested, depending on the detectors involved in their detection. In case of neutral particles, the timing information of the SEC is used. For charged particles the registration time in the PSB is utilized preferably. If that information is not available, the SEC time of the track is used instead. In order to ascertain whether the detected particles originate from the same event, the difference between the registration time of the ^{3}He nucleus in the forward detector and the time of the particles detected in the CD must be within a given time window. This window depends on the beam time as well as on the detectors that registered the particles, as illustrated in figures 6.32 and 6.33[7].

[7]Note that for charged particles a hit in the PSB was requested. If the PSB was not hit, the same time cuts were applied as for the neutral particles.

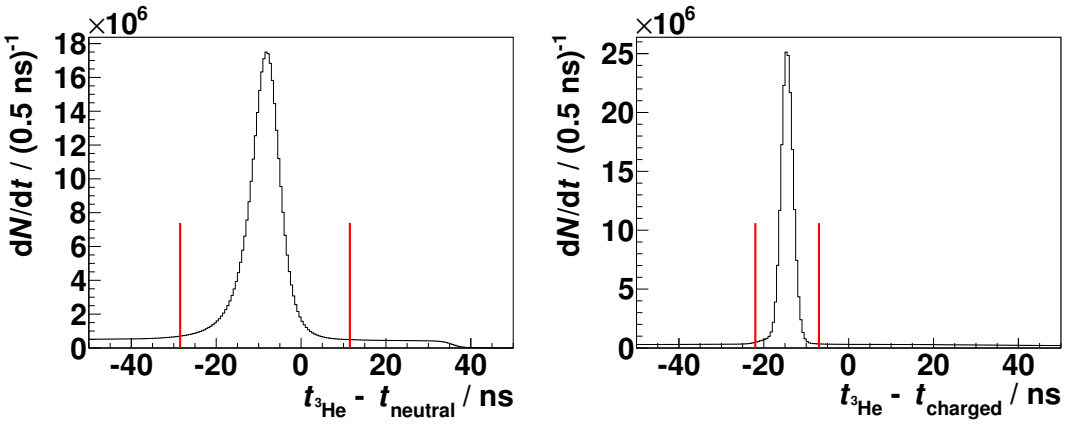

Figure 6.33.: Time difference between the ^{3}He nuclei detected in the forward detector and neutral or charged particles detected in the central detector for the 2009 data set (left and right figure, respectively). Only central detector particles in the time windows indicated by the red lines are used in the data analysis.

6.5.3. Momentum cut for charged particles

Reactions like the direct two-pion production $p + d \to {}^3He + \pi^+ + \pi^-$ have a different signature than the η meson decay of interest. However, split-offs of a charged particle's shower in the SEC can be misidentified as separate photon tracks (see chapter 6.5.5). Although certain cuts are applied to remove these photons, some misidentified photons remain afterwards. In particular, some events from the reaction $p + d \to {}^3He + \pi^+ + \pi^-$ pass the selection conditions due to the very high cross section of the reaction compared to the $p + d \to {}^3He + \eta$ cross section at the same beam energy[8].

According to Monte Carlo simulations, charged particles with large momenta are often reconstructed with very low energy losses in the SEC for some reaction channels. Reasons for the observed difference are split-off photons, which carry most of the charged particle's energy, as well as energy losses in the dead material of the SEC or outside of the detector. This effect is only observed for reactions with a too small or vanishing number of true decay photons, whereas reactions with the correct signature like $p+d \to {}^3He+\eta$ with $\eta \to \pi^+ + \pi^- + (\pi^0 \to \gamma + \gamma)$ do not show this behavior in simulations. This is visible in figure 6.34, where the energy loss of a charged particle in the SEC is plotted against its momentum times charge for

[8] According to [Pé14b, A$^+$15c], the cross section of the reaction $p + d \to {}^3He + \pi^0 + \pi^0$ is $\sigma\left({}^3He\pi^0\pi^0\right) = (2.28 \pm 0.04 \pm 0.40)\,\mu b$ at $\sqrt{s} = 3.416\,GeV$. For a rough estimate of the cross section of the reaction $p + d \to {}^3He + \pi^+ + \pi^-$ this value can be multiplied by an isospin factor of two.

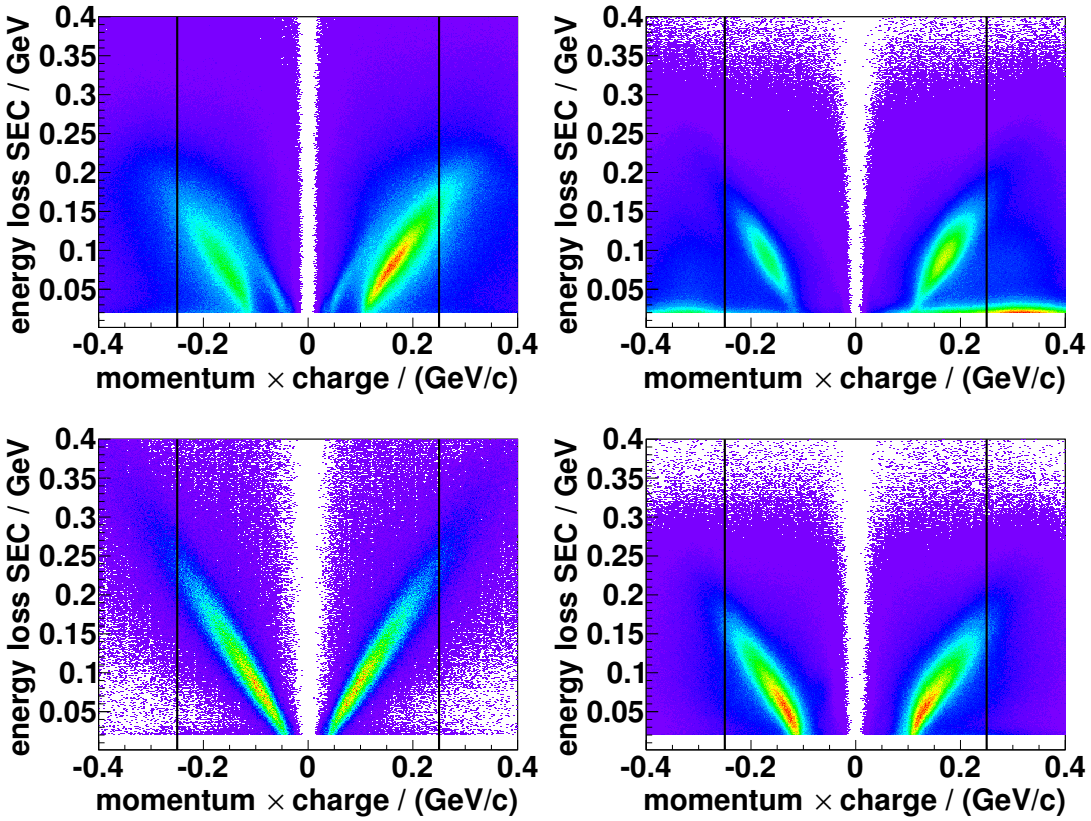

Figure 6.34.: Energy loss of charged particles in the SEC plotted against their momentum times charge for data recorded in 2008 (upper left), the simulated reaction $p+d \to {}^3He+\pi^+ +\pi^-$ (upper right), the simulated η decay $\eta \to \pi^0+e^+ +e^-$ (lower left), and the simulated η decay $\eta \to \pi^+ + \pi^- + \pi^0$ (lower right) in linear scale. All samples were preselected on the signature of the decay $\eta \to \pi^0 + e^+ + e^-$, and a ${}^3He$ nucleus detected in the FD was required (see chapters 6.5.2 and 6.5.1).

the simulated reaction $\mathrm{p} + \mathrm{d} \to {}^3\mathrm{He} + \pi^+ + \pi^-$ (upper right figure) and the η decay $\eta \to \pi^+ + \pi^- + \pi^0$ (lower right figure). However, in data no enhancement for high momenta and low energy losses in the SEC is observed (upper left figure). This is unexpected, as according to Monte Carlo fits to the data, a large number of events from the direct two-charged-pion production remains in data after applying all preselection conditions mentioned in this chapter 6.5 (see chapter 6.6.2) and, thus, such an enhancement should be seen in data, as well. The difference between data and Monte Carlo can be explained by energy losses and scattering in the detector not correctly assumed for charged particles with high momenta. It is reasonable to reject events with charged particles with such high momenta in the analysis, as the momentum and energy reconstruction in data and Monte Carlo are in good agreement for lower momenta. Therefore, a cut at $p = 0.25\,\mathrm{GeV}\,c^{-1}$ was applied to the charged particles detected in the central detector. Although most electrons and positrons from the decay $\eta \to \pi^0 + \mathrm{e}^+ + \mathrm{e}^-$ have lower momenta (see lower left plot of figure 6.34), this cut reduced the amount of signal events by about 39 % according to Monte Carlo simulations. While the normalization channel $\eta \to \pi^+ + \pi^- + \pi^0$ was reduced to a similar extent (by about 42 %), about 84 % of the direct two-charged-pion production events were rejected by this condition according to simulations. Systematic checks with respect to the above mentioned cut will be performed in chapter 7.1.3.

6.5.4. Conversion cut

Not all reconstructed electrons and positrons have to originate from the primary interaction vertex of the COSY proton beam and the deuteron pellet target. Photons may interact with the 1.2 mm thin beryllium beam pipe surrounding the interaction vertex and converge to an electron-positron pair. Since the probability for this is in the order of 1 %, these conversion electrons and positrons introduce an additional background. For example, the η meson decay $\eta \to \gamma + \gamma$ with one converging photon and a split-off photon (see chapter 6.5.5) passes the signature cut applied to the data (see chapter 6.5.2).

Figure 6.35 illustrates the decays $\eta \to \mathrm{e}^+ + \mathrm{e}^- + \gamma$ and $\eta \to \gamma + \gamma$. The electron and positron originate from the primary decay vertex in the first case, whereas they are produced in a conversion event of one photon in the beam pipe for the latter case.

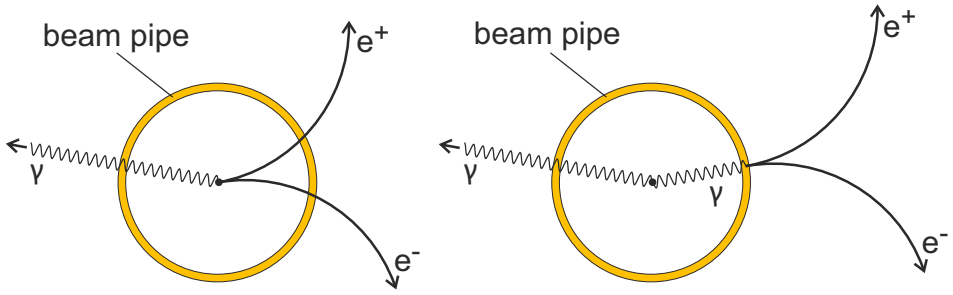

Figure 6.35.: Schematic diagram of the decay $\eta \to e^+ + e^- + \gamma$ (left) and the decay $\eta \to \gamma + \gamma$ with conversion of one decay photon to an electron-positron pair (right). The curvatures of the electron and positron tracks are determined by the magnetic field of the solenoid.

Different techniques to reduce the background caused by conversion are available. The method chosen in the PDEtaAnalysisBase class is based on two properties of the conversion positrons and electrons. The most intuitive property is the vertex position of the electron-positron pair in the x-y plane. If the charged particles originate from conversion in the beam pipe, this radial distance from the primary vertex should be about 30 mm, which corresponds to the radius of the beam pipe. In order to calculate the radial distance of the electron-positron vertex, the point of closest approach of the electron and positron helices reconstructed by the MDC is determined.

The second information utilized for the rejection of conversion electrons and positrons is the invariant mass of the electron-positron pair under the assumption that these particles originate from a conversion in the beam pipe. For true conversion particles this invariant mass should be compatible with zero.

In figure 6.36 the radial distance of the electron-positron vertex from the beam axis is plotted against the invariant mass of the electron-positron pair assuming an origin at the beam pipe for the two simulated decays $\eta \to e^+ + e^- + \gamma$ (left) and $\eta \to \gamma + \gamma$ (right). While the majority of electrons and positrons from the first decay have a radial vertex position below 28 mm and their invariant mass at the beam pipe is above 10 MeV, the radial vertex of the electron-positron pair from the two-photon decay is above 28 mm and their invariant mass at the beam pipe is smaller. Hence, in the analysis presented in this thesis the graphical cut indicated in both figures by the red lines was applied to reject the conversion electrons and positrons. Figure 6.37 shows the same histogram for a data sample recorded in 2008. It is visible that the graphical cut can separate the conversion electrons and positrons from primary vertex electrons and positrons very well.

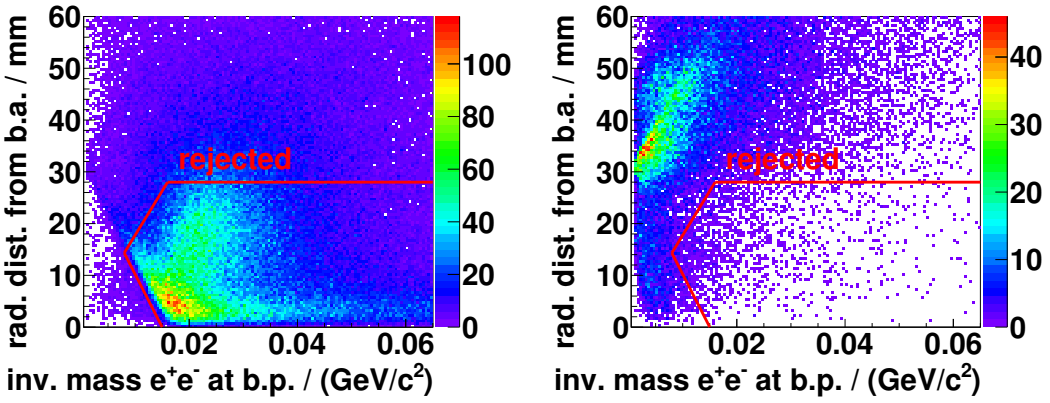

Figure 6.36.: Radial distance of the electron-positron vertex from the beam axis plotted against the invariant mass of the electron and positron at the beam pipe for the simulated decays $\eta \rightarrow e^+ + e^- + \gamma$ (left) and $\eta \rightarrow \gamma + \gamma$ (right). Events above and to the left of the red lines are rejected, whereas events inside the graphical cut remain. All presented samples were preselected requiring at least one positively and one negatively charged track reconstructed in the CD, as well as a ^{3}He nucleus detected in the FD (see chapter 6.5.1).

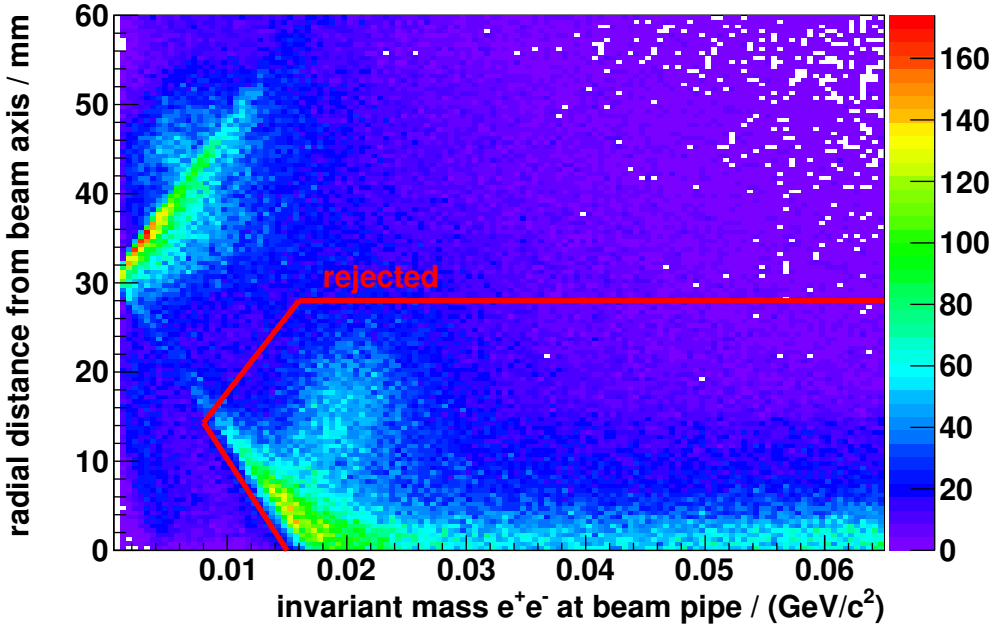

Figure 6.37.: Radial distance of the electron-positron vertex from the beam axis plotted against the invariant mass of the electron and positron at the beam pipe for a data sample recorded in 2008. Events above and to the left of the red lines are rejected, whereas events inside the graphical cut remain. The data were preselected requiring at least one positively and one negatively charged track reconstructed in the CD, as well as a ^{3}He nucleus detected in the FD (see chapter 6.5.1).

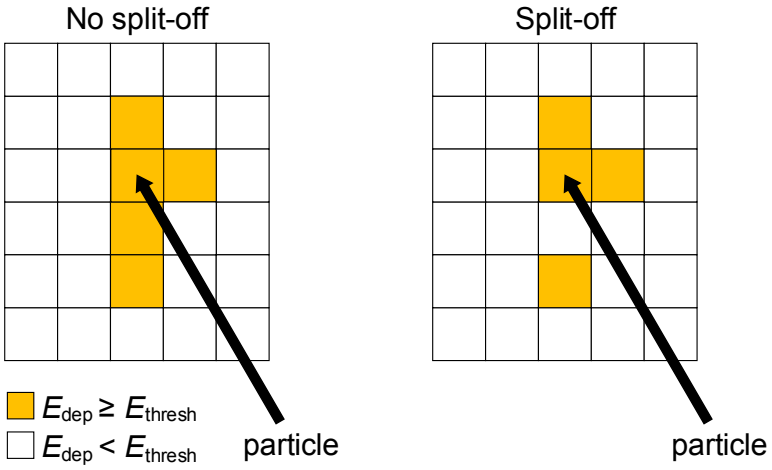

Figure 6.38.: Schematic diagram of a particle entering the calorimeter. Detector elements with an energy deposit above threshold are represented by orange squares, whereas those with an energy deposit below threshold are drawn in white. Left: A recorded cluster without a split-off. Right: An event with a split-off cluster in addition to the main cluster.

6.5.5. Split-off reduction

Particles with high energy entering the calorimeter produce a particle shower. The major production mechanisms of these showers are the conversion of photons to electron-positron pairs and bremsstrahlung. In case of charged pions the energy is mainly deposited by ionization.

During shower reconstruction the various hits in the calorimeter are grouped into clusters. It is possible that hits originating from the same shower are separated into two clusters. The second cluster has a lower deposited energy and can be misidentified as an additional neutral particle. This particle is called a split-off. In figure 6.38 such a split-off event is illustrated in comparison to a correctly reconstructed particle. While in the latter case all detector elements in which an energy of $E_{\mathrm{dep}} > E_{\mathrm{thresh}}$ was deposited are adjacent to each other (left figure), at least one element is geometrically separated from the main cluster in case of a split-off event (right figure).

An example of a decay passing the signature cut (see chapter 6.5.2) due to a split-off cluster is the η meson decay $\eta \rightarrow e^+ + e^- + \gamma$. The split-off track can either originate from a charged particle or a photon. In both cases the energy of the split-off cluster is small, as well as the angle between the parent track and

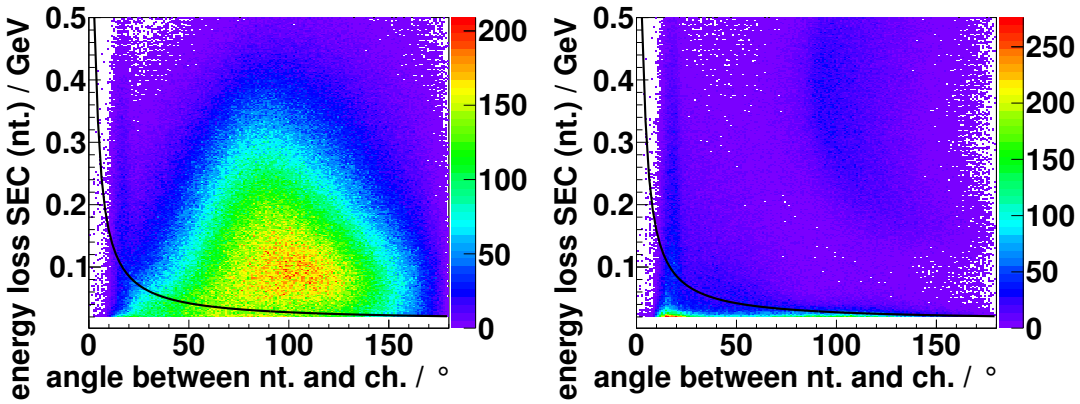

Figure 6.39.: Energy loss of a reconstructed neutral particle in the calorimeter plotted against the angle between its track and the track of a charged particle detected in the central detector for the simulated decays $\eta \to \pi^0 + e^+ + e^-$ and $\eta \to e^+ + e^- + \gamma$ (left and right figure, respectively). Neutral tracks with entries below the black cut line are rejected from the analysis. All samples were preselected on the signature of the decay $\eta \to \pi^0 + e^+ + e^-$, and a ^{3}He nucleus detected in the FD was required (see chapters 6.5.2 and 6.5.1).

the fake particle. Therefore, these properties can be used to separate the split-off photons from true decay photons.

Figures 6.39 and 6.40 show the energy of a neutral track deposited in the calorimeter plotted against the angle between this track and either a charged or a second neutral track, respectively, for the simulated decays $\eta \to \pi^0 + e^+ + e^-$ and $\eta \to e^+ + e^- + \gamma$. While most events are above the black cut line in case of the signal simulation, it is the opposite for the decay $\eta \to e^+ + e^- + \gamma$. In the presented analysis neutral tracks and particles X with

$$E_{\mathrm{dep}}^{\mathrm{SEC}} < \frac{1.45\,^\circ \times \mathrm{GeV}}{\angle(\mathrm{nt.}, \mathrm{X})} + 0.013\,\mathrm{GeV}\,, \tag{6.16}$$

with $\angle(\mathrm{nt.}, \mathrm{X})$ being the angle between the neutral track and the particle X detected in the CD, were rejected.

If a reconstructed track is a split-off of a charged track, the invariant mass of the charged and the neutral particle offers a further possibility to reject these misidentified photons. Assuming an electron mass for the charged particle, the invariant mass is expected to be small in comparison to the invariant mass of an electron or positron and a photon from the signal decay $\eta \to \pi^0 + e^+ + e^-$. Especially the contribution of reactions with charged pions like the η decay $\eta \to \pi^+ + \pi^- + \gamma$ to the background can be reduced.

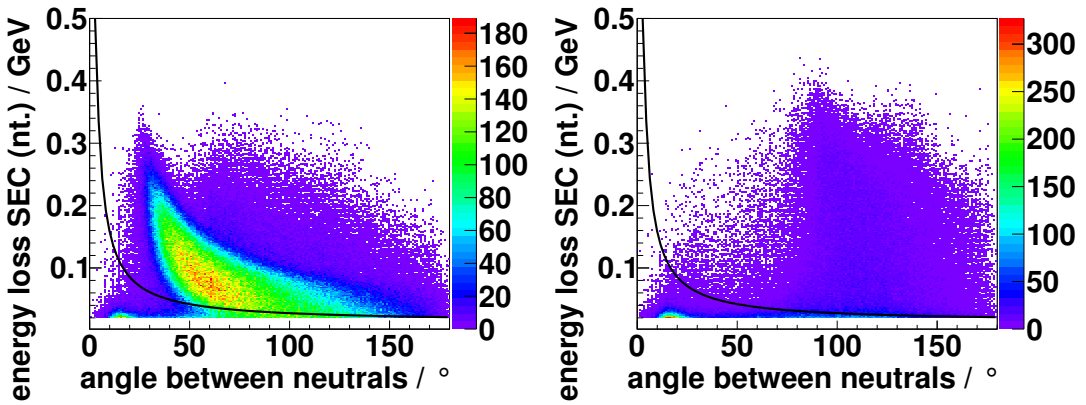

Figure 6.40.: Energy loss of a reconstructed neutral particle in the calorimeter plotted against the angle between its track and the track of a second neutral particle detected in the central detector for the simulated decays $\eta \to \pi^0 + e^+ + e^-$ and $\eta \to e^+ + e^- + \gamma$ (left and right figure, respectively). Neutral tracks with entries below the black cut line are rejected from the analysis. All samples were preselected on the signature of the decay $\eta \to \pi^0 + e^+ + e^-$, and a ^{3}He nucleus detected in the FD was required (see chapters 6.5.2 and 6.5.1).

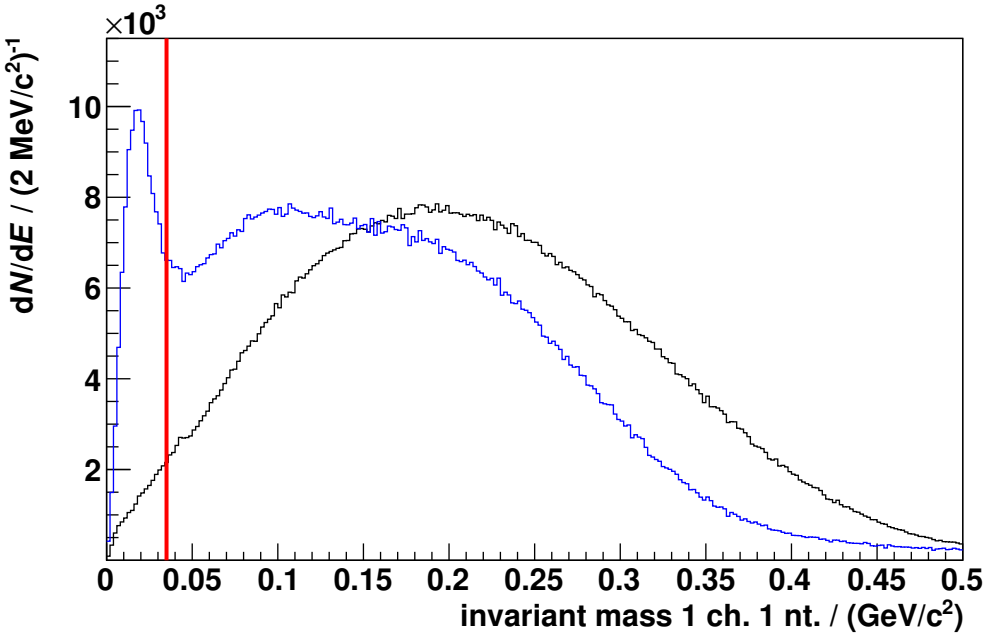

Figure 6.41.: Invariant mass of one neutral particle and one charged particle detected in the CD for the simulated decays $\eta \to \pi^0 + e^+ + e^-$ and $\eta \to \pi^+ + \pi^- + \gamma$ (black and blue histogram, respectively), assuming an electron mass for the charged particle. Note that the histogram of the signal decay is arbitrarily scaled to the latter. The red line illustrates the cut applied in the analysis. All samples were preselected on the signature of the decay $\eta \to \pi^0 + e^+ + e^-$, and a ^{3}He nucleus detected in the FD was required (see chapters 6.5.2 and 6.5.1).

In figure 6.41 the invariant mass of a reconstructed photon and a charged particle is plotted for the simulated decays $\eta \to \pi^0 + e^+ + e^-$ and $\eta \to \pi^+ + \pi^- + \gamma$ (black and blue histograms). The peak in the invariant mass distribution of the decay $\eta \to \pi^+ + \pi^- + \gamma$ at low masses corresponds to split-off events. Therefore, events with an invariant mass below 35 MeV c^{-2} were rejected from the analysis (illustrated by the red line).

6.5.6. Further preselection conditions

In chapter 6.6 the preselected 2008 and 2009 data sets will be fitted by Monte Carlo simulations. These fits are based on six different histograms. It is reasonable to limit the range of the utilized spectra to an appropriate one. Thus, the following conditions were applied to the data and Monte Carlo simulations:

- The ^{3}He missing mass must be in the range of 0.45 GeV c^{-2} to 0.60 GeV c^{-2},
- the invariant mass of two photons, one negatively and one positively charged particle reconstructed in the CD must be below 1.0 GeV c^{-2}, assuming an electron mass for the charged particles,
- the invariant mass of two photons reconstructed in the CD must be below 0.5 GeV c^{-2},
- the invariant mass of one negatively and one positively charged particle reconstructed in the CD must be below 1.0 GeV c^{-2}, assuming an electron mass for the charged particles,
- the smallest invariant mass of one charged particle and one photon of all four combinations possible for the signature of two photons, one negatively and one positively charged particle must be in the range of 0.035 GeV c^{-2} to 0.5 GeV c^{-2}, assuming an electron mass for the charged particle, and
- the missing mass squared $(p_\mathrm{p} + p_\mathrm{d} - p_{^3\mathrm{He}} - p_{\mathrm{e}^+} - p_{\mathrm{e}^-})^2$ must be in the range of $-0.1\,(\mathrm{GeV}/c^2)^2$ to $0.2\,(\mathrm{GeV}/c^2)^2$.

With these preselection conditions it is ascertained that all signal events remain and a sufficient range outside a possible signal region is available for a proper determination of the contributions of the different background reactions to the data.

6.6. Data description with Monte Carlo simulations

For the determination of the optimal selection conditions in the search for the decay $\eta \to \pi^0 + e^+ + e^-$ it is important to know the fraction of the different $p+d \to {}^3He+X$ background reactions contributing to the data. While the branching ratios of most η decay channels are well known [P+16] and the angular distribution of the reaction $p + d \to {}^3He + \eta$ was determined with high precision as part of this thesis (see chapter 5.1), the differential cross sections are known only with high uncertainties or not at all in case of the multi-pion production. Hence, the data were divided into ten angular ranges of $\cos\vartheta_\eta^{CMS}$ in which Monte Carlo simulations were fitted to the data.

It is important to note that the energy calibration of the first layer of the FRH was optimized with regard to the η meson production reaction $p + d \to {}^3He + \eta$. For an excess energy of about 60 MeV this equals energy losses of the ^{3}He nuclei in FRH1 of up to 0.3 GeV. ^{3}He ions originating from a multi-pion production reaction can have a higher energy loss in the FRH and, thus, their energy losses are reconstructed with larger uncertainties. Most of these events have a ^{3}He scattered in the angular range $0.6 < \cos\vartheta_{He}^{CMS} \leq 1$. On the other hand, only very few ^{3}He from the η meson production reaction are scattered in this angular range, namely less than 3 % (see chapter 5.1). Thus, to avoid systematic uncertainties, the angular range $0.6 < \cos\vartheta_{He}^{CMS} \leq 1$ ($-1 \leq \cos\vartheta_\eta^{CMS} < -0.6$) was excluded from the analysis.

6.6.1. Extraction of the number of $p + d \to {}^3He + \eta$ events in data for the different angular ranges

As the η decay $\eta \to \pi^+ + \pi^- + \pi^0$ has the same signature as the signal decay $\eta \to \pi^0 + e^+ + e^-$ of one positively charged, one negatively charged, and two neutral particles from the π^0 decay, it is utilized for the normalization. Before the number of events from the normalization channel will be determined, the number of reconstructed $p + d \to {}^3He + \eta$ reactions was extracted from ^{3}He missing mass spectra depending on $\cos\vartheta_\eta^{CMS}$.

For this purpose the background in the missing mass spectra was fitted by a third order polynomial. An example for such a fit is presented in the left of figure 6.42 for the angular range $-0.4 \leq \cos\vartheta_\eta^{CMS} < -0.2$ for the 2008 data set. The selected background environment is indicated by the black data points. After subtraction of the polynomial background from the data, the remaining peak was fitted by

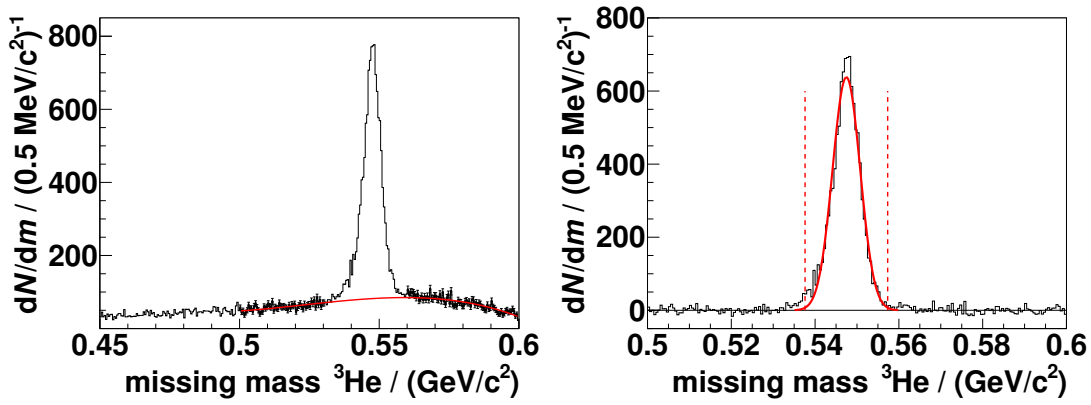

Figure 6.42.: Missing mass of ^{3}He for the angular range $-0.4 \leq \cos\vartheta_\eta^{\mathrm{CMS}} < -0.2$ for the 2008 data set. Left: Background fitted by a third order polynomial (red curve). The fit range is indicated by the black points. Right: Peak fitted by a Gaussian distribution after background subtraction (red curve). The left and right red dashed lines indicate the $\pm 3\sigma$ environment.

Table 6.9.: Number of extracted $\mathrm{p} + \mathrm{d} \to {}^3\mathrm{He} + \eta$ reactions depending on $\cos\vartheta_\eta^{\mathrm{CMS}}$ for the 2008 and 2009 data sets after preselection.

$\cos\vartheta_\eta^{\mathrm{CMS}}$	2008 data set	2009 data set
-0.6 – -0.4	7364 ± 112	$12\,828 \pm 148$
-0.4 – -0.2	$11\,000 \pm 126$	$19\,258 \pm 167$
-0.2 – 0.0	$13\,004 \pm 132$	$22\,625 \pm 174$
0.0 – 0.2	$13\,848 \pm 132$	$23\,837 \pm 175$
0.2 – 0.4	$13\,358 \pm 128$	$23\,863 \pm 172$
0.4 – 0.6	$11\,654 \pm 120$	$22\,089 \pm 165$
0.6 – 0.8	8368 ± 104	$16\,479 \pm 206$
0.8 – 1.0	4581 ± 77	9124 ± 112

a Gaussian distribution, and the events within the $\pm 3\sigma$ environment of the fit were counted and corrected to 100 % (see figure 6.42, right). In order to obtain the systematic uncertainties of the fit, the fit ranges were varied by up to 30 MeV, and the determined uncertainties were considered for the later analysis instead of the purely statistical uncertainties, if larger than the statistical uncertainties. The extracted numbers of $p + d \rightarrow {}^3He + \eta$ reactions are listed in table 6.9[9] and will be used as a constraint with the determined uncertainties for the fit of the data with Monte Carlo simulations as described in chapter 6.6.2.

6.6.2. Fitting of data spectra with Monte Carlo simulations

It is important to mention that the contributions of the different background channels to the data will be determined under the assumption of no contribution from the signal decay. This assumption is reasonable because of the current upper limit for the branching ratio of the signal of 4×10^{-5} [P+16], which results in an upper limit of 130 events expected in the full data set after preselection assuming a total number of produced η mesons of 3×10^7 [A+16b]. This number is well below the uncertainty of the number of reconstructed $p + d \rightarrow {}^3He + \eta$ reactions after preselection of about 600 events. Nevertheless, to avoid a bias of the fit, only every second data run (= about 50 % of the data) was utilized to extract the different background contributions. For these runs the number of produced η mesons was determined as described above. After the contributions of the various background reactions to the data were extracted by the Monte Carlo fit described in this chapter, these were corrected for the number of $p + d \rightarrow {}^3He + \eta$ reactions in the full data set. This method was applied to both the 2008 and the 2009 data set.

The description of the preselected data by Monte Carlo simulations is based on five quantities. These are listed in the following, and the corresponding histograms are illustrated in figure 6.43 for the 2008 data set and the angular range $-0.4 \leq \cos\vartheta_\eta^{\mathrm{CMS}} < -0.2$.

[9] The ratio of the extracted number of events for the 2009 data set compared to the number for the 2008 data set is about 1.75 for $-0.6 \leq \cos\vartheta_\eta^{\mathrm{CMS}} < 0.4$, whereas it is about 1.95 for $0.4 \leq \cos\vartheta_\eta^{\mathrm{CMS}} \leq 1.0$. Note that such differences can be explained by the different resolutions of the 2008 and 2009 data sets as well as by differences of the beam momenta and the amount of event overlap, leading to differences of the acceptance corrections that can vary depending on $\cos\vartheta_\eta^{\mathrm{CMS}}$. These acceptance corrections were not considered for the numbers presented here.

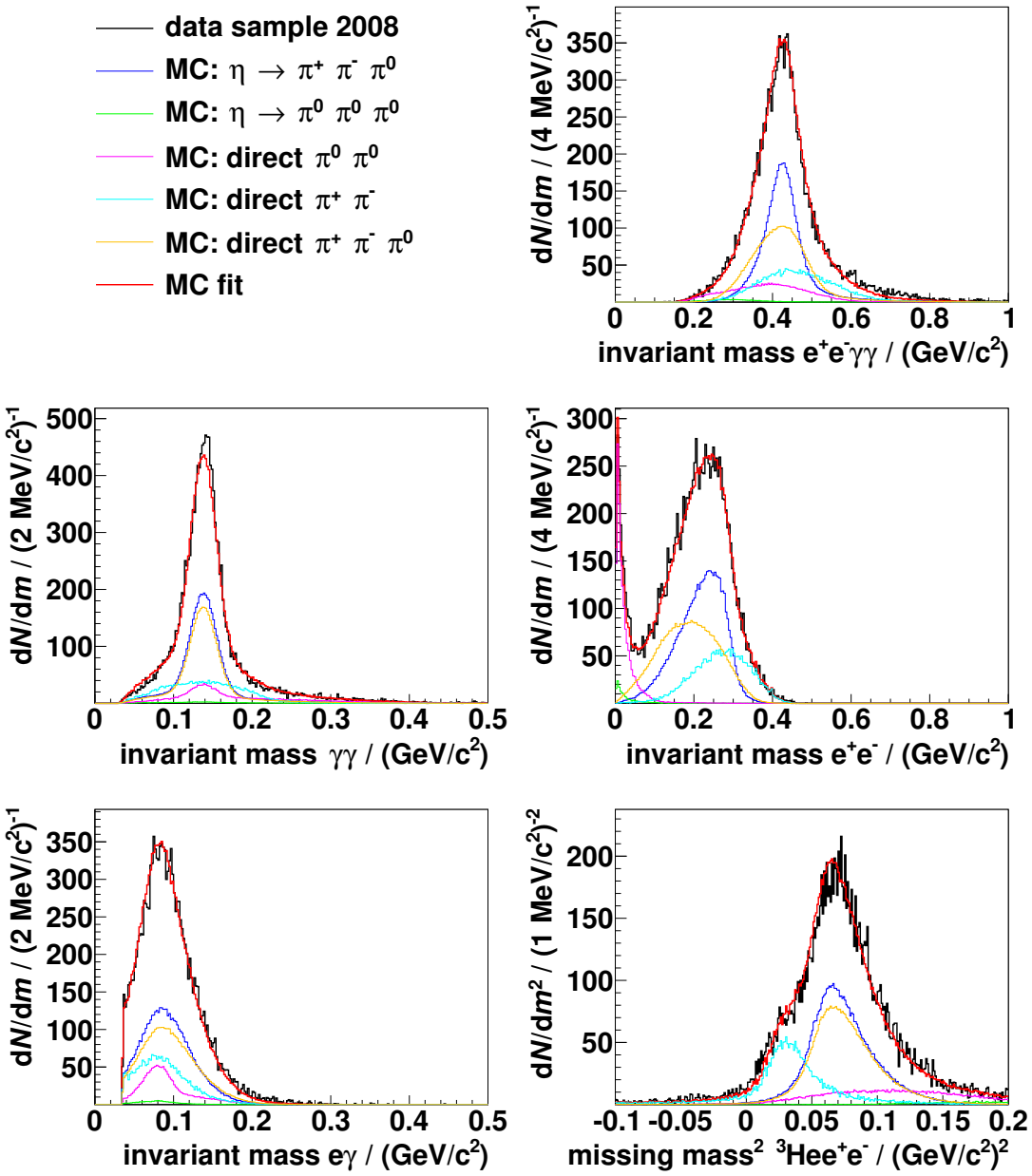

Figure 6.43.: Fit of Monte Carlo simulations to the 2008 data set for the angular range $-0.4 \leq \cos\vartheta_\eta^{\mathrm{CMS}} < -0.2$. Only the five reactions with the highest contribution to the fit are illustrated in detail (see color code, upper left). Upper right: invariant mass of two oppositely charged and two neutral CD particles. Middle left: invariant mass of two neutral CD particles. Middle right: invariant mass of two oppositely charged CD particles. Lower left: invariant mass of one charged and one neutral CD particle, smallest combination. Lower right: squared missing mass of ^{3}He and two oppositely charged CD particles. The charged CD particles were treated as electron and positron candidates. All data samples were preselected with the conditions described in chapter 6.5.

Invariant mass of $e^+e^-\gamma\gamma$

For the signal decay $\eta \to \pi^0 + e^+ + e^-$ the invariant mass of the electron, positron, and two photons is equal to the η mass $m_\eta = (547.862 \pm 0.017)\,\mathrm{MeV}\,c^{-2}$ [P+16]. However, the width of an observed signal peak is limited by the resolution of the central detector. In case of the decay $\eta \to \pi^+ + \pi^- + \pi^0$, which fulfills the signature conditions as well, a peak at a lower mass is expected in the invariant mass of the electron-positron pair candidate and the two neutral particles. This peak is clearly visible in the upper right of figure 6.43 (blue histogram). Other reactions with a different signature show no clear peak in the invariant mass of $e^+e^-\gamma\gamma$.

Invariant mass of $\gamma\gamma$

The second quantity used for the Monte Carlo fit is the invariant mass of two photons. For reactions and decays involving a π^0 meson a peak at the π^0 mass $m_{\pi^0} = (134.9766 \pm 0.0006)\,\mathrm{MeV}\,c^{-2}$ is observed in the invariant mass spectrum of two photons, as $(98.823 \pm 0.034)\,\%$ of the π^0 mesons decay to two photons [P+16] (see figure 6.43, middle left, blue, orange, magenta and green histogram). Reactions and decays not involving a π^0 meson contribute to a continuous background below the π^0 peak. Because of the preselection no further peak is expected in this invariant mass spectrum (see chapter 6.5).

Invariant mass of e^+e^-

The invariant mass of a pair of electron-positron candidates detected in the CD is an important quantity to distinguish between the different models of the decay $\eta \to \pi^0 + e^+ + e^-$ (see chapter 6.3.1). Furthermore, it allows for a separation between various background reaction channels. For instance, reactions with a Dalitz decay like $\pi^0 \to e^+ + e^- + \gamma$ or reactions with an electron-positron pair originating from conversion tend to have low values for the invariant mass of e^+e^- (see figure 6.43, middle right, magenta and green histogram), whereas reactions with charged pions tend to higher invariant masses (blue, light blue and orange histogram). Moreover, the shape of the distributions differ between the various reactions with charged pions involved.

Smallest invariant mass of eγ

As the fourth quantity utilized for the data description the invariant mass of one charged and one neutral particle detected in the CD was chosen. Only the smallest invariant mass of the four possible combinations is used. Similar to the other quantities the charged particle was treated as an electron or positron. Although the invariant mass distributions of eγ show only minor differences for the various reactions, these variations are sufficient to further distinguish these reaction channels (see figure 6.43, lower left).

Squared missing mass of ^{3}Hee^+e^-

Because of energy and momentum conservation the squared missing mass of the ^{3}He nucleus, the electron, and the positron peaks at the squared π^0 mass for the signal decay $\eta \to \pi^0 + e^+ + e^-$. In case of the direct $\pi^+\pi^-\pi^0$ production and the decay $\eta \to \pi^+ + \pi^- + \pi^0$, a peak at a higher mass is visible due to the mass difference between a charged pion and an electron for pions that were misidentified as an electron and a positron (see figure 6.43, lower right, blue and orange histogram).

The direct two-pion production $p + d \to {}^3He + \pi^+ + \pi^-$ only has the ^{3}He nucleus and two charged pions in the final state. Hence, the squared missing mass of these three particles is expected to peak at zero. Due to the mass differences of electrons and charged pions, a peak at a higher squared mass is visible (see figure 6.43, lower right, light blue histogram). For the direct $\pi^0\pi^0$ production and the η decay $\eta \to \pi^0 + \pi^0 + \pi^0$ continuous distributions are observed (see figure 6.43, lower right, green and magenta histogram).

A combination of the above mentioned spectra can be utilized for a fit of the preselected data with a cocktail of Monte Carlo simulations. Since no exact signature was required for the preselection, $n_{\mathrm{comb}} \geq 1$ combinations fulfilling the signature conditions are possible for each event with additional particles. Therefore, for data as well as simulations each entry in a histogram from a combination of four particles of an event, which was not rejected by the preselection, was weighted by the inverse number of possible combinations of this event ($1/n_{\mathrm{comb}}$), which passed the preselection. In this way the sum of all entries per one event in a histogram is always equal to unity.

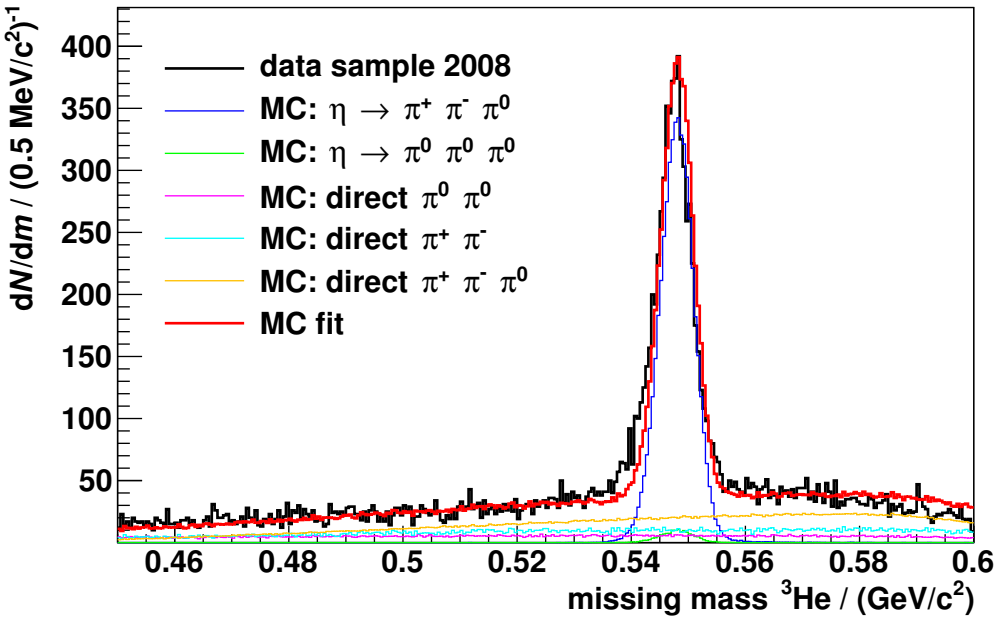

Figure 6.44.: Missing mass of ^{3}He for the angular range $-0.4 \leq \cos\vartheta_\eta^{\mathrm{CMS}} < -0.2$ for the 2008 data set fitted by Monte Carlo simulations. Only the five reactions with the highest contribution to the fit are illustrated in detail (see color code).

Histograms of the five quantities were created for data and simulations for eight angular bins in the range $-0.6 \leq \cos\vartheta_\eta^{\mathrm{CMS}} \leq 1$. All 40 data histograms were fitted by simulations at the same time. This was done separately for the 2008 and the 2009 data set. As the branching ratios of the most common η meson decays are well known, these were used as constraints for the fit respecting their uncertainties according to [P$^+$16]. Furthermore, the numbers of $\mathrm{p} + \mathrm{d} \rightarrow {}^3\mathrm{He} + \eta$ events as extracted in chapter 6.6.1 were used as constraints respecting their determined uncertainties. While the branching ratios of the η meson decays are independent of $\cos\vartheta_\eta^{\mathrm{CMS}}$ and, thus, global parameters were used for them, the parameters for the direct pion productions were determined for each angular range, since their angular distributions are unknown.

In chapter 6.3 it was discussed that events can overlap. Thus, a Monte Carlo sample was created with regard to event overlap. The ratio of pure events and events overlapping with particles from another event is unknown and was hence left as a free parameter of the fit. However, this ratio is independent of the angular range and must be varied as one global factor.

Figure 6.43 illustrates the five histograms for the angular range $-0.4 \leq \cos\vartheta_\eta^{\mathrm{CMS}} < -0.2$ for the 2008 data set fitted by Monte Carlo simulations (black

and red histograms). In addition, the contributions of the two η decay channels $\eta \to \pi^+ + \pi^- + \pi^0$ and $\eta \to \pi^0 + \pi^0 + \pi^0$ as well as of the direct pion production reactions $p + d \to {}^3He + \pi^0 + \pi^0$, $p + d \to {}^3He + \pi^+ + \pi^-$, and $p + d \to {}^3He + \pi^+ + \pi^- + \pi^0$ are presented (blue, green, magenta, light blue and orange histograms). The corresponding figures for the other seven angular bins and for the 2009 data set can be found in appendix B.2. It is visible that the combined cocktail of Monte Carlo simulations and simulations with event overlap leads to a good description of the data histograms. This can also be seen in the ${}^3He$ missing mass spectra, which were not used for the Monte Carlo fit, but only for the determination of the numbers of produced η mesons (see figure 6.44 and appendix B.2). The minor differences in the fit and the data can be explained by the uncertainties of the calibration of the detector elements.

The contributions of the different reactions to the data after preselection according to the fits by Monte Carlo simulations are listed in tables 6.10 and 6.11 for the 2008 and the 2009 data set, respectively. It is worthwhile to mention that the extracted contribution of the direct $\pi^0\pi^0$ production corresponds to a total cross section that is about four to five times larger than the $p+d \to {}^3He+\eta$ cross section at the same beam energy if the reconstruction efficiencies according to Monte Carlo simulations are considered. This factor is compatible with the total cross section of the reaction $p+d \to {}^3He+\pi^0+\pi^0$ as determined by E. Pérez del Río [Pé14b, A$^+$15c]. The largest deviation is seen for the angular range $0.8 \leq \cos\vartheta_\eta^{CMS} \leq 1$ where according to the Monte Carlo fit no contribution of the direct $\pi^0\pi^0$ production is seen in the 2008 data set. The mean value of the above mentioned factor over all angular bins and both data sets except for the mentioned range of the 2008 data set equals 4.7 ± 0.5.[10] For a discussion of the deviations, especially in the angular range $0.8 \leq \cos\vartheta_\eta^{CMS} \leq 1$ for the 2008 data set, see chapter 7.1.2.

The numbers of reconstructed $p + d \to {}^3He + \pi^+ + \pi^-$ reactions determined after preselection would suggest a cross section for this reaction which is up to 200 times larger than the cross section of $p + d \to {}^3He + \eta$. This is an order of magnitude larger than expected[11]. This discrepancy can be explained by the differences of the signature required in the preselection and the signature of the reaction $p + d \to {}^3He + \pi^+ + \pi^-$. Only events of this reaction channel with

[10] For a determination of the mean value the factors extracted for each angular range were weighted by the number of events in data without an η meson produced.

[11] For a rough estimate the cross section of $p + d \to {}^3He + \pi^0 + \pi^0$ as determined by E. Pérez del Río was multiplied by an isospin factor of two [Pé14b, A$^+$15c].

Table 6.10.: Numbers of events of the different reactions in the 2008 data set after preselection according to the fit by Monte Carlo simulations with their statistical uncertainties.

η decay channel	Number of events
$\eta \to \gamma + \gamma$	$1.5\ ^{+4.2}_{-1.2}$
$\eta \to \pi^0 + \pi^0 + \pi^0$	3647 ± 88
$\eta \to \pi^0 + \gamma + \gamma$	$1.8\ ^{+4.5}_{-1.5}$
$\eta \to \pi^+ + \pi^- + (\pi^0 \to \gamma + \gamma)$	$79\,029 \pm 409$
$\eta \to \pi^+ + \pi^- + (\pi^0 \to e^+ + e^- + \gamma)$	148 ± 18
$\eta \to \pi^+ + \pi^- + \gamma$	335 ± 27
$\eta \to e^+ + e^- + \gamma$	$15\ ^{+8}_{-5}$
$\eta \to \mu^+ + \mu^- + \gamma$	$0.08\ ^{+2.54}_{-0.07}$
$\eta \to e^+ + e^- + e^+ + e^-$	$0.07\ ^{+2.52}_{-0.06}$
$\eta \to \pi^+ + \pi^- + e^+ + e^-$	$2.8\ ^{+5.1}_{-2.1}$
Reaction channel	**Number of events**
$p + d \to {}^3He + \pi^0$	0
$p + d \to {}^3He + \pi^0 + \pi^0$	$18\,866 \pm 199$
$p + d \to {}^3He + \pi^0 + \pi^0 + \pi^0$	1796 ± 62
$p + d \to {}^3He + \pi^0 + \pi^0 + \pi^0 + \pi^0$	0
$p + d \to {}^3He + \pi^+ + \pi^-$	$31\,708 \pm 258$
$p + d \to {}^3He + \pi^+ + \pi^- + \pi^0$	$44\,989 \pm 308$
$p + d \to {}^3He + \pi^+ + \pi^- + \pi^0 + \pi^0$	0
$p + d \to {}^3He + \pi^+ + \pi^- + \pi^+ + \pi^-$	0

Table 6.11.: Numbers of events of the different reactions in the 2009 data set after preselection according to the fit by Monte Carlo simulations with their statistical uncertainties.

η decay channel	Number of events
$\eta \to \gamma + \gamma$	$3.2\ ^{+5.1}_{-2.2}$
$\eta \to \pi^0 + \pi^0 + \pi^0$	6819 ± 117
$\eta \to \pi^0 + \gamma + \gamma$	$3.3\ ^{+5.1}_{-2.3}$
$\eta \to \pi^+ + \pi^- + (\pi^0 \to \gamma + \gamma)$	$142\,303 \pm 537$
$\eta \to \pi^+ + \pi^- + (\pi^0 \to e^+ + e^- + \gamma)$	303 ± 25
$\eta \to \pi^+ + \pi^- + \gamma$	635 ± 36
$\eta \to e^+ + e^- + \gamma$	$31\ ^{+10}_{-8}$
$\eta \to \mu^+ + \mu^- + \gamma$	$0.17\ ^{+2.52}_{-0.14}$
$\eta \to e^+ + e^- + e^+ + e^-$	$0.12\ ^{+2.46}_{-0.10}$
$\eta \to \pi^+ + \pi^- + e^+ + e^-$	$5.7\ ^{+5.8}_{-3.2}$
Reaction channel	**Number of events**
$p + d \to {}^3He + \pi^0$	0
$p + d \to {}^3He + \pi^0 + \pi^0$	$41\,564 \pm 291$
$p + d \to {}^3He + \pi^0 + \pi^0 + \pi^0$	$0.2\ ^{+2.6}_{-0.2}$
$p + d \to {}^3He + \pi^0 + \pi^0 + \pi^0 + \pi^0$	0
$p + d \to {}^3He + \pi^+ + \pi^-$	$63\,769 \pm 360$
$p + d \to {}^3He + \pi^+ + \pi^- + \pi^0$	$85\,000 \pm 416$
$p + d \to {}^3He + \pi^+ + \pi^- + \pi^0 + \pi^0$	0
$p + d \to {}^3He + \pi^+ + \pi^- + \pi^+ + \pi^-$	0

two additional, misidentified photons can fulfill the signature requirements leaving only a very small amount of $\pi^+\pi^-$ production events according to simulations and, hence, leading to a very small reconstruction efficiency. Furthermore, the preselection conditions described in chapter 6.5 reduce the efficiency even more. The amount of reconstructed events heavily depends on the knowledge of the probability of split-off reactions with properties not common for these kinds of events. The properties of such special reactions within the WASA detector are only known with large uncertainties. Nevertheless, if no events from the direct $\pi^+\pi^-$ production remain after applying all selection conditions according to Monte Carlo simulations, there is no systematic effect in case of an upper limit determination for the branching ratio of the decay $\eta \to e^+ + e^- + \pi^0$ (see chapter 7).

According to the Monte Carlo fits, the η meson decays contributing most to the data are $\eta \to \pi^+ + \pi^- + \pi^0$ with $\pi^0 \to \gamma + \gamma$, $\eta \to \pi^0 + \pi^0 + \pi^0$, and $\eta \to \pi^+ + \pi^- + \gamma$. The highest contributions from the direct pion production are the reactions $p + d \to {}^3He + \pi^+ + \pi^- + \pi^0$ with the same signature as the signal decay and $p + d \to {}^3He + \pi^+ + \pi^-$ as well as $p + d \to {}^3He + \pi^0 + \pi^0$ because of their very high cross sections. When comparing the components of the 2008 data set and those of the 2009 data set, the factor between the event numbers of one reaction is about two for the η decays and these three pion production reactions. Smaller deviations of this factor from two can be explained by the different amount of event overlap during the two beam times: According to the fit, $61.7^{+1.0}_{-0.9}\,\%$ of the events in the 2008 data set have contributions from event overlap, whereas this value is $71.4^{+0.6}_{-0.5}\,\%$ for the 2009 data set[12]. The largest deviations are seen for the direct $\pi^0\pi^0\pi^0$ production. While $0.2^{+2.6}_{-0.2}$ events are seen in the 2009 data set, (1796 ± 62) events contribute to the 2008 data set according to the fit by Monte Carlo simulations. A discussion of the systematic uncertainties of the extracted contributions will be presented in chapter 7.1.2 in detail.

6.7. Selection conditions and optimization

In this chapter selection conditions for the reaction $p + d \to {}^3He + \eta$ and the decay $\eta \to (\pi^0 \to \gamma + \gamma) + e^+ + e^-$ will be presented. These will be applied after the preselection conditions described in chapter 6.5.

The identification of the signal reaction is based on the following quantities:

[12] For the determination of the quoted uncertainties see chapter 7.1.2.

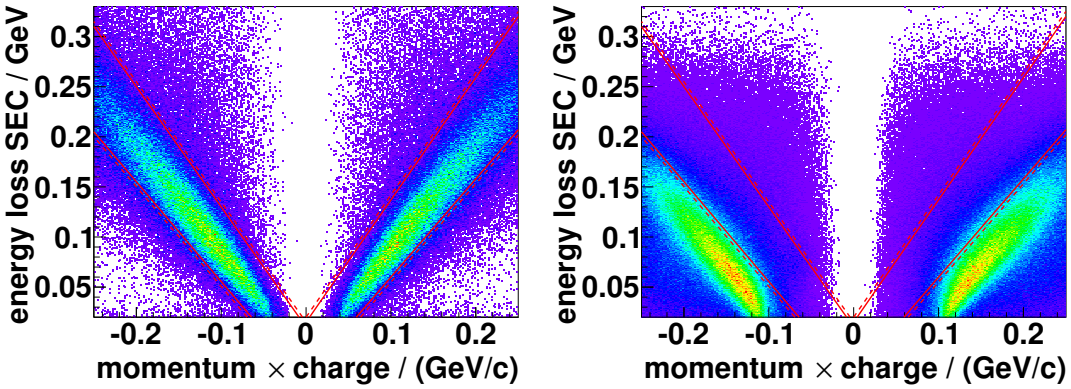

Figure 6.45.: Energy loss of charged particles in the SEC plotted against their momentum times charge for the simulated decays $\eta \rightarrow \pi^0 + e^+ + e^-$ (left) and $\eta \rightarrow \pi^+ + \pi^- + \pi^0$ (right). Both samples were preselected with the conditions presented in chapter 6.5. The selection conditions utilized in the analysis are illustrated by the red solid lines, whereas the red dashed lines indicate the cuts used during optimization of the other selection conditions (see chapter 6.7.1).

- The ^{3}He missing mass (m_X) to select the reaction $p + d \rightarrow {}^3He + \eta$,
- the invariant mass of two photons, a positron, and an electron candidate ($m_{ee\gamma\gamma}$) to identify the decay $\eta \rightarrow (\pi^0 \rightarrow \gamma + \gamma) + e^+ + e^-$,
- the invariant mass of two photons ($m_{\gamma\gamma}$) to ascertain the decay $\pi^0 \rightarrow \gamma + \gamma$,
- the invariant mass of an electron and a positron candidate (m_{ee}),
- the χ^2 probability of the kinematic fit with the hypothesis $p + d \rightarrow {}^3He + e^+ + e^- + \gamma + \gamma$ (*prob.*), and
- the energy loss of the charged decay particles in the calorimeter (E_{dep}^{SEC}) and the corresponding reconstructed momentum (p) utilized for the discrimination of electrons, positrons, and charged pions (particle identification, PID).

While the selection conditions for m_X, $m_{ee\gamma\gamma}$, $m_{\gamma\gamma}$, m_{ee}, and *prob.* were optimized with a software as described in chapter 6.7.1, those for the PID had been determined beforehand[13].

[13]Please note that all Monte Carlo plots presented here and in the following chapters were created with smearing settings obtained for an optimal agreement with the 2008 data set and without event overlap, if not stated otherwise. The corresponding plots for the 2009 data set and for simulations that include event overlap, respectively, show only minor differences. Hence, the presented plots for MC are sufficient for a valuation of the illustrated conditions.

As already discussed in chapter 6.5.3, an enhancement at low energy losses in the SEC and high momenta was observed in Monte Carlo simulations for the reaction $p+d \rightarrow {}^3He+\pi^+ +\pi^-$ if at least one positively charged, one negatively charged and two neutral particles detected in the CD were requested. Such an enhancement was not seen in data. Because of these deviations between simulations and measured data, charged particles with momenta above $0.25\,\mathrm{GeV}\,c^{-1}$ were rejected. In order to avoid systematic effects due to remaining pions of this reaction with momenta below this value, the selection conditions for the PID were chosen manually. In figure 6.45, showing the energy loss in the SEC of a charged particle plotted against its momentum times charge for the simulated decays $\eta \rightarrow \pi^0 + e^+ + e^-$ (left) and $\eta \rightarrow \pi^+ + \pi^- + \pi^0$ (right), these conditions are illustrated by red solid lines. All charged particles above the upper and below the lower cut line were rejected for the analysis. These are particles with:

$$E_{\mathrm{dep}}^{\mathrm{SEC}} > 1.200\,c \cdot p + 0.010\,\mathrm{GeV} \text{ or} \tag{6.17}$$

$$E_{\mathrm{dep}}^{\mathrm{SEC}} < 0.996\,c \cdot p - 0.044\,\mathrm{GeV} \text{ if negatively charged, and} \tag{6.18}$$

$$E_{\mathrm{dep}}^{\mathrm{SEC}} > 1.220\,c \cdot p + 0.015\,\mathrm{GeV} \text{ or} \tag{6.19}$$

$$E_{\mathrm{dep}}^{\mathrm{SEC}} < 0.980\,c \cdot p - 0.038\,\mathrm{GeV} \text{ if positively charged, respectively.} \tag{6.20}$$

The chosen conditions are stricter than conditions obtained by an optimization algorithm to ascertain that after application of all cuts ideally no charged pions remain. For the optimization of the other selection conditions looser requirements were utilized, illustrated by the red dashed lines in figure 6.45. In detail, the upper cut lines were shifted by $+5\,\mathrm{MeV}$, while the lower cut lines were shifted by $-5\,\mathrm{MeV}$ (see chapter 6.7.1).

6.7.1. Optimization procedure

The selection conditions for m_{X}, $m_{\mathrm{ee}\gamma\gamma}$, $m_{\gamma\gamma}$, m_{ee}, and *prob.* were determined with the aid of an optimization algorithm. First ideas of an optimization algorithm with respect to the decay $\eta \rightarrow \pi^0 + e^+ + e^-$ were discussed in a former diploma thesis [Ber09], and a first version was utilized in the analysis of the 2008 data set by A. Winnemöller [Win11]. The algorithm is purely based on Monte Carlo simulations, which were preselected with the conditions presented in chapter 6.5. In order to avoid a systematic bias of the result, only 40 % of the events of the simulated background reactions were utilized for the optimization, whereas the

other 60 % were used to determine the efficiency of the found cuts[14]. In case of the direct $\pi^0\pi^0$ production, additional 6×10^8 events were simulated and analyzed for the efficiency determination, as this reaction is the main contributor to the remaining events after applying all cuts (see chapter 7).

The cut optimization algorithm is based on the relative amount of events $S_\mathrm{R} = N_\mathrm{S}^\mathrm{cut}/N_\mathrm{S}^\mathrm{pres}$ of the decay $\eta \to \pi^0 + e^+ + e^-$ remaining after all cuts ($N_\mathrm{S}^\mathrm{cut}$) in relation to the number of events after preselection ($N_\mathrm{S}^\mathrm{pres}$) and the relative amount of events $B_\mathrm{R} = N_\mathrm{B}^\mathrm{cut}/N_\mathrm{B}^\mathrm{pres}$ from all background reactions remaining after all cuts ($N_\mathrm{B}^\mathrm{cut}$). For the latter the number of events in data after preselection according to the Monte Carlo fit presented in chapter 6.6 are used as reference ($N_\mathrm{B}^\mathrm{pres}$). In order to determine the optimum selection conditions, the signal-to-background ratio must be maximized, while at the same time as many signal events as possible should remain. This condition can be tested for each set of cuts by the evaluation function

$$G = S_\mathrm{R} \cdot \frac{S_\mathrm{R}}{B_\mathrm{R}} \,. \tag{6.21}$$

In case of an observation of the decay of interest, a maximization of this function leads to an optimal significance

$$S = \frac{N_\mathrm{S}}{\sqrt{N_\mathrm{B}}} \tag{6.22}$$

with the number of observed signal events N_S and the number of observed background events N_B.

In [Win11] the optimization was realized with a software that varied only one cut at once to find the maximum of G, while the other cuts were fixed. This process was performed for all cut variables. As the individual cuts change the shape of the distributions of the other quantities used for the event selection, the procedure was repeated until conversion was reached.

The maximization algorithm utilized in this thesis is based on the minimization tool Minuit available in the ROOT framework [BR97]. It allows to optimize all selection conditions at the same time. Together with a storage of the quantities of interest in a binary file format the performance of this algorithm is higher by orders of magnitude compared to the software used in [Win11]. Instead of about two weeks for five to six iterations, the algorithm requires less than one hour with over 1000 iteration steps.

[14] See chapter 6.3 for the list of simulated reactions.

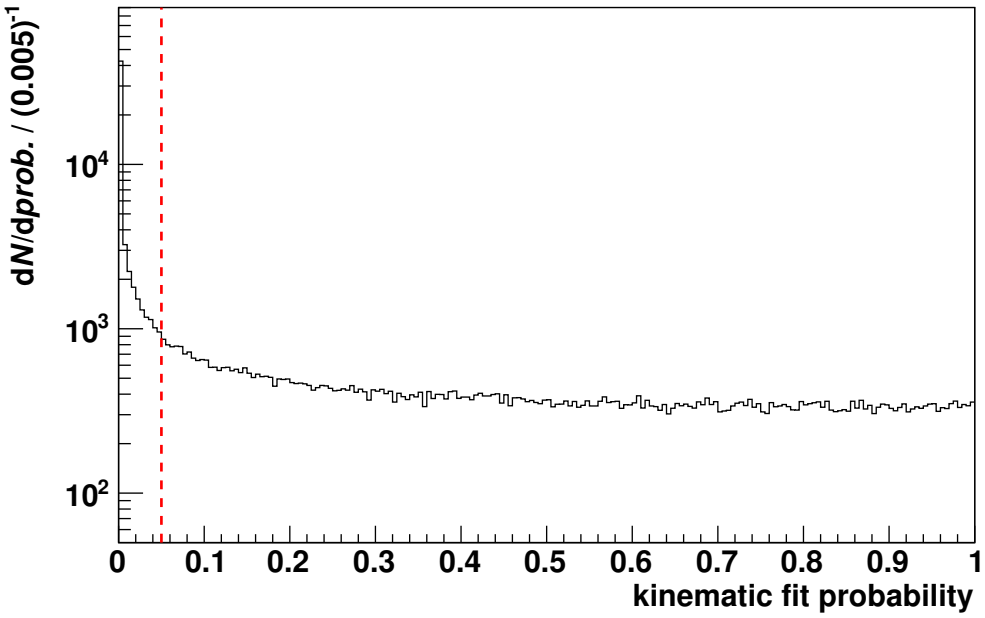

Figure 6.46.: χ^2 probability of the kinematic fit with the hypothesis $p + d \rightarrow {}^3He + e^+ + e^- + \gamma + \gamma$ for the simulated decay $\eta \rightarrow (\pi^0 \rightarrow \gamma + \gamma) + e^+ + e^-$. The minimum probability of 0.05 requested in the cut optimization is indicated by the red dashed line. The sample was preselected with the conditions presented in chapter 6.5.

Due to the higher statistics of the Monte Carlo simulation pool compared to the measured data, it is not reasonable to optimize the selection conditions until an absolute minimum of background events remain according to simulations. Instead, all combinations of selection conditions with a total amount of less than 0.2 events after all cuts according to the scaled Monte Carlo simulations were treated as if 0.2 events from all background reactions remained. Note that the limit for the precision of the cut optimization algorithm can be set to different values between zero and one event. Here 0.2 events was chosen as a limit, as 0.2 events equal one to four unscaled events[15] of the simulated reaction $p + d \rightarrow {}^3He + \pi^0 + \pi^0$, which is the main background for the analysis with regard to the decay $\eta \rightarrow \pi^0 + e^+ + e^-$ (see chapter 7). A value equaling less than one such unscaled Monte Carlo event is not reasonable for the limit of the precision of the optimization algorithm. However, it should be noted that limits for the precision in the range of 0.1 events to 0.5 events were found to lead to identical selection conditions.

[15] 0.2 events equal one event for simulations of the reaction $p + d \rightarrow {}^3He + \pi^0 + \pi^0$ with event overlap scaled to the 2009 data set, whereas 0.2 events equal four events for simulations of the reaction $p + d \rightarrow {}^3He + \pi^0 + \pi^0$ without event overlap scaled to the 2008 data set.

For the optimization process the selection conditions for the various quantities were limited to reasonable ranges. In case of the χ^2 probability of the kinematic fit with the hypothesis $\mathrm{p} + \mathrm{d} \to {}^3\mathrm{He} + \mathrm{e}^+ + \mathrm{e}^- + \gamma + \gamma$, a minimum probability of 0.05 was requested (see figure 6.46). This value is lower than a typical cut value of 0.1 as used in [Cod12], for example, but rejects events of the reaction $\mathrm{p}+\mathrm{d} \to {}^3\mathrm{He}+\eta$ with the decay $\eta \to (\pi^0 \to \gamma + \gamma) + \mathrm{e}^+ + \mathrm{e}^-$ that were reconstructed with four-momenta deviating significantly from the generated values.

It is important to note that the kinematic fit utilized for the presented analysis is purely based on kinematics without further constraints on the reaction particles. The error parametrization necessary for the kinematic fit was performed as part of the common base class PDEtaAnalysisBase by other members of the task force analyzing the data collected in 2008 and 2009 [BCHW17] and, hence, will not be discussed here. Further details about kinematic fits are given in chapter 2.6.

After applying a preliminary cut for the χ^2 probability of the kinematic fit at 0.05, limits for the selection conditions of the other quantities used in the analysis were defined. For this purpose the corresponding histograms of the simulated signal decay $\eta \to \pi^0 + \mathrm{e}^+ + \mathrm{e}^-$ were fitted by Gaussian distributions, and the maximum selection ranges allowed for the cut optimization were limited to the $\pm 3.3\sigma$ environment of the Gaussian distribution. This equals about 99.9 % of the events. Figure 6.47 illustrates the distributions for the ^{3}He missing mass (upper left figure), the invariant mass of two photons and an electron-positron pair candidate (upper right figure), and the invariant mass of two photons (lower figure) fitted by Gaussian distributions (red solid curves). The related maximum selection ranges are indicated by red dashed lines and correspond to:

$$0.539\,\mathrm{GeV}\,c^{-2} \leq m_{\mathrm{X}} \leq 0.557\,\mathrm{GeV}\,c^{-2}\,, \tag{6.23}$$

$$0.461\,\mathrm{GeV}\,c^{-2} \leq m_{\mathrm{ee}\gamma\gamma} \leq 0.646\,\mathrm{GeV}\,c^{-2}\,,\ \text{and} \tag{6.24}$$

$$0.092\,\mathrm{GeV}\,c^{-2} \leq m_{\gamma\gamma} \leq 0.185\,\mathrm{GeV}\,c^{-2}\,. \tag{6.25}$$

For the invariant mass of an electron-positron pair candidate only a minimum mass is requested in the later analysis (see chapter 6.7.2). As the distribution of the signal decay $\eta \to \pi^0 + \mathrm{e}^+ + \mathrm{e}^-$ starts at $0\,\mathrm{GeV}\,c^{-2}$, no further restrictions were implemented into the cut optimization algorithm. This is the case both for a decay according to three-particle phase space and for a decay via a virtual photon (see figure 6.48, orange shadowed and black lined histogram, respectively).

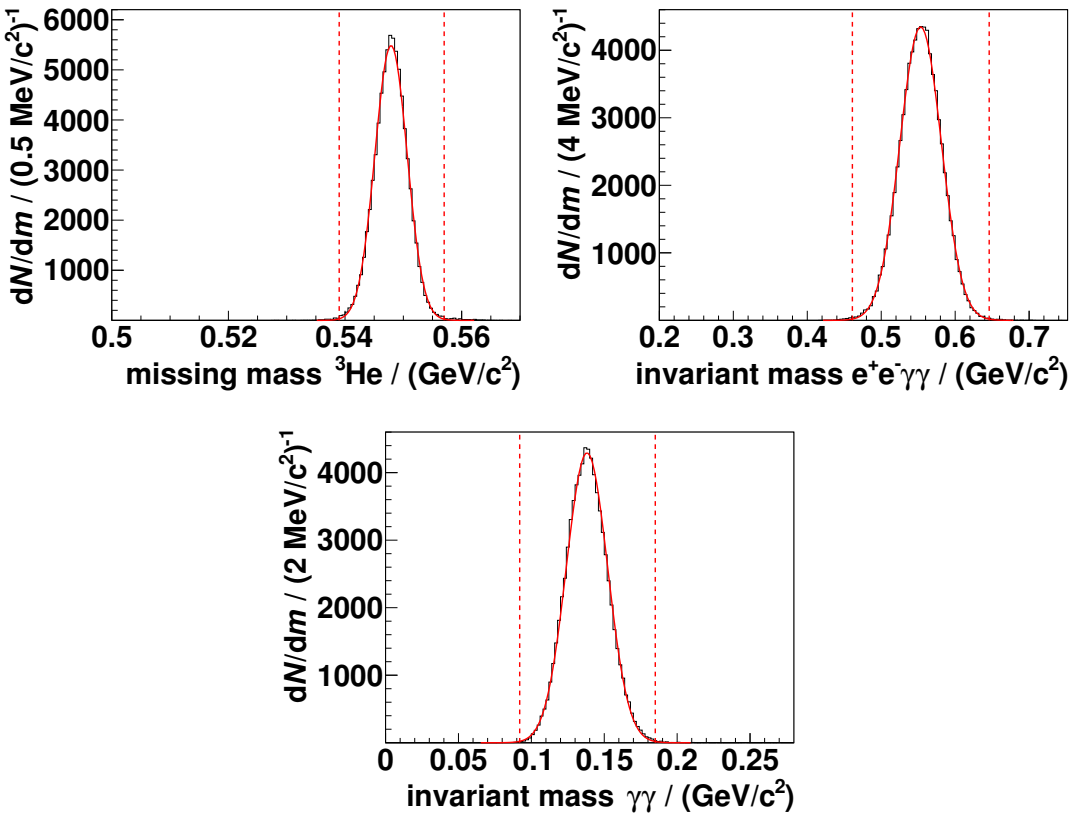

Figure 6.47.: ^{3}He missing mass (upper left), invariant mass of two photons and an electron-positron pair candidate (upper right), and invariant mass of two photons (lower figure) for the simulated reaction $p + d \rightarrow {}^3He + \eta$ with $\eta \rightarrow (\pi^0 \rightarrow \gamma + \gamma) + e^+ + e^-$. The spectra were fitted by a Gaussian distribution (red solid curves), and the corresponding $\pm 3.3\sigma$ environments of the Gaussians are illustrated by red dashed lines. The sample was preselected with the conditions presented in chapter 6.5, and a minimum χ^2 probability of 0.05 for the kinematic fit was requested.

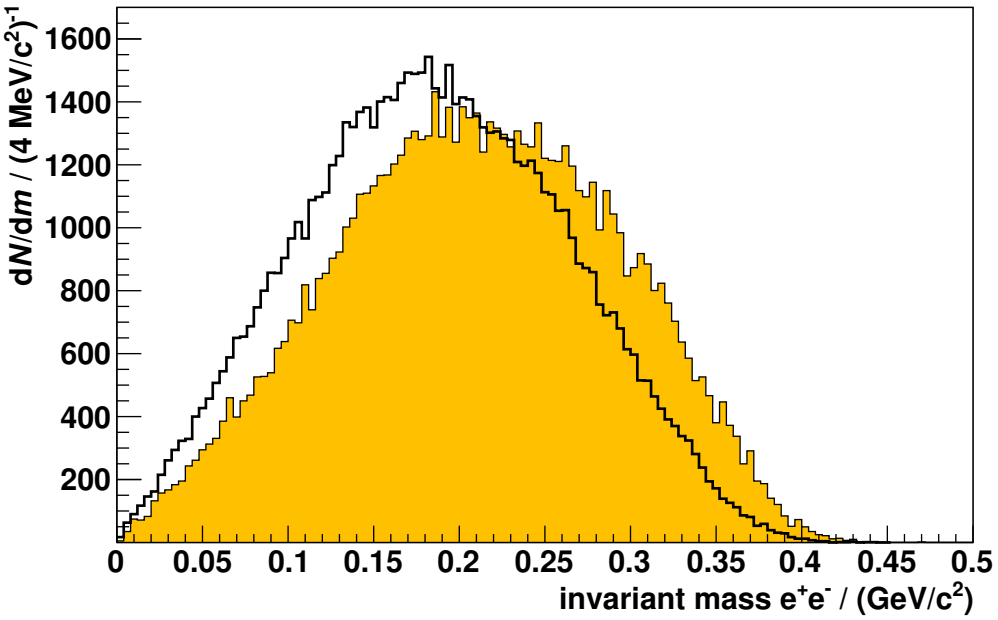

Figure 6.48.: Invariant mass of an electron-positron pair candidate for the simulated decay $\eta \to \pi^0 + e^+ + e^-$ assuming a decay according to three-particle phase space (shadowed in orange) and a decay via a virtual photon (black line). The samples were preselected with the conditions presented in chapter 6.5, and a minimum χ^2 probability of 0.05 for the kinematic fit was requested. The distribution for a decay via a virtual photon has been arbitrarily scaled to the other distribution.

Table 6.12.: Selection conditions for the analysis with regard to the decay $\eta \rightarrow (\pi^0 \rightarrow \gamma + \gamma) + e^+ + e^-$, assuming a decay according to three-particle phase space and for a decay via a virtual photon.

^{3}He missing mass (m_X)	$0.5414\,\mathrm{GeV}\,c^{-2} \leq$	m_X	$\leq 0.5561\,\mathrm{GeV}\,c^{-2}$
Invariant mass of $e^+e^-\gamma\gamma$ ($m_{ee\gamma\gamma}$)	$0.507\,\mathrm{GeV}\,c^{-2} \leq$	$m_{ee\gamma\gamma}$	$\leq 0.646\,\mathrm{GeV}\,c^{-2}$
Invariant mass of $\gamma\gamma$ ($m_{\gamma\gamma}$)	$0.0923\,\mathrm{GeV}\,c^{-2} \leq$	$m_{\gamma\gamma}$	$\leq 0.1574\,\mathrm{GeV}\,c^{-2}$
Invariant mass of e^+e^- (m_{ee})		m_{ee}	$\geq 0.096\,\mathrm{GeV}\,c^{-2}$
χ^2 probability of kinematic fit (*prob.*)		*prob.*	≥ 0.05
Particle identification of			
electron candidate	$0.996\,c \cdot p - 0.044\,\mathrm{GeV} \leq E_{dep}^{SEC} \leq 1.200\,c \cdot p + 0.010\,\mathrm{GeV}$		
positron candidate	$0.980\,c \cdot p - 0.038\,\mathrm{GeV} \leq E_{dep}^{SEC} \leq 1.220\,c \cdot p + 0.015\,\mathrm{GeV}$		

As already discussed at the beginning of chapter 6.7, the selection conditions for the electron and positron identification were fixed in the cut optimization software. The obtained selection conditions for all quantities will be presented and discussed in the following chapter 6.7.2.

6.7.2. Selection conditions

The optimization of the selection conditions described in chapter 6.7.1 was performed separately for a signal decay $\eta \rightarrow \pi^0 + e^+ + e^-$ assuming a decay according to three-particle phase space and for a decay via a virtual photon. For both cases the same set of selection conditions was found to have the best value for the evaluation function $G = S_R \cdot \frac{S_R}{B_R}$. These conditions are listed together with the manually chosen selection conditions for the PID in table 6.12 and will be discussed in the following.

In figure 6.49 the ^{3}He missing mass is plotted for the simulated reaction $p + d \rightarrow {}^3He + \eta$ with $\eta \rightarrow \pi^0 + e^+ + e^-$ (upper left), the simulated reaction $p + d \rightarrow {}^3He + \pi^0 + \pi^0$ (upper right), and for the 2008 and 2009 data sets (lower left and lower right, respectively). The range selected for the analysis is indicated by red cut lines. While the majority of events from the reaction $p + d \rightarrow {}^3He + \eta$ remain after application of the selection condition, most events from the direct pion production are rejected.

A cut on the invariant mass of two photons and an electron-positron pair candidate allows to reduce the contributions from the decay $\eta \rightarrow \pi^+ + \pi^- +$

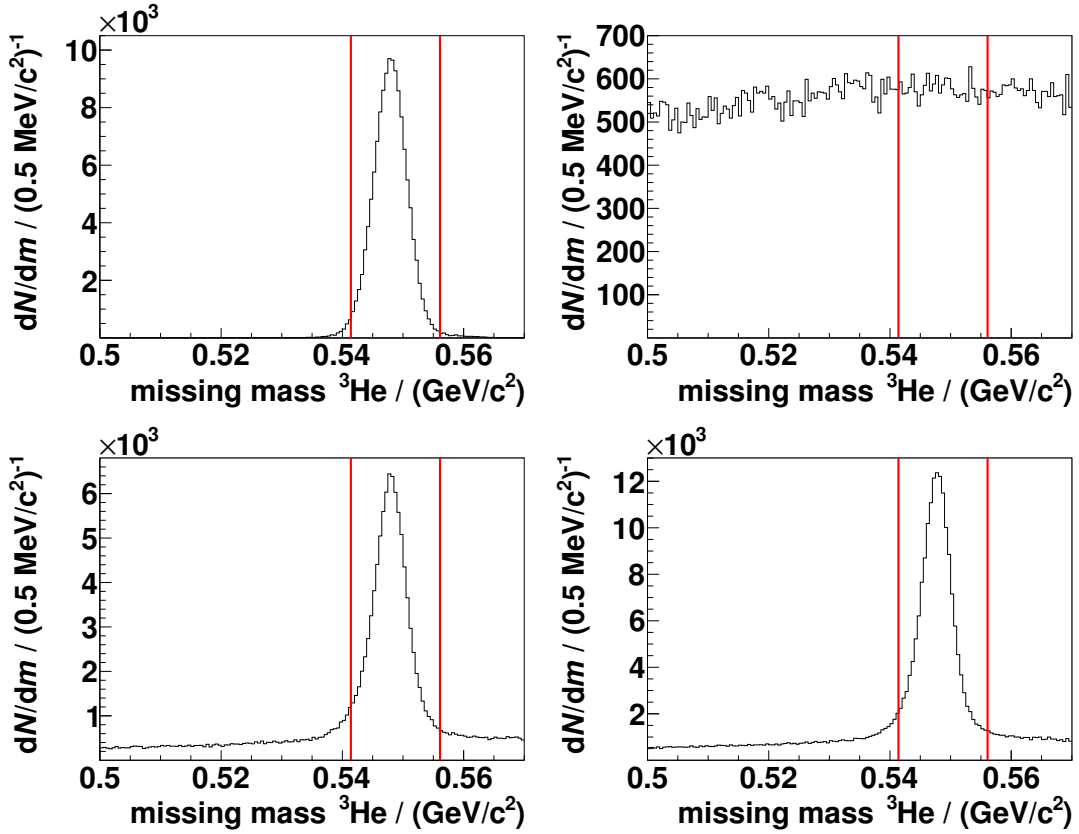

Figure 6.49.: ^{3}He missing mass for the simulated reaction $p + d \rightarrow {}^3He + \eta$ with $\eta \rightarrow \pi^0 + e^+ + e^-$ (upper left), the simulated reaction $p + d \rightarrow {}^3He + \pi^0 + \pi^0$ (upper right), and for the 2008 and 2009 data sets (lower left and lower right, respectively). Only events within the red lines are accepted in the analysis. All presented data samples were preselected with the conditions given in chapter 6.5.

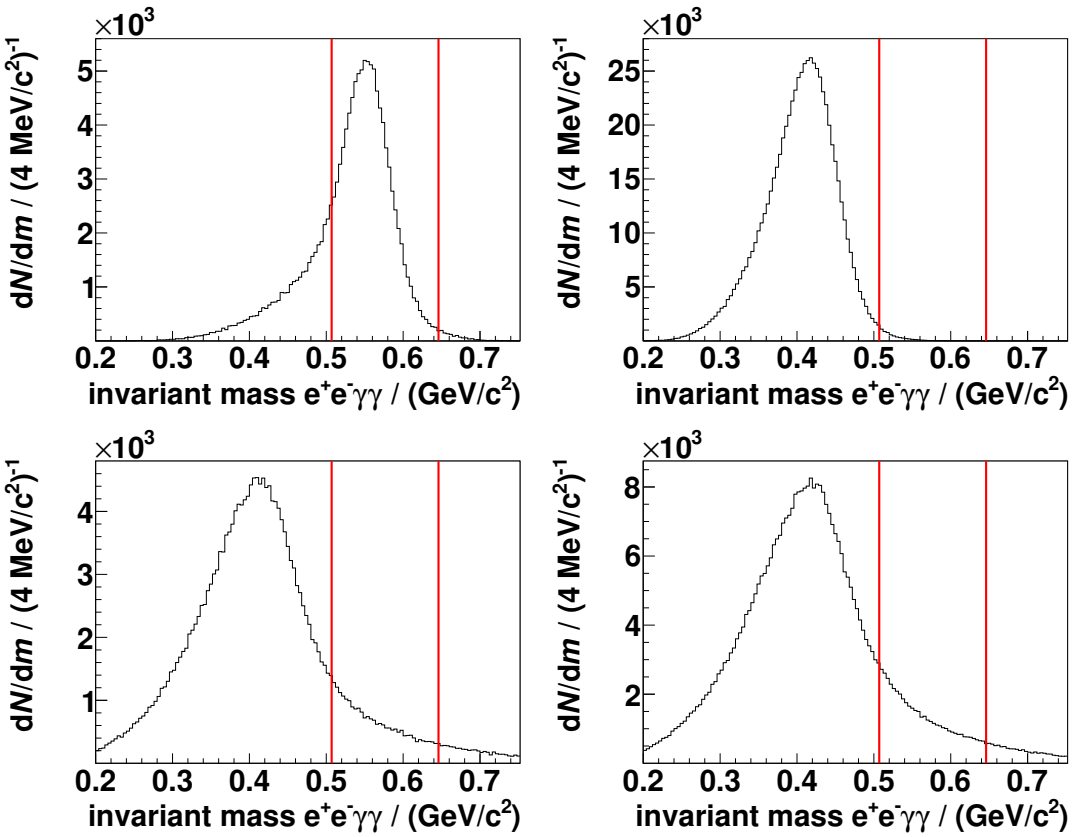

Figure 6.50.: Invariant mass of two photons and an electron-positron pair candidate for the simulated decays $\eta \to (\pi^0 \to \gamma + \gamma) + e^+ + e^-$ (upper left) and $\eta \to \pi^+ + \pi^- + (\pi^0 \to \gamma + \gamma)$ (upper right), as well as for the 2008 and 2009 data sets (lower left and lower right, respectively). Only events within the red lines are accepted in the analysis. All presented data samples were preselected with the conditions given in chapter 6.5.

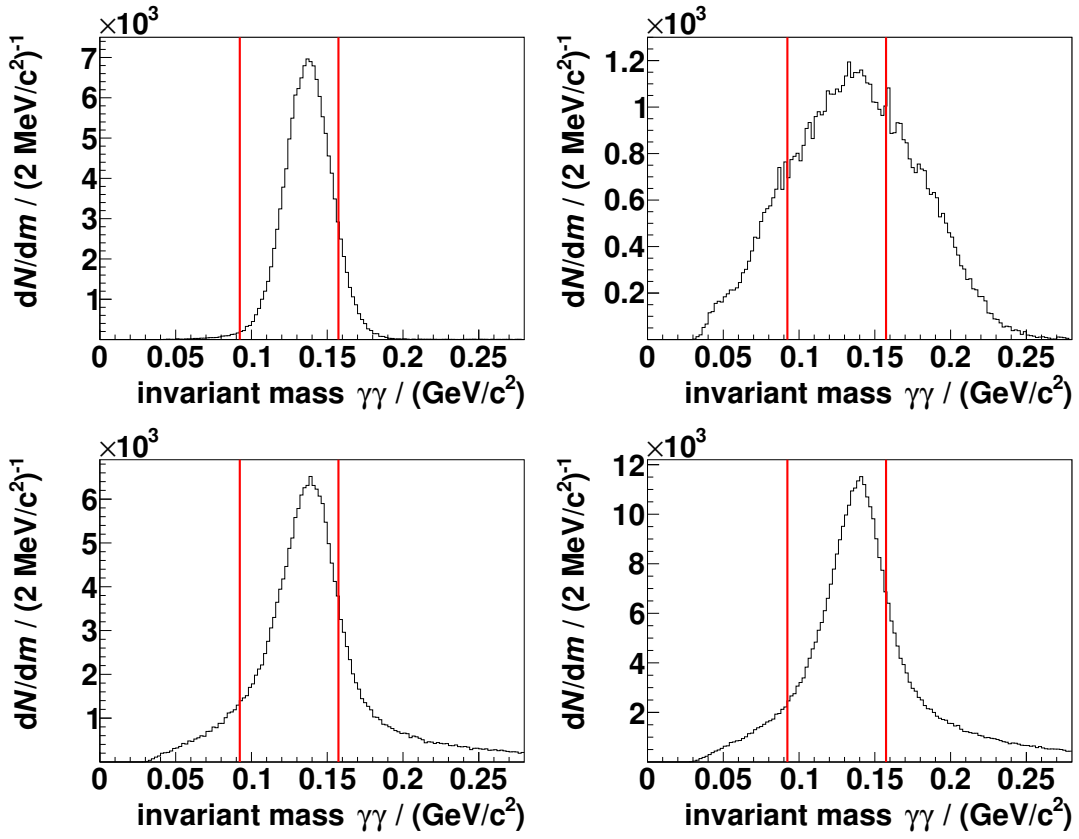

Figure 6.51.: Invariant mass of two photons for the simulated decay $\eta \to \pi^0 + e^+ + e^-$ (upper left), the simulated reaction $p + d \to {}^3He + \pi^+ + \pi^-$ (upper right), and the 2008 and 2009 data sets (lower left and lower right, respectively). Only events within the red lines are accepted in the analysis. All presented data samples were preselected with the conditions given in chapter 6.5.

$(\pi^0 \to \gamma + \gamma)$ to the data, whereas most events from the signal decay $\eta \to (\pi^0 \to \gamma + \gamma) + e^+ + e^-$ remain (see figure 6.50, upper right and upper left). Due to the difference between the charged pion and electron mass, the invariant mass distribution peaks at a lower mass than the η mass for the background decay. This peak is visible in the 2008 and 2009 data sets, as well (see figure 6.50, lower left and lower right, respectively).

In order to identify the decay $\pi^0 \to \gamma + \gamma$ and to reduce the contributions from reactions without a produced π^0, a cut on the invariant mass of two photons around the π^0 mass $m_{\pi^0} = (134.9766 \pm 0.0006)\,\mathrm{MeV}\,c^{-2}$ is applied [P+16]. As illustrated in figure 6.51, most events with a produced π^0 meson remain after application of the found selection conditions indicated by the red lines.

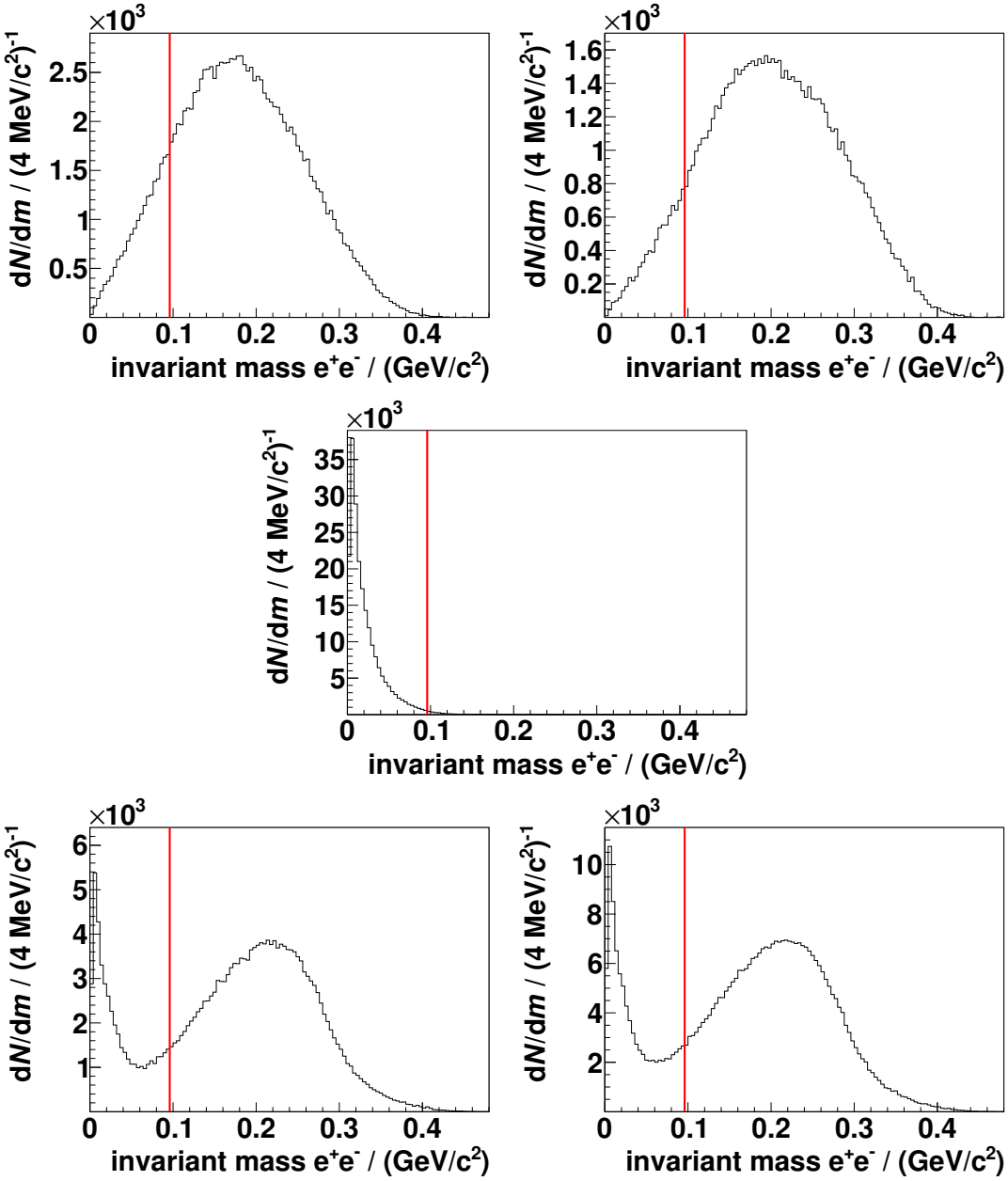

Figure 6.52.: Invariant mass of an electron-positron pair candidate for the simulated decay $\eta \to \pi^0 + e^+ + e^-$ via a virtual photon (upper left) and assuming a decay according to three-particle phase space (upper right), the simulated reaction $p + d \to {}^3He + \pi^0 + \pi^0$ (middle), and the 2008 and 2009 data sets (lower left and lower right, respectively). Events with an invariant mass below the mass indicated by the red line are rejected in the analysis. The presented data samples were preselected with the conditions given in chapter 6.5.

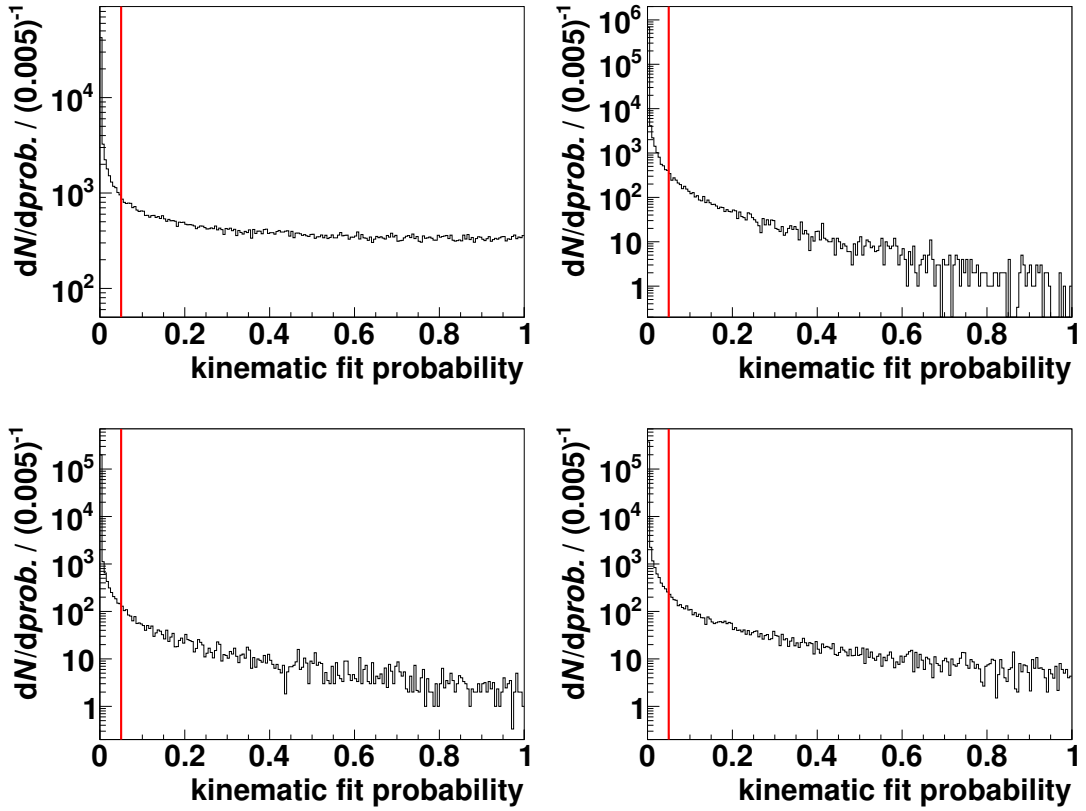

Figure 6.53.: χ^2 probability of the kinematic fit with the hypothesis $\mathrm{p} + \mathrm{d} \rightarrow {}^3\mathrm{He} + \mathrm{e}^+ + \mathrm{e}^- + \gamma + \gamma$ for the simulated decays $\eta \rightarrow (\pi^0 \rightarrow \gamma + \gamma) + \mathrm{e}^+ + \mathrm{e}^-$ (upper left) and $\eta \rightarrow \pi^+ + \pi^- + (\pi^0 \rightarrow \gamma + \gamma)$ (upper right), and for the 2008 and 2009 data sets (lower left and lower right, respectively). The minimum probability of 0.05 requested in the analysis is indicated by the red line. All samples were preselected with the conditions presented in chapter 6.5.

Figure 6.52 illustrates the distribution of the invariant mass of an electron-positron pair candidate. Both for the simulated decay $\eta \rightarrow \pi^0 + \mathrm{e}^+ + \mathrm{e}^-$ via a virtual photon (upper left) and assuming a decay according to three-particle phase space (upper right), the majority of events has an invariant mass above $0.096\,\mathrm{GeV}\,c^{-2}$, whereas the distribution of the simulated reaction $\mathrm{p} + \mathrm{d} \rightarrow {}^3\mathrm{He} + \pi^0 + \pi^0$ peaks close to $0\,\mathrm{GeV}\,c^{-2}$ (middle figure). Hence, the cut at a minimum invariant mass of $0.096\,\mathrm{GeV}\,c^{-2}$ rejects most events from this background reaction, which is also visible in data (lower left and lower right figure). The enhancement at higher masses originates from reactions with charged pions (see chapter 6.6.2).

According to the cut optimization algorithm, a minimum χ^2 probability of the kinematic fit of 0.05 in combination with the other selection conditions is sufficient

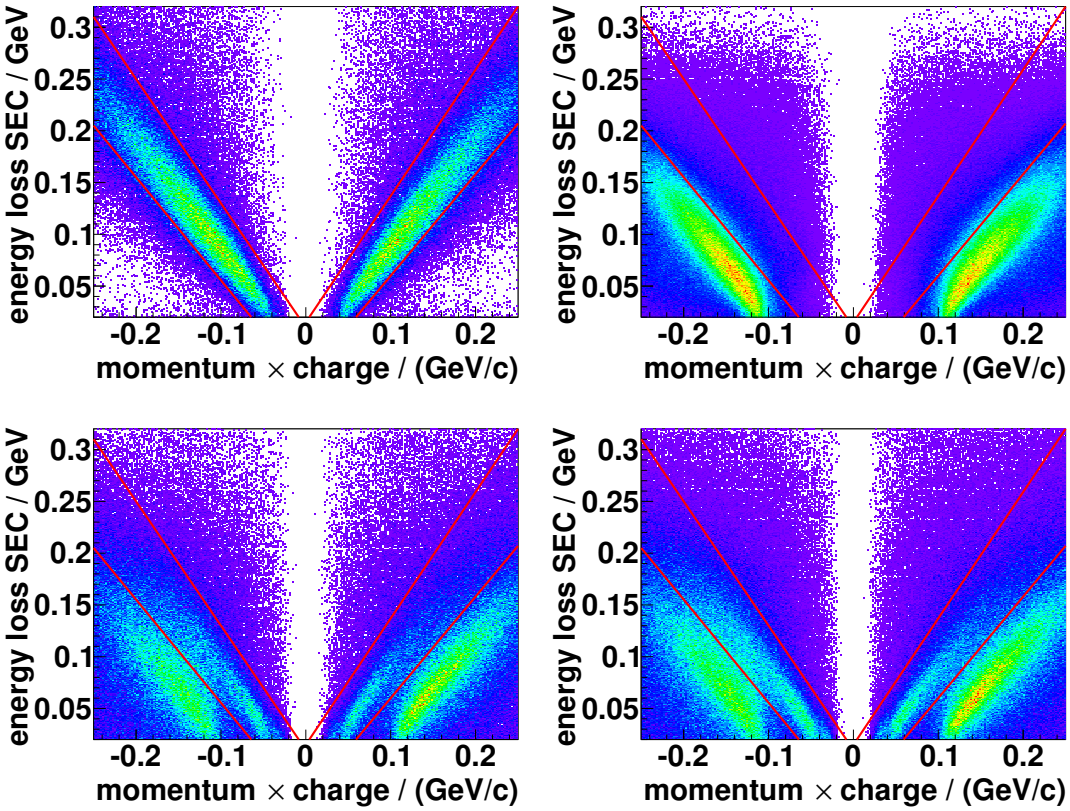

Figure 6.54.: Energy loss of charged particles in the SEC plotted against their momentum times charge for the simulated decays $\eta \to \pi^0 + e^+ + e^-$ (upper left) and $\eta \to \pi^+ + \pi^- + \pi^0$ (upper right) as well as for the 2008 and 2009 data sets (lower left and lower right, respectively) in linear scale. All data samples were preselected with the conditions presented in chapter 6.5. The selection conditions utilized in the analysis are illustrated by the red lines.

to suppress most background reactions. In figure 6.53 the according distributions are presented for the simulated decays $\eta \to (\pi^0 \to \gamma + \gamma) + e^+ + e^-$ (upper left figure) and $\eta \to \pi^+ + \pi^- + (\pi^0 \to \gamma + \gamma)$ (upper right figure), and for the 2008 and 2009 data sets (lower left and lower right figure, respectively). While for the signal decay the probability distribution is flat for higher probabilities, a continuous decrease of the distribution can be observed for the data recorded in 2008 and 2009, as expected from background reactions.

The last condition utilized in the analysis with regard to the decay $\eta \to \pi^0 + e^+ + e^-$ is the cut for the electron and positron identification. It is based on the energy loss of the charged particles in the SEC and their momentum and shown in figure 6.54. The chosen selection conditions, indicated by the red lines, allow to

reduce the contributions from reactions with charged pions to the data, whereas the majority of events from reactions with electrons and positrons remain after the selection conditions are applied.

7. Results and systematics of the analysis of the η meson decay $\eta \to \pi^0 + e^+ + e^-$

After the optimal selection conditions were determined (see chapter 6.7), they were applied both to the measured data and a Monte Carlo test sample. This test sample consisted of 60 % of all simulated background reactions listed in tables 6.2 and 6.3, whereas the optimization was based on the other 40 %. In case of the reaction $p + d \to {}^3He + \pi^0 + \pi^0$, additional 6×10^8 events were simulated and analyzed to further reduce the statistical uncertainty for this background reaction.

In table 7.1 the numbers of events remaining for the 2008 and 2009 data sets are compared to the numbers of events expected according to Monte Carlo simulations. In total three events of the data pass the preselection and selection conditions described in chapters 6.5 and 6.7.2, and the expected number of background events is 1.988 events[1]. These about two events originate from the direct $\pi^0\pi^0$ production, whereas contributions from other reactions can be neglected (see table 7.1, lower part). As this number is compatible with the three events seen in data, there is no observation of the decay $\eta \to \pi^0 + e^+ + e^-$ and, hence, no branching ratio for this decay will be determined, but an upper limit for the branching ratio.

Figure 7.1 illustrates the distributions of the quantities utilized for the event selection for the remaining events. The data are shown in black, and the Monte Carlo events, scaled according to the fit described in chapter 6.6.2, are presented in red. In addition, the selection conditions from table 6.12 are indicated by the blue dashed lines.

For comparison the missing mass, invariant mass and kinematic fit probability distributions of the remaining events for the simulated signal decay $\eta \to (\pi^0 \to \gamma + \gamma) + e^+ + e^-$ are shown in figure 7.2, both for a decay via a virtual

[1] The statistical and systematic uncertainties of this number are determined in chapter 7.1.2.

Table 7.1.: Numbers of events remaining after applying the preselection and selection conditions given in chapters 6.5 and 6.7.2. In the lower part of the table simulated reactions with more than zero events left are listed in detail. The numbers for the simulated reactions were scaled to the data according to the fit given in chapter 6.6.2. The statistical and systematic uncertainties of the numbers of remaining Monte Carlo events are discussed in chapter 7.1.2.

	Number of events		
Beam time	2008	2009	total
Data	1	2	3
Monte Carlo	0.755	1.233	1.988
pure	0.470	0.703	1.173
with event overlap	0.285	0.530	0.815
Direct $\pi^0\pi^0$ production	0.755	1.232	1.987
pure	0.470	0.702	1.172
with event overlap	0.285	0.530	0.815
$\eta \to e^+ + e^- + e^+ + e^-$	2.28×10^{-4}	3.44×10^{-4}	5.72×10^{-4}
pure	5.4×10^{-5}	3.2×10^{-5}	8.6×10^{-5}
with event overlap	1.74×10^{-4}	3.12×10^{-4}	4.86×10^{-4}
$\eta \to \pi^0 + \gamma + \gamma$	3.37×10^{-4}	4.68×10^{-4}	8.05×10^{-4}
pure	3.37×10^{-4}	4.68×10^{-4}	8.05×10^{-4}
with event overlap	0	0	0

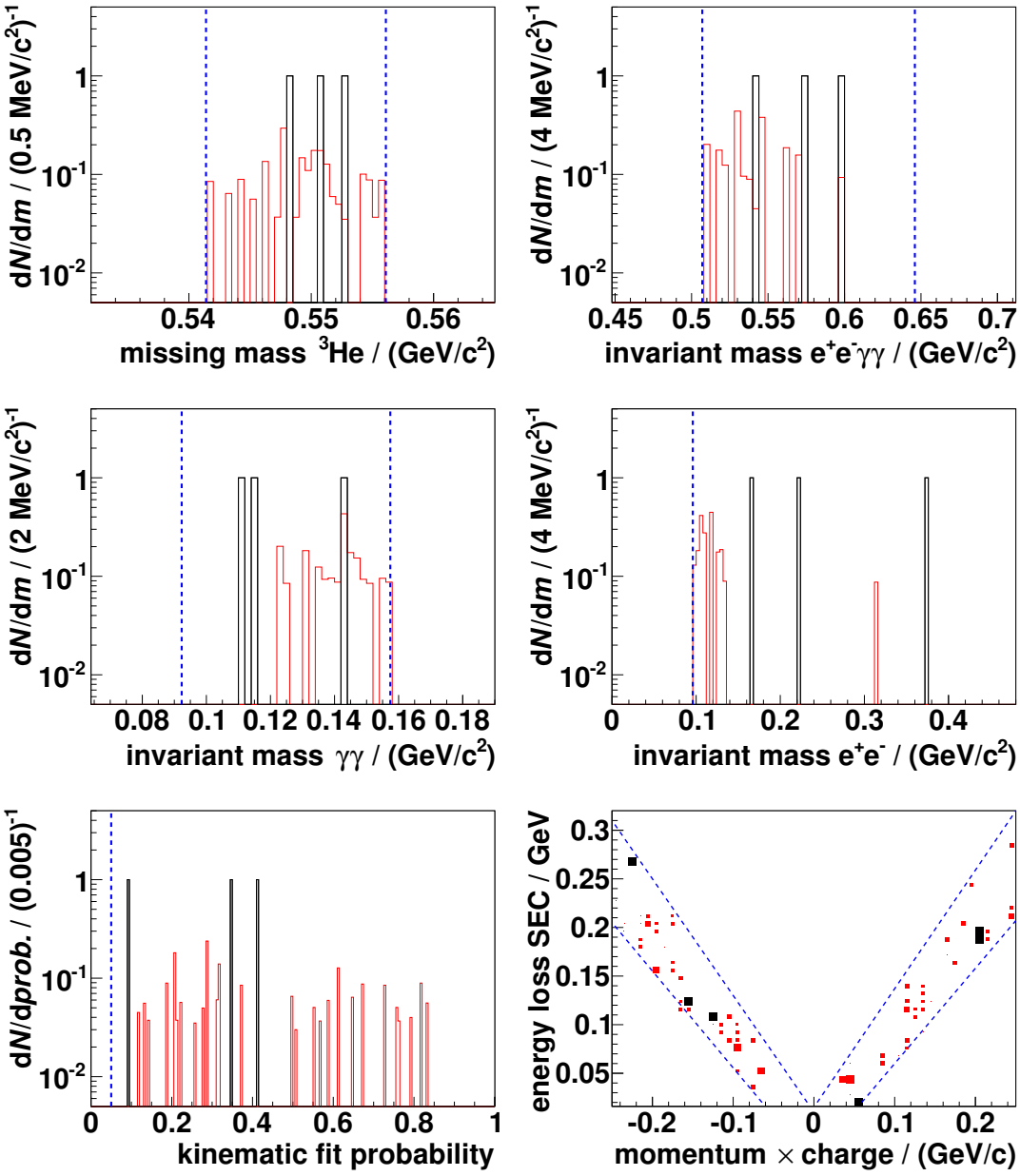

Figure 7.1.: Distributions of the different selection quantities for the measured data and Monte Carlo simulations, scaled according to the fit described in chapter 6.6.2, after application of the preselection and selection conditions given in chapters 6.5 and 6.7.2 (black and red histograms, respectively). The selection conditions are illustrated by blue dashed lines. Upper left: ^{3}He missing mass. Upper right: invariant mass of two oppositely charged and two neutral CD particles. Middle left: invariant mass of two neutral CD particles. Middle right: invariant mass of two oppositely charged CD particles. Lower left: χ^2 probability of the kinematic fit. Lower right: Energy loss of charged particles in the SEC plotted against their momentum times charge.

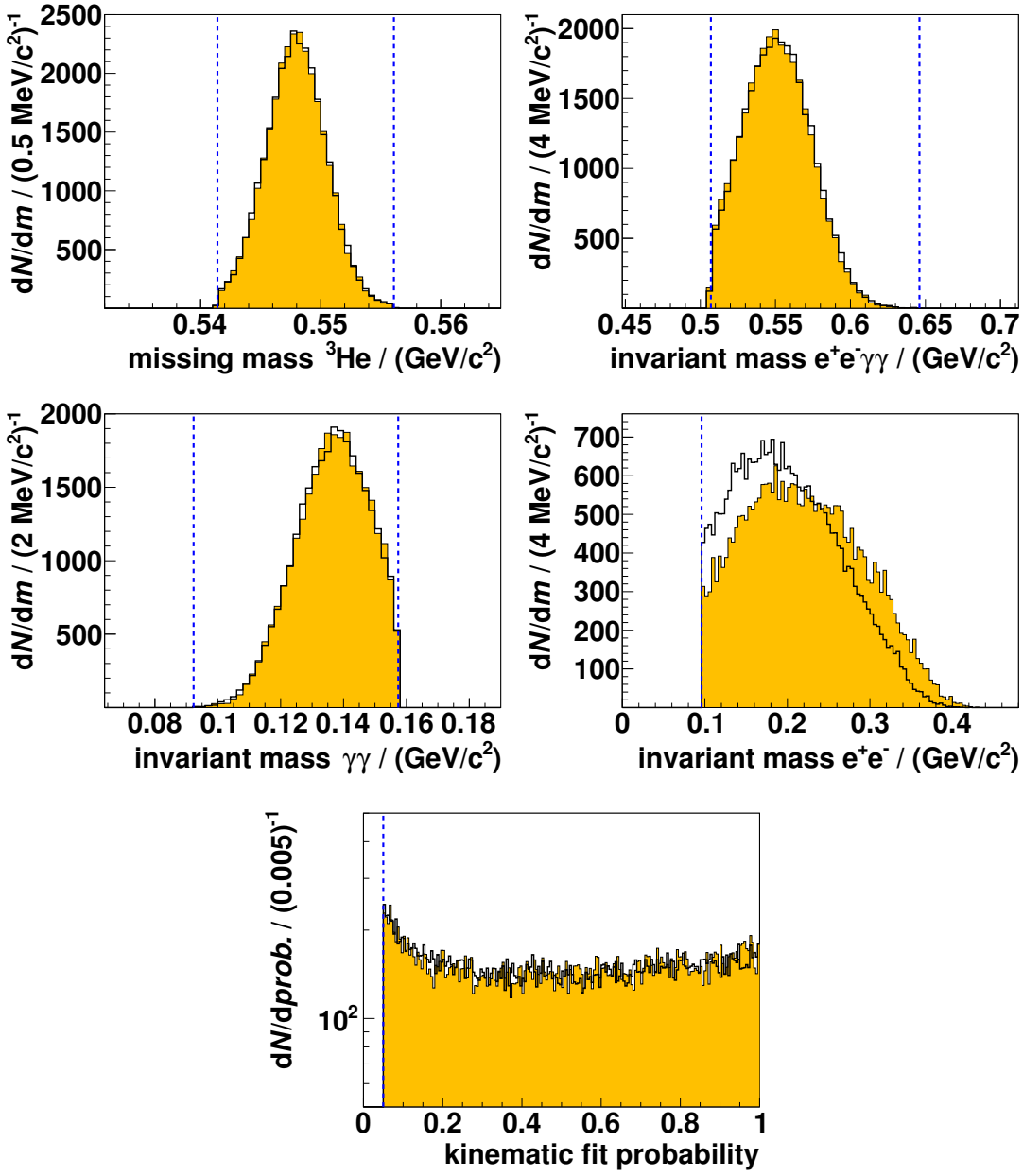

Figure 7.2.: Distributions of different selection quantities for the simulated decay $\eta \to (\pi^0 \to \gamma + \gamma) + e^+ + e^-$ assuming a decay via a virtual photon (black) and according to three-particle phase space (shadowed in orange, scaled to the former) after application of the preselection and selection conditions given in chapters 6.5 and 6.7.2. The selection conditions are illustrated by blue dashed lines. Upper left: ^{3}He missing mass. Upper right: invariant mass of two oppositely charged and two neutral CD particles. Middle left: invariant mass of two neutral CD particles. Middle right: invariant mass of two oppositely charged CD particles. Lower: χ^2 probability of the kinematic fit.

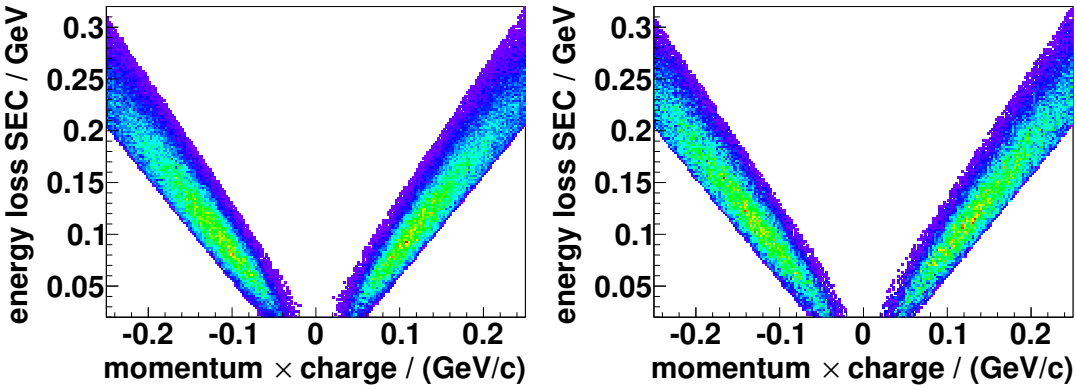

Figure 7.3.: Energy loss of charged particles in the SEC plotted against their momentum times charge for the simulated decay $\eta \to (\pi^0 \to \gamma + \gamma) + e^+ + e^-$ for a decay via a virtual photon (left) and according to three-particle phase space (right) after application of the preselection and selection conditions given in chapters 6.5 and 6.7.2. The histograms are presented in linear scale.

photon (black histograms) and for a decay according to three-particle phase space (histograms shadowed in orange). The histograms utilized for the PID for both decay models are presented in figure 7.3. For most quantities the distributions do not differ for the two decay models. The invariant mass of the electron-positron pair is an exception, as expected by the different models (see chapter 6.3.1). The difference in this distribution leads to a higher efficiency for the decay via one virtual photon of

$$\varepsilon_S^{\text{virtual}} = 0.023\,31(7) \tag{7.1}$$

compared to

$$\varepsilon_S^{\text{phase}} = 0.018\,44(7) \tag{7.2}$$

for the decay according to three-particle phase space for the analyzed angular range $-0.6 \leq \cos\vartheta_{\text{CMS}}^{\eta} \leq 1.0$. The given uncertainties are purely statistical.

In order to calculate an upper limit for the branching ratio of the decay $\eta \to \pi^0 + e^+ + e^-$, the decay $\eta \to \pi^+ + \pi^- + \pi^0$ is used for normalization. According to the MC fits presented in chapter 6.6.2, there are $(79\,029 \pm 409)$ events of the decay $\eta \to \pi^+ + \pi^- + (\pi^0 \to \gamma + \gamma)$ in the 2008 data set after preselection for the angular range $-0.6 \leq \cos\vartheta_{\text{CMS}}^{\eta} \leq 1.0$ and $(142\,303 \pm 537)$ events in the 2009 data set. A detailed list of the numbers of observed events of this decay channel for the various

angular ranges can be found in appendix B.3, tables B.1 and B.2, together with the individual efficiencies ε_{B}. According to these numbers, in total

$$N^{\text{produced}}_{\eta\to\pi^+\pi^-\pi^0} = (6.509 \pm 0.018) \times 10^6 \tag{7.3}$$

η mesons were produced in the 2008 and 2009 beam time that decayed via $\eta \to \pi^+ + \pi^- + (\pi^0 \to \gamma + \gamma)$ with $-0.6 \leq \cos\vartheta^{\eta}_{\mathrm{CMS}} \leq 1.0$.

For a proper determination of an upper limit the systematic uncertainties of the presented measurements and analyses have to be taken into account. This will be done in the following chapter 7.1.

7.1. Investigation of systematic effects

As discussed in chapter 2.8 the upper limit for the relative branching ratio $\Gamma(\eta \to \pi^0 + \mathrm{e}^+ + \mathrm{e}^-)/\Gamma(\eta \to \pi^+ + \pi^- + \pi^0)$ can be calculated by

$$\begin{aligned}
&\frac{\Gamma(\eta \to \pi^0 + \mathrm{e}^+ + \mathrm{e}^-)}{\Gamma(\eta \to \pi^+ + \pi^- + \pi^0)} \\
&= \frac{\Gamma(\eta \to (\pi^0 \to \gamma + \gamma) + \mathrm{e}^+ + \mathrm{e}^-)}{\Gamma(\eta \to \pi^+ + \pi^- + (\pi^0 \to \gamma + \gamma))} \cdot \frac{\Gamma(\pi^0 \to \gamma + \gamma)}{\Gamma(\pi^0 \to \gamma + \gamma)} \\
&= \frac{\Gamma(\eta \to (\pi^0 \to \gamma + \gamma) + \mathrm{e}^+ + \mathrm{e}^-)}{\Gamma(\eta \to \pi^+ + \pi^- + (\pi^0 \to \gamma + \gamma))} < \frac{N_{\mathrm{S,up}}}{N^{\text{produced}}_{\eta\to\pi^+\pi^-\pi^0} \cdot \varepsilon_{\mathrm{S}}}
\end{aligned} \tag{7.4}$$

with the number $N^{\text{produced}}_{\eta\to\pi^+\pi^-\pi^0}$ of produced η mesons decaying via $\eta \to \pi^+ + \pi^- + (\pi^0 \to \gamma + \gamma)$, the efficiency for the signal decay ε_{S}, and the upper limit for the number of signal events $N_{\mathrm{S,up}}$. The upper limit $N_{\mathrm{S,up}}$ depends on the number of events observed in data as well as on the number of events expected for the background according to simulations. Furthermore, for a proper determination of the upper limit $N_{\mathrm{S,up}}$ statistical and systematic uncertainties have to be considered. These can be separated into uncertainties by multiplicative effects, namely an uncertainty of the signal efficiency and an uncertainty of the number of $\eta \to \pi^+ + \pi^- + (\pi^0 \to \gamma + \gamma)$ events (see chapter 7.1.1), and an uncertainty by offset effects, which is an uncertainty for the number of events expected from background reactions (see chapter 7.1.2). In addition, to exclude systematic effects due to the choice of selection conditions, effects introduced by different conditions will be investigated (see chapter 7.1.3).

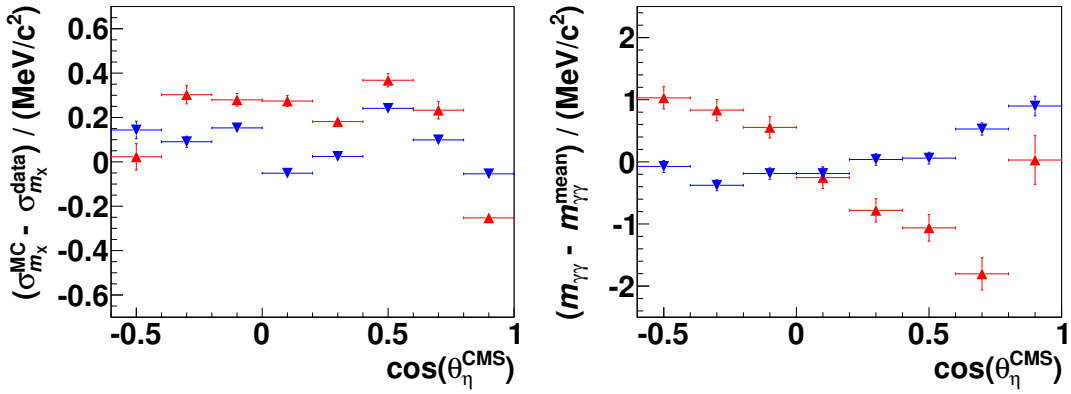

Figure 7.4.: Left: Residual $\sigma^{\mathrm{MC}}_{m_X} - \sigma^{\mathrm{data}}_{m_X}$ depending on $\cos\vartheta^{\mathrm{CMS}}_{\eta}$ for the 2008 and 2009 data sets (red triangles and blue inverted triangles, respectively). Right: Residual $m_{\gamma\gamma} - m^{\mathrm{mean}}_{\gamma\gamma}$ depending on $\cos\vartheta^{\mathrm{CMS}}_{\eta}$ for the 2008 and 2009 data sets (red triangles and blue inverted triangles, respectively). The horizontal error bars indicate the bin width, whereas the vertical error bars are statistical uncertainties.

7.1.1. Signal efficiency and number of $\eta \to \pi^+ + \pi^- + \pi^0$ events

The determination of reconstruction efficiencies depends on the precise knowledge of the detector resolution, as a different detector resolution can lead to a different efficiency. In the analysis presented in this thesis the efficiencies were determined by Monte Carlo simulations. The smearing parameters of these simulations were optimized to agree with the detector resolutions seen in data (see chapter 6.4). Since these parameters and the detector resolution can only be determined with a certain precision, the smearing parameters of the simulations will be varied to identify the influence on the efficiencies for the signal decay $\eta \to (\pi^0 \to \gamma + \gamma) + e^+ + e^-$ and the normalization channel $\eta \to \pi^+ + \pi^- + (\pi^0 \to \gamma + \gamma)$. It is important to note that the uncertainties of these two efficiencies are not independent and, therefore, will be investigated simultaneously.

Forward detector smearing parameters

In chapter 6.4.1 the MC smearing parameters for the forward detector were set to obtain a good agreement of the ^{3}He missing mass resolution of the η meson peak between simulations and data. Nonetheless, there are minor deviations of the standard deviation σ_{m_X} between Monte Carlo and data depending on $\cos\vartheta^{\mathrm{CMS}}_{\eta}$, as illustrated in the left of figure 7.4 for the 2008 and 2009 data sets for the analyzed angular range $-0.6 \leq \cos\vartheta^{\mathrm{CMS}}_{\eta} \leq 1.0$ (red triangles and blue inverted triangles,

Table 7.2.: Monte Carlo smearing parameter sets $\mathrm{FD}_{\mathrm{smear}}$ for the forward detector.

$\mathrm{FD}_{\mathrm{smear}}$	ΔE / MeV	ΔE_{rel}	*p.e.* / MeV	$\Delta\vartheta_{\mathrm{rel}}$ (2008)	$\Delta\vartheta_{\mathrm{rel}}$ (2009)
0	0.002 50	0.013	85	0.014	0.010
+	0.002 65	0.014	60	0.015	0.011
−	0.002 30	0.012	105	0.013	0.009

respectively). The mean of the residuals are $\Delta\sigma_{m_{\mathrm{X}}}^{\mathrm{mean}} = 0.26\,\mathrm{MeV}\,c^{-2}$ for the 2008 data set and $\Delta\sigma_{m_{\mathrm{X}}}^{\mathrm{mean}} = 0.13\,\mathrm{MeV}\,c^{-2}$ for the 2009 data set.

In order to test the systematics introduced by this uncertainty, the smearing parameters for the FD were varied to achieve a ^{3}He missing mass resolution which is larger (+) or smaller (−) by $\Delta\sigma_{m_{\mathrm{X}}} = 0.26\,\mathrm{MeV}\,c^{-2}$. Table 7.2 lists the corresponding parameters. The $\mathrm{FD}_{\mathrm{smear}}$ set marked by 0 is the default one and used in the main analysis.

Central detector smearing parameters

For the central detector the same MC smearing parameters were used for the 2008 and 2009 data sets. A test of these parameters was done by investigating the standard deviation $\sigma_{m_{\gamma\gamma}}$ of the π^0 meson peak in the distribution of the invariant mass of two photons. As the difference of $\sigma_{m_{\gamma\gamma}}$ between the 2008 and the 2009 data set is larger than the deviation between data and simulations, this is used as the uncertainty. It is

$$\begin{aligned} \sigma_{m_{\gamma\gamma}}^{2008} &= 18.0\,\mathrm{MeV}\,c^{-2} \\ \sigma_{m_{\gamma\gamma}}^{2009} &= 16.8\,\mathrm{MeV}\,c^{-2} \\ \Rightarrow \Delta\sigma_{m_{\gamma\gamma}} &= 1.2\,\mathrm{MeV}\,c^{-2}\,. \end{aligned} \tag{7.5}$$

Similar to the FD parameters, the CD smearing parameters were varied to obtain a standard deviation $\sigma_{m_{\gamma\gamma}}$ that is larger (+) or smaller (−) by $\Delta\sigma_{m_{\gamma\gamma}} = 1.2\,\mathrm{MeV}\,c^{-2}$ (see table 7.3, left). The $\mathrm{CD}_{\mathrm{smear}}$ set marked by 0 is the default one and used in the main analysis. Unlike for the FD, only the parameter for the average number of photo-electrons per MeV (*p.e.* / MeV) was varied, since it is the main smearing parameter for the central detector.

Table 7.3.: Left: Monte Carlo smearing parameter sets $\mathrm{CD}_{\mathrm{smear}}$ for the central detector. Right: Monte Carlo scaling parameter sets $\mathrm{CD}_{\mathrm{factor}}$ for the central detector.

$\mathrm{CD}_{\mathrm{smear}}$	ΔE / MeV	ΔE_{rel}	*p.e.* / MeV
0	0.0005	0.055	0.625
+	0.0005	0.055	0.494
−	0.0005	0.055	0.816

$\mathrm{CD}_{\mathrm{factor}}$	Scaling factor
0	1.142
+	1.150
−	1.134

Central detector scaling factor

Besides parameters for the detector smearing, a scaling factor for the energy loss in the SEC is used for the Monte Carlo simulations. For the investigation of systematic effects the π^0 meson peak in the invariant mass spectrum of two photons is checked again. Its position should be constant and independent of $\cos\vartheta_{\eta}^{\mathrm{CMS}}$. In the right of figure 7.4 the residual $m_{\gamma\gamma} - m_{\gamma\gamma}^{\mathrm{mean}}$ is plotted for the angular range $-0.6 \leq \cos\vartheta_{\eta}^{\mathrm{CMS}} \leq 1.0$ for the 2008 and 2009 data sets (red triangles and blue inverted triangles, respectively). Both for the 2008 and the 2009 data set a variance larger than the statistical uncertainties was observed. While the mean deviation for the 2008 data is $0.9\,\mathrm{MeV}\,c^{-2}$, it is $0.4\,\mathrm{MeV}\,c^{-2}$ for the 2009 data set.

To investigate the systematic effect of this deviation, the scaling factor was varied to achieve a mean peak position that is larger (+) or smaller (−) by $0.9\,\mathrm{MeV}\,c^{-2}$. In the right of table 7.3 the corresponding factors are listed. The $\mathrm{CD}_{\mathrm{factor}}$ set marked by 0 is the default one and used in the main analysis.

Since the systematic effects mentioned above can correlate, all possible combinations of $\mathrm{FD}_{\mathrm{smear}}$, $\mathrm{CD}_{\mathrm{smear}}$, and $\mathrm{CD}_{\mathrm{factor}}$ sets were tested, and the corresponding signal efficiencies and numbers of events of the decay $\eta \to \pi^+ + \pi^- + (\pi^0 \to \gamma + \gamma)$ were determined. These are listed in detail for the decay $\eta \to (\pi^0 \to \gamma + \gamma) + \mathrm{e}^+ + \mathrm{e}^-$ via a virtual photon and for a decay according to three-particle phase space in tables B.3 and B.4 in appendix B.4. To obtain the systematic uncertainty, the factor $1/\left(\varepsilon_{\mathrm{S}} \cdot N_{\eta\to\pi^+\pi^-\pi^0}\right)$ was calculated, as well as its relative deviation Δ_{rel} from the value of the standard set (0 0 0).

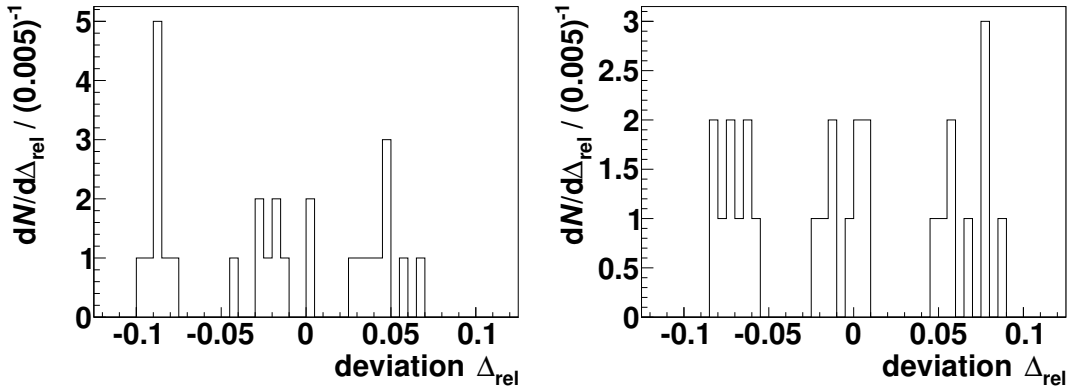

Figure 7.5.: Relative deviation Δ_{rel} of the factor $1/\left(\varepsilon_{\mathrm{S}} \cdot N_{\eta\to\pi^+\pi^-\pi^0}\right)$ for the different combinations of $\mathrm{FD_{smear}}$, $\mathrm{CD_{smear}}$ and $\mathrm{CD_{factor}}$ sets from the value for the standard set (0 0 0) for the decay $\eta \to (\pi^0 \to \gamma + \gamma) + \mathrm{e}^+ + \mathrm{e}^-$ via a virtual photon and for a decay according to three-particle phase space (left and right, respectively).

Figure 7.5 shows the corresponding distributions for the signal decay via a virtual photon and according to three-particle phase space (left and right, respectively). The relative variance for the decay via a virtual photon is

$$\mathrm{Var}_{\mathrm{rel}}^{\mathrm{virtual}}\left(\frac{1}{\varepsilon_{\mathrm{S}} \cdot N_{\eta\to\pi^+\pi^-\pi^0}}\right) = 0.059\,, \text{ and} \tag{7.6}$$

$$\mathrm{Var}_{\mathrm{rel}}^{\mathrm{phase}}\left(\frac{1}{\varepsilon_{\mathrm{S}} \cdot N_{\eta\to\pi^+\pi^-\pi^0}}\right) = 0.057 \tag{7.7}$$

for a decay according to three-particle phase space. These will be treated as systematic uncertainties for the upper limit determination.

Number of $\eta \to \pi^+ + \pi^- + \pi^0$ events

The number of $\eta \to \pi^+ + \pi^- + \pi^0$ events in the 2008 and 2009 data sets was determined after preselection (see chapter 6.6). To investigate systematics introduced by the preselection, less strict conditions were utilized instead for comparison, namely:

- For the energy loss of the neutral particles in the SEC a minimum energy of 10 MeV was requested instead of 20 MeV,
- no conditions for the momenta of the charged CD particles were applied,
- no conversion cut was utilized, and

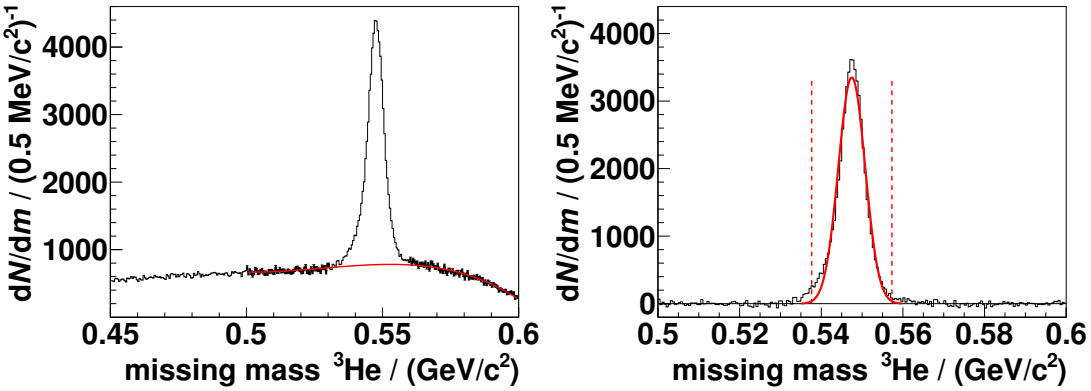

Figure 7.6.: Missing mass of ^{3}He for the angular range $-0.4 \leq \cos\vartheta_\eta^{\mathrm{CMS}} < -0.2$ for the 2008 data set. Left: Background fitted by a fourth order polynomial (red curve). The fit range is indicated by the black points. Right: Peak fitted by a Gaussian distribution after background subtraction (red curve). The left and right red dashed lines indicate the $\pm 3\sigma$ environment. The data were preselected with the conditions described in this chapter.

- no conditions to reduce background from split-off events from charged as well as from neutral particles were used. This also includes the cut on the invariant mass of a photon and a charged particle.

For the extraction of the numbers of $\mathrm{p + d \rightarrow {}^3He + \eta}$ events in the 2008 and 2009 data sets the same procedure as described in chapter 6.6.1 was used: The background below the η meson peak in the ^{3}He missing mass distributions was fitted by a polynomial for eight angular ranges ranging from $-0.6 \leq \cos\vartheta_\eta^{\mathrm{CMS}} < -0.4$ to $0.8 \leq \cos\vartheta_\eta^{\mathrm{CMS}} \leq 1.0$. For the fit a fourth order polynomial was utilized, as it leads to a slightly better description than a third order polynomial due to the larger background (see left of figure 7.6). After the background was subtracted, the peak was fitted by a Gaussian distribution and all events within the $\pm 3\sigma$ environment were counted (see right of figure 7.6).

In order to correct these numbers for the reconstruction efficiency, Monte Carlo simulations of the various η meson decays were analyzed with the same conditions and fitted by Gaussian distributions to count the number of events within the $\pm 3\sigma$ environment. These numbers were compared to the generated ones to receive the reconstruction efficiencies for each decay channel, and the efficiency corrections were applied to the numbers seen in data according to the branching ratios of the η decays listed in [P$^+$16]. According to this analysis, there were in total $(2.808 \pm 0.007) \times 10^7$ η mesons produced via the reaction $\mathrm{p + d \rightarrow {}^3He + \eta}$ in the angular range $-0.6 \leq \cos\vartheta_\eta^{\mathrm{CMS}} \leq 1.0$ in the analyzed 2008 and 2009 beam

Table 7.4.: Unscaled numbers of events for the simulated reaction $p + d \to {}^3He + \pi^0 + \pi^0$ remaining after applying the preselection and selection conditions given in chapters 6.5 and 6.7.2, and the corresponding confidence intervals according to Poisson statistics.

	Monte Carlo 2008		Monte Carlo 2009	
	pure	with overlap	pure	with overlap
Number of events	14	5	13	4
Poisson interval (CL = 68.27 %)	10.3 to 18.8	2.8 to 8.4	9.4 to 17.7	2.1 to 7.2

times. As the branching ratio for the decay $\eta \to \pi^+ + \pi^- + \pi^0$ is $(22.92 \pm 0.28)\,\%$ and $(98.823 \pm 0.034)\,\%$ for the decay $\pi^0 \to \gamma + \gamma$ [P+16], the number of produced η mesons that decayed via $\eta \to \pi^+ + \pi^- + (\pi^0 \to \gamma + \gamma)$ can be calculated as:

$$N^{\text{produced,sys}}_{\eta \to \pi^+\pi^-\pi^0} = (6.36 \pm 0.08) \times 10^6\,. \tag{7.8}$$

This number differs by 2.3 % from the $(6.509 \pm 0.018) \times 10^6$ η mesons, as determined in equation 7.3 at the beginning of chapter 7. Because this difference cannot be explained by statistical uncertainties and systematic uncertainties of the fitting procedures alone, it is treated as an additional systematic uncertainty for the upper limit determination.

7.1.2. Number of remaining $p + d \to {}^3He + \pi^0 + \pi^0$ events

As discussed at the beginning of chapter 7, about two events from the direct $\pi^0\pi^0$ production are estimated to remain in data after all preselection and selection conditions were applied, whereas no significant contributions from other background reactions are expected. Therefore, in this chapter the uncertainties for the number of $p + d \to {}^3He + \pi^0 + \pi^0$ events will be discussed.

Statistical uncertainty

The first uncertainties that need to be considered originate from the limited statistics of the Monte Carlo simulations. In table 7.4 the unscaled numbers of events of the simulated reaction $p + d \to {}^3He + \pi^0 + \pi^0$ that pass all cuts are listed together with the CL = 68.27 % confidence interval according to Poisson statistics.

In the program used for the upper limit determination the uncertainties due to Poisson statistics are considered.

Systematic uncertainty

As already mentioned in chapter 6.6.2, there are systematic uncertainties for the number of $p+d \rightarrow {}^3He+\pi^0+\pi^0$ events in the preselected data sets extracted by the Monte Carlo fit in addition to the statistical uncertainties. It is important to note that the fit parameters of the various simulations are correlated. Since these are several parameters, the uncertainties were not calculated directly, but a different method was chosen.

After the optimal fit with the best χ^2_{best} was found for a given angular range, the scaling parameter for the $\pi^0\pi^0$ production was fixed to a slightly different value than the optimal one. Afterwards the optimization of the fit was repeated to determine a new minimal χ^2_{sys}. This was done separately for all angular ranges for various values of the $\pi^0\pi^0$ fit parameter. All fit parameters with

$$\left|\chi^2_{\text{sys}} - \chi^2_{\text{best}}\right| \leq 1 \tag{7.9}$$

were considered for the determination of the systematic uncertainty. The maximal deviations of the numbers $N^{\text{sys}}_{\pi^0\pi^0}$ calculated using these parameters from the numbers $N_{\pi^0\pi^0}$ determined with the optimal fit parameters are defined as the positive and negative fit uncertainty ΔN_{fit}.

Tables 7.5 and 7.6 list the resulting fit uncertainties ΔN_{fit} for the extracted numbers of events $N_{\pi^0\pi^0}$ for the reaction $p + d \rightarrow {}^3He + \pi^0 + \pi^0$ depending on $\cos\vartheta_\eta^{\text{CMS}}$ for the 2008 and 2009 data sets. In case this uncertainty was larger than the corresponding statistical uncertainty ΔN_{stat}, the systematic uncertainty

$$\Delta N_{\text{sys,1}} = \sqrt{\Delta N^2_{\text{fit}} - \Delta N^2_{\text{stat}}} \tag{7.10}$$

was considered for the total systematic uncertainty. Otherwise $\Delta N_{\text{sys,1}}$ is equal to zero and left blank in the tables. Note that blank entries for ΔN_{fit} in table 7.6 correspond to uncertainty values below 20 events equaling the chosen minimal step size for the systematic tests of the fit parameters. This value is well below the statistical uncertainties ΔN_{stat} and, thus, was neglected.

In addition to the uncertainties of the $\pi^0\pi^0$ fit parameters, the parameter for the contribution of events with event overlap was investigated, both for the 2008

Table 7.5.: Extracted number of events $N_{\pi^0\pi^0}$ for the reaction $\mathrm{p+d} \to {}^3\mathrm{He}+\pi^0+\pi^0$ for the 2008 data set depending on the angular range with the statistical uncertainty ΔN_{stat}, the uncertainty ΔN_{fit} due to uncertainties of the fit parameters and the systematic uncertainty $\Delta N_{\mathrm{sys,1}}$ resulting thereof, as well as the systematic uncertainty $\Delta N_{\mathrm{sys,2}}$ introduced by differences between the fits of the 2008 and 2009 data sets.

$\cos\vartheta_\eta^{\mathrm{CMS}}$	$N_{\pi^0\pi^0}$	ΔN_{stat}	ΔN_{fit}	$\Delta N_{\mathrm{sys,1}}$	$\Delta N_{\mathrm{sys,2}}$
-0.6 – -0.4	3388	$+83$	$+67$	–	–
		-83	-67	–	–
-0.4 – -0.2	3219	$+83$	$+71$	–	–
		-83	-71	–	–
-0.2 – 0.0	2981	$+79$	$+68$	–	–
		-79	-68	–	–
0.0 – 0.2	2928	$+79$	$+77$	–	–
		-79	-77	–	–
0.2 – 0.4	2663	$+75$	$+77$	$+17$	–
		-75	-97	-60	–
0.4 – 0.6	1956	$+65$	$+266$	$+258$	$+356$
		-65	-230	-221	–
0.6 – 0.8	1731	$+60$	$+213$	$+205$	$+774$
		-60	-197	-187	–
0.8 – 1.0	0	$+1.1$	$+30$	$+30$	$+665$
		–	–	–	–

Table 7.6.: Extracted number of events $N_{\pi^0\pi^0}$ for the reaction $p + d \to {}^3He + \pi^0 + \pi^0$ for the 2009 data set depending on the angular range with the statistical uncertainty ΔN_{stat}, the uncertainty ΔN_{fit} due to uncertainties of the fit parameters and the systematic uncertainty $\Delta N_{sys,1}$ resulting thereof, as well as the systematic uncertainty $\Delta N_{sys,2}$ introduced by differences between the fits of the 2008 and 2009 data sets.

$\cos\vartheta_\eta^{CMS}$	$N_{\pi^0\pi^0}$	ΔN_{stat}	ΔN_{fit}	$\Delta N_{sys,1}$	$\Delta N_{sys,2}$
−0.6 – −0.4	6137	+113	+104	–	–
		−113	−26	–	–
−0.4 – −0.2	5715	+107	–	–	–
		−107	−26	–	–
−0.2 – 0.0	5495	+106	–	–	–
		−106	−26	–	–
0.0 – 0.2	5408	+105	–	–	–
		−105	−48	–	–
0.2 – 0.4	5122	+102	+105	+28	–
		−102	−21	–	–
0.4 – 0.6	5528	+106	+116	+48	–
		−106	−58	–	−852
0.6 – 0.8	5774	+108	–	–	–
		−108	–	–	−1785
0.8 – 1.0	2386	+69	+114	+91	–
		−69	−103	−76	−2386

Table 7.7.: Extracted number of events $N_{\pi^0\pi^0}$ for the reaction $p + d \to {}^3He + \pi^0 + \pi^0$ and $N_{\pi^0\pi^0\pi^0}$ for the reaction $p + d \to {}^3He + \pi^0 + \pi^0 + \pi^0$ for the 2008 and 2009 data sets depending on the angular range. The last column shows the ratio between the 2008 and 2009 data set for the reaction $p + d \to {}^3He + \pi^0 + \pi^0$.

	2008 data set		2009 data set		
$\cos\vartheta_\eta^{CMS}$	$N_{\pi^0\pi^0}$	$N_{\pi^0\pi^0\pi^0}$	$N_{\pi^0\pi^0}$	$N_{\pi^0\pi^0\pi^0}$	$\frac{N_{\pi^0\pi^0}(2009)}{N_{\pi^0\pi^0}(2008)}$
−0.6 – −0.4	3388	0	6137	0	$1.81^{+0.06}_{-0.06}$
−0.4 – −0.2	3219	0	5715	0	$1.78^{+0.06}_{-0.06}$
−0.2 – 0.0	2981	0	5495	0	$1.84^{+0.06}_{-0.06}$
0.0 – 0.2	2928	0	5408	0	$1.85^{+0.06}_{-0.06}$
0.2 – 0.4	2663	0	5122	0	$1.92^{+0.08}_{-0.07}$
0.4 – 0.6	1956	356	5528	0	$2.83^{+0.34}_{-0.4}$
0.6 – 0.8	1731	774	5774	0.2	$3.3^{+0.4}_{-0.4}$
0.8 – 1.0	0	665	2386	0	–

and the 2009 data set. For this purpose the same method as described above was used: The parameter for the contribution of event overlap was fixed to various values and the fit optimization was redone. Only parameters of fits that fulfilled equation 7.9 were used for the uncertainty determination. As already mentioned in chapter 6.6.2, the parameter for the event overlap contribution in the 2008 data set $par^{2008}_{overlap} = 61.7\,\%$ has an uncertainty of $^{+1.0}_{-0.9}\,\%$, whereas the parameter for the 2009 data set is $par^{2009}_{overlap} = 71.4^{+0.6}_{-0.5}\,\%$. The resulting uncertainty for $N_{\pi^0\pi^0}$ is less than 80 events, which is below the statistical uncertainty for both the 2008 and the 2009 data set. Therefore, this uncertainty can be neglected.

As stated in chapter 6.6.2, the contributions of the reaction $p + d \to {}^3He + \pi^0 + \pi^0 + \pi^0$ to the data according to the fits by MC simulations differ for the 2008 and 2009 data sets. Moreover, there are deviations of the $p + d \to {}^3He + \pi^0 + \pi^0$ contributions between the two data sets for some angular ranges. In table 7.7 the numbers of events for both reactions are listed for the 2008 and 2009 data sets depending on $\cos\vartheta_\eta^{CMS}$. In case of the reaction $p + d \to {}^3He + \pi^0 + \pi^0 + \pi^0$, the number of events $N_{\pi^0\pi^0\pi^0}$ is zero for all angular ranges in both data sets, except for the angular ranges $0.4 \leq \cos\vartheta_\eta^{CMS} < 0.6$, $0.6 \leq \cos\vartheta_\eta^{CMS} < 0.8$, and $0.8 \leq \cos\vartheta_\eta^{CMS} \leq 1.0$ in the 2008 data set. On the other hand, for the same angular ranges the ratio $N_{\pi^0\pi^0}(2009)/N_{\pi^0\pi^0}(2008)$ increases, whereas it is constant for the other angular ranges. These deviations are unexpected, as the branching ratios for

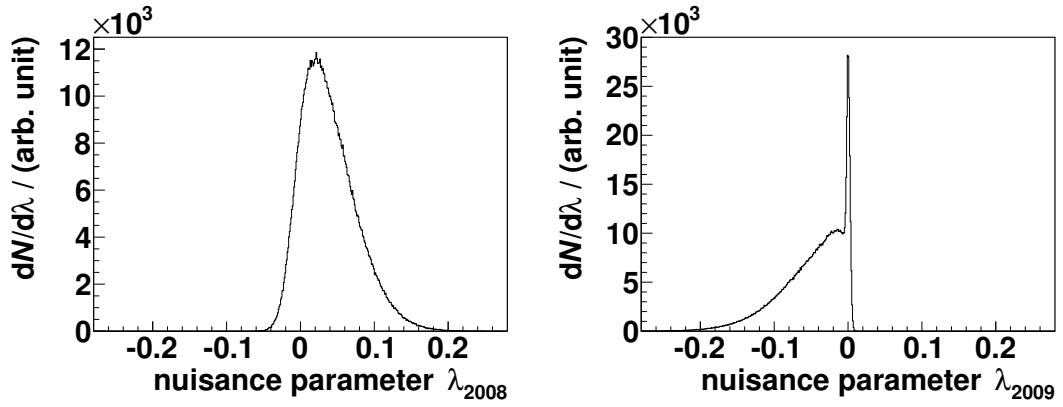

Figure 7.7.: Distributions of the nuisance parameters λ_{2008} and λ_{2009} for the systematic uncertainty of $N_{\pi^0\pi^0}$ in the 2008 and 2009 data sets (left and right, respectively).

both pion production reactions should be independent of the beam time. Since the extracted numbers of events for these two reactions are obviously correlated for these angular bins, the determined number $N_{\pi^0\pi^0\pi^0}$ was treated as an additional systematic uncertainty $\Delta N_{\mathrm{sys},2}$ of the number $N_{\pi^0\pi^0}$. It is possible that either the number $N_{\pi^0\pi^0}$ for the 2008 data set is too small by $N_{\pi^0\pi^0\pi^0}$, or that the number $N_{\pi^0\pi^0}$ for the 2009 data is too large by

$$\Delta N_{\mathrm{sys},2}(2009) = -N_{\pi^0\pi^0}(2009) \cdot \frac{N_{\pi^0\pi^0\pi^0}(2008)}{N_{\pi^0\pi^0}(2008) + N_{\pi^0\pi^0\pi^0}(2008)} \,. \tag{7.11}$$

The corresponding uncertainties are listed in the last column of tables 7.5 and 7.6.

Since the systematic uncertainties $\Delta N_{\mathrm{sys},1}$ and $\Delta N_{\mathrm{sys},2}$ are asymmetric, they cannot be added in quadrature to obtain the total systematic uncertainty of $N_{\pi^0\pi^0}$. Instead, the overall distribution of the nuisance parameters λ_{2008} and λ_{2009}, which correspond to the relative systematic uncertainties of $N_{\pi^0\pi^0}$, were determined with the aid of Monte Carlo simulations for the 2008 and the 2009 data set, respectively (see figure 7.7). While a distribution for a Gaussian uncertainty would be symmetric around zero, these distributions show a clear asymmetric behavior. Hence, no total systematic uncertainty for $N_{\pi^0\pi^0}$ will be given here, but the obtained distributions of these two nuisance parameters will be considered for the upper limit calculation in chapter 7.2.

7.1.3. Variation of the selection conditions

In chapters 6.5 and 6.7.2 the preselection and selection conditions utilized in the analysis were presented. To investigate possible systematic effects introduced by the choice of preselection and selection conditions, different conditions were tested and will be discussed in this chapter. In detail, one condition was varied at once and the number N_{data} of remaining events in the 2008 and 2009 data sets was compared to the number N_{MC} of remaining events according to Monte Carlo simulations. Since minor deviations are expected due to the limited statistics of both data and simulations, the variable κ was used as an indicator for possible systematic effects. It is defined as:

$$\kappa = \frac{N_{\text{data}} - N_{\text{MC}}}{\sqrt{\Delta N_{\text{data}}^2 + \Delta N_{\text{MC}}^2}} \,. \tag{7.12}$$

The uncertainties ΔN_{data} and ΔN_{MC} are given by the CL = 68.27 % confidence interval according to Poisson statistics. In case of the MC simulations, the uncertainties for the individual reactions were included with respect to their fit parameter used for scaling to data. Deviations with $|\kappa| \leq 2$ can be explained by statistical uncertainties and can be neglected, while larger deviations will be discussed. The systematic tests of the selection conditions were done separately for the 2008 and 2009 data sets.

^{3}He scattering angle ϑ_{LAB}

The first cut that was investigated were the selection conditions for the ^{3}He scattering angle ϑ_{LAB}. As the minimal scattering angle is limited by the COSY beam pipe, the conditions for this angle were varied from 2° to 4°, while the upper cut was fixed at the value used in the main analysis (17°). Tables B.6 and B.7 in appendix B.5 list the resulting numbers for the 2008 and 2009 data in detail. $|\kappa|$ remains below two for all conditions. Therefore, no systematic effect needs to be considered.

Energy loss E_{dep} of neutral and charged particles in the SEC

Typically stricter selection conditions result in a lower number of events remaining. However, the conditions used for the minimal energy loss of neutral and charged particles are applied before the check for split-off or conversion events. Since particles originating from split-off events typically have a low energy loss, fewer

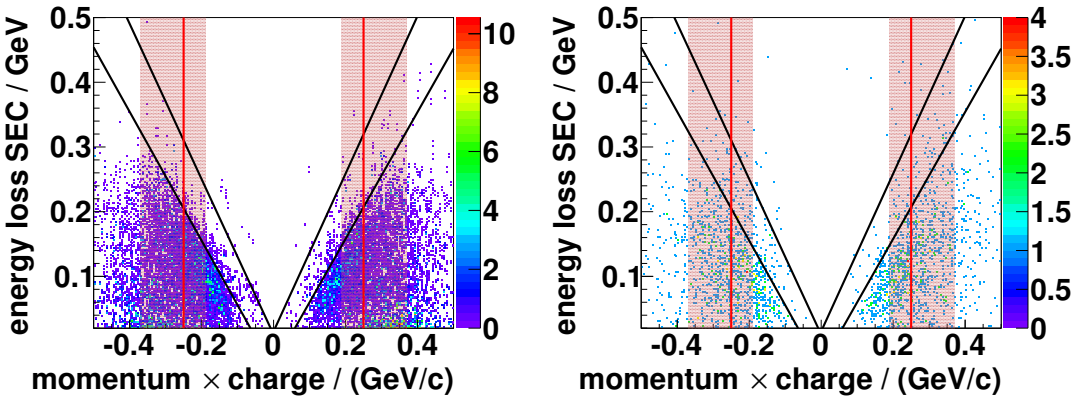

Figure 7.8.: Energy loss of charged particles in the SEC plotted against their momentum times charge after applying all preselection and selection conditions described in chapters 6.5 and 6.7.2, except for the cut on the momentum of charged particles and the PID cut. The latter is illustrated by black lines, while the standard momentum cut is presented by red lines. The red shaded area indicates the range used for the systematic checks. Left: Monte Carlo simulations scaled according to the fit to data (see chapter 6.6.2). Right: Combined plot for the 2008 and 2009 data sets.

events will be rejected by a cut used for the reduction of split-off events if a higher minimal energy loss is requested beforehand. Hence, a higher requested minimal energy loss can lead to an increasing number of events remaining after applying all selection conditions. Tables B.8, B.9, B.10, and B.11 in appendix B.5 list the corresponding values for the 2008 and 2009 data sets. No systematic effect is visible that needs to be considered.

Momentum p of charged particles

As discussed in chapter 6.5.3, a cut on the momentum p of charged particles was introduced to reject particles with higher momenta, because the energy loss distributions for these particles differ between MC and data. Thus, for systematic checks the condition for this cut was altered in the region indicated by the red shaded area in figure 7.8. Tables B.12 and B.13 in appendix B.5 list the resulting values for the 2008 and 2009 data sets. While $|\kappa|$ is below two for most tested conditions, it is $\kappa = 2.1$ for the momentum cut at $0.37\,\mathrm{GeV}\,c^{-1}$ for the 2009 data set. But this cut value is already far above the chosen selection condition of $p \leq 0.25\,\mathrm{GeV}\,c^{-1}$, whose purpose it is to reject events with systematic uncertainties. In order to test whether this deviation further increases for higher cut values, the selection condition $p \leq 0.50\,\mathrm{GeV}\,c^{-1}$ was investigated in addition. The resulting

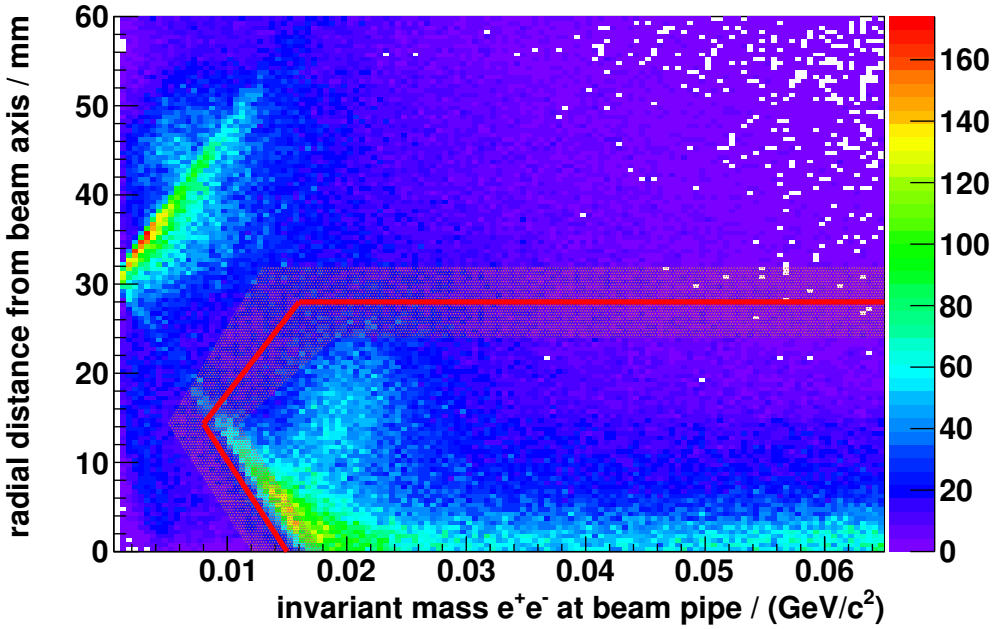

Figure 7.9.: Radial distance of the electron-positron vertex from the beam axis plotted against the invariant mass of the electron and positron at the beam pipe for a data sample recorded in 2008. Events above and to the left of the red lines are rejected, whereas events inside the graphical cut remain. For a systematic check the cut was varied within the range indicated by the red shaded area. The presented data were preselected requiring at least one positively and one negatively charged track reconstructed in the CD and a ^{3}He nucleus detected in the FD (see chapter 6.5.1).

$\kappa = 2.1$ for the 2009 data set is identical to the one for $p \leq 0.37\,\mathrm{GeV}\,c^{-1}$. Therefore, no systematic effects introduced by the cut of the momentum of charged particles need to be considered for the upper limit determination.

Conversion

In the preselection electrons and positrons from conversion of photons at the COSY beam pipe were rejected by the graphical cut, illustrated in figure 7.9 by the red lines (see chapter 6.5.4 for further details). This cut is defined by three prominent points, namely ($x_0 = 0.015\,\mathrm{GeV}\,c^{-2}$, $y_0 = 0.0\,\mathrm{mm}$), ($x_1 = 0.008\,\mathrm{GeV}\,c^{-2}$, $y_1 = 14.32\,\mathrm{mm}$), and ($x_2 = 0.016\,\mathrm{GeV}\,c^{-2}$, $d = 28.0\,\mathrm{mm}$). In order to investigate a possible systematic effect, different values for x_0, x_1, x_2, and d were tested as indicated in figure 7.9 by the red shaded area and listed in tables B.14, B.15, B.16, and B.17 in appendix B.5. No systematic effect was found.

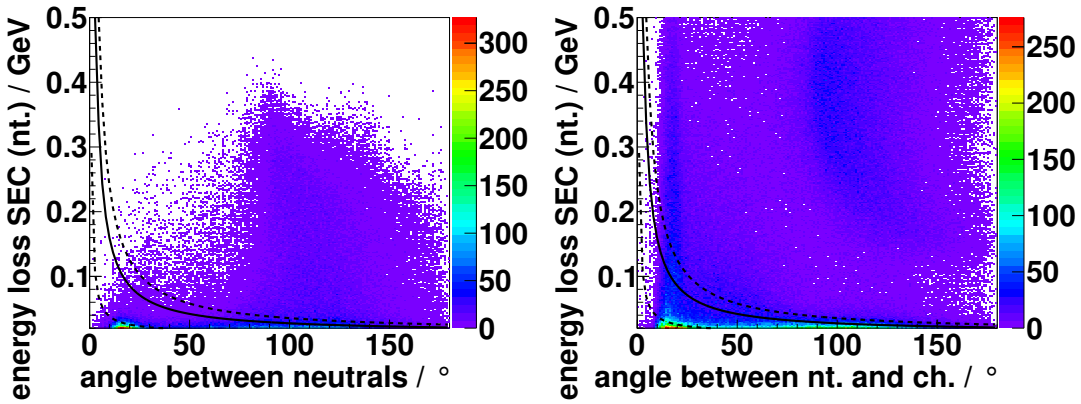

Figure 7.10.: Energy loss of a reconstructed neutral particle in the calorimeter plotted against the angle between its track and the track of a second neutral particle detected in the central detector (left) and plotted against the angle between its track and the track of a charged particle detected in the central detector (right) for the simulated decay $\eta \to e^+ + e^- + \gamma$. Neutral tracks with entries below the black cut line are rejected from the analysis. The black dashed lines indicate the range of tested parameters for the systematic checks. All samples were preselected on the signature of the decay $\eta \to \pi^0 + e^+ + e^-$, and a ^{3}He nucleus detected in the FD was required (see chapters 6.5.2 and 6.5.1).

Split-off events

For the rejection of split-off events two different selection conditions were utilized in the preselection (see chapter 6.5.5). The first one was based on the energy loss of a neutral particle and the angle between its track and the track of either a second neutral particle or a charged particle (see figure 7.10), whereas the second cut was based on the invariant mass of one neutral and one charged particle (see figure 7.11). Both conditions were varied for a systematic test within a certain range as indicated by the black dashed curves in figure 7.10 and the red shaded area in figure 7.11, respectively. The results for all tested cuts are given in tables B.18, B.19, B.20, B.21, B.22, and B.23 in appendix B.5. Since $|\kappa| \leq 2$ for all investigated conditions and cut values, no systematic effects need to be considered for the upper limit determination.

^{3}He missing mass

A cut on the ^{3}He missing mass was used in the analysis to select the reaction $p + d \to {}^3\mathrm{He} + \eta$ (see chapter 6.7.2). In order to investigate the systematics of this selection condition, the upper and lower cuts were varied independently within the range indicated by the red shaded areas in figure 7.12. The corresponding values are

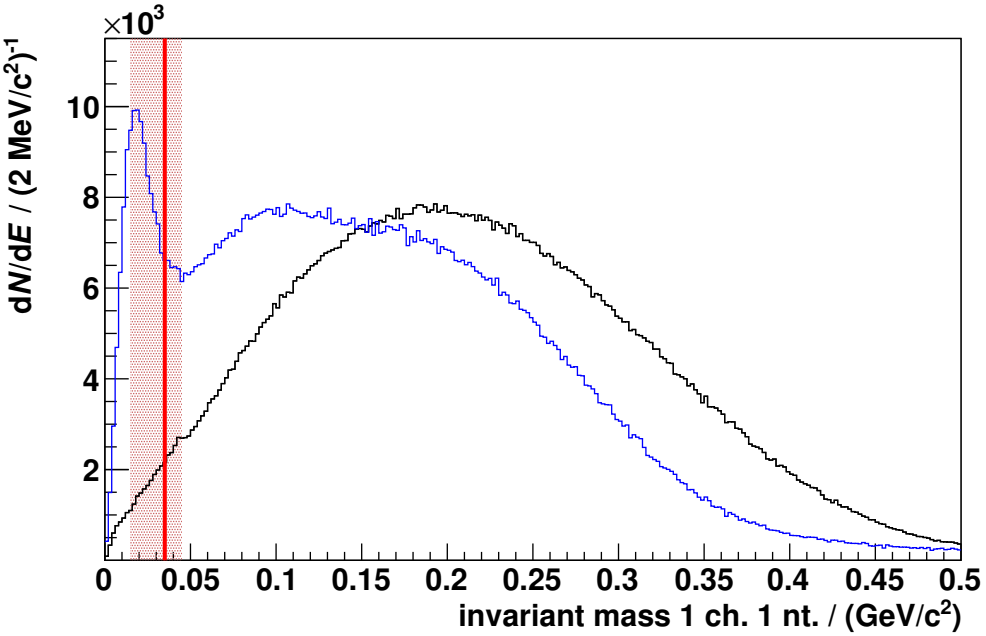

Figure 7.11.: Invariant mass of one neutral particle and one charged particle detected in the CD for the simulated decays $\eta \to \pi^0 + e^+ + e^-$ and $\eta \to \pi^+ + \pi^- + \gamma$ (black and blue histogram, respectively), assuming an electron mass for the charged particle. Note that the histogram of the signal decay is arbitrarily scaled to the latter. The red line illustrates the cut applied in the analysis, while the red shaded area indicates the range of cut values tested for the investigation of possible systematic effects. All samples were preselected on the signature of the decay $\eta \to \pi^0 + e^+ + e^-$, and a ^{3}He nucleus detected in the FD was required (see chapters 6.5.2 and 6.5.1).

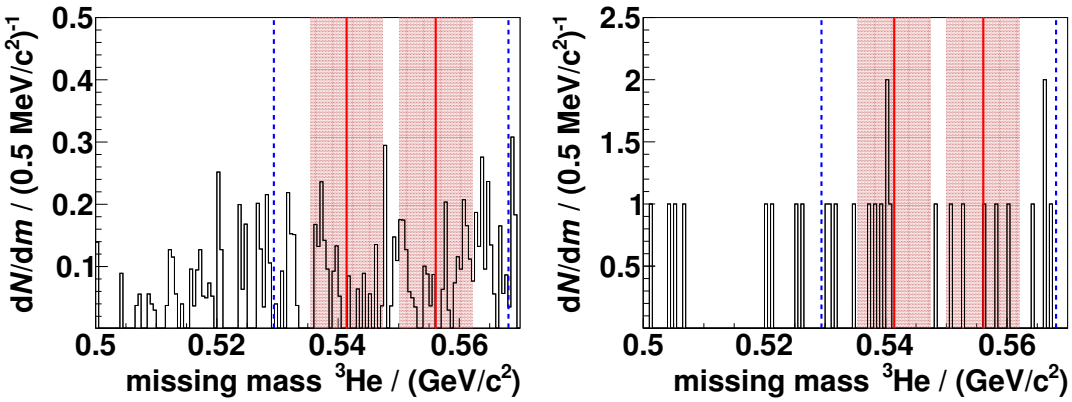

Figure 7.12.: ^{3}He missing mass distributions after application of the preselection and selection conditions described in chapters 6.5 and 6.7.2, except for the cut on m_{X}. Left: Monte Carlo simulation cocktail scaled according to the fit described in chapter 6.6.2. Right: Data measured in 2008 and 2009. The standard selection conditions used in the analysis are illustrated by red lines, while the cut range utilized for systematic tests is indicated by the red shaded areas. The blue dashed lines present the conditions used for an additional check of the 2008 data set.

given in tables B.24, B.25, B.26, and B.27 in appendix B.5. For most cut values it is $|\kappa| \leq 2$, except for two tested selection conditions, in particular $0.5374\,\mathrm{GeV}\,c^{-2} \leq m_{\mathrm{X}} \leq 0.5601\,\mathrm{GeV}\,c^{-2}$ and $0.5374\,\mathrm{GeV}\,c^{-2} \leq m_{\mathrm{X}} \leq 0.5581\,\mathrm{GeV}\,c^{-2}$, for which it is $\kappa = 2.1$ in case of the 2008 data set. Although it is $|\kappa| > 2$ for these cut ranges, this can possibly still be explained by statistical effects. To check this, a selection condition with a range wider by $\pm 60\,\mathrm{MeV}\,c^{-2}$ than the maximal tested range was investigated for the 2008 data set, namely $0.5294\,\mathrm{GeV}\,c^{-2} \leq m_{\mathrm{X}} \leq 0.5681\,\mathrm{GeV}\,c^{-2}$ (indicated by the blue dashed lines in figure 7.12, see table B.25 in appendix B.5). Utilizing this condition, 2.4 events are expected to remain according to MC and eight events remained after applying all cuts in data. The corresponding $\kappa = 1.4$ is well below two. Since the received κ values for $0.5374\,\mathrm{GeV}\,c^{-2} \leq m_{\mathrm{X}} \leq 0.5601\,\mathrm{GeV}\,c^{-2}$ and $0.5374\,\mathrm{GeV}\,c^{-2} \leq m_{\mathrm{X}} \leq 0.5581\,\mathrm{GeV}\,c^{-2}$ are only slightly above two and this deviation vanishes if the cut range is increased, this fluctuation can be explained by statistical effects and was not considered for the upper limit determination.

Invariant mass of $e^+e^-\gamma\gamma$

The next selection condition investigated for possible systematic effetcs is based on the invariant mass of an electron-positron pair candidate and two neutral particles

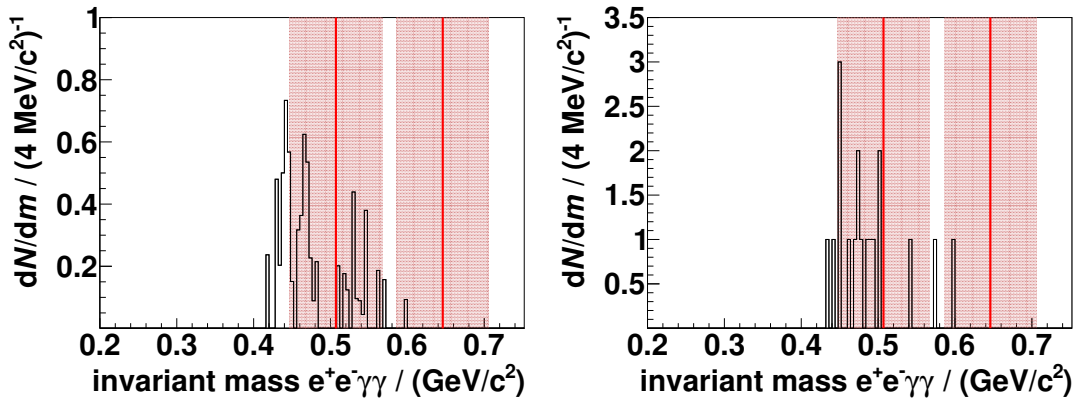

Figure 7.13.: Distributions for the invariant mass of an electron-positron pair candidate and two neutral particles after application of the preselection and selection conditions described in chapters 6.5 and 6.7.2, except for the cut on $m_{\mathrm{ee}\gamma\gamma}$. Left: Monte Carlo simulation cocktail scaled according to the fit described in chapter 6.6.2. Right: Data measured in 2008 and 2009. The standard selection conditions used in the analysis are illustrated by red lines, while the cut range utilized for systematic tests is indicated by the red shaded areas.

(see chapter 6.7.2). The standard conditions indicated by red lines in figure 7.13 were varied in the range illustrated by the red shaded areas. The corresponding values are listed in tables B.28, B.29, B.30, and B.31 in appendix B.5. Since $|\kappa| \leq 2$ for all tested conditions, no systematic uncertainty needs to be incorporated for the upper limit determination.

Invariant mass of $\gamma\gamma$

Similar to $m_{\mathrm{ee}\gamma\gamma}$, the tested selection conditions for the invariant mass of two photons show no systematic effect (see tables B.32, B.33, B.34, and B.35 in appendix B.5). Figure 7.14 presents the standard conditions used in the analysis (red lines) as well as the investigated cut range (red shaded area).

Invariant mass of e^+e^-

The cut on the invariant mass of an electron-positron pair candidate was used in the analysis to suppress events from background reactions with e^+e^- in the final state, especially from the direct $\pi^0\pi^0$ production (see chapter 6.7.2). The investigated cut values are given in tables B.36 and B.37 in appendix B.5 and are illustrated by the red shaded areas in figure 7.15. For the 2009 data set no systematic effect was found, whereas for the 2008 data set κ values of up to $\kappa = 2.2$ were received for cut

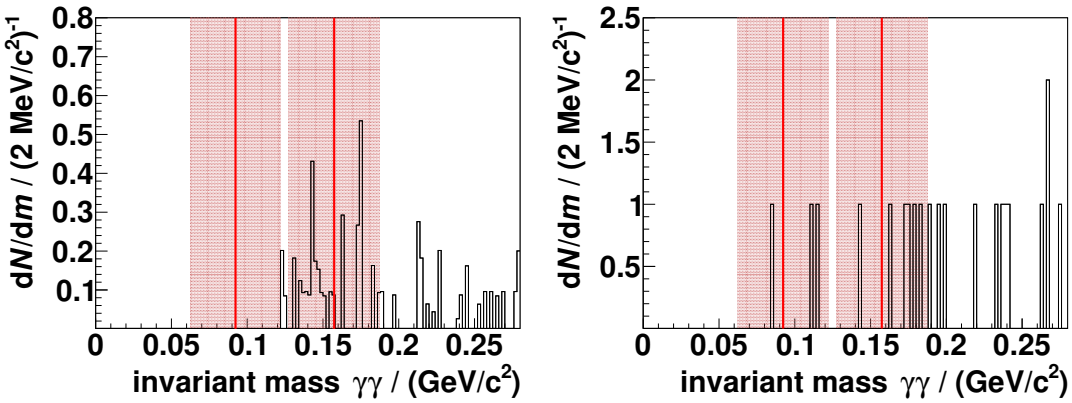

Figure 7.14.: Distributions for the invariant mass of two neutral particles after application of the preselection and selection conditions described in chapters 6.5 and 6.7.2, except for the cut on $m_{\gamma\gamma}$. Left: Monte Carlo simulation cocktail scaled according to the fit described in chapter 6.6.2. Right: Data measured in 2008 and 2009. The standard selection conditions used in the analysis are illustrated by red lines, while the cut range utilized for systematic tests is indicated by the red shaded areas.

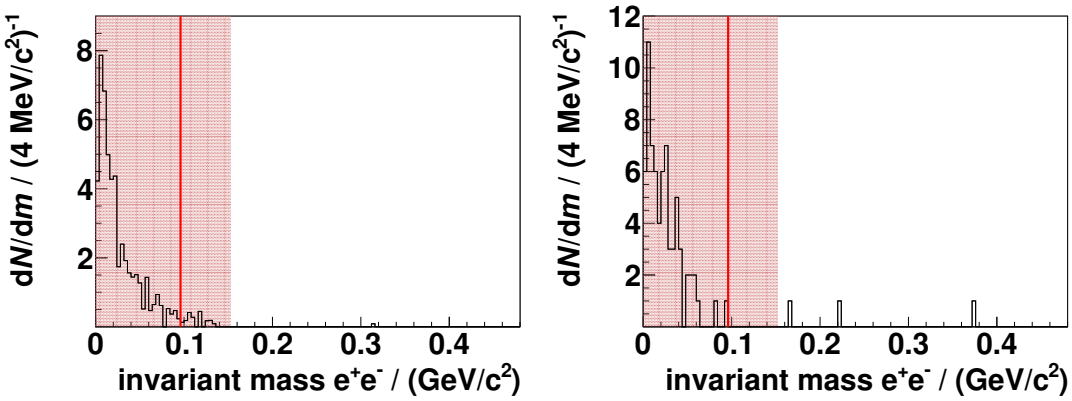

Figure 7.15.: Distributions for the invariant mass of an electron-positron pair candidate after application of the preselection and selection conditions described in chapters 6.5 and 6.7.2, except for the cut on m_{ee}. Left: Monte Carlo simulation cocktail scaled according to the fit described in chapter 6.6.2. Right: Data measured in 2008 and 2009. The standard selection condition used in the analysis is illustrated by the red lines, while the cut range utilized for systematic tests is indicated by the red shaded areas.

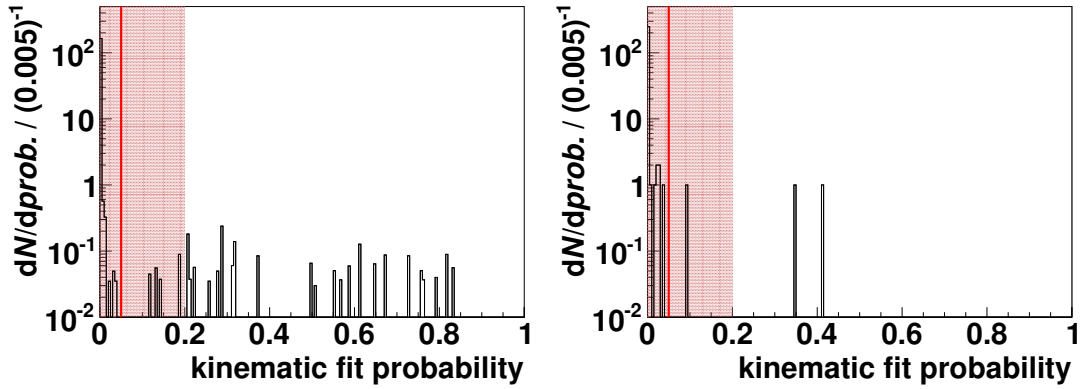

Figure 7.16.: Distributions for the χ^2 probability of the kinematic fit with the hypothesis $\mathrm{p+d} \to {}^3\mathrm{He+e^+ + e^- + \gamma + \gamma}$ after application of the preselection and selection conditions described in chapters 6.5 and 6.7.2, except for the cut on the χ^2 probability. Left: Monte Carlo simulation cocktail scaled according to the fit described in chapter 6.6.2. Right: Data measured in 2008 and 2009. The standard selection condition used in the analysis is illustrated by the red lines, while the cut range utilized for systematic tests is indicated by the red shaded areas.

values below $32\,\mathrm{MeV}\,c^{-2}$. However, these κ values are not significantly larger than two, and the corresponding cut values are less than a third of the standard cut value of $96\,\mathrm{MeV}\,c^{-2}$ presented by the red lines in figure 7.15. Thus, these deviations were not considered for the upper limit determination.

χ^2 probability of the kinematic fit

For the event selection in the analysis a minimal χ^2 probability of the kinematic fit of $prob.^{\mathrm{min}} = 0.05$ was requested (see chapter 6.7.2). In figure 7.16 this condition is presented by the red lines. The red shaded area indicates the range of conditions tested for the investigation of systematic effects, and the corresponding values are listed in tables B.38 and B.39 in appendix B.5. Both for the 2008 and the 2009 data set it is $|\kappa| \leq 2$ except for $prob.^{\mathrm{min}} = 0$. The larger deviations between data and MC for this cut value can be explained by events that were incorrectly reconstructed and should not be used in an analysis. Since the chosen cut at $prob.^{\mathrm{min}} = 0.05$ is well above zero and all cuts with $prob.^{\mathrm{min}} > 0$ do not show a deviation between data and MC that cannot be explained by statistics, this effect was not considered for the determination of systematic uncertainties.

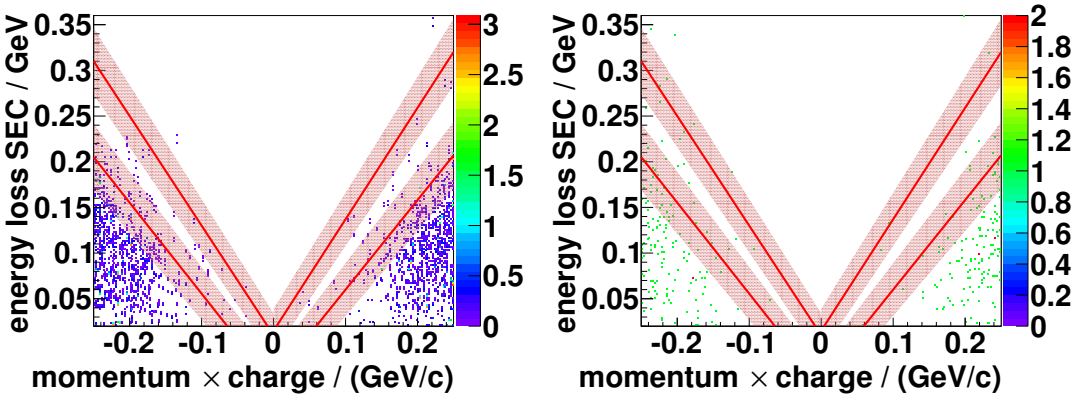

Figure 7.17.: Energy loss of charged particles in the SEC plotted against their momentum times charge after application of the preselection and selection conditions described in chapters 6.5 and 6.7.2, except for the PID cut. Left: Monte Carlo simulation cocktail scaled according to the fit described in chapter 6.6.2. Right: Data measured in 2008 and 2009. The standard selection conditions used in the analysis are illustrated by the red lines, while the cut ranges utilized for systematic tests are indicated by the red shaded areas.

Particle identification

The identification of electrons and positrons was realized in the analysis by a graphical cut depending on the energy loss of a charged particle in the SEC, its momentum, and its charge (see chapter 6.7.2). In detail, the used selection condition can be parametrized by:

$$l_0 + l_1 \cdot p \leq E_{\text{dep}}^{\text{SEC}} \leq u_0 + u_1 \cdot p \tag{7.13}$$

with independent conditions for negatively charged particles (neg) and positively charged particles (pos) as presented by the red lines in figure 7.17. For the investigation of the systematics of the PID the parameters for the upper and lower graphical cut lines were performed separately. This was done by varying the selection conditions within the range indicated by the red shaded areas in figure 7.17. The corresponding parameters for the upper cut are listed in tables B.40, B.41, B.42, and B.43 in appendix B.5, whereas the parameters for the lower cut are given in tables B.44, B.45, B.46, and B.47 in appendix B.5. In all cases it is $|\kappa| \leq 2$, and thus no systematic effect was found that needs to be considered for the upper limit determination.

Table 7.8.: Numbers of events for the simulated reaction p+d $\to$ ^{3}He+π^0+π^0 remaining after applying the preselection and selection conditions given in chapters 6.5 and 6.7.2, unscaled and scaled to data.

Number $N_{\pi^0\pi^0}$	Unscaled ($^{\mathrm{mc}}$)	Scaled to data ($^{\mathrm{data}}$)
2008, pure ($m_{2008,\mathrm{p}}$)	14	0.470
2008, with overlap ($m_{2008,\mathrm{o}}$)	5	0.285
2009, pure ($m_{2009,\mathrm{p}}$)	13	0.702
2009, with overlap ($m_{2009,\mathrm{o}}$)	4	0.530

7.2. Branching ratio of the decay $\eta \to \pi^0 + e^+ + e^-$

For the calculation of the upper limit of the branching ratio $\frac{\Gamma\left(\eta\to\pi^0+e^+e^-\right)}{\Gamma(\eta\to\pi^+\pi^-\pi^0)}$ according to equation 7.4, the upper limit for the number of signal events $N_{\mathrm{S,up}}$ needs to be determined. This was done with an algorithm written by A. Kupść [Kup17]. It calculates the posterior pdf based on equations 2.71 and 2.73 in chapter 2.8.1.

While the systematic uncertainty of the signal reconstruction efficiency ε_{S} is Gaussian distributed for the analysis presented in this thesis, the systematic uncertainty for the number of background events is asymmetric. Therefore, the pdf $f_{b'}(b, \sigma_b)$ in equation 2.73 was replaced by:

$$\begin{aligned} g_\lambda(b) = &\left[m^{\mathrm{data}}_{2008,\mathrm{p}} + m^{\mathrm{data}}_{2008,\mathrm{o}}\right] \cdot (1 + f_{\lambda_{2008}}(b_{2008})) \\ &+ \left[m^{\mathrm{data}}_{2009,\mathrm{p}} + m^{\mathrm{data}}_{2009,\mathrm{o}}\right] \cdot (1 + f_{\lambda_{2009}}(b_{2009})) \end{aligned} \tag{7.14}$$

with the distributions $f_{\lambda_{2008}}(b_{2008})$ and $f_{\lambda_{2009}}(b_{2009})$ of the nuisance parameters λ_{2008} and λ_{2009} for the 2008 and the 2009 data set, respectively (see chapter 7.1.2, figure 7.7). The numbers $m^{\mathrm{data}}_{2008,\mathrm{p}}$, $m^{\mathrm{data}}_{2008,\mathrm{o}}$, $m^{\mathrm{data}}_{2009,\mathrm{p}}$, and $m^{\mathrm{data}}_{2009,\mathrm{o}}$ are the numbers of events for the simulated reaction p + d $\to$ ^{3}He + π^0 + π^0 scaled to data according to the fit described in chapter 6.6.2 and remaining after applying the preselection and selection conditions given in chapters 6.5 and 6.7.2. Note that numbers with the index p correspond to remaining events from pure Monte Carlo simulations without event overlap and numbers with the index o to events from simulations with event overlap included. All numbers are listed in table 7.8 together with the corresponding unscaled numbers (index $^{\mathrm{mc}}$).

Table 7.9.: Summary of all systematic uncertainties for the analysis of the decay $\eta \to \pi^0 + e^+ + e^-$ via one virtual photon and for a decay according to three-particle phase space as obtained in chapter 7.1.

Systematic uncertainty	Virtual photon	Three-particle phase space
Signal efficiency (σ_ε)	0.059	0.057
Number $N_{\eta\to\pi^+\pi^-\pi^0}$ ($\sigma_{N_{\text{norm}}}$)	0.023	0.023
Number $N^{2008}_{\pi^0\pi^0}$ ($f_{\lambda_{2008}}(b_{2008})$)	see chapter 7.1.2, figure 7.7, left	
Number $N^{2009}_{\pi^0\pi^0}$ ($f_{\lambda_{2009}}(b_{2009})$)	see chapter 7.1.2, figure 7.7, right	

Due to the limited statistics of the Monte Carlo simulations, the numbers of expected events have statistical uncertainties. These can be incorporated by expanding equation 7.14 to:

$$\begin{aligned} g_{b',\lambda}(b) = &\left[\frac{m^{\text{data}}_{2008,\text{p}}}{m^{\text{mc}}_{2008,\text{p}}} \cdot P(m^{\text{mc}}_{2008,\text{p}}; b'_{2008,\text{p}}) + \frac{m^{\text{data}}_{2008,\text{o}}}{m^{\text{mc}}_{2008,\text{o}}} \cdot P(m^{\text{mc}}_{2008,\text{o}}; b'_{2008,\text{o}})\right] \\ &\cdot (1 + f_{\lambda_{2008}}(b_{2008})) \\ &+ \left[\frac{m^{\text{data}}_{2009,\text{p}}}{m^{\text{mc}}_{2009,\text{p}}} \cdot P(m^{\text{mc}}_{2009,\text{p}}; b'_{2009,\text{p}}) + \frac{m^{\text{data}}_{2009,\text{o}}}{m^{\text{mc}}_{2009,\text{o}}} \cdot P(m^{\text{mc}}_{2009,\text{o}}; b'_{2009,\text{o}})\right] \\ &\cdot (1 + f_{\lambda_{2009}}(b_{2009})) \ . \end{aligned} \tag{7.15}$$

Here the functions $P(m; b')$ are Poisson probability density functions of the type:

$$P(m; b') = e^{-m}\frac{m^{b'}}{b'!} \ . \tag{7.16}$$

In addition to the uncertainties of the signal reconstruction efficiency and the number of remaining background events, the systematic uncertainty $\sigma_{N_{\text{norm}}}$ of the number $N_{\eta\to\pi^+\pi^-\pi^0}$ of $\eta \to \pi^+ + \pi^- + \pi^0$ events in data has to be considered for the calculation of $N_{\text{S,up}}$. This is obtained by including the pdf $f_{N_{\text{norm}}}(1, \sigma_{N_{\text{norm}}})$ with the mean 1 and the standard deviation $\sigma_{N_{\text{norm}}}$ in equation 2.73. The resulting conditional pdf, which respects all mentioned uncertainties, is given by:

$$q\left(n|s\right)_b = \int_0^\infty \int_0^\infty \int_0^\infty \int_0^\infty p\left(n|s\varepsilon\right)_{b'} g_{b',\lambda}(b) f_\varepsilon(1, \sigma_\varepsilon) f_{N_{\text{norm}}}(1, \sigma_{N_{\text{norm}}}) \text{d}b' \text{d}\lambda \text{d}\varepsilon \text{d}N_{\text{norm}} \ . \tag{7.17}$$

Here the differentials $\mathrm{d}b'$ and $\mathrm{d}\lambda$ are short forms for

$$\mathrm{d}b' = \mathrm{d}b'_{2008,\mathrm{p}}\mathrm{d}b'_{2008,\mathrm{o}}\mathrm{d}b'_{2009,\mathrm{p}}\mathrm{d}b'_{2009,\mathrm{o}} \text{ and} \tag{7.18}$$

$$\mathrm{d}\lambda = \mathrm{d}\lambda_{2008}\mathrm{d}\lambda_{2009}\,. \tag{7.19}$$

Utilizing equations 7.14 and 7.17, the numbers of expected events listed in table 7.8, the systematic uncertainties given in table 7.9, and the fact that three events remain in the combined 2008 and 2009 data set, the upper limit $N_{\mathrm{S,up}}$ for the number of signal events was calculated to

$$N_{\mathrm{S,up}} = 4.97 \qquad (\mathrm{CL} = 90\,\%)\,, \tag{7.20}$$

both for the decay $\eta \to \pi^0 + \mathrm{e}^+ + \mathrm{e}^-$ via one virtual photon and for a decay according to three-particle phase space if the statistical uncertainties of the Monte Carlo simulations for the reaction $\mathrm{p} + \mathrm{d} \to {}^3\mathrm{He} + \pi^0 + \pi^0$ are not considered.

In the case that the statistical uncertainties of the Monte Carlo simulations for the reaction $\mathrm{p} + \mathrm{d} \to {}^3\mathrm{He} + \pi^0 + \pi^0$ are included and equation 7.15 is used, the resulting upper limit is

$$N_{\mathrm{S,up}} = 4.82 \qquad (\mathrm{CL} = 90\,\%)\,. \tag{7.21}$$

The lower value compared to equation 7.20 results from the properties of Poisson distributions for small numbers. In order to give a conservative upper limit for the branching ratio, equation 7.20 was used.

With this upper limit $N_{\mathrm{S,up}}$ the relative branching ratio was calculated as:

$$\begin{aligned} &\frac{\Gamma\left(\eta \to \pi^0 + \mathrm{e}^+ + \mathrm{e}^-\right)_{\mathrm{virtual}}}{\Gamma\left(\eta \to \pi^+ + \pi^- + \pi^0\right)} < \frac{N_{\mathrm{S,up}}}{N^{\mathrm{produced}}_{\eta\to\pi^+\pi^-\pi^0} \cdot \varepsilon_{\mathrm{S}}^{\mathrm{virtual}}} = \frac{4.97}{6.509 \times 10^6 \times 0.023\,31} \\ \Rightarrow\ &\frac{\Gamma\left(\eta \to \pi^0 + \mathrm{e}^+ + \mathrm{e}^-\right)_{\mathrm{virtual}}}{\Gamma\left(\eta \to \pi^+ + \pi^- + \pi^0\right)} < 3.28 \times 10^{-5} \qquad (\mathrm{CL} = 90\,\%) \end{aligned} \tag{7.22}$$

for the decay via one virtual photon and

$$\begin{aligned} \frac{\Gamma\left(\eta \to \pi^0 + \mathrm{e}^+ + \mathrm{e}^-\right)_{\mathrm{phase}}}{\Gamma\left(\eta \to \pi^+ + \pi^- + \pi^0\right)} &< \frac{N_{\mathrm{S,up}}}{N^{\mathrm{produced}}_{\eta\to\pi^+\pi^-\pi^0} \cdot \varepsilon^{\mathrm{phase}}_{\mathrm{S}}} = \frac{4.97}{6.509 \times 10^6 \times 0.018\,44} \\ \Rightarrow \frac{\Gamma\left(\eta \to \pi^0 + \mathrm{e}^+ + \mathrm{e}^-\right)_{\mathrm{phase}}}{\Gamma\left(\eta \to \pi^+ + \pi^- + \pi^0\right)} &< 4.14 \times 10^{-5} \qquad (\mathrm{CL} = 90\,\%) \end{aligned} \tag{7.23}$$

for the decay according to three-particle phase space.

Inserting the branching ratio $\frac{\Gamma(\eta\to\pi^+ + \pi^- + \pi^0)}{\Gamma(\eta\to\mathrm{all})} = 0.2292(28)$ [P$^+$16] gives

$$\frac{\Gamma\left(\eta \to \pi^0 + \mathrm{e}^+ + \mathrm{e}^-\right)_{\mathrm{virtual}}}{\Gamma\left(\eta \to \mathrm{all}\right)} < 7.52 \times 10^{-6} \qquad (\mathrm{CL} = 90\,\%) \tag{7.24}$$

for the decay via one virtual photon and

$$\frac{\Gamma\left(\eta \to \pi^0 + \mathrm{e}^+ + \mathrm{e}^-\right)_{\mathrm{phase}}}{\Gamma\left(\eta \to \mathrm{all}\right)} < 9.49 \times 10^{-6} \qquad (\mathrm{CL} = 90\,\%) \tag{7.25}$$

for the decay according to three-particle phase space, which is smaller than the current upper limit of 4×10^{-5} (CL = 90 %) [P$^+$16] by a factor of four to six.

8. Summary and outlook

The studies presented in this thesis are separated into two major topics. In the first part of the thesis the production reaction $p + d \to {}^3He + \eta$ was investigated and differential cross sections as well as the total cross section ratio were determined for the excess energies $Q = 48.8\,\mathrm{MeV}$ and $Q = 59.8\,\mathrm{MeV}$. The second topic covered the search for the C parity violating decay $\eta \to \pi^0 + e^+ + e^-$. As a result, it was possible to determine a new upper limit for the branching ratio of this decay channel. All measurements utilized for the analyses presented in this thesis were obtained with the WASA-at-COSY experimental setup.

8.1. Analysis of the production reaction $p + d \to {}^3He + \eta$

The analysis of the production reaction $p + d \to {}^3He + \eta$ presented in this thesis was based on a part of the data collected in the beam time of 2009. These data runs were collected at the two excess energies $Q = 48.8\,\mathrm{MeV}$ and $Q = 59.8\,\mathrm{MeV}$. In order to determine the differential cross section distributions of this reaction, the data were divided into 23 angular bins ranging from $\cos\vartheta_\eta^{\mathrm{CMS}} = -0.92$ to $\cos\vartheta_\eta^{\mathrm{CMS}} = 0.92$ and the numbers of events were extracted with the ^3He missing mass method. For this purpose the data were fitted by Monte Carlo simulations of the reaction $p + d \to {}^3He + \eta$ and background reactions. The resulting differential distributions for both excess energies could be obtained with high precision and are in good agreement with each other. Especially the differential distribution at $Q = 48.8\,\mathrm{MeV}$ was determined with a much higher precision than the results extracted in a previous experiment [B$^+$00]. It was found that polynomials of third order are sufficient to describe the forward peaking shape of the distribution both at $Q = 48.8\,\mathrm{MeV}$ and at $Q = 59.8\,\mathrm{MeV}$.

Apart from the differential cross section distributions, the ratio of the total cross sections for the reaction $p + d \to {}^3He + \eta$ was extracted for the two excess energies

$Q = 48.8\,\mathrm{MeV}$ and $Q = 59.8\,\mathrm{MeV}$ by a relative normalization utilizing the reaction $\mathrm{p} + \mathrm{d} \rightarrow {}^3\mathrm{He} + \pi^0$. The ratio

$$\frac{\sigma_\eta\,(48.8\,\mathrm{MeV})}{\sigma_\eta\,(59.8\,\mathrm{MeV})} = 0.77 \pm 0.06 \tag{8.1}$$

determined in this thesis does not agree with an enhancement of the total cross section at $Q = 48.8\,\mathrm{MeV}$, as possibly indicated by data measured with GEM [B$^+$00], but suggests the presence of a distinct change of the total cross section for excess energies between 20 MeV and 60 MeV. This variation might indicate a change of the production mechanisms involved. As part of this thesis the results of the analysis have been published in the European Physical Journal A in 2014 [A$^+$14b].

Because of the open questions introduced by the results obtained in this thesis for the total cross section ratio and the differential cross sections, new measurements were performed with WASA-at-COSY in 2014 at 15 excess energies ranging from 13.6 MeV to 80.9 MeV [Hü17]. The goal of these measurements is to extract differential distributions for further excess energies with the same high precision as the results presented in this thesis. Furthermore, changes to the WASA detector setup and further optimizations of the data acquisition for these measurements will allow for an alternative normalization by using the pd elastic scattering for cross checks. Very first preliminary results for the differential cross section distributions are in good agreement with the results of this thesis. Nonetheless, the analysis of these data and the normalization are ongoing.

8.2. Analysis of the decay $\eta \rightarrow \pi^0 + \mathrm{e}^+ + \mathrm{e}^-$

The analysis with regard to the η meson decay channel $\eta \rightarrow \pi^0 + \mathrm{e}^+ + \mathrm{e}^-$ was based on the full $\mathrm{p} + \mathrm{d} \rightarrow {}^3\mathrm{He} + \eta$ data set recorded in the beam times of 2008 and 2009 at an excess energy of $Q = 59.8\,\mathrm{MeV}$. The goal of this analysis was the search for a C parity violating decay process and the determination of either the branching ratio of this decay or the upper limit thereof. As a result of this thesis a new upper limit for the decay $\eta \rightarrow \pi^0 + \gamma^* \rightarrow \pi^0 + \mathrm{e}^+ + \mathrm{e}^-$ and the decay $\eta \rightarrow \pi^0 + \mathrm{e}^+ + \mathrm{e}^-$ according to three-particle phase space was determined.

The analysis was based on the common analysis base class PDEtaAnalysisBase, which had been developed together with fellow researchers. This base class includes optimized calibrations for all WASA detector components. As part of this thesis

an optimal calibration of the forward detector for the full data sets was obtained and implemented in the base class, allowing for an ideal reconstruction of the ^{3}He nuclei four-momenta.

For the analysis two different variants of the decay channel $\eta \to \pi^0 + e^+ + e^-$ were simulated, namely a decay via one virtual photon and a decay according to three-particle phase space. In addition, several billion events of Monte Carlo simulations were created for the various background reactions. This way limitations of the extracted results by the statistics of the simulations were avoided.

In the first step of the analysis both the measured data and the simulations were preselected with regard to a pure $p + d \to {}^3He + X$ data sample with the signature of the decay of interest and suppressing events with contribution of conversion reactions and split-off events. Afterwards a part of the data was fitted by Monte Carlo simulations to extract the contributions of the different background reactions to the data. The determined ratios of the reactions were utilized in an algorithm that optimized selection conditions with regard to the signal decay $\eta \to \pi^0 + e^+ + e^-$. While these optimizations were based on 40 % of the MC pool, the efficiency determination was performed with the remaining 60 % of the simulation pool. Thereby a bias of the received result could be avoided.

Including all systematic effects and normalizing to the decay channel $\eta \to \pi^+ + \pi^- + \pi^0$, a new upper limit for the branching ratio of the decay $\eta \to \pi^0 + e^+ + e^-$ was determined, which is

$$\frac{\Gamma\left(\eta \to \pi^0 + e^+ + e^-\right)_{\text{virtual}}}{\Gamma\left(\eta \to \text{all}\right)} < 7.52 \times 10^{-6} \qquad (\text{CL} = 90\,\%) \tag{8.2}$$

for the decay via one virtual photon and

$$\frac{\Gamma\left(\eta \to \pi^0 + e^+ + e^-\right)_{\text{phase}}}{\Gamma\left(\eta \to \text{all}\right)} < 9.49 \times 10^{-6} \qquad (\text{CL} = 90\,\%) \tag{8.3}$$

for the decay according to three-particle phase space. For both cases the obtained upper limit of the branching ratio is smaller than the current best upper limit of 4×10^{-5} (CL = 90 %) [P$^+$16] by a factor of four to six. Therefore, a publication of these results is currently in preparation [B$^+$17].

Apart from the $p+d \to {}^3He+\eta$ data sets utilized for the analysis presented in this thesis, data were collected for the reaction $p+p \to p+p+\eta$ with WASA-at-COSY. These data sets contain a larger number of produced η mesons, but have a higher

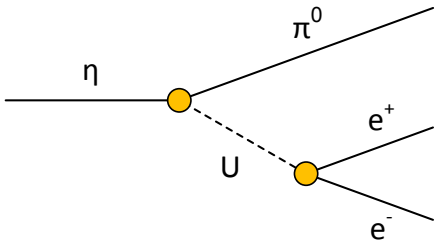

Figure 8.1.: Schematic diagram of the η meson decay $\eta \to \pi^0 + e^+ + e^-$ for a decay via a hypothetical C violating dark boson U.

relative background and a lower reconstruction efficiency for the decay analysis in comparison to the $p + d \to {}^3He + \eta$ data. An analysis of the $p + p \to p + p + \eta$ data sets with regard to the decay $\eta \to \pi^0 + e^+ + e^-$ is currently being performed by K. Demmich [Dem17] and is based on the methods developed during this thesis. In parallel, a part of the collected data has been investigated by J. Stepaniak in a first analysis, confirming the potential of the high statistics $p + p \to p + p + \eta$ data sets [Ste17].

8.3. Outlook: the C violating decay $\eta \to \pi^0 + U \to \pi^0 + e^+ + e^-$

In this thesis an upper limit for the decay $\eta \to \pi^0 + e^+ + e^-$ was determined for a decay via one virtual photon and for a decay according to three-particle phase space (see chapter 7.2). However, besides the C parity violating decay $\eta \to \pi^0 + \gamma^* \to \pi^0 + e^+ + e^-$ and the C parity conserving decay $\eta \to \pi^0 + \gamma^* + \gamma^* \to \pi^0 + e^+ + e^-$, a decay via a hypothetical dark boson U in the intermediate state with a mass

$$m_U < m_\eta - m_{\pi^0} \approx 413\,\mathrm{MeV}\,c^{-2} \tag{8.4}$$

might be a possibility (see figure 8.1). Since this dark boson, which decays to an electron-positron pair, has negative C parity, the decay would violate the C parity conservation, similar to the decay via one virtual photon.

For the Monte Carlo simulation of the decay $\eta \to \pi^0 + \mathrm{U} \to \pi^0 + \mathrm{e}^+ + \mathrm{e}^-$ the decay amplitude squared from equation 2.55 can be used with

$$\frac{|f_1(q^2)|^2}{(q^2)^2} = \frac{e^2\varepsilon^4\lambda^2}{\left(q^2 - m_\rho^2\right)^2 + q^2\Gamma_\rho^2(q^2)} \cdot \frac{(q^2)^2}{(q^2 - m_\mathrm{U}^2)^2 + q^2\Gamma_\mathrm{U}^2} \tag{8.5}$$

with the coupling constant ε and the width Γ_U of the U boson [Wir17]. For the calculation vector meson dominance was assumed, which is dominated by the ρ meson for the given q range. As q is in the range of the expected U boson mass m_U, the width Γ_U has to be considered in the calculations and equation 8.5. The resulting decay amplitude squared is

$$\begin{aligned}&\left|\mathcal{A}\left(\eta \to \pi^0 + \mathrm{U} \to \pi^0 + \mathrm{e}^+ + \mathrm{e}^-\right)\right|^2 \\ &= \frac{e^2\varepsilon^4\lambda^2}{\left(q^2 - m_\rho^2\right)^2 + q^2\Gamma_\rho^2(q^2)} \cdot \frac{(q^2)^2}{(q^2 - m_\mathrm{U}^2)^2 + q^2\Gamma_\mathrm{U}^2} \cdot 2e^2\left(-4m_\eta^2 q^2 + 16m_\eta^2 E_{\mathrm{e}^+}E_{\mathrm{e}^-}\right).\end{aligned} \tag{8.6}$$

While the mass m_U of the U boson is unknown and can vary in the range from $0\,\mathrm{MeV}\,c^{-2}$ to $413\,\mathrm{MeV}\,c^{-2}$, the dark boson is expected to have a width Γ_U in the order of eV according to theoretical investigations [Wir17]. Because this is in the same order as the width of the π^0 meson, the hypothetical dark boson can be assumed to decay at about the interaction vertex of the COSY beam with the deuterium pellets, too.

As an example the decay for an assumed U boson mass of $m_\mathrm{U} = 150\,\mathrm{MeV}\,c^{-2}$ will be discussed in the following. For the simulations a width of $\Gamma_\mathrm{U} = 100\,\mathrm{keV}\,c^{-2}$ was used, which is above the expected width, but well below the resolution of the WASA central detector. Figure 8.2 shows the invariant mass distribution of the electron-positron pair for the simulated decay $\eta \to \pi^0 + \mathrm{U} \to \pi^0 + \mathrm{e}^+ + \mathrm{e}^-$ as generated (shadowed in orange) and after reconstruction and applying the preselection conditions as presented in chapter 6.5 (black histogram). Obviously, the width of the reconstructed invariant mass is solely limited by the resolution of the WASA detector. For the analysis in total 121 306 events were generated with Monte Carlo[1], and the same preselection and selection conditions as described in chapters 6.5 and 6.7.2 were used. Since a peak at the mass $m_\mathrm{U} = 150\,\mathrm{MeV}\,c^{-2}$ is

[1]For technical reasons a minimum number of generated events was required in Pluto instead of an exact number of events.

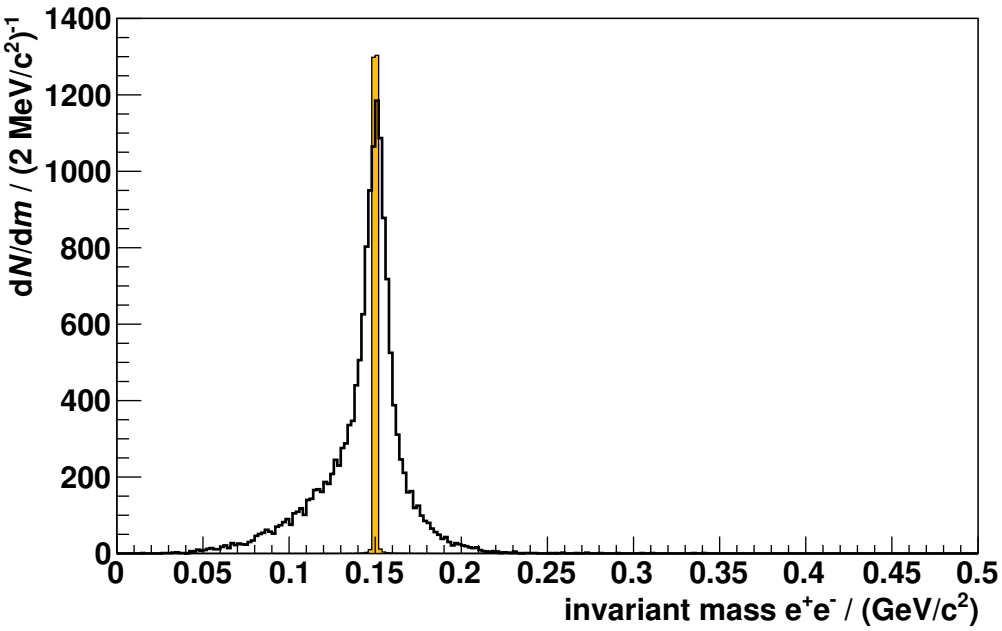

Figure 8.2.: Invariant mass of the e^+e^- pair of the simulated η meson decay $\eta \rightarrow \pi^0 + U \rightarrow \pi^0 + e^+ + e^-$ with a U boson mass of $m_U = 150\,\mathrm{MeV}\,c^{-2}$ and a width of $\Gamma_U = 100\,\mathrm{keV}\,c^{-2}$. The generated distribution is illustrated by the orange shadowed area, while the reconstructed distribution after applying the preselection cuts presented in chapter 6.5 is shown in black. Note that the generated distribution is arbitrarily scaled for more visibility.

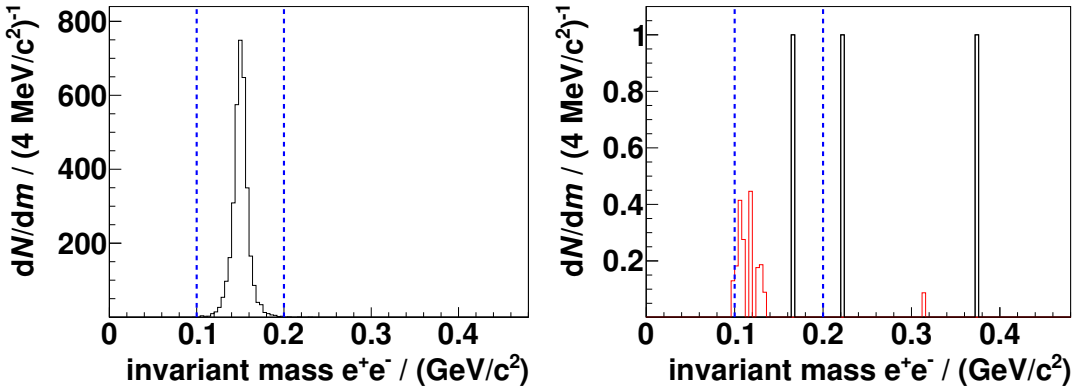

Figure 8.3.: Invariant mass of the e^+e^- pair after application of the preselection and selection conditions given in chapters 6.5 and 6.7.2. Left: Monte Carlo simulations of the decay $\eta \to \pi^0 + U \to \pi^0 + e^+ + e^-$. Right: Data and Monte Carlo simulations of all background reactions, scaled according to the fit described in chapter 6.6.2, after application of the preselection and selection conditions given in chapters 6.5 and 6.7.2 (black and red histogram, respectively). The additional selection conditions for m_{ee} are illustrated by blue dashed lines.

Table 8.1.: Numbers of events for the simulated reaction $p+d \to {}^3He+\pi^0+\pi^0$ remaining after applying the preselection and selection conditions given in chapters 6.5 and 6.7.2 and in this chapter, unscaled and scaled to data.

Number $N_{\pi^0\pi^0}$	Unscaled (^{mc})	Scaled to data (^{data})
2008, pure ($m_{2008,p}$)	12	0.400
2008, with overlap ($m_{2008,o}$)	4	0.240
2009, pure ($m_{2009,p}$)	11	0.602
2009, with overlap ($m_{2009,o}$)	4	0.530

expected for the signal decay, the invariant mass of e^+e^- was requested additionally to be in the range of 100 MeV c^{-2} to 200 MeV c^{-2}.

In figure 8.3 this condition for m_{ee} is represented by blue dashed lines. According to the Monte Carlo simulations of the background reactions (weighted to the data, see chapter 6.6.2), about 1.772 events are expected to remain from the reaction $p + d \to {}^3He + \pi^0 + \pi^0$ after applying all preselection and selection conditions including this cut, while one event is seen in data. A detailed list for the numbers of remaining events for the simulated reaction $p+d \to {}^3He+\pi^0+\pi^0$, unscaled and

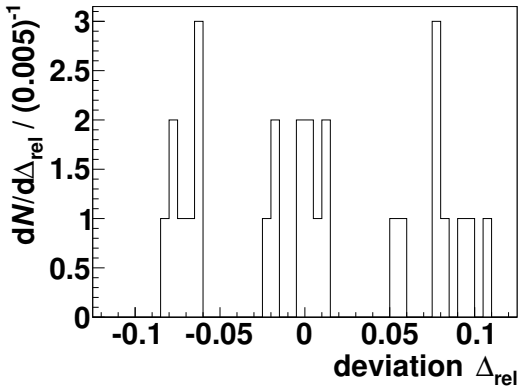

Figure 8.4.: Relative deviation Δ_{rel} of the factor $1/\left(\varepsilon_{\mathrm{S}} \cdot N_{\eta\to\pi^+\pi^-\pi^0}\right)$ for the different combinations of $\mathrm{FD_{smear}}$, $\mathrm{CD_{smear}}$ and $\mathrm{CD_{factor}}$ sets from the value for the standard set (0 0 0) for the decay $\eta \to (\pi^0 \to \gamma + \gamma) + \mathrm{e}^+ + \mathrm{e}^-$ via a dark boson.

scaled to data, is given in table 8.1. The efficiency for the simulated signal decay $\eta \to \pi^0 + \mathrm{U} \to \pi^0 + \mathrm{e}^+ + \mathrm{e}^-$ was determined to be

$$\varepsilon_{\mathrm{S}}^{\mathrm{dark}} = 0.037\,02(30)\,. \tag{8.7}$$

The systematic uncertainties of the analysis with regard to the decay $\eta \to \pi^0 + \mathrm{U} \to \pi^0 + \mathrm{e}^+ + \mathrm{e}^-$ are identical to those determined in chapter 7.1 for the number of remaining events from the reaction $\mathrm{p} + \mathrm{d} \to {}^3\mathrm{He} + \pi^0 + \pi^0$ and the number of events from the decay $\eta \to \pi^+ + \pi^- + \pi^0$ used for normalization (see also table 7.9 in chapter 7.2), whereas the systematic uncertainty of the signal efficiency ε_{S} introduced by uncertainties of the detector resolution and the statistical uncertainty of remaining $\pi^0\pi^0$ events differ. In order to obtain the systematic uncertainty of $\varepsilon_{\mathrm{S}}^{\mathrm{dark}}$ due to uncertainties of the WASA detector resolution, the same method as described in chapter 7.1.1 was used.

Table B.5 in appendix B.4 lists the resulting numbers for the tested detector smearing sets, and in figure 8.4 the relative deviations Δ_{rel} of the factor $1/\left(\varepsilon_{\mathrm{S}} \cdot N_{\eta\to\pi^+\pi^-\pi^0}\right)$ are plotted for these sets. The relative variance for the decay via a dark boson is

$$\mathrm{Var}_{\mathrm{rel}}^{\mathrm{dark}}\left(\frac{1}{\varepsilon_{\mathrm{S}} \cdot N_{\eta\to\pi^+\pi^-\pi^0}}\right) = 0.061 \tag{8.8}$$

and was treated as the systematic uncertainty of $\varepsilon_{\mathrm{S}}^{\mathrm{dark}}$.

Utilizing equations 7.17 and 7.14 in chapter 7.2 as well as the above mentioned information, the upper limit $N_{\mathrm{S,up}}^{\mathrm{dark}}$ for the number of signal events was calculated to

$$N_{\mathrm{S,up}}^{\mathrm{dark}} = 3.06 \qquad (\mathrm{CL} = 90\,\%)\,. \tag{8.9}$$

This results in an upper limit for the relative branching ratio of

$$\begin{aligned} &\frac{\Gamma\left(\eta \to \pi^0 + \mathrm{e}^+ + \mathrm{e}^-\right)_{\mathrm{dark}}}{\Gamma\left(\eta \to \pi^+ + \pi^- + \pi^0\right)} < \frac{N_{\mathrm{S,up}}^{\mathrm{dark}}}{N_{\eta\to\pi^+\pi^-\pi^0}^{\mathrm{produced}} \cdot \varepsilon_{\mathrm{S}}^{\mathrm{dark}}} = \frac{3.06}{6.509 \times 10^6 \times 0.037\,02} \\ \Rightarrow\ &\frac{\Gamma\left(\eta \to \pi^0 + \mathrm{e}^+ + \mathrm{e}^-\right)_{\mathrm{dark}}}{\Gamma\left(\eta \to \pi^+ + \pi^- + \pi^0\right)} < 1.27 \times 10^{-5} \qquad (\mathrm{CL} = 90\,\%) \end{aligned} \tag{8.10}$$

for the decay $\eta \to \pi^0 + \mathrm{U} \to \pi^0 + \mathrm{e}^+ + \mathrm{e}^-$ with $m_{\mathrm{U}} = 150\,\mathrm{MeV}\,c^{-2}$. The corresponding absolute branching ratio is

$$\frac{\Gamma\left(\eta \to \pi^0 + \mathrm{e}^+ + \mathrm{e}^-\right)_{\mathrm{dark}}}{\Gamma\left(\eta \to \mathrm{all}\right)} < 2.91 \times 10^{-6} \qquad (\mathrm{CL} = 90\,\%) \tag{8.11}$$

if the branching ratio $\frac{\Gamma(\eta\to\pi^+ + \pi^- + \pi^0)}{\Gamma(\eta\to\mathrm{all})} = 0.2292(28)$ [P$^+$16] is inserted in equation 8.10.

This result for the decay $\eta \to \pi^0 + \mathrm{U} \to \pi^0 + \mathrm{e}^+ + \mathrm{e}^-$ with $m_{\mathrm{U}} = 150\,\mathrm{MeV}\,c^{-2}$ shows the potential of the WASA-at-COSY experimental setup for the search for a C violating decay with a dark boson U involved. Therefore, it is planned to utilize the higher statistics $\mathrm{p} + \mathrm{p} \to \mathrm{p} + \mathrm{p} + \eta$ data collected with WASA-at-COSY not only for the search for a C parity violating decay $\eta \to \pi^0 + \mathrm{e}^+ + \mathrm{e}^-$ via one virtual photon, but also for a decay via a hypothetical dark boson U [Dem17].

A. Appendix A: $p + d \rightarrow {}^3He + \eta$ cross section analysis

A.1. Investigation of the influence of beam momentum shifts on the resulting cross section

In this chapter the influence of a minor shift of the beam momentum assumed in the data analysis will be discussed. For this purpose the results presented in chapter 5, which were obtained assuming a beam momentum of $p_{\mathrm{beam}} = 1.673\,\mathrm{GeV}\,c^{-1}$ (and, thus, a beam energy of $T_{\mathrm{beam}} = 980\,\mathrm{MeV}$ and an excess energy of $Q = 48.8\,\mathrm{MeV}$), are compared to analysis results under the assumption of a beam momentum of $p_{\mathrm{beam}} = 1.670\,\mathrm{GeV}\,c^{-1}$ (corresponding to a beam energy of $T_{\mathrm{beam}} = 977.3\,\mathrm{MeV}$ and an excess energy of $Q = 47.3\,\mathrm{MeV}$).

In case of the determination of the η meson angular distribution, a shift of the beam momentum by about $3\,\mathrm{MeV}\,c^{-1}$ (0.2 %) can lead to a deviation of the determined efficiencies for the various angular bins by up to 1.6 %. The extracted angular distributions (shown in table 5.1, chapter 5.1) were obtained with an uncertainty of the beam momentum of 0.1 %, which results in an uncertainty of the acceptance of 0.8 %. The uncertainties given in table 5.1 vary from 3.2 % to 33 % and are dominated by the statistical uncertainty of the measured data and the uncertainty related to the extraction procedure of the number of produced η mesons. Hence, the angular distributions derived with an excess energy of $Q = 47.3\,\mathrm{MeV}$ instead of 48.8 MeV do in fact agree with the distribution derived with the original assumption within the given uncertainties. Furthermore, the larger uncertainty of the beam momentum does not significantly influence the overall uncertainty.

According to equation 4.11, the extracted η meson cross section ratio depends on the obtained η meson yields, the π^0 meson yields at $\cos\vartheta^{\pi^0}_{\mathrm{CMS}} = -1$, and the cross section ratio of the reaction $p + d \rightarrow {}^3He + \pi^0$ at $\cos\vartheta^{\pi^0}_{\mathrm{CMS}} = -1$. As shown

for the differential η meson yields, a shift of the beam momentum by 0.2 % has no significant impact on the total η meson yield. In case of the reaction $\mathrm{p} + \mathrm{d} \to {}^3\mathrm{He} + \pi^0$, the acceptances for $Q = 48.8\,\mathrm{MeV}$ and $Q = 59.8\,\mathrm{MeV}$ corresponding to a much larger beam momentum change agree within their uncertainties, as has been shown in chapter 4.11.3.

Using the fit function to the differential cross sections for $\cos\vartheta^{\pi^0}_{\mathrm{CMS}} = -1$ derived in chapter 4.11.4 (see figure 4.31), a differential cross section ratio

$$\frac{\sigma_{\pi^0}\left(T_{\mathrm{beam}} = 977.3\,\mathrm{MeV}\right)}{\sigma_{\pi^0}\left(T_{\mathrm{beam}} = 1000\,\mathrm{MeV}\right)} = 0.903 \pm 0.010 \tag{A.1}$$

can be extracted. Within the uncertainties this ratio agrees with the one obtained in chapter 4.11.4, namely equation 4.10

$$\frac{\sigma_{\pi^0}\left(T_{\mathrm{beam}} = 980\,\mathrm{MeV}\right)}{\sigma_{\pi^0}\left(T_{\mathrm{beam}} = 1000\,\mathrm{MeV}\right)} = 0.914 \pm 0.009\,. \tag{A.2}$$

With this differential cross section ratio a cross section ratio for a beam energy of 977.3 MeV can be calculated as

$$\begin{aligned}
\frac{\sigma_\eta\left(47.3\,\mathrm{MeV}\right)}{\sigma_\eta\left(59.8\,\mathrm{MeV}\right)} &= \frac{\sigma_{\pi^0}\left(T_{\mathrm{beam}} = 977.3\,\mathrm{MeV}\right)}{\sigma_{\pi^0}\left(T_{\mathrm{beam}} = 1000\,\mathrm{MeV}\right)} \cdot \frac{N_{\pi^0}\left(T_{\mathrm{beam}} = 1000\,\mathrm{MeV}\right)}{N_{\pi^0}\left(T_{\mathrm{beam}} = 977.3\,\mathrm{MeV}\right)} \\
&\quad \cdot \frac{N_\eta\left(47.3\,\mathrm{MeV}\right)}{N_\eta\left(59.8\,\mathrm{MeV}\right)} \\
&= (0.903 \pm 0.010) \cdot (8.6 \pm 0.6) \cdot \frac{N_\eta\left(47.3\,\mathrm{MeV}\right)}{N_\eta\left(59.8\,\mathrm{MeV}\right)} \\
&= 0.76 \pm 0.06\,.
\end{aligned} \tag{A.3}$$

By scaling the $Q = 59.8\,\mathrm{MeV}$ WASA-at-COSY data to the $Q = 59.4\,\mathrm{MeV}$ ANKE data [R+09] as described in chapter 5.2, a total cross section for $Q = 47.3\,\mathrm{MeV}$ could be calculated as

$$\sigma\left(47.3\,\mathrm{MeV}\right) = (294 \pm 24 \pm 48)\,\mathrm{nb}\,. \tag{A.4}$$

Compared to the published cross section $\sigma\left((48.8 \pm 0.8)\,\mathrm{MeV}\right) = (298 \pm 24 \pm 49)\,\mathrm{nb}$ [A+14b] this value deviates by just 4 nb, which is much smaller than both the statistical and the systematic uncertainty. Therefore, changes to the resulting cross sections and subsequent conclusions as published in [A+14b] and presented in this thesis due to a possible shift of the beam momentum by 0.2 % can be neglected.

A.2. Lists of runs used for the $p + d \rightarrow {}^3He + \eta$ cross section analysis

Table A.1.: List of all used $Q = 59.8\,\mathrm{MeV}$ runs.

run_14403	run_14414	run_14424	run_14434	run_14444	run_14450
run_14451	run_14452	run_14453	run_14454	run_14455	run_14456
run_14457	run_14458	run_14459	run_14460	run_14461	run_14462
run_14463	run_14464	run_14465	run_14466	run_14467	run_14468
run_14469	run_14475	run_14485	run_14497	run_14507	run_14517
run_14530	run_14540	run_14554	run_14564	run_14574	run_14591
run_14601	run_14611	run_14621	run_14635	run_14645	run_14655
run_14671	run_14682	run_14692	run_14702	run_14712	run_14722
run_14734	run_14751	run_14761	run_14771	run_14781	run_14791
run_14802	run_14812	run_14830	run_14840	run_14850	run_14860
run_14873	run_14883	run_14894	run_14904	run_14916	run_14926
run_14936	run_14946	run_14956	run_14970	run_14980	run_14990
run_15000	run_15010	run_15022	run_15034	run_15044	run_15054
run_15064	run_15074	run_15086	run_15098	run_15109	run_15119
run_15129	run_15139	run_15151	run_15161	run_15171	run_15181
run_15192	run_15202	run_15212	run_15222	run_15232	run_15242
run_15252	run_15262	run_15272	run_15303	run_15314	run_15324
run_15334	run_15344	run_15356	run_15366	run_15376	run_15386
run_15396	run_15406	run_15416	run_15427	run_15438	run_15448
run_15459	run_15469	run_15482	run_15492	run_15505	run_15515
run_15525	run_15535	run_15545	run_15555	run_15565	run_15575
run_15616	run_15626	run_15637	run_15648	run_15660	run_15672
run_15682	run_15692	run_15702	run_15713	run_15723	run_15733
run_15743	run_15753	run_15763	run_15773	run_15788	run_15798
run_15808	run_15818	run_15828	run_15838	run_15848	run_15859
run_15869	run_15879	run_15890	run_15904	run_15915	run_15931
run_15941					

Table A.2.: List of all used $Q = 48.8\,\mathrm{MeV}$ runs.

run_15277	run_15279	run_15281	run_15283	run_15285
run_15287	run_15288	run_15289	run_15290	run_15291
run_15292	run_15293	run_15294	run_15295	run_15296

B. Appendix B: $\eta \to \pi^0 + e^+ + e^-$ decay analysis

B.1. Calculations for the amplitude of the decay $\eta \to \pi^0 + \gamma^* \to \pi^0 + e^+ + e^-$

The expression $(p_\eta + p_\pi)^\mu \, \mathcal{O}_{\mu\mu'}(e^+e^-) \, (p_\eta + p_\pi)^{\mu'}$ used for the calculation of the absolute amplitude squared in chapter 2.4.2 can be calculated as described in the following. For the calculation the following variables were used:

- the four-momentum $p_{\eta,\mu}$ and the mass m_η of the η meson,
- the four-momentum $p_{\pi,\mu}$ of the π^0 meson,
- the four-momentum $p^+_{e,\mu}$, the mass m_e, and the energy E_{e^+} of the positron,
- the four-momentum $p^-_{e,\mu}$, the mass m_e, and the energy E_{e^-} of the electron, and
- the four-momentum sum $p_{e,\mu} = p^+_{e,\mu} + p^-_{e,\mu}$.

Furthermore, the expression $(p_\eta + p_\pi)^\mu \, \mathcal{O}_{\mu\mu'}(e^+e^-) \, (p_\eta + p_\pi)^{\mu'}$ was solved in the η rest frame and the following relations were used:

$$(p^+_e)^2 = (p^-_e)^2 = m_e^2 \,, \tag{B.1}$$

$$p_\eta^2 = m_\eta^2 \,, \tag{B.2}$$

$$q_\mu = p_{e,\mu} \,, \tag{B.3}$$

$$q_\mu = p_{\eta,\mu} - p_{\pi,\mu}$$

$$\Rightarrow p_{\eta,\mu} + p_{\pi,\mu} = 2p_{\eta,\mu} - q_\mu = 2p_{\eta,\mu} - p_{e,\mu} \,, \tag{B.4}$$

$$p_\eta p_e^\pm = m_\eta E_{e^\pm} \text{ , and} \tag{B.5}$$

$$(p_\eta + p_\pi)^\mu \, g_{\mu\mu'} \, (p_\eta + p_\pi)^{\mu'} = (p_\eta + p_\pi)^2 \,. \tag{B.6}$$

With these relations $(p_\eta + p_\pi)^\mu \, \mathcal{O}_{\mu\mu'}(\mathrm{e}^+\mathrm{e}^-) \, (p_\eta + p_\pi)^{\mu'}$ was calculated as described below.

$$
\begin{aligned}
&(p_\eta + p_\pi)^\mu \, \mathcal{O}_{\mu\mu'}(\mathrm{e}^+\mathrm{e}^-) \, (p_\eta + p_\pi)^{\mu'} \\
&= (p_\eta + p_\pi)^\mu \, 2e^2 p_\mathrm{e}^2 \left[- \left(g_{\mu\mu'} - \frac{p_{\mathrm{e},\mu} p_{\mathrm{e},\mu'}}{p_\mathrm{e}^2} \right) - \frac{\left(p_\mathrm{e}^+ - p_\mathrm{e}^-\right)_\mu \left(p_\mathrm{e}^+ - p_\mathrm{e}^-\right)_{\mu'}}{p_\mathrm{e}^2} \right] (p_\eta + p_\pi)^{\mu'} \\
&= 2e^2 p_\mathrm{e}^2 \left(- (p_\eta + p_\pi)^2 + \frac{\left[(p_\eta + p_\pi) \, p_\mathrm{e} \right]^2}{p_\mathrm{e}^2} - \frac{\left[(p_\eta + p_\pi) \left(p_\mathrm{e}^+ - p_\mathrm{e}^-\right) \right]^2}{p_\mathrm{e}^2} \right) \\
&= 2e^2 p_\mathrm{e}^2 \left(- (p_\eta + p_\pi)^2 + \frac{\left[(p_\eta + p_\pi) \left(p_\mathrm{e}^+ + p_\mathrm{e}^-\right) \right]^2}{p_\mathrm{e}^2} - \frac{\left[(p_\eta + p_\pi) \left(p_\mathrm{e}^+ - p_\mathrm{e}^-\right) \right]^2}{p_\mathrm{e}^2} \right) \\
&= 2e^2 p_\mathrm{e}^2 \Bigg(- (p_\eta + p_\pi)^2 \\
&\qquad + \frac{\cancel{\left[(p_\eta + p_\pi) \, p_\mathrm{e}^+ \right]^2} + 2 \left[(p_\eta + p_\pi) \, p_\mathrm{e}^+ \right] \left[(p_\eta + p_\pi) \, p_\mathrm{e}^- \right] + \cancel{\left[(p_\eta + p_\pi) \, p_\mathrm{e}^- \right]^2}}{p_\mathrm{e}^2} \\
&\qquad - \frac{\cancel{\left[(p_\eta + p_\pi) \, p_\mathrm{e}^+ \right]^2} - 2 \left[(p_\eta + p_\pi) \, p_\mathrm{e}^+ \right] \left[(p_\eta + p_\pi) \, p_\mathrm{e}^- \right] + \cancel{\left[(p_\eta + p_\pi) \, p_\mathrm{e}^- \right]^2}}{p_\mathrm{e}^2} \Bigg) \\
&= 2e^2 p_\mathrm{e}^2 \left(- (p_\eta + p_\pi)^2 + 4 \frac{\left[(p_\eta + p_\pi) \, p_\mathrm{e}^+ \right] \left[(p_\eta + p_\pi) \, p_\mathrm{e}^- \right]}{p_\mathrm{e}^2} \right) \\
&= 2e^2 p_\mathrm{e}^2 \left(- (2p_\eta - p_\mathrm{e})^2 + 4 \frac{\left[(2p_\eta - p_\mathrm{e}) \, p_\mathrm{e}^+ \right] \left[(2p_\eta - p_\mathrm{e}) \, p_\mathrm{e}^- \right]}{p_\mathrm{e}^2} \right) \\
&= 2e^2 p_\mathrm{e}^2 \left(-4p_\eta^2 + 4p_\eta p_\mathrm{e} - p_\mathrm{e}^2 + 4 \frac{\left[2p_\eta p_\mathrm{e}^+ - \left(p_\mathrm{e}^+ + p_\mathrm{e}^-\right) p_\mathrm{e}^+ \right] \left[2p_\eta p_\mathrm{e}^- - \left(p_\mathrm{e}^+ + p_\mathrm{e}^-\right) p_\mathrm{e}^- \right]}{p_\mathrm{e}^2} \right) \\
&= 2e^2 p_\mathrm{e}^2 \Bigg(-4m_\eta^2 + 4m_\eta \left(E_{\mathrm{e}^+} + E_{\mathrm{e}^-} \right) - p_\mathrm{e}^2 \\
&\qquad + 4 \frac{\left[2m_\eta E_{\mathrm{e}^+} - \left(m_\mathrm{e}^2 + p_\mathrm{e}^+ p_\mathrm{e}^- \right) \right] \left[2m_\eta E_{\mathrm{e}^-} - \left(m_\mathrm{e}^2 + p_\mathrm{e}^+ p_\mathrm{e}^- \right) \right]}{p_\mathrm{e}^2} \Bigg) \\
&= 2e^2 p_\mathrm{e}^2 \Bigg(-4m_\eta^2 + 4m_\eta \left(E_{\mathrm{e}^+} + E_{\mathrm{e}^-} \right) - p_\mathrm{e}^2 \\
&\qquad + 4 \frac{\left[2m_\eta E_{\mathrm{e}^+} - \frac{1}{2} \left(m_\mathrm{e}^2 + 2p_\mathrm{e}^+ p_\mathrm{e}^- + m_\mathrm{e}^2 \right) \right] \left[2m_\eta E_{\mathrm{e}^-} - \frac{1}{2} \left(m_\mathrm{e}^2 + 2p_\mathrm{e}^+ p_\mathrm{e}^- + m_\mathrm{e}^2 \right) \right]}{p_\mathrm{e}^2} \Bigg)
\end{aligned}
$$

$$
\begin{aligned}
&= 2e^2 p_{\mathrm{e}}^2 \left(-4m_\eta^2 + 4m_\eta \left(E_{\mathrm{e}^+} + E_{\mathrm{e}^-}\right) - p_{\mathrm{e}}^2 \right. \\
&\qquad \left. + 4\frac{\left[2m_\eta E_{\mathrm{e}^+} - \frac{1}{2}\left(p_{\mathrm{e}}^+ + p_{\mathrm{e}}^-\right)^2\right]\left[2m_\eta E_{\mathrm{e}^-} - \frac{1}{2}\left(p_{\mathrm{e}}^+ + p_{\mathrm{e}}^-\right)^2\right]}{p_{\mathrm{e}}^2} \right) \\
&= 2e^2 q^2 \left(-4m_\eta^2 + 4m_\eta \left(E_{\mathrm{e}^+} + E_{\mathrm{e}^-}\right) - q^2 + 4\frac{\left[2m_\eta E_{\mathrm{e}^+} - \frac{1}{2}q^2\right]\left[2m_\eta E_{\mathrm{e}^-} - \frac{1}{2}q^2\right]}{q^2} \right) \\
&= 2e^2 q^2 \left(-4m_\eta^2 + 4m_\eta \left(E_{\mathrm{e}^+} + E_{\mathrm{e}^-}\right) - q^2 + 4\frac{4m_\eta^2 E_{\mathrm{e}^+} E_{\mathrm{e}^-} - m_\eta q^2 \left(E_{\mathrm{e}^+} + E_{\mathrm{e}^-}\right) + \frac{q^4}{4}}{q^2} \right) \\
&= 2e^2 q^2 \left(-4m_\eta^2 + \cancel{4m_\eta \left(E_{\mathrm{e}^+} + E_{\mathrm{e}^-}\right)} - \cancel{q^2} + \frac{16m_\eta^2 E_{\mathrm{e}^+} E_{\mathrm{e}^-}}{q^2} - \cancel{4m_\eta \left(E_{\mathrm{e}^+} + E_{\mathrm{e}^-}\right)} + \cancel{q^2} \right)
\end{aligned}
$$

$$
\Rightarrow \boxed{\left(p_\eta + p_\pi\right)^\mu \mathcal{O}_{\mu\mu'}(\mathrm{e}^+\mathrm{e}^-)\left(p_\eta + p_\pi\right)^{\mu'} = 2e^2\left(-4m_\eta^2 q^2 + 16m_\eta^2 E_{\mathrm{e}^+} E_{\mathrm{e}^-}\right)} \qquad \text{(B.7)}
$$

B.2. Monte Carlo fits to the 2008 and 2009 data

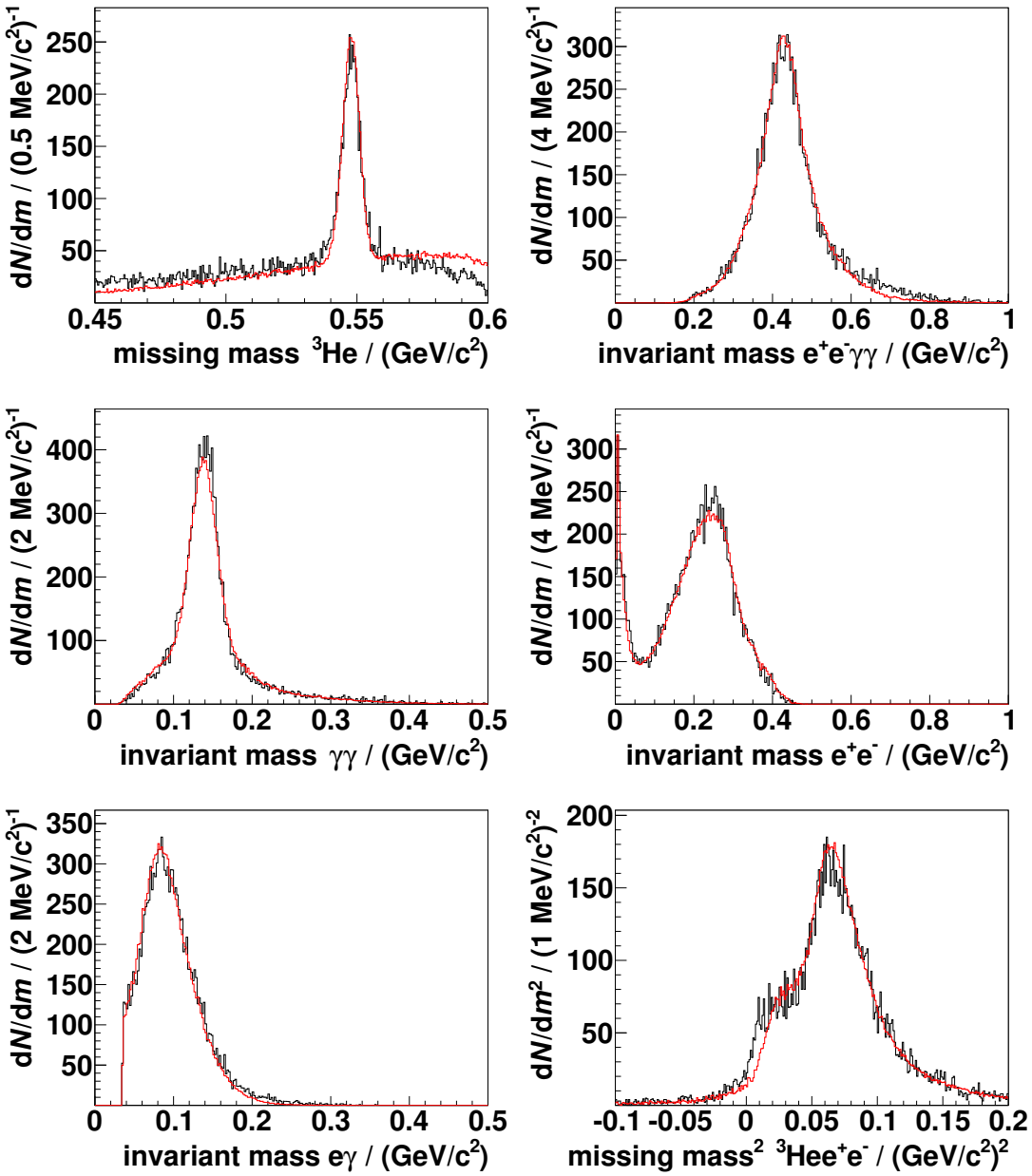

Figure B.1.: Fit by Monte Carlo simulations (red) to the 2008 data set (black) for the angular range $-0.6 \leq \cos\vartheta_\eta^{\mathrm{CMS}} < -0.4$. Upper left: ^{3}He missing mass. Upper right: invariant mass of two oppositely charged and two neutral CD particles. Middle left: invariant mass of two neutral CD particles. Middle right: invariant mass of two oppositely charged CD particles. Lower left: invariant mass of one charged and one neutral CD particle, smallest combination. Lower right: squared missing mass of ^{3}He and two oppositely charged CD particles. For the charged CD particles an electron mass was assumed. All data samples were preselected with the conditions described in chapter 6.5. For fit details see chapter 6.6.

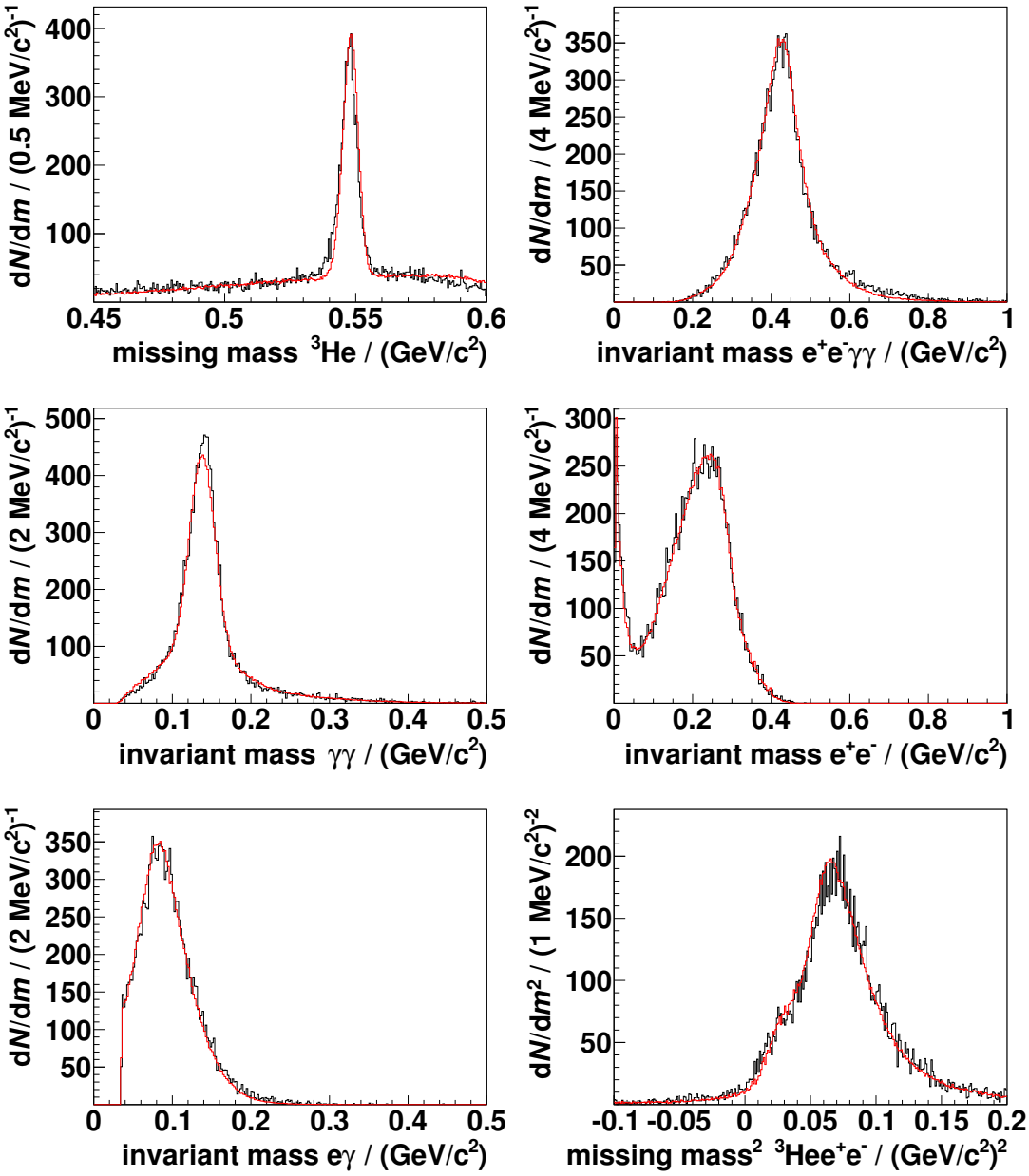

Figure B.2.: Fit by Monte Carlo simulations (red) to the 2008 data set (black) for the angular range $-0.4 \leq \cos\vartheta_{\eta}^{\mathrm{CMS}} < -0.2$. Upper left: ^{3}He missing mass. Upper right: invariant mass of two oppositely charged and two neutral CD particles. Middle left: invariant mass of two neutral CD particles. Middle right: invariant mass of two oppositely charged CD particles. Lower left: invariant mass of one charged and one neutral CD particle, smallest combination. Lower right: squared missing mass of ^{3}He and two oppositely charged CD particles. For the charged CD particles an electron mass was assumed. All data samples were preselected with the conditions described in chapter 6.5. For fit details see chapter 6.6.

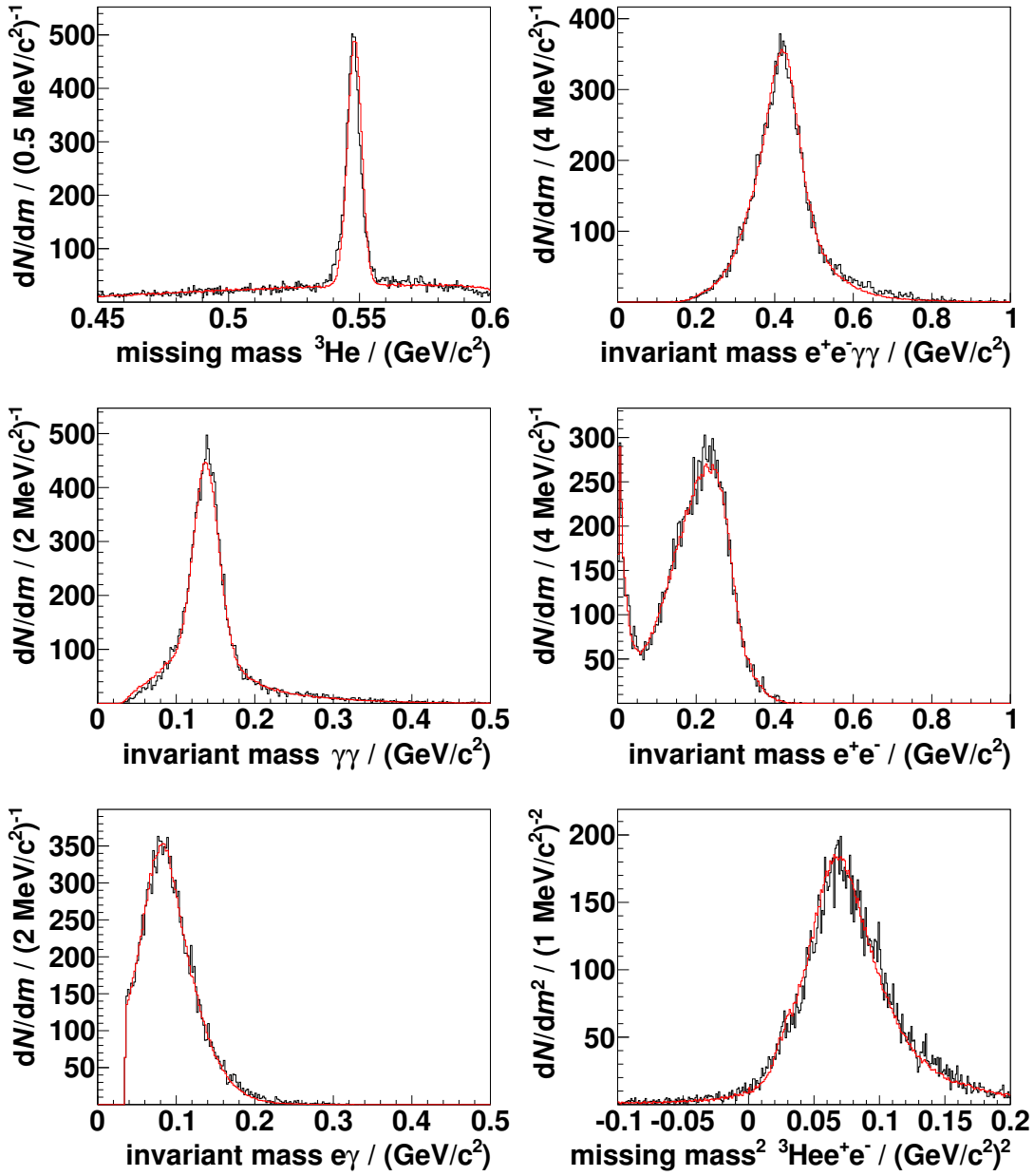

Figure B.3.: Fit by Monte Carlo simulations (red) to the 2008 data set (black) for the angular range $-0.2 \leq \cos\vartheta_\eta^{\mathrm{CMS}} < 0.0$. Upper left: ^{3}He missing mass. Upper right: invariant mass of two oppositely charged and two neutral CD particles. Middle left: invariant mass of two neutral CD particles. Middle right: invariant mass of two oppositely charged CD particles. Lower left: invariant mass of one charged and one neutral CD particle, smallest combination. Lower right: squared missing mass of ^{3}He and two oppositely charged CD particles. For the charged CD particles an electron mass was assumed. All data samples were preselected with the conditions described in chapter 6.5. For fit details see chapter 6.6.

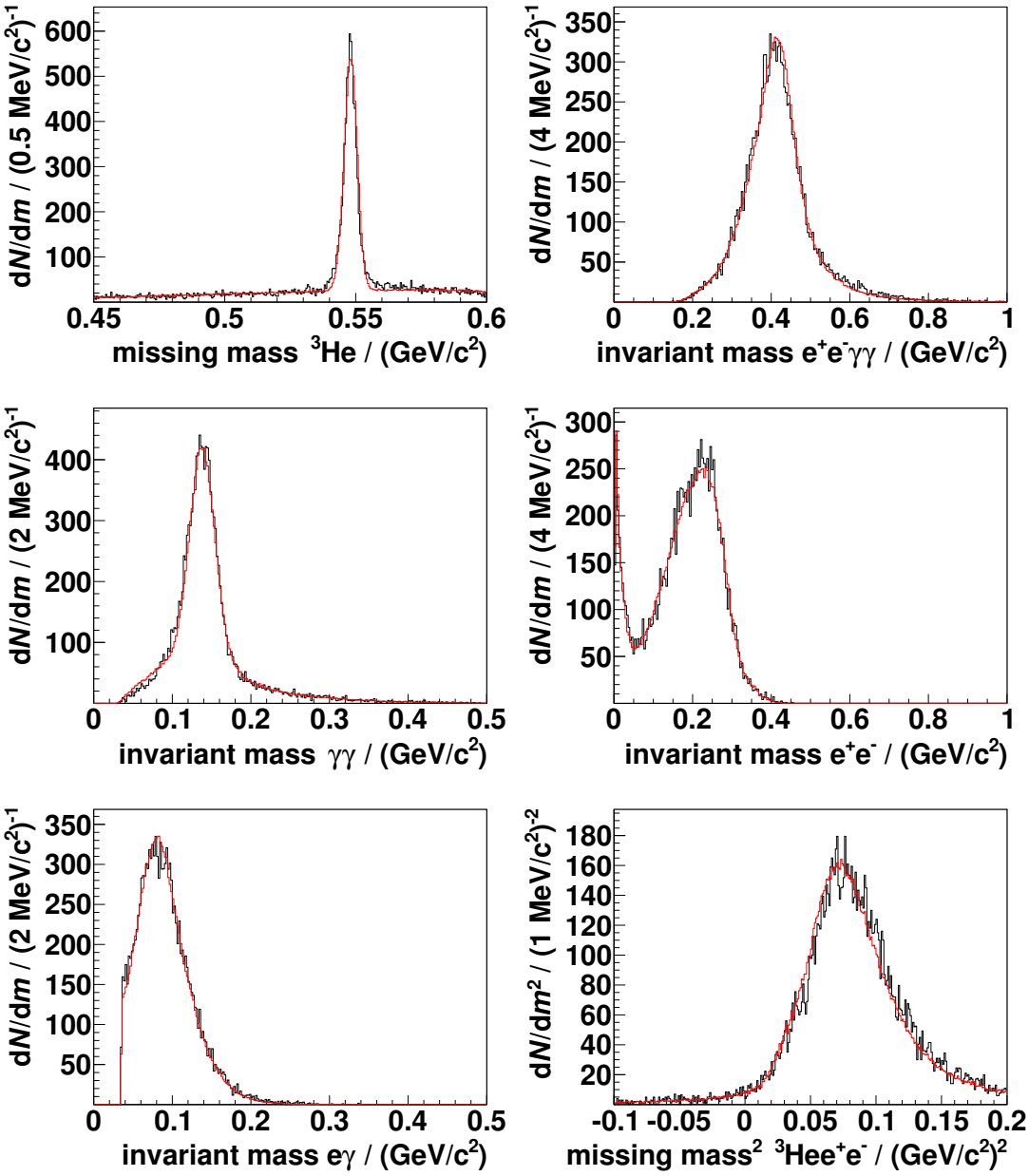

Figure B.4.: Fit by Monte Carlo simulations (red) to the 2008 data set (black) for the angular range $0.0 \leq \cos\vartheta_{\eta}^{\mathrm{CMS}} < 0.2$. Upper left: ^{3}He missing mass. Upper right: invariant mass of two oppositely charged and two neutral CD particles. Middle left: invariant mass of two neutral CD particles. Middle right: invariant mass of two oppositely charged CD particles. Lower left: invariant mass of one charged and one neutral CD particle, smallest combination. Lower right: squared missing mass of ^{3}He and two oppositely charged CD particles. For the charged CD particles an electron mass was assumed. All data samples were preselected with the conditions described in chapter 6.5. For fit details see chapter 6.6.

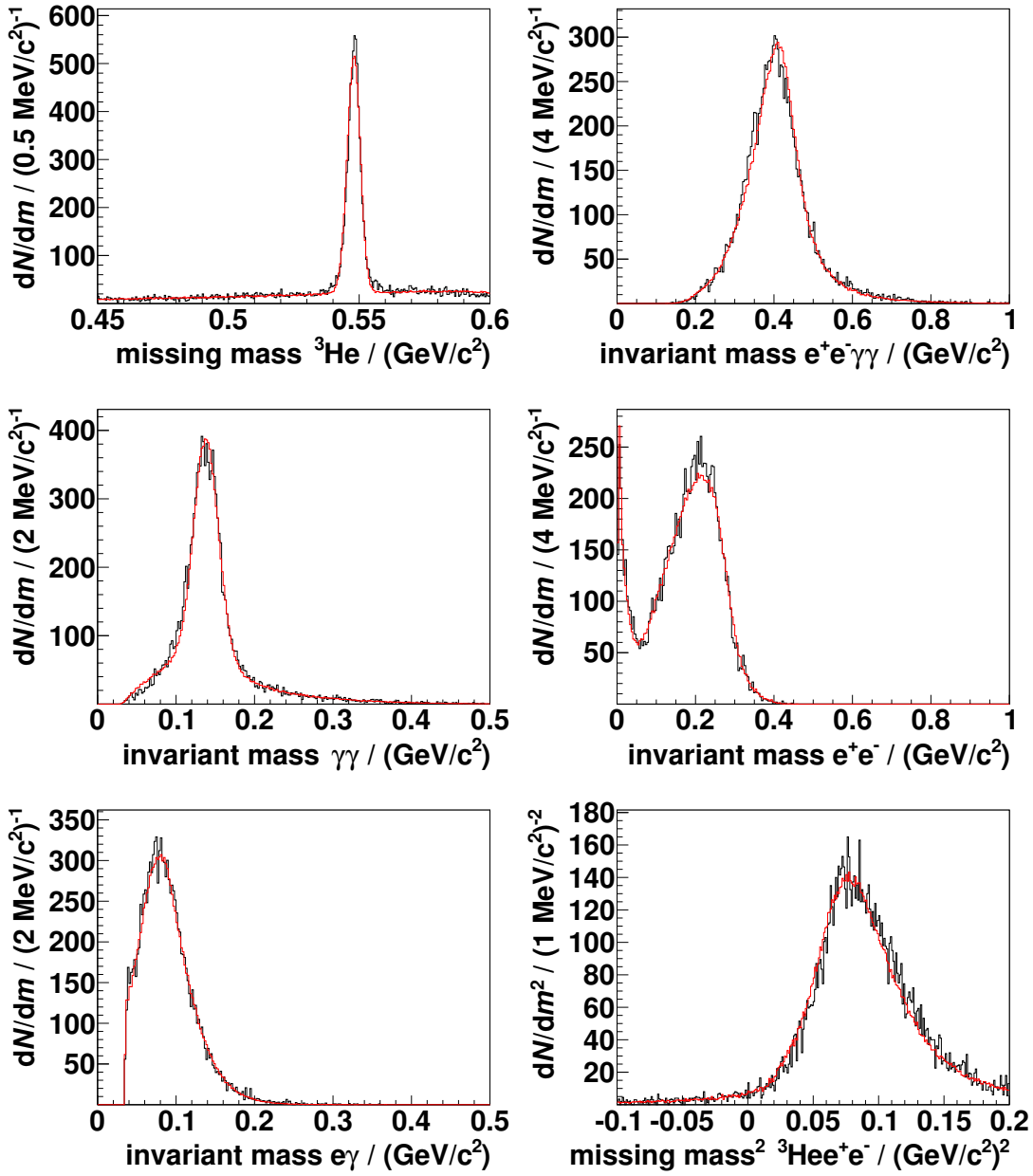

Figure B.5.: Fit by Monte Carlo simulations (red) to the 2008 data set (black) for the angular range $0.2 \leq \cos\vartheta_\eta^{\mathrm{CMS}} < 0.4$. Upper left: ^{3}He missing mass. Upper right: invariant mass of two oppositely charged and two neutral CD particles. Middle left: invariant mass of two neutral CD particles. Middle right: invariant mass of two oppositely charged CD particles. Lower left: invariant mass of one charged and one neutral CD particle, smallest combination. Lower right: squared missing mass of ^{3}He and two oppositely charged CD particles. For the charged CD particles an electron mass was assumed. All data samples were preselected with the conditions described in chapter 6.5. For fit details see chapter 6.6.

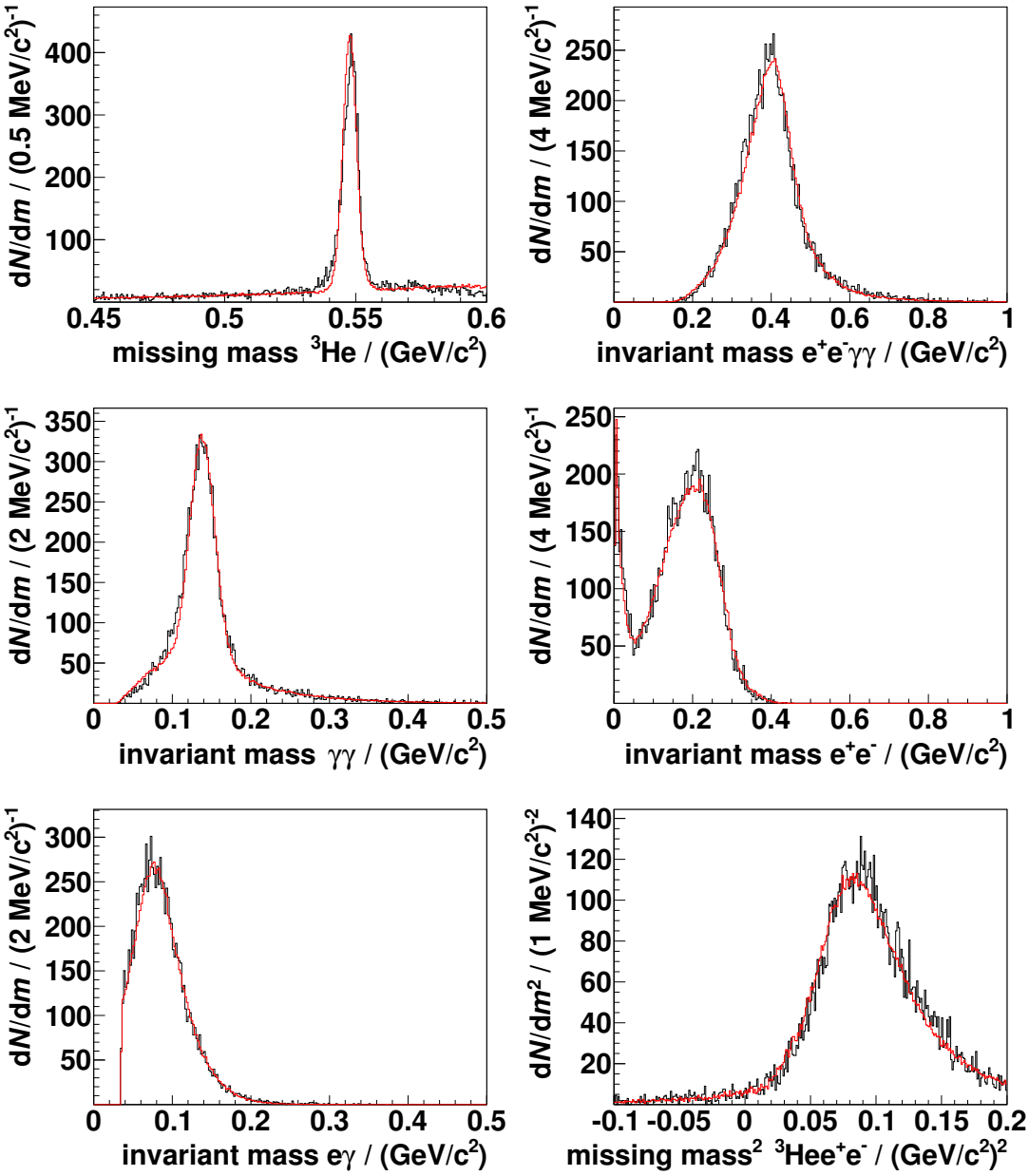

Figure B.6.: Fit by Monte Carlo simulations (red) to the 2008 data set (black) for the angular range $0.4 \leq \cos\vartheta_{\eta}^{\mathrm{CMS}} < 0.6$. Upper left: ^{3}He missing mass. Upper right: invariant mass of two oppositely charged and two neutral CD particles. Middle left: invariant mass of two neutral CD particles. Middle right: invariant mass of two oppositely charged CD particles. Lower left: invariant mass of one charged and one neutral CD particle, smallest combination. Lower right: squared missing mass of ^{3}He and two oppositely charged CD particles. For the charged CD particles an electron mass was assumed. All data samples were preselected with the conditions described in chapter 6.5. For fit details see chapter 6.6.

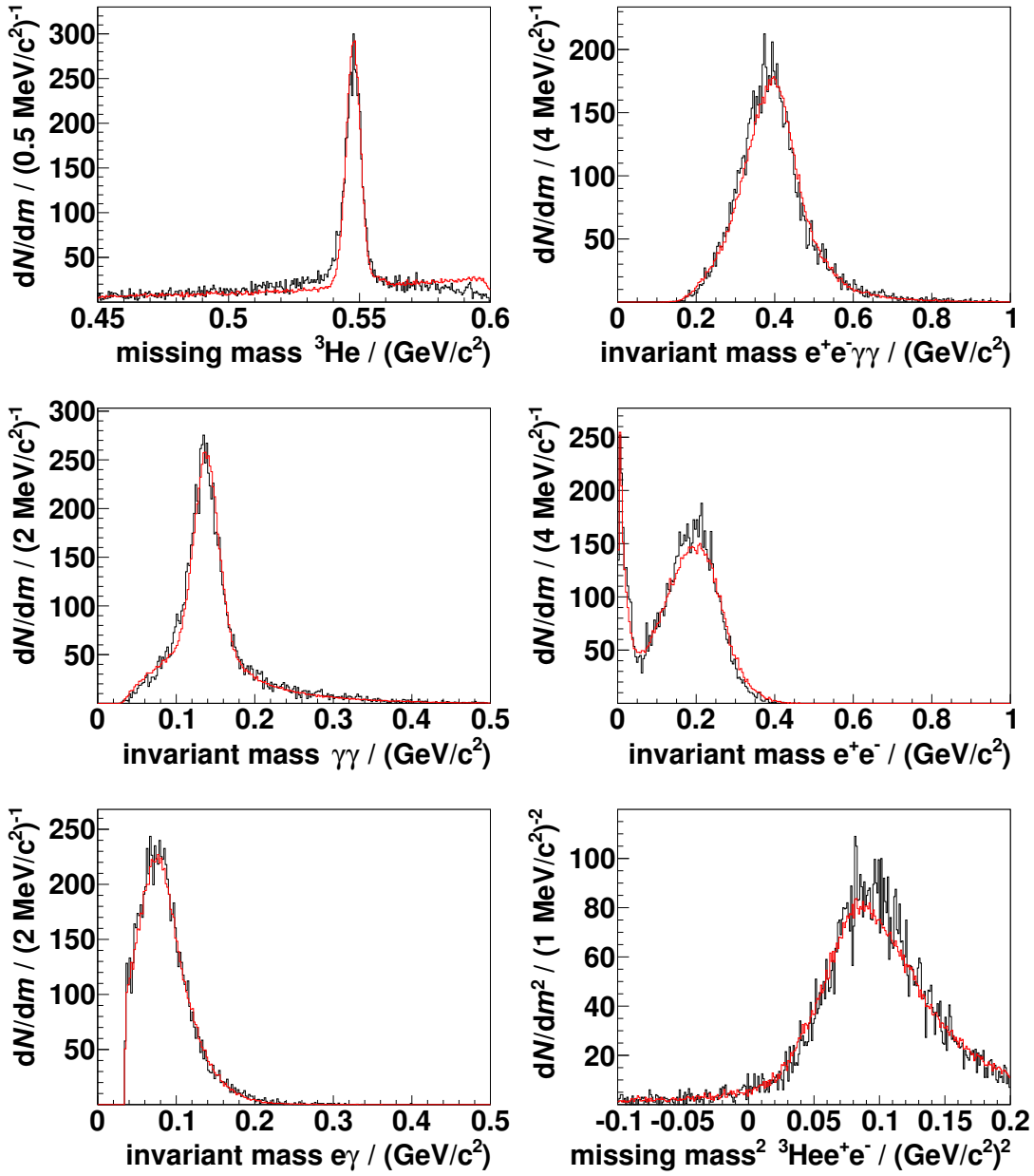

Figure B.7.: Fit by Monte Carlo simulations (red) to the 2008 data set (black) for the angular range $0.6 \leq \cos\vartheta_\eta^{\mathrm{CMS}} < 0.8$. Upper left: ^{3}He missing mass. Upper right: invariant mass of two oppositely charged and two neutral CD particles. Middle left: invariant mass of two neutral CD particles. Middle right: invariant mass of two oppositely charged CD particles. Lower left: invariant mass of one charged and one neutral CD particle, smallest combination. Lower right: squared missing mass of ^{3}He and two oppositely charged CD particles. For the charged CD particles an electron mass was assumed. All data samples were preselected with the conditions described in chapter 6.5. For fit details see chapter 6.6.

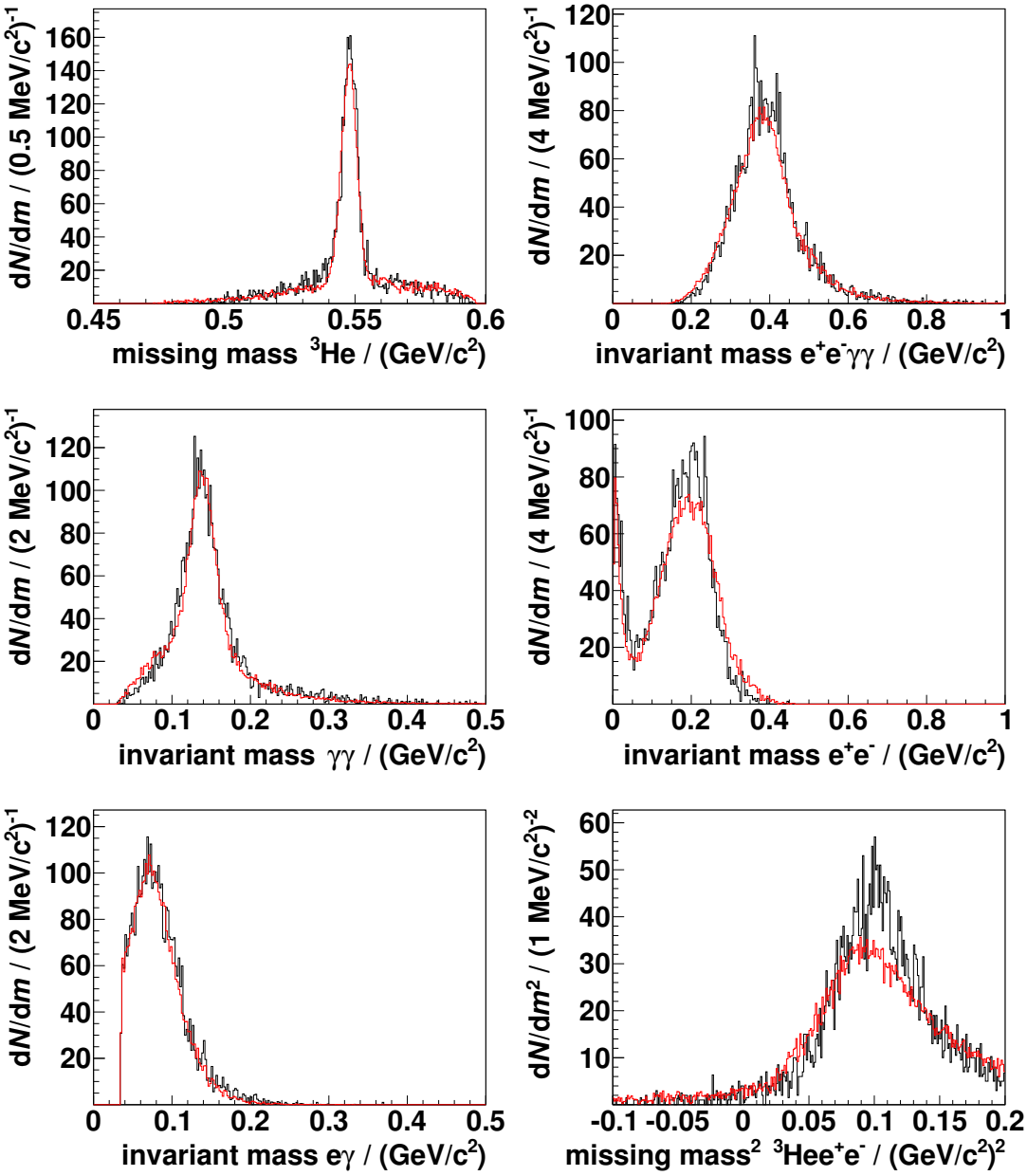

Figure B.8.: Fit by Monte Carlo simulations (red) to the 2008 data set (black) for the angular range $0.8 \leq \cos\vartheta_{\eta}^{\mathrm{CMS}} \leq 1.0$. Upper left: ^{3}He missing mass. Upper right: invariant mass of two oppositely charged and two neutral CD particles. Middle left: invariant mass of two neutral CD particles. Middle right: invariant mass of two oppositely charged CD particles. Lower left: invariant mass of one charged and one neutral CD particle, smallest combination. Lower right: squared missing mass of ^{3}He and two oppositely charged CD particles. For the charged CD particles an electron mass was assumed. All data samples were preselected with the conditions described in chapter 6.5. For fit details see chapter 6.6.

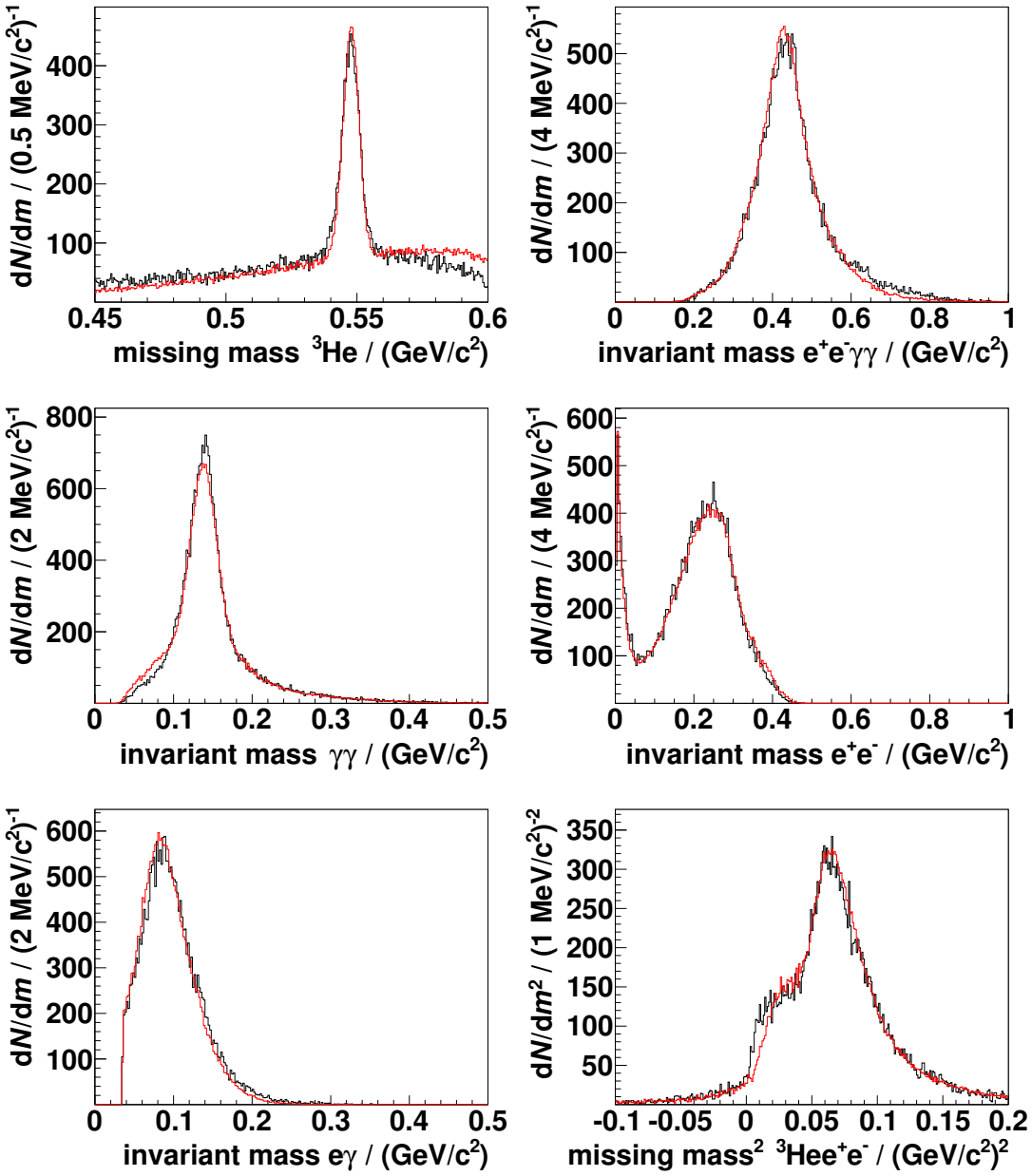

Figure B.9.: Fit by Monte Carlo simulations (red) to the 2009 data set (black) for the angular range $-0.6 \leq \cos\vartheta_\eta^{\mathrm{CMS}} < -0.4$. Upper left: ^{3}He missing mass. Upper right: invariant mass of two oppositely charged and two neutral CD particles. Middle left: invariant mass of two neutral CD particles. Middle right: invariant mass of two oppositely charged CD particles. Lower left: invariant mass of one charged and one neutral CD particle, smallest combination. Lower right: squared missing mass of ^{3}He and two oppositely charged CD particles. For the charged CD particles an electron mass was assumed. All data samples were preselected with the conditions described in chapter 6.5. For fit details see chapter 6.6.

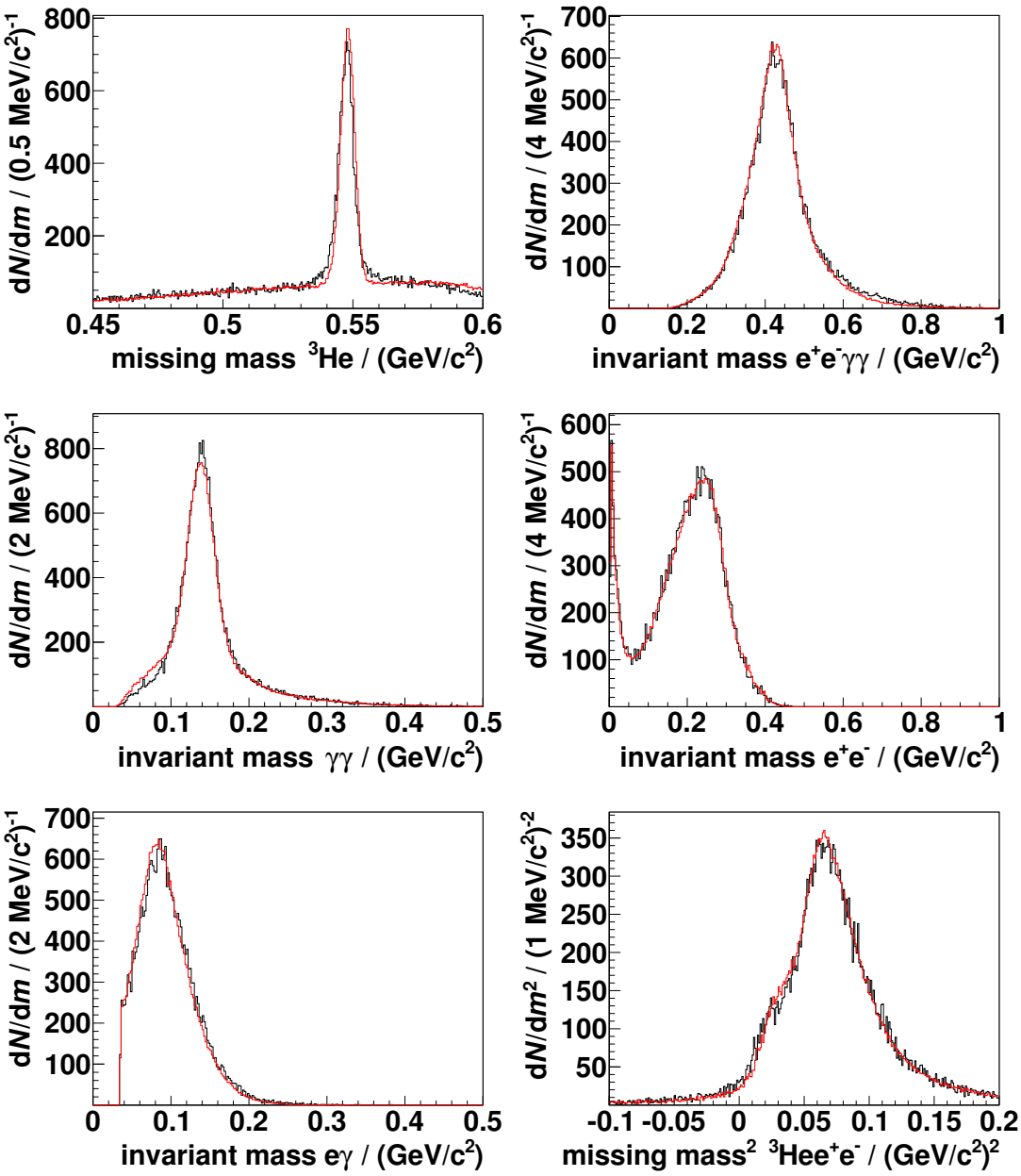

Figure B.10.: Fit by Monte Carlo simulations (red) to the 2009 data set (black) for the angular range $-0.4 \leq \cos\vartheta_{\eta}^{\mathrm{CMS}} < -0.2$. Upper left: ^{3}He missing mass. Upper right: invariant mass of two oppositely charged and two neutral CD particles. Middle left: invariant mass of two neutral CD particles. Middle right: invariant mass of two oppositely charged CD particles. Lower left: invariant mass of one charged and one neutral CD particle, smallest combination. Lower right: squared missing mass of ^{3}He and two oppositely charged CD particles. For the charged CD particles an electron mass was assumed. All data samples were preselected with the conditions described in chapter 6.5. For fit details see chapter 6.6.

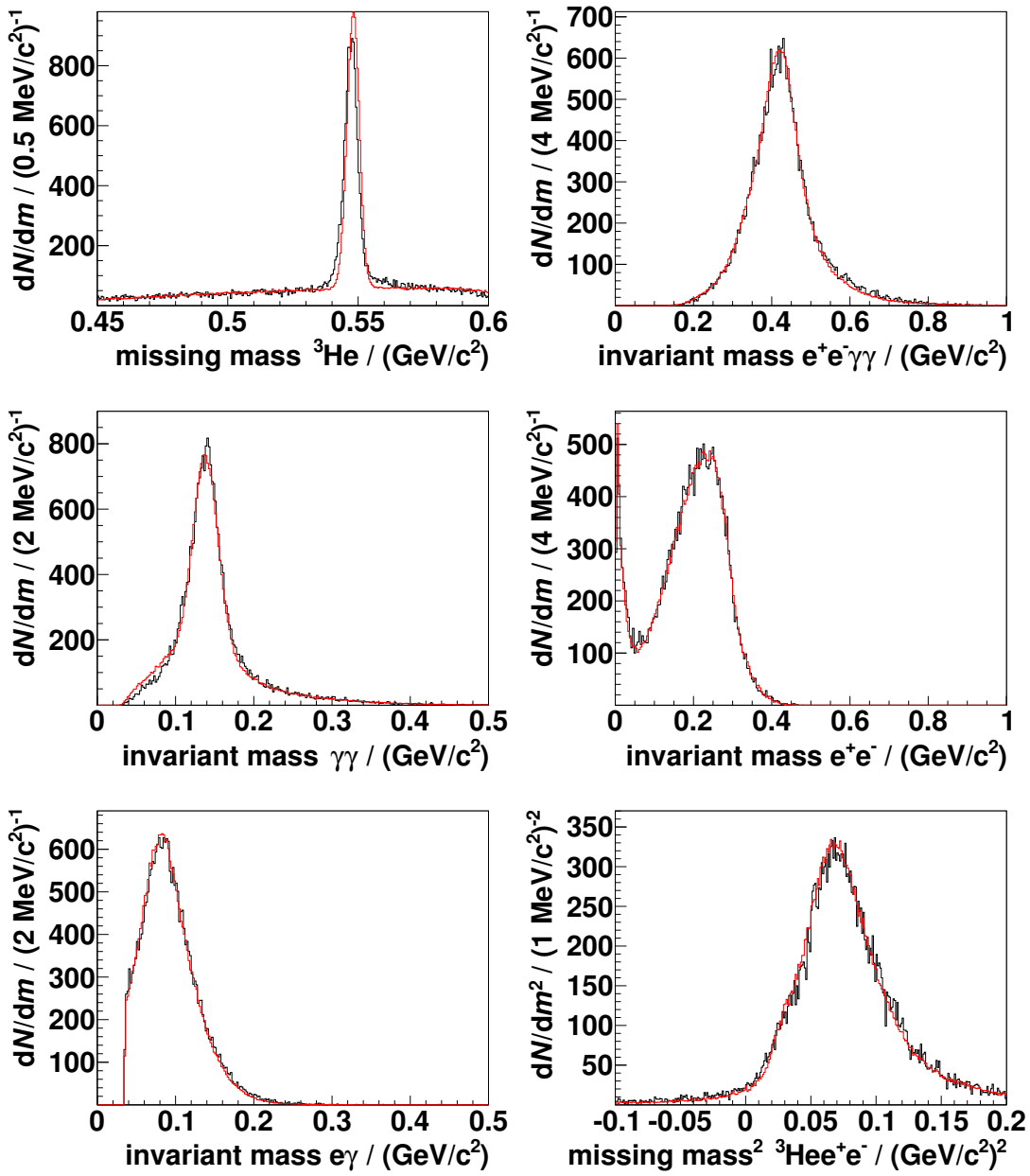

Figure B.11.: Fit by Monte Carlo simulations (red) to the 2009 data set (black) for the angular range $-0.2 \leq \cos\vartheta_{\eta}^{\mathrm{CMS}} < 0.0$. Upper left: ^{3}He missing mass. Upper right: invariant mass of two oppositely charged and two neutral CD particles. Middle left: invariant mass of two neutral CD particles. Middle right: invariant mass of two oppositely charged CD particles. Lower left: invariant mass of one charged and one neutral CD particle, smallest combination. Lower right: squared missing mass of ^{3}He and two oppositely charged CD particles. For the charged CD particles an electron mass was assumed. All data samples were preselected with the conditions described in chapter 6.5. For fit details see chapter 6.6.

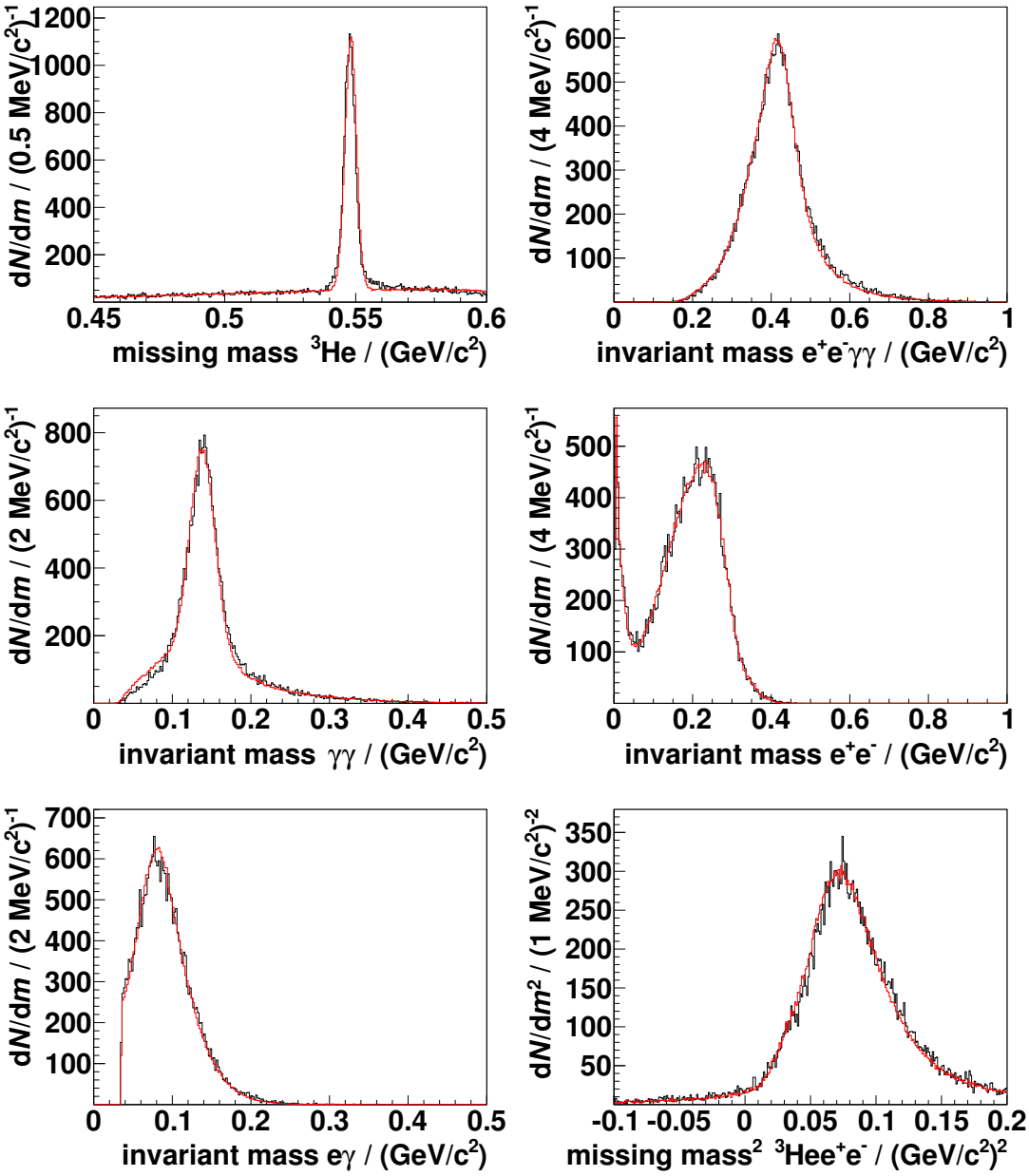

Figure B.12.: Fit by Monte Carlo simulations (red) to the 2009 data set (black) for the angular range $0.0 \leq \cos\vartheta_{\eta}^{\mathrm{CMS}} < 0.2$. Upper left: ^{3}He missing mass. Upper right: invariant mass of two oppositely charged and two neutral CD particles. Middle left: invariant mass of two neutral CD particles. Middle right: invariant mass of two oppositely charged CD particles. Lower left: invariant mass of one charged and one neutral CD particle, smallest combination. Lower right: squared missing mass of ^{3}He and two oppositely charged CD particles. For the charged CD particles an electron mass was assumed. All data samples were preselected with the conditions described in chapter 6.5. For fit details see chapter 6.6.

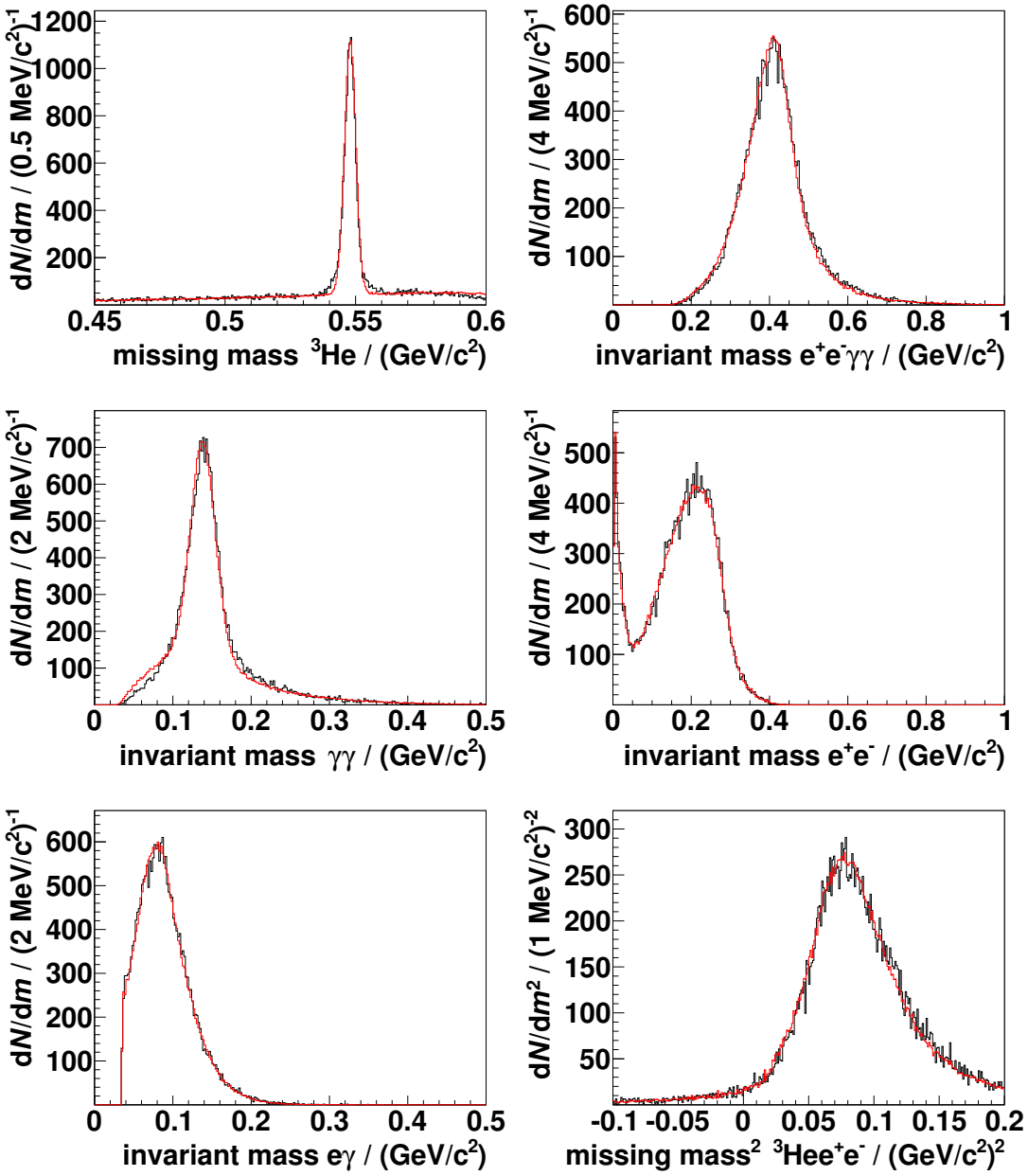

Figure B.13.: Fit by Monte Carlo simulations (red) to the 2009 data set (black) for the angular range $0.2 \leq \cos\vartheta_\eta^{\mathrm{CMS}} < 0.4$. Upper left: ^{3}He missing mass. Upper right: invariant mass of two oppositely charged and two neutral CD particles. Middle left: invariant mass of two neutral CD particles. Middle right: invariant mass of two oppositely charged CD particles. Lower left: invariant mass of one charged and one neutral CD particle, smallest combination. Lower right: squared missing mass of ^{3}He and two oppositely charged CD particles. For the charged CD particles an electron mass was assumed. All data samples were preselected with the conditions described in chapter 6.5. For fit details see chapter 6.6.

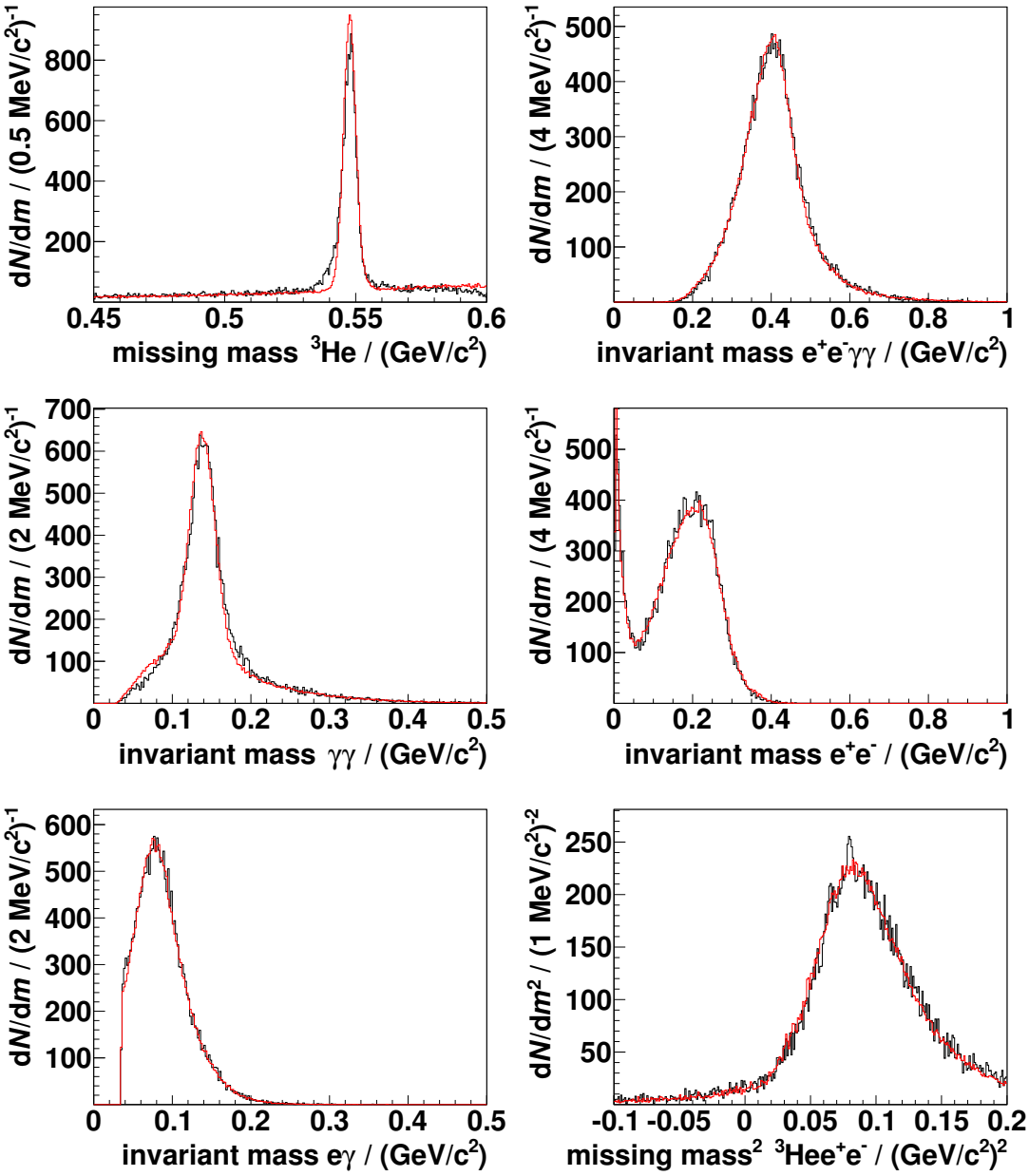

Figure B.14.: Fit by Monte Carlo simulations (red) to the 2009 data set (black) for the angular range $0.4 \leq \cos\vartheta_{\eta}^{\mathrm{CMS}} < 0.6$. Upper left: ^{3}He missing mass. Upper right: invariant mass of two oppositely charged and two neutral CD particles. Middle left: invariant mass of two neutral CD particles. Middle right: invariant mass of two oppositely charged CD particles. Lower left: invariant mass of one charged and one neutral CD particle, smallest combination. Lower right: squared missing mass of ^{3}He and two oppositely charged CD particles. For the charged CD particles an electron mass was assumed. All data samples were preselected with the conditions described in chapter 6.5. For fit details see chapter 6.6.

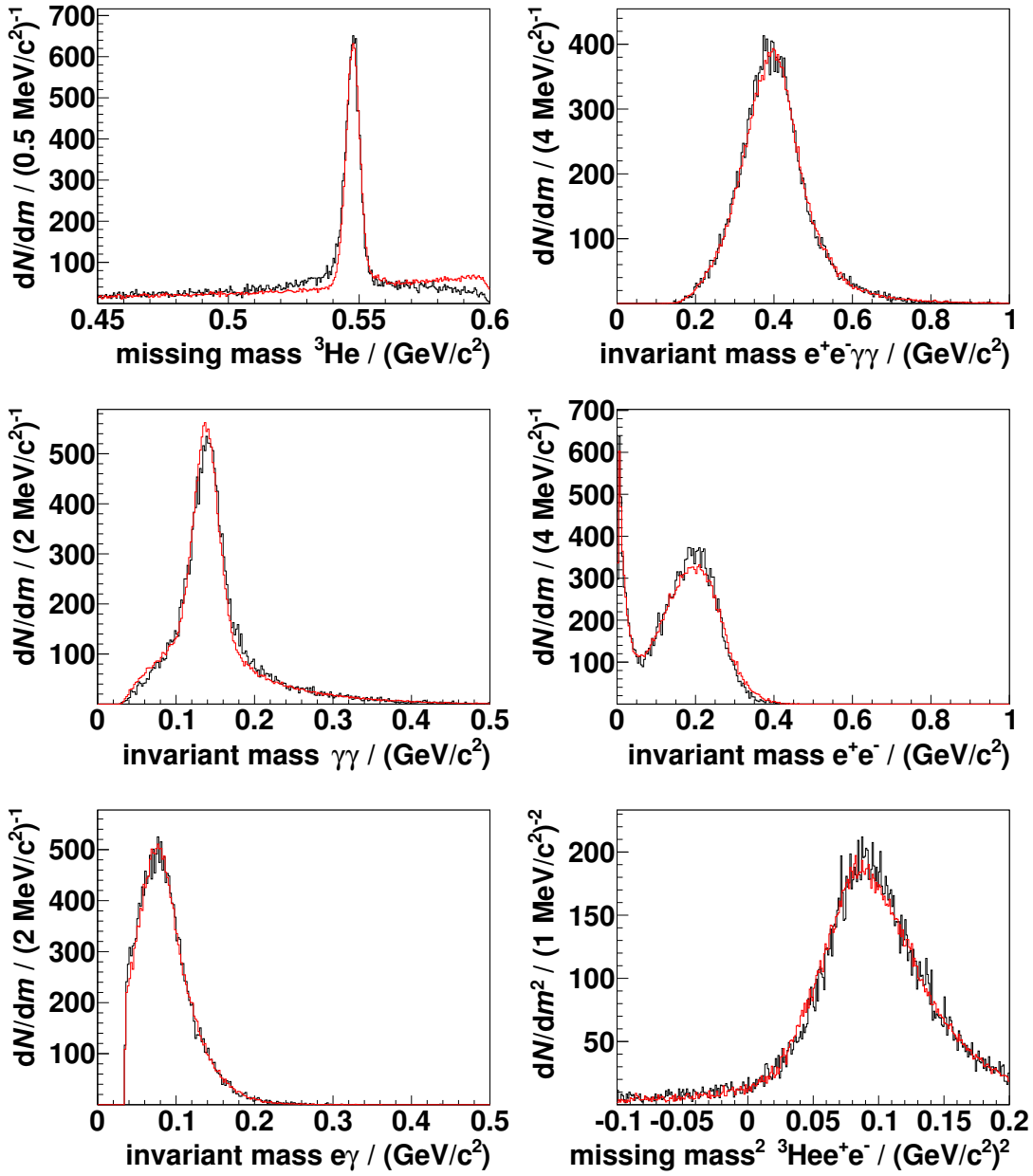

Figure B.15.: Fit by Monte Carlo simulations (red) to the 2009 data set (black) for the angular range $0.6 \leq \cos\vartheta_\eta^{\mathrm{CMS}} < 0.8$. Upper left: ^{3}He missing mass. Upper right: invariant mass of two oppositely charged and two neutral CD particles. Middle left: invariant mass of two neutral CD particles. Middle right: invariant mass of two oppositely charged CD particles. Lower left: invariant mass of one charged and one neutral CD particle, smallest combination. Lower right: squared missing mass of ^{3}He and two oppositely charged CD particles. For the charged CD particles an electron mass was assumed. All data samples were preselected with the conditions described in chapter 6.5. For fit details see chapter 6.6.

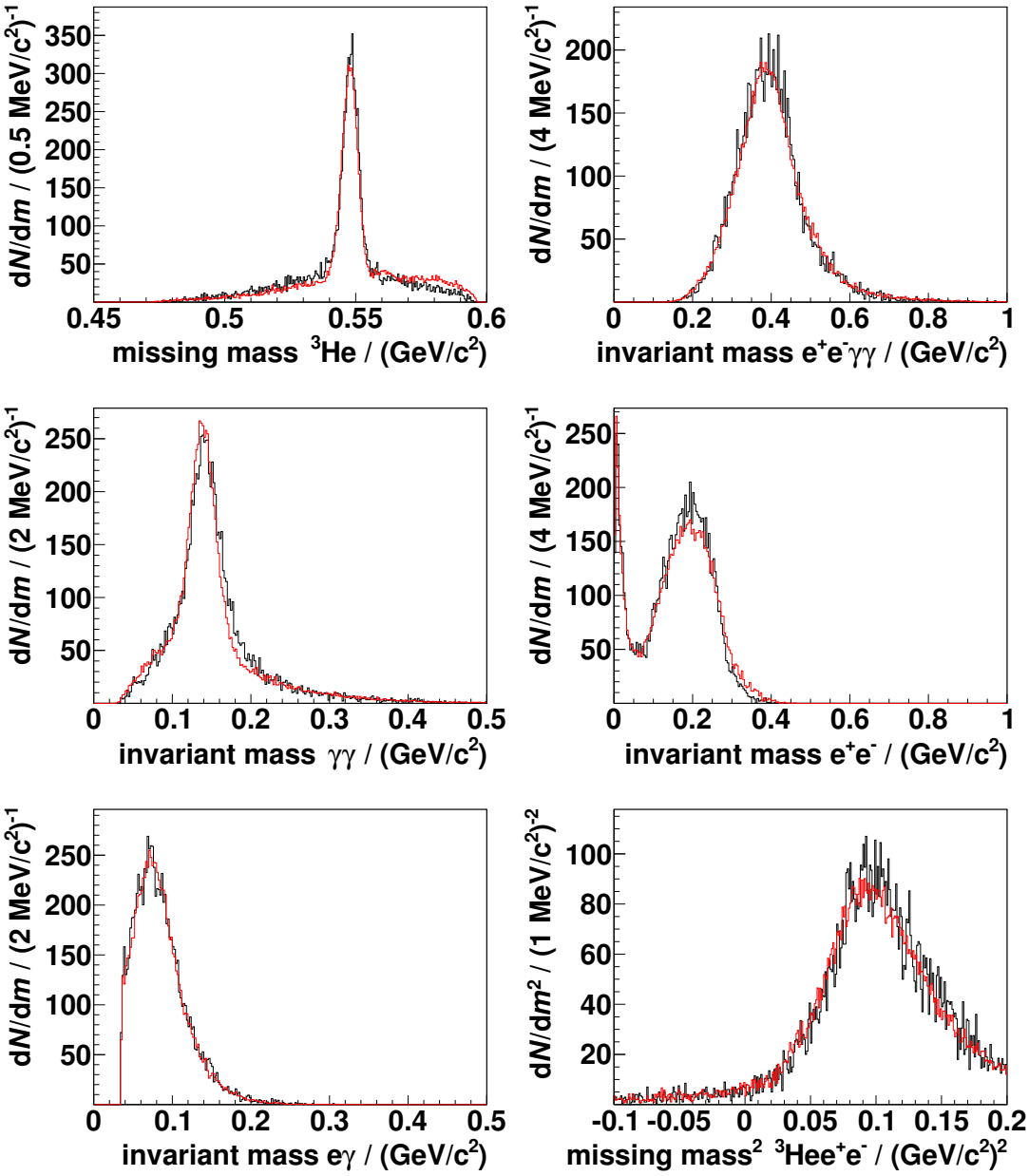

Figure B.16.: Fit by Monte Carlo simulations (red) to the 2009 data set (black) for the angular range $0.8 \leq \cos\vartheta_{\eta}^{\mathrm{CMS}} \leq 1.0$. Upper left: ^{3}He missing mass. Upper right: invariant mass of two oppositely charged and two neutral CD particles. Middle left: invariant mass of two neutral CD particles. Middle right: invariant mass of two oppositely charged CD particles. Lower left: invariant mass of one charged and one neutral CD particle, smallest combination. Lower right: squared missing mass of ^{3}He and two oppositely charged CD particles. For the charged CD particles an electron mass was assumed. All data samples were preselected with the conditions described in chapter 6.5. For fit details see chapter 6.6.

B.3. Number of $\eta \to \pi^+ + \pi^- + \pi^0$ events

Table B.1.: Number of events of the η decay $\eta \to \pi^+ + \pi^- + (\pi^0 \to \gamma + \gamma)$ in the 2008 data set depending on the angular range. The observed numbers $N^{\text{observed}}_{\eta\to\pi^+\pi^-\pi^0}$ are separated in events without event overlap and events with event overlap. For both cases the corresponding efficiencies ε_{B} according to Monte Carlo simulations are given. The given uncertainties are purely statistical.

	pure events		events with event overlap		
$\cos\vartheta_\eta^{\text{CMS}}$	$N^{\text{observed}}_{\eta\to\pi^+\pi^-\pi^0}$	ε_{B}	$N^{\text{observed}}_{\eta\to\pi^+\pi^-\pi^0}$	ε_{B}	$N^{\text{produced}}_{\eta\to\pi^+\pi^-\pi^0}$
-0.6 – -0.4	3682 ± 61	0.1132(4)	3485 ± 59	0.066 75(33)	$84\,741 \pm 1072$
-0.4 – -0.2	5426 ± 74	0.097 10(31)	5233 ± 72	0.058 19(24)	$145\,801 \pm 1513$
-0.2 – 0.0	6365 ± 80	0.078 42(23)	6173 ± 79	0.047 28(18)	$211\,747 \pm 2026$
0.0 – 0.2	6687 ± 82	0.062 90(18)	6564 ± 81	0.038 48(14)	$276\,922 \pm 2576$
0.2 – 0.4	6339 ± 80	0.049 13(15)	6323 ± 80	0.030 52(12)	$336\,204 \pm 3196$
0.4 – 0.6	5407 ± 74	0.036 50(12)	5501 ± 74	0.023 08(10)	$386\,471 \pm 3955$
0.6 – 0.8	3796 ± 62	0.025 81(10)	3915 ± 63	0.016 59(8)	$383\,077 \pm 4644$
0.8 – 1.0	2015 ± 45	0.013 90(7)	2117 ± 46	0.009 08(6)	$378\,050 \pm 6253$
-0.6 – 1.0	$39\,718 \pm 199$	0.047 00(24)	$39\,311 \pm 198$	0.028 95(15)	$2\,203\,012 \pm 10\,035$

Table B.2.: Number of events of the η decay $\eta \to \pi^+ + \pi^- + (\pi^0 \to \gamma + \gamma)$ in the 2009 data set depending on the angular range. The observed numbers $N^{\text{observed}}_{\eta\to\pi^+\pi^-\pi^0}$ are separated in events without event overlap and events with event overlap. For both cases the corresponding efficiencies ε_{B} according to Monte Carlo simulations are given. The given uncertainties are purely statistical.

	pure events		events with event overlap		
$\cos\vartheta_\eta^{\text{CMS}}$	$N^{\text{observed}}_{\eta\to\pi^+\pi^-\pi^0}$	ε_{B}	$N^{\text{observed}}_{\eta\to\pi^+\pi^-\pi^0}$	ε_{B}	$N^{\text{produced}}_{\eta\to\pi^+\pi^-\pi^0}$
-0.6 – -0.4	5046 ± 71	0.1123(4)	7431 ± 86	0.066 34(32)	$156\,925 \pm 1554$
-0.4 – -0.2	7462 ± 86	0.096 55(31)	$11\,181 \pm 106$	0.057 86(24)	$270\,502 \pm 2198$
-0.2 – 0.0	8693 ± 93	0.077 94(23)	$13\,098 \pm 114$	0.046 98(18)	$390\,309 \pm 2937$
0.0 – 0.2	9025 ± 95	0.062 61(18)	$13\,758 \pm 117$	0.038 28(14)	$503\,523 \pm 3702$
0.2 – 0.4	8860 ± 94	0.048 87(15)	$13\,731 \pm 117$	0.030 36(12)	$633\,577 \pm 4691$
0.4 – 0.6	7994 ± 89	0.036 30(12)	$12\,652 \pm 112$	0.022 99(10)	$770\,558 \pm 5997$
0.6 – 0.8	5832 ± 76	0.025 70(10)	9327 ± 97	0.016 49(8)	$792\,597 \pm 7178$
0.8 – 1.0	3120 ± 56	0.013 85(7)	5094 ± 71	0.009 05(6)	$788\,133 \pm 9693$
-0.6 – 1.0	$56\,032 \pm 237$	0.045 50(19)	$86\,271 \pm 294$	0.028 06(10)	$4\,306\,124 \pm 15\,265$

B.4. Investigation of systematic effects: Tables for the Monte Carlo smearing

Table B.3.: Combinations of $\mathrm{FD_{smear}}$, $\mathrm{CD_{smear}}$ and $\mathrm{CD_{factor}}$ sets with the corresponding efficiencies ε_S for the decay $\eta \to (\pi^0 \to \gamma + \gamma) + e^+ + e^-$ via a virtual photon in the angular range $-0.6 \leq \cos\vartheta_\eta^\mathrm{CMS} \leq 1.0$, the number $N_{\eta\to\pi^+\pi^-\pi^0}$ of produced η mesons decaying via the channel $\eta \to \pi^+ + \pi^- + (\pi^0 \to \gamma + \gamma)$ in the angular range $-0.6 \leq \cos\vartheta_\eta^\mathrm{CMS} \leq 1.0$, the quotient $1/\left(\varepsilon_\mathrm{S} \cdot N_{\eta\to\pi^+\pi^-\pi^0}\right)$, and the relative difference Δ_rel of this quotient from the quotient determined for the set (0 0 0), which is listed in the last row of the table. In addition, the relative variance for the quotient is given.

Set						
$\mathrm{FD_{smear}}$	$\mathrm{CD_{smear}}$	$\mathrm{CD_{factor}}$	ε_S	$N_{\eta\to\pi^+\pi^-\pi^0}$	$\frac{1}{\varepsilon_\mathrm{S}\cdot N_{\eta\to\pi^+\pi^-\pi^0}}$	Δ_rel
+	0	0	0.0235	6.55×10^6	6.50×10^{-6}	−0.0136
−	0	0	0.0239	6.47×10^6	6.46×10^{-6}	−0.0197
0	+	0	0.0221	6.59×10^6	6.86×10^{-6}	0.0409
+	+	0	0.0222	6.51×10^6	6.92×10^{-6}	0.0494
−	+	0	0.0226	6.49×10^6	6.81×10^{-6}	0.0339
0	−	0	0.0258	6.40×10^6	6.06×10^{-6}	−0.0798
+	−	0	0.0256	6.50×10^6	6.00×10^{-6}	−0.0894
−	−	0	0.0259	6.39×10^6	6.05×10^{-6}	−0.0826
0	0	+	0.0239	6.46×10^6	6.48×10^{-6}	−0.0171
+	0	+	0.0234	6.47×10^6	6.60×10^{-6}	0.0019
−	0	+	0.0244	6.41×10^6	6.40×10^{-6}	−0.0284
0	+	+	0.0221	6.56×10^6	6.91×10^{-6}	0.0483
+	+	+	0.0218	6.52×10^6	7.03×10^{-6}	0.0664
−	+	+	0.0226	6.49×10^6	6.82×10^{-6}	0.0350
0	−	+	0.0261	6.37×10^6	6.02×10^{-6}	−0.0861
+	−	+	0.0255	6.52×10^6	6.01×10^{-6}	−0.0885
−	−	+	0.0260	6.40×10^6	6.02×10^{-6}	−0.0867
0	0	−	0.0237	6.59×10^6	6.41×10^{-6}	−0.0271
+	0	−	0.0236	6.57×10^6	6.45×10^{-6}	−0.0215
−	0	−	0.0243	6.53×10^6	6.30×10^{-6}	−0.0435
0	+	−	0.0217	6.67×10^6	6.91×10^{-6}	0.0484
+	+	−	0.0220	6.52×10^6	6.95×10^{-6}	0.0551
−	+	−	0.0225	6.57×10^6	6.76×10^{-6}	0.0253
0	−	−	0.0257	6.53×10^6	5.96×10^{-6}	−0.0954
+	−	−	0.0255	6.51×10^6	6.02×10^{-6}	−0.0865
−	−	−	0.0257	6.50×10^6	5.99×10^{-6}	−0.0912
0	0	0	0.0233	6.51×10^6	6.59×10^{-6}	Var: 0.059

Table B.4.: Combinations of $\mathrm{FD_{smear}}$, $\mathrm{CD_{smear}}$ and $\mathrm{CD_{factor}}$ sets with the corresponding efficiencies ε_S for the decay $\eta \to (\pi^0 \to \gamma + \gamma) + e^+ + e^-$ according to three-particle phase space in the angular range $-0.6 \leq \cos\vartheta_\eta^\mathrm{CMS} \leq 1.0$, the number $N_{\eta\to\pi^+\pi^-\pi^0}$ of produced η mesons decaying via the channel $\eta \to \pi^+ + \pi^- + (\pi^0 \to \gamma + \gamma)$ in the angular range $-0.6 \leq \cos\vartheta_\eta^\mathrm{CMS} \leq 1.0$, the quotient $1/\left(\varepsilon_\mathrm{S} \cdot N_{\eta\to\pi^+\pi^-\pi^0}\right)$, and the relative difference Δ_rel of this quotient from the quotient determined for the set (0 0 0), which is listed in the last row of the table. In addition, the relative variance for the quotient is given.

Set						
$\mathrm{FD_{smear}}$	$\mathrm{CD_{smear}}$	$\mathrm{CD_{factor}}$	ε_S	$N_{\eta\to\pi^+\pi^-\pi^0}$	$\frac{1}{\varepsilon_\mathrm{S}\cdot N_{\eta\to\pi^+\pi^-\pi^0}}$	Δ_rel
+	0	0	0.0187	6.55×10^6	8.18×10^{-6}	−0.0181
−	0	0	0.0186	6.47×10^6	8.29×10^{-6}	−0.0047
0	+	0	0.0171	6.59×10^6	8.89×10^{-6}	0.0674
+	+	0	0.0171	6.51×10^6	8.96×10^{-6}	0.0754
−	+	0	0.0177	6.49×10^6	8.71×10^{-6}	0.0451
0	−	0	0.0200	6.40×10^6	7.82×10^{-6}	−0.0612
+	−	0	0.0202	6.50×10^6	7.63×10^{-6}	−0.0842
−	−	0	0.0202	6.39×10^6	7.73×10^{-6}	−0.0724
0	0	+	0.0184	6.46×10^6	8.41×10^{-6}	0.0087
+	0	+	0.0185	6.47×10^6	8.35×10^{-6}	0.0020
−	0	+	0.0190	6.41×10^6	8.22×10^{-6}	−0.0136
0	+	+	0.0170	6.56×10^6	8.96×10^{-6}	0.0759
+	+	+	0.0170	6.52×10^6	9.05×10^{-6}	0.0861
−	+	+	0.0176	6.49×10^6	8.76×10^{-6}	0.0515
0	−	+	0.0203	6.37×10^6	7.73×10^{-6}	−0.0728
+	−	+	0.0197	6.52×10^6	7.79×10^{-6}	−0.0649
−	−	+	0.0201	6.40×10^6	7.77×10^{-6}	−0.0677
0	0	−	0.0184	6.59×10^6	8.24×10^{-6}	−0.0108
+	0	−	0.0181	6.57×10^6	8.40×10^{-6}	0.0078
−	0	−	0.0188	6.53×10^6	8.13×10^{-6}	−0.0246
0	+	−	0.0170	6.67×10^6	8.82×10^{-6}	0.0585
+	+	−	0.0171	6.52×10^6	8.98×10^{-6}	0.0772
−	+	−	0.0173	6.57×10^6	8.79×10^{-6}	0.0554
0	−	−	0.0200	6.53×10^6	7.65×10^{-6}	−0.0821
+	−	−	0.0196	6.51×10^6	7.85×10^{-6}	−0.0579
−	−	−	0.0200	6.50×10^6	7.70×10^{-6}	−0.0757
0	0	0	0.0184	6.51×10^6	8.33×10^{-6}	Var: 0.057

Table B.5.: Combinations of $\mathrm{FD_{smear}}$, $\mathrm{CD_{smear}}$ and $\mathrm{CD_{factor}}$ sets with the corresponding efficiencies ε_S for the decay $\eta \to (\pi^0 \to \gamma + \gamma) + e^+ + e^-$ via a hypothetical dark boson with a mass of $m_\mathrm{U} = 150\,\mathrm{MeV}\,c^{-2}$ in the angular range $-0.6 \leq \cos\vartheta_\eta^\mathrm{CMS} \leq 1.0$, the number $N_{\eta\to\pi^+\pi^-\pi^0}$ of produced η mesons decaying via the channel $\eta \to \pi^+ + \pi^- + (\pi^0 \to \gamma + \gamma)$ in the angular range $-0.6 \leq \cos\vartheta_\eta^\mathrm{CMS} \leq 1.0$, the quotient $1/\left(\varepsilon_\mathrm{S} \cdot N_{\eta\to\pi^+\pi^-\pi^0}\right)$, and the relative difference Δ_rel of this quotient from the quotient determined for the set (0 0 0), which is listed in the last row of the table. In addition, the relative variance for the quotient is given.

Set						
$\mathrm{FD_{smear}}$	$\mathrm{CD_{smear}}$	$\mathrm{CD_{factor}}$	ε_S	$N_{\eta\to\pi^+\pi^-\pi^0}$	$\frac{1}{\varepsilon_\mathrm{S}\cdot N_{\eta\to\pi^+\pi^-\pi^0}}$	Δ_rel
+	0	0	0.0365	6.55×10^6	4.19×10^{-6}	0.0099
−	0	0	0.0367	6.47×10^6	4.21×10^{-6}	0.0146
0	+	0	0.0333	6.59×10^6	4.56×10^{-6}	0.0981
+	+	0	0.0343	6.51×10^6	4.48×10^{-6}	0.0789
−	+	0	0.0352	6.49×10^6	4.37×10^{-6}	0.0538
0	−	0	0.0408	6.40×10^6	3.83×10^{-6}	−0.0768
+	−	0	0.0402	6.50×10^6	3.83×10^{-6}	−0.0774
−	−	0	0.0401	6.39×10^6	3.90×10^{-6}	−0.0604
0	0	+	0.0373	6.46×10^6	4.15×10^{-6}	−0.0009
+	0	+	0.0369	6.47×10^6	4.19×10^{-6}	0.0104
−	0	+	0.0374	6.41×10^6	4.17×10^{-6}	0.0045
0	+	+	0.0332	6.56×10^6	4.59×10^{-6}	0.1073
+	+	+	0.0343	6.52×10^6	4.47×10^{-6}	0.0780
−	+	+	0.0344	6.49×10^6	4.47×10^{-6}	0.0774
0	−	+	0.0405	6.37×10^6	3.87×10^{-6}	−0.0665
+	−	+	0.0394	6.52×10^6	3.90×10^{-6}	−0.0604
−	−	+	0.0384	6.40×10^6	4.07×10^{-6}	−0.0185
0	0	−	0.0373	6.59×10^6	4.07×10^{-6}	−0.0183
+	0	−	0.0368	6.57×10^6	4.13×10^{-6}	−0.0039
−	0	−	0.0378	6.53×10^6	4.05×10^{-6}	−0.0244
0	+	−	0.0341	6.67×10^6	4.40×10^{-6}	0.0598
+	+	−	0.0341	6.52×10^6	4.49×10^{-6}	0.0825
−	+	−	0.0336	6.57×10^6	4.53×10^{-6}	0.0907
0	−	−	0.0397	6.53×10^6	3.86×10^{-6}	−0.0703
+	−	−	0.0396	6.51×10^6	3.88×10^{-6}	−0.0648
−	−	−	0.0403	6.50×10^6	3.81×10^{-6}	−0.0812
0	0	0	0.0370	6.51×10^6	4.15×10^{-6}	Var: 0.061

B.5. Investigation of systematic effects: Tables for the selection conditions

In the following tables the standard selection conditions are indicated by bold numbers.

Table B.6.: Investigation of various conditions for the ^{3}He scattering angle ϑ_{LAB} for the 2008 data set with regard to systematic effects.

$\vartheta^{\mathrm{min}}_{\mathrm{LAB}}/^\circ$	$\vartheta^{\mathrm{max}}_{\mathrm{LAB}}/^\circ$	MC events	data events	κ
2	17	0.76	1	0.17
2.5	17	0.76	1	0.17
3	**17**	**0.76**	**1**	**0.17**
3.5	17	0.76	1	0.17
4	17	0.76	1	0.17

Table B.7.: Investigation of various conditions for the ^{3}He scattering angle ϑ_{LAB} for the 2009 data set with regard to systematic effects.

$\vartheta^{\mathrm{min}}_{\mathrm{LAB}}/^\circ$	$\vartheta^{\mathrm{max}}_{\mathrm{LAB}}/^\circ$	MC events	data events	κ
2	17	1.2	2	0.27
2.5	17	1.2	2	0.27
3	**17**	**1.2**	**2**	**0.27**
3.5	17	1.2	2	0.27
4	17	1.2	2	0.27

Table B.8.: Investigation of various conditions for the energy loss E_{dep} of neutral particles in the calorimeter for the 2008 data set with regard to systematic effects.

$E_{\text{dep}}^{\text{min}}$/GeV	MC events	data events	κ
0	0.76	1	0.17
0.01	0.76	1	0.17
0.02	**0.76**	**1**	**0.17**
0.03	1.1	1	−0.05
0.04	1.4	1	−0.16
0.05	1.6	1	−0.26
0.06	1.5	1	−0.21

Table B.9.: Investigation of various conditions for the energy loss E_{dep} of neutral particles in the calorimeter for the 2009 data set with regard to systematic effects.

$E_{\text{dep}}^{\text{min}}$/GeV	MC events	data events	κ
0	1.2	2	0.27
0.01	1.2	2	0.27
0.02	**1.2**	**2**	**0.27**
0.03	2.1	1	−0.5
0.04	2.8	3	0.06
0.05	3.5	4	0.14
0.06	3.2	2	−0.4

Table B.10.: Investigation of various conditions for the energy loss E_{dep} of charged particles in the calorimeter for the 2008 data set with regard to systematic effects.

$E_{\text{dep}}^{\text{min}}$/GeV	MC events	data events	κ
0.01	0.82	1	0.13
0.015	0.82	1	0.13
0.02	**0.76**	**1**	**0.17**
0.025	0.76	1	0.17
0.03	0.76	1	0.17
0.035	0.72	1	0.2
0.04	0.72	1	0.2

Table B.11.: Investigation of various conditions for the energy loss E_{dep} of charged particles in the calorimeter for the 2009 data set with regard to systematic effects.

$E_{\mathrm{dep}}^{\mathrm{min}}$/GeV	MC events	data events	κ
0.01	1.4	2	0.22
0.015	1.4	2	0.22
0.02	**1.2**	**2**	**0.27**
0.025	1.2	1	−0.1
0.03	1.2	1	−0.1
0.035	1.2	1	−0.08
0.04	1.2	1	−0.08

Table B.12.: Investigation of various conditions for the momentum p of charged particles for the 2008 data set with regard to systematic effects.

p^{min}/GeV c^{-1}	MC events	data events	κ
0.19	0.39	0	−0.33
0.2	0.53	0	−0.5
0.21	0.58	1	0.29
0.22	0.66	1	0.24
0.23	0.66	1	0.24
0.24	0.66	1	0.24
0.25	**0.76**	**1**	**0.17**
0.26	0.82	1	0.13
0.27	0.82	2	0.7
0.28	0.97	3	1
0.29	1	3	1
0.3	1.1	3	0.9
0.31	1.1	3	0.9
0.32	1.1	4	1.3
0.33	1.3	4	1.2
0.34	1.3	4	1.2
0.35	1.3	4	1.2
0.36	1.3	4	1.2
0.37	1.3	4	1.2
0.5	1.4	5	1.5

Table B.13.: Investigation of various conditions for the momentum p of charged particles for the 2009 data set with regard to systematic effects.

$p^{\min}/\mathrm{GeV}\,c^{-1}$	MC events	data events	κ
0.19	0.63	1	0.14
0.2	0.81	1	0.07
0.21	0.94	1	0.024
0.22	1	1	0.019
0.23	1	2	0.34
0.24	1	2	0.34
0.25	**1.2**	**2**	**0.27**
0.26	1.2	4	0.9
0.27	1.2	4	0.9
0.28	1.2	4	0.9
0.29	1.3	4	0.8
0.3	1.5	4	0.8
0.31	1.5	6	1.3
0.32	1.5	6	1.3
0.33	1.5	6	1.3
0.34	1.5	7	1.5
0.35	1.5	8	1.7
0.36	1.5	9	1.9
0.37	1.5	10	2.1
0.5	1.7	10	2.1

Table B.14.: Investigation of various conditions for the reduction of conversion events for the 2008 data set with regard to systematic effects.

d/ mm	x_0/ GeV c^{-2}	x_1/ GeV c^{-2}	x_2/ GeV c^{-2}	MC events	data events	κ
24	0.012	0.005	0.013	0.68	1	0.22
24	0.012	0.005	0.016	0.68	1	0.22
24	0.012	0.005	0.019	0.68	1	0.22
24	0.015	0.008	0.013	0.68	1	0.22
24	0.015	0.008	0.016	0.68	1	0.22
24	0.015	0.008	0.019	0.68	1	0.22
24	0.018	0.011	0.013	0.68	1	0.22
24	0.018	0.011	0.016	0.68	1	0.22
24	0.018	0.011	0.019	0.68	1	0.22
26	0.012	0.005	0.013	0.68	1	0.22
26	0.012	0.005	0.016	0.68	1	0.22
26	0.012	0.005	0.019	0.68	1	0.22
26	0.015	0.008	0.013	0.68	1	0.22
26	0.015	0.008	0.016	0.68	1	0.22
26	0.015	0.008	0.019	0.68	1	0.22
26	0.018	0.011	0.013	0.68	1	0.22
26	0.018	0.011	0.016	0.68	1	0.22
26	0.018	0.011	0.019	0.68	1	0.22
28	0.012	0.005	0.013	0.76	1	0.17
28	0.012	0.005	0.016	0.76	1	0.17
28	0.012	0.005	0.019	0.76	1	0.17
28	0.015	0.008	0.013	0.76	1	0.17
28	**0.015**	**0.008**	**0.016**	**0.76**	**1**	**0.17**
28	0.015	0.008	0.019	0.76	1	0.17
28	0.018	0.011	0.013	0.76	1	0.17
28	0.018	0.011	0.016	0.76	1	0.17
28	0.018	0.011	0.019	0.76	1	0.17
30	0.012	0.005	0.013	0.76	1	0.17
30	0.012	0.005	0.016	0.76	1	0.17
30	0.012	0.005	0.019	0.76	1	0.17
30	0.015	0.008	0.013	0.76	1	0.17
30	0.015	0.008	0.016	0.76	1	0.17
30	0.015	0.008	0.019	0.76	1	0.17
30	0.018	0.011	0.013	0.76	1	0.17
30	0.018	0.011	0.016	0.76	1	0.17
30	0.018	0.011	0.019	0.76	1	0.17

Table B.15.: Investigation of various conditions for the reduction of conversion events for the 2008 data set with regard to systematic effects, continued.

d/ mm	x_0/ GeV c^{-2}	x_1/ GeV c^{-2}	x_2/ GeV c^{-2}	MC events	data events	κ
32	0.012	0.005	0.013	0.83	1	0.12
32	0.012	0.005	0.016	0.83	1	0.12
32	0.012	0.005	0.019	0.83	1	0.12
32	0.015	0.008	0.013	0.83	1	0.12
32	0.015	0.008	0.016	0.83	1	0.12
32	0.015	0.008	0.019	0.83	1	0.12
32	0.018	0.011	0.013	0.83	1	0.12
32	0.018	0.011	0.016	0.83	1	0.12
32	0.018	0.011	0.019	0.83	1	0.12

Table B.16.: Investigation of various conditions for the reduction of conversion events for the 2009 data set with regard to systematic effects.

d/ mm	x_0/ GeV c^{-2}	x_1/ GeV c^{-2}	x_2/ GeV c^{-2}	MC events	data events	κ
24	0.012	0.005	0.013	1.1	2	0.31
24	0.012	0.005	0.016	1.1	2	0.31
24	0.012	0.005	0.019	1.1	2	0.31
24	0.015	0.008	0.013	1.1	2	0.31
24	0.015	0.008	0.016	1.1	2	0.31
24	0.015	0.008	0.019	1.1	2	0.31
24	0.018	0.011	0.013	1.1	2	0.31
24	0.018	0.011	0.016	1.1	2	0.31
24	0.018	0.011	0.019	1.1	2	0.31

Table B.17.: Investigation of various conditions for the reduction of conversion events for the 2009 data set with regard to systematic effects, continued.

d/ mm	x_0/ GeV c^{-2}	x_1/ GeV c^{-2}	x_2/ GeV c^{-2}	MC events	data events	κ
26	0.012	0.005	0.013	1.1	2	0.31
26	0.012	0.005	0.016	1.1	2	0.31
26	0.012	0.005	0.019	1.1	2	0.31
26	0.015	0.008	0.013	1.1	2	0.31
26	0.015	0.008	0.016	1.1	2	0.31
26	0.015	0.008	0.019	1.1	2	0.31
26	0.018	0.011	0.013	1.1	2	0.31
26	0.018	0.011	0.016	1.1	2	0.31
26	0.018	0.011	0.019	1.1	2	0.31
28	0.012	0.005	0.013	1.2	2	0.27
28	0.012	0.005	0.016	1.2	2	0.27
28	0.012	0.005	0.019	1.2	2	0.27
28	0.015	0.008	0.013	1.2	2	0.27
28	**0.015**	**0.008**	**0.016**	**1.2**	**2**	**0.27**
28	0.015	0.008	0.019	1.2	2	0.27
28	0.018	0.011	0.013	1.2	2	0.27
28	0.018	0.011	0.016	1.2	2	0.27
28	0.018	0.011	0.019	1.2	2	0.27
30	0.012	0.005	0.013	1.2	2	0.27
30	0.012	0.005	0.016	1.2	2	0.27
30	0.012	0.005	0.019	1.2	2	0.27
30	0.015	0.008	0.013	1.2	2	0.27
30	0.015	0.008	0.016	1.2	2	0.27
30	0.015	0.008	0.019	1.2	2	0.27
30	0.018	0.011	0.013	1.2	2	0.27
30	0.018	0.011	0.016	1.2	2	0.27
30	0.018	0.011	0.019	1.2	2	0.27
32	0.012	0.005	0.013	1.5	2	0.19
32	0.012	0.005	0.016	1.5	2	0.19
32	0.012	0.005	0.019	1.5	2	0.19
32	0.015	0.008	0.013	1.5	2	0.19
32	0.015	0.008	0.016	1.5	2	0.19
32	0.015	0.008	0.019	1.5	2	0.19
32	0.018	0.011	0.013	1.5	2	0.19
32	0.018	0.011	0.016	1.5	2	0.19
32	0.018	0.011	0.019	1.5	2	0.19

Table B.18.: Investigation of various conditions for the rejection of split-off tracks of charged particles for the 2008 data set with regard to systematic effects.

min. split charged / $^\circ \times$ GeV	MC events	data events	κ
0	1.2	2	0.5
0.25	1.2	2	0.5
0.45	1.1	2	0.5
0.65	1.1	2	0.5
0.85	1	2	0.6
1.05	0.9	2	0.6
1.25	0.8	1	0.14
1.45	**0.76**	**1**	**0.17**
1.65	0.66	1	0.24
1.85	0.66	1	0.24
2.05	0.6	1	0.28
2.25	0.6	1	0.28

Table B.19.: Investigation of various conditions for the rejection of split-off tracks of charged particles for the 2009 data set with regard to systematic effects.

min. split charged / $^\circ \times$ GeV	MC events	data events	κ
0	2.1	4	0.6
0.25	2.1	4	0.6
0.45	2	3	0.33
0.65	2	3	0.33
0.85	1.8	3	0.4
1.05	1.6	2	0.16
1.25	1.4	2	0.23
1.45	**1.2**	**2**	**0.27**
1.65	1.1	1	−0.024
1.85	1.1	1	−0.024
2.05	0.92	1	0.032
2.25	0.92	1	0.032

Table B.20.: Investigation of various conditions for the rejection of split-off tracks of neutral particles for the 2008 data set with regard to systematic effects.

min. split neutral / $^\circ \times$ GeV	MC events	data events	κ
0	1.1	2	0.5
0.25	1	2	0.5
0.45	1	2	0.6
0.65	1	2	0.6
0.85	0.86	2	0.7
1.05	0.78	2	0.7
1.25	0.76	2	0.7
1.45	**0.76**	**1**	**0.17**
1.65	0.72	1	0.2
1.85	0.62	1	0.26
2.05	0.62	1	0.26
2.25	0.62	1	0.26

Table B.21.: Investigation of various conditions for the rejection of split-off tracks of neutral particles for the 2009 data set with regard to systematic effects.

min. split neutral / $^\circ \times$ GeV	MC events	data events	κ
0	1.8	6	1.2
0.25	1.7	6	1.2
0.45	1.7	6	1.2
0.65	1.7	6	1.2
0.85	1.3	6	1.4
1.05	1.2	6	1.4
1.25	1.2	5	1.1
1.45	**1.2**	**2**	**0.27**
1.65	1.2	1	−0.08
1.85	1	0	−0.8
2.05	1	0	−0.8
2.25	1	0	−0.8

Table B.22.: Investigation of various conditions for the invariant mass $m_{e\gamma}$ for the 2008 data set with regard to systematic effects.

$m_{e\gamma}^{min}/\mathrm{GeV}\,c^{-2}$	MC events	data events	κ
0.015	0.76	2	0.7
0.02	0.76	2	0.7
0.025	0.76	2	0.7
0.03	0.76	2	0.7
0.035	**0.76**	**1**	**0.17**
0.04	0.76	1	0.17
0.045	0.76	1	0.17

Table B.23.: Investigation of various conditions for the invariant mass $m_{e\gamma}$ for the 2009 data set with regard to systematic effects.

$m_{e\gamma}^{min}/\mathrm{GeV}\,c^{-2}$	MC events	data events	κ
0.015	1.2	2	0.27
0.02	1.2	2	0.27
0.025	1.2	2	0.27
0.03	1.2	2	0.27
0.035	**1.2**	**2**	**0.27**
0.04	1.2	2	0.27
0.045	1.2	2	0.27

Table B.24.: Investigation of various conditions for the ^{3}He missing mass m_x for the 2008 data set with regard to systematic effects.

$m_x^{\min}$/GeV c^{-2}	$m_x^{\max}$/GeV c^{-2}	MC events	data events	κ
0.5354	0.5621	1.6	7	1.9
0.5354	0.5601	1.3	7	2
0.5354	0.5581	1.2	7	2
0.5354	0.5561	1.1	6	1.8
0.5354	0.5541	1	6	1.9
0.5354	0.5521	0.94	5	1.6
0.5354	0.5501	0.84	5	1.7
0.5374	0.5621	1.4	7	2
0.5374	0.5601	1.2	7	2.1
0.5374	0.5581	1.1	7	2.1
0.5374	0.5561	1	6	1.9
0.5374	0.5541	0.9	6	1.9
0.5374	0.5521	0.82	5	1.7
0.5374	0.5501	0.73	5	1.7
0.5394	0.5621	1.3	5	1.5
0.5394	0.5601	0.99	5	1.6
0.5394	0.5581	0.9	5	1.7
0.5394	0.5561	0.83	4	1.4
0.5394	0.5541	0.72	4	1.5
0.5394	0.5521	0.64	3	1.2
0.5394	0.5501	0.55	3	1.2
0.5414	0.5621	1.2	2	0.5
0.5414	0.5601	0.91	2	0.6
0.5414	0.5581	0.82	2	0.7
0.5414	**0.5561**	**0.76**	**1**	**0.17**
0.5414	0.5541	0.64	1	0.25
0.5414	0.5521	0.56	0	−0.5
0.5414	0.5501	0.47	0	−0.4
0.5434	0.5621	1.2	2	0.5
0.5434	0.5601	0.88	2	0.6
0.5434	0.5581	0.78	2	0.7
0.5434	0.5561	0.72	1	0.19
0.5434	0.5541	0.61	1	0.27
0.5434	0.5521	0.53	0	−0.5
0.5434	0.5501	0.43	0	−0.4

Table B.25.: Investigation of various conditions for the ^{3}He missing mass m_x for the 2008 data set with regard to systematic effects, continued.

$m_x^{\min}/\mathrm{GeV}\,c^{-2}$	$m_x^{\max}/\mathrm{GeV}\,c^{-2}$	MC events	data events	κ
0.5454	0.5621	1.1	2	0.5
0.5454	0.5601	0.84	2	0.7
0.5454	0.5581	0.75	2	0.7
0.5454	0.5561	0.68	1	0.22
0.5454	0.5541	0.57	1	0.3
0.5454	0.5521	0.49	0	−0.4
0.5454	0.5501	0.4	0	−0.34
0.5474	0.5621	1	2	0.6
0.5474	0.5601	0.74	2	0.7
0.5474	0.5581	0.64	2	0.8
0.5474	0.5561	0.58	1	0.29
0.5474	0.5541	0.47	1	0.4
0.5474	0.5521	0.39	0	−0.33
0.5474	0.5501	0.29	0	−0.25
0.5294	0.5681	2.4	8	1.4

Table B.26.: Investigation of various conditions for the ^{3}He missing mass m_x for the 2009 data set with regard to systematic effects.

$m_x^{\min}/\mathrm{GeV}\,c^{-2}$	$m_x^{\max}/\mathrm{GeV}\,c^{-2}$	MC events	data events	κ
0.5354	0.5621	2.6	5	0.7
0.5354	0.5601	2.2	4	0.6
0.5354	0.5581	2.1	3	0.29
0.5354	0.5561	1.9	3	0.4
0.5354	0.5541	1.8	3	0.4
0.5354	0.5521	1.7	3	0.4
0.5354	0.5501	1.3	2	0.26
0.5374	0.5621	2.3	4	0.6
0.5374	0.5601	1.9	3	0.4
0.5374	0.5581	1.8	2	0.08
0.5374	0.5561	1.6	2	0.15
0.5374	0.5541	1.4	2	0.2
0.5374	0.5521	1.4	2	0.22
0.5374	0.5501	0.93	1	0.025

Table B.27.: Investigation of various conditions for the ^{3}He missing mass m_x for the 2009 data set with regard to systematic effects, continued.

$m_x^{\min}$/GeV c^{-2}	$m_x^{\max}$/GeV c^{-2}	MC events	data events	κ
0.5394	0.5621	2	4	0.6
0.5394	0.5601	1.7	3	0.4
0.5394	0.5581	1.5	2	0.16
0.5394	0.5561	1.3	2	0.23
0.5394	0.5541	1.2	2	0.29
0.5394	0.5521	1.1	2	0.31
0.5394	0.5501	0.69	1	0.12
0.5414	0.5621	1.9	4	0.7
0.5414	0.5601	1.6	3	0.5
0.5414	0.5581	1.4	2	0.2
0.5414	**0.5561**	**1.2**	**2**	**0.27**
0.5414	0.5541	1.1	2	0.33
0.5414	0.5521	1	2	0.35
0.5414	0.5501	0.59	1	0.16
0.5434	0.5621	1.9	4	0.7
0.5434	0.5601	1.5	3	0.5
0.5434	0.5581	1.4	2	0.22
0.5434	0.5561	1.2	2	0.29
0.5434	0.5541	1	2	0.35
0.5434	0.5521	0.98	2	0.4
0.5434	0.5501	0.54	1	0.18
0.5454	0.5621	1.7	4	0.7
0.5454	0.5601	1.3	3	0.6
0.5454	0.5581	1.2	2	0.28
0.5454	0.5561	1	2	0.35
0.5454	0.5541	0.85	2	0.4
0.5454	0.5521	0.8	2	0.4
0.5454	0.5501	0.36	1	0.24
0.5474	0.5621	1.6	4	0.8
0.5474	0.5601	1.3	3	0.6
0.5474	0.5581	1.1	2	0.3
0.5474	0.5561	0.95	2	0.4
0.5474	0.5541	0.79	2	0.4
0.5474	0.5521	0.74	2	0.4
0.5474	0.5501	0.3	1	0.27

Table B.28.: Investigation of various conditions for the invariant mass $m_{ee\gamma\gamma}$ for the 2008 data set with regard to systematic effects.

$m^{\min}_{ee\gamma\gamma}/\mathrm{GeV}\,c^{-2}$	$m^{\max}_{ee\gamma\gamma}/\mathrm{GeV}\,c^{-2}$	MC events	data events	κ
0.447	0.706	2.1	7	1.7
0.447	0.686	2.1	7	1.7
0.447	0.666	2.1	7	1.7
0.447	0.646	2.1	7	1.7
0.447	0.626	2.1	7	1.7
0.447	0.606	2.1	7	1.7
0.447	0.586	2.1	7	1.7
0.467	0.706	1.1	4	1.3
0.467	0.686	1.1	4	1.3
0.467	0.666	1.1	4	1.3
0.467	0.646	1.1	4	1.3
0.467	0.626	1.1	4	1.3
0.467	0.606	1.1	4	1.3
0.467	0.586	1.1	4	1.3
0.487	0.706	0.76	2	0.7
0.487	0.686	0.76	2	0.7
0.487	0.666	0.76	2	0.7
0.487	0.646	0.76	2	0.7
0.487	0.626	0.76	2	0.7
0.487	0.606	0.76	2	0.7
0.487	0.586	0.72	2	0.7
0.507	0.706	0.76	1	0.17
0.507	0.686	0.76	1	0.17
0.507	0.666	0.76	1	0.17
0.507	**0.646**	**0.76**	**1**	**0.17**
0.507	0.626	0.76	1	0.17
0.507	0.606	0.76	1	0.17
0.507	0.586	0.72	1	0.2
0.527	0.706	0.55	1	0.32
0.527	0.686	0.55	1	0.32
0.527	0.666	0.55	1	0.32
0.527	0.646	0.55	1	0.32
0.527	0.626	0.55	1	0.32
0.527	0.606	0.55	1	0.32
0.527	0.586	0.51	1	0.34

Table B.29.: Investigation of various conditions for the invariant mass $m_{ee\gamma\gamma}$ for the 2008 data set with regard to systematic effects, continued.

$m^{\min}_{ee\gamma\gamma}/\mathrm{GeV}\,c^{-2}$	$m^{\max}_{ee\gamma\gamma}/\mathrm{GeV}\,c^{-2}$	MC events	data events	κ
0.547	0.706	0.13	0	−0.12
0.547	0.686	0.13	0	−0.12
0.547	0.666	0.13	0	−0.12
0.547	0.646	0.13	0	−0.12
0.547	0.626	0.13	0	−0.12
0.547	0.606	0.13	0	−0.12
0.547	0.586	0.097	0	−0.08
0.567	0.706	0.075	0	−0.07
0.567	0.686	0.075	0	−0.07
0.567	0.666	0.075	0	−0.07
0.567	0.646	0.075	0	−0.07
0.567	0.626	0.075	0	−0.07
0.567	0.606	0.075	0	−0.07
0.567	0.586	0.038	0	−0.033

Table B.30.: Investigation of various conditions for the invariant mass $m_{ee\gamma\gamma}$ for the 2009 data set with regard to systematic effects.

$m^{\min}_{ee\gamma\gamma}/\mathrm{GeV}\,c^{-2}$	$m^{\max}_{ee\gamma\gamma}/\mathrm{GeV}\,c^{-2}$	MC events	data events	κ
0.447	0.706	2.8	9	1.5
0.447	0.686	2.8	9	1.5
0.447	0.666	2.8	9	1.5
0.447	0.646	2.8	9	1.5
0.447	0.626	2.8	9	1.5
0.447	0.606	2.8	9	1.5
0.447	0.586	2.7	8	1.4
0.467	0.706	1.9	8	1.6
0.467	0.686	1.9	8	1.6
0.467	0.666	1.9	8	1.6
0.467	0.646	1.9	8	1.6
0.467	0.626	1.9	8	1.6
0.467	0.606	1.9	8	1.6
0.467	0.586	1.9	7	1.4

Table B.31.: Investigation of various conditions for the invariant mass $m_{ee\gamma\gamma}$ for the 2009 data set with regard to systematic effects, continued.

$m^{\min}_{ee\gamma\gamma}/\mathrm{GeV}\,c^{-2}$	$m^{\max}_{ee\gamma\gamma}/\mathrm{GeV}\,c^{-2}$	MC events	data events	κ
0.487	0.706	1.2	5	1.1
0.487	0.686	1.2	5	1.1
0.487	0.666	1.2	5	1.1
0.487	0.646	1.2	5	1.1
0.487	0.626	1.2	5	1.1
0.487	0.606	1.2	5	1.1
0.487	0.586	1.2	4	0.9
0.507	0.706	1.2	2	0.27
0.507	0.686	1.2	2	0.27
0.507	0.666	1.2	2	0.27
0.507	**0.646**	**1.2**	**2**	**0.27**
0.507	0.626	1.2	2	0.27
0.507	0.606	1.2	2	0.27
0.507	0.586	1.2	1	−0.08
0.527	0.706	0.94	2	0.4
0.527	0.686	0.94	2	0.4
0.527	0.666	0.94	2	0.4
0.527	0.646	0.94	2	0.4
0.527	0.626	0.94	2	0.4
0.527	0.606	0.94	2	0.4
0.527	0.586	0.89	1	0.04
0.547	0.706	0.3	2	0.6
0.547	0.686	0.3	2	0.6
0.547	0.666	0.3	2	0.6
0.547	0.646	0.3	2	0.6
0.547	0.626	0.3	2	0.6
0.547	0.606	0.3	2	0.6
0.547	0.586	0.25	1	0.29
0.567	0.706	0.18	2	0.7
0.567	0.686	0.18	2	0.7
0.567	0.666	0.18	2	0.7
0.567	0.646	0.18	2	0.7
0.567	0.626	0.18	2	0.7
0.567	0.606	0.18	2	0.7
0.567	0.586	0.12	1	0.34

Table B.32.: Investigation of various conditions for the invariant mass $m_{\gamma\gamma}$ for the 2008 data set with regard to systematic effects.

$m_{\gamma\gamma}^{\min}/\mathrm{GeV}\,c^{-2}$	$m_{\gamma\gamma}^{\max}/\mathrm{GeV}\,c^{-2}$	MC events	data events	κ
0.0623	0.1874	1.3	2	0.4
0.0623	0.1774	1.1	2	0.5
0.0623	0.1674	0.85	1	0.1
0.0623	0.1574	0.76	1	0.17
0.0623	0.1474	0.62	1	0.27
0.0623	0.1374	0.23	0	−0.2
0.0623	0.1274	0.099	0	−0.09
0.0723	0.1874	1.3	2	0.4
0.0723	0.1774	1.1	2	0.5
0.0723	0.1674	0.85	1	0.1
0.0723	0.1574	0.76	1	0.17
0.0723	0.1474	0.62	1	0.27
0.0723	0.1374	0.23	0	−0.2
0.0723	0.1274	0.099	0	−0.09
0.0823	0.1874	1.3	2	0.4
0.0823	0.1774	1.1	2	0.5
0.0823	0.1674	0.85	1	0.1
0.0823	0.1574	0.76	1	0.17
0.0823	0.1474	0.62	1	0.27
0.0823	0.1374	0.23	0	−0.2
0.0823	0.1274	0.099	0	−0.09
0.0923	0.1874	1.3	2	0.4
0.0923	0.1774	1.1	2	0.5
0.0923	0.1674	0.85	1	0.1
0.0923	**0.1574**	**0.76**	**1**	**0.17**
0.0923	0.1474	0.62	1	0.27
0.0923	0.1374	0.23	0	−0.2
0.0923	0.1274	0.099	0	−0.09
0.1023	0.1874	1.3	2	0.4
0.1023	0.1774	1.1	2	0.5
0.1023	0.1674	0.85	1	0.1
0.1023	0.1574	0.76	1	0.17
0.1023	0.1474	0.62	1	0.27
0.1023	0.1374	0.23	0	−0.2
0.1023	0.1274	0.099	0	−0.09

Table B.33.: Investigation of various conditions for the invariant mass $m_{\gamma\gamma}$ for the 2008 data set with regard to systematic effects, continued.

$m_{\gamma\gamma}^{\min}/\mathrm{GeV}\,c^{-2}$	$m_{\gamma\gamma}^{\max}/\mathrm{GeV}\,c^{-2}$	MC events	data events	κ
0.1123	0.1874	1.3	2	0.4
0.1123	0.1774	1.1	2	0.5
0.1123	0.1674	0.85	1	0.1
0.1123	0.1574	0.76	1	0.17
0.1123	0.1474	0.62	1	0.27
0.1123	0.1374	0.23	0	−0.2
0.1123	0.1274	0.099	0	−0.09
0.1223	0.1874	1.3	2	0.4
0.1223	0.1774	1.1	2	0.5
0.1223	0.1674	0.85	1	0.1
0.1223	0.1574	0.76	1	0.17
0.1223	0.1474	0.62	1	0.27
0.1223	0.1374	0.23	0	−0.2
0.1223	0.1274	0.098	0	−0.09

Table B.34.: Investigation of various conditions for the invariant mass $m_{\gamma\gamma}$ for the 2009 data set with regard to systematic effects.

$m_{\gamma\gamma}^{\min}/\mathrm{GeV}\,c^{-2}$	$m_{\gamma\gamma}^{\max}/\mathrm{GeV}\,c^{-2}$	MC events	data events	κ
0.0623	0.1874	2	7	1.3
0.0623	0.1774	2	5	0.9
0.0623	0.1674	1.4	4	0.8
0.0623	0.1574	1.2	3	0.6
0.0623	0.1474	0.95	3	0.7
0.0623	0.1374	0.36	3	0.9
0.0623	0.1274	0.19	3	0.9
0.0723	0.1874	2	7	1.3
0.0723	0.1774	2	5	0.9
0.0723	0.1674	1.4	4	0.8
0.0723	0.1574	1.2	3	0.6
0.0723	0.1474	0.95	3	0.7
0.0723	0.1374	0.36	3	0.9
0.0723	0.1274	0.19	3	0.9

Table B.35.: Investigation of various conditions for the invariant mass $m_{\gamma\gamma}$ for the 2009 data set with regard to systematic effects, continued.

$m_{\gamma\gamma}^{\min}/\mathrm{GeV}\,c^{-2}$	$m_{\gamma\gamma}^{\max}/\mathrm{GeV}\,c^{-2}$	MC events	data events	κ
0.0823	0.1874	2	7	1.3
0.0823	0.1774	2	5	0.9
0.0823	0.1674	1.4	4	0.8
0.0823	0.1574	1.2	3	0.6
0.0823	0.1474	0.95	3	0.7
0.0823	0.1374	0.36	3	0.9
0.0823	0.1274	0.19	3	0.9
0.0923	0.1874	2	6	1.1
0.0923	0.1774	2	4	0.6
0.0923	0.1674	1.4	3	0.5
0.0923	**0.1574**	**1.2**	**2**	**0.27**
0.0923	0.1474	0.95	2	0.4
0.0923	0.1374	0.36	2	0.6
0.0923	0.1274	0.19	2	0.6
0.1023	0.1874	2	6	1.1
0.1023	0.1774	2	4	0.6
0.1023	0.1674	1.4	3	0.5
0.1023	0.1574	1.2	2	0.27
0.1023	0.1474	0.95	2	0.4
0.1023	0.1374	0.36	2	0.6
0.1023	0.1274	0.19	2	0.6
0.1123	0.1874	2	5	0.9
0.1123	0.1774	2	3	0.33
0.1123	0.1674	1.4	2	0.2
0.1123	0.1574	1.2	1	−0.1
0.1123	0.1474	0.95	1	0.02
0.1123	0.1374	0.36	1	0.24
0.1123	0.1274	0.19	1	0.31
0.1223	0.1874	2	4	0.6
0.1223	0.1774	2	2	0.012
0.1223	0.1674	1.4	1	−0.18
0.1223	0.1574	1.2	0	−1
0.1223	0.1474	0.95	0	−0.8
0.1223	0.1374	0.36	0	−0.31
0.1223	0.1274	0.19	0	−0.16

Table B.36.: Investigation of various conditions for the invariant mass m_{ee} for the 2008 data set with regard to systematic effects.

$m_{\mathrm{ee}}^{\mathrm{min}}/\mathrm{GeV}\,c^{-2}$	MC events	data events	κ
0	18	29	2.1
0.008	14	23	1.9
0.016	9.6	19	2.1
0.024	6.7	16	2.2
0.032	5.4	13	2
0.04	4.3	7	0.9
0.048	3.3	5	0.7
0.056	2.8	4	0.5
0.064	2.1	2	−0.04
0.072	1.6	2	0.25
0.08	1.3	2	0.4
0.088	1	2	0.6
0.096	**0.76**	**1**	**0.17**
0.104	0.62	1	0.26
0.112	0.35	1	0.5
0.12	0.21	1	0.6
0.128	0.13	1	0.6
0.136	0.037	1	0.7
0.144	0.037	1	0.7
0.152	0.037	1	0.7

Table B.37.: Investigation of various conditions for the invariant mass m_{ee} for the 2009 data set with regard to systematic effects.

$m_{\mathrm{ee}}^{\mathrm{min}}/\mathrm{GeV}\,c^{-2}$	MC events	data events	κ
0	35	44	1.2
0.008	27	33	1
0.016	19	24	0.9
0.024	13	17	0.7
0.032	11	10	−0.12
0.04	8.1	8	−0.04
0.048	6.2	7	0.22
0.056	4.9	4	−0.28
0.064	3.7	3	−0.23
0.072	2.7	3	0.11
0.08	2.3	3	0.24
0.088	1.7	2	0.11
0.096	**1.2**	**2**	**0.27**
0.104	1.1	2	0.34
0.112	0.64	2	0.5
0.12	0.33	2	0.6
0.128	0.23	2	0.6
0.136	0.051	2	0.7
0.144	0.051	2	0.7
0.152	0.051	2	0.7

Table B.38.: Investigation of various conditions for the χ^2 probability (*prob.*) of the kinematic fit for the 2008 data set with regard to systematic effects.

$prob.^{\min}$	MC events	data events	κ
0	52	80	2.9
0.005	0.96	2	0.6
0.01	0.89	2	0.6
0.015	0.79	2	0.7
0.02	0.79	2	0.7
0.025	0.79	2	0.7
0.03	0.79	2	0.7
0.035	0.79	2	0.7
0.04	0.76	1	0.17
0.045	0.76	1	0.17
0.05	**0.76**	**1**	**0.17**
0.055	0.76	1	0.17
0.06	0.76	1	0.17
0.065	0.76	1	0.17
0.07	0.76	1	0.17
0.075	0.76	1	0.17
0.08	0.76	1	0.17
0.085	0.76	1	0.17
0.09	0.76	1	0.17
0.095	0.76	1	0.17
0.1	0.76	1	0.17
0.12	0.71	1	0.2
0.14	0.71	1	0.2
0.16	0.67	1	0.23
0.18	0.67	1	0.23
0.2	0.64	1	0.25

Table B.39.: Investigation of various conditions for the χ^2 probability (*prob.*) of the kinematic fit for the 2009 data set with regard to systematic effects.

$prob.^{\min}$	MC events	data events	κ
0	98	148	4
0.005	2	8	1.6
0.01	1.5	7	1.5
0.015	1.3	7	1.6
0.02	1.3	6	1.4
0.025	1.3	4	0.9
0.03	1.3	2	0.25
0.035	1.2	2	0.27
0.04	1.2	2	0.27
0.045	1.2	2	0.27
0.05	**1.2**	**2**	**0.27**
0.055	1.2	2	0.27
0.06	1.2	2	0.27
0.065	1.2	2	0.27
0.07	1.2	2	0.27
0.075	1.2	2	0.27
0.08	1.2	2	0.27
0.085	1.2	2	0.27
0.09	1.2	2	0.27
0.095	1.2	1	−0.1
0.1	1.2	1	−0.1
0.12	1.2	1	−0.1
0.14	1.2	1	−0.08
0.16	1.2	1	−0.08
0.18	1.2	1	−0.08
0.2	1.1	1	−0.05

Table B.40.: Investigation of various conditions for the upper graphical cut for the PID of positively and negatively charged particles for the 2008 data set with regard to systematic effects.

$u^{\max}_{\text{pos0}}$/GeV	$u^{\max}_{\text{pos1}}/c$	$u^{\max}_{\text{neg0}}$/GeV	$u^{\max}_{\text{neg1}}/c$	MC events	data events	κ
−0.009	1.17	−0.014	1.15	0.55	1	0.31
−0.009	1.195	−0.014	1.175	0.55	1	0.31
−0.009	1.22	−0.014	1.2	0.58	1	0.29
−0.009	1.245	−0.014	1.225	0.58	1	0.29
−0.009	1.27	−0.014	1.25	0.58	1	0.29
−0.003	1.17	−0.008	1.15	0.55	1	0.31
−0.003	1.195	−0.008	1.175	0.58	1	0.29
−0.003	1.22	−0.008	1.2	0.58	1	0.29
−0.003	1.245	−0.008	1.225	0.58	1	0.29
−0.003	1.27	−0.008	1.25	0.63	1	0.26
0.003	1.17	−0.002	1.15	0.64	1	0.25
0.003	1.195	−0.002	1.175	0.64	1	0.25
0.003	1.22	−0.002	1.2	0.64	1	0.25
0.003	1.245	−0.002	1.225	0.72	1	0.19
0.003	1.27	−0.002	1.25	0.76	1	0.17
0.009	1.17	0.004	1.15	0.68	1	0.23
0.009	1.195	0.004	1.175	0.68	1	0.23
0.009	1.22	0.004	1.2	0.72	1	0.19
0.009	1.245	0.004	1.225	0.76	1	0.17
0.009	1.27	0.004	1.25	0.76	1	0.17
0.015	1.17	0.01	1.15	0.68	1	0.23
0.015	1.195	0.01	1.175	0.72	1	0.19
0.015	**1.22**	**0.01**	**1.2**	**0.76**	**1**	**0.17**
0.015	1.245	0.01	1.225	0.76	1	0.17
0.015	1.27	0.01	1.25	0.76	1	0.17
0.021	1.17	0.016	1.15	0.76	1	0.17
0.021	1.195	0.016	1.175	0.76	1	0.17
0.021	1.22	0.016	1.2	0.76	1	0.17
0.021	1.245	0.016	1.225	0.79	1	0.14
0.021	1.27	0.016	1.25	0.79	1	0.14
0.027	1.17	0.022	1.15	0.79	1	0.14
0.027	1.195	0.022	1.175	0.79	1	0.14
0.027	1.22	0.022	1.2	0.79	1	0.14
0.027	1.245	0.022	1.225	0.79	1	0.14
0.027	1.27	0.022	1.25	0.79	2	0.7

Table B.41.: Investigation of various conditions for the upper graphical cut for the PID of positively and negatively charged particles for the 2008 data set with regard to systematic effects, continued.

$u^{\max}_{\text{pos0}}$/GeV	$u^{\max}_{\text{pos1}}/c$	$u^{\max}_{\text{neg0}}$/GeV	$u^{\max}_{\text{neg1}}/c$	MC events	data events	κ
0.033	1.17	0.028	1.15	0.79	1	0.14
0.033	1.195	0.028	1.175	0.79	1	0.14
0.033	1.22	0.028	1.2	0.79	1	0.14
0.033	1.245	0.028	1.225	0.79	2	0.7
0.033	1.27	0.028	1.25	0.79	2	0.7
0.039	1.17	0.034	1.15	0.79	1	0.14
0.039	1.195	0.034	1.175	0.79	1	0.14
0.039	1.22	0.034	1.2	0.79	2	0.7
0.039	1.245	0.034	1.225	0.79	2	0.7
0.039	1.27	0.034	1.25	0.79	2	0.7

Table B.42.: Investigation of various conditions for the upper graphical cut for the PID of positively and negatively charged particles for the 2009 data set with regard to systematic effects.

$u^{\max}_{\text{pos0}}$/GeV	$u^{\max}_{\text{pos1}}/c$	$u^{\max}_{\text{neg0}}$/GeV	$u^{\max}_{\text{neg1}}/c$	MC events	data events	κ
−0.009	1.17	−0.014	1.15	0.96	1	0.016
−0.009	1.195	−0.014	1.175	1	1	−0.0032
−0.009	1.22	−0.014	1.2	1	1	−0.0032
−0.009	1.245	−0.014	1.225	1	1	−0.0032
−0.009	1.27	−0.014	1.25	1	2	0.35
−0.003	1.17	−0.008	1.15	1	1	−0.0032
−0.003	1.195	−0.008	1.175	1	1	−0.0032
−0.003	1.22	−0.008	1.2	1	1	−0.0032
−0.003	1.245	−0.008	1.225	1	2	0.35
−0.003	1.27	−0.008	1.25	1.1	2	0.34

Table B.43.: Investigation of various conditions for the upper graphical cut for the PID of positively and negatively charged particles for the 2009 data set with regard to systematic effects, continued.

$u^{\max}_{\text{pos0}}$/GeV	$u^{\max}_{\text{pos1}}/c$	$u^{\max}_{\text{neg0}}$/GeV	$u^{\max}_{\text{neg1}}/c$	MC events	data events	κ
0.003	1.17	−0.002	1.15	1.1	1	−0.06
0.003	1.195	−0.002	1.175	1.2	1	−0.08
0.003	1.22	−0.002	1.2	1.2	2	0.29
0.003	1.245	−0.002	1.225	1.2	2	0.27
0.003	1.27	−0.002	1.25	1.2	2	0.27
0.009	1.17	0.004	1.15	1.2	1	−0.08
0.009	1.195	0.004	1.175	1.2	2	0.27
0.009	1.22	0.004	1.2	1.2	2	0.27
0.009	1.245	0.004	1.225	1.2	2	0.27
0.009	1.27	0.004	1.25	1.2	2	0.27
0.015	1.17	0.01	1.15	1.2	2	0.27
0.015	1.195	0.01	1.175	1.2	2	0.27
0.015	**1.22**	**0.01**	**1.2**	**1.2**	**2**	**0.27**
0.015	1.245	0.01	1.225	1.2	2	0.27
0.015	1.27	0.01	1.25	1.2	2	0.27
0.021	1.17	0.016	1.15	1.2	2	0.27
0.021	1.195	0.016	1.175	1.3	2	0.25
0.021	1.22	0.016	1.2	1.3	2	0.25
0.021	1.245	0.016	1.225	1.3	2	0.25
0.021	1.27	0.016	1.25	1.3	2	0.25
0.027	1.17	0.022	1.15	1.3	2	0.25
0.027	1.195	0.022	1.175	1.3	2	0.25
0.027	1.22	0.022	1.2	1.3	2	0.25
0.027	1.245	0.022	1.225	1.3	2	0.25
0.027	1.27	0.022	1.25	1.3	2	0.25
0.033	1.17	0.028	1.15	1.3	2	0.25
0.033	1.195	0.028	1.175	1.3	2	0.25
0.033	1.22	0.028	1.2	1.3	2	0.25
0.033	1.245	0.028	1.225	1.3	2	0.25
0.033	1.27	0.028	1.25	1.3	2	0.25
0.039	1.17	0.034	1.15	1.3	2	0.25
0.039	1.195	0.034	1.175	1.3	2	0.25
0.039	1.22	0.034	1.2	1.3	2	0.25
0.039	1.245	0.034	1.225	1.3	2	0.25
0.039	1.27	0.034	1.25	1.3	2	0.25

Table B.44.: Investigation of various conditions for the lower graphical cut for the PID of positively and negatively charged particles for the 2008 data set with regard to systematic effects.

$l^{\min}_{\text{pos0}}$/GeV	$l^{\min}_{\text{pos1}}/c$	$l^{\min}_{\text{neg0}}$/GeV	$l^{\min}_{\text{neg1}}/c$	MC events	data events	κ
−0.062	0.93	−0.068	0.946	2.8	4	0.5
−0.062	0.955	−0.068	0.971	2.2	4	0.8
−0.062	0.98	−0.068	0.996	1.9	3	0.5
−0.062	1.005	−0.068	1.021	1.6	3	0.7
−0.062	1.03	−0.068	1.046	1.2	2	0.5
−0.056	0.93	−0.062	0.946	2.1	4	0.8
−0.056	0.955	−0.062	0.971	1.8	3	0.6
−0.056	0.98	−0.062	0.996	1.5	2	0.3
−0.056	1.005	−0.062	1.021	1.2	2	0.5
−0.056	1.03	−0.062	1.046	0.94	1	0.04
−0.05	0.93	−0.056	0.946	1.8	3	0.6
−0.05	0.955	−0.056	0.971	1.4	2	0.34
−0.05	0.98	−0.056	0.996	1.1	2	0.5
−0.05	1.005	−0.056	1.021	0.94	1	0.04
−0.05	1.03	−0.056	1.046	0.85	1	0.1
−0.044	0.93	−0.05	0.946	1.3	2	0.4
−0.044	0.955	−0.05	0.971	1.1	2	0.5
−0.044	0.98	−0.05	0.996	0.85	1	0.1
−0.044	1.005	−0.05	1.021	0.76	1	0.17
−0.044	1.03	−0.05	1.046	0.71	1	0.2
−0.038	0.93	−0.044	0.946	0.98	1	0.017
−0.038	0.955	−0.044	0.971	0.76	1	0.17
−0.038	**0.98**	**−0.044**	**0.996**	**0.76**	**1**	**0.17**
−0.038	1.005	−0.044	1.021	0.67	1	0.23
−0.038	1.03	−0.044	1.046	0.58	1	0.29
−0.032	0.93	−0.038	0.946	0.76	1	0.17
−0.032	0.955	−0.038	0.971	0.67	1	0.23
−0.032	0.98	−0.038	0.996	0.64	1	0.25
−0.032	1.005	−0.038	1.021	0.54	1	0.32
−0.032	1.03	−0.038	1.046	0.48	1	0.4
−0.026	0.93	−0.032	0.946	0.64	1	0.25
−0.026	0.955	−0.032	0.971	0.6	1	0.28
−0.026	0.98	−0.032	0.996	0.54	1	0.32
−0.026	1.005	−0.032	1.021	0.44	1	0.4
−0.026	1.03	−0.032	1.046	0.37	1	0.4

Table B.45.: Investigation of various conditions for the lower graphical cut for the PID of positively and negatively charged particles for the 2008 data set with regard to systematic effects, continued.

$l^{\min}_{\text{pos0}}$/GeV	$l^{\min}_{\text{pos1}}/c$	$l^{\min}_{\text{neg0}}$/GeV	$l^{\min}_{\text{neg1}}/c$	MC events	data events	κ
−0.02	0.93	−0.026	0.946	0.6	1	0.28
−0.02	0.955	−0.026	0.971	0.51	1	0.34
−0.02	0.98	−0.026	0.996	0.41	1	0.4
−0.02	1.005	−0.026	1.021	0.37	0	−0.32
−0.02	1.03	−0.026	1.046	0.37	0	−0.32
−0.014	0.93	−0.02	0.946	0.51	1	0.34
−0.014	0.955	−0.02	0.971	0.41	0	−0.35
−0.014	0.98	−0.02	0.996	0.33	0	−0.29
−0.014	1.005	−0.02	1.021	0.27	0	−0.23
−0.014	1.03	−0.02	1.046	0.2	0	−0.17

Table B.46.: Investigation of various conditions for the lower graphical cut for the PID of positively and negatively charged particles for the 2009 data set with regard to systematic effects.

$l^{\min}_{\text{pos0}}$/GeV	$l^{\min}_{\text{pos1}}/c$	$l^{\min}_{\text{neg0}}$/GeV	$l^{\min}_{\text{neg1}}/c$	MC events	data events	κ
−0.062	0.93	−0.068	0.946	4.5	10	1.3
−0.062	0.955	−0.068	0.971	4	9	1.2
−0.062	0.98	−0.068	0.996	3.3	7	1
−0.062	1.005	−0.068	1.021	2.5	6	1
−0.062	1.03	−0.068	1.046	1.9	6	1.2
−0.056	0.93	−0.062	0.946	3.7	9	1.3
−0.056	0.955	−0.062	0.971	3.3	6	0.8
−0.056	0.98	−0.062	0.996	2.4	6	1
−0.056	1.005	−0.062	1.021	1.9	5	0.9
−0.056	1.03	−0.062	1.046	1.7	5	1

Table B.47.: Investigation of various conditions for the lower graphical cut for the PID of positively and negatively charged particles for the 2009 data set with regard to systematic effects, continued.

$l^{\min}_{\text{pos0}}$/GeV	$l^{\min}_{\text{pos1}}/c$	$l^{\min}_{\text{neg0}}$/GeV	$l^{\min}_{\text{neg1}}/c$	MC events	data events	κ
−0.05	0.93	−0.056	0.946	2.9	6	0.9
−0.05	0.955	−0.056	0.971	2.4	6	1
−0.05	0.98	−0.056	0.996	1.7	5	1
−0.05	1.005	−0.056	1.021	1.6	4	0.7
−0.05	1.03	−0.056	1.046	1.6	3	0.5
−0.044	0.93	−0.05	0.946	2.2	4	0.6
−0.044	0.955	−0.05	0.971	1.7	4	0.7
−0.044	0.98	−0.05	0.996	1.6	4	0.8
−0.044	1.005	−0.05	1.021	1.3	2	0.25
−0.044	1.03	−0.05	1.046	1.2	2	0.29
−0.038	0.93	−0.044	0.946	1.8	4	0.7
−0.038	0.955	−0.044	0.971	1.5	3	0.5
−0.038	**0.98**	**−0.044**	**0.996**	**1.2**	**2**	**0.27**
−0.038	1.005	−0.044	1.021	1.1	2	0.34
−0.038	1.03	−0.044	1.046	0.92	1	0.032
−0.032	0.93	−0.038	0.946	1.2	2	0.27
−0.032	0.955	−0.038	0.971	1.2	1	−0.08
−0.032	0.98	−0.038	0.996	1.1	1	−0.024
−0.032	1.005	−0.038	1.021	0.86	1	0.05
−0.032	1.03	−0.038	1.046	0.75	1	0.09
−0.026	0.93	−0.032	0.946	1.1	1	−0.06
−0.026	0.955	−0.032	0.971	1	1	0.0
−0.026	0.98	−0.032	0.996	0.81	1	0.07
−0.026	1.005	−0.032	1.021	0.7	1	0.11
−0.026	1.03	−0.032	1.046	0.7	1	0.11
−0.02	0.93	−0.026	0.946	0.95	1	0.02
−0.02	0.955	−0.026	0.971	0.76	1	0.09
−0.02	0.98	−0.026	0.996	0.7	1	0.11
−0.02	1.005	−0.026	1.021	0.7	1	0.11
−0.02	1.03	−0.026	1.046	0.64	0	0.5
−0.014	0.93	−0.02	0.946	0.76	1	0.09
−0.014	0.955	−0.02	0.971	0.7	1	0.11
−0.014	0.98	−0.02	0.996	0.59	1	0.16
−0.014	1.005	−0.02	1.021	0.45	0	0.4
−0.014	1.03	−0.02	1.046	0.28	0	0.24

Bibliography

[A+95] Amsler, C. et al.: *η-decays into three pions.* Physics Letters B, 346(1-2):203–207, March 1995.

[A+07] Adam, H.-H. et al.: *Hadronic $^3He\eta$ production near threshold.* Physical Review C, 75:014004, January 2007.

[A+09] Adolph, C. et al.: *Measurement of the $\eta \to 3\pi^0$ Dalitz plot distribution with the WASA detector at COSY.* Physics Letters B, 677(1-2):24–29, June 2009.

[A+11] Adlarson, P. et al.: *Abashian-Booth-Crowe Effect in Basic Double-Pionic Fusion: A New Resonance?* Physical Review Letters, 106:242302, June 2011.

[A+12a] Adlarson, P. et al.: *Abashian-Booth-Crowe resonance structure in the double pionic fusion to ^4He.* Physical Review C, 86:032201, September 2012.

[A+12b] Adlarson, P. et al.: *Exclusive measurement of the $\eta \to \pi^+\pi^-\gamma$ decay.* Physics Letters B, 707(2):243–249, January 2012.

[A+12c] Adlarson, P. et al.: *$\pi^0\pi^0$ Production in proton-proton collisions at $T_p = 1.4$ GeV.* Physics Letters B, 706(4-5):256–262, January 2012.

[A+13a] Adlarson, P. et al.: *Investigation of the $dd \to {}^3He n\pi^0$ reaction with the FZ Jülich WASA-at-COSY facility.* Physical Review C, 88:014004, July 2013.

[A+13b] Adlarson, P. et al.: *Isospin decomposition of the basic double-pionic fusion in the region of the ABC effect.* Physics Letters B, 721(4-5):229–236, April 2013.

[A+13c] Adlarson, P. et al.: *Measurement of the $pn \to pp\pi^0\pi^-$ reaction in search for the recently observed resonance structure in $d\pi^0\pi^0$ and $d\pi^+\pi^-$ systems.* Physical Review C, 88:055208, November 2013.

[A+13d] Adlarson, P. et al.: *Search for a dark photon in the $\pi^0 \to e^+e^-\gamma$ decay.* Physics Letters B, 726(1-3):187–193, October 2013.

[A+13e] Adlarson, P. et al.: *Search for η-mesic ^{4}He with the WASA-at-COSY detector.* Physical Review C, 87:035204, March 2013.

[A+14a] Adlarson, P. et al.: *Charge symmetry breaking in $dd \to {}^4He\pi^0$ with WASA-at-COSY.* Physics Letters B, 739:44–49, December 2014.

[A+14b] Adlarson, P. et al.: *Cross section ratio and angular distributions of the reaction $p + d \to {}^3He + \eta$ at 48.8 MeV and 59.8 MeV excess energy.* The European Physical Journal A, 50:100, June 2014. Material re-used with kind permission of The European Physical Journal (EPJ). © SIF, Springer-Verlag Berlin Heidelberg, 2014.

[A+14c] Adlarson, P. et al.: *Evidence for a New Resonance from Polarized Neutron-Proton Scattering.* Physical Review Letters, 112:202301, May 2014.

[A+14d] Adlarson, P. et al.: *Measurement of the $\eta \to \pi^+\pi^-\pi^0$ Dalitz plot distribution.* Physical Review C, 90:045207, October 2014.

[A+14e] Adlarson, P. et al.: *Neutron-proton scattering in the context of the $d^*(2380)$ resonance.* Physical Review C, 90:035204, September 2014.

[A+15a] Aad, G. et al.: *Combined Measurement of the Higgs Boson Mass in pp Collisions at $\sqrt{s} = 7$ and 8 TeV with the ATLAS and CMS Experiments.* Physical Review Letters, 114:191803, May 2015.

[A+15b] Aaij, R. et al.: *Observation of $J/\psi p$ Resonances Consistent with Pentaquark States in $\Lambda_b^0 \to J/\psi K^- p$ Decays.* Physical Review Letters, 115:072001, August 2015.

[A+15c] Adlarson, P. et al.: *ABC effect and resonance structure in the double-pionic fusion to ^{3}He.* Physical Review C, 91:015201, January 2015.

[A+15d] Adlarson, P. et al.: *Measurement of the $np \to np\pi^0\pi^0$ reaction in search for the recently observed $d^*(2380)$ resonance.* Physics Letters B, 743:325–332, April 2015.

[A+16a] Adlarson, P. et al.: *Measurement of the $\vec{n}p \to d\pi^0\pi^0$ reaction with polarized beam in the region of the $d^*(2380)$ resonance.* The European Physical Journal A, 52:147, May 2016.

[A+16b] Adlarson, P. et al.: *Measurements of branching ratios for η decays into charged particles.* Physical Review C, 94:065206, December 2016.

[A+16c] Adlarson, P. et al.: *Search for an isospin $I = 3$ dibaryon.* Physics Letters B, 762:455–461, November 2016.

[A+17] Adlarson, P. et al.: *Search for η-mesic ^4He in the $dd \to {}^3He n\pi^0$ and $dd \to {}^3He p\pi^-$ reactions with the WASA-at-COSY facility.* Nuclear Physics A, 959:102–115, March 2017.

[ABC60] Abashian, A., N. E. Booth and K. M. Crowe: *Possible anomaly in meson production in $p + d$ collisions.* Physical Review Letters, 5(6):258–260, September 1960.

[aca01] acam-messelectronic GmbH: *TDC-F1 Functional description - scientific version*, 2001.

[aca06] acam-messelectronic GmbH: *TDC-GPX Datasheet*, 2006.

[Adl12] Adlarson, P.: *Studies of the Decay $\eta \to \pi^+\pi^-\pi^0$ with WASA-at-COSY.* Doctoral thesis, Uppsala Universitet, Sweden, 2012.

[ATL12] ATLAS Collaboration: *Observation of a new particle in the search for the Standard Model Higgs boson with the ATLAS detector at the LHC.* Physics Letters B, 716(1):1–29, September 2012.

[B+67a] Baglin, C. et al.: *Further results in direct search for C violating decay mode $\eta^0 \to \pi^0 e^+ e^-$.* Physics Letters, 24B(12):637–638, June 1967.

[B+67b] Billing, K. D. et al.: *Search for the decay mode $\eta^0 \to \pi^0 e^+ e^-$.* Physics Letters, 25B(6):435–439, October 1967.

[B+68] Bazin, M. J. et al.: *An evaluation of searches for C nonconservation in eta decay.* Physical Review Letters, 20(16):895–898, April 1968.

[B+73] Banaigs, J. et al.: *A study of the reactions $d + p \to \tau + \pi^0$ and $d + p \to \tau + \eta^0$.* Physics Letters, 45B(4):394–398, August 1973.

[B+85] Berthet, P. et al.: *Very backward π^0 and η^0 production by proton projectiles on a deuterium target at intermediate energies.* Nuclear Physics A, 443(4):589–600, October 1985.

[B+88] Berger, J. et al.: *Identification of the $d + p \to {}^3He + \eta$ Reaction Very Near Threshold: Cross Section and Deuteron Tensor Analyzing Power.* Physical Review Letters, 61(8):919–922, August 1988.

[B+00] Betigeri, M. et al.: *Measurement of $pd \to {}^3He\eta$ in the S_{11} resonance.* Physics Letters B, 472(3-4):267–272, January 2000.

[B+02] Bilger, R. et al.: *Measurement of the $pd \to {}^3He\eta$ cross section between 930 and 1100 MeV.* Physical Review C, 65:044608, March 2002.

[B+03] Bräutigam, W. et al.: *Status and perspectives of the cyclotron JULIC as COSY injector.* NUKLEONIKA, 48:123–126, 2003.

[B+04] Bilger, R. et al.: *Measurement of the $pd \to pd\eta$ cross section in complete kinematics.* Physical Review C, 69:014003, January 2004.

[B+09] Bergmann, F. et al.: *The WASA-at-COSY pellet target.* FZ Jülich IKP: Annual Report 2008 (Jül-4282), 2009.

[B+17] Bergmann, F. et al.: *Search for C violation in the decay $\eta \to \pi^0 + e^+ + e^-$ with WASA-at-COSY.* In preparation, 2017.

[BAC61] Booth, N. E., A. Abashian and K. M. Crowe: *Anomaly in meson production in $p + d$ collisions.* Physical Review Letters, 7(1):35–39, July 1961.

[Bar02] Barnes, J.: *Early Greek Philosophy.* Penguin Classics, September 2002.

[BCHW17] Bergmann, F. S., D. Coderre, M. Hodana and P. Wurm: *Measurements of Charged Decays in $pd \to {}^3He\eta$ with WASA-at-COSY.* Private Communication, 2017.

[Ber06] Berger, C.: *Elementarteilchenphysik*. Springer, second edition, 2006.

[Ber09] Bergmann, F. S.: *Studien zum seltenen Zerfall des η-Mesons $\eta \to \pi^0 + e^+ + e^-$ am Experimentaufbau WASA-at-COSY*. Diploma thesis, Westfälische Wilhelms-Universität Münster, Germany, August 2009.

[BFL65] Bernstein, J., G. Feinberg and T. D. Lee: *Possible C, T Noninvariance in the Electromagnetic Interaction*. Physical Review, 139(6B):B1650–B1659, September 1965.

[BP63] Bayes, T. and R. Price: *An Essay towards Solving a Problem in the Doctrine of Chances. By the Late Rev. Mr. Bayes, F. R. S. Communicated by Mr. Price, in a Letter to John Canton, A. M. F. R. S.* Philosophical Transactions, 53:370–418, January 1763.

[BR97] Brun, R. and F. Rademakers: *ROOT - An Object Orientated Data Analysis Framework, Proceedings AIHENP'96 Workshop, Lausanne*. Nuclear Instruments and Methods in Physics Research A, 389(1-2):81–86, April 1997. See also http://root.cern.ch/.

[Bro95] Brodowski, W. B. U.: *Design und Aufbau einer Vetowand für den WASA/PROMICE-Detektor am CELSIUS-Speicherring und erste Messungen der Reaktion $pp \to pp\pi^-\pi^+$*. Diploma thesis, Eberhard Karls Universität Tübingen, Germany, August 1995.

[BT66] Barrett, B. and T. N. Truong: *Analysis of η^0, $X^0 \to \pi^+\pi^-\gamma$ with Possible C Violation*. Physical Review, 147(4):1161–1165, July 1966.

[BT92] Box, G. E. P. and G. C. Tiao: *Bayesian Inference in Statistical Analysis*. Wiley-Interscience, first edition, 1992.

[C+94] Chiavassa, E. et al.: *Measurement of the $pp \to pp\eta$ total cross section between 1.265 and 1.50 GeV*. Physics Letters B, 322(3):270–274, February 1994.

[C+96] Calén, H. et al.: *Detector setup for a storage ring with an internal target*. Nuclear Instruments and Methods in Physics Research A, 379(1):57–75, September 1996.

[C+98] Caso, C. et al.: *Review of Particle Physics.* The European Physical Journal C, 3(1), 1998. 1999 update.

[C+07] Calén, H. et al.: *Upgrade of the Forward Range Hodoscope of the WASA-at-COSY facility.* FZ Jülich IKP: Annual Report 2006 (Jül-4234), 2007.

[Cal08] Calén, H.: *Pellet Beam Dump modification.* WASA-at-COSY Collaboration WIKI - ID: Pelletdump_HC080107, January 2008.
URL: http://wasasrv.ikp.kfa-juelich.de/WasaWiki/.

[Car06] Carman, D. S.: *GlueX: The Search for Gluonic Excitations at Jefferson Laboratory.* AIP Conference Proceedings, 814:173–182, February 2006.

[CER93] CERN Application Software Group Computing and Networks Division: *GEANT - Detector Description and Simulation Tool.* CERN Program Library Long Writeup W5013, 1993.

[Cha35] Chadwick, J.: *The neutron and its properties.* Nobel Lecture, December 1935.

[Che67] Cheng, T. P.: *C-Conserving Decay $\eta \to \pi^0 e^+ e^-$ in a Vector-Meson-Dominant Model.* Physical Review, 162(5):1734–1738, October 1967.

[CMS12] CMS Collaboration: *Observation of a new boson at a mass of 125 GeV with the CMS experiment at the LHC.* Physics Letters B, 716(1):30–61, September 2012.

[Cod12] Coderre, D.: *The Branching Ratio and CP-Violating Asymmetry of $\eta \to \pi^+\pi^- e^+ e^-$.* Doctoral thesis, Ruhr-Universität Bochum, Germany, 2012.

[ÇT05] Çengel, Y. A. and R. H. Turner: *Fundamentals of thermal-fluid sciences.* McGraw-Hill Education, second edition, 2005.

[CW09] Chao, K.-T. and Y. Wang: *Physics at BES-III.* International Journal of Modern Physics A, 24(1 supp), May 2009.

[D+94] Dahmen, M. et al.: *A three layer circular scintillator hodoscope.* Nuclear Instruments and Methods in Physics Research A, 348(1):97–104, August 1994.

[D+02] Dahmen, B. et al.: *Ion Sources at COSY-Jülich.* FZ Jülich IKP: Annual Report 2001 (Jül-3978), 2002.

[Dem13] Demmich, K.: *Energy Calibration for the Forward Detector at WASA-at-COSY with particular Consideration of the Reaction* $p + d \rightarrow {}^3He + \eta'$. Master's thesis, Westfälische Wilhelms-Universität Münster, Germany, March 2013.

[Dem17] Demmich, K.: *In preparation.* Doctoral thesis in preparation, Westfälische Wilhelms-Universität Münster, Germany, 2017.

[DPP97] Diakonov, D., V. Petrov and M. Polyakov: *Exotic anti-decuplet of baryons: prediction from chiral solitons.* Zeitschrift für Physik A, 359(3):305–314, September 1997.

[E+96] Ekström, C. et al.: *Hydrogen pellet targets for circulating particle beams.* Nuclear Instruments and Methods in Physics Research A, 371(3):572–574, March 1996.

[EB64] Englert, F. and R. Brout: *Broken symmetry and the mass of gauge vector mesons.* Physical Review Letters, 13(9):321–323, August 1964.

[EW88] Ericson, T. and W. Weise: *Pions and Nuclei.* International Series of Monographs on Physics 74. Clarendon Press - Oxford, 1988.

[F+07] Fröhlich, I. et al.: *Pluto: A Monte Carlo Simulation Tool for Hadronic Physics.* XI International Workshop on Advanced Computing and Analysis Techniques in Physics Research, April 2007.

[FC98] Feldman, G. J. and R. D. Cousins: *Unified approach to the classical statistical analysis of small signals.* Physical Review D, 57(7):3873–3889, April 1998.

[Fra02] Fransson, K.: *The Trigger System of the CELSIUS/WASA Detector.* Physica Scripta, T99:176–182, 2002.

[Fri17] Fritzsch, C.: *In preparation.* Doctoral thesis in preparation, Westfälische Wilhelms-Universität Münster, Germany, 2017.

[FW95] Fäldt, G. and C. Wilkin: *The reaction* $pd \rightarrow {}^3He\eta$ *near threshold.* Nuclear Physics A, 587(4):769–786, May 1995.

[G+89] Goldman, T. et al.: *"Inevitable" nonstrange dibaryon.* Physical Review C, 39(5):1889–1895, May 1989.

[Gla61] Glashow, S. L.: *Partial-symmetries of weak interactions.* Nuclear Physics, 22(4):579–588, February 1961.

[GM64] Gell-Mann, M.: *A schematic model of baryons and mesons.* Physics Letters, 8(3):214–215, February 1964.

[GW89] Germond, J.-F. and C. Wilkin: *The $dp \to {}^3He\eta$ reaction at threshold.* Journal of Physics G: Nuclear and Particle Physics, 15(4):437–447, April 1989.

[Hü17] Hüsken, N.: *In preparation.* Doctoral thesis in preparation, Westfälische Wilhelms-Universität Münster, Germany, 2017.

[HHM03] Hejny, V., M. Hartmann and A. Mussgiller: *RootSorter: A New Analysis Framework for ANKE.* FZ Jülich IKP: Annual Report 2002 (Jül-4052), 2003.

[Hig64a] Higgs, P. W.: *Broken symmetries and the masses of gauge bosons.* Physical Review Letters, 13(16):508–509, October 1964.

[Hig64b] Higgs, P. W.: *Broken symmetries, massless particles and gauge fields.* Physics Letters, 12(2):132–133, September 1964.

[Hod12] Hodana, M.: *Study of the $\eta \to e^+e^-\gamma$ decay using WASA-at-COSY detector system.* Doctoral thesis, Jagiellonian University in Kraków, Poland, 2012.

[HR+04] Höistad, B., J. Ritman et al.: *Proposal for the Wide Angle Shower Apparatus (WASA) at COSY-Jülich "WASA at COSY".* Technical Report, Forschungszentrum Jülich, October 2004.

[J+75] Jane, M. R. et al.: *A new upper limit for the branching ratio for the decay $\eta \to \pi^0 e^+ e^-$.* Physics Letters, 59B(1):99–102, October 1975.

[Jac04] Jacewicz, M.: *Measurement of the Reaction $pp \to pp\pi^+\pi^-\pi^0$ with CELSIUS/WASA at 1.36 GeV.* Doctoral thesis, Uppsala Universitet, Sweden, 2004.

[Jan10] Janusz, M.: *Study of the η meson decay into $\pi^+\pi^-e^+e^-$ using WASA-at-COSY detector system.* Doctoral thesis, Jagiellonian University in Kraków, Poland, 2010.

[Jay68] Jaynes, E. T.: *Prior Probabilities.* IEEE Transactions on Systems Science and Cybernetics, SSC-4(3):227–241, September 1968.

[Jef46] Jeffreys, H.: *An invariant form for the prior probability in estimation problems.* Proceedings of the Royal Society of London Series A, 186(1007):453–461, September 1946.

[Jef98] Jeffreys, H.: *The Theory of Probability.* Oxford University Press, third edition, 1998.

[JS02] Jarlskog, C. and E. Shabalin: *On Search for CP, T, CPT and C Violation in Flavour-Changing and Flavour-Conserving Interactions.* Physica Scripta, T99:23–33, 2002.

[K+86] Kerboul, C. et al.: *Deuteron tensor analyzing power for the collinear $\vec{d}p \to {}^3He\pi^0$ reaction at intermediate energies.* Physics Letters B, 181(1-2):28–32, November 1986.

[K+06] Kleines, H. et al.: *The New DAQ System for WASA at COSY.* IEEE Transactions on Nuclear Science, 53(3):893–897, June 2006.

[K+08] Kleines, H. et al.: *Performance Issues of the New DAQ System for WASA at COSY.* IEEE Transactions on Nuclear Science, 55(1):261–264, February 2008.

[K+13] Kelkar, N. G. et al.: *Interaction of eta mesons with nuclei.* Reports on Progress in Physics, 76:066301, May 2013.

[Kho09] Khoukaz, A.: *Gas system of the ANKE cluster jet target.* Private Communication, 2009.

[KKJ03] Khemchandani, K. P., N. G. Kelkar and B. K. Jain: *Three-body mechanism of η production.* Physical Review C, 68:064610, December 2003.

[KKJ07] Khemchandani, K. P., N. G. Kelkar and B. K. Jain: *Comment on "Hadronic ${}^3He\eta$ production near threshold".* Physical Review C, 76:069801, December 2007.

[KKJ12] Khemchandani, K. P., N. G. Kelkar and B. K. Jain. Private Communication, 2012.

[KM14] Khoukaz, A. and P. Moskal: *Proposal 220 and Proposal 186.3.* In *Minutes of the 42nd Meeting of the COSY Programme Advisory Committee (PAC).* IKP, Forschungszentrum Jülich, February 2014.

[KN91] Kilian, K. and H. Nann: *Meson production and velocity matching.* AIP Conference Proceedings: Particle production near threshold, 221:185–191, April 1991.

[Koc04] Koch, I.: *Measurements of $2\pi^0$ and $3\pi^0$ Production in Proton-Proton Collisions at a Center of Mass Energy of 2.465 GeV.* Doctoral thesis, Uppsala Universitet, Sweden, 2004.

[Kup95] Kupść, A.: *Note on kinematical fit.* WASA-at-COSY Collaboration internal note, November 1995.

[Kup17] Kupść, A. Private Communication, 2017.

[KW11] Kupść, A. and A. Wirzba: *Tests of the fundamental symmetries in η meson decays.* Journal of Physics: Conference Series, 335:012017, December 2011.

[Lal10] Lalwani, K.: *Measurement of the branching ratio of a rare decay $\eta \to \pi^0\gamma\gamma$ with WASA-at-COSY.* Doctoral thesis, Indian Institute of Technology Bombay, India, 2010.

[Lee65] Lee, T. D.: *Possible C-Noninvariant Effects in the 3π Decay Modes of η^0 and ω^0.* Physical Review, 139(5B):B1415–B1420, September 1965.

[Ler14] Lersch, D.: *Investigation of Dipion Final State Interactions in $pp \to pp\eta\,[\eta \to \pi^+\pi^-\gamma]$ with the WASA-at-COSY Facility.* Doctoral thesis, Bergische Universität Wuppertal, Germany, October 2014.

[LL88] Laget, J. M. and J. F. Lecolley: *Direct Evidence for Three-Body Mechanisms in the Reaction $p + \vec{d} \to {}^3He + \eta$.* Physical Review Letters, 61(18):2069–2072, October 1988.

[M+96] Mayer, B. et al.: *Reactions $pd \to {}^3He\eta$ and $pd \to {}^3He\pi^+\pi^-$ near the η threshold.* Physical Review C, 53(5):2068–2074, May 1996.

[M+07] Mersmann, T. et al.: *Precision Study of the η ^{3}He System Using the $dp \to {}^3He\eta$ Reaction.* Physical Review Letters, 98:242301, June 2007.

[Mai97] Maier, R.: *Cooler synchrotron COSY - performance and perspectives.* Nuclear Instruments and Methods in Physics Research A, 390(1-2):1–8, May 1997.

[Mer07] Mersmann, T.: *Untersuchung der Wechselwirkung zwischen η-Mesonen und ^{3}He-Kernen am Experimentaufbau ANKE.* Doctoral thesis, Westfälische Wilhelms-Universität Münster, Germany, 2007.

[Nar00a] Narsky, I.: *Estimation of upper limits using a Poisson statistic.* Nuclear Instruments and Methods in Physics Research A, 450(2-3):444–455, August 2000.

[Nar00b] Narsky, I.: *Expected Coverage of Bayesian Confidence Intervals for the Mean of a Poisson Statistic in Measurements with Background.* arXiv:hep-ex/0005019v1, May 2000. SMUHEP-00-03.

[Ney37] Neyman, J.: *Outline of a Theory of Statistical Estimation Based on the Classical Theory of Probability.* Philosophical Transactions of the Royal Society of London Series A, 236(767):333–380, August 1937.

[Nor04] Norman, G.: *Pellet Target Documentation.* Internal document, April 2004.

[NP93] Ng, J. N. and D. J. Peters: *Study of $\eta \to \pi^0\gamma\gamma$ decay using the quark-box diagram.* Physical Review D, 47(11):4939–4948, June 1993.

[P+00] Prasuhn, D. et al.: *Electron and stochastic cooling at COSY.* Nuclear Instruments and Methods in Physics Research A, 441(1-2):167–174, February 2000.

[Pé09] Pérez del Río, E.: *Upgrade of the Forward Veto Hodoscopes at WASA.* Master's thesis, Eberhard Karls Universität Tübingen, Germany, 2009.

[Pé14a] Pérez del Río, E. Private Communication, 2014.

[Pé14b] Pérez del Río, E.: *ABC Effect and d^* Resonance in Double-Pionic Fusion to ^{3}He.* Doctoral thesis, Eberhard Karls Universität Tübingen, Germany, 2014.

[P+16] Patrignani, C. et al.: *Review of Particle Physics.* Chinese Physics C, 40:100001, 2016.

[PAN09] PANDA Collaboration: *Physics Performance Report for: $\overline{P}$ANDA Strong Interaction Studies with Antiprotons.* arXiv:hep-ex/0903.3905, March 2009.

[Pas10] Passfeld, A.: *Bestimmung von totalen und differentiellen Wirkungsquerschnitten der Reaktion $p + d \rightarrow {}^3He + \eta$ bei 49 und 60 MeV Überschussenergie am Experimentaufbau WASA-at-COSY.* Diploma thesis, Westfälische Wilhelms-Universität Münster, Germany, 2010.

[Pau06] Pauly, C.: *Light Meson Production in pp Reactions at CELSIUS/WASA above the η Threshold.* Doctoral thesis, Universität Hamburg, Germany, 2006.

[PC65] Price, L. R. and F. S. Crawford, Jr.: *Search for $\eta^0 \rightarrow e^+ + e^- + \pi^0$.* Physical Review Letters, 15(3):123–125, July 1965.

[Pet10] Petri, T.: *Anomalous decays of pseudoscalar mesons.* Diploma thesis, Rheinische Friedrich-Wilhelms-Universität Bonn, Germany, July 2010.

[Pri10] Pricking, A.: *Double Pionic Fusion to ${}^4He$ Kinematically Complete Measurements over the Energy Region of the ABC Effect.* Doctoral thesis, Eberhard Karls Universität Tübingen, Germany, 2010.

[R+09] Rausmann, T. et al.: *Precision study of the $dp \rightarrow {}^3He\eta$ reaction for excess energies between 20 and 60 MeV.* Physical Review C, 80:017001, July 2009.

[Rau09] Rausmann, T.: *Untersuchung der Reaktion $d + p \rightarrow {}^3He + \eta$ im Bereich zwischen 20 und 60 MeV Überschussenergie am Experiment ANKE.* Doctoral thesis, Westfälische Wilhelms-Universität Münster, Germany, December 2009.

[Red10] Redmer, C. F.: *In search of the Box-Anomaly with the WASA facility at COSY.* Doctoral thesis, Bergische Universität Wuppertal, Germany, March 2010.

[RK65] Rittenberg, A. and G. R. Kalbfleisch: *Search for C-invariance violation in $\eta(958\,MeV)$ and $\eta(549\,MeV)$ decays.* Physical Review Letters, 15(13):556–560, September 1965.

[Rub99] Ruber, R.: *An ultra-thin-walled superconducting solenoid for meson-decay physics.* Doctoral thesis, Uppsala Universitet, Sweden, 1999.

[Rut11] Rutherford, E.: *The Scattering of α and β Particles by Matter and the Structure of the Atom.* Philisophical Magazine Series 6, 21:669–688, May 1911.

[S+07] Smyrski, J. et al.: *Measurement of the $dp \to {}^3He\eta$ reaction near threshold.* Physics Letters B, 649(4):258–262, June 2007.

[S+08] Stassen, R. et al.: *The HESR rf-system and tests in COSY.* Proceedings of EPAC08, Genoa, Italy, A04 Circular Accelerators:361–363, 2008.

[Sak64] Sakurai, J. J.: *Invariance Principles and Elementary Particles.* Princeton University Press, Princeton, New Jersey, 1964.

[Sit15] Sitterberg, K.: *The Fusion Reaction $pd \to {}^3He\pi^0$ examined with the WASA-at-COSY Experiment.* Master's thesis, Westfälische Wilhelms-Universität Münster, Germany, November 2015.

[SJ01] Santra, A. B. and B. K. Jain: *η production in proton-deuteron collisions.* Physical Review C, 64:025201, July 2001.

[Smi68] Smith, J.: *C-Conserving Decay Modes $\eta \to \pi^0 e^+ e^-$ and $\eta \to \pi^0 \mu^+ \mu^-$.* Physical Review, 166(5):1629–1632, February 1968.

[Ste17] Stepaniak, J. Private Communication, 2017.

[SW64] Salam, A. and J. C. Ward: *Electromagnetic and weak interactions.* Physics Letters, 13(2):168–171, November 1964.

[The16] The GlueX Collaboration: *First Results from The GlueX Experiment.* AIP Conference Proceedings, 1735(1):020001, May 2016.

[Tho01] Thomson, J. J.: *On bodies smaller than atoms.* The Popular Science Monthly, 59:323–335, August 1901.

[Tro95] Trostell, B.: *Vacuum injection of hydrogen micro-sphere beams.* Nuclear Instruments and Methods in Physics Research A, 362(1):41–52, August 1995.

[Vla08] Vlasov, P. N.: *Analysis of the $\eta \to 3\pi^0$ decay in the pp interaction.* Doctoral thesis, Ruhr-Universität Bochum, Germany, September 2008.

[W+08a] Winnemöller, A. et al.: *The WASA-at-COSY pellet target.* FZ Jülich IKP: Annual Report 2007 (Jül-4262), 2008.

[W+08b] Wolke, M. et al.: *First Experiments with the WASA Detector.* FZ Jülich IKP: Annual Report 2007 (Jül-4262), 2008.

[WAS17] WASA-at-COSY Collaboration: *WASA-at-COSY Collaboration WIKI*, April 2017.
URL: http://wasasrv.ikp.kfa-juelich.de/WasaWiki/index.php.

[Wei67] Weinberg, S.: *A model of leptons.* Physical Review Letters, 19(21):1264–1266, November 1967.

[Win11] Winnemöller, A.: *Analyse des verbotenen η-Meson Zerfalls $\eta \to \pi^0 + e^+ + e^-$ am Experimentaufbau WASA-at-COSY.* Doctoral thesis, Westfälische Wilhelms-Universität Münster, Germany, January 2011.

[Wir17] Wirzba, A. Private Communication, 2017.

[Wol07] Wolke, M.: *Beam-time request 136.5.* In *Minutes of the 33rd Meeting of the COSY Programme Advisory Committee (PAC).* IKP, Forschungszentrum Jülich, May 2007.

[Wur13] Wurm, P.: *Measurement of the $\eta \to e^+e^-e^+e^-$ double Dalitz decay and the search for new physics beyond the Standard Model in $\eta \to e^+e^-$ with WASA-at-COSY.* Doctoral thesis, Universität zu Köln, Germany, 2013.

[Yua15] Yuan, C.-Z.: *Study of the XYZ states at the BESIII.* Frontiers of Physics, 10(6):101401, December 2015.

[Yur11] Yurev, L. S.: *Study of the decay $\eta \to e^+e^-e^+e^-$ with WASA-at-COSY.* Doctoral thesis, Universität zu Köln, Germany, 2011.

[Z+94] Zwoll, K. et al.: *Flexible Data Acquisition System for Experiments at COSY*. IEEE Transactions on Nuclear Science, 41(1):37–44, February 1994.

[Zhe09] Zheng, C.: *Matching Trigger Efficiency of Forward Detector of WASA-at-COSY*. FZ Jülich IKP: Annual Report 2008 (Jül-4282), 2009.

[Zhu07] Zhu, Y.: *Upper limit for Poisson variable incorporating systematic uncertainties by Bayesian approach*. Nuclear Instruments and Methods in Physics Research A, 578(1):322–328, July 2007.

[Zwe64] Zweig, G.: *An SU_3 model for strong interaction symmetry and its breaking*. CERN Report No. CERN-TH-401, January 1964.
URL: http://cdsweb.cern.ch/record/352337.

List of Figures

List of Tables

Acknowledgments - Danksagung

„Zum Abschluss möchte ich mich bei allen bedanken, die mich bei meiner ~~Diplom~~arbeit ***Doktorarbeit*** unterstützt haben.“[Ber09]

Zuallererst möchte ich Prof. Dr. Alfons Khoukaz danken für die Betreuung und fortlaufende Unterstützung während meiner gesamten Promotionszeit sowie schon zuvor während meiner Diplomarbeitszeit. Einen besseren Doktorvater kann sich, glaube ich, niemand wünschen.

Weiterhin möchte ich Herrn Prof. Dr. Johannes P. Wessels für die Übernahme des Korreferats und Herrn Priv.-Doz. Dr. Jochen Heitger für den Einsatz als Drittprüfer danken.

Furthermore, I would like to thank the whole WASA collaboration. I would like to mention especially Dr. Magnus Wolke, Dr. Volker Hejny, who is always willing to help with programming and other problems, Dr. Andrzej Kupść for the fruitful discussions and support with plenty physics and other questions, and Dr. Andreas Wirzba for the theoretical support. A big thank you to Farha, Ira, Maria, and everybody else who helped me enjoy my time in Jülich. And of course, a respectful thank you to the WASA pellet target. Without you and your friend the COSY Hilton telephone, I would have slept way too much - and nobody wants to do that.

Ein großer Dank geht natürlich auch an die COSY-Crew sowie Guido D’Orsaneo und Dirk Spölgen, die mich immer wieder bereitwillig bei Reparaturen des WASA Pellettargets unterstützt haben.

Selbstverständlich gilt mein Dank ebenfalls allen aktuellen und ehemaligen Mitgliedern der Arbeitsgruppe, die zur großartigen und freundschaftlichen Arbeitsatmosphäre beigetragen haben. Erwähnen möchte ich die aktuellen Mitglieder Marcel Rump, Benny Hetz, Anky Hergemöller, B.A. Silke Grieser, Christopher the Machine Fritzsch, Daniel Bonaventura, Daniel-1 Schröer, Lukas Mordrog Leßmann, Johannes Kellers und Robin Balske. Ein besonderer Dank gilt Kay-le Katarn Demmich und Niels Hüsken, die bereitwillig die hier vorliegende epische Geschichte Korrektur gelesen haben und mit denen ich immer wieder hilfreiche Diskussionen

über und um die Mythen der WASA Analyse führen konnte. Ein großer Dank geht an Dr. Alexander Winnemöller, der mir die WASA Analyse nahegebracht hat und mich zusammen mit Dr. Tobias Rausmann (dieses Mal hoffentlich korrekt geschrieben) in die Geheimnisse des Pellettargets eingeführt hat, Dr. Timo Mersmann, der auch nach seiner aktiven Zeit in der Arbeitsgruppe immer mal wieder vorbeischaut, um über dieses und jenes zu diskutieren, Dr. Alexander Täschner, der bei Computer- und Programmierfragen immer ein offenes Ohr für mich hatte, Dr. Michael Papenbursch (auch dir Danke für die illustren Warhammer Runden), die bisher noch nicht genannten Pellettarget-Buddies Dr. Paul Gos*love*ski, Annika Passfeld (danke für den grandiosen P. . .splot), Karsti Sitterberg und Christina Tienchen Husmann sowie Dr. Malte Mielke und Dr. Esco Köhler. Von den mittlerweile zahlreichen ehemaligen Bachelorstudenten unserer Arbeitsgruppe, die ich in meiner Danksagung nicht außen vorlassen will, möchte ich gesondert die von mir betreuten Bachelor Florian Schepers und Patrice Hüsemann nennen, mit denen ich viele weitere Geheimnisse der Pelletdüsen entdecken durfte, und natürlich Michael Evilmikey Evelt, dessen *Faszination* für Age of S. . .mar ich bis heute nicht so ganz verstehe.

Ein herzliches Dankeschön geht zudem an „die Geseker“, die während meines Studiums und meiner Promotion über eine so lange Zeit stets Geduld mit mir hatten, die SIGler für die entspannenden Runden und Diskussionen am PC nach Feierabend sowie an meine Show Ladies ♡. Das Training, die Turniere und generell die schöne Zeit mit euch haben mir immer wieder neue Kraft für meine Promotion gegeben.

Ein ganz besonders herzlicher Dank geht an meine Familie für die Unterstützung während meines gesamten Studiums und darüber hinaus. - Auch an dich, Minosch. Moreover, vielen Dank für die Korrekturen. Very good. Very, very good corrections.

Abschließen möchte ich mit den Worten von Peter Q. Taggart, dem Commander der NSEA-Protector:

„Niemals aufgeben, niemals kapitulieren!“

(Martin Keßler, Synchronsprecher für Tim Allen alias Jason Nesmith alias Commander Peter Quincy Taggart in Galaxy Quest, 1999)